AN INTEGRATIVE APPROACH FOR UNDERSTANDING THE ADVERSE OUTCOME PATHWAYS IN ALGAE

by

STEFAN SCHADE

A thesis submitted to
the University of Birmingham
for the degree of
DOCTOR OF PHILOSOPHY

School of Biosciences

College of Life and Environmental Sciences

The University of Birmingham

September 2019

UNIVERSITY OF
BIRMINGHAM

University of Birmingham Research Archive

e-theses repository

This unpublished thesis/dissertation is copyright of the author and/or third parties. The intellectual property rights of the author or third parties in respect of this work are as defined by The Copyright Designs and Patents Act 1988 or as modified by any successor legislation.

Any use made of information contained in this thesis/dissertation must be in accordance with that legislation and must be properly acknowledged. Further distribution or reproduction in any format is prohibited without the permission of the copyright holder.

Abstract

Conventional environmental hazard assessment practices focus on determining intrinsic danger of chemicals via induction of crude apical endpoints. A novel chemical safety assessment paradigm is pioneering the understanding of molecular mechanisms fundamentally driving such endpoints to increase quality of future chemical safety assessment. To achieve stakeholder acceptance of new technologies such as *omics* to drive discovery of toxicological mechanisms, there is a need for evaluation of experimental approaches tailored towards this end, using environmentally relevant models such as microalgae. The research goal of this thesis was to propose the development, characterization and application of an experimental design and a suitable physical algal exposure system tailored towards hypothesis of acute chemical mode of action (MoA) and key events in adverse outcome pathways (AOPs) driven by time-resolved multi-*omics* profiling of algae. An experimental design aligned with the AOP framework was delineated, and a customized algal vial exposure system developed and rigorously validated. The developed system generated highly similar metabolomics profiles in a repeat-exposure study, and existing differences could be mitigated via an internal normalization strategy. Markers driving the adverse phenotype after exposure could be reproducibly identified from the study. Applying the experimental design via the developed exposure system, large-scale and highly time-resolved multi-*omics* (metabolomics, lipidomics and transcriptomics) exposure experiments of *Chlamydomonas reinhardtii* to the baseline-toxicant chlorobenzene and the herbicide norflurazon were conducted. Acute chemical MoA and draft AOPs were successfully constructed, using generated and retrieved literature data. Results emphasized discrete (primarily chloroplast-based oxidative stress for norflurazon, general metabolic inhibition and membrane-disruptive effects for chlorobenzene) however to a degree shared molecular stress signatures (inhibition of cellular motility, activation of autophagy and apoptosis). Finally, the utility and limitations of the presented discovery approach for application in hazard assessment were discussed, suggesting high utility to future prioritization of testing and to chemical read-across of hazard using *omics*-signatures, pending further validation of the method, including application to new model toxicants, putative biomarker identification from the *omics* datasets, and targeted manual validation of the latter.

Acknowledgements

I hereby thank my supervisors, Prof. Dr. M. Viant, Prof. Dr. J. Colbourne, Dr. E. Butler and Dr. G. Hodges for their invaluable academic help and support throughout the birth, childhood, adolescence, and final leaving-the-house of this thesis.

I thank Dr. A. Perotti, Dr. K. Gkrintzalis and Dr. M. Jones the many inside jokes, something of a social life, and helping to build DIY lab equipment.

Lastly, I want to thank my family and my significant other, Elena, for unwavering moral support, making me laugh when I wanted none of it, asking the right questions, and being there when it mattered. Buy the ticket, take the ride…

Table of contents

Chapter 1 – Introduction
1. Introduction to hazard assessment 2
1.2. Chemical risk and hazard assessment and their legislative background 2
1.2. Conventional approaches to inform environmental hazard assessment 4
2. Shortcomings of conventional hazard assessment strategy 6
2.1. High demands for financial expenditure, test subjects and time 6
2.2. Limited reliability of data 7
2.3. Limited generalizability of data 8
3. Conceptual and technological advances to drive a new chemical safety assessment paradigm 9
3.1. Integrated approaches to hazard assessment and the adverse outcome pathway concept 10
3.2. Technological advances to support a paradigm shift 14
4. Requirements and needs towards regulatory acceptance of omics 15
5. Model species selection to showcase utility of omics to environmental hazard assessment 17
6. Omics platforms to enable hypothesis of chemical MoA and molecular markers predictive of adverse outcome 20
6.1. Metabolomics and lipidomics 21
6.2. Next-generation-sequencing transcriptomics 23
6.3. Integration of multiple omics data 25
7. The research goal and scientific objectives of this project 29

Chapter 2 – Experimental design, methods and materials
1. General methods and materials 32
1.1. Algae culturing 32
1.2. Direct-infusion mass-spectrometry (DIMS) metabolomics and lipidomics 34
1.3. Illumina transcriptomics 37
2. Outlining the experimental design for omics-driven chemical MoA and putative molecular key event hypotheses 40
2.1. Overall strategy for showcasing omics-driven MoA and key event hypothesis 40
2.2. Aligning experimental design with assumptions of the AOP concept 44
2.3. Summary: Requirements for an algal exposure system to suit and support parameters of the outlined experimental design 54

Chapter 3 – Improved Algal Toxicity Test System for Robust Omics-Driven Mode-of-Action Discovery in *Chlamydomonas reinhardtii*
1. Introduction 57
2. Materials and Methods 61
2.1. Algae Culturing and inoculation of test cultures 61
2.2. Initial optimization of *C. reinhardtii* homogenization yields 61
2.3. Determination of required biomass for omics platforms 62
2.4. Development of a customized growth medium CGM 64
2.5. Optimization of the sample purity for mass spectrometric analyses 65
2.6. Comparison of synchronized and non-synchronized cell cultures 65
2.7. Vial Exposures for concentration-response experiments 66
2.8. Measurement of chlorobenzene exposure concentrations over time 67
2.9. Variability characterization of tailored closed-vial exposure system 68
3. Results and Discussion 70
3.1. Designating margins of minimally required biomass for omics platforms 70
3.2. Development of a customized growth medium for closed-vial exposures ...74
3.3. Cell cycle synchronization enables phenotypic anchoring in a single-generation test 78
3.4. Synchronized vs. non-synchronized cultures for molecular studies 83
3.5. Application of tailored exposure system to volatile and reference toxicants .87
3.6. Repeatability of *C. reinhardtii* metabolic phenotypes in tailored exposure system 91
4. Conclusion 98

Chapter 4 – A time-resolved multi-omics approach confirms and extends existing knowledge on the chemical MoA of norflurazon
1. Introduction 100
2. Materials and Methods 102
2.1. Algae culturing 102
2.2. Norflurazon range-finding experiment 102
2.3. Multi-omics time-course exposure experiment 102
2.4. Multi-omics sampling procedure and instrumental analysis 103
2.5. Metabolomics and lipidomics statistical data analyses 103
2.6. Transcriptomics statistical data analyses 104
2.7. Quantitation of norflurazon medium concentrations 105
3. Results and Discussion 107
3.1. Determination of optimal NF exposure concentrations 107
3.2. Quality assurance of omics data acquired from time-course exposure experiment 108
3.3. Confirmation of exposure concentration and adverse outcome induction .112
3.4. Global effects of norflurazon on *C. reinhardtii* biology 113
3.5. Time-course analysis of norflurazon toxicity on algae 120
3.6. Time-course multi-omics exposure data support existing understanding of acute NF chemical MoA and aid construction of a hypothetical AOP in *C. reinhardtii* 143
4. Conclusion 148

Chapter 5 - Time-resolved multi-omics profiling of the *Chlamydomonas reinhardtii* stress response to chlorobenzene drives chemical MoA hypothesis
1. Introduction 150
2. Materials and Methods 151
2.1. Algae culturing 151
2.2. Multi-omics time-course exposure experiment 151
2.3. Multi-omics sampling procedure and instrumental analysis 151
2.4. Metabolomics, lipidomics and transcriptomics processing and data analysis 152
3. Results and Discussion 153
3.1. Quality assurance of omics data acquired from time-course exposure experiment 153
3.2. Confirmation of exposure concentration and adverse outcome induction 156
3.3. Global effects of chlorobenzene on *C. reinhardtii* biology 158
3.4. Time-course analysis of chlorobenzene toxicity on algae 163
3.5. Hypothesizing an acute chemical MoA for chlorobenzene toxicity and constructing draft AOP for baseline toxicity 174
4. Conclusion 177

Chapter 6 – Overall conclusions and outlook
1. Introduction 180
2. Evaluation of scientific objectives 1. and 2. 181
3. Evaluation of scientific objective 3. 186
4. Evaluation of the overall research goal 188
5. Outlook 191

Appendix
A.1. Supplementary Figures 193
A.2. Supplementary Tables 239

References 269

List of Figures

Figure 1. Simplified schematic of the chemical safety assessment process under REACH legislation, spanning initial data collection, hazard assessment (hazard identification and concentration-response characterization), exposure estimation and risk assessment to guide regulatory decision-making. Figure after ref. [5]..... 3

Figure 2. Schematic of human hazard and risk assessment within the new chemical safety assessment paradigm. Similar considerations were envisioned for safety assessment of chemicals in an environmental context. Figure from ref. [51]. 11

Figure 3. Structure of an adverse outcome pathway. Interaction of a chemical substance (toxicant) with an organism causes a molecular initiating event, which induces a chain of discrete and causally linked key events. The key events ultimately lead to induction of an adverse outcome relevant to risk assessment. Figure from ref. [108], modified. 12

Figure 4. Chlamydomonas reinhardtii liquid culture at 200-fold magnification. Visible are vegetative cells from various position in the cell cycle, including ciliated cells in cell cycle stages of biomass accumulation and photosynthetic activity (Top, Middle), or unciliated daughter cells (zoospores) post-division still contained in the membrane of the mother cell (Bottom)..... 18

Figure 5. Domains functional units of biomolecules involved in biological processes and pathways, and the concordant omics technologies that are intended to interrogate patterns of the specific types of biomolecules. Figure from ref. [419]. 20

Figure 6. Overview of the different main approaches to targeted mass spectrometry and untargeted metabolomics and lipidomics analyses. Juxtaposed are their specific technologies, strengths and pitfalls in application. Figure from ref. [569]. 22

Figure 7. Inter-relation of the different domains of molecular functional units, and by extension omics layers, in the description of adverse molecular and apical phenotypes. The adverse phenotypes are here depicted for various human health aetiologies, but the schematic can be used synonymously for apical endpoints of an organism relevant to environmental hazard assessment, such as growth inhibition in algae. Figure from ref. [309]. 26

Figure 8. Individual steps for centrifugal concentration, cell density measurement, dilution, seeding of *C. reinhardtii* cell cultures into T101/V4 vials, and incubation of vials on a lined tray. Biological replicates in vials were generated from independent flask cultures. 33

Figure 9. Abstract overview of the experimental design chosen for the project, including remodeling of the algal growth inhibition test to a single-generation test on synchronized cell populations, description of the time-series sampling profile, factoring or replication and exposure concentrations, selection of chemical MoA and model toxicants, selection and quantification of AO induction, and requirements for generation of biological material for downstream omics analysis. 42

Figure 10. Abstract representation of the conventional and remodeled algal exposure schemes. (A) The conventional 72h test for algal growth inhibition conducted in continuous light conditions [12,360] generates samples with molecular signatures averaged over population and algal generations. The (B) single-generation test with light:dark cycling (effecting synchronized cell cultures) generates samples with precise molecular signatures specific to biological processes in cell cycle, and molecular effects are clearly linked to induction of a single window of AO induction (i.e. cell division events). 49

Figure 11. Schematic representation of the sampling profile and frequency aligned to the cell cycle of C. reinhardtii up to cell division (window of AO occurrence, experimentally determined in Chapter 3). Experiment comprised culture seeding and exposure to chemical-spiked growth medium and linear sampling over 9 time-points. The last 3 time-points were slightly more frequent to capture specific molecular effects related to nuclear and cellular division (cytokinesis), which are functionally related to AO induction. These occur within narrow time-windows, and normally-distributed over an algal cell populations within these windows. 52

Figure 12. Comparison of efficiency of homogenization methods. (A) Downstream metabolite and lipid extraction efficiency by proxy of optical absorption (arbitrary units a.u.) at 450nm of suspended plant pigments in 71% methanol:water solution (5.25 x 10^6 cells), comparing 1.4mm ceramic beads, 0.5mm glass beads or 2.8mm steel beads. (B) Extraction efficiency of 0.5mm glass beads, QIAshredder homogenization and no homogenization, measured by total RNA extraction yields from 1 x 10^7 cells in 20 µL eluate using Nanodrop-8000. 70

Figure 13. Scatterplot (A) of extracted *C. reinhardtii* cells vs. extractable total RNA as measured by Nanodrop 8000 (n = 1-4 per group). A linear regression line along 95%-confidence interval was plotted for all sample groups. The RNA integrity number equivalent (RINe) plotted as boxplot (B) over all groups, with indication of the minimal RINe = 6.5 threshold required for transcriptome sequencing (https://www.bgi.com/us/sequencing-services/rna-sequencing-solutions/transcriptome-sequencing/; Accessed 07/05/18). 73

Figure 14. pH drift of *C. reinhardtii* cell suspensions in CGM containing 92.5%-reduced phosphate supplementation (open flask culturing), over varying MOPS-buffer supplementation (n=2). Only 20mM MOPS supplementation showed a pH drift of acceptable magnitude as per OECD guideline below 0.5 over the targeted test duration of 24h, which was hereafter used for all further experiments. 75

Figure 15. Growth rates (n=3) of *C. reinhardtii* in (A, B) completely-filled vials, or (C, D) vials with variable air headspace (HS). CGM was further supplemented with (A, C) 250 mg/L or (B, D) 500 mg/L NaHCO3 supplementation. In completely filled vials, neither level of inorganic carbon addition was sufficient to raise population growth rates above GR > 0.92/day at higher cell densities, the OECD-recommended validity criterion for healthy growth. When air headspace (HS) in the vial was applied, growth rates increased substantially. For an inoculation density of 7.5 x 10^5 cells/mL along 5% HS and 500 mg/L NaHCO3 supplementation (D), growth rates exceeded the desired threshold. 76

Figure 16. Growth rates (A) and pH drift (B) over 24 h growth of synchronized *C. reinhardtii* cultures in capped vials with varying size of air headspace, inoculated at 7.5 x 10^5 cells/mL in CGM. 2.5-fold growth per day (GR = 0.92/d) as validity criterion and acceptable pH drift are marked as dotted lines. 77

Figure 17. Cell density (Top) and number of distinct peaks in PI fluorescence intensity (Bottom; ~ amount of genomic material found in each zoosporangium or zoospore) indicating genomic division events during multiple-fission cycles for non-synchronized (A) or synchronized (B) cultures. For synchronized cultures, light:dark transition occurred at 12 h. 79

Figure 18. Abstract representation of the time-windows of potential molecular key events and adverse outcome within algal cell cycle, as induced by exposure to toxicants. The schematic is overlayed growth curves for (A) non-synchronised and (B) synchronized cell cultures. 81

Figure 19. Metabolic fingerprints for pellet wash optimization. A first study comprising synchronized control cultures seeded in vials was performed to assess the influence of the number of washing steps on the metabolomics data quality. Cell cultures were concentrated as above from a single stock, seeded at 7.5 x 10^5 cells/mL in 30 capped vials and incubated for 3 h. Next, 5.25 x 10^6 cells were sampled from each test vial and a varying number of pellet washes performed before flash-freezing: None (red), once (blue) or twice (green). 83

Figure 20. PCA scores plots comparing the DIMS metabolic phenotypes of (A) synchronized algal cell cultures grown in alternating light:dark conditions, and of (B) non-synchronized algal cell cultures grown in constant light. Plotted are PCA scores for samples taken at 4 h 15 min ±15 min (red), 8 h 15 min ±15 min (green)) and 12 h 15 min ±15 min (blue). 85

Figure 21. Dose-response curve (4 parameter log-logistic model) of 24 h algal growth inhibition experiments for (A) 3,5-DCP, (B) $K_2Cr_2O_7$, and (C) three independent experiments for chlorobenzene (n = 4 per concentration). Error bars correspond to 95%-confidence intervals of fitted curve. 90

Figure 22. Violin-plot of relative standard deviations (RSD) of *m/z* features per experimental batch (B1/2/3, comparing three identical and independently- repeated batches of exposure experiments), median RSD values over all features are labelled per group. “Control” vs “Exposed” (CB), n = 10 per group. Each violin plot shows the value range (vertical lines), density of values (width of plot), and the 25^{th}, 50^{th} and 75^{th} percentile of values (horizontal lines) 91

Figure 23. PCA scores plots (PC1 vs. PC2) visualizing (**A**) the metabolic differences across three exposure studies (termed biological batches), with each batch comprising of control (n = 10) and CB-exposed (n = 10) samples; (**B**) only the control samples from each batch. Sample groups are biological batch 1 Control (Purple) and CB (Green), batch 2 Control (Yellow) and CB (Orange), and batch 3 Control (Red) and CB (Blue). 93

Figure 24. To increase comparability of exposure effects over the three repeated experiments, *m/z* feature intensities in CB groups were normalized to their batch-respective control groups by calculating the $\log_2$ fold-change of *m/z* features: (**A**) density distribution of LFC values for each batch ($\log_2$ (median[Int_{CB}]/median[$Int_{Control}$]), per *m/z* feature) ; (**B**) PCA scores plot from analysis of LFC values of all three batches ($\log_2$ (Int_{CB}/median[$Int_{Control}$]), for each *m/z* feature and for each of 10 CB samples). Batch 1 = green, Batch 2 = orange, Batch 3 = purple 95

Figure 25. PLS-DA scores plot visualizing the group-separation of metabolic phenotype in *C. reinhardtii* following exposure to 25 mg/L chlorobenzene (red circles) relative to unexposed controls (green circles). All samples from three independent exposure experiments (biological batches) were pooled in this analysis. R2 = variance explained by the model, Q2 = quality of model fit after permutation testing 96

Figure 26. 4-parameter log-logit dose-concentration model of 3 independent norflurazon growth rate inhibition experiments. The lowest observable effect occurred at 50 µg/L, while the EC_{75} was approached at ca. 12mg/L. For the experiment, 1000µgl and 2000µg/L were chosen. 107

Figure 27. m/z drift (measured in ppm in relation to average m/z value per peak over total multi-analytical-batch run) and occurrence of missing values (“NA”) over run of the positive ion mode metabolomics assay, after peak alignment in the dataset with a 2ppm tolerance window. Specifically, a relatively large drift of instrumental m/z measurements was observed over the first ~50 injections and over the last ~250 injections, inducing loss of retained peaks in the dataset due to the large Euclidean distance to cluster centroids, which generated large numbers of missing values. This effect was observable over the complete m/z range. Regions with high numbers of missing values were excluded from further analysis, as indicated in the figure. 108

Figure 28. RSD distribution and Quality Control sample (QC) RSD metrics per DIMS assay (Lipidomics, positive- or negative ion mode metabolomics). QC mRSD are at or below 13.9% for all assays, indicating high technical quality. RSD distributions for sample batches B1/2/3 are drastically higher as these groups contain diverse samples from all exposure groups and time-points randomized over run sequence, i.e. they are expected to reflect a relatively high biological metabolic variation. 110

Figure 29. Phred scores of the total dataset (norflurazon and chlorobenzene [Chapter 5] samples as a single analytical batch). Phred scores indicate the likelihood of a correct base call in Illumina RNAseq technology, Phred score at 30 or above suggest at least 99.9% likelihood of a correct call (= 100%*(1-(10^(-Phred_Score/10))). Only a single sample showed decreased scores (two technical replicates of 'NF8L4'), with scores at all time still >25 (99.7% likelihood of correct call). Color guide: Green = Very good quality calls, Orange = easonable quality calls, Red = poor quality calls. 111

Figure 30. '(A) Boxplots of exposure concentrations per group over time-course, measured by LC-MS/MS, and (B) boxplots of growth rate inhibition measured via CASY cell counting at 24h, post induction of the adverse outcome (inhibition of cell division). Marked in (A) is the limit of detection (LOD) for the applied LC-MS/MS method. 112

Figure 31. PCA of complete dataset ("NF" = Norflurazon, Time-point "TP" 1-9, "C"=Control, "L"=Low, "H"=High), for (A) Transcriptomics, (B) Lipidomics, (C) Metabolomics positive ion mode, (D) Metabolomics negative ion mode. Colored regions indicate the 95%-confidence intervals. Scaling differences between RNA and metabolite/lipid data stem from different data processing pipelines and are not indicative of quantity of molecular effects 113

Figure 32. PCA plots of (A) transcriptomics, (B) lipidomics, (C) positive ion metabolomics and (D) negative ion metabolomics, using the complete collapsed dataset (time variable omitted). Principal components were selected that highlight the underlying effects of increasing NF concentrations consistent over time-course. 114

Figure 33. Significantly different variables between exposure groups (Top = Low-vs-Control comparison, Bottom = High-vs-Control comparison), as represented by differentially expressed genes for RNA data (FDR ≤ 0.05, $\log_2$-fold change ≥ 2) and as spectral peaks significant between groups (Welch's t-test, FDR ≤ 0.05)..... 115

Figure 34. Venn diagrams of significantly different spectral peaks in (A) lipidomics data, (B) positive metabolomics data, (C) negative metabolomics data, and of differentially expressed genes in (D) transcriptomics data. Comparisons of "High"-concentration to "Control" ("High/Ctrl") and of "Low"-concentration to "Control" ("Low/Ctrl") are shown, intersections of circles show numbers of the differences that could be found within both comparisons 116

Figure 35. JGI-GO enrichments of NF-induced changes in the collapsed transcriptomics dataset, identified by parametric gene set enrichment analysis (PGSEA; [508]). Gene ontologies are presented and ranked along their FDR. PGSEA allowed first insight into exposure effects even when collapsing the time variable, and indicated monotonous changes from Control gene expression over increase in exposure concentration. However, strong time-dependence of molecular perturbation can still be observed, indicating the present weakness of omitting time-course in analysis. Red = relative higher expression of gene, blue = relative lower expression of gene. Time-points are plotted from TP1 to TP9 per group from left to right. 118

Figure 36. Time-course plot of maSigPro gene "Cluster07", functionally enriched with gene ontologies involving cell projection, cilium assembly, -regeneration and ciliary motility (Fig. 37) Plotted are replicate medians of all genes per time-point, and the median over replicate medians per time-point connected by a line per group. Significant changes in expression (ANOVA) are indicated by * (FDR<0.05), ** (FDR<0.01) or *** (FDR<0.001)..... 120

Figure 37. 'Network representation of JGI-GO categories related to cellular motility as discovered by maSigPro time-profile clustering ("Cluster07"). Distance of the lines ("edges") is a measure of similarity, size of the nodes (bright green) suggests significance of enrichment of the ontology term 121

Figure 38. Heatmap of the cell motility gene cluster, showing relatively increased (Red) and decreased (Blue) gene expression profiles of “Control”, “Low” and “High" groups over the normalized complete dataset. Indicated are time-points 8 and 9 (TP8/9) in exposed groups, showing slight increases of gene expression at these late time-points in the "Low” group, but also for parts of the gene cluster in the “High” group. 123

Figure 39. Time-course plot, median of genes per replicate and median of medians with connection line. Showing expression for (A) “Lipid catabolism" and "b-oxidation" JGI-GOs, and (B) Sulphur metabolism (combined JGI-GOs “Glutathione metabolic process”, “Sulfur Synthesis“, “Methionine Metabolism” and “Sulfur Amino Acid Synthesis”). Significant changes in expression (ANOVA) are indicated by * (FDR<0.05), ** (FDR<0.01) or *** (FDR<0.001). 124

Figure 40. Comparison of oxidative stress markers from 3 cellular compartments in *C. reinhardtii.* Time-points with significant differences between exposure groups (ANOVA) are shaded yellow. Chloroplast markers have a trend for upregulation from TP2, whereas significant differences were observable at TP3 and TP5-9. Cytosolic and mitochondrial markers overall were appreciable only considerably later (from TP5 and TP6, respectively), suggesting initiation of ROs in the chloroplast compartment and propagation of ROS damage at later time-stages into neighbouring compartments. Significant changes in expression (ANOVA) are indicated by * (FDR<0.05), ** (FDR<0.01) or *** (FDR<0.001). 126

Figure 41. Time-course plot, median of genes per replicate and median of medians with connection line, showing expression of the genes in maSigPro “Cluster05” enriching KEGG pathway “Carotenoid synthesis”. Significant changes in expression (ANOVA) are indicated by * (FDR<0.05), ** (FDR<0.01) or *** (FDR<0.001)..... 128

Figure 42. Time-course profile of NF’s molecular target, phytoene desaturase (PDS1). Significant changes in expression (ANOVA) are indicated by * (FDR<0.05), ** (FDR<0.01) or *** (FDR<0.001). 129

Figure 43. Normalised peak intensities of spectral peaks putatively annotated as (A) geranylgeranyl diphosphate (B) dihydro-geranylgeranyl diphosphate, and their precursor 2-C-Methylerythritol 4-phosphate (MEP), over time-course. Significant changes in peak intensity (ANOVA) are indicated by * (FDR<0.05), ** (FDR<0.01) or *** (FDR<0.001). 130

Figure 44. Increased intensities of spectral peaks putatively annotated as (A) Mg-Protoporphyrin IX and (B) pheophorbide-a, two chlorophyll synthesis pathway intermediates. Significant changes in peak intensity (ANOVA) are indicated by * (FDR<0.05), ** (FDR<0.01) or *** (FDR<0.001). 131

Figure 45. Shared generally applicable pathway enrichment analysis of lipid, metabolite and RNA expression data on the KEGG pathway for porphyrin and chlorophyll pigment synthesis (FDR = 0.027). Up- or down-regulation of genes is marked by green or red coloration, lower or higher spectral peak intensities are marked by blue or yellow coloration. Green enzyme names reflect ‘KEGG common enzyme names’..... 134

Figure 46. (A) Heatmap and (B) JGI-GO enrichment tree (along FDR) of a gene cluster significantly downregulated from TP5 to TP9 in the collapsed dataset. Color red indicates relatively increased expression, color blue indicates relative reduction in gene expression. Size of the nodes indicates degree of significance, the distance of the clusters connected by the branches of the dendogram is relative to th ontological similarity of gene sets 137

Figure 47. Representation of the genes associated with JGI-GOs comprising autophagic mechanisms and catabolism of organic substances. (A) Network map for, and (B) expression heatmap of maSigPro “Cluster01” genes enriching said JGI-GOs, indicating relative increase (red) or reduction (blue) in gene expression. Time-points 8 and 9 (TP8/9) are marked on the heatmap for exposure groups “Low” and “High”. Distance of the lines (“edges”) is a measure of similarity, size of the nodes (bright green) is relative to significance of enrichment of the ontology term. 138

Figure 48. Heatmap (A) of gene expression (blue = relative reduction, red = relative increase) and (B) network map of JGI-GOs enriched by a gene cluster discovered by hierarchical cluster analysis, signalling activity of macromolecular mitotic processes including microtubule-/ cytoskeletal binding and chromosome organization processes, with increased expression almost exclusively only observable in control cultures. Distance of the lines (“edges”) is a measure of similarity, size of the nodes (bright green) is relative to significance of enrichment of the ontology term 139

Figure 49. Time-course profiles of maSigPro (A) “Cluster02” and (B) “Cluster06”, both strongly enriched with JGI-GOs related to DNA repair mechanisms, cell cycle checkpoint activity, and mitotic and chromosomal organization (see Suppl. Fig. SI-45). Significant changes in gene expression (ANOVA) are indicated by * (FDR<0.05), ** (FDR<0.01) or *** (FDR<0.001). 140

Figure 50. Heatmap of GO comprising apoptotic mechanisms, visible induction only at “Low” and “High” concentrations at the last time-points, TP8 and TP9. Time-points 8 and 9 (TP8/9) are marked, color red indicates relatively increased gene expression, blue relatively decreased. 142

Figure 51. Time-resolved chemical MoA hypothesis of norflurazon toxicity in *C. reinhardtii.* The intensity of molecular effects (marked by increasing or decreasing width of the bars) and direction of change (marked by color of bars) is represented over the sampling time-course. The molecular effects here are anchored to both the 12h: 12h light:dark cycle (at the beginning of the 12h light period and transition into the 12h dark period) and the window of adverse outcome occurrence (inhibition of algal cell division and decrease of population growth rate), with cellular and nuclear division occurring slightly before, during and after the light:dark transition. 144

Figure 52. A potential AOP draft for “Phytoene desaturase inhibition leading to algal growth inhibition”, along with an indication of whether the new phenotypically-anchored *omics* data juxtaposed to literature support and/or Weight of Evidence (WoE; a conceptual framework to rate confidence in data and specifically key events, including strength of “Evidence”, and “Quantitative understanding” of key events and key event relationships [175,603,604]) have contributed to the derivation of that knowledge. PDS = Phytoene desaturase. 146

Figure 53. DIMS lipidomics sample acquisition over randomised sample sequence and effects of instable nESI spray in analytical batch 1, compared with higher data quality after increased nESI capillary voltage in batches 2 and 3. The top panel describes the m/z-distance of each individual mass spectral peak to its assigned peak cluster centroid during global dataset peak alignment at a 2ppm tolerance window. Strong loss of peak-cluster assignments is visible here in the first analytical batch (specifically higher m/z features), reinforced by a consistent reduction in the number of measurable spectral peaks (middle panel) and increased generation of missing values post peak alignment over the dataset (bottom panel). 154

Figure 54. Violin-plot of RSD distribution and Quality Control sample (QC) RSD metrics per DIMS assay (Lipidomics, positive and negative ion mode metabolomics). QC mRSD were at or below 14.7% for all assays. RSD distributions for sample batches 1/2/3 are drastically higher as these groups contain diverse samples from all exposure groups and time-points randomised over run sequence. Each violin plot shows the value range (vertical lines), density of values (width of plot), and the 25th, 50th and 75th percentile of values (horizontal lines). Due to data loss and discarding during instrumental acquisition, batch 1 in the lipidomics dataset is missing 155

Figure 55. (A) Boxplot of exposure concentrations per group over time-course, measured by GC-MS, and (B) boxplots of growth rate inhibition measured via CASY cell counting at 24h, post induction of the adverse outcome. Marked in (A) is the limit of detection (LOD) for the applied GC-MS method. 156

Figure 56. PCA of complete dataset (time-point “TP” 1-9, “C” = Control, “L” = Low, “H” = High), for (A) transcriptomics, (B) lipidomics, (C) metabolomics positive ion mode, (D) metabolomics negative ion mode. Colored regions indicate the 95%-confidence intervals. Scaling differences between Illumina and DIMS data stem from different data processing pipelines and are not indicative of quantity of molecular effects 158

Figure 57. Significantly different variables between exposure groups (Top = Low vs Control, Bottom = High vs Control), as represented by differentially expressed genes for RNA data (FDR ≤ 0.05, log2-fold change ≥ 2) and as spectral peaks significant between groups (t-test, FDR ≤ 0.05)..... 159

Figure 58. Venn diagrams of significantly different spectral peaks in (A) lipidomics data, (B) positive metabolomics data, and of differentially expressed genes in (C) transcriptomics data. Comparisons of “High”-concentration to “Control” (“High/Ctrl”) and of “Low”-concentration to “Control” (“Low/Ctrl”) are shown, intersections of circles show numbers of the differences that could be found within both comparisons. Negative metabolomics data showed no significantly different spectral peaks of the Low vs. Control comparison over the collapsed dataset. 160

Figure 59. JGI-GO enrichments of CB-induced changes in the collapsed transcriptomics dataset, identified by parametric gene set enrichment analysis (PGSEA). Gene ontologies are presented and ranked along their FDR. PGSEA allowed first insight into exposure effects even when collapsing the time variable, and indicated monotonous changes from “Control” over “Low” and “High” exposures in most GO categories. Time-points plotted from TP1-9 per group left to right. 162

Figure 60. Time-profile plots of maSigPro gene clusters (A) “Cluster08”, (B) “Cluster09” along significant differences of expression at each time-point (ANOVA), and (C) hierarchical enrichment tree of JGI-GO enrichments of genes pooled from both clusters. FDR of JGI-GO enrichments are displayed next to JGI-GO labels. Significant changes in gene expression (ANOVA) are indicated by * (FDR<0.05), ** (FDR<0.01) or *** (FDR<0.001). Size of the nodes indicates degree of significance, the distance of the clusters connected by the branches of the dendogram is relative to the ontological similarity of gene sets. 164

Figure 61. Time-course plot, median of genes per replicate and median of medians with connection line. Showing expression of genes within the JGI-GOs 'Polyol metabolic process' and ‘Protein N-linked glycolization’ (as identified by PGSEA at TP2), using the CB transcriptomics dataset. Significant changes in expression (ANOVA) are indicated by * (FDR<0.05), ** (FDR<0.01) or *** (FDR<0.001). 166

Figure 62. Time-course plot, median of genes per replicate and median of medians with connection line. Showing expression of genes within maSigPro (A) “Cluster02” and (B) “Cluster07”, comprising various elements of the photosynthetic machinery (Suppl. Table SI-T21). Significant changes in expression (ANOVA) are indicated by * (FDR<0.05), ** (FDR<0.01) or *** (FDR<0.001). 169

Figure 63. Time-course plot, median of genes per replicate and median of medians with connection line of genes enriching “RNA-polymerase”- and “Proteasome” KEGG pathways. Significant changes in expression (ANOVA) are indicated by * (FDR<0.05), ** (FDR<0.01) or *** (FDR<0.001). 171

Figure 64. Hierarchical cluster plot of JGI-GOs enriched by genes of maSigPro time-profile “Cluster05”, along their FDR. Size of the nodes indicates degree of significance, the distance of the clusters connected by the branches of the dendogram is relative to the ontological similarity of gene sets. . 173

Figure 65. Time-resolved chemical MoA hypothesis of chlorobenzene toxicity in *C. reinhardtii.* The intensity of molecular effects (marked by increasing or decreasing width of the bars) and direction of change (marked by color of bars) is represented over the sampling time-course. The molecular effects here are anchored to both the 12h: 12h light:dark cycle (at the beginning of the 12h light period and transition into the 12h dark period) and the window of adverse outcome occurrence (inhibition of algal cell division and decrease of population growth rate), with cellular and nuclear division occurring slightly before, during and after the light:dark transition. 175

Figure 66. A potential AOP draft for “Baseline toxicity inducing algal growth inhibition”, along indication of discoverability by omics. Delineated are the AOP draft from molecular initiating event (MIE) over multiple hypothesized key events up to the adverse outcome (AO) of algal growth inhibition. Overall, perceived strength of evidence and quantitative understanding was rated low for many elements of the AOP due to high variance in the dataset and lack of existing supporting knowledge informing the construction of this AOP draft. 178

List of Tables

Table 1. Overview of common NGS technologies and their characteristics. Each platform provides advantages and disadvantages towards specific purposes such as *de-novo* transcriptome assembly or low-level transcript detection Table adapted from ref. [296]. 24

Table 2. Commonly applied endpoints on higher levels of biological organization for measuring algal toxicity induced by chemical compounds. Juxtaposed are type of endpoint, variables measured, required instrumentation and degree of biological insight gained. 45

Table 3. Unique *m/z* features in positive ion mode DIMS spectra, from samples featuring various degrees of dilution of injection solvent. Shown are peak numbers after alignment, after blank and after 100% sample filter (average of n = 3). A reconstitution volume of 50 µL ("Neat") injection solvent was found to result in the maximal number of unique *m/z* features post-processing. 72

Table 4. ANOVA results comparing PC1, -2 and -3 scores of control samples or CB samples only (in each case between the independently-repeated identical exposure experiments), and CB samples normalized to their batch-specific controls. Mitigation of initially significant inter-experimental variability (excluding PC2) could be achieved using this normalization. 94

Table 5. Enrichment analysis applied to three metabolomics datasets following exposure of *C. reinhardtii* to chlorobenzene (three independently repeated and identical exposure experiments; batches 1, 2, 3). Ranked lists of *m/z* feature LFC were calculated (S_{B1}–S_{B3} for batches 1–3) and every list was compared against every other list to determine whether S_{B1}-S_{B3} were enriched with elements of the other sets. Significance of enrichment was assessed using 1000 random permutations of *m/z* values in LFC-ranked lists, and false-discovery rates are reported. NES = normalized enrichment score, degree of metabolite enrichment of S within dataset. LE = leading edge, subset of *m/z* features in S that are most impactful towards a high NES. 97

Table 6. Gradient of mobile phase B over 21.5min analytical runtime in LC-MS/MS analysis. Total carrier phase = % phase A + % phase B (% phase A = 1 - % phase B).. 106

Abbreviations

3,5-DCP.....3,5-Dichlorophenol

ANOVA.....Analysis of variance

AO .....Adverse Outcome

AOP ..... Adverse Outcome Pathway

ATG .....Autophagy-related genes

BBM.....Bold's basal medium

CASY..... Cell counting technology by Hoffmann-la-Roche AG

CB..... Chlorobenzene

cDNA .....complementary DNA (deoxy-ribonucleic acid)

CGM ..... *Chlamydomonas* growth medium

CoA.....Co-enzyme A

CPM.....Counts per million

CRISPR..... clustered regularly interspaced short palindromic repeat.

CSA .....Chemical safety assessment

DEG.....Differentially expressed genes

DIMS..... Direct-infusion mass spectrometry

DMSO.....Dimethylsulfoxide

EC.....Effect concentration

ECHA..... European Chemicals Agency

eco-TTC.....Ecological threshold for toxicological concern

EHA .....Environmental hazard assessment

ER.....Endoplasmatic reticulum

ETC ..... electron-transport chain

EU.....European Union

FDR .....False discovery rate

GAGE ..... Generally-applicable gene-set enrichment analysis

GC-MS.....Gas-chromatography mass spectrometry

GGPP .....Geranylgeranyl diphosphate

GRS.....Geranylgeranyl reductase

GSH..... Glutathione

GST .....Glutathione-S-transferase

glog..... generalized log transformation

Hac .....Acetate

HPLC.....High-pressure liquid chromatography

HSM..... High salt medium

IATA..... Integrated Approaches to Testing and Assessment

ISO ..... International Organization for Standardization

JGI-GO .....Joint Genome Institute Gene Ontology terms

$K_2Cr_2O_7$..... Potassium dichromate

KE.....Key event

KEGG ..... Kyoto Encyclopedia of Genes and Genomes

LC-MS/MS.....Liquid-chromatography tandem mass spectrometry

LE ..... Leading edge

LFC ..... Log-fold change

Lhc ..... Light-harvesting complex

LINCS ..... Library of Integrated Network-Based Cellular Signatures

LOESS ..... Locally-estimated scatterplot smoothing

MGDG ..... Monogalactosyldiacylglycerols

MI-Pack ..... Metabolite identification software

MIE ..... Molecular initiating event

MoA ..... Mode of Action

mRSD ..... Median relative standard deviation

MS ..... Mass spectrometry

NA value ..... Missing value (‘Not available’)

NAM ..... New Approach Methodology

NES ..... Normalized enrichment score

nESI ..... nano-Electrospray ionization

nESI-DIMS ..... nano-Electrospray Ionization coupled to DIMS

NF ..... Norflurazon

NGS ..... Next Generation (Nucleobase) Sequencing

OECD ..... Organization for Economic Co-operation and Development

PCA ..... Principal component analysis

PGSEA ..... Parametric gene set enrichment analysis

PDS ..... Phytoene desaturase

PLS ..... Partial least squares

PLS-DA ..... Partial least squares – linear discriminant analysis

PS ..... Photosystem

QC ..... Quality control

QSAR ..... Quantitative structure-activity relationship

REACH ..... Registration, Evaluation, Authorization and Restriction of Chemicals

ROS ..... Reactive oxygen species

rlog ..... regularized log transformation

RSD ..... Relative standard deviation (~Coefficient of variation)

RNA ..... Ribonucleic acid

RNA-Seq ..... RNA sequencing technology

SB ..... Set batch

SGC ..... Single genome copy

SIMstitch ..... Single-Ion Monitoring window stitching

SNARE ..... soluble N-ethylmaleimide-sensitive-factor attachment protein receptor

TOR kinase ..... Target-of-rampamycin kinase

TP ..... (Sampling) Time-point

Chapter 1

Introduction

1. Introduction to hazard assessment

1.1 Chemical risk and hazard assessment and their legislative background

Environmental health status is heavily impacted by anthropogenic actions, prominently by intentional or accidental release of synthetic chemical substances into natural ecosystems, where these commonly do not occur naturally or at high concentrations. Life in aquatic ecosystems is a fundamental element of local and global food cycles, comprising primary producers to tertiary consumers [1,2]. Regrettably, chemical pollution of surface and groundwaters has become omnipresent [3] and represents a major threat to aquatic organisms and by extension terrestrial food chains [4].

To protect the aquatic and general environments from potential man-made chemical pollution on the European level, a number of legislations were enacted. Notable among these are the Water Framework Directive [5] to guide future water protection policy, and the Registration, Evaluation, Authorization and Restriction of Chemicals (REACH [6]). According to REACH, any chemical substance produced in or imported into the EU above one ton per year requires an assessment of its potential to induce toxic effects relevant to human and environmental health, and submission of these data to the European Chemicals Agency (ECHA) for registration. The core concept of this chemical safety assessment process in REACH was carried over from the Existing Substances Regulation by the European Economic Community. Importantly however, among many other changes, REACH shifts the burden of conducting chemical safety assessment onto producers and importers, away from regulatory agencies.

The chemical safety assessment process involves hazard and risk assessment of a chemical substance, where hazard is defined as the capability of causing a given adverse environmental or human health effect, and risk as the probability of that hazard occurring at a given exposure to the chemical substance. The formal and iterative chemical safety assessment process (Figure 1) comprises hazard assessment, exposure estimation, and ultimately risk assessment in the context of an

initial problem formulation with the purpose of guiding regulatory decision-making [7,8]. REACH regulates the registration of substances and detailed requirements for chemical safety assessment in dependence of production or import volume, and level of concern. High production or import volumes, and highly toxic substances (reproductive toxins, carcinogens and mutagens) require full chemical safety assessment of the substance in question [9,10].

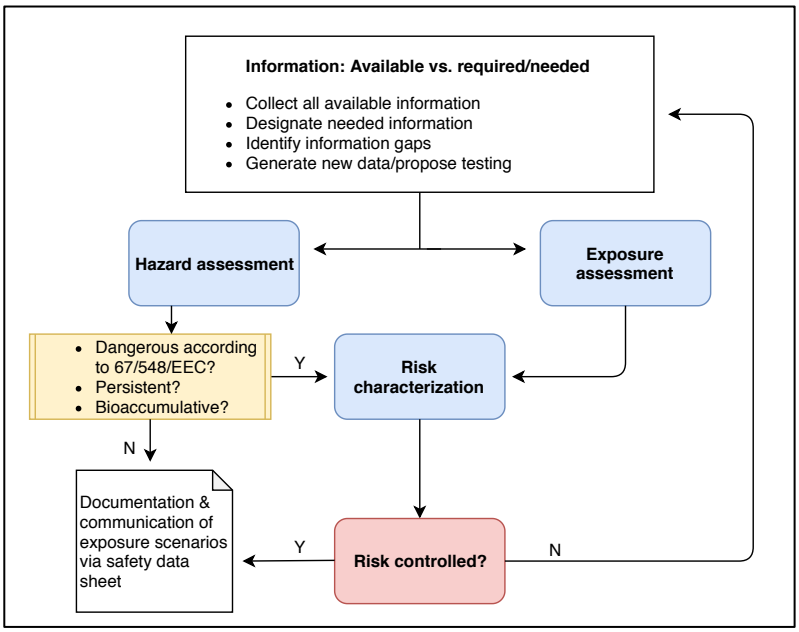


Figure 1. Simplified schematic of the chemical safety assessment process under REACH legislation, spanning initial data collection, hazard assessment (hazard identification and concentration-response characterization), exposure estimation and risk assessment to guide regulatory decision-making. Figure after ref. [5].

Any substance with tonnages as low as one ton per year requires an environmental hazard assessment on aquatic organisms, specifically algae, daphnids and fish, as detailed in REACH annex VII [11]. To harmonize test procedures and data collection for submission to ECHA, the Organization for Economic Co-Operation and Development (OECD) and the International Organization for Standardization (ISO) provide official guidelines prescribing test conditions to conduct the specific toxicity tests for environmental hazard assessment. For instance, OECD guideline 201 and ISO/DIS 8692 [12,13] prescribe specific conditions and validity requirements for conducting a hazard assessment regarding algal growth inhibition of chemical substances in the context of aquatic toxicity. Overall, environmental hazard

assessment plays a pivotal role in the authorization or restriction of chemical substances within the regulatory decision-making framework, and an accurate assessment of chemicals is critical for protecting all environmental compartments, including diverse aquatic ecosystems.

1.2 Conventional approaches to inform environmental hazard assessment

The data used to evaluate the intrinsic hazard of a chemical substance to human and environmental health are routinely gained from standardized toxicity tests (bioassays). In the conventional environmental hazard assessment practice, bioassays are laid out in the format of phenotype-focused whole organism tests. These seek to characterize environmental hazard by exposing a sentinel organism to a range of concentrations of a chemical substance, and measuring the associated induction of observable adverse phenotypes (i.e. apical endpoints). The particular apical endpoints to be measured depend on the type of environmental hazard that is sought to be identified and characterized, and on the test organism. Examples for such apical endpoints relevant to environmental hazard assessment are growth inhibition of algal populations [12,13], immobilization or reproductive inhibition in daphnids [14,15], changes in bodyweight or mortality in birds [16], or short- and long-term reproductive inhibition and somatic malformations in fish [17–21]. These phenotype-focused bioassays form the core of conventional EHA strategy and the basis for further chemical risk assessment.

Additional information on substance hazard may be submitted by registrants to support the chemical safety assessment in the form of data from alternative testing strategies. Such commonly involve biochemical experimentation (potentially employing novel technologies) or *in-silico* predictions of hazard [22,23] to gain insight into chemical mode of action (MoA). The MoA of a chemical substance describes its initial interaction with molecular biological targets in an organism and the subsequently induced effects on cells and tissue in the organism, and is helpful in extrapolating information on toxicity to other chemical substances and species [24]. Literature search reveals a wealth of research studies suggesting biochemical follow-up methods to phenotype-focused bioassays in environmental hazard assessment for the

deduction of MoA, e.g. in algae [25–37], fish [38–40], or even for multi-species assessments [41–44].

Additional prediction of MoA and potential hazard may be granted by *in-silico* models, which derive information from characteristics of the chemical substance other than its toxicity. Prominently, quantitative structure-activity relationship (QSAR) models seek to predict and categorize chemical activity (apical endpoint induction, MoA, environmental stability *etc*.) from the molecular structure of a chemical, thus seeking to avoid expenditure from additional laboratory testing. Well-established examples for such categorization approaches are the OECD QSAR toolbox, or the Mode of Action and Toxicity (MOAtox) database by the United States Environmental Protection Agency (USEPA), although new models are constantly under development [45–47].

Even simple alternative testing strategies as described above can be valuable to increase confidence in environmental hazard assessment of a chemical substance by improving understanding of MoA. The regulatory acceptance of alternative testing strategies though is a slow process, requiring thorough grasp of the science behind the biological processes under scrutiny, and reliable comparability of alternative model systems to full organism tests [48–50]. Thus, despite an encouragement of submission of alternative test data to support chemical safety assessments, such remains at the level of secondary supporting information, and the primary regulatory reliance on and prescription of phenotype-focused bioassays is still characteristic of REACH and most other chemical legislations globally [51,52].

2. Shortcomings of conventional hazard assessment strategy

The specific test guidelines for phenotype-focused bioassays have been methodologically refined since their initial conception. However, the toxicological problem formulation of what information is relevant for defining environmental hazard of a chemical substance, and how to interpret it, was principally left unchanged for decades [53]. Phenotype-focused bioassays were and are generally regarded as adequate for their originally intended purpose, i.e. the characterization of environmental hazard solely by proxy of crude apical endpoint induction. However, the latter is a relatively insensitive measure of chemical toxicity in and of itself [48], and has been criticized by the wider research community heavily for its shortcomings as a viable tool for future environmental hazard assessment [52–54]. These may be summarized as a) unacceptably high demands for expenditure, time and test resources, and limited b) reliability and c) generalizability of data generated in phenotype-focused bioassays.

2.1 High demands for financial expenditure, test subjects and time

In spring of 2019, over 22,000 chemical substances had been registered under REACH in the European Union [55]. Regardless, over 140,000 commercial chemicals (excluding mixtures) are handled daily on a global scale, for ten-thousands of which there is only little, if any, toxicological information available [56–59].

First-tier hazard screening frameworks, such as the ecological threshold for toxicological concern (eco-TTC [60,61]) exist to triage inherently dangerous or high-production volume chemicals for prioritized testing. Despite the ensuing reduction of substances requiring detailed chemical safety assessment though, conventional approaches to environmental hazard and risk assessment are still insufficient to cope with testing of prioritized substances in a reasonable time-frame and budget [58,62]. In the example of REACH, up to 80,000€ are required to merely conduct hazard assessment to aquatic organisms for a single test substance [11].

Additionally, chemical substances may induce multiple apical endpoints in different species, at various exposure concentrations or duration [63]. Here, avoiding false negatives or undetected MoA in hazard assessment requires application of large test batteries of bioassays involving multiple species and exposure scenarios, in turn leading to geometric increases in demands of funds, time and test subjects [64,65]. An estimated 5000 test animals are required per chemical substance registration under REACH, leading to yearly test subject demands in the range of hundred-thousands merely in the EU [66,67].

As a result, a large number of potentially dangerous substances are handled daily on a world-wide scale - safety evaluation of which, according to current paradigms, will be extremely difficult to achieve due to financial, ethical and time constraints [57,68,69].

2.2 Limited reliability of data

Phenotype-focused bioassays were further likened to black-box models, restricting assessment of chemical hazard to a narrative or phenomenological description [70–72]. Knowledge of molecular mechanisms and cause-effect chains within chemical MoA can augment confidence in hazard assessment substantially [73], mechanistic insight however can only be gained minimally from said bioassays.

As indicated, alternative testing approaches can help bridging the gap of inferring MoA [56,74,75], but merely a limited number of *in-vitro* and *in-silico* methods are accepted to supplement chemical safety assessment. Of those, most *in-vitro* methods impose prior assumptions on the particular chemical MoA, and many *in-silico* approaches serve mainly to predict apical endpoint induction [60]. Thus, characterization of hazard with reliance on conventional environmental hazard assessment practices might result in failure to detect unknown or secondary MoA [57,76]. Lack of mechanistic insight, limited coverage of screened hazard types, and dependence on prior knowledge for MoA elucidation effect high uncertainty factors during successive risk characterization [77,78].

2.3 Limited generalizability of data

Another major shortcoming of hazard assessment based on induction of crude apical endpoints is the limited predictive power when attempting to extrapolate hazard to other species and chemicals. Ideal coverage of potentially inducible types of hazard across genetically diverse organisms would require parallel testing of millions of environmental species [79]. Realistically, hazard assessment can thus only be performed on sentinel species that biologically closely resemble most organisms in their ecological niche [80,81], followed by extrapolation of data onto other species. For phenotype-focused bioassays, cross-species extrapolation comes with certain limitations. Due to differential physiology, cellular architecture and/or metabolic and genotypic diversity, a given chemical hazard (or chemical MoA inferred from phenotype) detected by bioassays may not be relevant to other organisms, or remain completely undetected in a given species [82]. The result is increased likelihood for detection of false positives, or waiving false negatives.

Confidence in cross-species extrapolation can be drastically increased when based on mechanism, in order to distinguish which molecular targets of, and interactions with chemical substances are relevant to other organisms [83,84]. However, the focus on apical endpoint induction in conventional EHA strategy leads to gaps in understanding mechanism in chemical MoA, again augmenting over-conservative uncertainty factors and safety thresholds in risk characterization [85–88]. Similarly, substantial obstacles exist in effective extrapolation of hazard from chemicals with known effects onto untested chemicals. ‘Chemical read-across’ is based on structural similarity of substances, and has proven valuable for cost-effective triage, waiving chemical safety assessment of chemicals and data-gap filling [45]. Nonetheless, legacy *in-silico* models in regulatory decision-making frequently attempt to perform chemical hazard grouping on the basis of predicting proxy markers of toxicity, e.g. apical endpoint induction or environmental fate. Grouping of chemical hazard in this approach bears inherent uncertainty, as it remains largely ignorant of complex molecular interactions between chemical and organism, including idiosyncratic chemical MoA, multiple induced chemical MoA, chronic- and mixture toxicity [89,90]. Comparisons of the predictive power of major digital classification

platforms (e.g. OECD QSAR Toolbox, USEPA ECOSAR, -EPISUITE or -ASTER) concluded overall utility for application in first-tier screening, however discordance between model predictions, risk of misclassification, incomplete coverage of the chemical MoA-space and ignorance of chemical metabolism were also attributed [91–94]. Again, hazard prediction from descriptors based on interactions at the molecular chemical-organism interface would improve reliability of *in-silico* tools drastically [60,91,95–99], however regulatory acceptance of alternative approaches such as new *in-silico* models is slow [9,100].

In conclusion, reliance on data from highly resource-intensive phenotype-focused bioassays or proxy hazard markers detached from biological response often leads to over-conservative and disputable safety assessments in regulatory decision-making [52,101].

3. Conceptual and technological advances to drive a new chemical safety assessment paradigm

A re-evaluation of basic assumptions underlying the current chemical safety assessment paradigm in toxicological sciences is required to address described shortcomings, specifically of the standards of what information should drive chemical safety assessment. Over the last decades, novel conceptual and technological approaches have revolutionized the wider field of molecular biology [102]. As a response, the National Academy of Science published a seminal report [51] detailing a strategy to use these new approaches to modernize chemical safety assessment. Specifically, it highlighted a paradigm shift towards mechanistic understanding of adverse effects of chemicals on humans (Fig. 2), while decreasing cost and animal sacrifice [48]. Next to calling for a change of emphasis towards defining chemical MoA of toxicants, more comprehensive and realistic procedures to exposure assessment and translation of concentration-response data from animal and *in vitro* models to

human (dosimetry) were described [103–105]. The report was well-received by the scientific and regulatory community, and implementation was rapidly initiated in human toxicological sciences [23,106,107]. In the field of environmental toxicology, the new paradigm arrived with somewhat lower momentum [54,67]. However, the same progression towards focus on mechanism using novel technological and conceptual advances is endeavored within environmental hazard assessment. The new elements of such mechanism-based hazard assessment thus should include chemical characterization and the assessment of chemical MoA via understanding perturbation of biological pathways (Fig. 2).

3.1 Integrated approaches to hazard assessment and the adverse outcome pathway concept

Pathway-based approaches form the heart of mechanism-based hazard assessment. For environmental toxicology, the adverse outcome pathway (AOP [108]) has established itself as conceptual framework to organize, centralize and harmonize toxicological information [109]. AOPs represent abstract schematics of perturbed biological pathways, linking the basal toxicological interaction of toxicants with biomolecular structures (molecular initiating event; MIE) mechanistically to an adverse outcome observable on the phenotypical level (Fig. 3). The adverse outcome (AO) is located on the higher levels of biological organization, and reflects a relevant endpoint for regulatory intervention, i.e. organism-, population or community level effects. Importantly, MIE and AO are connected by a chain of modular and discretized key events (KE), which represent irreversible aberrations from correct biological functioning and are causally and successively associated.

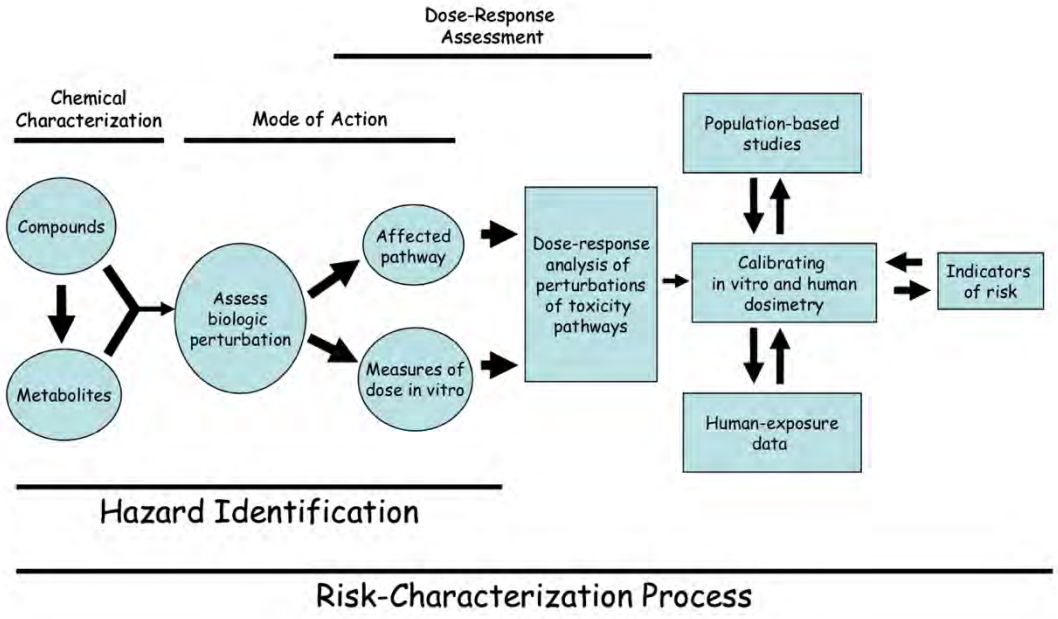


Figure 2. Schematic of human hazard and risk assessment within the new chemical safety assessment paradigm. Similar considerations were envisioned for safety assessment of chemicals in an environmental context. Figure from ref. [51].

AOPs have the potential to become prime tools for predicting adverse chemical effects. They enable a plausible cause-effect understanding of perturbance of biological pathways, and thus can be of high utility for regulatory decision-making [96,110–114]. As they are non-specific to individual chemicals but rather to MIE, individual or networks of AOPs (i.e. AOPs sharing MIEs, KEs or AOs) could provide toxicological information and predictive power for a multitude of chemicals and more generally MoAs [114–116]. Thus, AOPs represent leveraged models that could aid chemical read-across and generalization of MoA over large sets of untested substances or those with minimal information on hazard [109]. Invaluably, by focusing on mechanism and contextualization of biological pathway conservation across different environmental species, the AOP concept has the potential to improve confidence in cross-species extrapolation while decreasing testing expenditure [84,111,113], help in interpreting species-sensitivity distributions, and understand discrepancies of MoA in different species [117]. In addition to mechanistic insight, AOPs enable quantitative prediction of chemical hazard including low-dose- and sublethal effects [110,111], allow more accurate classification and hazard assessment

of chemical mixtures [114,118,119], and may be extended to incorporate toxicokinetic and exposure information [120–122].

Overall, due to their non-linear and flexible structure, AOPs and AOP-networks can incorporate both inherent chemical substance properties (e.g. multiple MIEs induced by single toxicant) and the complexity, dynamics, kinetics and non-linearity of the biological response system they are aimed to reflect, in a centralized block of information.

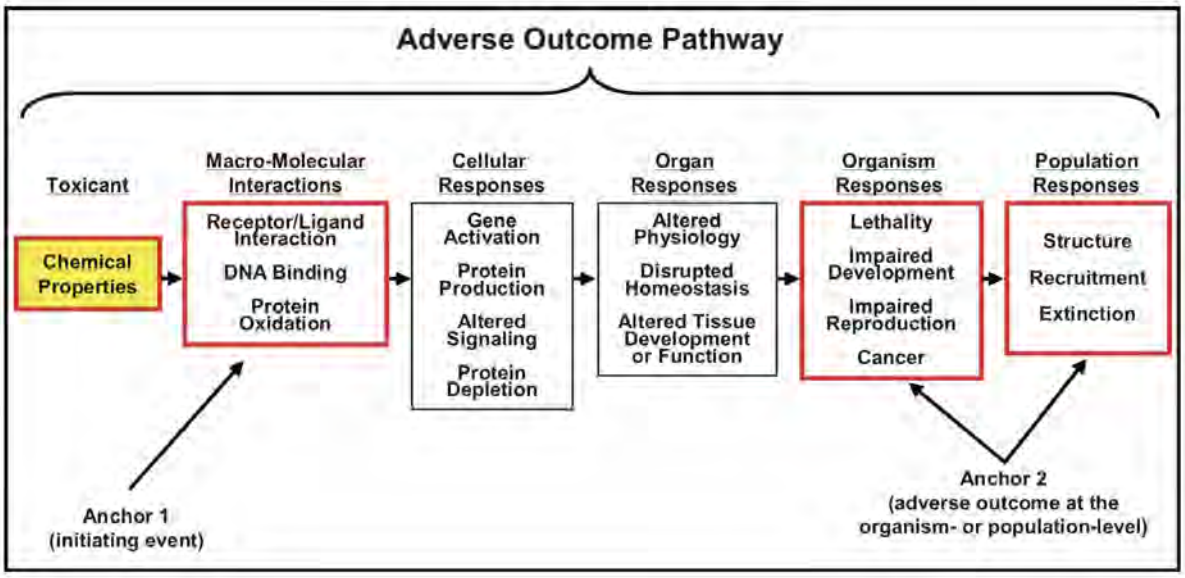


Figure 3. Structure of an adverse outcome pathway. Interaction of a chemical substance (toxicant) with an organism causes a molecular initiating event, which induces a chain of discrete and causally linked key events. The key events ultimately lead to induction of an adverse outcome relevant to risk assessment. Figure from ref. [108], modified.

The new paradigm of chemical safety assessment aims to avoid utilization of data from phenotype-focused bioassays as sole basis for hazard assessment. However, single alternative testing methods cannot supplant these due to the inherent biological complexity of adverse effects of chemicals. To bridge this gap, the concept of Integrated Approaches to Testing and Assessment (IATA) has evolved. IATA are combinatory approaches that optimize chemical hazard assessment in order to reduce redundancy, cost and animal sacrifice in testing, while improving confidence in regulatory decision-making and handling of uncertainty [10,11,109,123–125]. IATA integrate the utilization of diverse existing data on a chemical with the guided

generation of new data on chemical hazard and evaluation thereof, both originating from a diverse set of sources such as *in-silico* toxicokinetic models and predictive QSARs, *in-vitro* assays, high-throughput-screening, or pan-genomic molecular profiling [126].

Adverse outcome pathways, in their role as knowledge frameworks, can serve as fundaments for IATA by organizing available toxicological information, and evaluating the latter for adequacy towards regulatory decision-making using weight-of-evidence approaches [123,127]. The modular nature of AOPs can point towards an optimal combination of testing techniques for a given type of hazard. For instance, key events in AOPs may indicate biomarkers predictive of hazard, and suggest batteries consisting of various laboratory assays to develop mechanism-based rapid targeted testing strategies [113,127]. Molecular initiating events may aid in constructing *in-silico* tools within IATA, i.e. by guiding the generation of QSARs for predicting MIE-induction of chemicals [128–132] to facilitate chemical read-across and grouping for screening and prioritization [133]. AOPs further enrich IATA by flagging up gaps in the understanding of adverse chemical effects, and guide targeted data gap filling [45,111,113,117]. AOPs go hand in hand with IATA to reduce cost (time, money, animal life) of, and increase confidence in chemical safety assessment, by facilitating the construction of mechanism-based predictive tools and testing strategies, focusing on data gaps, avoiding duplicate testing, and utilizing of the most predictive resources for a given problem formulation [75,110,134].

IATA are structured approaches to testing, however do not enable mechanistic understanding without the help of mechanism-based tools such as AOPs [135]. Previously, AOP-driven guidance of IATA was successfully achieved, and the concept showed promising potential as starting point for modern chemical safety assessment [109,134,135].

3.2 Technological advances to support a paradigm shift

Next to described conceptual developments, recent technological advances from the field of molecular biology are increasingly manifesting themselves in application to toxicological sciences, in an effort to modernize chemical safety assessment [51,106]. These 'New Approach Methodologies' (NAMs) comprise a variety of *in-vitro, in-chemico* and *in-silico* approaches [136]. Prominent examples are robotic high-throughput platforms such as ToxCast [8,137] or LINCS [138] that utilize extensive batteries of pathway-specific *in-vitro* tests for chemical and drug MoA screening, three-dimensional tissue test systems [139], *in-silico* predictions based on sophisticated QSARs employing molecular descriptors [46,100,140], or *omics* technologies enabling global profiling of biological stress responses to toxicants.

Omics are analytical platforms that allow untargeted and hypothesis-free profiling of molecular signatures, amongst others, gene transcription (transcript*omics*), protein levels (prote*omics*), or metabolite and lipid concentration (metabol*omics* and lipid*omics*). The range of molecular markers measured in parallel is commonly in the range of thousands. Generated datasets are distinctly precise in profiling global molecular states of cells, tissues or whole organisms [65], owing to high instrumental sensitivity and avoidance of proxy biomarkers. Historically, the various *omics* research domains and platforms have evolved independently in different contexts of application, and their utility in uncovering molecular dynamics and processes was demonstrated repeatedly [49,141–144]. Amid the NAMs considered for toxicological purposes, *omics* stand out for their unique capacity of comprehensive molecular analysis, and unbiased, *a priori* discovery of biological processes.

As molecular NAMs, *omics* technologies bear great potential to inform and support the construction of AOPs. Untargeted analysis is envisioned to play a vital role in IATA by supporting mechanistic hypotheses and global chemical MoA deduction [134]. As an unbiased discovery tool, *omics* data can unveil completely new and unexpected molecular mechanisms [145], granting *a priori* discovery of chemical MoA. Further, *omics* can improve hazard assessment by informing mechanism-based cross-species extrapolation and chemical read-across [76,88,146–148], guide the development of IATA, or even be part of first-tier screening in IATA. *Omics* might

provide strong supporting evidence in the construction of AOPs, if not be a primary driver of it. Untargeted molecular fingerprints might allow the discovery of biomarkers diagnostic of chemical MoA and predictive of apical endpoint (e.g. hypothesize on key events predictive of AO in AOPs), or enable the inference of MIEs for the design of QSARs - thereby enabling the compilation of biologically-informed targeted *in-vitro* test panels or *in-silico* tools for IATA [97,123,149,150]. Moreover, untargeted *in-vitro* assays could be part of hazard screening within IATA. Classification of chemical MoA and chemical grouping could be achieved using similarity in global molecular fingerprints indicative of MoA, allowing chemical read-across, chemical MoA hypothesis and rapid chemical prioritization for further testing [113,127,145,151–153].

Overall, *omics* could increase confidence in cause–effect analyses and hazard assessment by providing mechanistic evidence on the harmful effects of chemicals. However, the application of *omics* to toxicological sciences has so far largely been limited to isolated case studies demonstrating effects of model chemicals [145,154,155].

4. Requirements and needs towards regulatory acceptance of *omics*

Omics may prove highly valuable for application in environmental hazard assessment of harmful chemicals, for instance in prioritization and read-across, and research interest on *omics*-driven MoA elucidation and chemical safety assessments is increasing from various stakeholders [57]. Despite the publication of first framework proposals for *omics* data generation and evaluation towards application in chemical safety assessment [146,156], ECHA and other regulatory institutions consider molecular NAMs - including *omics* - not yet sufficiently developed and reliable to inform chemical safety assessments [49,136]. This very perception is yet the highest barrier to utilization of *omics* datasets in regulatory decision-making [23,49,155]. A number of

obstacles remain to be overcome in order to achieve this regulatory acceptance, among them more technical requirements including the overarching standardization of soft- and hardware platforms, or the introduction of good laboratory conventions in data generation, -processing and -curation in the generation of mechanistic data to inform and support construction of AOPs [157–160].

On the practical side, two requirements for facilitating more frequent and assured application of *omics* to environmental hazard assessment purposes are regularly noted as (1) establishment of tailored experimental designs and testing systems suitable for *omics*-driven hypothesis of chemical MoA, and (2) associated demonstration that *omics* applying said designs and systems can reliably discover chemical MoA and thus be of utility to hazard assessment. Discovery of molecular mechanisms requires the development of new protocols towards robust, precise, reproducible and scalable experimental designs, to support factoring of exposure concentrations, biological replication and time-resolution in single experiments [49,146,157,161–164]. Specifically, explorations of the temporal domain (time-course analysis) and concentration-response behavior are highly valuable - yet frequently neglected - considerations in *omics* research examining processes molecular perturbations induced by chemicals [108,165]. Thereafter applying these experimental designs, proof-of-concept studies using model toxicants are required to demonstrate reproducible and reliable *omics*-driven chemical MoA hypothesis and discovery of molecular markers of toxicity such as molecular key events predictive of adverse outcome [70,111,124,127]. Following the hypothesis of chemical MoA by *omics* in such studies, targeted post-hoc tests though would be required to evaluate and characterize putative biomarkers and their relationships if they are to be integrated into mechanism-based hazard assessment, e.g. for design of targeted regulatory tests specific to a chemical MoA or even AOP [109,134,146,166–168].

Ultimately, pending regulatory acceptance of *omics* as fit for purpose, they are expected to bear great inherent value for supporting chemical safety assessment. These include but are not limited to deduction of MoA, providing supportive weight of evidence for AOPs, aiding IATA by improving precision in screening, chemical read-

across and relevant cross-species hazard extrapolation, or classification and labelling of dangerous chemicals as per REACH legislation [49,145,146,165,169–172].

5. Model species selection to showcase utility of *omics* to environmental hazard assessment

When selecting model organisms for the purpose of showcasing NAM-driven identification of chemical MoA and AOP, specific criteria need to be regarded to improve applicability of research results. Characteristics of an optimal model species include widespread environmental occurrence, extensive availability of information on biological pathways and their evolutionary conservation, and ideally placement of the species within the three classic tiers of test organisms applied in environmental hazard assessment (freshwater algae, water flea and fish) to achieve a degree of comparability to existing hazard assessment practices [173–176]. Certain sentinel species were recently established as prime model organisms in the specific context of AOP development, for instance the invertebrates *Daphnia* sp. and *Caenorhabditis elegans* [177,178], zebrafish [179], or the algae *Chlamydomonas reinhardtii* [180]. Algae are key components of aquatic food chains. The more than 70,000 algal species assume critical roles in global carbon fixation, primary production of biomass and bio-indication of local aquatic pollution [1,181–183]. As a result, algae have become internationally established test organisms in chemical safety assessment [12,13,184].

C. reinhardtii (Fig. 4) is the algae that has received most attention in any algal research endeavor to date [185], and looks back at over a century of research in various contexts. The ciliated freshwater phytoplantic species is characterized by a haploid and relatively small ~120-megabase nuclear genome, containing approximately 14,500 protein-coding genes [186,187]. Availability of nuclear-, mitochondrial- and chloroplast genome sequence, the algae's simple and rapid life-cycle, and ready available methods for genetic manipulation including CRISPR/Cas9 [188,189] render *C. reinhardtii* a superb model organism for molecular studies and an

established reference species for genetics research [186,190,191]. Furthermore, *C. reinhardtii* is a model for exploring cellular morphology of green algae, chloroplast-based photosynthesis, function and structure of cilia and centrioles, algal diurnal cycles and cell cycle control [185,186,192–202], and various research in biomedical and biotechnological sciences [203–207]. *C. reinhardtii* was the first algal species with a dedicated genome project [186,208,209], which public availability along extensive metabolic pathway information was of immeasurable value as basis for exploration of biological processes in algae using *omics*. As a result, this algal species has received widespread attention as an algal model in the research areas of evolutionary genomics [186,210–215], functional genomics [193,215–218], transcriptomics [219–231], metabolomics [232–241], and proteomics [234,242–244].

Further, research efforts to describe the effects of model toxicants on the molecular stress response of *C. reinhardtii* using *omics* approaches have recently become more frequent. Landmark studies include those exploring effects of metals

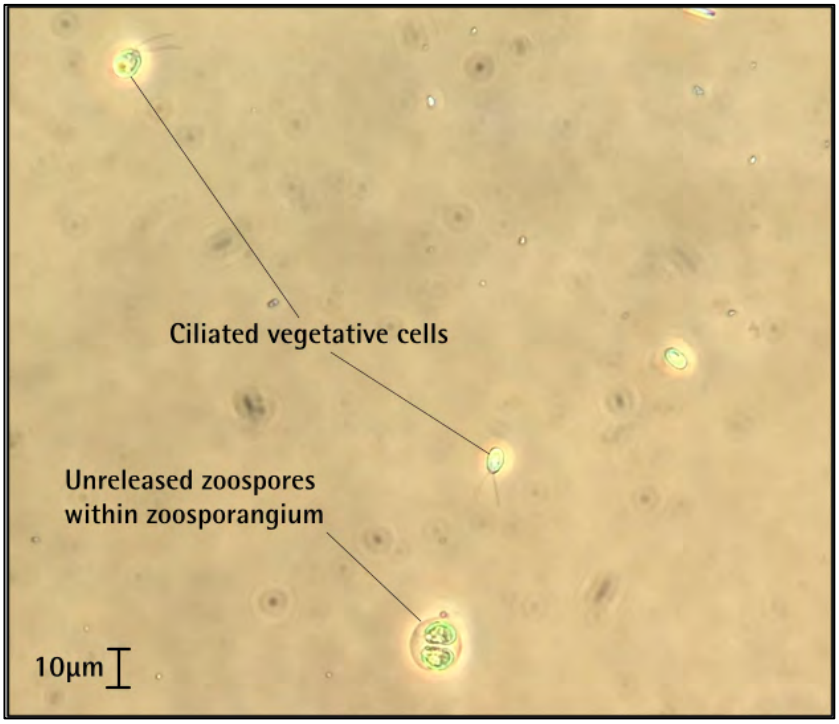


Figure 4. *Chlamydomonas reinhardtii* liquid culture at 200-fold magnification. Visible are vegetative cells from various position in the cell cycle, including ciliated cells in cell cycle stages of biomass accumulation and photosynthetic activity (Top, Middle), or unciliated daughter cells (zoospores) post-division still contained in the membrane of the mother cell (Bottom).

[245–251], pesticides [252–255], or nanoparticles [256,257]. Most experimental approaches using *omics* to describe chemical effects on *C. reinhardtii*, and microalgae in general, show a number of limitations towards the purpose of informing AOPs or guiding IATA. These include limited or missing temporal resolution [246,252,253,256,258–260], exposure and sampling strategies with little biological justification [248,250,251,254,255,261,262], lack of matched life stages [231,243,245,257,263], or restricted scalability, among others.

It is evident that there is a need for the establishment of tailored experimental designs and testing systems as mentioned in Section 4. Once this need has been addressed appropriately, the extensive biochemical and molecular characterization of *C. reinhardtii* can be leveraged for *omics*-driven chemical MoA or putative molecular key event hypotheses, and emphasizes the value of selecting this algal species as environmentally-relevant model for this project.

6. *Omics* platforms to enable hypothesis of chemical MoA and molecular markers predictive of adverse outcome

Biological pathways involve multiple interacting domains of molecular functional units such as genes, gene products, metabolites or enzymes (Fig. 5). Perturbation of these pathways leads to a biological stress response that is often mediated by complicated feedback cycles, which in turn cannot be sufficiently described by isolated functional units such as changes in protein levels or gene expression alone [65]. To achieve optimal coverage and understanding of chemical effects, parallel interrogation of complementary *omics* 'lenses' on an organisms stress response are warranted therefore to form a more complete picture [264,265].

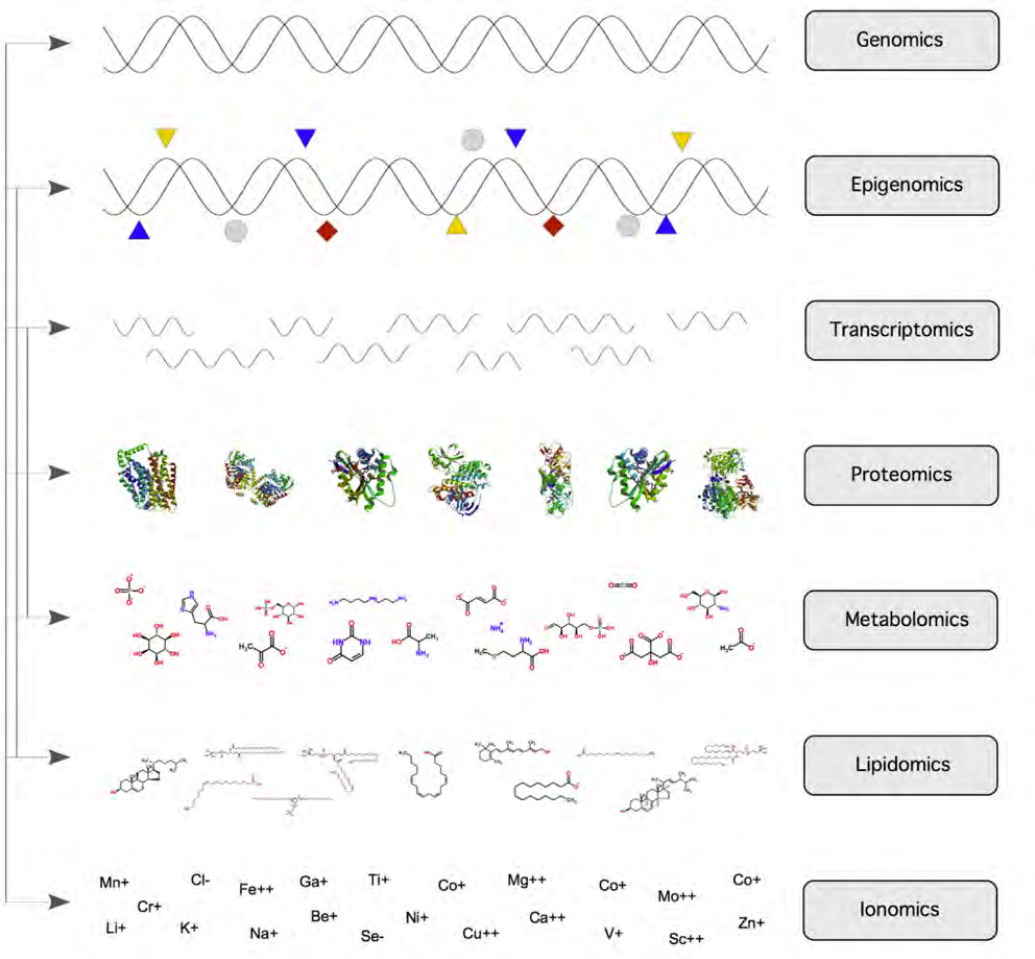


Figure 5. Domains functional units of biomolecules involved in biological processes and pathways, and the concordant omics technologies that are intended to interrogate patterns of the specific types of biomolecules. Figure from ref. [419].

6.1 Metabolomics and lipidomics

The metabolome and lipidome respectively comprise a diverse variety of low- and high molecular weight endogenous chemicals, which in turn constitute the substrates, intermediates and products of an organisms enzymatic machinery. By definition, metabolism is functionally located downstream of genes and gene products within biological pathways [266]. Consequentially, the metabolome and lipidome are the domains of molecular functional units with highest proximity to phenotype [159,267–269], and thus can be optimal descriptors of biological pathway perturbation and chemical MoA [270].

Metabolomics and lipidomics apply state-of-the-art technology to record global metabolite or lipid levels in samples. Ideally, these technologies can combine comprehensive coverage, minimal sample preparation requirements, rapid analysis time, low chemical group bias, high sensitivity, -resolution, -dynamic range, and -compound identification capacity [271]. As relatively nascent *omics* branches though, no single platform can provide all these requirements singularly, and a number of different platforms for analysis of metabolic phenotypes have established themselves with varying degree of applicability for specific purposes (Fig. 6). Overall, current bottlenecks are laborious and time-consuming processes of metabolite and lipid annotation, and unavailability of reference standards [272]. However, continuous optimization efforts are made towards overcoming these, along achievement of ever higher sensitivity and resolution in analyses [270].

Direct-infusion mass-spectrometry (DIMS) enables untargeted and unbiased ‘shotgun’ metabolomics and lipidomics profiling of a sample, via complementary assays featuring only minimal preparational and operational differences. For DIMS, a solvent-resuspended sample extract is introduced into an ionization source without prior chromatographic separation of analytes to grant shorter analysis time. The generated positive or negative analyte ions are transferred through ion optics and mass filters to the mass analyzer for detection of ion-specific mass-to-charge values (*m/z*). Utilization of high-resolution high-sensitivity mass analyzers for DIMS, such as orbitrap (e.g. Thermo Fisher Orbitrap Elite MS instrumentation), provides high accuracy in measurements of analyte *m/z* during data acquisition of unfractionated

extracts for metabolomics [273,274]. Inherent to the simultaneous *m/z*-analysis of thousands of ions during direct sample infusion are matrix effects, e.g. signal suppression of low-concentration analytes by high-concentration analytes in the mass analyzer, and concomitantly increasing probability of analyte *m/z* overlap and decreasing sensitivity and accuracy in analyzing complex biological sample matrices [274,275]. However, such can be overcome by application of spectral selective-ion-monitoring stitching (SIM-stitch) strategy to grant analysis of wide dynamic ranges of *m/z* values while ensuring high mass accuracy, resolution and sensitivity of orbitrap analyzers [276]. Resulting increased runtime and required sample volumes can be satisfactorily compensated by sample introduction via nano-electrospray ionization source (nESI) applying minimal sample flow rates [276,277].

Despite certain reduced capability for peak annotation of e.g. isomers and intrinsic problems with identification, nESI-SIMstitch-DIMS stands out from other platforms as a highly effective approach for its primary purpose of untargeted 'shotgun' metabolomics, featuring lower cost while ensuring comprehensive analysis

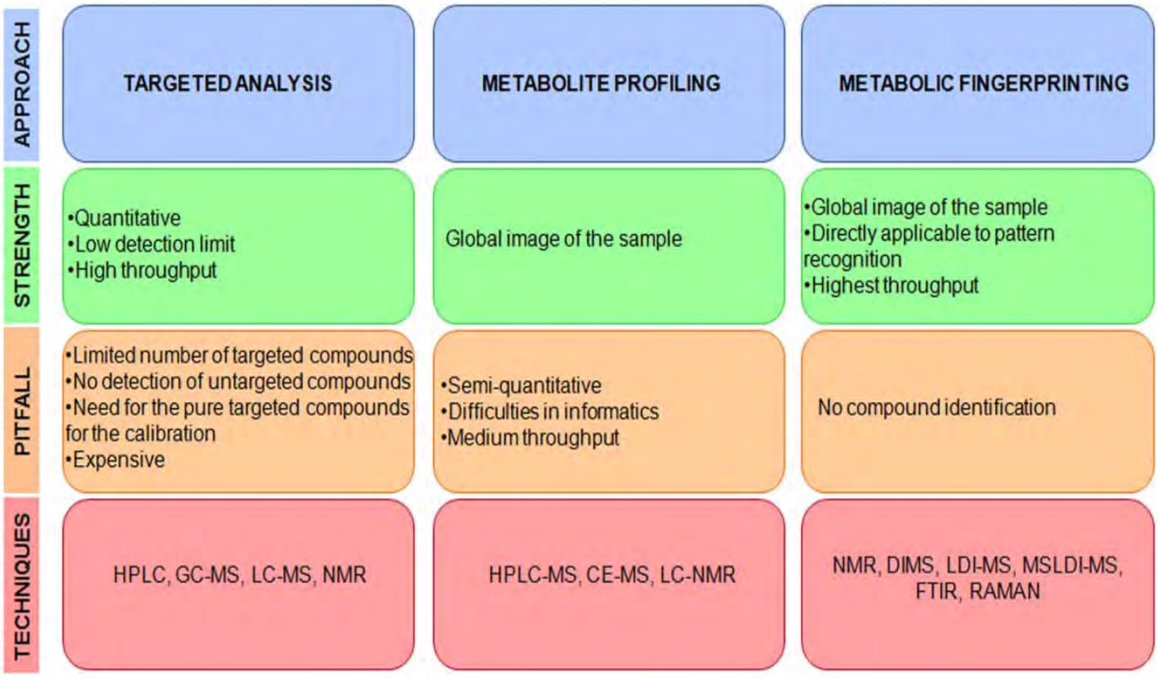


Figure 6. Overview of the different main approaches to targeted mass spectrometry and untargeted metabolomics and lipidomics analyses. Juxtaposed are their specific technologies, strengths and pitfalls in application. Figure from ref. [569].

performance and increased coverage of analytes, shorter analysis runtime and thus higher sample throughput, requiring less sample pre-treatment, and avoiding chromatographic bias [159,278–281]. Specifically, when using sophisticated mass analyzers such as orbitrap, additional characterization and annotation of *m/z* features of interest can be established using selective fragmentation (MS^n) strategies in follow-up studies of untargeted metabolomics. As additional value to this work, DIMS has been repeatedly and successfully applied to analyze untargeted metabolite and lipid fingerprints of algae extracts [273,282–285], increasing tailored applicability to this project.

6.2 Next-generation-sequencing transcriptomics

Changes in gene transcripts represent another facet of the molecular response of an organism to environmental stressors, and hence are a prime lens for scrutinizing perturbed biological pathways while maintaining proximity to genotype in analysis. The study of pan-genomic gene expression (transcriptomics) has been applied over the last decades to a diverse array of research areas - including evolutionary biology and phenotypic plasticity, ecological research, personalized medicine, and more recently human and environmental toxicology [141,176,286–289].

The field was long limited by its requirement for *a priori* knowledge of a sequenced genome (e.g. microarray technology), which led to radical restrictions and bias of analysis [290,291]. However, the advent of next generation sequencing (NGS) technologies and their operational independence from *a priori* sequence information, ever-growing public availability of sequenced genomes to annotate gene products, and continuous efforts to improve data processing and interpretation methods have revolutionized transcriptomics to a high-content and high-throughput tool with great potentially value to modern environmental toxicology [290,292,293].

The various NGS technologies grant precision and accuracy in analysis similar to real-time quantitative polymerase chain reaction technology [219,294], next to high sample throughput, decreased cost and time for analysis, and reduced analytical artefacts [295]. RNA sequencing (RNA-Seq) has become an umbrella term for a

number of NGS platforms supplied by different sequencing technology developers (Table 1) to perform various tasks, such as *de-novo* transcriptome assembly or gene expression analysis.

Table 1. Overview of common NGS technologies and their characteristics. Each platform provides advantages and disadvantages towards specific purposes such as *de-novo* transcriptome assembly or low-level transcript detection. Table adapted from ref. [296].

Platform	Illumina MiSeq	Ion Torrent PGM	PacBio RS	Illumina GAIIx	Illumina HiSeq 2000
Instrument Cost	$128 K	$80 K	$695 K	$256 K	$654 K
Sequence yield per run	1.5-2Gb	20-50 Mb on 314 chip, 100-200 Mb on 316 chip, 1Gb on 318 chip	100 Mb	30Gb	600Gb
Sequencing cost per G	$502	$1000 (318 chip)	$2000	$148	$41
Run Time	27 hours	2 hours	2 hours	10 days	11 days
Reported Accuracy	Mostly > 1 in 1000	Mostly 1 in 100	< 1 in 10	Mostly > 1 in 1000	Mostly > 1 in 1000
Observed Raw Error Rate	0.80 %	1.71 %	12.86 %	0.76 %	0.26 %
Read length	up to 150 bases	~200 bases	Average 1500 bases	up to 150 bases	up to 150 bases
Paired reads	Yes	Yes	No	Yes	Yes
Insert size	up to 700 bases	up to 250 bases	up to 10 kb	up to 700 bases	up to 700 bases
Typical nucleotide requirements	50-1000 ng	100-1000 ng	~1 µg	50-1000 ng	50-1000 ng

Illumina RNA sequencing technology uses cDNA sequences complementary to generated fragments of extracted sample RNA, which are ligated with sample-specific adapter sequences (library generation). These ligated sequences are introduced to a flow cell where they bind with surface-attached oligomers, and are amplified by initial polymerase-driven chain extension and repeated cycles of enzymatic bridge-amplification. The tight clusters of formed amplification products are cyclically sequenced using optical signals from hybridizing fluorescently-tagged nucleotides.

The different available platforms are again tailored for specific purposes in relation to cost of analysis. The long read lengths of PacBio's single molecule sequencing technology for instance show great applicability for *de-novo* genome or transcriptome assembly in short runtimes at a relatively high cost [296]. Illumina RNA-Seq platforms (e.g. HiSeq-4000, Mi-Seq) and their short-read RNA fragment analysis were developed earlier than comparable technologies in the field, and had the opportunity to evolve for longer stretches of time [296]. Thus, Illumina's sequencing technology is accredited with outstanding performance and flexibility for a variety of applications (despite relatively small drawbacks such as longer runtimes or proportionally higher background noise) - specifically for low-cost, high-throughput and high-accuracy study of pan-genomic gene expression, while featuring lower false positive error rates than comparable platforms and higher sequencing depth to allow low-level transcript analysis [290,296–300]. As benefit to this project, Illumina RNA-Seq has prior been repeatedly and successfully applied to explore responses of the algal transcriptome to various environmental influences and stressors [221,264,301,302].

6.3 Integration of multiple omics data

The different *omics* layers and their analytical platforms have varying advantages and disadvantages regarding their applicability to, and precision and accuracy in a given problem formulation. Towards deducing chemical MoA and hypothesizing predictive biomarkers of apical endpoints (e.g. key events in AOPs), the combination and integration of multiple complementary *omics* data (Fig. 7) is sensible to yield a realistic representation of biological systems and their perturbation [165,303]. Studying metabolism and gene transcription in an integrated approach does not and cannot lead to an association of each measured metabolic- to a transcriptional change, however a response close to molecular phenotype can be anchored in its functional root response close to genotype, establishing indication of toxic mechanism [159,269,304]. Integration of *omics* data from untargeted metabolic and transcriptional profiling has been performed successfully in ecological studies [142,220,305–308] and

more importantly in various investigations of chemical effects in human or environmental toxicology [250,304,309–315].

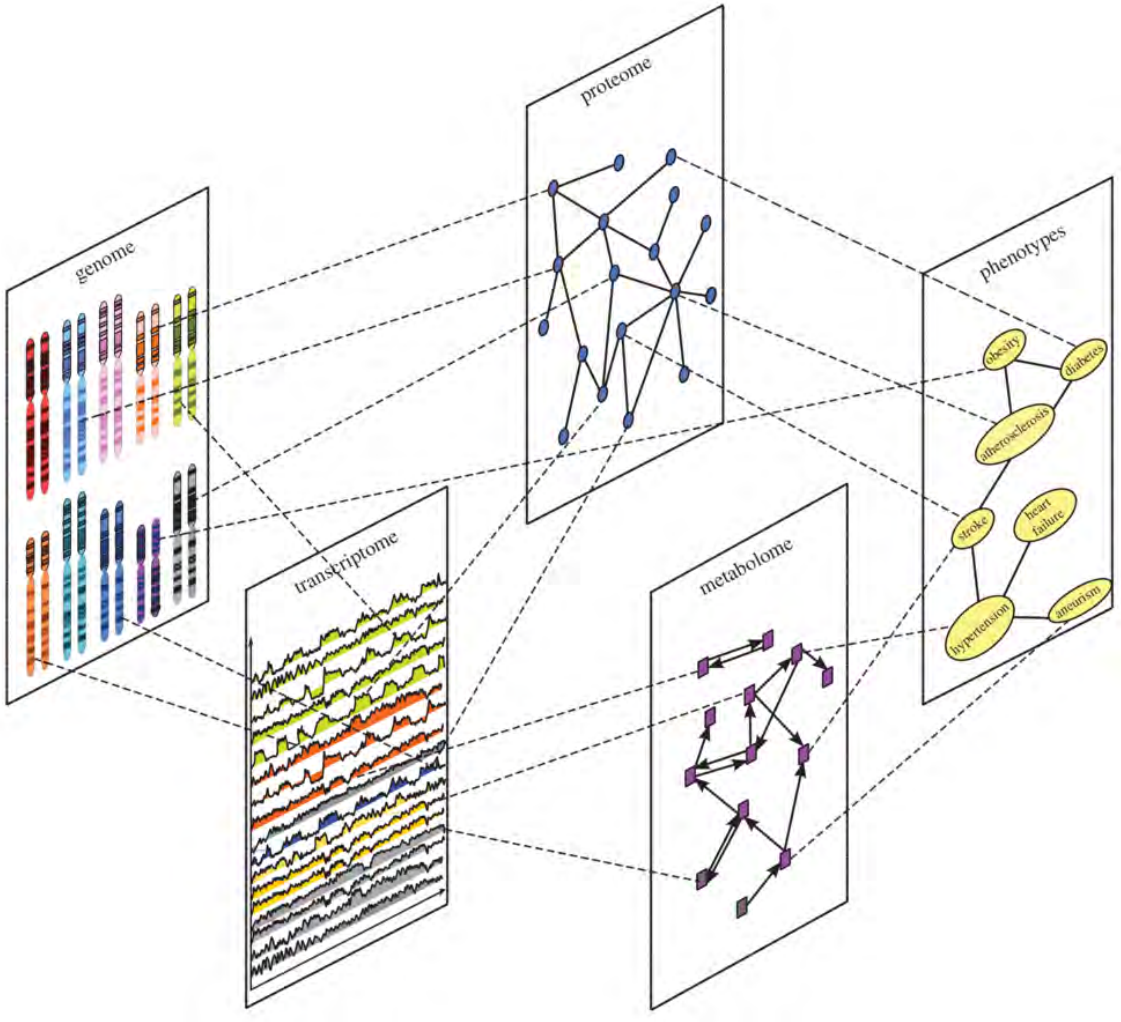


Figure 7. Inter-relation of the different domains of molecular functional units, and by extension omics layers, in the description of adverse molecular and apical phenotypes. The adverse phenotypes are here depicted for various human health aetiologies, but the schematic can be used synonymously for apical endpoints of an organism relevant to environmental hazard assessment, such as growth inhibition in algae. Figure from ref. [309].

The ever evolving computational tools relevant to integrate data from multiple *omics* platforms open up the opportunity to shed light on potential molecular mechanisms and toxicological effect patterns from a perspective impossible to achieve from an isolated *omics* analysis [265,316,317,318]. Exploratory data- and time-course analysis can discern wider patterns of toxicant-induced changes on highly-dimensional and multivariate datasets such as those covering the metabolome or the

transcriptome. Commonly applied statistical approaches here comprise principal-component analysis (PCA) to perform dimensionality reduction of the thousands of variables gained through omics into small subsets of variables that cause the essential majority of variability in the dataset, partial least squares discriminant analysis (PLS-DA) to extract the variables most important for group separation between exposure groups, or basic statistical testing using two- (Welch's t-test for low sample size) or multi-group comparisons (ANOVA) of spectral peaks for significant differences. Hierarchical clustering, another common tool in multivariate data analysis, conducts an iterative (hierarchical) comparison in similarity of samples based on numerical differences in the measured spectral peaks and transcripts of the samples, which can be applied to pinpoint groups of variables behaving quantitatively similar independent of sample group- or analytical time-point membership. These methods are applied using open-source software such as R and SLIDE [331, 509]. To efficiently utilize an experimental design employing multiple analytical time-points, the software MetaboClust [501] and R package maSigPro [510,511] amongst other published tools are highly valuable in identifying and hierarchically clustering spectral peaks or gene transcripts with similar time-expression/-intensity profiles along dose-dependent changes of spectral intensity or transcript levels across exposed toxicant concentrations.

More in-depth interpretation of the here yielded results can be gained through application of more sophisticated bioinformatics approaches. Metaboanalyst [332] grants putative annotation of spectral peaks to plant metabolites such as *Arabidopsis thaliana*, and enables pathway-overrepresentation analysis of identified groups of spectral peaks and putative annotations to the Kyoto Encyclopedia of Genes and Genomes (KEGG). The iDEP interface [508] aids interpretation of transcriptomics data, enabling differentially-expressed-gene (DEG) analysis between toxicant exposure groups, applying the DESeq2 R package [502,503]. Further, iDEP offers parametric gene set enrichment analysis (PGSEA), a novel multi-group approach to generally-applicable gene set enrichment analysis (GAGE). PGSEA performs gene set enrichment analysis, filters out non-significant gene sets by permutation testing, performs a multi-group comparison of variance (ANOVA) using the generated variable enrichment z-scores, and finally ranks gene sets by standard deviation i.e. variability

of the z-scores, in order to achieve biologically-meaningful insight [508, 446]. Gained gene sets from PGSEA or DEG can thereafter be checked for gene enrichments on biological pathways of a selected species, such as the *C. reinhardtii* genome from the Joint Genome Institute gene ontology database[1]. Lastly, a concatenated table containing both putatively annotated spectral peaks and transcripts of interest can be submitted to generally applicable set enrichment analysis on KEGG pathways using pathview software [500,506,507], to gain the most leveraged and biologically conclusive analysis of an existing multi-omics dataset of toxicant-induced changes on an organism such as *C. reinhardtii*.

Provided a suitable experimental design, an integrated approach utilizing DIMS and Illumina RNASeq platforms leveraged by the computational integration of generated metabolomics, lipidomics and transcriptomics datasets applying discussed or further available statistical bioinformatics approaches should be able to provide the sufficient sensitivity, resolution and accuracy to enable robust and reproducible diagnosis of chemical MoA and discovery of biomarkers predictive of apical endpoints in algal populations.

[1] http://www.jgi.doe.gov/

7. The research goal and scientific objectives of this project

The work in this project was conducted with the view to facilitate more frequent and assured application of *omics* technologies in environmental hazard assessment, by attempting to address two practical requirements for regulatory acceptance as described in Section 4. These are (1) the establishment of tailored experimental designs and testing systems effective for *omics*-driven diagnosis of chemical MoA and hypothesis of putative key events in AOPs, and (2) the associated demonstration that *omics* applying developed approaches can in fact reliably and reproducibly deduce chemical MoA and suggest such key events of importance to hazard assessment. A more specific perspective was assumed to enable clear boundaries of the carried-out work to achieve the overarching research goal:

> **To develop and trial an integrated multi-*omics*-driven algal toxicity testing approach for hypothesis of acute chemical MoA and putative molecular key events to support construction of AOPs.**

The following scientific objectives were identified in order to successfully achieve the research goal:

- **I.** Outline a tailored experimental design that is effective for *omics*-driven chemical MoA diagnosis and molecular key event hypothesis in algal toxicity testing.
- **II.** Develop and validate a rigorously-defined algal exposure system suitable to support the specific requirements of the outlined experimental design.
- **III.** Apply the developed toxicity testing approach to selected model toxicants as an attempt to diagnose acute chemical MoA and hypothesize putative molecular key events to support construction of AOPs.

This thesis document has been structured according to the following chapter outline:

- Chapter 1 serves as introduction to the research topic, and lays out the research goal and scientific objectives of the project.
- Chapter 2 describes the general methods and materials employed throughout the project. Further, it outlines the developed tailored experimental design for multi-*omics*-driven chemical MoA and molecular key event hypothesis in algae, along the detailed considerations and criteria that were taken into account in its conception (**Scientific Objective I**).
- Chapter 3 describes the development and evaluation of a rigorously-defined *C. reinhardtii* exposure system that is suitable to fulfil the specific requirements of the above experimental design (**Scientific Objective II**).
- Chapter 4 and 5 comprise proof-of-concept case studies for applying the developed experimental design and algal exposure system to two selected model toxicants, featuring either well-described primary chemical MoA (Ch. 4), or poorly-understood MoA in algae (Ch. 5). This was to demonstrate capability of the approach to diagnose chemical MoA and hypothesize putative molecular key events to support construction of AOPs (**Scientific Objective III**).
- Chapter 6 provides a general discussion and conclusions of the overall project, discusses the limitations and applicability, and indicates potential for future work.

Chapter 2

Experimental design, methods and materials

1. General methods and materials

1.1. Algae culturing

1.1.1. Agar culture and preparation of growth medium

Axenic *Chlamydomonas reinhardtii* Dangeard (1888) CC-125 wild type mt+ was purchased from the Culture Collection of Algae and Protozoa (CCAP, Dunbeg, UK). The strain was maintained heterotrophically on agar plates (1.5% w/v agar in tris-acetate-phosphate media) on laboratory shelves at 23 °C until liquid inoculation.

A modified *Chlamydomonas* growth medium (CGM) was developed as described in Chapter 3, based on Sueoka's high salt medium supplemented with Kropat's trace elements [319,320] with the following modifications. The final concentrations of the divalent inorganic salts $CaCl_2*2H_2O$ and $MgSO_4*7H_2O$ were increased to 50 mg/L and 100 mg/L, and the concentration of total phosphates was reduced by 92.5% to 54 mg/L KH_2PO_4 and 108 mg/L K_2HPO_4 to decrease both palmelloid formation and mass spectrometric ion suppression due to phosphate accumulation in *C. reinhardtii* cells [238,321–323]. To increase inorganic carbon levels, the growth medium was supplemented with 500 mg/L Na-HCO_3. As *C. reinhardtii* growth is optimal between pH 5.5 to 9 [324,325], pH was adjusted to 6 to shift carbon equilibrium towards photosynthetically-available carbonic acid species [326]. To retain buffer capacity for a photosynthesis-driven change in medium pH, CGM was supplemented with 20 mM MOPS buffer, similar to ref. [238]. The growth medium was sterilized by 0.22 µm-filtration to avoid degradation of MOPS, salt precipitation and shift of the carbon equilibrium caused by autoclaving [327].

1.1.2. Inoculation of liquid test cultures

Inoculation of stock cultures, open-flask experimental and vial experimental cultures were conducted as individually described in Chapters 3, 4 and 5. Overall, agar cultures were inoculated in 35 mL CGM within foam-bunged 250 mL wide-neck glass flasks for inoculation of initial liquid stock cultures. Cultures were incubated in a

Multitron Pro rotary shaking incubator (Infors HT, Bottmingen-Basel, Switzerland) at 25°C and 200rpm orbital shaking. Lighting conditions were either set as constant lighting (non-synchronized cell cycles), or as a 12h:12h light:dark cycle (synchronized cell cycles), as described individually in each chapter. Light color temperature was 8500K. Algae were adapted to this lighting and autotrophic growth conditions in liquid cultures for at least 120h prior to experiments.

Further experiments were conducted in a tailored vial exposure system as developed in Chapter 3 (Fig. 8). Briefly, before start of individual experiments, cell cultures were concentrated by centrifugal separation at 1200-g for 3min (Eppendorf 5920r, Eppendorf UK). The supernatant was decanted, and cells were resuspended as quadruplicates in CGM (or toxicant-spiked CGM for exposure experiments) in clear 10.5mL glass vials with aluminum cap inlay (T101/V4, Scientific Glass Laboratories, UK) to yield a final cell concentration of $7.5x10^5$ cells/mL and 10% total gas phase volume within each vial. Vials were capped and incubated for 24h, rolling free on a lined tray in the rotary incubator to maintain cell suspension. Exposure to individual toxicants, specific sampling time-points, sample size and amount of harvested cell suspension for downstream analyses are described individually in each chapter. For each sampling event, vials were of sacrificial nature to maintain carbon equilibrium.

Culture cell density for inoculations was scrupulously controlled and growth rates measured in technical duplicate using CASY TT cell counting technology (Roche Innovatis AG, Switzerland), which operates via electric pulse area analysis to count suspended particles.

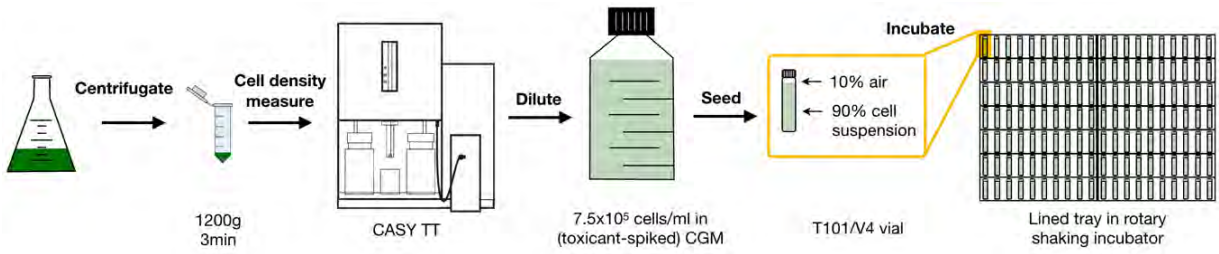


Figure 8. Individual steps for centrifugal concentration, cell density measurement, dilution, seeding of *C. reinhardtii* cell cultures into T101/V4 vials, and incubation of vials on a lined tray. Biological replicates in vials were generated from independent flask cultures.

Growth rates were calculated as

$$GR = ln(\frac{CD_{24h}}{CD_{Inoculation}})/\Delta t$$

where CD = cell density determined by CASY. With Δt = 1 day, the formula can be simplified to

$$GR = ln(\frac{CD_{24h}}{CD_{Inoculation}})$$

For exposure experiments, % growth rate inhibition was calculated as

$$GRI = \frac{GR_{Control} - GR_{Exposed}}{GR_{Control}} * 100\%$$

1.2. Direct-infusion mass-spectrometry (DIMS) metabolomics and lipidomics

1.2.1. Sampling procedure

Modifying the procedure in ref. [235], algal cell suspensions were quenched by injection into an equivalent volume of -78°C 70:30 methanol:water (HPLC-grade, Fisher Scientific, UK) solution in 15mL tubes over dry ice. Quenched cell suspensions were centrifuged at 3800*g* and -11°C for 3min, and the supernatant aspirated. The number of cell pellet washes was first optimized in a pilot experiment (see results in Chapter 3), a single pellet wash was determined as optimal and used for all further experiments in this project. The wash comprised of resuspension of the cell pellet in 10mL of -20°C 35% methanol:water, then repeating the centrifugation and supernatant aspiration (described above). Between centrifugation and aspiration steps, samples were stored in a custom mobile thermal bath between -20°C aluminum beads to minimize metabolic activity and avoid freezing of suspension and thus risk of cell lysis caused by lower temperatures. After aspiration, pellets were flash-frozen in liquid nitrogen, and all samples stored at -80°C until metabolite and lipid extraction.

1.2.2. Metabolite and lipid extractions

Biphasic metabolite extractions were performed with a final solvent ratio of methanol:chloroform:water (Chloroform HPLC-grade, Fisher Scientific) of 2:2:1.8 [328]. Cell pellets were thawed in randomized subsets of 24 tubes on ice, resuspended in 970µL ice-cold 70:30 methanol:water, and transferred into ice-cold homogenization tubes with 0.5 mm glass beads (VK05, Stretton Scientific, UK) on ice. Homogenization efficiency was found to be optimal using 0.5 mm glass beads as compared in an initial experiment (see Chapter 3), and thus used for all further experiments. Samples were immediately homogenized at 6800rpm for 2x15sec bursts using a Precellys-24 tissue homogenizer (Bertin, Montigny-le-Bretonneux, France). Samples were placed back on ice for 2min, then the supernatant (742µL) was transferred to a 1.8mL glass vial (aluminum-lined caps) containing 795µL of ice-cold 1:2 water:chloroform, to yield the final solvent ratio of 2:2:1.8. Vials were vortexed for 30sec and centrifuged for 15min at 2585g at 4°C to achieve phase separation. Half the polar phases each were aliquoted to two 2mL Eppendorf tubes using a glass syringe for metabolomics of the polar metabolite fraction for each untargeted assays using positive or negative ion mode. The nonpolar phase was aliquoted to a 1.8mL glass vial using a different glass syringe for untargeted lipidomics analysis. Syringes were washed in methanol or chloroform, respectively, between samples. Polar aliquots were dried in a SPD11V SpeedVac sample concentrator (Thermo Fisher Scientific, Waltham, USA) at room temperature, nonpolar extracts were dried using a nitrogen evaporator (VLM, Bielefeld, Germany). Extracts were stored at -80°C until reconstitution in injection solvent (see below). The same procedure was performed to generate an extraction blank sample for every phase aliquot.

1.2.3 Direct-infusion mass-spectrometry (DIMS)

Sample preparation, direct infusion mass spectrometric analyses and data processing were performed after the procedure of Ref. [276]. Reconstitution solvents for the polar fraction were prepared as 80:20 methanol:water containing 0.25% v/v formic acid (98%; VWR, Lutterworth, UK) for positive ion mode and 80:20 methanol:water containing 20mM ammonium acetate (98%; VWR, Lutterworth, UK)

for negative ion mode. Reconstitution solvent for the nonpolar fraction was 3:1 methanol:chloroform containing 5mM ammonium acetate. To maximize the number of reproducibly detected *m/z* features, the dilution of the reconstituted algal extracts was first optimized using polar extracts (see results in Chapter 3). A reconstitution volume of 50µL injection solvent was found to result in the maximal number of unique *m/z* features post-processing, therefore this option was used for preparation of all further samples.

Reconstituted samples were vortexed for 30sec, centrifuged at 22,000g for 10min, and 10 µl of each sample was combined into an intra-study quality control (QC) sample pool stored on wet-ice. All samples (biological, blank, QC) were plated as technical quadruplicates (10µl volume) on 384-well Abgene microtiter plates (Eppendorf, Stevenage, UK) in randomized order. Samples were bracketed by two QC samples at each beginning and end of each plate and interspersed by a QC samples at every 10^{th} position. Plates were sealed with aluminum foil and stored at 4°C until analysis. Untargeted metabolomics and lipidomics analyses were performed using an Orbitrap Elite mass spectrometer (Thermo Fisher Scientific, Waltham, USA) with prefixed direct-infusion nano-electrospray ionization (nESI) device (Triversa; Advion Bisociences, Ithaca, USA) controlled by Chipsoft software (Advion Bisociences, Ithaca, USA). Samples were cooled to 10°C during the analytical run.

Polar and nonpolar fractions of samples were run in either positive or negative ionization mode, respectively, as described individually in Chapters 3, 4 and 5. Acquisition conditions were for positive ion mode: 7µl of sample was aspirated and delivered to the chip-based nESI with a rate of 300nl/min, 0.3psi backpressure and voltage of +1.5kV (positive ion mode), or -1.5kV (negative ion mode). Voltage was supplied to the chip to maintain a stable current of 100 to 300nA. Sample acquisition was controlled by XCalibur software (Thermo Fisher Scientific, Waltham, USA) using an optimised spectral stitching method [276] to achieve increased sensitivity of the mass spectrometer towards low-concentration metabolites and increased resolution as compared to full scan collection of untargeted metabolomics and lipidomics data in DIMS.

1.2.4. Raw data processing and exploratory statistical analysis

Individual SIM-windows of samples were stitched into single mass spectra ranging 50-620 m/z for the polar assays and 190-1200 *m/z* for the nonpolar assay [276]. Spectra were ≥75% replicate filtered, global peak aligned with a 2ppm error tolerance, purity-filtered (peak bin-membership = 1), extraction blank filtered, QC-based locally-estimated scatterplot smoothing- (LOESS) signal corrected [329], and ≥80% QC sample-based peak filtered. Features with ≥20% missing-values were filtered out, and probabilistic quotient normalization applied [330]. RSD values for each *m/z* feature and median RSD were calculated for quality control of the data, and features in QC samples with RSD values >30% omitted from the data. For multivariate data analysis, missing values imputation (k-NN) was performed and the generalized log (glog) transformation applied. Outliers were removed if their measurements exceeded the 95% confidence interval derived for all the biological samples, within each dataset. Statistical tests (Welch's *t*-test, Kruskal-Wallis test, ANOVA) were performed using R [331] and the R-Stats base package [331], PCA and PLS-DA conducted using MetaboAnalyst [332]. Further data analysis steps were undertaken as described in the individual chapters.

1.3. Illumina transcriptomics

1.3.1. Sampling procedure and RNA extraction

Cell suspensions were centrifuged in 4mL cryovials at 2,600*g* for 3min at 23°C, the supernatant aspirated and cell pellets flash frozen in liquid nitrogen. Sample were homogenized using QIAshredder columns (Qiagen, Hilden, Germany) which was found to supply optimal homogenization yields in an initial comparative experiment (See Chapter 3). Total RNA was extracted using RNeasy Plant Mini Kit (Qiagen, Hilden, Germany), and genomic DNA removed using RNase-Free DNase Set (Qiagen, Hilden, Germany), both as per manufacturer's instructions. Extracted total RNA was eluted in 20µl of RNAse-free water (Qiagen, Hilden, Germany) and stored at -80°C. Estimation of total RNA concentration in RNA extracts samples was done using a Nanodrop-8000 Spectrophotometer (ND-8000-GL; Thermo Fisher Scientific,

Waltham, USA). Aliquots of each sample were diluted to 5ng/µl and tested upon an Agilent Tapestation 2200 (G2964AA; Agilent Technologies, Stockport, UK) using High-Sensitivity RNA screentape (5067-5579; Agilent Technologies, Stockport, UK) to ascertain that the RNA Integrity was of sufficient quality for downstream analyses (RNA integrity number equivalent RINe > 6.5).

1.3.2. Illumina RNASeq

Samples were purified by use of the NEBNext® Poly(A) mRNA Magnetic Isolation Module (E7490L; New England Biolabs, Ipswich, USA) immediately prior to library construction. All RNA libraries were produced using the Biomek FxP (A31842; Beckman Coulter Ltd., High Wycombe, UK) with NEBNext Ultra II Directional RNA Library Prep Kit (E7420L; New England Biolabs, Ipswich, USA) and NEBnext Multiplex Oligos for Illumina Dual Index Primers (E7600S ; New England Biolabs, Ipswich, USA), using manufacturers instruction and 500ng of total RNA. Constructed libraries were assessed for quality using the Tapestation 2200 with High Sensitivity D1000 DNA screentape (5067-5584; Agilent Technologies, Stockport, UK). Multiplex library clustering and sequencing was performed upon the HiSeq4000 by BGI Copenhagen. Read counts were generated using paired-end strategy with reads of 50bp length and 5 million reads per sample. All samples were multiplexed, the multiplex was sequenced on two lanes for technical replication [333]. Data were delivered as *.fastq format files.

1.3.3. Raw data processing and statistical analysis

Trimmomatic v0.32 [334] was used to process raw reads to remove adapters and poor quality reads. FastQC v0.11.8 software[2] was used to check read quality and generate quality plots. The reference genome of *C. reinhardtii* v5.5.42 [186] was

[2] bioinformatics.babraham.ac.uk/projects/fastqc

downloaded from ensembl genome database[3], including non-protein coding genes. Gffread [335] was used to correct and change gff3 to gtf format, and STAR aligner v2.6.0 [336] was used for mapping reads. Resulting BAM files were used to generate read counts using featureCount software [337]. In-house R scripts were used to merge read counts of samples from the two lanes by summation and change format for downstream analysis. Steps for further data analysis are described in the individual chapters.

[3] plants.ensembl.org

2. Outlining the experimental design for *omics*-driven chemical MoA and putative molecular key event hypotheses

To optimize the capability of the experimental design to effectively hypothesize on chemical MoA and molecular key events for aiding construction of AOPs using the model *C. reinhardtii*, a number of criteria and parameters were considered (Figure 9). This section briefly discusses important considerations and justifications for the experimental design in line with Scientific Objective I of this thesis, and lists the requirements which the physical algal exposure system subsequently needed to fulfil to be suitable to support it.

2.1. Overall strategy for showcasing omics-driven MoA and key event hypothesis

2.1.1. Multi-omics driven fingerprinting of the algal stress response

As presented in Chapter 1, combined fingerprinting of the algal metabolome, lipidome and transcriptome during toxicant exposure appeared adequate to reveal molecular changes diagnostic of acute chemical MoA and hypothesize on putative for molecular key events to support construction of AOPs. This was here conducted using nESI-SIM-stitch-DIMS and Illumina HiSeq4000 platforms, characteristics of which are detailed in Chapter 1. The application of each however required a minimum of extractable *C. reinhardtii* / algal biomass per individual sample to generate reproducible signal and high-quality data, which needed to be confirmed experimentally (see Chapter 3) and supplied by the exposure system for each biological replicate.

2.1.2. Selection of the specific molecular algal stress responses that were subjected to *omics* analysis during this project

Molecular effects of toxicity (i.e. chemical MoA) were the primary subjects of *omics* interrogation in this investigation. Selection of these was guided by Scientific Objective III., i.e. showcasing *omics*-driven chemical MoA and putative molecular key

event hypotheses. For increasing generalizability of and confidence in the proposed approach, this was conducted from two opposite perspectives (Chapters 4 and 5).

First, to enable comparability of *omics*-discovered toxicological information to existing knowledge and thus ‘calibrate’ the data analysis approach, the herbicidal MoA of carotenoid synthesis inhibition was selected as a well-described acute chemical MoA. Carotenoid biosynthesis is a pigment synthesis pathway generating critical intermediates and pigments to enable photoprotection and functional coloration in algae and the wider plant kingdom, thus conveying environmental relevance [338]. Various inhibitors of metabolic reactions in carotenoid biosynthesis are commercially available herbicides, and the caused chemical perturbations are well-described biochemically [339–342]. Evaluation of chemical-induced stress profiles measured with *omics* by comparison to existing knowledge thus promised to be an adequate starting point for trialing the here described experimental approach

The second perspective assumed was *de-novo* generation of information – the hypothesis of chemical MoA and putative molecular key events in AOPs from *omics* data using a toxicant with poorly-understood toxic effects in algae. Baseline toxicity describes the molecular effects on organisms of a class of non-reactive chemicals which are ubiquitous in industrial applications - approximately 60% of all industrial chemicals globally are estimated to primarily exhibit baseline toxicity [343]. A molecular mechanism of toxicity has to date not been elucidated in the plant kingdom.

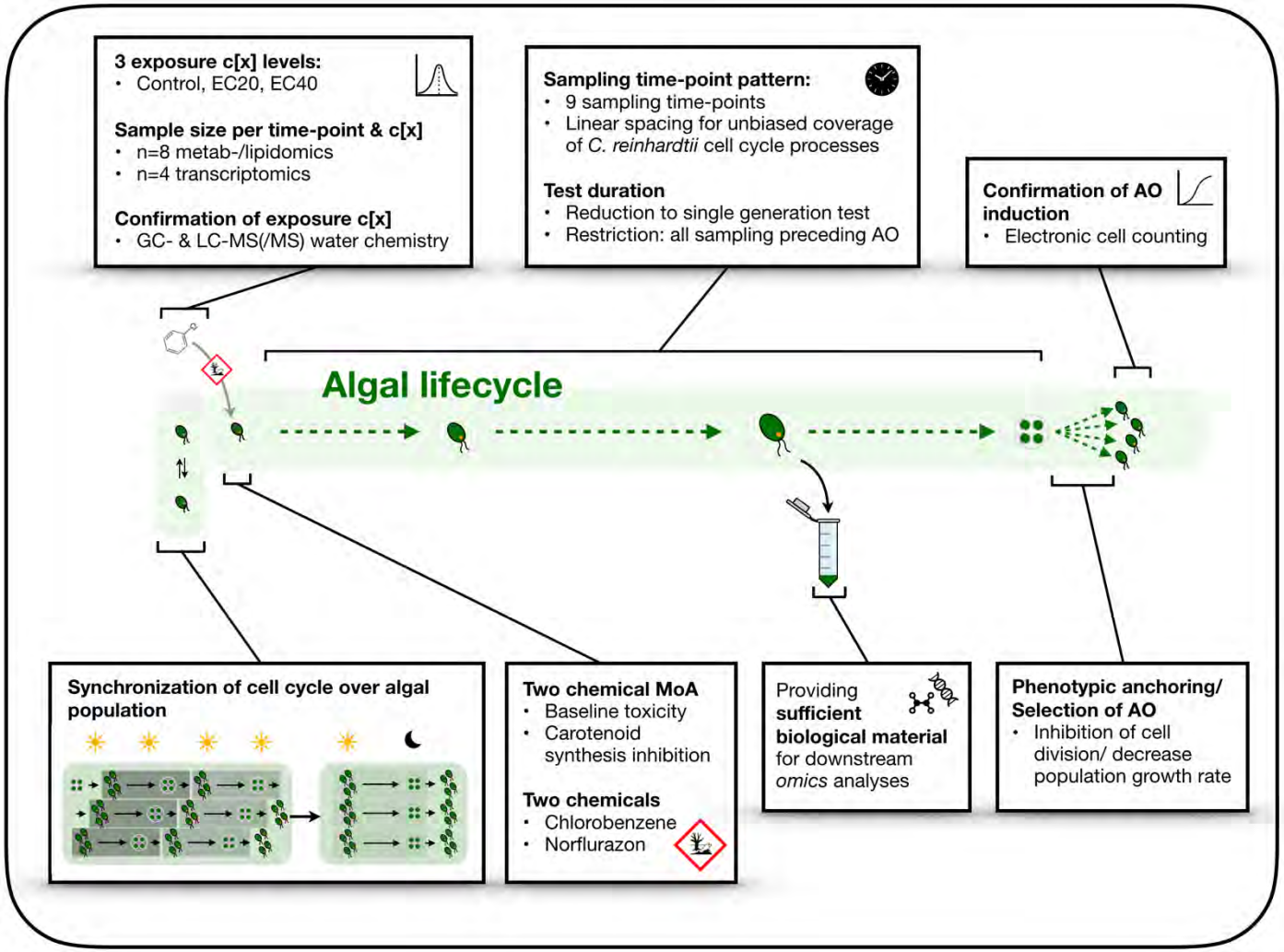


Figure 9. Abstract overview of the experimental design chosen for the project, including remodeling of the algal growth inhibition test to a single-generation test on synchronized cell populations, description of the time-series sampling profile, factoring or replication and exposure concentrations, selection of chemical MoA and model toxicants, selection and quantification of AO induction, and requirements for generation of biological material for downstream omics analysis.

2.1.3. Maximizing applicability to chemical space, and selection of model toxicants

A set of model toxicants grouped was selected for the chosen chemical MoA with regard to financial feasibility and available time for carrying out experimental work. A small selection of toxicants along a more rigorous experimental investigation of the same is generally preferred for mechanistic investigations [168]. Further, the algal exposure system was required to feature coverage for a maximal chemical space, i.e. have capacity to reproducibly test various test compounds of varying physio-chemical properties, such as volatile or poorly water-soluble chemicals [79,344]. Two suitable chemicals, one for each of the selected MoA, were selected after reviewing a large set of candidate chemicals belonging to each chemical MoA grouping. Chlorobenzene is a nonpolar baseline toxicant belonging to the halogenated aromatic organic compounds. Its speculated molecular non-specificity [345,346], recalcitrance against catabolism in aquatic organisms [347], and high volatility (K_H = 3.7E-3 atm*m^3/mol [348]) render it a promising model for generating *de novo* information on baseline toxicity in algae using a tailored exposure system. Norflurazon (4-chloro-5-(methylamino)-2-(alpha, alpha, alpha-trifluoro-m-tolyl)-3(2H)-pyridazinone) is a known inhibitor of the enzyme phytoene desaturase in algae and plants, and belongs to the carotenoid synthesis inhibitor herbicide class. Norflurazon is characterized by poor water-solubility (S = 33.7mg/L), and similarly low aquatic biodegradability [349]. The effects of the inhibition of the target enzyme is well-understood [339,350,351], knowledge on off-target and downstream effects of norflurazon on the other hand is scarce [34,252], rendering norflurazon an ideal candidate for confirmation of existing and generation of *de novo* toxicity data.

2.2. Aligning experimental design with assumptions of the AOP concept

2.2.1. Phenotypic anchoring

A structural assumption of the AOP framework is that the molecular effects driving adverse phenotypical endpoints occur temporally prior to the latter. To align an experimental design for hypothesis of acute chemical MoA and putative molecular key events to support construction of AOPs, molecular signatures indicative of chemical exposure needed to be biologically linked to the adverse phenotype (i.e. adverse outcome AO), resembling the terminal anchor of the cause-effect chain of perturbation [108,165,352–355]. This phenotypic anchoring serves two purposes when considering novel methodologies for application in hazard assessment. First, it establishes mechanistic association of molecular to apical effects, so that abstract molecular phenomena can be considered predictive of regulatory endpoints per se. Second, it achieves a degree of comparability to existing test practices in order to judge and facilitate their applicability [49,353,356–358].

For this project, the AO of algal growth inhibition (determined as decrease in population growth rate) was selected from a panel of endpoints commonly applied in environmental toxicology (Table 2). Compared to other proxy endpoints, algal growth inhibition has a direct association to population health (population-level AO), a clear linkage to organism-level AO (rooted in inhibition of cellular division and equivalent of reproductive output), is reflective of algae's ecological importance in aquatic food webs, and an established phenotypical endpoint in chemical safety assessment [359,360]. Further, this AO was simple to determine by automated cell density measurements post cell division events.

Table 2. Commonly applied endpoints on higher levels of biological organization for measuring algal toxicity induced by chemical compounds. Juxtaposed are type of endpoint, variables measured, required instrumentation and degree of biological insight gained.

Type	Endpoint	Variable measured; instrumentation required	Biological insightfulness
Sub-apical endpoints	Lipid accumulation as stress response	Lipid body size; FACS of lipid dyed cells	Only spurious association with chemical MoA
Whole-cell or population apical endpoints	Photo-respirative inhibition	Oxygen evolution; specific physical setup for chemical, optical or mechanical sensors	Proxy measure for cellular metabolism; may be confounded by chemical MoA
	Inhibition of cell division (decrease of population growth rate)	Cell density; automated cell counting or hemocytometer	Direct relation to reproductive output
	Reduction in total population biomass	Dry biomass; e.g. ammonium-bicarbonate method [361]	Direct relation to reproductive output
		Chlorophyll absorbance; spectrophotometer	May be confounded by chemical MoA or by high-cell density self-shading; only partially correlated with biomass [362]
		Chlorophyll-fluorescence; spectrophotometer or pulse amplitude modulated (PAM) fluorescence devices	
		DIC uptake; CO_2 sensors	Proxy measure for population growth, may be confounded by chemical MoA
		Carbon fixation; C^{14} labelling	Proxy measure for population growth, may be confounded by chemical MoA
	Elemental composition	CNP ratio; elemental analyzer	Only spurious association with chemical MoA

Induction of AO in an exposure experiment ultimately needed to be confirmed to establish authenticity of recorded molecular fingerprints as stress profiles resulting from toxic insult. For such confirmation, twofold measures were integrated into the experimental design. First, AO induction (inhibition of population growth) was measured post cell division using CASY electronic cell counting, which is optimal regarding accuracy and counting speed for relatively homogenous cell populations of

structurally integer cells [363]. Second, associated exposure levels of the model exposure chemicals were confirmed by quantifying analytes in cell suspensions using gas-chromatography mass spectrometry (GC-MS, for volatile chlorobenzene) or liquid-chromatography tandem mass spectrometry (LC-MS/MS, for norflurazon).

2.2.2 Remodeling of the conventional algal growth inhibition exposure system

Conventional regulatory guidelines for conducting algal growth inhibition tests are provided by OECD and ISO [359,360]. In brief, exposure of an algal species in exponential growth phase to a range of toxicant concentrations over a period of 72h under constant lighting conditions is prescribed. Measurement of biomass, cell density or other apical endpoints is performed at 24h-intervals. Though invaluable for standardization of environmental hazard assessment in the past, said guidelines were originally not designed towards the purpose of discriminating molecular markers of toxicological interest. For the hypothesis of chemical MoA and key events predictive of algal growth inhibition, molecular stress signatures of algal cell populations needed to be related to the terminal occurrence of the AO. This bore two important corollaries for an effective experimental design - the population-wide synchronization of cell cycle and physiological cell release, and the alignment of total test duration to cell cycle.

2.2.2.1. Synchronization of algal cell cultures

Exposure and effect analysis of multiple life-stages within the same experiment are commonly avoided in environmental toxicity assessments due to introduction of confounding factors (differing activity of biological processes, vulnerability *etc*.), and initial matching of test organisms by life-stage is prescribed in the standardized OECD test criteria for virtually any employed environmental model organisms such as water flea [364,365], birds [366,367], bee [368,369], annelids [370,371], springtail [372], molluscs [373], amphibia [374,375] or fish [376–380]. As one of the few cell-based *in vivo* systems, test conditions for microalgal bioassays [359] do not have such requirement of initial matching of life-stage/cell-cycle. The conventional green algae growth inhibition test as prescribed by OECD and ISO [359,360] comprises exposure

of a microalgal species (commonly *Raphidocelis subcapitata* or *Desmodesmus subspicatus*) in exponential growth phase to a range of toxicant concentrations over a period of 72h under constant lighting conditions.

For the recommended test species and other green algae (e.g. genera *Chlamydomonas*, *Scenedesmus*, *Chlorella*), the phenomenon of population-wide light-driven synchronization of cell cycle and cellular division in form of multiple-fission cycles has been described extensively for cultures grown in defined alternating light:dark conditions [381–383]. Upon onset of light, metabolic energy is allocated to photosynthesis and cellular growth processes until the environment becomes deprived of light. Transition to dark triggers multiple rounds of replication and mitosis, release of daughter cells (zoospores) from the parent cell (zoosporangium), and basal respiration until the onset of light [384–386]. The degree of entrained coordination between cells in a given population is close to absolute [381].

The importance of aligning cell cycles across cell populations is common practice in other cellular models such as yeast or human cells [387], and its importance has been emphasized before for investigations into biological processes [388,389]. In algae, prior research efforts have leveraged the benefits of synchronized cultures for investigations into cell-cycle processes [197,386,390–393], for minimization of variability in metabolic profiles [394], for the improvement of toxicokinetic models [120,395], or for select toxicological studies [253–255,396,397]. However, only limited considerations of, and no conceptual argumentation for, the explicit importance of utilizing synchronized cell cultures for toxicological investigations appear to have been made thus far. As per the algal growth inhibition assay guidelines [359,360], algae are grown under continuous lighting conditions. Such culturing regimen leads to misalignment of cell cycle in algal populations and non-synchronized cell cultures, and thus non-specificity of molecular signatures from a particular sampling time-point to specific biological processes [398]. It stands to reason that such loss of the temporal dimension in analysis of biological and toxicological pathways diminishes potential for deduction of key events mechanistically associated with adverse outcomes [167,168]. Further, the recommended constant lighting conditions are not representative of natural environments, and overall lead to suboptimal metabolic efficiency in

microalgae [399]. Synchronizing cell cycles in algal populations (Fig. 10B) aligns time-dependent cell cycle processes between all cells of an algal population [381,386], and in theory should grant the desired benefit of aligning potential chemical-induced perturbations of specific cell cycle processes over the population. Overall, expected benefits include increased specificity of *omics* signatures from given sampling time-points to molecular functions and their perturbations, decreased confounding signals from overlaying cell-cycles, strongly improved capacity to investigate molecular temporal cause-effect chains inducing AO, and ultimately increased precision in hazard assessment using *omics.*

On these grounds, a specific investigation of the benefit of synchronized algal cultures for insightfulness of *omics*-profiles was warranted (conducted in Chapter 3). Consequently, *C. reinhardtii* cultures in this project were adapted for at least 120h to alternating light:dark conditions (12h light:12h dark cycling) prior to experiments to achieve cell cycle synchronization, and were tested under such conditions (Fig. 10B).

2.2.2.2. Alignment of test duration to cell cycle and introduction of the single generation test format

The conventionally-applied 72h exposure duration (Fig. 10A) may prove additionally unfavorable in uncovering acute chemical MoA, and may generate high redundancy in information when using synchronized cell cultures. The 72h test duration prescribed by test guidelines [359,360] was designed to assess hazard via apical-endpoint induction using non-synchronized algal populations. In the context of capturing molecular effects of toxicity (indicative of acute chemical MoA) predictive of adverse outcome, this prescribed duration becomes arbitrary.

Ultimately, for a mechanistic investigation of acute toxic effects and determination of molecular key events that are predictive of successive induction growth inhibition, the answer does not lie in the absolute length of the exposure duration but in the biological anchoring, i.e. the duration which is minimally required to link molecular stress responses to successive phenotypical effects in a cause-effect chain. Work in this research project was restricted to investigation of acute toxicity (as manifested by the AO of growth inhibition) in algae induced by chemicals; investigation into other

manifestations of toxicity (including chronic-, trans-generational effects, etc.), or suggesting key events predictive of these, was not in the scope of this project. The definition of 'acute' toxicity/ MoA was here the significant inhibition of population growth of *C. reinhardtii* upon completion of a single cell cycle/generation. Molecular effects predictive of AO need to temporally precede the induction of adverse phenotype [400], in turn molecular effects occurring after AO induction are only relevant to next cell cycle/generation and were considered redundant molecular information in the induction of the preceding AO.

Reducing the test duration to encompass a single algal generation from newly-released cells (first life-stage after division) up to cell division (temporal locus of AO), was considered sufficient for an acute chemical MoA investigation. The test duration of exposure experiments in this project was thus anchored to a single algal generation up the actual window of cell division/ AO occurrence (Fig 10B). This is assumed to harbor all molecular effects causative of AO in acute chemical MoA, i.e. the onset of cellular division in a single generation of *C. reinhardtii* cells in a given light:dark cycle. For the algal exposure system to enable such experimental design, experimental

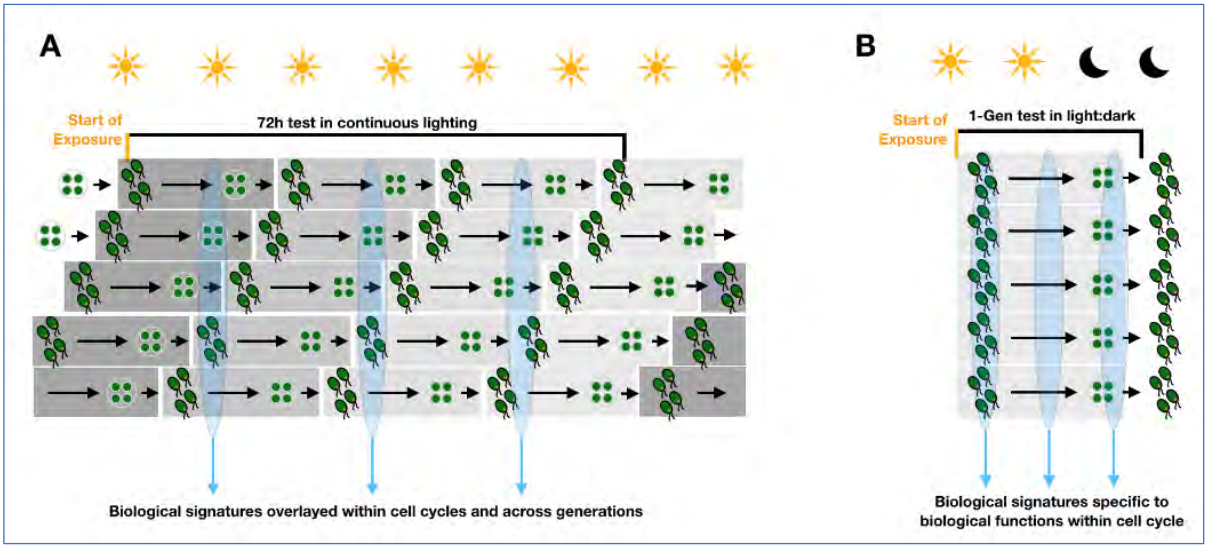


Figure 10. Abstract representation of the conventional and remodeled algal exposure schemes. (A) The conventional 72h test for algal growth inhibition conducted in continuous light conditions [12,360] generates samples with molecular signatures averaged over population and algal generations. The (B) single-generation test with light:dark cycling (effecting synchronized cell cultures) generates samples with precise molecular signatures specific to biological processes in cell cycle, and molecular effects are clearly linked to induction of a single window of AO induction (i.e. cell division events).

discovery of the locus of cell division in *C. reinhardtii* under experimental conditions was warranted (conducted in Chapter 3).

2.2.3. Factoring and balancing temporal resolution, concentration-response analysis and replication

Scientific and regulatory circles called for *omics* experimental designs suitable for mechanistic investigation [49,146,157]. Specifically, these need to reflect scalable setups to support extensive factoring of exposure concentrations, sampling time-points and replication to optimize biological insight into toxicological effects [161–164,401]. Such investigations into concentration-response dynamics and temporal resolution of toxicological effects can be challenging and are often neglected [165,402].

2.2.3.1. Need for time-resolved investigation of toxicological processes in algae

Chemical MoA and associated AO-induction (as captured by AOPs) in organisms are no static phenomena and represent processes occurring over time [403]. Moreover, critical chemical MoA-dependent perturbation of molecular processes (e.g. such as those occurring over algal cell cycle) may be restricted to narrow time windows during exposure, or effects on different *omics* layers may be phase-shifted in time - and not measurable at single time-point designs [404]. Thus, time-course analysis was required for detailed characterization of dynamics and kinetics of molecular stress response. Unfortunately, this is rarely conducted in a well-resolved manner in *omics* research [108,165]. Two main considerations stood out for outlining the time-series that should be employed in this project.

First, the overall sampling pattern required careful construction, including the allocation of start and end of time-series in relation to *C. reinhardtii* lifecycle, and the spacing of the sampling time-points. This pattern should be free of prior assumptions, i.e. unbiased for *omics* discovery, and encompass a maximum of *C. reinhardtii* life-stages between preceding and successive clonal generations. In practice, the time-series required an anchoring of the earliest-feasible sampling time-point past the test

culture inoculation so as to not intervene the state of light-driven *C. reinhardtii* cell cycle progression, and anchoring of the latest-feasible time-point capturing nuclear division of cells, the biological event immediately preceding cellular division (cytokinesis) and thus window of AO occurrence. The latter was experimentally determined in Chapter 3.

Second, the frequency of sampling required consideration. Possibility of discriminating transient or phase-shifted molecular effects (e.g. downstream effects within different *omics* layers) from permanent changes (e.g. steadily increasing metabolite accumulation) increases with sampling frequency. On the other hand, physical feasibility of sampling played a role. A single time-point entailed cell harvest for multi-omics analyses (metabol-, lipid- and transcriptomics) along water chemistry samples for confirmation of exposure concentrations. The resulting time interval required for the sampling procedure needed to be less than the spacing between time-points. Moreover, requirements of the data analysis strategy that was used to evaluate generated time series had an impact on selection of time-point frequency. Here, the project endeavored to distinguish molecular differences between chemical exposure levels over time-course by using an optimal combination of statistics- and biology-driven analysis strategies [405]. These included exploratory multivariate analysis, determination of significant features (differential gene expression, significance testing), time-profile and phase-shift clustering, and metabolic pathway and gene ontology enrichment analyses of identified clusters and significant differences. Specific computational algorithms to conduct time-profile analysis of single- or multi-*omics* data overall perform best with temporal resolution of more than 8 sampling time-points [406]. Lastly, temporal resolution had to be balanced both with per-group replication (see below) to retain statistical power [404], and with available project funding. Considering the above, the experimental design was adjusted to accommodate a linearly-spaced sampling pattern to minimize missing of effect windows associated with biased patterns [400], with a moderately high number of 9 sampling time-points (Fig. 11).

The first sampling time-point was anchored to the commencement of the 12h culture illumination phase. The prior required inoculation of test cultures was not

feasible in the dark phase without exposing algae to light and initiating light-regulated cell cycle progression [200,386], whereas an inoculation of the test cultures at the prior clonal generation would have been penalized with inaccuracy in culture cell density and loss of control of exponential growth patterns at required high cell densities for the tailored physical exposure system (see Chapter 3). Furthermore, algal biological activity in complete darkness is indicated to be largely limited to mitochondrial energy metabolism, which is maintained throughout the light phase [385,407–410]. Consequently, the proposed time-frame from commencement of light phase to sporulation covered the single largest set of molecular and cellular functions within a cell cycle that chemicals may perturb. The last sampling time-point was anchored to the time of cell cycle stage of nuclear division immediately preceding cell division and potential AO occurrence, as investigated in Chapter 3, with sampling frequency increased from 1.5h to 1h for the last 3 time-points to capture specific molecular effects related to nuclear and cellular division, which are functionally related to AO induction.

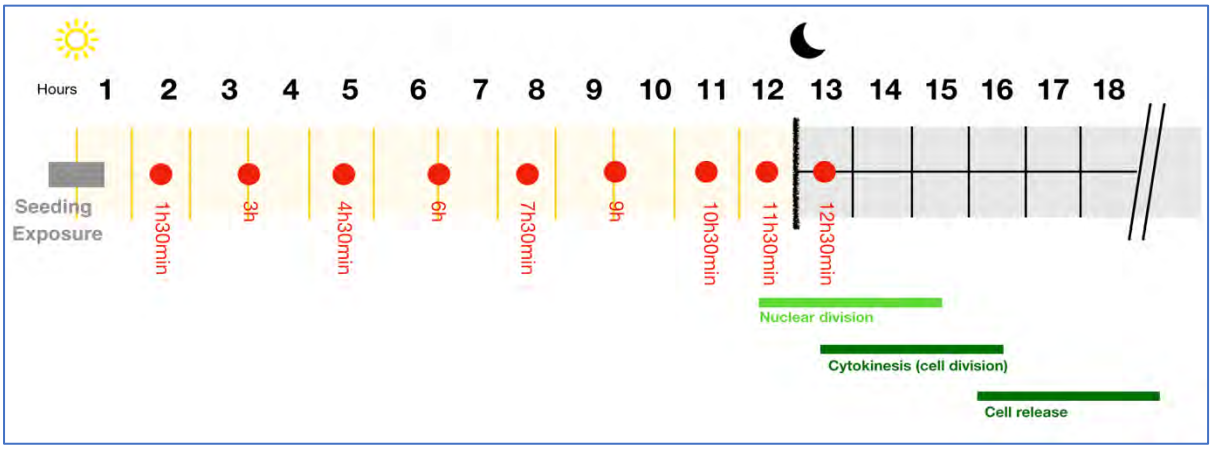


Figure 11. Schematic representation of the sampling profile and frequency aligned to the cell cycle of C. reinhardtii up to cell division (window of AO occurrence, experimentally determined in Chapter 3). Experiment comprised culture seeding and exposure to chemical-spiked growth medium and linear sampling over 9 time-points. The last 3 time-points were slightly more frequent to capture specific molecular effects related to nuclear and cellular division (cytokinesis), which are functionally related to AO induction. These occur within narrow time-windows, and normally-distributed over an algal cell populations within these windows.

2.2.3.2. Exploration of concentration-response dynamics of molecular effects

A critical criterion for increasing confidence in chemical MoA deductions and predictivity of hypothesized molecular key events for aiding construction of AOPs, and to distinguish adaptive from adverse responses, is the clear determination of concentration-response relationships [57,165,167,168,411–413]. The selection of exposure concentration levels to achieve phenotypic anchoring in this project was directed to enable overall concentration-response analysis (≥ 3 levels for indicating monotonic trends), and to induce a substantial effect size of molecular changes while avoiding acute cytotoxicity and necrotic effects in cells [414]. Accordingly, the application of 3 concentration levels (Control, EC_{20}, EC_{40})[4] was selected. Individual concentrations for chlorobenzene and norflurazon were determined by range-finding in Chapters 4 and 5.

2.2.3.3. Optimizing replication per experimental group

The main criteria for selection of replication per sampling time-point and exposure concentrations was the available funding to the project and expected variance specific to each *omics* platform. There is unclarity in the specific application of power analysis to complex multi-*omics* datasets involving multi-factorial designs (concentration levels vs. time-points). Classical power analysis applies univariate statistical tests to simple Control-Treatment designs, and existing extensions of such approaches to *omics* experiments recording highly-dimensional multivariate datasets result in low statistical power [415]. When performing exploratory data analysis employing such datasets and experimental designs as for instance in the case of chemical MoA hypothesis, the nature and extent of the expected effects is not known, and attempting an association of statistical power with biological meaningfulness using these existing methods of power analysis would thus likely result in unrealistically-high numerical estimates on required replication. Metabolomics and lipidomics sample size in human- and

[4] EC_x = Effect concentration x, i.e. concentration that induces adverse phenotype in x% of the population

environmental toxicology investigations are frequently n ≥ 5 per group. To balance maximally possible statistical power with available funding, here a sample size of n = 8 was chosen for metabolomics and lipidomics data per time-point per concentration. Funds were further limited for the more costly Illumina RNASeq platform. However, low inter-group variance in next generation sequencing data is currently well-achievable with lower sample sizes [389,406,416], thus transcriptomics sample size was restricted to n = 4. To avoid batch effects and increase data comparability, a split-sample strategy was chosen to enable analysis of a split portion of the same biological replicates with each employed *omics* platform [304].

2.3. Summary: Requirements for an algal exposure system to suit and support parameters of the outlined experimental design

Overall, the outlined experimental design had the following requirements for the physical algal exposure system, as developed in Chapter 3:

1) *Supply of sufficient C. reinhardtii sample biomass*
   - *Determination of common sample biomass ranges for each omics platform*
   - *Confirmation of these regarding high quality extractable RNA and metabolites/lipids for C. reinhardtii in this study*
   - *Adjustment of algal exposure system to supply sufficient biomass per sample*
2) *Physical scalability of exposure system*
   - *Generation of sufficient sample biomass at 9 sampling time-points, for 3 exposure concentration levels, and 8 biological replicates*
   - *Capacity for inclusion of additional replicate vessels (3 exposure concentrations, n=4) for measurement of AO induction, and additional medium sampling volume for exposure concentration analytics*
3) *Support for soluble and volatile test chemicals via a closed test system*

Further, two experimental investigations as conducted in Chapter 3 needed to be performed for a finalization of experimental design parameters:

- *Indicate the benefit of synchronized algal cultures (12:12h light conditions) for omics-based fingerprinting studies*
- *Pinpoint window of cellular division and thus of chemical-induced AO occurrence within C. reinhardtii cell cycle under experimental condition, towards allocate of sampling profile prior AO induction and specifically the terminal sampling time-point to locus of nuclear division (immediately preceding cell division i.e. AO occurrence window)*

Chapter 3

Improved Algal Toxicity Test System for Robust Omics-Driven Mode-of-Action Discovery in *Chlamydomonas reinhardtii* [5]

[5] Contents (text, data, figures, tables) of this chapter were published in *Metabolites*, DOI: 10.3390/metabo9050094 [417].

1. Introduction

Algae are internationally established test organisms in chemical risk assessment [13,184,359]. Toxicity test guidelines incorporating algae are largely focused on traditional apical endpoints such as growth rates following a 72-hour chemical exposure. By consequence, no knowledge is obtained on the causes of chemical toxicity, nor on the generality of the chemical effects on other species. Increasingly, chemical risk assessment is sought to include New Approach Methodologies (NAMs) such as *omics* technologies to improve precision in the prioritization and chemical categorization of chemicals [418]. One application of NAMs is to increase confidence in cause–effect analyses by providing mechanistic evidence on the harmful effects of chemicals. This transition, from traditional whole organism endpoint-based to molecular pathway-based (eco)toxicology, is motivated by the application of high-content transcriptomics and metabolomics, which have demonstrated a capability to discover biological processes [49,419,420].

There is an overarching need for the establishment of tailored experimental designs and testing systems effective for *omics*-driven diagnosis of chemical MoA and hypothesis of putative key events predictive of adverse outcome on one hand, and associated demonstrations that *omics* applying developed approaches can in fact reliably and repeatably deduce chemical MoA and suggest such key events in AOPs of importance to hazard assessment. To develop a robust and scalable test system for *omics*-driven discovery of chemical MoA and toxicological key events in algae, a rigorously characterized algae culturing and exposure protocol with biological processes synchronized across all cells within a test population was first required, so to minimize molecular variation for the pathway-based cause-effect assessments. The exposure system was further required to feature minimal test duration to facilitate rapid measurements, and matching of the same to an algal lifecycle to allow accurate linking of the molecular perturbations to growth inhibition to address regulatory requirements of phenotypic anchoring [49,352–354,356]. Moreover, the exposure system needed to both support testing of insoluble and volatile toxicants to increase applicability of the system to a wider chemical space, such as the here selected volatile model baseline toxicant chlorobenzene, and feature high scalability towards extensive factoring of

exposure levels, sampling time-points and biological replicates such as those required by the outlined experimental design in Chapter 2. Lastly, exposure vessels needed to supply sufficient biological material for downstream multi-*omics* analyses, while exhibiting healthy population growth parameters. The successful design of such a robust test guideline should facilitate the generation of highly repeatable, high-quality multi-*omics* data.

As discussed in detail in Chapter 2, current algal growth inhibition test guidelines [13,359] recommend culturing in constant lighting, a condition that induces rapid drift and loss of cell-cycle alignment over a population of algae that are responsive to light-regulation of the cell cycle [398]. In such a culturing regimen, samples for molecular analyses taken at any given time-point over the test duration will contain a cross-section of individual cells performing simultaneously all of the biological functions in the algal cell cycle, leading to averaged molecular signatures that are non-specific to biological functions or condition dependent perturbations (Fig. 10A). Equally, apical endpoints (e.g., inhibition of cell division in algae) will be observable throughout this time course, preventing the possibility of biological and temporal anchoring of hypothesized putative molecular cause-effect chains to the adverse outcome (AO). To emphasize the challenging nature of interpreting molecular results from such experiments, an analogy is drawn to a hypothetical rodent bioassay with inclusion of ante-natal, neonatal, adolescent, middle-aged, old-aged and pregnant animal subjects, and pooling tissue samples from all of these life-stages to infer a chemical MoA. Loss of the temporal dimension in biological and toxicological pathways diminishes potential for deduction of biomarkers mechanistically associated with adverse outcomes [421,422]. There is a logical argument that just as life stage is controlled in vertebrate and invertebrate animal testing, similar considerations should be given to algal toxicity testing, which regrettably have so far been limited in scope [394,395]. Additional to culturing in constant lighting conditions, the 72h test duration prescribed by official test guidelines (OECD, ISO) may prove unfavorable, and generate high redundancy in information, when extending the conventional algal growth inhibition test towards investigations into chemical MoA that is associated with acute growth inhibition in a synchronized cell population. Following introduction of cell cycle synchronization, the aim here was to align test duration with the algal cell cycle,

to ultimately enable discovery of key events occurring before (and that are predictive of) acute growth inhibition. Here, the prime consideration was the biological anchoring of the test duration to the life-cycle of a single algal generation (Fig. 10B).

While *omics* technologies hold considerable promise for the discovery of chemical MoA [128,156,259,423], to date the majority of *omics* studies have been too small-scale to deliver on this promise in algae research. Seminal studies in microalgal toxico-*omics* include those by Nestler et al. [424], Jamers et al. [425] and Pillai et al. [426]. However, the majority of past study designs either tended to (i) scrutinize only single snapshots of molecular perturbation [246,253,256,258–260,424], (ii) apply test durations which lack a biologically-justified anchoring of sampling time-points [251,254,255,261,262,425,427], and/or (iii) utilize non-synchronized cultures over time-course experiments [231,243,257,263,426]. Overall, new robust, miniaturized and scalable designs in routine algal toxicity testing are required to allow extensive factoring of exposure concentration and biological replication over wide a time-response surface to increase statistical power [146,428]. However, large scale studies factoring time and toxicant exposure are currently not supported by conventional microalgal toxicity test practices. For instance, recent multi-*omics* studies on *C. reinhardtii* feature experimental designs restricted in sample size, analytical methodology, and sampling time-points primarily due to lack of generatable biomass [250,427].

The challenge of generating sufficient biological material for *omics* analysis is particularly aggravated during the testing of volatile toxicants. Due to the CO_2-dependence of natural photoautotrophic growth, existing volatile test systems are incompatible with above-mentioned experimental designs. Conventional agitation- and aeration-based exposure vessel systems become highly cumbersome to maintain with increasing experimental scale, and maintenance of stable medium toxicant concentrations is difficult to non-feasible in open flask culturing. Historically, a variety of solutions has been proposed to reconcile autotrophic growth requirements with testing of volatiles, including modified flask culture with 2L air space [429], custom bipartite flasks [430], CO_2-enrichment of the flask air-space [431], no-air-space testing without bicarbonate enrichment [432–436] or with

bicarbonate enrichment [437,438], or test tubes with extremely large air space [439,440]. The application of all of the above methods to large-scale and highly-replicated multi-time-point (multi-)*omics* studies featuring extensive factoring over time and concentration levels is regrettably precluded. This is due to low cell densities and thus unfeasibly-high sampling volumina, problematic physical scalability and cost of idiosyncratic vessel set-up, disturbance of phase equilibria during repeat-sampling procedures, strong pH drift over experimental durations, and often a combination thereof.

This chapter, in line with Scientific Objective II, covers the development and evaluation of a rigorously-defined *C. reinhardtii* exposure system that is suitable to fulfil the specific requirements of the outlined experimental design (Fig. 9).

2. Materials and Methods

2.1. Algae Culturing and inoculation of test cultures

Chlamydomonas reinhardtii was cultured and test cultures prepared and inoculated as outlined in Chapter 2.

2.2. Initial optimization of C. reinhardtii homogenization yields

Initially, optimization steps were undertaken to increase extraction yields of *C. reinhardtii* metabolites, lipids and total RNA from cellular biomass towards downstream omics analyses. To maximize metabolite and lipid extraction yield, homogenization efficiency of 3 types of homogenization beads was compared. Prior to development of CGM medium (See Chapter 2 and below), algae were grown Bold's Basal medium (BMM) supplemented with 15 mg/L NH_4Cl and Kropat's trace elements ([320,441]). 20 mL of cell suspension of was sampled from exponential growth phase, centrifuged at 3800 x *g* for 3min (23 °C), and the cell pellet diluted with phosphate-buffered saline (PBS, pH 7.4; Sigma-Aldrich, Gillingham, UK) to a density of 5.25 x 10^6 cells/mL. 1 mL of the suspension was centrifuged at 3800 x g for 3min, the supernatant aspirated, and the cell pellet flash frozen. The cells were resuspended with 1mL ice-cold 71%, and the resuspension filled into the different ice-cold homogenization tubes (n=4) containing either 2.8mm steel beads, 1.4mm ceramic beads or 0.5mm glass beads (MK28R, CK14, VK05; Stretton Scientific, Stretton, UK). Samples were homogenized at 6500rpm for 2x15sec bursts on a Precellys-24 tissue homogenizer (Bertin, Montigny-le-Bretonneux, France). 750 µl of supernatant were transferred to 1.5mL tubes, centrifuged at centrifuged at 7000 × g for 3 min (4 ◦C). The supernatant was transferred to another 1.5mL tube, and diluted with 3.25 mL of ice-cold 71% methanol:water. The 4 mL sample was transferred to a quartz cuvette and optical density measured at 450nm (OD_{450nm}) as proxy to determine relative amounts of various polar and non-polar plant pigments in the liquid phase [442]. OD_{450nm} measurements were taken on a Biochrom Uv/vis Spectrophotometer (Libra S32; Biochrom Ltd., Cambridge, UK). Homogenization with 0.5 mm glass beads was found

to lead to the highest homogenization efficiency by proxy of OD_{450nm}, and was used for all further experiments in this work.

To maximize extraction yield of total RNA, three types of homogenization protocols were compared. 20 mL algae grown in BBM (see above) were sampled from exponential growth phase, centrifuged at 3800 x *g* for 3min (23 °C), and the cell pellet diluted in PBS to yield a cell concentration of 1 x 10^7 cells/mL. 1 mL (n = 4 per group) of this suspension was sampled to a 4mL cryovial, centrifuged at 2,585 x *g* for 3min (23°C), and supernatant aspirated. The cell pellet was flash frozen in liquid nitrogen, then resuspended in 450 µL RLT-buffer (Qiagen, Hilden, Germany) with 1:100 parts β-mercapto-ethanol (Sigma-Aldrich, Gillingham, UK) and thawed at room temperature. N = 4 samples were not mechanically homogenized at all, n = 4 samples homogenized using QIAshredder columns (Qiagen, Hilden, Germany), and n = 4 samples were homogenized using 0.5 mm glass beads in homogenization tubes (VK05; Stretton Scientific, Stretton, UK) using the Precellys-24 tissue homogenizer. Total RNA extraction of all sample groups was then performed using RNeasy Plant Mini Kit (Qiagen, Hilden, Germany), including genomic DNA removal using RNase-Free DNase Set as per manufacturer instructions (Qiagen, Hilden, Germany). Total RNA concentration of 20 µL eluate was measured on Nanodrop as described in Chapter 2. Homogenization using QIAshredder columns was found to yield highest homogenization efficiency regarding total RNA, and was used for all further experiments in this work. Statistical significance of differences was assessed using Welch's t-test in R software.

2.3. Determination of required biomass for omics platforms

An experiment was conducted to confirm the amounts of total RNA extractable from *C. reinhardtii* biomass and sufficient for downstream analysis by Illumina HiSeq4000 and DIMS platforms. Literature research was conducted and service providers (BGI Copenhagen, RNA sequencing service) contacted. The sufficiency of retrieved ranges of *C. reinhardtii* biomass and the associated extractable biological material were experimentally confirmed as follows. Here, prior to the development of CGM growth media (outlined in Chapter 2), algae were initially cultured in BBM as

describe above. Cells were grown under 12 h:12 h light:dark conditions to stationary phase and harvested by centrifugation at 3800 x *g* for 3min in 50 mL tubes. Statistical significance of differences was assessed using Welch's t-test in R software.

For confirmation of extractable total RNA towards transcriptomics analyses, cell pellets were diluted in BBM and cell densities measured using CASY cell counting to yield a range of total cell numbers (encompassing retrieved ranges) per tube of 1 x 10^7 cells, 5 x 10^6, 3.72 x 10^6, 2.5 x 10^6, 1.86 x 10^6, 1.25 x 10^6, 9.3 x 10^5 and 4.8 x 10^5 cells (n = 4). Cells were centrifuged, flash frozen, total RNA extracted, and RNA concentration and integrity determined as outlined in Chapter 2.

For confirmation of the sufficiency of extractable metabolites (from retrieved *C. reinhardtii* biomass recommended ranges towards metabolomics analyses), cell pellets were diluted in BBM and cell densities measured using CASY cell counting to yield a final total cell number of 5.25 × 10^6 per tube (n = 3). Cells were centrifuged at 3800 x *g* for 3min, supernatant aspirated and pellets flash frozen in liquid nitrogen. Metabolite extraction and DIMS analysis of the polar fraction was performed as described in Chapter 2. The effects of dilution of the reconstituted metabolite extracts on the detectability of unique *m/z* features in positive ion mode DIMS analysis were characterized. Polar sample extracts of triplicate samples were reconstituted in each 50 µL injection solvent (neat) and diluted 3-fold, 9-fold, 27-fold and 81-fold with injection solvent. Numbers of unique features before pre-processing (after peak alignment, including blank features), and after blank- and sample filtering that retain only features found in 100% of samples were calculated. The 'neat' resuspension volume (50 µL) yielded the highest number (4602) of unique *m/z* features after sample filter, with decreasing number of features with increasing dilution (3-fold = 3813, 9-fold = 2204, 27-fold = 1540, 81-fold = 694). Therefore, this option was used for preparation of all further metabolomics samples.

2.4. Development of a customized growth medium CGM

Sueoka's base HSM medium with Kropat's trace elements [319,320] was modified towards development of a custom growth medium CGM as described in Chapter 2. To minimize occurrence of palmelloids (non-released zoospores within parent cell membrane) and phosphate ion-suppression in mass spectrometric analysis, experimental comparisons were made between 3 different levels of phosphate supplementation, were algae were grown in 12 h:12 h light:dark cycles in CGM containing either 1.44 g/L K_2HPO_4 and 0.72 g/L KH_2PO_4 (Equivalent to Sueoka's HSM), 108 mg/L K_2HPO_4 and 54 mg/L KH_2PO_4 (92.5% reduction from HSM), or 48mg/L K_2HPO_4 and 24 mg/L KH_2PO_4 (96.6% reduction from HSM). Cells were seeded in open flasks under 12 h:12 h light:dark cycles at 1.5 x 10^4 cells/mL, and cell density was counted for > 120 h (n=4). Samples were checked for occurrence of palmelloids using CASY, the latter confirmed by light microscopy (DM750M; Leica Camera AG, Wetzlar, Germany). pH was measured using an Orion Star benchtop pH meter (A211; Thermo Scientific, Rugby, UK), and growth curves were plotted using Graphpad Prism 6 software. A further experiment was conducted, comparing pH drift (n = 2) of algal cell cultures incubated for 72h in open flasks, inoculated at 1.5 x 10^4 cells/mL over varying levels of MOPS buffer (20mM, 6.6mM, 2mM, 0.66mM) in CGM containing 92.5%-reduced phosphate levels, pH 6.

To optimize growth of *C. reinhardtii* seeded in closed vials, three experiments were conducted and algae seeded in vials as described in Chapter 2. In the first experiment, cells were grown in vials filled to the brim (no air space) over a range of inoculation cell densities from 3 x 10^5, 4.5 x 10^5, 6 x 10^5, 7.5 x 10^5 and 1 x 10^6 cells/mL, in CGM supplemented with either 250 mg/L or 500 mg/L $NaHCO_3$ and pH adjusted to 6 to shift carbon equilibrium towards photosynthetically-available carbonic acid species [326]. In the second experiment, cells were grown in vials with either 0%, 5% or 10% air-space over a range of inoculation cell densities from 7.5 x 10^5, 1 x 10^6 and 1.25 x 10^6 cells/mL with either 250 mg/L or 500 mg/L $NaHCO_3$ supplementation at pH 6. In the third experiment, cells were grown in vials at 7.5 x 10^5 cells/mL and 500 mg/L $NaHCO_3$ supplementation (pH 6) over a range of either 0%, 2.5%, 5%, 7.5%, 10%, 12.5% or 15% vial air-space.

2.5. Optimization of the sample purity for mass spectrometric analyses

Another experiment was conducted to reduce influence of sample contaminants from growth medium and consumables on mass spectrometric analyses. Here, the number of washes of the cell pellet before flash freezing was optimized in a pilot study by comparing n = 10 samples (each 7mL of 7.5 x 10^5 cells/mL from exponential growth phase) from each of three groups: no wash, single wash of cell pellet, or two washes. Samples were first centrifuged and supernatant aspirated as described in Chapter 2, then different washing regiment of the cell pellet (no wash, single or double wash) were applied per group. “No wash” cell pellets were flash frozen in liquid nitrogen immediately. For “single-“ or “double wash” groups, each wash comprised of resuspension of the cell pellet in 10 mL of –20 °C 35% methanol:water, then repeating the centrifugation and supernatant aspiration steps before flash freezing. Metabolite extractions, DIMS analysis of the polar metabolite fraction (positive ionization mode) and data processing was performed as described in Chapter 2. A single pellet wash was determined as optimal and used for all further experiments in this study.

2.6. Comparison of synchronized and non-synchronized cell cultures

The next experiment compared the metabolic phenotypes and mitotic activity of cell cultures grown under continuous lighting versus those grown under alternating 12 h:12 h light:dark cycles. Algae grown in either condition were seeded in vials as described in Chapter 2. Samples were taken at 4 h 15 min (±15 min), 8 h 15 min (±15 min) and 12 h 15 min (±15 min) post-seeding. 5.25 × 10^6 (7 mL) were taken from synchronized samples at every time-point, and sampling volumina of the non-synchronized samples were adjusted to match this cell number by prior CASY electronic cell counting. As described in Chapter 2, cells were harvested and stored at –80 °C until combined metabolite extractions. DIMS analysis of the polar metabolite fraction (positive ionization mode) and data processing was carried out as described in Chapter 2.

Over the course of this study, further samples were taken for flow cytometric measurements of genomic material in cell particles at 4 h, 8 h, 12 h and 16 h post-

seeding for non-synchronized cultures, and 3 h, 6 h, 9 h, 11 h, 13 h, 14.5 h, 16 h, 18 h post-seeding for synchronized cultures. 1×10^6 cells were sampled (n = 3), centrifuged at 7000× *g* for 3 min (23 °C), pellets washed once in 1 mL PBS, and cells fixed in 70/30 ethanol:water (HPLC-grade; Fisher Scientific, Loughborough, UK) for 24 h at 4 °C. This last step served to permeabilize cells for propidium iodide (PI) and to extract chlorophylls which might interfere with the PI emission spectrum [443]. The cells were washed again in 1 mL PBS and incubated in the dark for 30 min in 500 µL PBS containing 0.1 mg/mL RNAse-A (Qiagen, Hilden, Germany) and 0.01 mg/mL PI in water (94%; Sigma-Aldrich, Gillingham, UK). For 1×10^4 particles per sample, PI fluorescence was measured using a Becton Dickinson FACS-Calibur (488 nm excitation, bandpass filter 610/10), and analyzed using open-source Flowing Software[6] v2.5.1. Absence of chlorophyll interference was confirmed with non-stained cell samples. Due to haploidy of *C. reinhardtii* vegetative cells, discrete peaks in per-particle fluorescence intensity histograms from cells sampled at a given time were equated either to the number of genome copies present within each cell particle (zoosporangia or zoospores) post nuclear division. Fluorescence areas in between discrete peaks were assigned as cells currently undergoing DNA replication and assigned as 'S-phase'. Growth curves of both culture regimen were determined using CASY cell-counting, at 2–4 h intervals for non-synchronized cultures and at higher resolution (30 min intervals) at the light:dark transition for synchronized cultures.

For each sampling time-point, vials were of sacrificial nature to maintain carbon equilibrium. Synchronized cell culturing was determined as a preferable option to non-synchronized cultures for this project as described in the results section, and used in all further experiments in this work.

2.7. Vial Exposures for concentration-response experiments

To expose cells, quadruplicate independent culture batches of synchronized cultures were grown in open flask culture, and seeded in vials as described in Chapter

[6] flowingsoftware.btk.fi

2. Preparation steps were restricted to a maximum duration of 30 min within the onset of light phase. Culture cell density for inoculation was scrupulously controlled and growth rates measured in technical duplicate using CASY cell counting.

Experiments conducting toxicity tests on synchronized cell cultures were performed using chlorobenzene (CB, 99.9%; Sigma-Aldrich, Gillingham, UK) as a volatile substance, and 3,5-dichlorophenol (3,5-DCP, 97%; Sigma-Aldrich, Gillingham, UK) and potassium dichromate ($K_2Cr_2O_7$, 99%; Sigma-Aldrich, Gillingham, UK) as reference substances. All tests were performed with biological quadruplicates. *C. reinhardtii* was exposed to 3,5-DCP at 0, 0.6, 1.2, 2.4, 4.8 and 9.6 mg/L. Cells were exposed to $K_2Cr_2O_7$ 0.05, 0.16, 1 and 10 mg/L, using CGM devoid of the chelating agent EDTA. Cells were exposed to CB in three independent experiments at individual concentration ranges: 0, 15, 24, 38, 60, 95 mg/L (repeat 1, for range-finding); 0, 3.5, 7, 10.5, 14, 17.5, 21, 25, 37.5, 50 mg/L (repeat 2, adjusted range to encompass curve slope); 0, 1.5, 3, 6, 12, 18, 25, 36, 48 mg/L (repeat 3, for focus on environmentally-relevant lower end of concentration-response curve). 4-parameter log-logistic concentration-response modeling and effective concentration (EC) estimation was performed using open-source R software [331] and the drc package [444].

2.8. Measurement of chlorobenzene exposure concentrations over time

To measure concentrations of chlorobenzene in test medium and stability of concentrations in vials over time, algae were incubated in vials with growth medium spiked with 14 mg/L or 24 mg/L CB (nominal) for 12 h 15 min. At 0 h and 12 h 15 min, 100 µL (n = 4) was injected into 20 mL headspace vials with PTFE-lined septa (Scientific Glass Laboratories, Stoke-On-Trent, UK) containing 9.7 mL CGM and 100 µL 0.8M H_2SO_4 for fixation. Samples were stored in the dark at 4 °C. 100 µL of 10 mg/L d_5-chlorobenzene (99 atom-%; Sigma-Aldrich) in CGM was added prior to analysis (final concentration 0.1 mg/L). Headspace GC-MS was performed on an Agilent 5975B inert XL MSD, using a DB-624 column (30 m × 0.25 mm i.d. × 1.4 µm) and Gerstel Autosampler MPS2. Analytes were identified using target *m/z* = 112 and qualifier *m/z* = 77 (CB); target *m/z* = 117 and qualifier *m/z* = 82 (d_5-CB). The sample

sequence was randomized, and quantification of chlorobenzene was performed relative to d_5-chlorobenzene.

2.9. Variability characterization of the tailored closed-vial exposure system

A further exposure experiment was conducted to compare the metabolite phenotypes of synchronized cell cultures in pure growth medium (control) versus cells exposed to 25 mg/L CB, repeated three times, to characterize the metabolic variability and repeatability of data generated in the exposure vial system. Ten biological replicates for each of the control and CB groups were seeded in capped vials, incubated for 3 h, harvested, and cell pellets stored at –80 °C until metabolite extraction as described in Chapter 2. This experiment was repeated three times in identical set-up with a duration of 5d between experiments. Metabolite extraction was performed for all samples of the three repeats combined. DIMS analysis of the polar metabolite fraction (positive ionization mode) and data processing was carried out as described in Chapter 2.

Statistical tests (Welch's *t*-test, Kruskal-Wallis test, ANOVA) were performed using R and the R-Stats base package, and PCA and PLS-DA were conducted using MetaboAnalyst v4.0 [445]. Set enrichment analysis was performed with the Broad Institute Java-based GSEA tool [446]. This method calculates an enrichment score of a supplied set S of variables against test data, to determine whether variables of S occur tendentially within the *m/z* features that are high-ranking in importance for separation of phenotype in the test data. S commonly comprises elements of a biological pathway (pathway enrichment analysis), however may contain individually defined variables. Here, S comprised *m/z* features with high LFC of one biological batch, which were checked for enrichment against LFC-ranked lists of *m/z*-values in the other biological batches. Thus, it was determined whether those *m/z*-values that were responsible for LFC-driven phenotype-separation in one biological batch were equally important in the other biological batches. Strength of the enrichment was calculated using NES metric (normalized enrichment score), significance determined by estimating false-discovery rate corrected p-values using 1000-fold permutation of

the *m/z* features. *m/z* features within S deemed most impactful towards a high enrichment metric NES are referred to as the leading edge subset (LE, [446]).

3. Results and Discussion

3.1. Designating margins of minimally required biomass for omics platforms

An approximate lower margin of required *C. reinhardtii* biomass to achieve reproducible data in metabolomics and lipidomics studies has been reported at *ca.* 2-2.5 x 10^6 algal cells per assay [235,284], i.e. 4-5 x 10^6 algal cells for split-phase ion mode metabolomics and lipidomics assays. Similar values were reported for transcriptomics [221,225,386,447] or proteomics [242,253], and a recommended minimum for the desired Illumina transcriptome sequencing was indicated at >500ng total RNA per sample (BGI, personal communication). For this project, these values were slightly raised to the desired benchmark of 5.25 x 10^6 cells per sample for DIMS metabolomics and lipidomics, and to 750ng extractable total RNA per sample Illumina RNAseq. This was to allow for potential differences in applied methodology, loss of material during sampling, or extraction inefficiencies.

To confirm sufficiency of the retrieved values for downstream DIMS and Illumina RNASeq, the homogenization processes of both metabolites/lipids and total RNA were first optimized before conducting trial extractions to target desired biomass

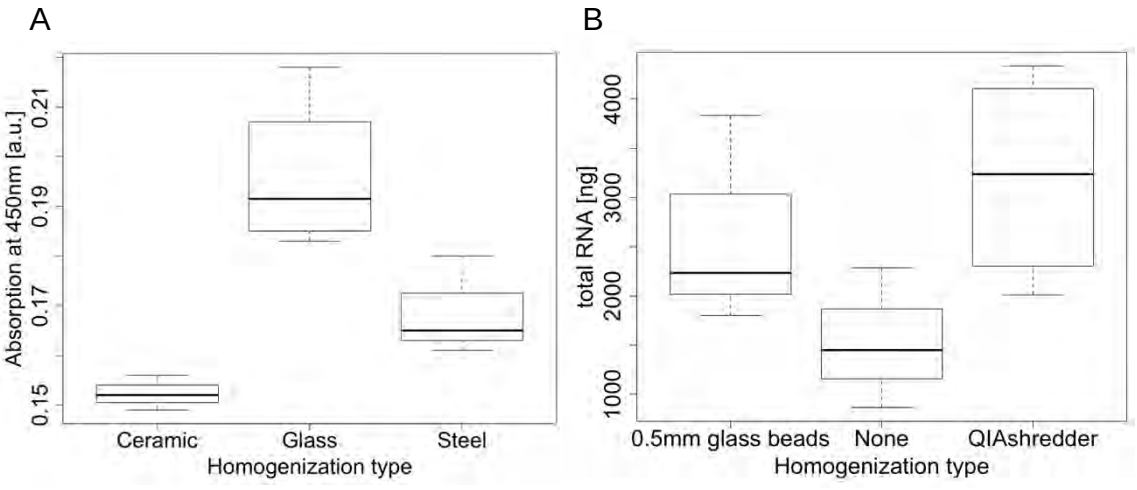


Figure 12. Comparison of efficiency of homogenization methods. (A) Downstream metabolite and lipid extraction efficiency by proxy of optical absorption (arbitrary units a.u.) at 450nm of suspended plant pigments in 71% methanol:water solution (5.25 x 10^6 cells), comparing 1.4mm ceramic beads, 0.5mm glass beads or 2.8mm steel beads. (B) Extraction efficiency of 0.5mm glass beads, QIAshredder homogenization and no homogenization, measured by total RNA extraction yields from 1 x 10^7 cells in 20 µL eluate using Nanodrop-8000.

benchmarks. Metabolite, lipid and total RNA extraction processes have been developed extensively for larger amounts of algal biomass, however less so for algal cell homogenization of small cell pellets [235,328,448]. Towards metabolite and lipid extraction, homogenization efficiency of a cell pellet containing 5.25×10^6 cells using 2.8 mm steel, 1.4 mm ceramic and 0.5mm glass bead was assessed by comparing optical density at 450nm of homogenized cell suspensions (Fig. 12A), a wavelength at which manifold polar and non-polar plant pigments are responsive in their respective absorption spectra [442]. 0.5 mm glass bead homogenization yielded a clearly observable and statistically significant maximum in OD_{450nm} when compared to ceramic or steel beads (Welch's t-test; $p = 9.94 \times 10^{-3}$, $p = 3.79 \times 10^{-2}$, respectively), and was thus selected for all further experiments. For cell pellet homogenization efficiency towards total RNA extractions, non-homogenized cell pellets of 1×10^7 cells were compared to those homogenized by Qiagen QIAshredder columns, or homogenization by 0.5mm glass beads (Fig. 12B). A reduced but non-zero amount of RNA extraction was to be expected in non-homogenized samples undergoing cell lysis by thaw-freeze processes [449] and lysis buffer. Concordantly, the relatively lowest but still substantial total RNA yields were observable for this group of samples. QIAshredder homogenization yielded the highest total RNA yields, although neither statistically significant from bead homogenization (Welch's t-test; $p = 5.15 \times 10^{-1}$) nor from no homogenization ($p = 5.8 \times 10^{-2}$). However, given ease of use of QIAshredder columns in contrast to bead homogenization and an observable trend towards higher total RNA extraction yields, this option was selected for all subsequent experiments.

Table 3. Unique *m/z* features in positive ion mode DIMS spectra, from samples featuring various degrees of dilution of injection solvent. Shown are peak numbers after alignment, after blank and after 100% sample filter (average of n = 3). A reconstitution volume of 50 µL ("Neat") injection solvent was found to result in the maximal number of unique *m/z* features post-processing.

Dilution	After alignment, incl. blank	After blank filter	After sample filter (100%)
Neat	14115	7649	4602
3x	12986	6409	3813
9x	11563	4888	2204
27x	10008	3310	1540
81x	9591	2881	694

Next, after selecting optimal homogenization procedures, the sufficiency of the desired cell number benchmarks for DIMS metabolomics and lipidomics was confirmed. N = 3 cell pellets of 5.25 x 10^6 cells were extracted, sample extracts resuspended and analyzed along 3 dilution levels in DIMS (positive ionization mode) for maximum of measurable *m/z* features. Table 3 supports the conclusion that a 50 µL resuspension volume did not induce substantial ion suppression in the mass spectrometer nor inhibit nESI spray stability. The numbers of measurable *m/z* features post data processing were within expected ranges [276] and can be assumed approximately equivalent for the negative ion assay. Following from this, a cell pellet of 5.25 x 10^6 cells was designated as a sufficient benchmark for downstream DIMS analyses.

Second, the desired total RNA yield benchmark (750ng) per sample required towards Illumina transcriptomics was translated to cell density equivalents. Total RNA was extracted from cell pellets comprising a range of 5 x 10^5 to 1 x 10^7 cells (Fig. 13A). Increases in extractable total RNA were linear with increasing cell number, despite loss of samples during extractions for some groups. RNA integrity (RINe) was > 9 for all samples, suggesting a high-quality RNA extraction process (Fig. 13B). The desired value of 750ng total RNA for downstream Illumina RNASeq was anchored here to the lower margin of 95%-confidence interval of a linear regression-model of the cell curve,

i.e. ~ 2 x 10^6 cells (Fig. 13A), in line with material amounts previously reported as sufficient for *C. reinhardtii* transcriptomics [221,225,386,447].

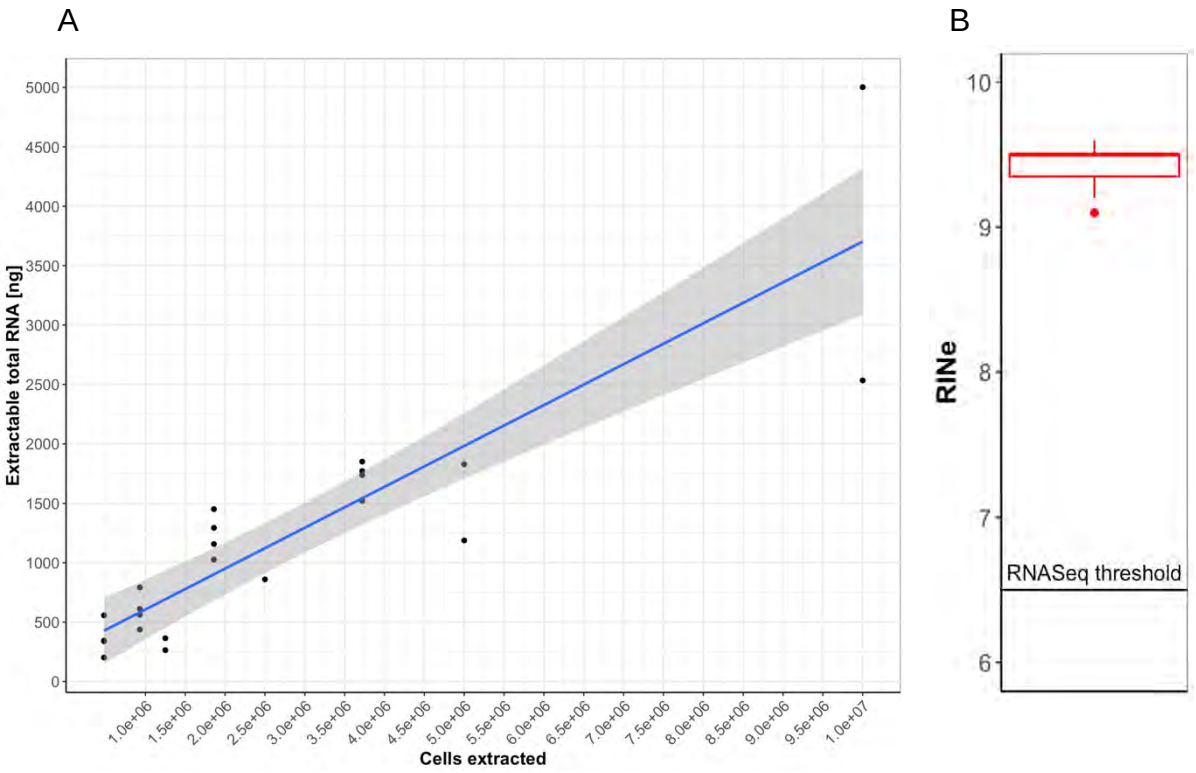


Figure 13. Scatterplot (A) of extracted *C. reinhardtii* cells vs. extractable total RNA as measured by Nanodrop 8000 (n = 1-4 per group). A linear regression line along 95%-confidence interval was plotted for all sample groups. The RNA integrity number equivalent (RINe) plotted as boxplot (B) over all groups, with indication of the minimal RINe = 6.5 threshold required for transcriptome sequencing (https://www.bgi.com/us/sequencing-services/rna-sequencing-solutions/transcriptome-sequencing/; Accessed 07/05/18).

In sum, a suitable exposure system was required here to supply 2 x 10^6 + 5.25 x 10^6 = 7.25 x 10^6 cells per individual sample. As discussed in Chapter 2, a type of miniaturized exposure vessel was further needed that could allow generation of this minimally required biomass, permit an experiment running 228 vessels in parallel (3 concentration levels, 9 time-points, n = 8 per group, +12 vessels for AO measures), and have low to no volatilization loss of volatile chemicals over test duration. Among commercially available vessels, T101/V4 10.5mL glass vials were found as optimal compromise between vial size/ scalability (for free-rolling incubation on a custom-made lined vial tray) and contained liquid and gas volumina.

3.2. Development of a customized growth medium for closed-vial exposures

A custom growth medium CGM was developed to enable generation (upscaling) of healthy *C. reinhardtii* biomass in open flask culture and in subsequent closed-vial experiments. Sueoka's high salt medium HSM [319] was used as foundation for a high-nutrient density medium, and a revised trace element supplementation was selected for maximizing population growth rates [320]. First, calcium and magnesium salt concentrations were increased above equivalent concentrations of the chelating agent ethylenediamine-tetra-acetic acid (EDTA), to avoid induction of palmelloid cell aggregates of exponentially dividing cells that remain within the mother cell membrane after division and generally progress slowly through cell cycle [322,323,450]. The latter would confound molecular signatures and their temporal trajectory when interrogating algal cell populations for cell-cycle specific effects indicative of acute chemical MoA.

Phosphate ion levels were reduced to further decrease palmelloid formation and ion-suppression in mass spectrometry [238,321,323,450]. Renberg et al. [238] reduced phosphate concentrations by 94% of HSM medium, inducing no apparent inhibitive effect on *C. reinhardtii* population growth rates. These values were used here as benchmark, and comparative incubation experiments to minimize phosphate supplementation were conducted (Suppl. Fig. SI-1) of *C. reinhardtii* grown under 12h: 12h light:dark cycles in open flasks, containing CGM along HSM-equivalent- ("High phosphate"), 92.5%-reduced-, or 96.6% reduced-phosphate supplementation. Complete lack of palmelloids was achieved with either of the reduced-phosphate supplementation, as compared to high phosphate levels, where presence of cell aggregates was appreciable in CASY and confirmed via light microscopy. Slight lag of population growth in *C. reinhardtii* grown on even higher reduction of phosphate levels (98%-reduction from HSM) was previously observed [238]. A similar effect was appreciable here for the 96.6%-reduced phosphate group (Suppl. Fig. SI-1), additionally growth did not reach the same ultimate cell density at begin of stationary phase. Maximal growth rates were achieved in 92.5%-reduced phosphate medium, hence this level of supplementation was selected for all further experiments.

To increase pH-buffering capacity resulting from reduced phosphate levels, the growth medium was further supplemented with MOPS buffer. A comparison of various levels of MOPS supplementation resulted in pH drift of >0.5 per day in open flasks for all groups except 20mM (Fig. 14), and strong instability of pH over 72h for 2.2mM MOPS and below. pH drift in culturing for test preparation or over test duration should ideally not exceed <0.5 as per OECD test guideline [12], larger pH drift up- or downwards may change toxicant bioavailability or affect healthy growth of algae [451,452]. Accordingly, 20mM MOPS supplementation was selected for all further studies.

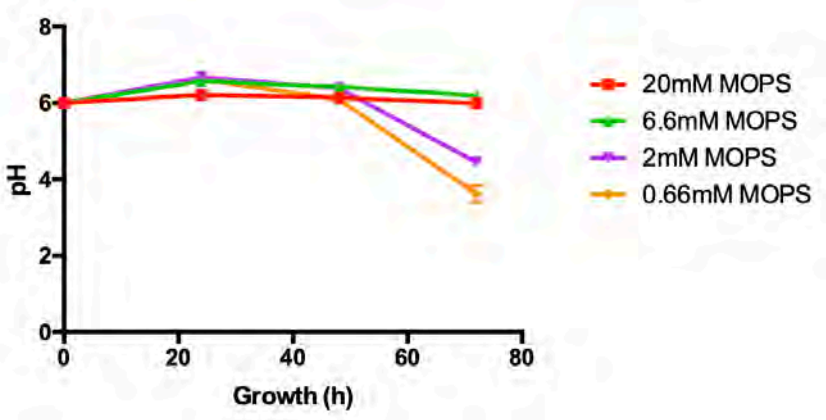


Figure 14. pH drift of *C. reinhardtii* cell suspensions in CGM containing 92.5%-reduced phosphate supplementation (open flask culturing), over varying MOPS-buffer supplementation (n=2). Only 20mM MOPS supplementation showed a pH drift of acceptable magnitude as per OECD guideline below 0.5 over the targeted test duration of 24h, which was hereafter used for all further experiments.

Next, CGM was modified to achieve healthy growth parameters under experimental conditions in selected T101/V4 vials, and to enable supply of sufficient biomass of ≥ 7.25 x 10^6 cells per vial for downstream *omics* analyses. The mean true vial volume of T101/V4 vials, including volume of the inner neck and cap structure, was experimentally determined as 11.14mL (n = 10; Suppl. Table SI-T1). $NaHCO_3$ supplementation was added to CGM to increase photosynthetically-available carbonic acid species at pH 6, specifically towards growth in vials without air exchange [326,437]. In an initial range-finding experiment using open flask culturing, $NaHCO_3$-

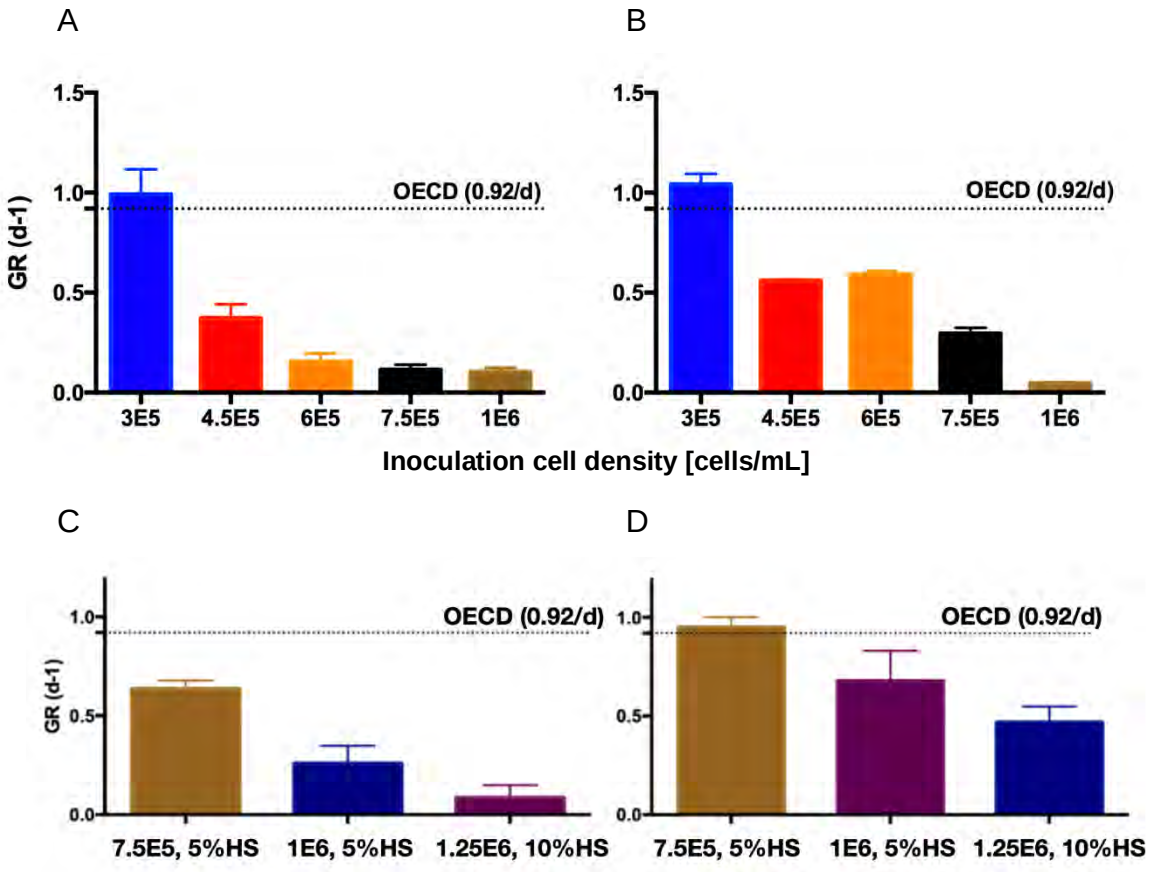


Figure 15. Growth rates (n=3) of *C. reinhardtii* in (A, B) completely-filled vials, or (C, D) vials with variable air headspace (HS), each in quadruplicate. CGM was further supplemented with (A, C) 250 mg/L or (B, D) 500 mg/L NaHCO3 supplementation. In completely filled vials, neither level of inorganic carbon addition was sufficient to raise population growth rates above GR > 0.92/day at higher cell densities, the OECD-recommended validity criterion for healthy growth. When air headspace (HS) in the vial was applied, growth rates increased substantially. For an inoculation density of 7.5 x 10^5 cells/mL along 5% HS and 500 mg/L NaHCO3 supplementation (D), growth rates exceeded the desired threshold.

supplementation was optimal at 250-500 mg/L, and growth rates did not increase with higher NaHCO3-supplementation, however morphological changes of cells were appreciable at and above substantially higher concentrations, as observed previously for algae [453] (Suppl. Fig. SI-2).

In completely-filled vials T101/V4, $NaHCO_3$-supplementation alone was not sufficient to enable *C. reinhardtii* growth rates (GR) to achieve the validity criterion of 2.5-fold growth over 24h period, or GR ≥ 0.92^{-d} (Fig. 15 A and B). However, application of 5% air headspace (HS; Fig. 15D) in the vials along 500 mg/L carbon supplementation subsequently led to *C. reinhardtii* achieving growth rates above the desired threshold (average GR = 0.97^{-d}, n = 3), at a cell density of 7.5 x 10^5 cells/mL that would allow for the closed-vial test system supply sufficient biomass vial to downstream *omics* platforms. To select an optimal and final configuration, the previous vial growth experiment was repeated using 7.5 x 10^5 cells/mL inoculation density, 500 mg/L $NaHCO_3$-supplementation, and a range of vial air headspace of HS 0-15% (Fig. 16). A 10% air headspace was selected as optimal trade-off between size of growth rate *vs*. vial liquid and minimal gas compartments, featuring adequate growth rates of >0.92^{-d} (mean 1.14^{-d}; n = 4) and a pH drift < 0.5 (mean 0.25; n = 4) over a 24 h incubation period, thus meeting generally-accepted specifications for healthy growth

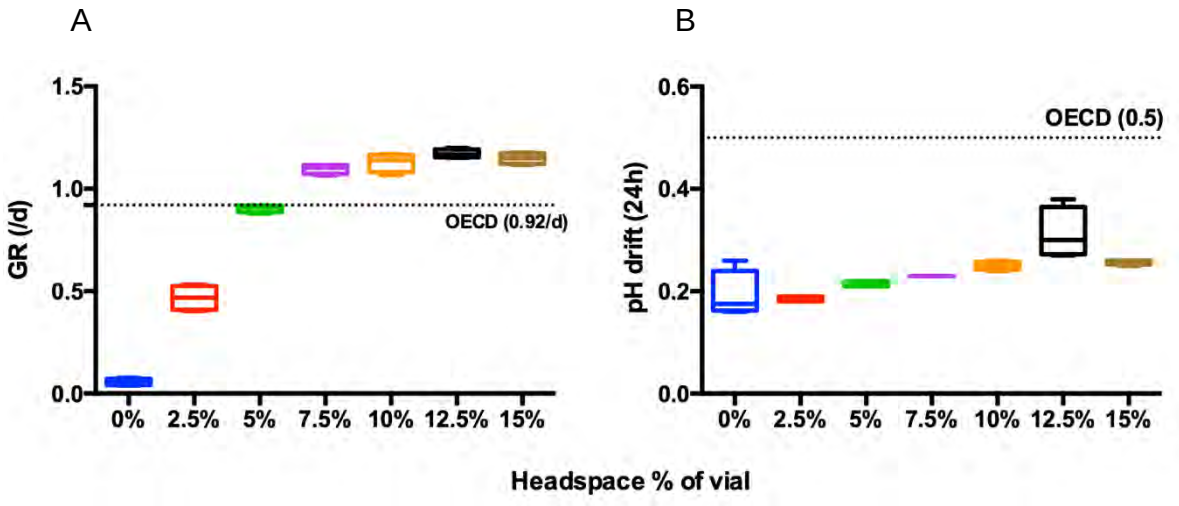


Figure 16. Growth rates (A) and pH drift (B) over 24 h growth of synchronized *C. reinhardtii* cultures in capped vials (n = 3 per group) with varying size of air headspace, inoculated at 7.5 x 10^5 cells/mL in CGM. 2.5-fold growth per day (GR = 0.92/d) as validity criterion and acceptable pH drift are marked as dotted lines.

conditions [359]. Applying a 10% air headspace, 10.03 mL of liquid phase inoculated with 7.5 x 10^5 cells/mL could generate a maximum of 7.52 x 10^6 harvestable cells per vial, meeting the initially desired benchmark of 7.25 x 10^6 cells for downstream *omics* platforms, including additional cell suspension for water chemistry sampling in order to confirm actual exposure concentrations. The achieved biomass of >7.5 × 10^6 harvestable cells per test vial has been substantially increased from comparable vial systems [437–439] and is sufficient to generate biological material for the demands of DIMS and Illumina RNASeq in parallel. Further, the low pH drift achieved precludes risk of changing bioavailability due to photosynthesis-driven pH changes, an issue more likely observed in other volatile test systems [432,454,455].

3.3. Cell cycle synchronization enables phenotypic anchoring in a single-generation test

After defining medium and inoculation parameters of the tailored exposure system, the overall test format (duration, light conditions) was conceptually adapted towards application in toxicological investigations striving for hypothesis of acute chemical MoA and putative molecular key events to support construction of AOPs. For various unicellular green algae commonly applied in growth inhibition tests (e.g., genera *Chlamydomonas, Raphidocelis*, *Desmodesmus*, *Scenedesmus*, *Chlorella*), the phenomenon of light-driven cell cycle synchronization is a known manifestation of evolutionary adaptation to scarcity of light in natural environments that can be experimentally induced by introduction of alternating light:dark cycles during incubation [456–458]. The degree of induced coordination between cells is close to absolute [197], nonetheless the explicit benefits of this algal population synchronization to the context of environmental toxicology have previously only been given brief consideration [394]. Exposure and effect analysis of multiple life-stages within the same experiment are commonly avoided in toxicity assessments due to introduction of various confounding factors [459]. Initial matching of test organisms by life-stage is prescribed in the standardized OECD test criteria for most environmental model organisms, such as water flea, birds, bee, annelids, springtail, molluscs, amphibia, or fish [460]. As one of the few cell-based *in vivo* systems, microalgal

bioassays do currently not feature the requirement for life-stage/cell-cycle matching [13,359]. Commonly prescribed test conditions, including constant lighting, may further be considered non-representative of natural environments, and drive suboptimal metabolic efficiency and rapid cell cycle misalignment [398,461,462]

In the here conducted experiments, cells grown in vials under constant lighting or alternating 12 h:12 h light:dark conditions were compared regarding time-point specificity of zoospore release (i.e., increase in cell number and density) and mitotic activity, over a time-course of 24 h. A clear logarithmic increase of cell density over the whole measurement period (thus a constant presence of zoospore hatching events) were observed in the cell populations grown in constant light (Fig. 17A). By contrast, for cell cultures grown in alternating 12 h:12 h light:dark conditions (Fig. 17B), an increase in cell number occurred exclusively after the light:dark transition in a narrow time window of approximately 2.5–3 h starting around the 16 h time-point, indicating a high population-wide coordination of zoospore release from zoosporangia within the experimental time-frame.

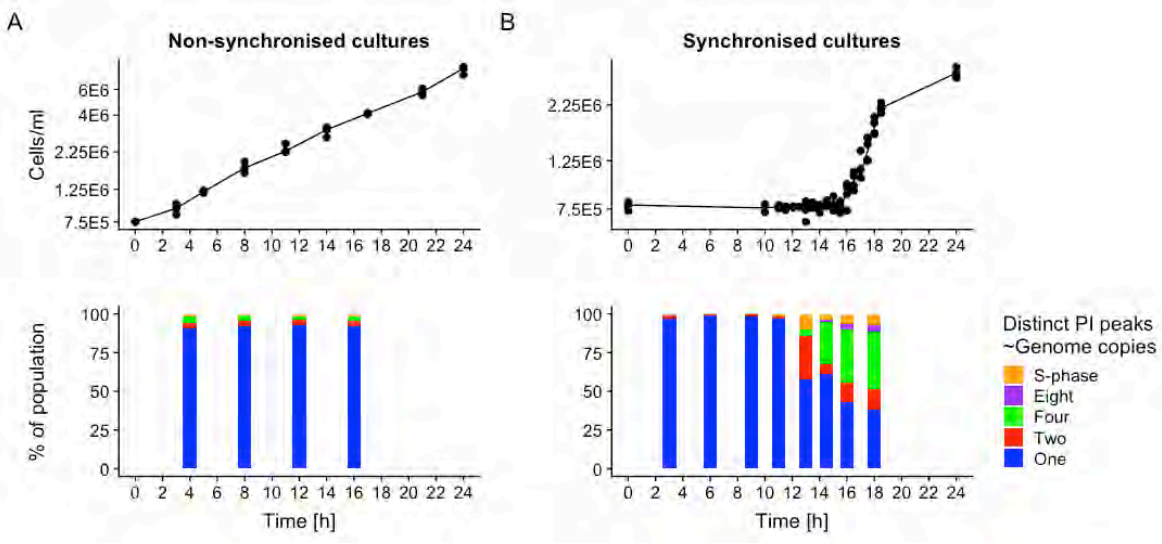


Figure 17. Cell density (Top) and number of distinct peaks in PI fluorescence intensity (Bottom; ~ amount of genomic material found in each zoosporangium or zoospore) indicating genomic division events during multiple-fission cycles for non-synchronized (A) or synchronized (B) cultures. For synchronized cultures, light:dark transition occurred at 12 h. N = 3 per group.

A similar, although phase-shifted, dynamic process was observed when mitotic activity between the two culturing regimens was compared with flow cytometric measurements (Fig. 17 A and B). Cells were analyzed for fluorescence of the DNA-intercalating fluorophore propidium iodide after a nucleotide staining procedure and enzymatic RNA degradation. Cell cultures grown in constant lighting conditions comprised either single cell zoospores, zoosporangia enclosing two or four zoospores, or cell particles undergoing S-phase, to narrowly-defined percentages over the whole course of the experiment (single genome copy zoospores 92.07 ± 0.77% of population, two-genome copy zoosporangia 3.25 ± 0.26%, four copy 3.21 ± 0.77%, cells in S-phase 1.48 ± 0.26%). Cell cultures from alternating light:dark conditions were composed of a time-dependent cell population, dominated by cells containing a single genome copy (SGC zoospores) at all time-points before the light:dark transition at 12 h (97.06 ± 1.53%). Yet at the 13 h time-point, these SGC zoospores comprised only 58% of the population, with a concordant increase in cell particles in S-phase, or zoosporangia containing two or four genome copies.

In the presented data, coordination of genomic division and sporulation events over the complete algal population in cultures grown in light:dark cycles, and lack thereof in cultures grown in constant light, was confirmed via electronic cell counting and flow-cytometry. This difference was indicative of cell cycle synchronization in algae grown under alternating light cycles [197]. From the perspective of mechanistic (eco-)toxicology, one significant benefit of the observed population-wide coordination of nuclear division and sporulation is the ensuing occurrence and measurability of the algal adverse phenotypic endpoint within a narrow time-window across the cell population (Fig. 17B). This in turn enables temporal phenotypic anchoring of the AO to prior molecular perturbations, thereby defining structure of AOPs and increasing cause-effect associations in chemical MoA hypotheses [354]. In contrast, described coordination and opportunity of mechanistic anchoring is lost in algal cell culturing using constant light regimes [398], due to consistent occurrence of nuclear division and sporulation over the entire experimental time-frame (Fig. 17 A). Flow-cytometric measurements were here utilized to allocate the final sampling time-point of the sampling profile in the outlined experimental design (see Chapter 2, Section 2.2.3.1.). When algal growth inhibition i.e. inhibition of algal cell division is selected as adverse

outcome to which to link molecular perturbations, cytokinesis of a cell (post nuclear- and organelle division) resembles the window of occurrence of possible toxicant-induced adverse outcome, as measured later by increase in cell density after release of the divided zoospores from zoosporangia by cell counting. Flow cytometry indicated start of replication activity as early as 11 h into the light-phase (Fig. 17B; cells in S-phase at 11 h significantly increased from 9 h, Welch's t-test $p = 2.7 \times 10^{-3}$). First nuclear division events were observed at merely 1 h after the light:dark transition (13 h time-point), as evidenced by substantial presence of zoosporangia containing multiple genome copies (two or four zoospores). The number of cells containing ever greater numbers of genome copies grew exponentially at later time-points, concordant with the nature of multiple-fission cycle division of C. reinhardtii [197]. By comparison, zoospore hatching (release from zoosporangia) and respective increase in cell density was only observed after 15.5 h. With cytokinetic events already observed as early as 1 h after light:dark transition, it was concluded that the last sampling time-point of the sampling profiles for later *omics* studies on norflurazon and chlorobenzene (Chapters 4 and 5) should be allocated at max. 12 h 30 min after exposure (i.e. 30 min after light:dark transition) to capture potential molecular perturbations of nuclear division along minimal overlay with the cytokinesis and zoospore release time window i.e. occurrence window of induced adverse outcome (Fig. 18).

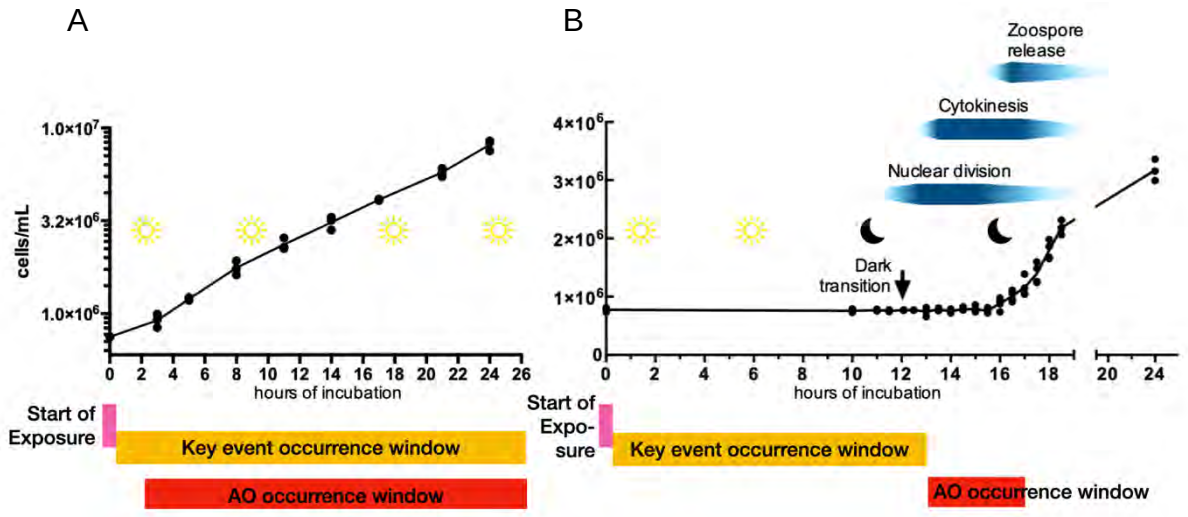


Figure 18. Abstract representation of the potential time-windows of molecular key events and adverse outcome within algal cell cycle, as induced by exposure to toxicants. The schematic is overlayed growth curves for (A) non-synchronised and (B) synchronized cell cultures.

Reducing the duration of a conventional algal test protocol would increase sample throughput and thus facilitate applicability for high throughput *omics* technologies, e.g., for applications in read-across and prioritization. When applied to the purpose of hypothesizing chemical MoA and key events predictive of apical endpoints (i.e. AO) in synchronized cultures, the commonly prescribed 72 h test duration designed for non-synchronized cell cultures [12,13] becomes an arbitrary timeframe. Given the selection of inhibition of cellular division as the AO for microalgal toxicity, it can be assumed that AO-inducing key events must occur and be measurable within perturbations of preceding biological functions [168,463] and thus within previous cell cycle stages. Justification of the test duration in microalgal exposure studies aiming to hypothesize on acute chemical MoA and molecular key events, therefore, should not hinge upon absolute length, but on biological anchoring, i.e., the minimal time required to link molecular stress responses to successive phenotypic effects, and thereby satisfying the regulatory requirement of phenotypic anchoring [49,352–354,356]. The reduction of test duration encompassing a single generation of synchronized cells (Fig. 18B, and Fig. 10B in Chapter 2) is proposed in this context. It may be argued that an optimal sampling strategy would extend exposure and sampling to the respective dark phase of the alternating light:dark cycle after sporulation, allowing the effects of a chemical on dark cycle processes to be examined. The practical implementation of such a protocol is not readily feasible, risking activation of biological functions in algae exposed even to minimal light indicative of a commencing cell growth cycle [218,386]. Furthermore, algal biological activity in complete darkness is indicated to be largely limited to mitochondrial energy metabolism, which is maintained throughout the light phase [386,408–410]. Consequently, the proposed time-frame from commencement of light phase to sporulation covers the single largest set of molecular and cellular functions within a cell cycle that chemicals may perturb.

3.4. Synchronized vs. non-synchronized cultures for molecular studies

3.4.1. Initial optimization of the cell wash procedure

Before conducting metabolic phenotyping experiments, the cell harvesting procedure was optimized to reduce influence of extracellular compounds or extraneous contaminants from growth medium or consumables on mass spectrometric profiles [464]. Using the established measure of median relative standard deviation (mRSD) of measured metabolite features as a descriptor of variance [465], the mRSD value of unwashed cell pellets was 28.08%, decreased to 21.22% for pellets washed once, and to 16.76% for pellets washed twice. No pellet washing led to high sample variation in multivariate space (Fig. 19). When comparing variance scores in multivariate analysis (PCA; principal component analysis) of polar metabolite *m/z* features, a significant difference was discovered between the three wash groups along PC1 (ANOVA; $p = 6.19 \times 10^{-9}$), capturing 47.6% variance in the dataset, but not along PC2 ($p = 0.2$), capturing only 11.2% variance. Despite the reduction in mRSD between one and two pellet washes, no substantial difference in clustering could be found between these two wash conditions, however PC2 scores (not PC1) were significantly different between one and two washing steps (t-test, $p = 0.06$).

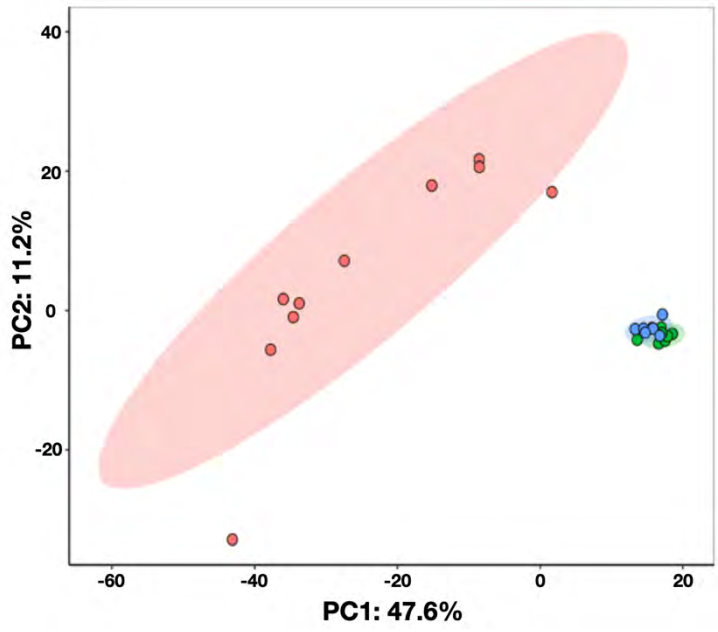


Figure 19. Metabolic fingerprints for pellet wash optimization. A first study comprising synchronized control cultures seeded in vials was performed to assess the influence of the number of washing steps on the metabolomics data quality. Cell cultures were concentrated as above from a single stock, seeded at 7.5×10^5 cells/mL in 30 capped vials and incubated for 3 h. Next, 5.25×10^6 cells were sampled from each test vial and a varying number of pellet washes performed before flash-freezing: None (red), once (blue) or twice (green).

The most substantial reduction of sample variance could be achieved using a single pellet wash as compared to no wash, as observed previously for other cell types [464,466,467]. As additional washing steps would relatively increase time demands of the sampling process per time-point and introduce higher complexity to the protocol, a single wash step was selected as sufficient compromise for all further metabolomics and lipidomics experiments.

3.4.2. The benefit of synchronized algae cultures for molecular studies

To analyze the impact of light-induced cell cycle synchronization on the metabolic phenotypes of algal cultures, direct infusion mass spectrometry (DIMS) based metabolomics was applied to cells grown in alternating light:dark conditions (synchronized cell cycles) versus grown in constant lighting (non-synchronized). Basal (unexposed) algal cultures were sampled from each culturing regimen at 4 h 15 min (±15 min), 8 h 15 min (±15 min) and 12 h 15 min (±15 min) post-seeding (n = 8 for each light regime and time-point). Intra-study quality control samples (QC) were derived from a single pool of aliquots from each biological sample. Technical variability over the dataset was estimated from mRSD of QC samples [276], and total (dominated by biological) metabolic variability was assessed from groups of biological samples. mRSD of all *m/z* features for the QC samples in the analysis of the synchronized cell cultures was 9.1%, while QC mRSD for analysis of non-synchronized cell cultures was 12.1%. These results indicate low technical variability and hence high quality of the DIMS metabolomics data, as previously described by Ref. [465]. Total mRSD for synchronized cultures was as follows: 25.1% (4 h 15 min ± 15 min), 27.4% (8 h 15 min ± 15 min) and 30.6% (12 h 15 min ± 15 min); while for non-synchronized cultures: 36.2% (4 h 15 min ±15 min), 27.6% (8 h 15 min ±15 min) and 33.8% (12 h 15 min ± 15 min). These values indicate a slightly higher biological variability in non-synchronized cultures *versus* synchronized cultures. Unsupervised multivariate analysis (PCA) compared the metabolic phenotypes of the algae as a function of lighting regime and time-course (Fig. 20). Outliers were removed if their measurements exceeded the 95% confidence interval derived for all the biological

samples, within each dataset (4 samples in non-synchronized study, 2 samples in synchronized).

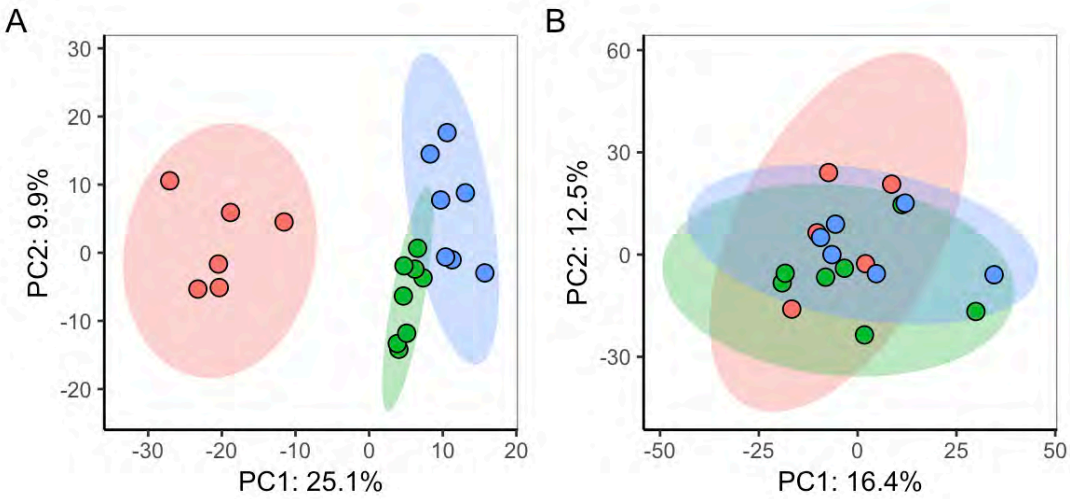


Figure 20. PCA scores plots comparing the DIMS metabolic phenotypes of (A) synchronized algal cell cultures grown in alternating light:dark conditions, and of (B) non-synchronized algal cell cultures grown in constant light. Plotted are PCA scores for samples taken at 4 h 15 min ±15 min (red), 8 h 15 min ±15 min (green)) and 12 h 15 min ±15 min (blue).

No metabolic separation of time-points was observed for non-synchronized cell cultures grown in constant lighting conditions. However, for cells grown in alternating light:dark conditions, a progression of their metabolic phenotypes was discovered over time (along PC1). Statistical analysis of the PC scores for each sample indicated significant differences in PC1 (ANOVA; $p = 1.8 \times 10^{-11}$) and PC2 ($p = 6.39 \times 10^{-3}$) scores between metabolic phenotypes of the time-points for cells with synchronized cell-cycles, but not for non-synchronized cell cultures (PC1 p = 0.84, PC2 p = 0.85). This result indicates homogeneity of the metabolic composition of samples from non-synchronized cultures, and discrete compositions over time of those from synchronized cultures. Given the data, all subsequent studies were conducted using synchronized cell cultures.

In mammalian cell models, synchronization is routinely applied to enable detailed investigations into specific phases of the cell cycle [387]. In microalgae such as *C. reinhardtii,* synchronization of cell cycle was applied to study various biological processes [386,392,393,468,469], however its explicit importance for toxicological investigations remains undervalued [394,395]. The here conducted experiments

comparing the metabolite phenotypes from *C. reinhardtii* grown under the two culturing regimens emphasized substantial and significant changes in the molecular composition in the synchronized *C. reinhardtii* cultures through time. Cells are tightly aligned in their progress through the entire cell cycle up to nuclear and cellular division [470] and characteristically evolving metabolic and transcriptomic patterns have previously been linked to this progression in *C. reinhardtii* [386,407]. In both pro- and eukaryotic cells, evidence is mounting that metabolic activity is not merely affected by position in the cell cycle, but a major driver of it [471,472]. Accordingly, distinct changes of metabolic patterns along the cell cycle were discernable in the scope of metabolomics analysis of synchronized cell populations. However, a complete lack of such an effect was apparent in cultures grown in constant light as prescribed by regulatory guidelines. Under non-nutrient-limited exponential growth conditions, non-synchronized cultures grown in constant light will comprise algal cells from every possible stage of the cell cycle, irrespective of experimental time-point. Although individual cells still progress through cell cycle, extracted samples for molecular studies comprise cross-sections over the whole complement of cell cycle-dependent biological functions, as evidenced by the high similarity of metabolic profiles between successive time-points over the experimental time-frame.

Metabolic phenotypes from samples of synchronized algae cultures taken at specific time-points during the exposure period were representative of narrow windows of biological functions anchored to cell cycle. The equivalent is true for perturbations of cellular functions (molecular key events), which temporal occurrence can be precisely measured over respective time-course analyses. Light:dark cycle-induced algal cell cycle synchronization should thus be able improve *omics*-driven time-course analysis of key events by avoiding phase-shifts of molecular signals in the test system [388,389]. In non-synchronized cultures, discrete sampling intervals cannot be precisely rooted to cell-cycle-dependent biological processes. There, the interpretation of toxicological mechanisms remains limited to snapshots of overlaying molecular cross-sections of algal populations (Fig. 10 in Chapter 2), and molecular phenotypes are averaged over the heterogeneous cell population within a sampling time-point. It is concluded that synchronized cell cultures in this context represent an approach to study molecular biological processes and their perturbations with strongly

reduced variability, enabling increased analytical and temporal resolution of biological processes and their perturbances.

3.5. Application of tailored exposure system to volatile and reference toxicants

Past studies to hypothesize on chemical MoA in algae were frequently limited in exploring the temporal dynamics of toxicity. Many existing multi-*omics* studies attempting to deduce MoA of chemicals as dynamic processes in *C. reinhardtii* have employed experimental designs with relatively low numbers of sampling time-points [246,250,253,256,258,397,424,425]. Again, large-scale experimental designs are not sufficiently supported by conventional microalgal toxicity test practices, and the scarcity of existing publications with time-series analyses of algae is partly due to a relative lack of physical scalability. Specifically, algal toxicity testing of volatile chemicals has consistently proven an obstacle in the past due to the CO_2-dependence of natural photoautotrophic growth. Conventional agitation- and aeration-based exposure vessel systems become highly cumbersome to maintain with increasing experimental scale, and the stability of mid-concentration exposures is difficult in open flask culturing. A variety of solutions has been proposed to address the issue, including tailored complex flasks [429,455,473] and variants of bottle or tube testing [432,437–439,474–478]. The application of these existing methods to large-scale (multi-)*omics* studies is regrettably precluded, due to low applied inoculation cell densities, problematic physical scalability, disturbance of phase equilibria during repeat-sampling procedures, strong pH drift, or a combination thereof.

Here, a tailored sacrificial closed-vial testing system using custom growth media was developed below to address shortcomings of existing systems, and enable application to the large-scale experimental design presented in Chapter 2. The volatile testing system reported here represents a miniaturized and abbreviated variant of the conventional algal growth inhibition test, reorienting its focus on molecular events predictive of a measurable acute adverse outcome in a single clonal generation of *C. reinhardtii.* By utilizing small glass vials, parallelizability of test vessels and thus factorization of experimental variables can in principle be drastically increased in individual experiments. Capacity to test hundreds of vial replicates in parallel, per

individual toxicity test, has been achieved (see Chapters 4 and 5), enabling experimental designs to accommodate for high replication, temporal resolution and multiple exposure concentrations.

First, the suitability of the capped-vial exposure system for maintaining stable concentrations of a volatile toxicant in the medium over the required test duration was assessed. GC-MS analysis was conducted on chlorobenzene levels in the medium of these sacrificial vials sampled at the beginning (0 h) and after 12 h 15 min incubation. Algal exposures were conducted and samples taken at each time-point for both “Low’ (14 mg/L) and “High” (24 mg/L) nominal chlorobenzene concentrations (n = 4 for each time-point and concentration; Suppl. Fig. SI-66).

Measurements of chlorobenzene levels at the start of the experiment were lower than nominal (“Low” group measured at 12.32 ±0.31 mg/L; “High” group nominal measured at 20.87 ±1.78 mg/L), however the levels did not change significantly over the 12 h 15 min incubation period (Welch’s t-test, “Low” p = 0.39, “High” p = 0.24). This indicates chemical loss during initial stock preparations, however high stability of concentration levels over the incubation period. According to Henry’s law constant, fraction of chlorobenzene in the gas phase is calculated as $\%CB_g = V_g/(V_g + (V_L \cdot R \cdot T/K_H))$ with V_g = 10% vial gas phase, V_L = 90% vial liquid phase, T = 298.15K, R = 8.205 ± 10^{-5} m^3·atm/(K·mol), K_H = 3.7 × 10^{-3} atm·m^3/mol [479]. At equilibrium, only 1.65% of chlorobenzene theoretically partitions into the gas phase. Similar calculation for the expected partitioning of 204 Volatile Organic Compounds [480] suggests that 85% would partition less than 6% into the gas phase of the proposed exposure system. Concluding, stable exposure over the time-course of the experiment was well achievable using the designed capped-vial testing system, and minimal partitioning into the gas phase occurs during the experimental timeframe. Anticipation of and correction for initial volatilization loss during stock preparation of highly volatile chemicals at inoculation is advised for further studies.

To demonstrate the generation of repeatable biological results by the designed testing approach for soluble and volatile toxicants, concentration-response experiments of 3,5-DCP, $K_2Cr_2O_7$ (recommended reference toxicants [12,13]) and the volatile chlorobenzene were performed to compare generated data to existing

knowledge. The exposure period used was 24 h, aligning with both the cell culture studies presented above. EC_{50} value for the reference substance 3,5-DCP was estimated at 0.93 ±0.09 mg/L (Fig. 21A) using a 4-parameter log-logistic model, well within the range of 0.5 to 6.1 mg/L (48 to 72 h-EC_{50}) observed for *C. reinhardtii* and other green algae [481]. Effective dose-estimation for $K_2Cr_2O_7$ exposures led to an 24 h-EC_{50} value of 3.56 ±4.26 mg/L (Fig. 21B), encompassing literature background [481,482] but displaying a relatively large standard deviation.

The determined 24 h-EC_{50} of the highly volatile chemical chlorobenzene for *C. reinhardtii* was estimated at 32.52 ±3.64 mg/L (combined data of three repeats, Fig. 21C), again within range of published closed-test system data (*P. subcapitata* 48 h-EC_{50} = 14.4 mg/L [478]; *Selenastrum capricornutum* 96 h-EC_{50} = 12.5 mg/L, [429]), and drastically reduced compared to results derived from open-flask testing (*S. capricornutum* 96 h-EC_{50} = 224 mg/L [483]). When accounting for inter-species variability in sensitivity and differences in test exposure durations and physical setups [429], the estimated EC_{50} suggests adequate performance of the vial exposure system within expected ranges of variation. Of particular note is the high repeatability (low variation) in the growth data derived from the synchronized culture test system, individual experiments led to estimation of EC_{50} values of 45.46 ±20.13 mg/L (Exp. 1), 37.85 ±8.56 mg/L (Exp. 2) and 37.42 ±20.86 mg/L (Exp. 3).

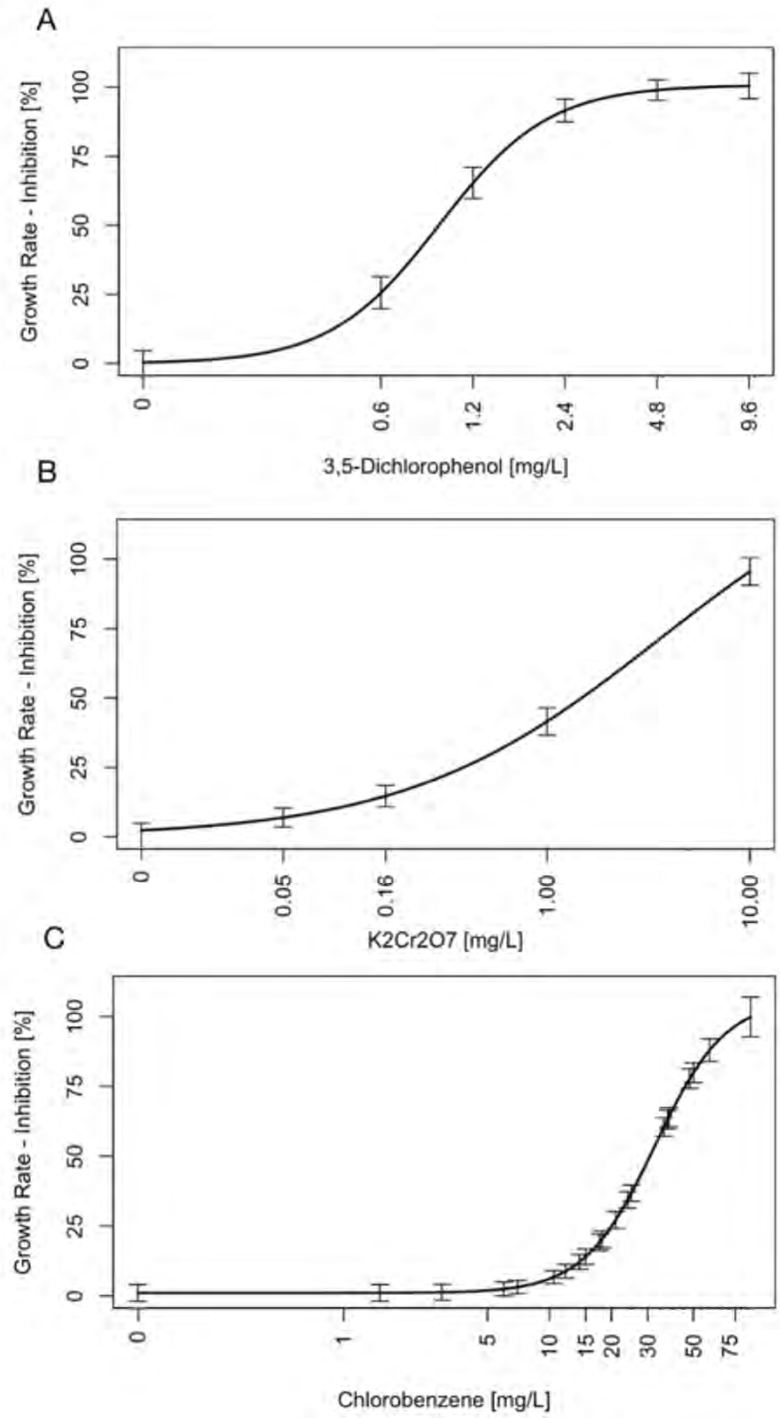


Figure 21. Dose-response curve (4 parameter log-logistic model) of 24 h algal growth inhibition experiments for (A) 3,5-DCP, (B) $K_2Cr_2O_7$, and (C) three independent experiments for chlorobenzene (n = 4 per concentration). Error bars correspond to 95%-confidence intervals of fitted curve.

3.6. Repeatability of C. reinhardtii metabolic phenotypes in tailored exposure system

Robust and reproducible determination of molecular markers diagnostic of chemical MoA and predictive of adverse outcome, and consideration of *omics* analytical and biological variability of is paramount for downstream utilization of the generated data to support environmental hazard assessments [484]. To characterize the reproducibility of the metabolite phenotypes of synchronized *C. reinhardtii* cultures grown in the capped-vial exposure system, DIMS metabolomics was conducted on samples generated over three independent experiments. To minimize experimental cost, it was here assumed that variability as compared of biological signatures as described by metabolomics was comparable to those of other *omics* platforms. Each biological batch comprised of highly replicated algal cultures in pure growth medium (control, n = 10) and cultures exposed to 25 mg/L chlorobenzene (CB, n = 10), with all samples harvested after a 3 h incubation. This exposure concentration was selected based on the previous concentration-response study (Fig. 21C) with the 3 h time-point assumed to capture early metabolic perturbations induced by the baseline toxicant; exposures were conducted early in the light phase of the 12 h:12 h light:dark cycle. Algal cell samples of each biological batch were stored at –80 °C, then all samples were extracted and DIMS metabolomics analysis (positive ion mode) performed as a

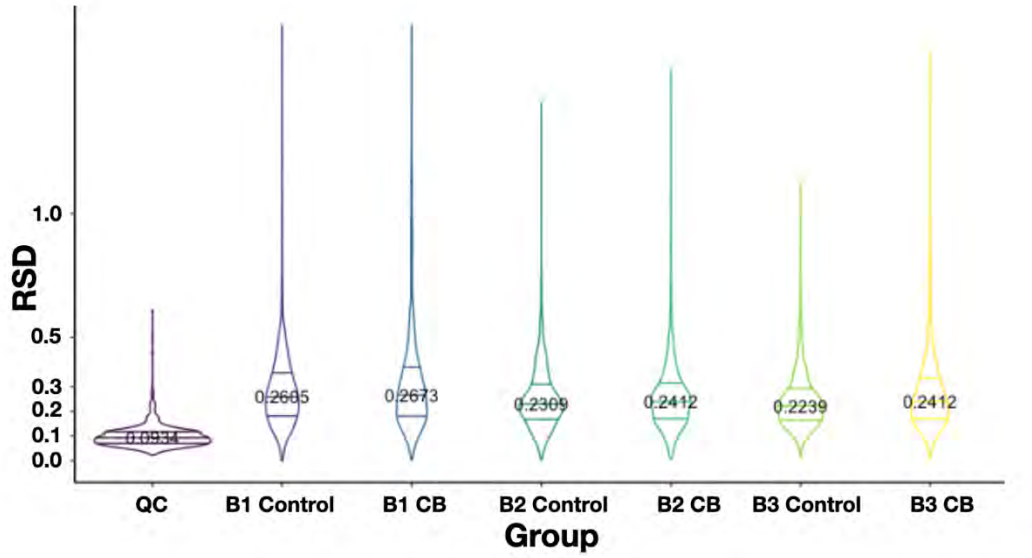


Figure 22. Violin-plot of relative standard deviations (RSD) of *m/z* features per experimental batch (B1/2/3, comparing three identical and independently- repeated batches of exposure experiments), median RSD values over all features are labelled per group. “Control” vs “Exposed” (CB), n = 10 per group. Each violin plot shows the value range (vertical lines), density of values (width of plot), and the 25th, 50th and 75th percentile of values (horizontal lines).

single analytical batch. This design allowed biological variation between the exposure experiments to be isolated and identified.

First, RSD and median RSD values were calculated for all batches and groups to characterize technical and total (dominated by biological) metabolic variability. mRSD of all *m/z* features within intra-study QC samples was 9.3%, confirming low technical variability and high quality of the instrumental analysis (Fig. 22). RSD distributions and mRSD values suggested observable, although small, differences between biological batches, with batches 2 and 3 displaying lower mRSD than batch 1. mRSD values in biological batches 1, 2 and 3 were for Control groups 26.0%, 23.1% and 22.4%, and for CB groups 26.7%, 24.1% and 24.1%. Ranges of recorded median RSD values (20.86% to 24.99%) lay within the expected ranges for test organisms and cells, e.g., median RSD values have been reported for algal and other cells between 20-22% [465,485].

To characterize the reproducibility of data gained from the developed exposure system, differences in the metabolite phenotypes between three repeated exposure studies were compared. PCA was applied to study the metabolic variability inherent to the complete dataset. Two outliers were removed (batch 1, CB samples) as they exceeded the 95% confidence interval of the complete dataset, and PCA conducted on the 56 remaining samples. The PCA scores plot (Fig. 23A, Suppl. Fig. SI-3A) revealed that the three batches were not identical, with batch 1 CB samples showing the highest intra-group variance as well as differing from the batch 2 and 3 CB samples in multivariate space. Additionally, while the metabolic effects of CB relative to the control samples were apparent for batches 1 and 3, a minimal difference between controls and CB-treated samples was observed for batch 2. To further investigate, PCA was conducted on the control samples alone, from all three biological batches (Fig. 23B and Suppl. Fig. SI-3B), to determine the extent to which the baseline algal metabolome varied across studies. ANOVA of the PC scores for the three control groups indicated significant differences along PC1 and PC3 ($p = 7.15 \times 10^{-6}$ and 3.84×10^{-4}, respectively; Table 4), indicating certain inter-batch metabolic variation between the three biological batches. Similarly, PCA and subsequent ANOVA of PC scores were

applied to just the CB samples, which also revealed significance of metabolic differences between the three biological batches (Suppl. Fig. SI-4, Table 4).

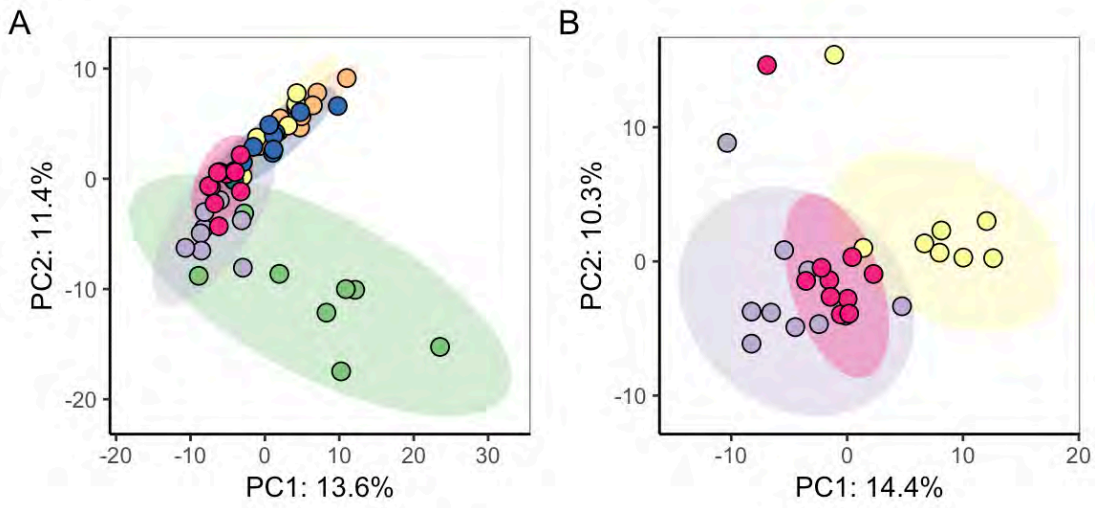


Figure 23. PCA scores plots (PC1 vs. PC2) visualizing (**A**) the metabolic differences across three exposure studies (termed biological batches), with each batch comprising of control (n = 10) and CB-exposed (n = 10) samples; (**B**) only the control samples from each batch. Sample groups are biological batch 1 Control (Purple) and CB (Green), batch 2 Control (Yellow) and CB (Orange), and batch 3 Control (Red) and CB (Blue).

Overall, small batch effects could be observed between the baseline metabolic phenotypes across the three repeats of the exposure experiment when compared in PCA. A number of possible factors might have contributed to these differences, including subtle changes in laboratory maintenance that unknowingly affected the growth and biological activity of the algal cultures, as reported previously for microalgal bioassays [486]. Furthermore, batch differences in algae exposure studies can be impacted by various biotic and abiotic confounding variables. Algae are sensitive for instance to minimal variations in prepared growth media, specific position of cells within the culture growth curve, or minor deviations in culture handling by the operator during maintenance or inoculation [487–490].

Table 4. ANOVA results comparing PC1, -2 and -3 scores of control samples or CB samples only (in each case between the independently-repeated identical exposure experiments), and CB samples normalized to their batch-specific controls. Mitigation of initially significant inter-experimental variability (excluding PC2) could be achieved using this normalization.

Samples Analyzed by PCA (All Three Batches)	*PC1*	*PC2*	*PC3*
Controls only	$p = 7.15 \times 10^{-6}$	$p = 0.11$	$p = 3.84 \times 10^{-4}$
CB only	$p = 1.72 \times 10^{-7}$	$p = 0.20$	$p = 0.048$
CB normalized to batch-specific controls	$p = 0.20$	$p = 0.015$	$p = 0.11$

To achieve the high level of repeatability required for toxicity testing, the effect of normalizing each batch of exposure data to the corresponding control metabolic phenotypes was explore. First, the $\log_2$ fold-change (LFC) for every *m/z* feature (peak) was calculated, specifically by determining $\log_2$ of the ratio of the median feature intensity in the CB group over the median intensity in the respective control group ($\log_2$ (median[Int_{CB}]/median[$Int_{Control}$]), for each *m/z* feature). This calculation was repeated for each of the three batches. The resulting density distributions of LFC values, one for each biological batch, were visually similar (Fig. 24A). Yet upon statistical testing, these LFC batch values were still significantly different (Kruskal-Wallis test; $p = 1.38 \times 10^{-12}$). To further explore the effect of normalizing each batch of exposure data to the corresponding control metabolic phenotypes, specifically using PCA, $\log_2$ fold-changes were recalculated individually for the metabolite features of each of the n = 10 samples in the CB group relative to the median feature intensity of their respective control group ($\log_2$ (Int_{CB}/median[$Int_{Control}$])). This allowed PCA of these LFC values to reveal any metabolic differences between the effects of CB-treatment normalized to each batch-control, for all three batches (Fig. 24B), with the scores plot now highlighting the significant overlap and therefore consistency of the batches. Indeed, ANOVA indicated no significant differences between PC1 and PC3 scores (Table 4; PC1 p = 0.20, PC3 p = 0.11). However, slight batch differences were still detectable along PC2 (p = 0.015). Importantly, initial batch effects in PCA (Fig. 23 A and B) were greatly decreased by applying this normalization strategy to the relevant batch-

controls (Fig. 24B). This demonstrated normalization of the observed differences in algal stress response, by calculating log_2 fold-change of the measured *m/z* feature intensities to their batch-specific biological baseline (controls), proved to at least partially mitigate existing batch differences in unsupervised multivariate analysis.

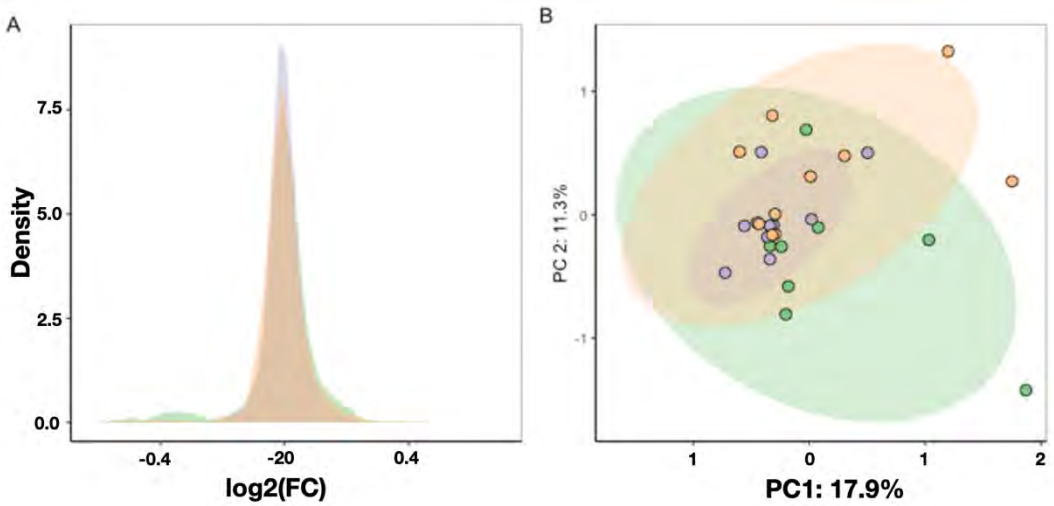


Figure 24. To increase comparability of exposure effects over the three repeated experiments, *m/z* feature intensities in CB groups were normalized to their batch-respective control groups by calculating the log_2 fold-change of *m/z* features: (**A**) density distribution of LFC values for each batch (log_2 (median[Int_{CB}]/median[$Int_{Control}$]), per *m/z* feature); (**B**) PCA scores plot from analysis of LFC values of all three batches (log_2 (Int_{CB}/median[$Int_{Control}$]), for each *m/z* feature and for each of 10 CB samples). Batch 1 = green, Batch 2 = orange, Batch 3 = purple.

Next, the repeatability of the CB-induced metabolic perturbations in the three exposure experiments from the context of a) supervised multivariate analysis, and b) molecular biomarker discovery was evaluated. Partial least squares-discriminant analysis (PLS-DA) was conducted on *m/z* features of all of the samples from the three biological batches. Here it was endeavored to evaluate the metabolic perturbations in the three exposure experiments using a supervised multivariate analysis, which focuses on the most consistent changes induced in the CB-treated samples. The algorithm selected an optimum of 5 latent variables for the classification model. While the control and CB samples were clearly separated in the PLS-DA scores plot of latent variable 1 vs. 2 (Fig. 25), a robust interpretation of these results required any over-fitting of the PLS model to be assessed. Following 10-fold internal cross-validation, the PLS model yielded an $R^2 = 0.99$ (amount of variation in data explained by model) and $Q^2 = 0.72$ (goodness of fit), which indicated good generalizability. Despite the

small batch effects in PCA, the algal metabolic stress response appeared to be regulated by a consistent mechanism across studies, as indicated by PLS-DA on pooled data

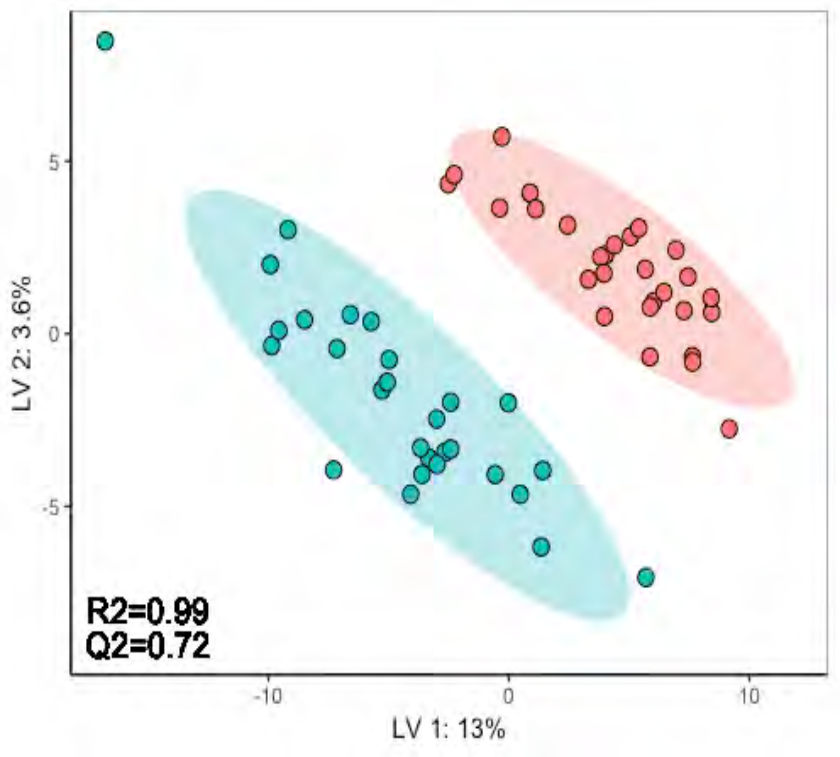


Figure 25. PLS-DA scores plot visualizing the group-separation of metabolic phenotype in *C. reinhardtii* following exposure to 25 mg/L chlorobenzene (red circles) relative to unexposed controls (green circles). All samples from three independent exposure experiments (biological batches) were pooled in this analysis. R2 = variance explained by the model, Q2 = quality of model fit after permutation testing.

Lastly, molecular biomarkers of the three biological batches were compared. This was achieved by applying set enrichment analysis [446] to the metabolomics data, an approach originally developed for analyzing gene set enrichment [446] which lately has become increasingly applied in metabolomics [491–494]. This statistical process of comparing the rank order of genes, based on the magnitude or significance of their responses to multiple experimental conditions, was here applied on the rank order of mass over charge (*m/z)* metabolic features. Three comparisons were made (Table 5).

Table 5. Enrichment analysis applied to three metabolomics datasets following exposure of *C. reinhardtii* to chlorobenzene (three independently repeated and identical exposure experiments; batches 1, 2, 3). Ranked lists of *m/z* feature LFC were calculated (S_{B1}–S_{B3} for batches 1–3) and every list was compared against every other list to determine whether S_{B1}-S_{B3} were enriched with elements of the other sets. Significance of enrichment was assessed using 1000 random permutations of *m/z* values in LFC-ranked lists, and false-discovery rates are reported. NES = normalized enrichment score, degree of metabolite enrichment of S within dataset. LE = leading edge, subset of *m/z* features in S that are most impactful towards a high NES.

Metabolite set	*Metric*	*Batch 1*	*Batch 2*	*Batch 3*
	NES	-	1.39	1.33
S_{B1}	LE	-	11 features	72 features
	FDR	-	0.004	0.006
	NES	1.41	-	1.96
S_{B2}	LE	53 features	-	43 features
	FDR	<0.001	-	<0.001
	NES	1.38	2.02	-
S_{B3}	LE	61 features	50 features	-
	FDR	<0.001	<0.001	-

First, the top 100 LFC *m/z* features from batch 1 were designated as metabolite set (termed set batch 1, or S_{B1}), and used to interrogate the rank order of *m/z* metabolic features obtained from the other two batches. The significance of this set enriching the leading edges (LE) of each of the two batches was calculated using the normalized enrichment score (NES) and by estimating a false discovery rate (FDR). This enrichment test was twice repeated, for S_{B2} and S_{B3}. The enrichment analysis was conducted to characterize the overall degree of similarity of whole sets of metabolic markers associated with chlorobenzene exposure between the repeat experiments. The results indicate that top 100 LFC *m/z* features for from each batch are strongly and significantly enriching all biological batch-metabolite set combinations (Table 5). This led to the conclusion that a common and consistent subset of metabolic markers

as a toxicological signal was discovered across all the biological batches, and further support was added to the conclusion that, despite small batch effects in PCA, a consistent toxicological effect could be measured over all experimental repeats of the exposure experiments.

4. Conclusion

Firstly, a miniaturized and scalable closed-vial chemical exposure system using custom growth media was designed, which is suitable to support the requirements of the outlined experimental design (Chapter 2) towards hypothesis of acute chemical MoA and putative molecular toxicological key events to support construction of AOPs. It allows for sufficient growth of *C. reinhardtii* (at high inoculation cell densities) for multi-*omics* assays, while aligning test duration to algal cell cycle and minimizing chemical volatilization. The latter was proven by stable exposure concentrations to chlorobenzene over the test duration. Further, the repeatability of this *C. reinhardtii* exposure system was examined by comparing phenotypical endpoint induction standard 24 h-algal growth inhibition assays using the developed exposure system, and identifying batch variation when applying unsupervised multivariate analyses to the metabolomics data. These unwanted effects could be reduced by normalizing each biological batch to its respective control data. Furthermore, set enrichment analysis as well as supervised multivariate analysis was applied to demonstrate the consistency of the metabolic markers discovered in three repeat exposures to chlorobenzene. Secondly, the utilization of synchronized algal cell cultures grown in alternating light:dark cycles allowed explicit adjustment of sampling time-profiles to the algal cell cycle to achieve phenotypic anchoring, and it was demonstrated that the application of an *omics* technology to such synchronized algal cell cultures can detect characteristic metabolic phenotypes that evolve through the cell-cycle. This should in theory benefit the interpretability of molecular data in terms of hypothesizing chemical MoA and molecular key events that are anchored to, and predictive of, the algal adverse phenotype of reduced growth and might serve beneficial in aiding construction of AOPs.

Chapter 4

A time-resolved multi-omics approach confirms and extends existing knowledge on the chemical MoA of norflurazon

1. Introduction

Omics technologies are expected to have high utility in profiling chemical-induced perturbations of biological processes [57]. In this context, they could become valuable tools to support chemical safety assessment of novel and existing chemicals specifically in the areas of first-tier prioritization of testing, or read-across of chemical hazard based on the similarity of biological signatures. However, most “New Approach Methodologies” such as *omics* are still considered insufficiently developed to aid the regulatory decision-making process [49,136]. Amongst the different challenges that are limiting the wider adoption of *omics* into environmental chemical safety science, is general scarcity of work showcasing *omics*-driven chemical MoA hypothesis, thereby enabling discovery of molecular markers that are specific to a chemical’s MoA and predictive of adverse outcome. Not only could such molecular markers provide a tangible tool for risk assessment, they would also be beneficial to aiding construction of AOPs [111,124,127,495].

Previous studies attempting *omics*-driven deduction of toxicant-induced effects in algae conducted by various research groups (notably refs. [424–426]) were overall limited in scale and experimental designs to discover time-dependent effects. As discussed in Chapters 2 and 3, a large drawback observed in numerous algal toxico-*omics* studies was a lack of cell cycle synchronization within algal test cultures [231,243,257,263,426]. Consequently, confidence in derivable cause-effect relationships was limited by these characteristics, specifically within the context of understanding temporal dynamics of molecular perturbations and their specificity to biological processes within the algal cell cycle. This further resulted in a lack of biologically-justified anchoring of sampling time-points to time-windows prior to the induction (and hence measurability) of the adverse outcome [251,254,255,261,262,425,427]. Last, time-course analysis in existing studies was restricted to at most 3 sampling time-points [426], with most research employing single time-point designs for analyzing toxicant-induced molecular perturbation [246,253,256,258–260,424]. This low number of sampling time-points is suboptimal, arguably insufficient, for computational analysis of temporal trajectories of biological processes using multivariate data [406].

The purpose of this chapter was to address these limitations and to offer a new perspective into molecular stress profiling of *C. reinhardtii* by means of an exposure of synchronized cell cultures to the herbicide norflurazon (NF) coupled to a highly-time-resolved multi-*omics* analysis. NF is a herbicide known for its inhibition of phytoene desaturase enzyme inhibition within the carotenoid synthesis pathway, however knowledge of off-target and downstream effects is relatively scarce [34,424], making it an ideal candidate for anchoring molecular effects discoverable by *omics* to existing toxicity information and potentially extend the latter. The overall aim, in line with Scientific Objective III (see Chapter 1) was to apply the delineated multi-*omics* experimental design (Chapter 2) using the prior-developed tailored algal exposure system (Chapter 3) to showcase *omics*-driven hypothesis of a time-resolved acute chemical MoA for NF toxicity, and to illustrate aided construction of a draft AOP for phytoene desaturase inhibition, supported by *omics* data. This was conducted within the context of the dual nature of the experimental design, using a model toxicant (NF) with well-understood molecular effects to guide and "calibrate" the mode of data analysis and evaluate how effectively the multi-*omics* approach can reproduce known effects of toxicity. The work presented in this chapter was subsequently intended to enable a subsequent "blind" application (Chapter 5) of the presented *omics* approach for the elucidation and identification of an unknown or poorly characterized MoA of a chemical in algae. This dual approach should increase confidence in the generated data and the proposed mode of their interpretation

2. Materials and Methods

2.1. Algae culturing

C. reinhardtii cultures were incubated in liquid CGM under a 12 h:12 h light:dark cycle as described in Chapter 2.

2.2. Norflurazon range-finding experiment

To expose cells, quadruplicate independent batches of synchronized cultures were grown in open flask culture, and seeded in vials as described in Chapter 2. Preparation steps were restricted to a maximum duration of 30 min within the onset of light phase. Culture cell density for inoculation was precisely controlled and growth rates measured in technical duplicate using CASY cell counting. Toxicity tests were performed using norflurazon (NF; Sigma-Aldrich, Gillingham, UK), and all tests were performed with biological quadruplicates. Prior to addition to CGM, NF was dissolved in DMSO as carrier solvent and then added to CGM, effecting a final DMSO concentration of 0.35%, non-toxic to *C. reinhardtii* [496]. The range-finding experiment was conducted over the following exposure concentration range: 0, 0.05, 0.15, 0.45, 1, 2, 6, 12 and 20 mg/L NF. Cell density was measured using CASY at 24 h, and growth rate inhibition was calculated as described in Chapter 2. A 4-parameter log-logistic concentration-response model was calculated using open-source R software [331] and the drc package [444].

2.3. Multi-omics time-course exposure experiment

To expose cells for the multi-*omics* profiling exposure experiment, synchronized cell cultures were grown in open flask culture and seeded in vials as described in Chapter 2. Preparation steps were restricted to a maximum duration of 30 min within the onset of light phase. The experimental design for this experiment was described in Chapter 2. Exposure concentrations were aligned with results from the range-finding experiment and set to 0mg/L (“Control”), 1 mg/L (“Low”) and 2 mg/L (“High”) to achieve

exposure levels observed to induce no (EC_0), ~20% (EC_{20}) and ~40% (EC_{40}) of growth inhibition. To generate the toxicant-spiked media solutions, a single batch of growth medium was split, spiked with the respective amounts of toxicant, and culture cell density for inoculation precisely controlled and growth rates measured in technical duplicate using CASY cell counting (see Fig. 8, Chapter 2). For each exposure level, a total of 72 vials were inoculated to enable n = 8 replicates for each of the 9 sampling time-points, an additional 4 vials per concentration were inoculated to enable post-adverse outcome growth inhibition measures at 24 h. In total, 228 vials were inoculated in parallel.

2.4. Multi-omics sampling procedure and instrumental analysis

Cell cultures were sampled at 9 time-points (TP1-9), at 1.5/ 3/ 4.5/ 6/ 7.5/ 9/ 10.5/ 11.5/ 12.5 h post commencement of light cycle, translating to 1/ 2.5/ 4/ 5.5/ 7/ 8.5/ 10/ 11/ 12 h post-exposure. As the last timepoint was allocated to the dark-phase of the light cycle, sampling procedure was conducted using minimal laboratory lighting. At each time-point, n = 8 exposure vials were opened, n = 4 samples (3 mL) were collected for transcriptomics analysis, and n = 8 samples (6.9 mL) were collected for direct-infusion mass-spectrometry (DIMS) metabolomics and lipidomics. Sampling procedure, metabolite/lipid/RNA extraction, instrumental analysis and data processing steps were performed as described in Chapter 2. Additionally at each time-point, 80 µl of cell suspension was collected for measure medium NF concentration levels using liquid-chromatography tandem-mass-spectrometry, as described below.

2.5. Metabolomics and lipidomics statistical data analyses

Prior to data analysis, spectral peaks arising from NF and its main metabolite des-methyl-NF [497] were removed from the dataset (see Suppl. Table SI-T2 for filtered adducts per ion mode). Statistical tests (Welch's *t*-test, Kruskal-Wallis test, ANOVA) and PCA were conducted using R and the R-Stats base package [331]. Spectral peaks were putatively annotated using MI-Pack software [498] and the ChlamyCyc metabolic pathway and spectral feature database [187], using a 5ppm

error tolerance on possible adducts [M+H]+, [M+Na]+ and [M+K]+ (positive ion mode) or [M-H]-, [M+Cl]-, [M+Na-2H]-, [M+K-2H]- and [M+Hac-H]- (negative ion mode; Hac = acetate). For multiple assigned putative annotations per spectral peak, the putative annotation with lowest ppm error was selected. Spectral peaks with multiple annotations with equal ppm-error were excluded from analysis. Compound names were translated to KEGG-IDs for pathway-overrepresentation analysis using *Arabidopsis* KEGG pathways [499] in MetaboAnalyst [332], and for metabolite set enrichment analysis on KEGG pathways using Pathview software [500]. Clustering of spectral peaks with similar time-intensity profiles but significantly different peak intensities between exposure groups were identified using metaboClust software [501], using a custom filtering condition for concentration-response behavior as 'log2-fold change [High-vs-Control] > log2-fold change [Low-vs-Control]' and limitation of found clusters to k = 9 (analysis report in Suppl. Table SI-T3 and Suppl. Figs. SI-5/-6/-7). All analyses were conducted using a threshold of false discovery rate FDR ≤ 0.05 (method = Benjamini-Hochberg).

2.6. Transcriptomics statistical data analyses

Transcriptomics instrumental data collection and raw data processing for norflurazon samples were conducted together with samples for the chlorobenzene time-course exposure experiment (Chapter 5). Before exploratory data analysis (PC K-means clustering and hierarchical clustering), counts were normalized using regularized log (rlog) transformation and low-count genes filtered out below 0.5 counts per million [502]. Differentially expressed genes (false discovery rate FDR ≤ 0.05, log2-fold change ≥ 2) were determined using DESeq2 [502] and apeglm packages [503]. Scatter- and PCA plots were generated using R and the R-Stats base package. ANOVA on single gene expression between exposure groups at individual time-points in time-course analysis were conducted on rlog-transformed data to satisfy assumptions of normal distribution. To perform enrichment analyses, PlantsEnsembl gene IDs were first converted to Joint Genome Institute (JGI) v5 IDs using custom R-script, then to GeneBank accession IDs using Algal Functional Annotation Tool [504], and finally to Entrez IDs using DAVID [505]. Generally-applicable gene-set enrichment

(GAGE) analysis on KEGG pathways using individual or shared lipid, metabolite or RNA expression data was conducted using Pathview software [500,506,507]. Parametric gene set enrichment analysis (PGSEA) over all treatment groups on Joint Genome Institute biological process gene ontologies (JGI-GO) were performed using iDEP software [508]. Hierarchical clustering using Euclidean distance as a similarity measure was performed using SLIDE software [509]. Time-profile clustering of genes with similar time-expression profiles significantly different between exposure groups were identified using maSigPro package for R [510,511] using default settings (CPM filter = 0.0, design type = multiple-series time-course, significance level = 0.05, R-squared cutoff = 0.7, clustering method = hierarchical clustering, clusters = 9; analysis report in Suppl. Table SI-T4). JGI-GO network representations were drawn using ShinyGO software [512]. All analyses were conducted using a threshold of false discovery rate FDR ≤ 0.05.

2.7. Quantitation of norflurazon medium concentrations

To confirm exposure concentrations of NF in growth medium of all three concentration groups (“Control”/”Low”/”High”), liquid-chromatography tandem mass spectrometry (LC-MS/MS) analysis was conducted on spent growth media sampled at each experimental timepoint. 100 µl of cell suspension was sampled, centrifuged at 15000 rpm, and 80µl of growth media supernatant injected into vials containing 10 µl of 100 mM NaN3 in CGM for biological fixation. Samples were stored at -20 °C in the dark until analysis. Before instrumental data acquisition, 10 µl of 10 mg/L solution of isotopically labelled NF-13C,-d3 (dissolved inn 0.35% DMSO in CGM) was added as internal standard to each sample. Detector linearity was achieved across the range of 7.8125 – 125 ng/mL, and thus samples were further diluted by a factor of 32:1. Samples were analyzed using a Waters Xevo TQ coupled to ACQUITY UPLC with C-18 Agilent ZORBAX RRHT Eclipse XDB-C-18 (2.1 mm x 10 0mm x 1.8 µm) reverse-phase column and guard column (2.1 mm, 1.8 µm). Mobile phases were (A) 0.1% formic acid (98%; VWR) in ultrapure H2O (LCMS grade; Sigma-Aldrich, Gillingham, UK) and pH adjusted to 5.5 with NH_4OH (29±1% NH3; Sigma-Aldrich, Gillingham, UK), and (B) 0.1% formic acid in acetonitrile (LCMS grade; Sigma-Aldrich, Gillingham,

UK). Column temperature was set at 40°C, flow rate = 0.3 mL / min, and injection volume was 1µl. LC-MS/MS analysis was run as a gradient (Table 6), with a retention time of NF at 10.3 min. Mass spectrometry parameters were: Positive ion ESI, capillary voltage 3.5kV, mass range 100 – 500 amu. Single reaction monitoring was conducted using ions *m/z* = 304.0 (precursor) and *m/z* = 284.1 (quantifier) at a collision energy of 31 V. The sample sequence was randomized, and quantification of NF was performed relative to the isotopically-labelled internal standard.

Table 6. Gradient of mobile phase B over 21.5min analytical runtime in LC-MS/MS analysis. Total carrier phase = % phase A + % phase B (% phase A = 1 - % phase B).

Time (min)	%B
0	0
15	100
20	100
21.5	0

3. Results and Discussion

3.1. Determination of optimal NF exposure concentrations

To enable phenotypic anchoring of molecular effects to the adverse outcome of algal growth inhibition at levels below acute cytotoxicity [414], an initial range-finding exposure experiment was conducted (Fig. 26). NF induced a concentration-response behavior in *C. reinhardtii* typical of pesticidal action, with an increase of the model slope above ~1000µg/L (~EC_{20}) and within the range of effective concentrations observed before [34]. The present data was used to inform the exposure concentrations of the subsequent multi-*omics* experiment. Two midrange concentrations (1000µg/L ~EC_{20}, 2000µg/L ~EC_{40}) were chosen as optimal exposures (termed “Low”, “High” levels) within the boundaries of the delineated experimental design (See Chapter 2). These concentrations inducted measurable adverse outcome, an important component of the experimental design.

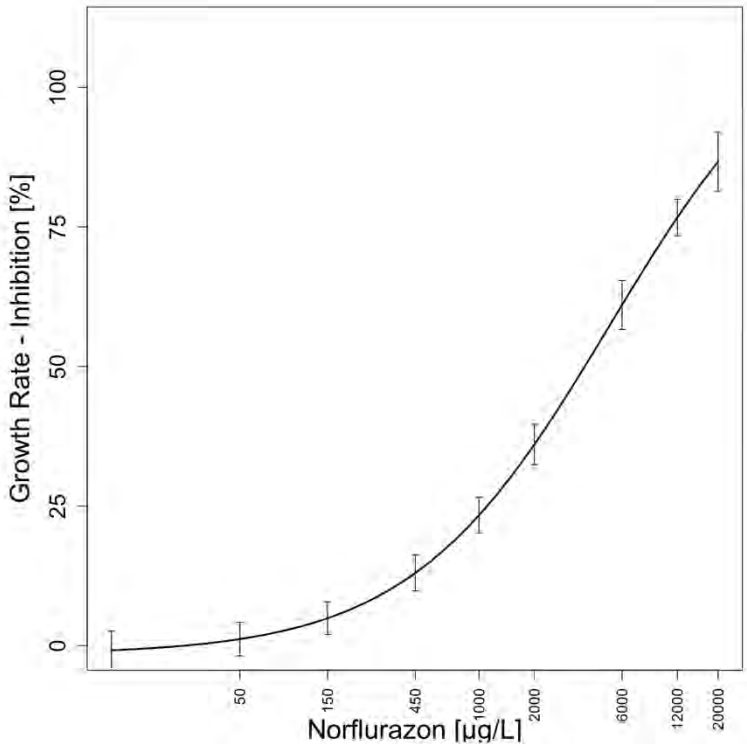


Figure 26. 4-parameter log-logit dose-concentration model pooling 3 independent norflurazon growth rate inhibition experiments. The lowest observable effect occurred at 50 µg/L, while the EC_{75} was approached at ca. 12mg/L. For the experiment, 1000µgl and 2000µg/L were chosen.

3.2. Quality assurance of omics data acquired from time-course exposure experiment

Prior to interpretation of the biological stress response of *C. reinhardtii* to NF exposure over a time-course, the quality of the multi-*omics* data from these experiments was assessed for the individual *omics* platforms, and low-quality samples and variables excluded.

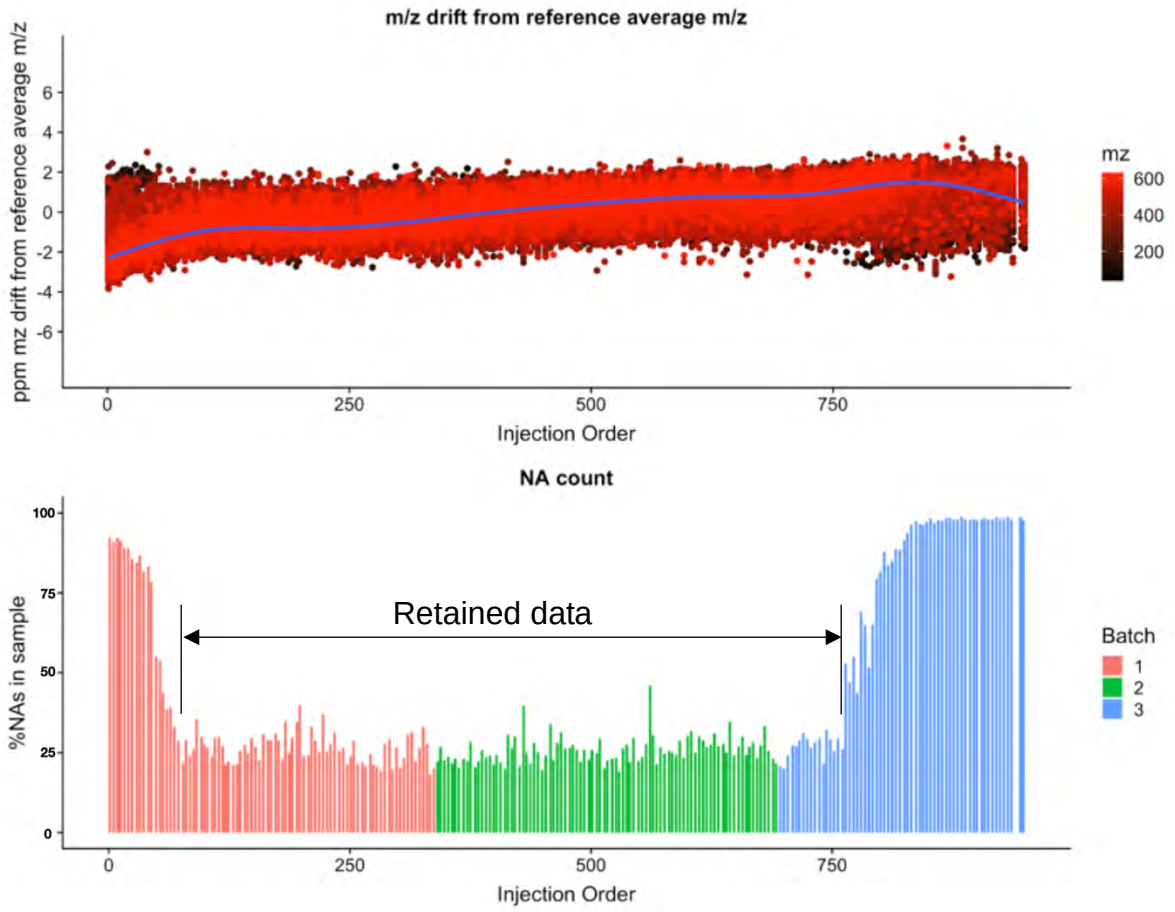


Figure 27. m/z drift (measured in ppm in relation to average m/z value per peak over total multi-analytical-batch run) and occurrence of missing values ("NA") over run of the positive ion mode metabolomics assay, after peak alignment in the dataset with a 2ppm tolerance window. Specifically, a relatively large drift of instrumental m/z measurements was observed over the first ~50 injections and over the last ~250 injections, inducing loss of retained peaks in the dataset due to the large Euclidean distance to cluster centroids, which generated large numbers of missing values. This effect was observable over the complete m/z range. Regions with high numbers of missing values were excluded from further analysis, as indicated in the figure.

3.2.1. Quality assurance – Mass spectrometry data

High spectral peak *m/z* accuracy and precision are paramount for confidence in downstream (putative) annotation of spectral peaks in DIMS. However, substantial drift of the *m/z* calibration of peaks could be observed over the multi-batch sequence for the positive ion mode metabolomics assay in DIMS post-analysis (Fig. 27), but not in the negative ion mode metabolomics- or the lipidomics assay. Drift of this instrumental *m/z* calibration generated a large number of missing values (50-100% of peak intensities missing) in parts of the positive ion mode metabolomics dataset after global peak alignment using a 2ppm *m/z* tolerance window. LOESS batch correction was in this case unsuccessful to correct this problem, as the method filters missing-value measurements to apply spline-based correction on peak intensity drift using QC pool samples which are evenly spaced throughout the sample sequence [329]. Increasing the width of the ppm tolerance window alleviated the problem when above a width of >3.5ppm, however this in effect would lead to high probability of misclassification of spectral peaks (and their drifting *m/z* calibration) during the spectral binning process in global peak alignment, and ultimately erroneous annotations. To retain stringent ppm tolerance parameters during peak alignment, the high missing-value sequence sections in the analysis sequence were removed from the dataset (Fig. 27). Additionally, only spectral peaks which could be uniquely assigned to a single hierarchical clustering bin during peak alignment were retained, to avoid mis-classification of peaks due to drift of instrumental *m/z* measurements over runtime. The subsequent LOESS batch correction performed efficiently hereafter (Suppl. Figs. SI-8 and SI-9). Due to randomization of analysis sequence and inclusion of 4 technical replicates per sample, the complete loss of samples from the dataset could be limited.

After all of the data processing steps and outlier removal, the following numbers of samples were retained in the dataset: Lipidomics assay = 187 of 216 samples (86% retained), metabolomics negative ion mode assay = 201 of 216 (93% retained), and 162 of 216 (75% retained) in the positive ion metabolomics assay. Overall, RSD distributions (as a measure of technical instrument variance using QC samples, see Chapter 3 [276,465]) confirmed that the filtered datasets were of high technical quality

for all three DIMS assays (Fig. 28), with median values (mRSD) of 8.8% (positive ion metabolomics), 9.9% (lipidomics) and 13.9% (negative ion metabolomics).

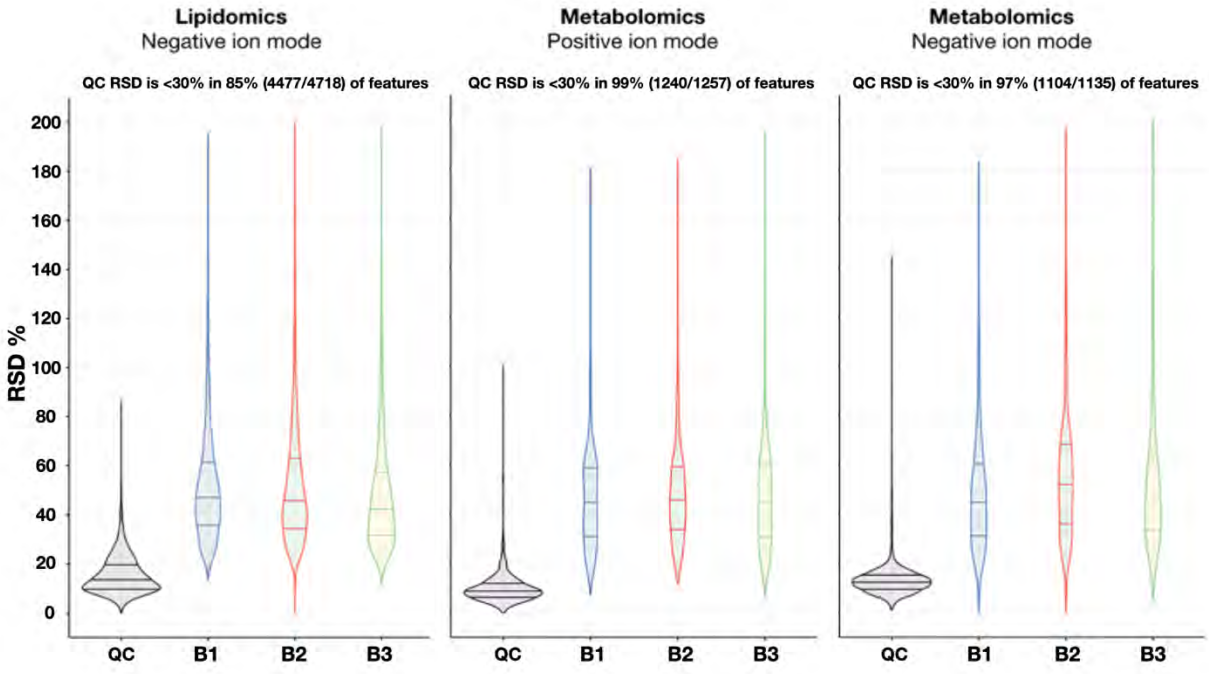


Figure 28. RSD distribution and Quality Control sample (QC) RSD metrics per DIMS assay (Lipidomics, positive- or negative ion mode metabolomics). QC mRSD are at or below 13.9% for all assays, indicating high technical quality. RSD distributions for sample batches B1/2/3 are drastically higher as these groups contain diverse samples from all exposure groups and time-points randomized over run sequence, i.e. they are expected to reflect a relatively high biological metabolic variation.

Data were categorized into time-points, and significantly different spectral peaks (Welch's t-test, FDR ≤ 0.05) were determined between exposure groups (High-vs-Control, Low-vs-Control) per time point, and putative peak annotations were attempted using *ChlamyCyc* spectral database and MI-Pack [187,498] with an error tolerance < 5 ppm. Significantly different spectral peaks were uniquely and putatively annotated with low- to moderate success rate per sampling time-point: 0 - 6.75% for lipidomics datasets, 0 - 16.4% for the positive ion metabolomics assay, and 0 - 20.6% for the negative ion metabolomics assays (Suppl. Tables SI-T5, SI-T6, and SI-T7), in line with DIMS metabolomics studies in other species.

3.2.2. Quality assurance – Transcriptomics data

Data acquisition and raw data processing of norflurazon and chlorobenzene samples (Chapter 5) was conducted as a single analytical batch. In the NF dataset, 25 samples experienced substantial loss of sample material during either sampling or RNA extractions (Suppl. Fig. SI-10), leading to insufficient material for RNASeq library generation. Ultimately, 83 of 108 NF experimental samples (77%) could be successfully sequenced. For the dataset, metrics suggested that the transcriptomics data were of high quality. Phred scores above 35 (likelihood of correct base call = 99.97%) were measured for all samples except a single (NF Time-point 8 “Low” replicate 4), which showed a Phred score = 25 but was retained in analysis (Fig. 29). Per-sequence GC content was in the range of 60-70% for the dataset, well within the expected range of the *C. reinhardtii* genome at 64-65% and higher than most multicellular eukaryotes [513,514]. Per-base N-content was close to zero for the overall dataset, the sequence length distribution had its single maximum at sequencing length minus trimmed adapter length. A median of 83.29% of reads over all NF samples could be uniquely mapped to the species genome. The group at time-point 2 “Low” contained a single replicate, for DEG calculation this replicate was temporarily merged with “High” samples, and the group termed “Treatment”.



Figure 29. Phred scores of the total dataset (norflurazon and chlorobenzene [Chapter 5] samples as a single analytical batch). Phred scores indicate the likelihood of a correct base call in Illumina RNAseq technology, Phred score at 30 or above suggest at least 99.9% likelihood of a correct call (= 100%*(1-(10^(-Phred_Score/10))). Only a single sample showed decreased scores (two technical replicates of ‘NF8L4’), with scores at all time still >25 (99.7% likelihood of correct call). Color guide: Green = Very good quality calls, Orange = reasonable quality calls, Red = poor quality calls.

3.3. Confirmation of NF exposure concentrations and adverse outcome induction

Measurements of an adverse outcome induction (growth rate inhibition) as well as quantifying the concentration of NF in the medium samples were both conducted to increase confidence in the experimental results and achieve phenotypic anchoring. Measured medium concentrations of NF (Fig. 30A) were well within range of the nominal exposure concentrations (1mg/L “Low”, 2mg/L “High”) with a slight upward trend overall, however the measured induction of growth rate inhibition (Fig. 30B) of the “High” concentration was higher than initially expected. Such divergence between results of individual growth inhibition assays have been observed before, owing to some differences in culturing of sensitive algal species [486,487,489,490] and were not unexpected considering the relatively steep slope of the concentration-response curve measured for NF (Fig. 26) and slight upward trend of measured NF concentrations from nominal.

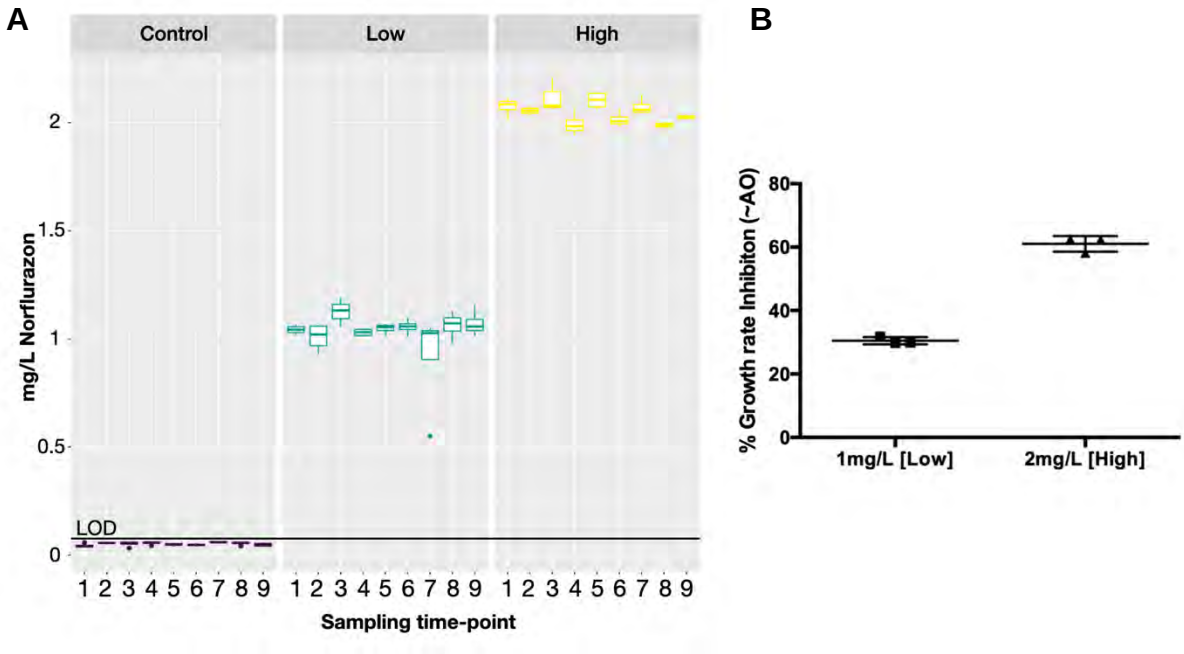


Figure 30. (A) Boxplots of exposure concentrations per group over time-course, measured by LC-MS/MS, and (B) boxplots of growth rate inhibition measured via CASY cell counting at 24h, post induction of the adverse outcome (inhibition of cell division). Marked in (A) is the limit of detection (LOD) for the applied LC-MS/MS method.

3.4. Global effects of norflurazon on C. reinhardtii biology

When comparing the complete datasets generated by the various *omics* platforms and applying unsupervised dimensionality reduction using principal component analysis (PCA), the maximal variance in the data could be described by

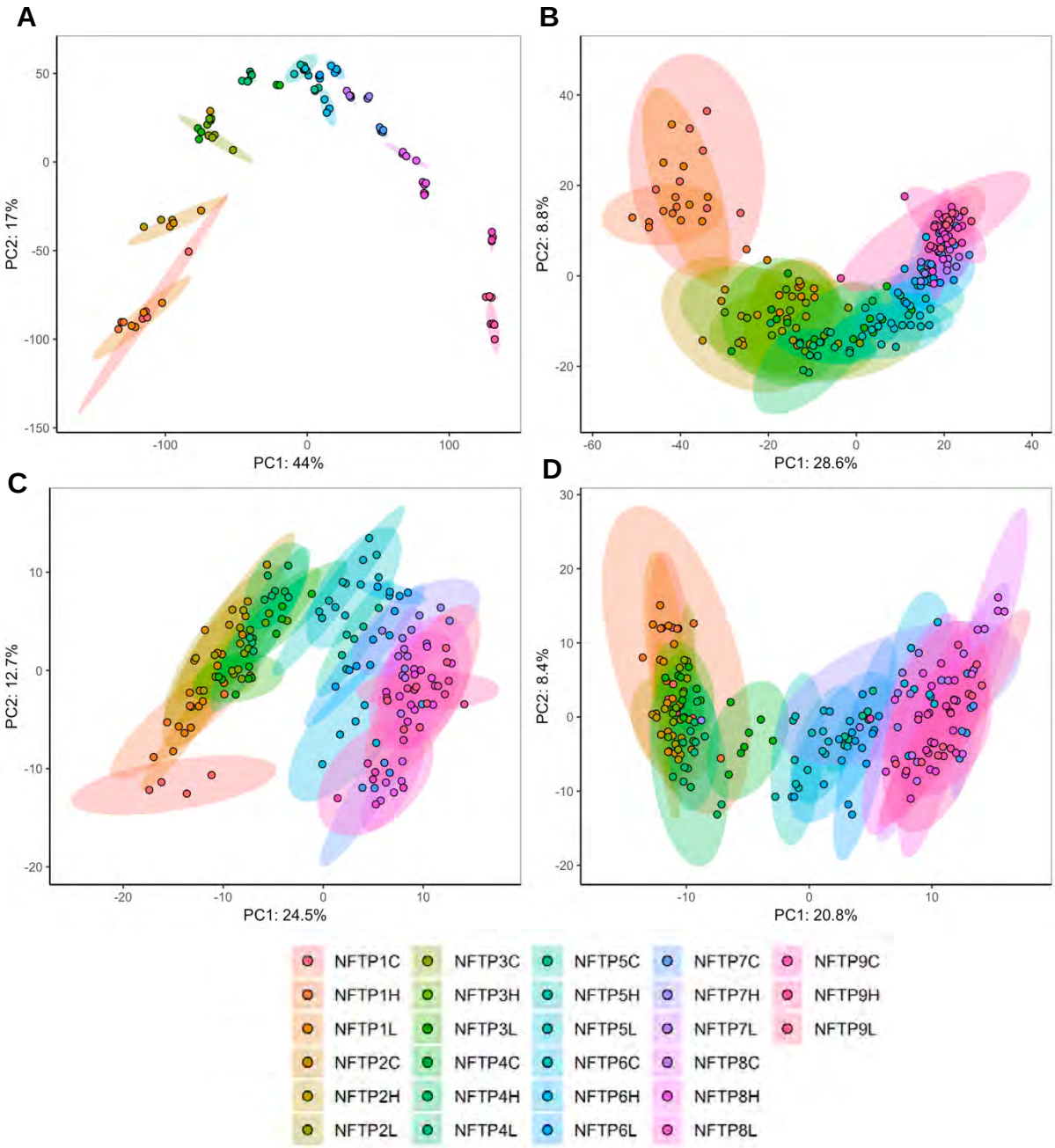


Figure 31. PCA of complete dataset (“NF” = Norflurazon, Time-point “TP” 1-9, “C”=Control, “L”=Low, “H”=High), for (A) Transcriptomics, (B) Lipidomics, (C) Metabolomics positive ion mode, (D) Metabolomics negative ion mode. Colored regions indicate the 95%-confidence intervals. Scaling differences between RNA and metabolite/lipid data stem from different data processing pipelines and are not indicative of quantity of molecular effects.

the developmental trajectory of *C. reinhardtii* cells progressing through the different sampling timepoints (Fig. 31). The global dataset with omission of the 'time'-variable was here further termed the 'collapsed dataset'. The crescent-shaped trajectory of PC scores was indicative of the underlying biological and developmental changes driving growth and position in cell cycle, as has been similarly observed for *C. reinhardtii* or other plants before [390,515]. For transcriptomics data, specifically time-points (TP) 8 and 9 segregated themselves from the rest of the dataset, occurring immediately before the dark-light transition (TP80 and after entering dark-phase (TP9),

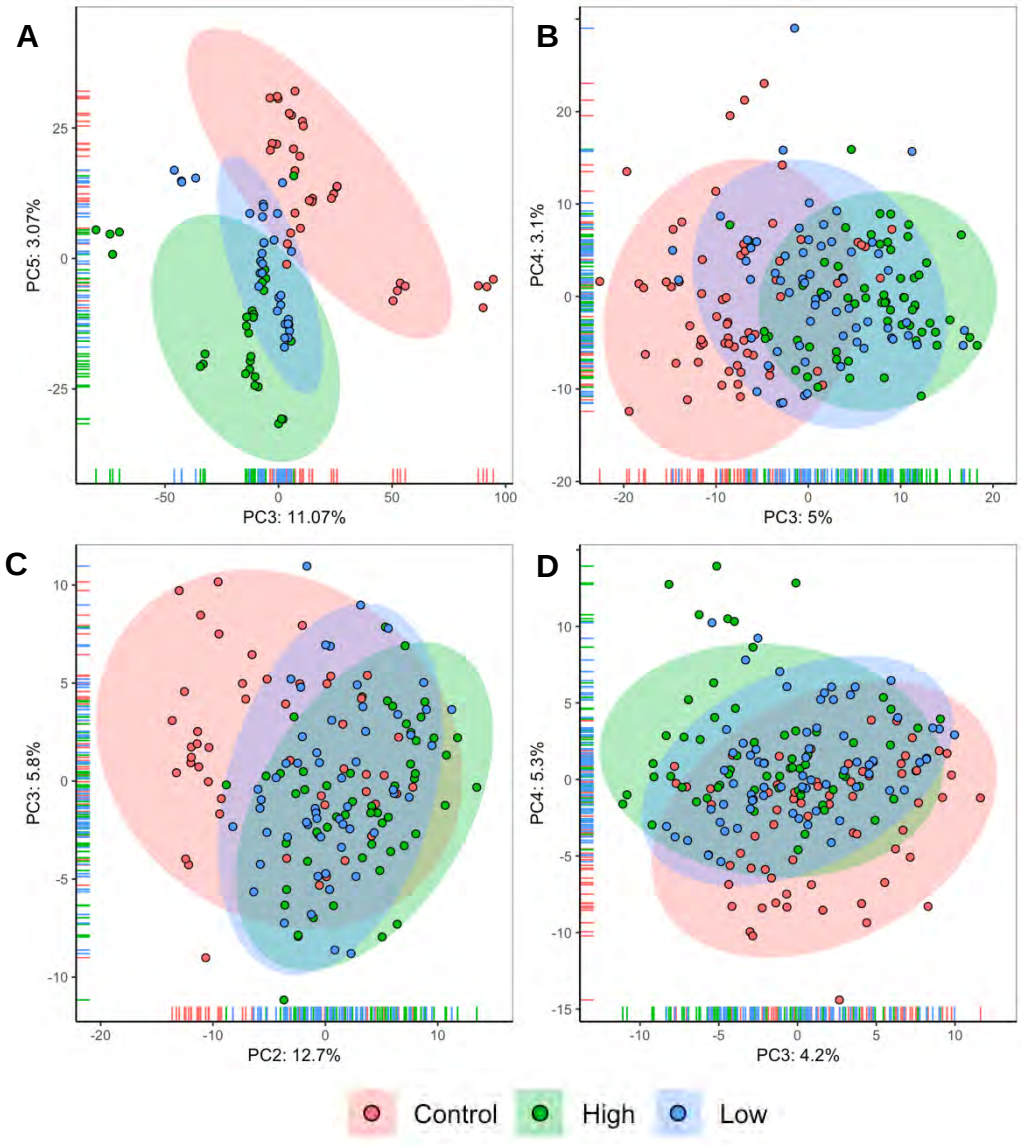


Figure 32. PCA plots of (A) transcriptomics, (B) lipidomics, (C) positive ion metabolomics and (D) negative ion metabolomics, using the complete collapsed dataset (time variable omitted). Principal components were selected that highlight the underlying effects of increasing NF concentrations consistent over time-course.

representing the drastic changes cells are undergoing during this transition [193,197]. Upon isolated analysis of the “Control”-group, periodicity and time-dependence of specific biological processes could be traced over mid- and late cell cycle using k-means clustering and gene ontology enrichment analyses (Suppl. Fig. SI-11), with results in agreement with previous profiling of *C. reinhardtii* cell cycle progression [193,218,390,391].

When collapsing the dataset, scrutiny of principal components 2-5 reveals that subtle but underlying NF-exposure related molecular effects were appreciable in the *omics* measurements. Specifically, PC3 and PC5 for transcriptomics data, PC2 and PC4 for the positive and negative ion metabolomics assays, respectively, and PC3 for the lipidomics data indicate an exposure-dependent effect consistent over all timepoints (Fig. 32), with transcriptomics data showing the most pronounced effects.

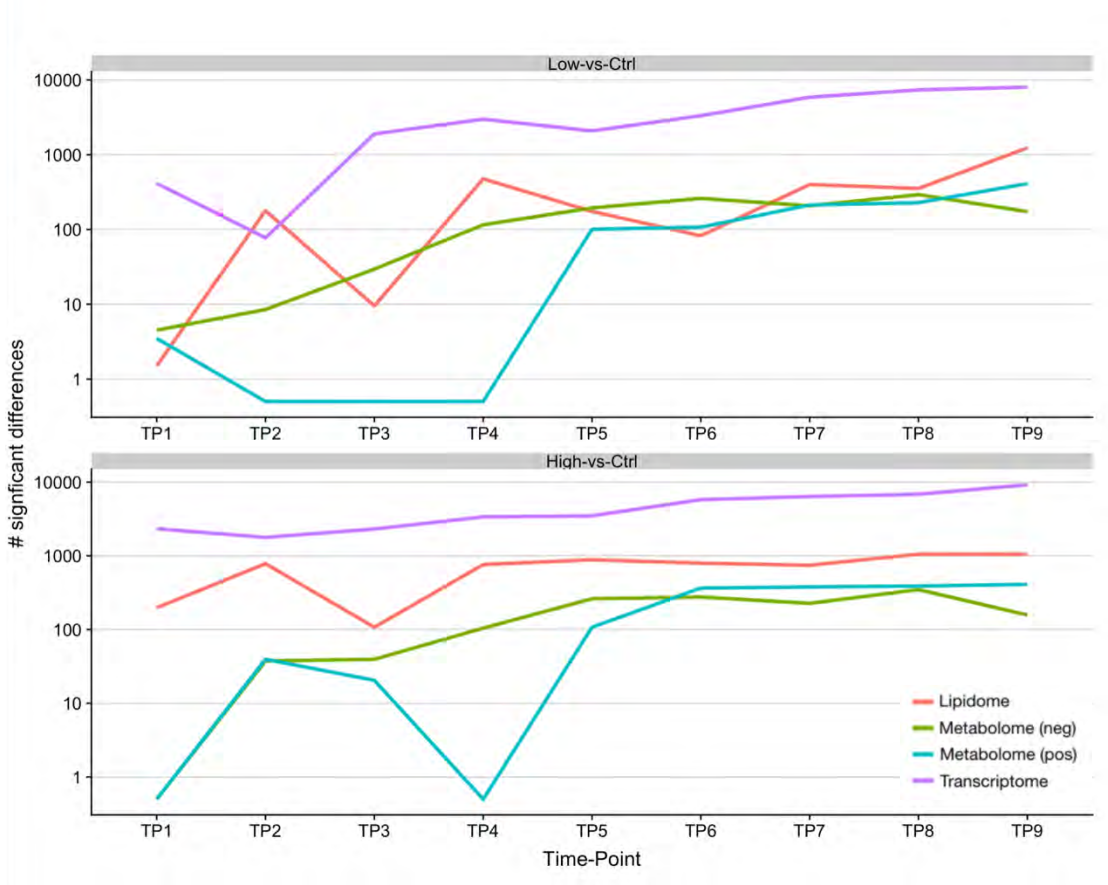


Figure 33. Significantly different variables between exposure groups (Top = Low-vs-Control comparison, Bottom = High-vs-Control comparison), as represented by differentially expressed genes for RNA data (FDR ≤ 0.05, $\log_2$-fold change ≥ 2) and as spectral peaks significant between groups (Welch’s t-test, FDR ≤ 0.05).

In line with this observation, an immediate, consistent and substantial response of the transcriptome to NF exposure was appreciable early from TP1 in PCA (Suppl. Fig. SI-12) and when calculating differentially expressed genes (DEG) over time-course (Fig. 33), indicating high sensitivity of either the transcriptome itself as a result of exposure, high analytical precision of the instrumental platform, or both. Specifically, the “High” exposure group showed a highly consistent presence of DEG over the time-course with ever increasing number of DEGs over exposure time. The “Low” group showed 10-fold increase in DEG (and later almost 100-fold) only beyond TP2, indicating possible activation thresholds of discrete adaptive/adverse effects in dependence of exposure concentration, or cumulative effects of toxicity [426].

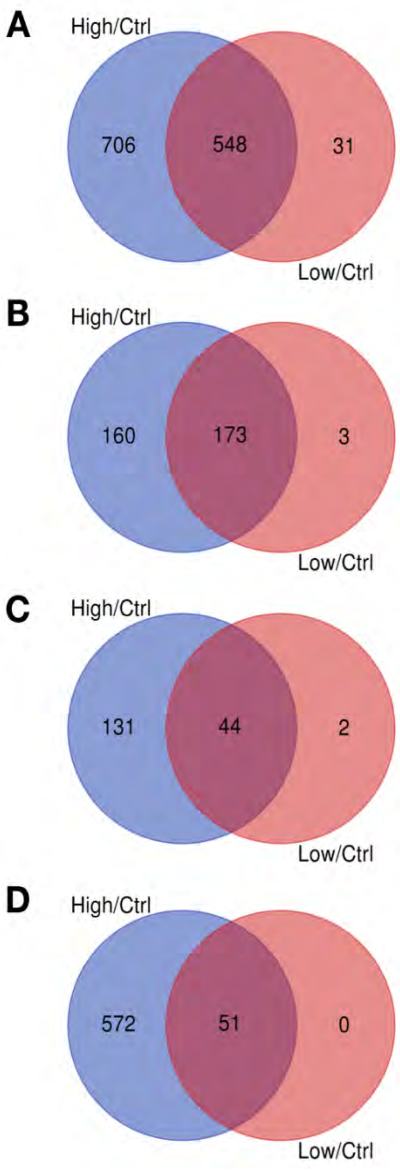


Figure 34. Venn diagrams of significantly different spectral peaks in (A) lipidomics data, (B) positive metabolomics data, (C) negative metabolomics data, and of differentially expressed genes in (D) transcriptomics data. Comparisons of “High”-concentration to “Control” (“High/Ctrl”) and of “Low”-concentration to “Control” (“Low/Ctrl”) are shown, intersections of circles show numbers of the differences that could be found within both comparisons.

When collapsing the dataset and drawing Venn diagrams of NF-induced significantly changing spectral peak intensities and DEG (Fig. 34), the considerable overlap between the High-vs-Control and the Low-vs-Control comparisons in all the *omics* the suggests similar NF-induced molecular effects at both exposure levels, with the higher NF exposure levels mediating a more diverse biological stress profile of *C. reinhardtii*. This high consistency of the molecular measurements of High-vs-Control and Low-vs-Control also builds further confidence in the technical quality of the exposures and subsequent *omics* measurements. Gene enrichment analysis of DEG in the collapsed transcriptomics dataset (Suppl. Fig. SI-13) using Joint Genome Institute biological process gene ontologies (JGI-GOs) indicated apparent down-regulation of processes involved with cellular motility and cell cycle checkpoint progression, and upregulation of lipid metabolism and redox processes in the High-vs-Control comparison, whereas downregulation of processes involved with cell cycle checkpoint progression marked the most-strongly enriched JGI-GO terms in the Low-vs-Control comparison. However, DEG analysis and omission of ‘time’ as a descriptor variable could give here at best an initial insight when analyzing a time-course dataset. The large-magnitude oscillations of gene expression during growth and developmental trajectory (biological signal) in the collapsed dataset did likely overshadow the more subtle “Low”-concentration effects (toxicological signal) due to the primary reliance of DEG-calculation on significance and log2-fold change [446,516], whereas more diverse toxicological signals could be determined in the “High”-exposure group due to larger effect size of molecular changes vs. changes over time. When applying parametric gene set enrichment analysis (PGSEA) to a multi-group comparison [508], more nuanced insights into molecular changes induced by NF could be observed (Fig. 35), due the focus of PGSEA on impact of individual biological pathways rather than

statistical significance [446,517]. As visible in the PGSEA heatmap, developmental patterns of gene expression over time-course still confound this mode of analysis strongly. However, PGSEA suggested that many observable changes were dose-dependent and increased gradually over concentration. The top-30 FDR-ranked JGI-GOs affected involved cellular motility, peroxisomal activity, membrane transport processes and general energy metabolism, some of which were reported previously as effects of NF-toxicity or general toxicant stresses [424,518,519] but could not here be precisely anchored in a time-dependent cause-effect progression using the

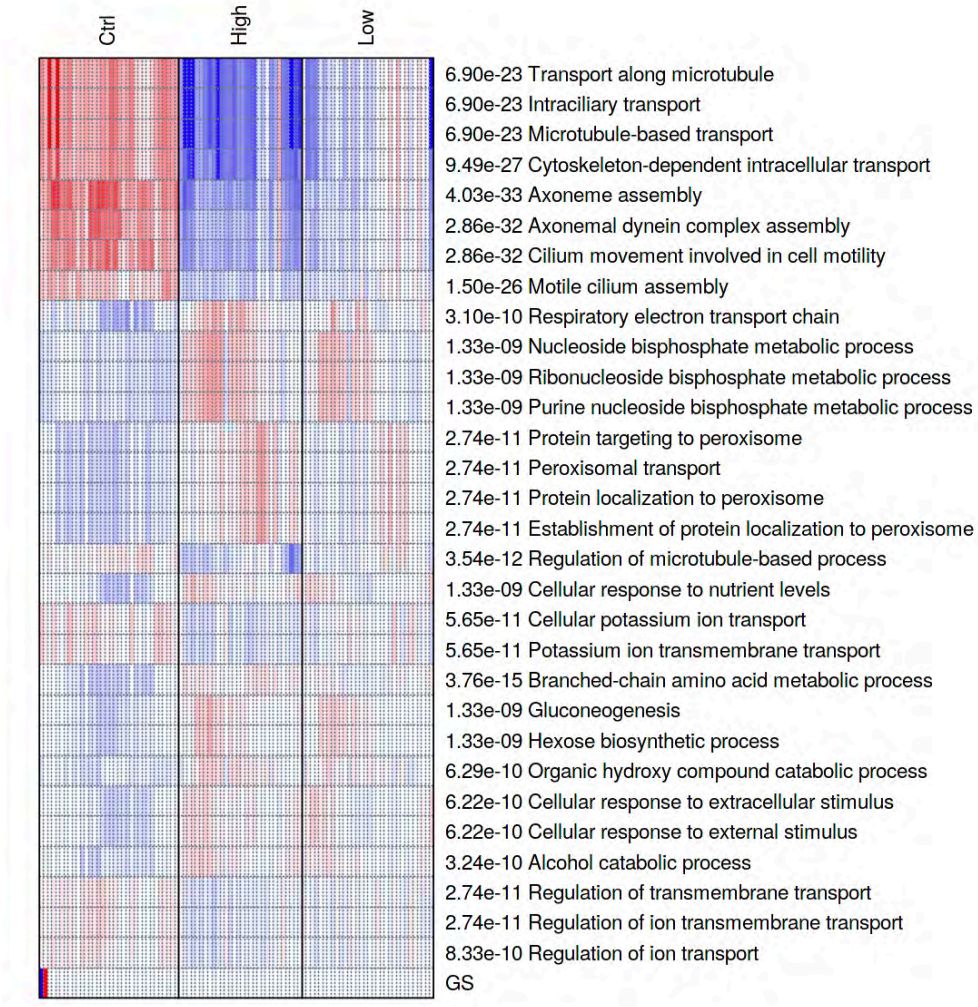


Figure 35. JGI-GO enrichments of NF-induced changes in the collapsed transcriptomics dataset, identified by parametric gene set enrichment analysis (PGSEA; [508]). Gene ontologies are presented and ranked along their FDR. PGSEA allowed first insight into exposure effects even when collapsing the time variable, and indicated monotonous changes from Control gene expression over increase in exposure concentration. However, strong time-dependence of molecular perturbation can still be observed, indicating the present weakness of omitting time-course in analysis. Red = relative higher expression of gene, blue = relative lower expression of gene. Time-points are plotted from TP1 to TP9 per group from left to right.

collapsed global dataset. Specifically, reduction of cellular motility appeared to be one of the major NF-induced changes on the transcriptome.

The *C. reinhardtii* metabolome and lipidome appeared to be less sensitive to NF-induced changes in the collapsed dataset as well at individual sampling time-points, with stronger effects by measure of significantly different spectral peaks between building after time-point TP4 (Fig. 33). Specifically, the positive ion metabolomics assay was less sensitive to changes at early time-points, which was potentially partially caused by the reduced sample size from *m/z* calibration drift corrective measures. At “Low” concentration, both the lipidome and the negative ion metabolome exhibited less than ten significantly different spectral peaks in immediate response to exposure at TP1. At “High” concentration the lipidome appeared most sensitive to NF, with consistently high numbers of significantly different spectral peaks throughout the time-course. However at and after TP5, all DIMS assays indicated higher numbers of significantly different spectral peaks (e.g.in the high hundreds of peaks), with classes significantly separating in PCA according to ANOVA of PC scores (Suppl. Fig. SI-12). The relatively higher analytical variance of DIMS (vs. RNA-Seq) likely played a further role in the reduced responsiveness of the metabolome and lipidome [355], with the PCA indicating relatively close clustering of groups in contrast to the transcriptomics data during the time-course pre-TP5, and much larger in-group variance as compared to the transcriptomics data. Overall, metabolite set enrichment analysis of significant features between groups (collapsed dataset without time variable) indicated no significantly enriched metabolic pathways, likely due to low putative spectral peak annotation success (Suppl. Tables SI-T5 /-T6/ -T7) and limited statistical power of the collapsed global dataset ignoring the time resolution provided by the experimental design.

3.5. Time-course analysis of norflurazon toxicity on algae

To enable a deeper interrogation of the multi-*omics* datasets, time-points were analyzed independently regarding gene-/metabolite set enrichment and DEGs, genes and spectral peaks were clustered according to their similarity in time-course profiles, and variables of interest submitted to enrichment analyses. Clusters of spectral peaks with similar time-profiles identified by metaboClust software could not be satisfactorily annotated and showed no significant metabolic pathway enrichments (Suppl. Table SI-T3, Suppl. Figs. SI-5/-6/-7).

3.5.1. Cell motility inhibition dominates NF-induced changes on transcriptome

As indicated above for transcriptomics (not for lipidomics or metabolomics data), the apparent inhibition of cell motility was one of the strongest and consistent effects over time when scrutinizing both the collapsed dataset (Fig. 35) and individual time-points. maSigPro time-profile clustering identified “Cluster07” (Fig. 36) that comprises genes showing significantly decreased expression at almost all sampling time-points and enriching over 30 JGI-GOs related to cellular motility and flagellar assembly

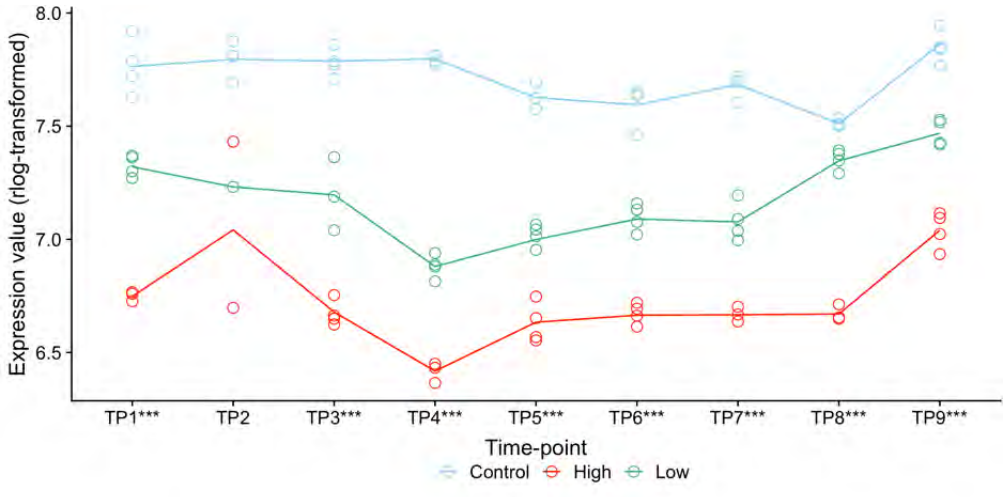


Figure 36. Time-course plot of maSigPro gene “Cluster07”, functionally enriched with gene ontologies involving cell projection, cilium assembly, -regeneration and ciliary motility (Fig. 37) Plotted are replicate medians of all genes per time-point, and the median over replicate medians per time-point connected by a line per group. Significant changes in expression (ANOVA) are indicated by * (FDR<0.05), ** (FDR<0.01) or *** (FDR<0.001).

(Suppl. Table SI-T10). Accordingly, similar enrichments were found in DEG (Table SI-T8) between the High-vs-Control comparison (significant at all sampling time points and within collapsed dataset), the Low-vs-Control comparison (significant at all time point except TP2, TP8 and TP9), and in the top-30 gene sets in PGSEA (collapsed dataset and at all sampling time points except TP2, TP7 and TP9; see Table SI-T9). The effect showed a consistent concentration-dependency (larger effect in “High” concentration) over NF exposure concentration for the entire time-course, including as early as 1 h after the NF exposure started (Fig. 36). The identified gene “Cluster07” enriched over 30 JGI-GOs including “Microtubule-based process”, “Microtubule-based transport”, “Cilium of flagellum-dependent cell motility”, “Locomotion”, etc. (Fig. 37). The gene cluster specifically contained genes coding proteins related to *C. reinhardtii* flagellar function, including flagellar axoneme/microtubule proteins (e.g. TUBA/TUBB), dyneins (e.g. DHC10, IDA7), and those involved in intra-flagellar transport (e.g. IFT122).

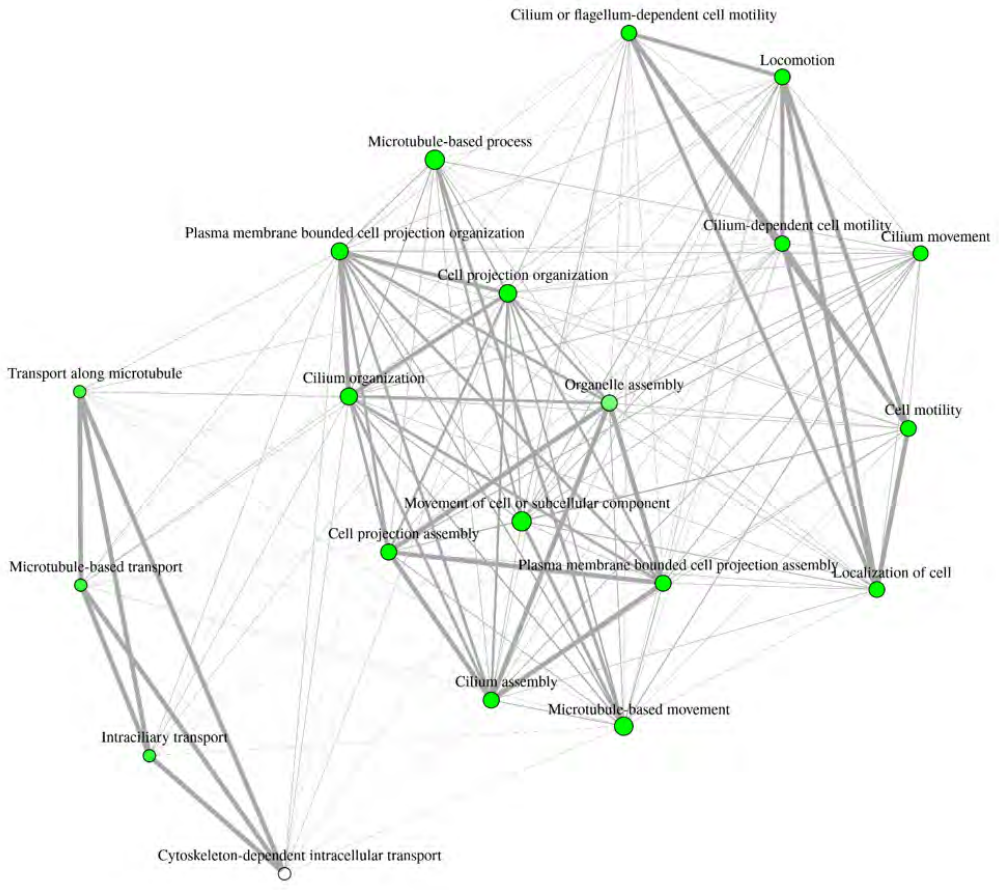


Figure 37. Network representation of JGI-GO categories related to cellular motility as discovered by maSigPro time-profile clustering (“Cluster07”). Distance of the lines (“edges”) is a measure of similarity, size of the nodes (bright green) is relative to significance of enrichment of the ontology term.

Inhibition of *C. reinhardtii* cellular motility on a phenotypical level has been reported for exposure to *Anabaena* toxin [520], selenite [521] or in other algae exposed to heavy metals [522,523]. Flagellar regeneration and algal cell motility was reported previously as one of the most substantially impacted biological processes on the transcriptome of *C. reinhardtii* after toxicant exposure. For instance, exposure to inorganic and organic mercury species led to significant and substantial downregulation of gene ontologies comprising flagellar constitution, growth control and regeneration processes, involving axonemal dynein synthesis, flagellar ATPases, motor proteins, basal bodies and intra-flagellar-associated proteins [246,247,524]. Similarly, exposure to copper or lithium led to significant reduction of cellular motility and flagellar growth [525,526].

In healthy cells, structural microtubular proteins of *C. reinhardtii* flagella (e.g. TUBA/TUBB, dyneins) undergo a dynamic cycle of loss and re-construction due to environmental influences, attrition and intra-cellular protein recycling [192,527–529]. Reduction in TUBA/TUBB biosynthesis and intra-flagellar protein shuttling by the IFT gene family [530] thus likely leads to cumulative loss of flagella regeneration over cell cycle, as potentially observed here. Flagellar assembly (including axoneme, basal bodies and intra-flagellar transports) in healthy cultures was previously reported to increase briefly in activity immediately before, during and after cytokinesis, indicating growth of flagellar of divided cells after retraction of the same before cytokinesis [193]. Fig. 38 shows a similar increase in gene expression in “Low” and “High” at TP8 and TP9, however reduced as compared to “Control” cultures. Concordant lack of related gene ontologies from DEG enrichments of the “Low” group at TP8/9 (Suppl. Table SI-T8), and from the top-30 gene sets in PGSEA at TP9 was appreciable. These last sampling time-points are located at and shortly after the light-dark transition, and are marking cell cycle stages of nuclear and cellular division in synchronized cell cultures [193,197,198,470].

Such molecular effects have to date not been reported before for *C. reinhardtii* or more generally for microalgae exposed to NF. Overall, multiple possible scenarios could result in inhibition of cellular motility, for instance potential existence of a secondary molecular target of NF on the pathway of flagellar protein synthesis,

requiring targeted follow-up studies to evaluate this hypothesis. More likely however, given the previous observations of reduced motility following a wide range of chemical stressors (see above) is the general redirection of energetic flux from the metabolic cost of cellular movement (microtubule synthesis, intra-flagellar protein transport, etc.) towards adaptive and compensatory responses to toxicant exposure during the cellular growth phase of cell cycle (TP1 – TP7). Partial, but compared to “Control” reduced re-activation of these pathways in exposed cultures (mainly in “Low” and to a much lesser degree in “High” group) was observed at the later time-points (TP8 and TP9) during flagella synthesis, the latter being required for newly-divided cells (zoospores).

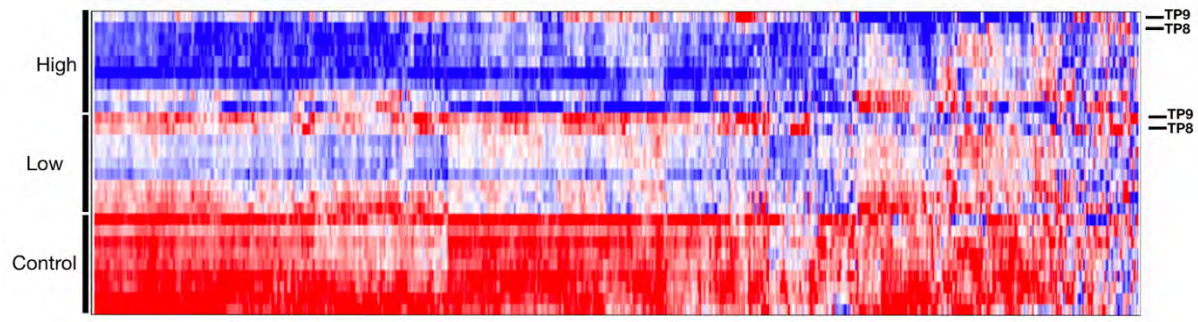


Figure 38. Heatmap of the cell motility gene cluster, showing relatively increased (Red) and decreased (Blue) gene expression profiles of “Control”, “Low” and “High" groups over the normalized complete dataset. Indicated are time-points 8 and 9 (TP8/9) in exposed groups, showing slight increases of gene expression at these late time-points in the "Low” group, but also for parts of the gene cluster in the “High” group.

3.5.2. Norflurazon induces oxidative stress and perturbs redox homeostasis and lipid metabolism

A second prominent effect of NF on *C. reinhardtii* was a delayed but significant induction of genes enriching ontologies related to lipid catabolism and lipid β-oxidation processes. Upregulated DEGs at time-points 5-9 (TP8 only in “High”; Suppl. Table SI-T8), in the collapsed dataset (“High” group), and in the top-30 gene sets in PGSEA at time-points 4-7 (Suppl. Table SI-T9) were found enriched with these and closely-related ontologies. When analyzing the time-course behavior of these genes, NF concentration- and time-dependency of effects were found, with a significant upregulation and departure from “Control” expression levels at and after TP3 and highest expression levels reached at the latest sampling time-points (Fig. 39A). A similar but delayed relationship was observed for the JGI-GO “Oxidation-reduction process”, significantly upregulated from TP5 to TP9 (Suppl. Fig. SI-14).

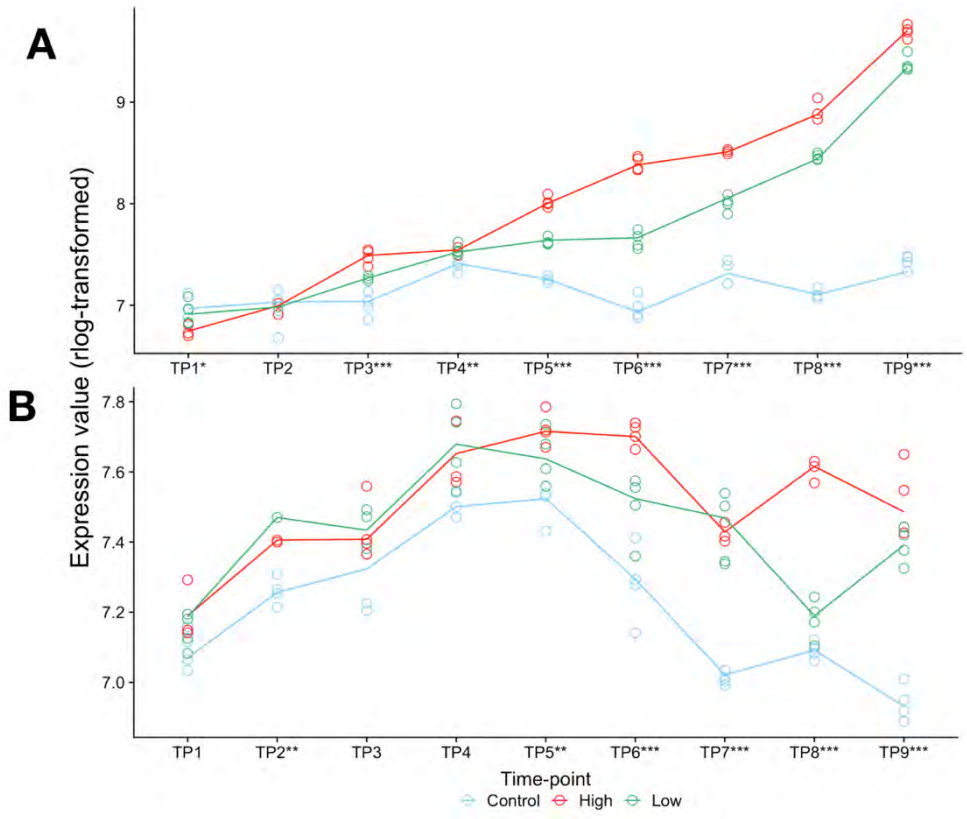


Figure 39. Time-course plot, median of genes per replicate and median of medians with connection line. Showing expression for (A) “Lipid catabolism" and "b-oxidation" JGI-GOs, and (B) Sulphur metabolism (combined JGI-GOs “Glutathione metabolic process”, “Sulfur Synthesis“, “Methionine Metabolism” and “Sulfur Amino Acid Synthesis”). Significant changes in expression (ANOVA) are indicated by * (FDR<0.05), ** (FDR<0.01) or *** (FDR<0.001).

Upregulation of various markers of oxidative stress caused by norflurazon were previously reported, including chloroplastic peroxiredoxin PRX1, thioredoxins TRXf and TRXm, and superoxide dismutase FSD1, cytosolic TRXh, mitochondrial PRX7, and downregulation of cytosolic PRX2 [424]. The new data collected data agreed overall with existing findings, however more nuanced differences were found in the time-course analysis of synchronized cultures (Suppl. Fig. SI-15 to -23). In the chloroplast, PRX1 was upregulated from TP4 to TP8, and downregulated at TP9, TRXf/x/y were upregulated from TP4 to TP9, and FSD1 was upregulated from TP5 to TP9 [531]. Cytosolic PRX2 and TRXh were as well upregulated from TP5-9, whereas mitochondrial TRXo and PRx7 were upregulated only at later time-points, from TP6 to TP9. Time-course plots of oxidative stress markers split per organellar compartment (Fig. 40) suggest delayed response to oxidative stress in cytosol and mitochondria as compared to earlier onset in the chloroplast, pointing to chloroplast-initiated oxidative stress.

Markers for increased sulfur metabolism were found as part of the homeostatic response to reactive oxygen species (ROS) [192], with the “Glutathione metabolic process” JGI-GO identified within the top-30 gene sets in PGSEA as upregulated at TP3, “Sulfur Synthesis“ and “Methionine Metabolism” upregulated at TP5, and “Sulfur Amino Acid Synthesis” upregulated at TP6 and TP8 (Suppl. Table SI-T9). A set of genes enriching the KEGG pathway “Sulfur metabolism” and JGI-GO “Sulfur compound transport” was further identified by maSigPro “Cluster01” (Suppl. Tables SI-T10 and TI-11, Suppl. Fig. SI-25). In a previous investigation in non-synchronized cells, a lack of *C. reinhardtii* glutathione-S-transferase (GST) stimulation was observed in response to NF exposure [424]. Here, upregulation of GST and mitochondrial GSTm at TP5 to TP8 and related enzymes such as glutathione synthetase GSH1 (upregulated at TP5 to TP9) were measured. Combining non-redundant genes from JGI-GOs “Glutathione metabolic process”, “Sulfur Synthesis“, “Methionine Metabolism” and “Sulfur Amino Acid Synthesis” and plotting expression over time (Fig. 39B), a trend towards increased expression is observed as early as TP1, with group differences significant and increasing at TP2, and clearly evident from TP5 to TP9. More support for an oxidative-damage driven mechanism was the presence of upregulated antioxidant synthesis. The JGI-GO “Flavin-compound biosynthesis” was

in the top-30 gene sets in PGSEA at TP3-5 (Suppl. Table SI-T9), with riboflavin specifically promoting the degradation of norflurazon [532,533].

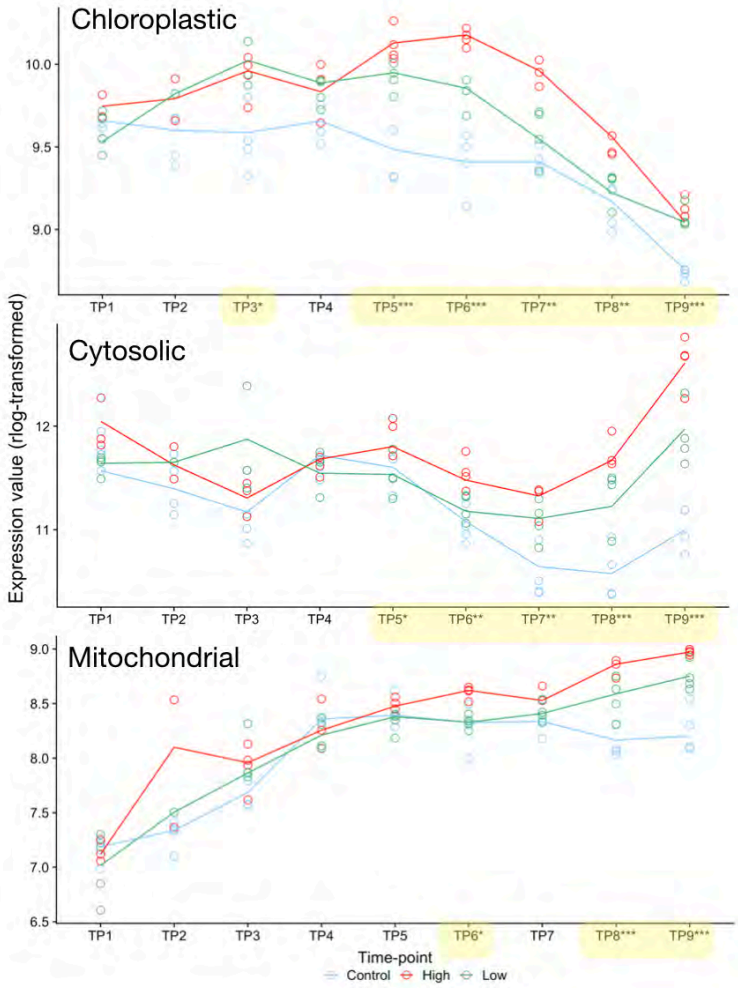


Figure 40. Comparison of oxidative stress markers from 3 cellular compartments in *C. reinhardtii.* Time-points with significant differences between exposure groups (ANOVA) are shaded yellow. Chloroplast markers have a trend for upregulation from TP2, whereas significant differences were observable at TP3 and TP5-9. Cytosolic and mitochondrial markers overall were appreciable only considerably later (from TP5 and TP6, respectively), suggesting initiation of ROs in the chloroplast compartment and propagation of ROS damage at later time-stages into neighbouring compartments. Significant changes in expression (ANOVA) are indicated by * (FDR<0.05), ** (FDR<0.01) or *** (FDR<0.001).

NF is known to induce oxidative stress through inhibiting photo-protectant carotenoid compound synthesis [350]. The early increase in sulfur metabolism was here indicative of an immediate defensive response in reaction to ROS. Algal fatty acids are synthesized in the chloroplast stroma [534], the observed β-oxidation and lipid catabolism was thus proposed here as the resulting molecular detoxification and degradation mechanism of oxidized fatty acids, themselves resulting from oxidative damage to membrane lipids of the sensitive chloroplast thylakoids [535]. Decrease of chloroplastic lipids like monogalactosyldiacylglycerols (MGDG) as seen in NF-treated soy bean [536] was measurable here as well on the lipidome of *C. reinhardtii*, recording a trend over time of decreasing levels of two measured spectral peaks putatively annotated as 18:2-MGDG species (Suppl. Figs. SI-26 and SI-27). With,

significant differences were present at most but not all sampling time-points, potentially owing to the higher variance of lipidomics measurements.

Concurrent to (membrane) lipid damage, protein degradation was ranked high in the top-30 gene sets in PGSEA using the collapsed dataset (Fig. 35), with significantly upregulated JGI-GOs for “Peroxisomal transport” and “Protein targeting to peroxisome” steadily increasing after TP5 (Suppl. Fig. SI-28). Peroxisomes are the site of protein- but also of further fatty acid degradation in algae [537–539]. As identified by KEGG pathway enrichments of maSigPro “Cluster03” genes (Suppl. Fig. SI-29, Suppl. Table SI-T12), fatty acid biosynthesis was upregulated significantly from TP3 to TP7, and downregulated thereafter. This stimulation of lipid synthesis and lipid metabolism was observed previously for algae exposed to NF, other ROS-inducing herbicides, or high-light stress [424,538,540,541], and is proposed here as compensatory mechanism resulting from oxidative damage initially localized to chloroplast membranes and membrane proteins. Further proposed is a downstream overpowering of the homeostatic lipid and protein catabolism capacity in chloroplasts and peroxisomes (recycling of damaged species) over time. A steady accumulation of ROS, as suggested by increasing gene expression of lipid catabolism and redox markers (Figs. 39 and 40) likely led to a tipping point and propagation chains of oxidative damage to neighboring cellular compartments [396,542], as indicated by delayed oxidative stress markers in cytosol and mitochondria (Fig. 40).

3.5.3. Norflurazon impacts pigment metabolism up- and downstream of molecular target

Carotenoids are pigments that act as plastid photoprotectants via ROS quenching and non-photochemical excess energy dissipation [543]. The primary mechanism of NF is the inhibition of the enzyme phytoene desaturase (PDS), effecting accumulation of its substrate phytoene and overall depletion of downstream carotenoids [338,544–546] in the carotenoid synthesis pathway (Suppl. Fig. SI-65). In this dataset, few carotenoids could be measured using DIMS, likely due to limited ionization of long-chained lipids in the electrospray source [547]. In the collapsed global dataset, pathway overrepresentation analysis of significant spectral peaks in "Low" and "High" groups on *Arabidopsis* metabolic pathways indicated dysregulation of carotenoid metabolism, however highly non-significant (FDR = 0.93 and 1, respectively). Transcriptomics data maSigPro time-profile clustering identified a "Cluster05" containing genes enriching the KEGG pathway "Carotenoid Synthesis" (Fig. 41, Suppl. Table SI-T13). Dysregulation (Up: TP1, TP2-TP8; Down for "High": TP9, Down for "Low": TP8) of the gene cluster was significant at all time-points except TP2, which may have been caused by the low sample size in both exposure groups (Fig. 41). Enrichment of JGI-GO "Carotenoid biosynthetic process" was further found in the top-30 gene sets in PGSEA at time-points TP1 and TP4-7 (Suppl. Table SI-T9).

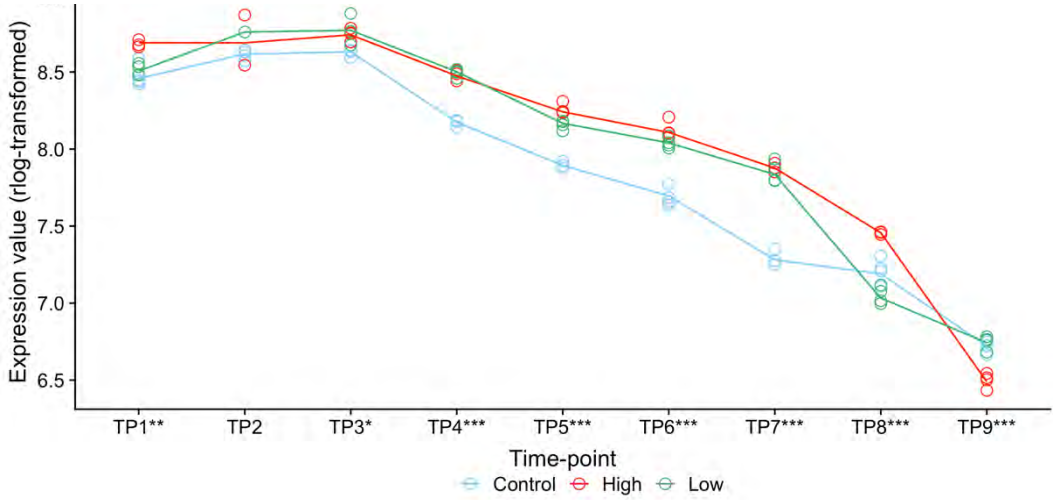


Figure 41. Time-course plot, median of genes per replicate and median of medians with connection line, showing expression of the genes in maSigPro "Cluster05" enriching KEGG pathway "Carotenoid synthesis". Significant changes in expression (ANOVA) are indicated by * (FDR<0.05), ** (FDR<0.01) or *** (FDR<0.001).

Previous *omics* investigation did not indicate any specific disruption of the carotenoid synthesis pathway and NF's molecular target PDS following NF exposure [424], stressing difficulty of discovering molecular targets (MIE in AOPs) using *omics*. Targeted biochemical analysis in other plants on occasion found downregulated PDS after NF treatment [545,548]. Differences in overall experimental design, analytical technology, computational analysis or simply cross-species differences might partially explain such observations, however overall, an increase of PDS expression stands to reason after NF exposure and is to be expected in the plant kingdom [338]. Here, the enzyme PDS was significantly upregulated at all timepoints except TP2 (low n) and TP3 (Fig. 42), and was element of the identified maSigPro "Cluster05". Overall, the genes in the KEGG carotenoid synthesis pathway (KEGG 'cre00906') were significantly upregulated at all time-points prior to TP8 (Suppl. Fig. SI-31). A spectral peak putatively annotated as the upstream precursor substrate compound of the carotenoid pathway, geranylgeranyl diphosphate (GGPP) and its intermediate dihydro-geranylgeranyl diphosphate, were found at lower levels in NF-exposed algae than in control cultures (significant at multiple time-points), suggesting depletion of free substrate as overcompensation to downstream pathway activation (Fig. 43A and B). Similarly, the non-mevalonate pathway including its key pathway enzymes CMS and MEcPP synthase involved upstream in GGPP-synthesis [549–551] were found significantly upregulated at all time-points except TP2 and -3 (Suppl. Fig. SI-32), whereas peak intensities of the spectral peak putatively annotated as its pathway

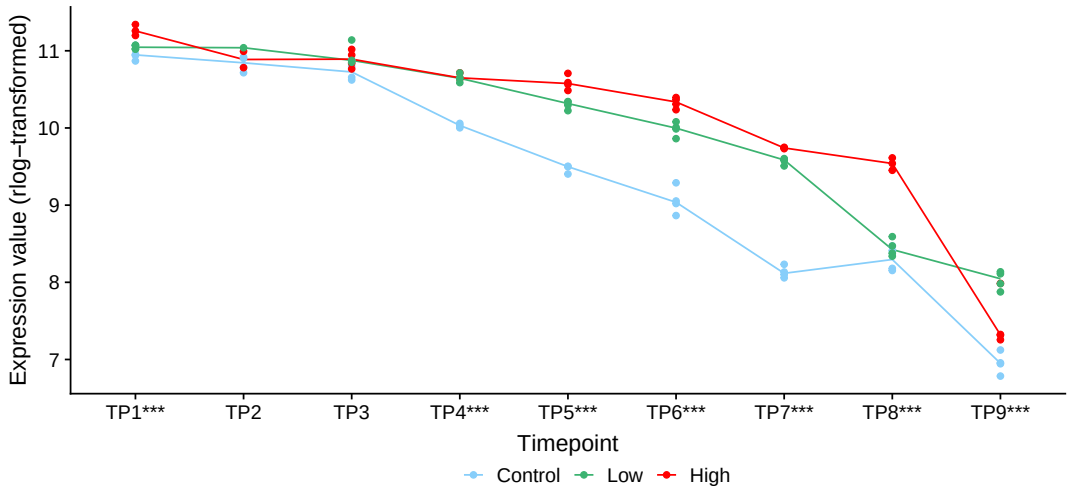


Figure 42. Time-course profile of NF's molecular target, phytoene desaturase (PDS1). Significant changes in expression (ANOVA) are indicated by * (FDR<0.05), ** (FDR<0.01) or *** (FDR<0.001).

intermediate 2-C-methylerythritol 4-phosphate (MEP) were significantly reduced at all time-points compared to “Control” (Fig. 32 C). Overall, rapid clearance of pigment precursors and pathway intermediates was indicated to compensate for lack of generated carotenoids, terpenoids and other related downstream phytochemicals [552].

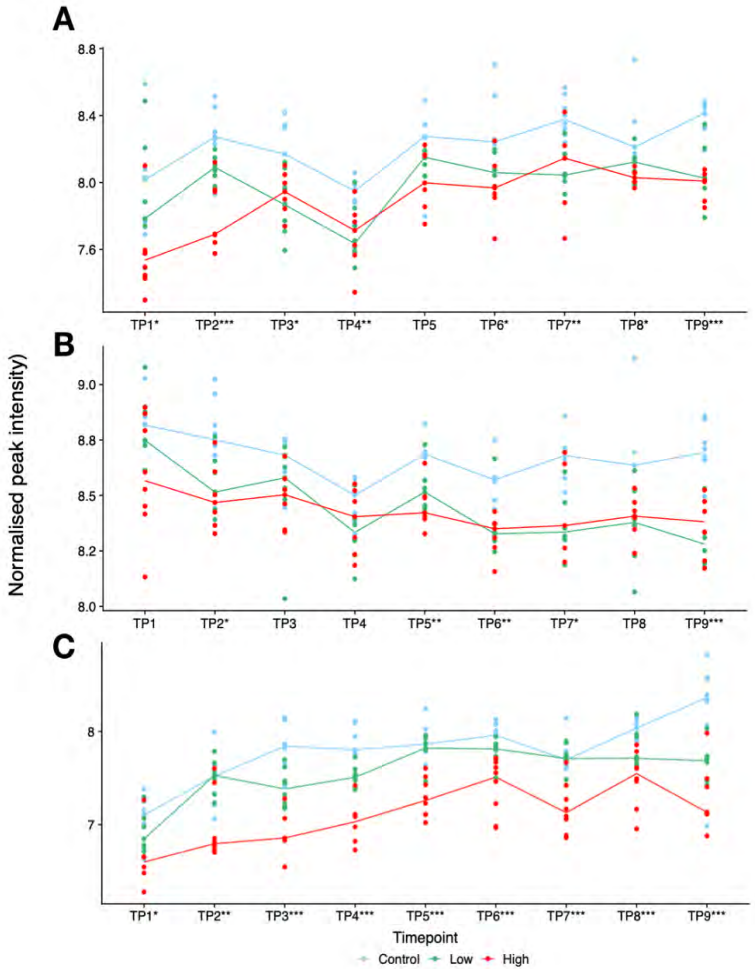


Figure 43. Normalised peak intensities of spectral peaks putatively annotated as (A) geranylgeranyl diphosphate (B) dihydro-geranylgeranyl diphosphate, and their precursor 2-C-Methylerythritol 4-phosphate (MEP), over time-course. Significant changes in peak intensity (ANOVA) are indicated by * (FDR<0.05), ** (FDR<0.01) or *** (FDR<0.001).

The overall reduction of photoprotectants has a marked downstream effects on photosynthesis - catabolism of photosynthetic apparatus, deterioration of the lamellar system and decrease of energy yield from electron-transport in photosystem I and II (PS-I/II) are generic effects induced by NF exposure [553–555]. In the collapsed metabolomics and lipidomics datasets, DIMS data pathway overrepresentation analysis of “High” (but not “Low”) group differences from “Control” cultures indicated significant enrichment of “Porphyrin and chlorophyll metabolism” (FDR = 4.7 x 10^{-16}),

showing increased intensities of spectral peaks putatively annotated as various photosynthetic pigments and pathway intermediates, including pheophorbide-a, Mg-protoporphyrin, primary fluorescent chlorophyll- and red chlorophyll catabolites, divinyl chlorophyllide-a, or chlorophyll-a. The pathway was also significant enriched in overrepresentation analysis when analyzing significant spectral peaks at individual time-points, for group “Low” at TP4 and TP9 (FDR = 0.0035 and 0.019, respectively), and group “High” at TP6, TP8 and TP9 (FDR = 0.0009, 0.004 and 0.0006, respectively). This pathway was not enriched in DEG analysis nor in the top-30 enriched gene sets of PGSEA of the collapsed transcriptomics dataset (Fig. 35, Suppl. Fig. SI-13), however maSigPro time-profile “Cluster03” genes enriched KEGG pathways “Photosynthesis”, “Porphyrin and chlorophyll metabolism” (Fig. 45), “Carbon fixation” and “Photosynthesis – antenna proteins”, amongst others significantly upregulated at TP3 to TP7 (Suppl. Fig. SI-29 and Suppl. Table SI-T12). PGSEA of individual time-points showed upregulated gene sets for various JGI-GOs involving formation of

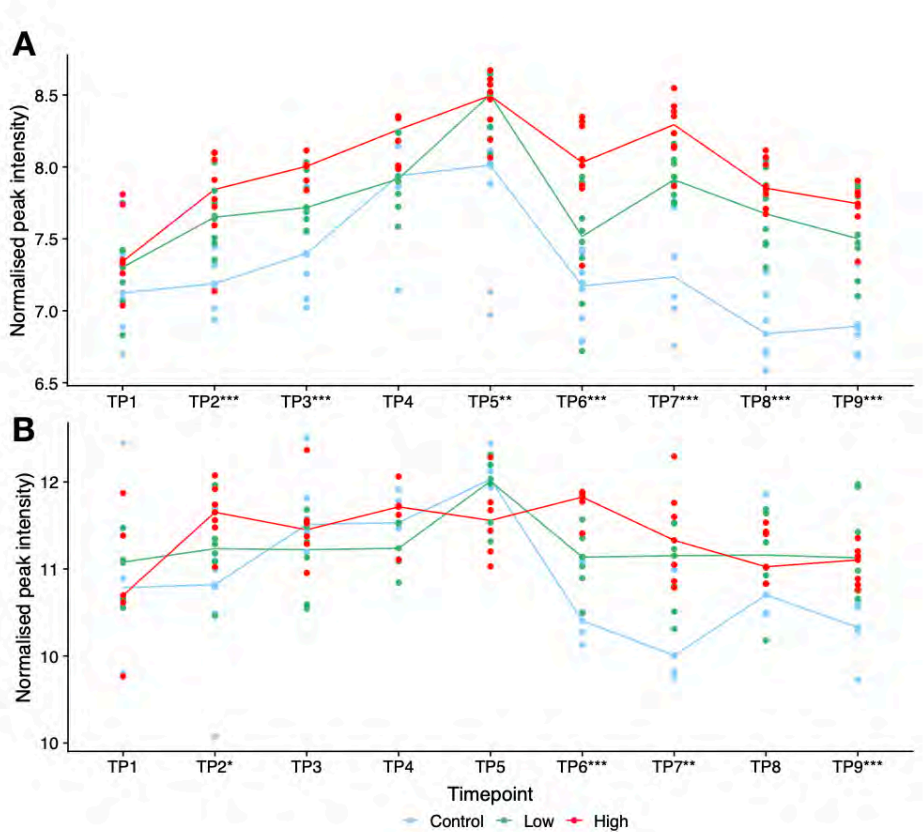


Figure 44. Increased intensities of spectral peaks putatively annotated as (A) Mg-Protoporphyrin IX and (B) pheophorbide-a, two chlorophyll synthesis pathway intermediates. Significant changes in peak intensity (ANOVA) are indicated by * (FDR<0.05), ** (FDR<0.01) or *** (FDR<0.001).

thylakoid and plastid structures, and “Regulation of Photosynthesis” at TP1 and TP3-6 (Suppl. Table SI-T9). DIMS here tended to detect consistent accumulation or depletion of putatively annotated pigment intermediates at all time-points including dark-zone (Figs. 43 and 44), whereas transcriptomics analysis indicated that the primary response to lack of photo-protectants was localized during the light zone primarily (TP1-TP8; Suppl. Fig. SI-29 and Suppl. Table SI-T12).

Induction of porphyrin- and chlorophyll biosynthesis appears to be a compensatory mechanism to NF-induced chlorophyll oxidation by ROS [424,518], with the metabolic pathway enriched by significant changes on the metabolome, transcriptome and lipidome as indicated by generally applicable set enrichment analysis on multi-*omics* data (FDR=0.027, Fig. 45). Precursor metabolism was equally upregulated as shown by increase in geranylgeranyl reductase (GGR) expression (Suppl. Fig. SI-33), similar to Ref. [424]. Further, accumulation of a chlorophyll spectral peak putatively annotated as the pathway intermediate, Mg-protoporphyrin IX (Fig. 44A), appears to have played a role here in chloroplast-nucleus signaling of chloroplast remodeling processes [550,556–559]. The concordant accumulation of pheophorbide-a [560] was likely an additional result of NF-induced porphyrin metabolism upregulation (Fig. 44B, Suppl. Fig. SI-31). The latter as observed here is likely a redirection of metabolic flux to increase pigment levels for scavenging reactive intermediates and protect photosynthetic apparatus [519,545].

Up-regulated gene expression of chloroplast- and thylakoid membrane proteins as a likely concomitant compensatory reaction to NF-induced ROS damage [424] was reflected by enrichments of maSigPro time-profile “Cluster03” and “Cluster08” genes (Suppl. Figs. SI-29 and SI-34, Suppl. Tables SI-T12 and SI-T14), comprising subunits of photosystem antenna proteins, cytochrome-b6f and light-harvesting complex proteins, emphasizing perturbation and regenerative activity of photosystem subunits to sustain of function during cell growth after NF exposure [545]. Most carotenoids and all chlorophylls are bound to antenna proteins, which themselves are situated in thylakoid membrane [561,562]. Due to ROS damage to proteins and membrane lipids, synthesis of these components and general plastid maintenance was likely increased [563–565]. Previously, NF-exposure and perturbance of the carotenoid synthesis

pathway in *C. reinhardtii* was associated with decreased presence of all nine chlorophyll-binding- (light-harvesting complex; lhc) along deterioration of other thylakoid membrane proteins [566–570], the former suggested as biomarkers of chloroplast ROS generation [424,550,566,567,569].

Experiments in non-synchronized *C. reinhardtii* cultures found further evidence of photosystem damage by measuring increased levels of VIPP1, an enzyme associated with thylakoid formation and remodeling [424,571]. In the present experiment using synchronized cultures, large-magnitude upregulation of VIPP1 was specifically found only at the last two sampling time-points TP8 and TP9 (Suppl. Fig. SI-35), suggesting this gene as a marker of accumulative ROS damage specifically measurable during chloroplast organelle repair and division prior to cell division [192,572]. In this context, upregulation of the JGI-GO “Lysine biosynthesis” was present within the top-30 gene sets in PGSEA of TP3-7 (Suppl. Table SI-T9 and Suppl. Fig. SI-36), and found enriched by maSigPro “Cluster05” genes (Suppl. Table SI-T13, Suppl. Fig. SI-30), which along with its support proteins ETFa/-b (upregulated from TP6 to TP9; Suppl. Fig. SI-37) was recently associated with chloroplast maintenance [573,574].

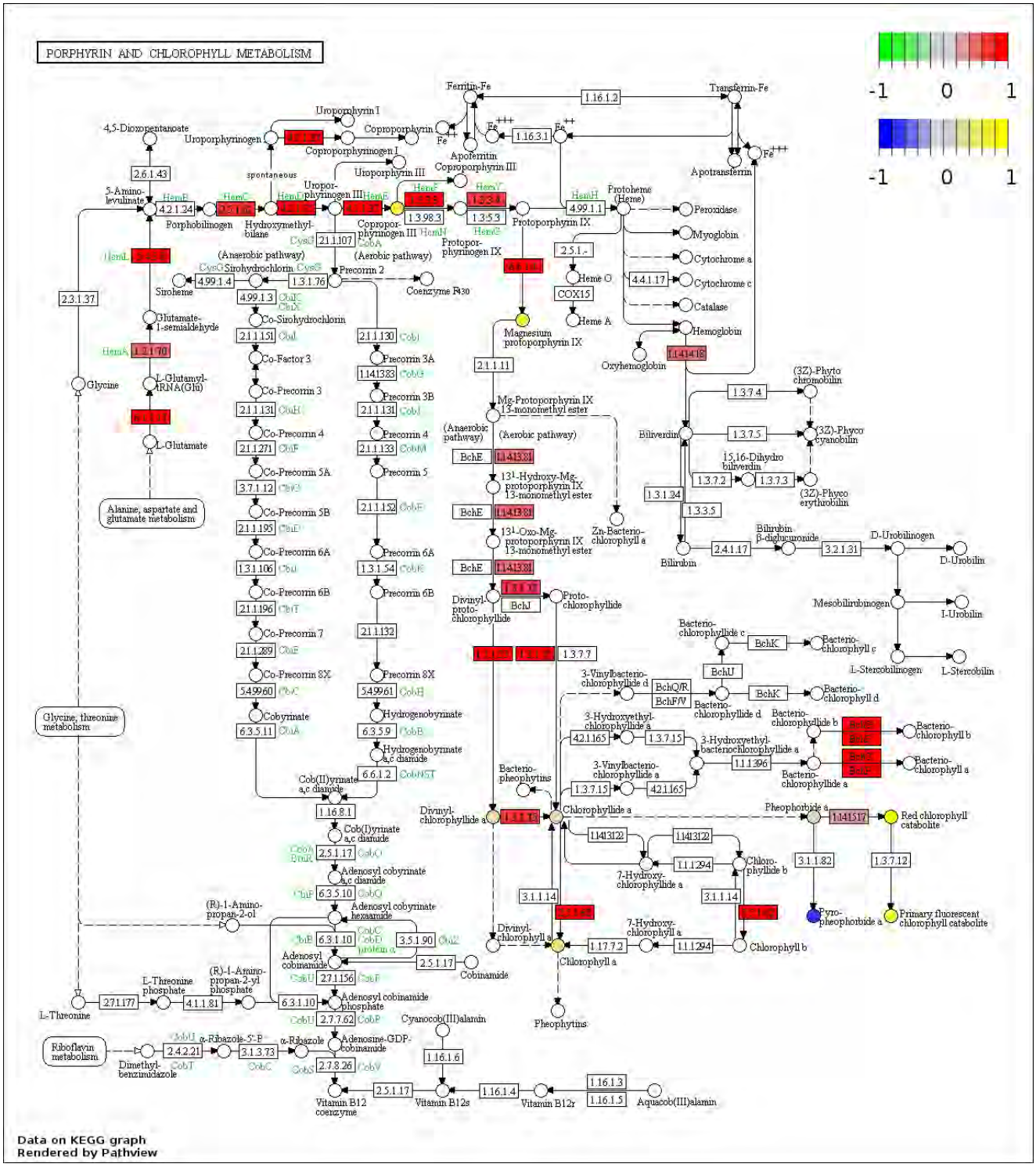


Figure 45. Shared generally applicable pathway enrichment analysis of lipid, metabolite and RNA expression data on the KEGG pathway for porphyrin and chlorophyll pigment synthesis (FDR = 0.027). Up- or down-regulation of genes is marked by green or red coloration, lower or higher spectral peak intensities are marked by blue or yellow coloration. Green enzyme names reflect 'KEGG common enzyme names'.

3.5.4. Homeostatic activation of gene expression and protein synthesis

NF-induced toxic insult had a non-centralized stimulative effect on general gene expression activity and protein synthesis, likely related to adaptive mechanisms to toxicant exposure. Metabolism and synthesis of amino acids was enriched by maSigPro “Cluster05” genes (Suppl. Table SI-T13, Suppl. Fig. SI-30), specifically KEGG pathways “Biosynthesis of amino acids”, “Phenylalanine, tyrosine and tryptophan biosynthesis”, “Aminoacyl-tRNA metabolism”, “Ribosome” and “Protein export”, upregulated from TP3-8 and downregulated at TP9, and “Branched-chain amino acid metabolic process” as identified by PGSEA top-30 gene sets of the collapsed global transcriptomics dataset (Fig. 35). Stimulation of protein synthesis was observed previously in NF-treated *C. reinhardtii,* involving cytosolic, plastidic and mitochondrial ribosomal activity [424], and specifically increase of various protein precursors in chloroplasts [575]. Additionally, lower levels of the protein trafficking markers SEC23-/24A could be associated to NF exposure [424], which expression was here found to be downregulated only at late TP8 and TP9 (Suppl. Fig. SI-38). This, at large, underscores a general increase in gene expression and protein translation, activation and modification towards homeostatic regulatory processes as response to NF-induced cellular stress.

3.5.5. Downstream effects on energy metabolism, metabolic flux and transport processes

Changes on different energy pathways were recorded in the present data using the global collapsed transcriptomics dataset, and various individual time-points (Fig. 24, Suppl. Tables SI-T8 and SI-T9). Expression of the membrane transporter AMTF1 for ammonium, the primary nitrogen source for *C. reinhardtii* strain CC-125, was reduced over the complete sampling time-course (Suppl. Fig. SI-39), in contrast to observed induced amino acid synthesis but in line with previous findings [424]. This might suggest a to-date unexplored nitrogen homeostatic mechanism as stress response, and/or potential cross-talk between dysregulated nitrogen and carbon assimilatory metabolism [576,577]. Metabolism and uptake of carbon was strongly altered by NF exposure. CCP1/2, markers of inorganic carbon metabolism in algae

[192,578–581], were significantly downregulated in the light- and photosynthetic phase of cell cycle from TP2-TP7 (CCP2 not at TP4 and TP5), with downregulation at later time-points TP6 and TP7 (Suppl. Fig. SI-40). On the other hand, activity of carbonic anhydrase CAH3 specific to chloroplast inorganic carbon uptake and concentration, and markers for calvin cycle activity FBP1 were significantly upregulated at TP3-TP8 (Suppl. Fig. SI-41) [192,424]. CCP1/2 are required for overall cellular growth but not for photosynthesis [579], suggesting rechanneling of metabolic energy from cell growth towards carbon pooling for increase in photosynthetic activity as response to chloroplastic NF ROS stress.

Upregulation of glycolysis, pyruvate- and propionate metabolism was identified in maSigPro “Cluster03” gene enrichments (Suppl. Fig. SI-29, Suppl. Table SI-T12), and pentose-phosphate and glyceraldehyde-3- phosphate (g3p) metabolism by PGSEA at TP6 (Suppl. Table SI-T9). Pyruvate is the breakdown product of glycolysis, but also a fermentation product in chloroplasts, mitochondria and cytosol for energy generation in darkness [390]. The upregulation of glycolysis, pentose-phosphate pathway from TP3-7 (Suppl. Fig. SI-29) and g3p at TP1 and TP4 to TP9 (Suppl. Fig. SI-42) could be indicative of general increase in energy generation to meet the metabolic cost of ROS defensive mechanisms. G3p-, glycolysis and pyruvate metabolism though are additionally required for generation of substrates for the non-mevalonate pathway and GGPP-synthesis for porphyrin-, carotenoid- and terpenoid synthesis, thus are likely associated with observed upregulation of various pigment synthesis. Further, pyruvate has been suggested to protect mitochondria from ROS in human cells [582] - a potentially similar role in plants or algae though remains to be demonstrated.

A downregulation of expression of calcium-binding-, calcium transmembrane transport proteins and calcium channel kinases was further discovered by cluster analysis (Fig 46). Calcium serves in plants as general regulatory signaling molecule, e.g. in feedback mechanisms involving successful photosynthesis and carbon fixation [583,584]. Specifically, it was previously associated with cytosol-mitochondrion calcium-potential modulation in response to ROS or heat shock [585–587], or correct functioning of flagellar motility and regeneration [192,588]. Overall, down-regulation of

calcium signaling and membrane-transport processes appears here as a result of systemic metabolic disruption, modulating further downstream adaptive or adverse responses, potentially including upregulation of chloroplast remodeling or reduction of flagellar regeneration.

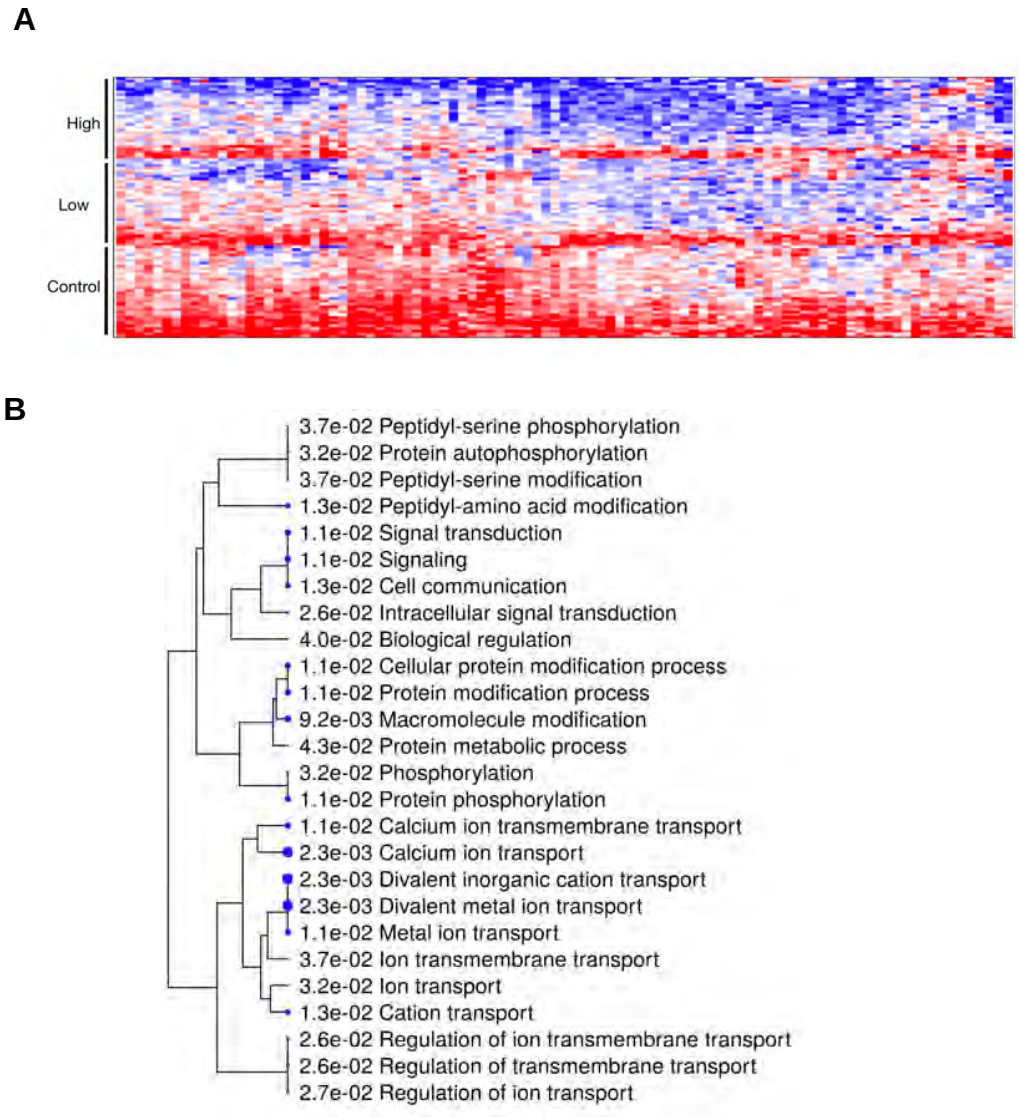


Figure 46. (A) Heatmap and (B) JGI-GO enrichment tree (along FDR) of a gene cluster significantly downregulated from TP5 to TP9 in the collapsed dataset. Color red indicates relatively increased expression, color blue indicates relative reduction in gene expression. Size of the nodes indicates degree of significance, the distance of the clusters connected by the branches of the dendogram is relative to the ontological similarity of gene sets.

3.5.6 Genomic damage, cellular catabolism and apoptosis conclude the cell cycle of NF-exposed *C. reinhardtii*

Delayed onset downstream effects of cumulative oxidative stress damage were appreciable over the time-course experiment. DEGs of TP8 and TP9 enriched for both exposure groups multiple JGI-GOs, including “Macroautophagy”, “Autophagosome assembly” or “Organic substance catabolic processes” – these GOs were also located within the top-30 gene sets in PGSEA for these time-points (Suppl. Tables SI-T8 and SI-T9), as well as found enriched by genes of maSigPro “Cluster01” (Fig. 47, Suppl. Fig. SI-24). Autophagy is an auxiliary homeostatic response mechanism, and in algae is specifically linked to the upregulation of the autophagy-related genes (ATG) in processes of general metabolic adaptation to cellular stress and recycling of degraded cellular components [543,566,589,590]. Specifically in context of NF-/Carotenoid-

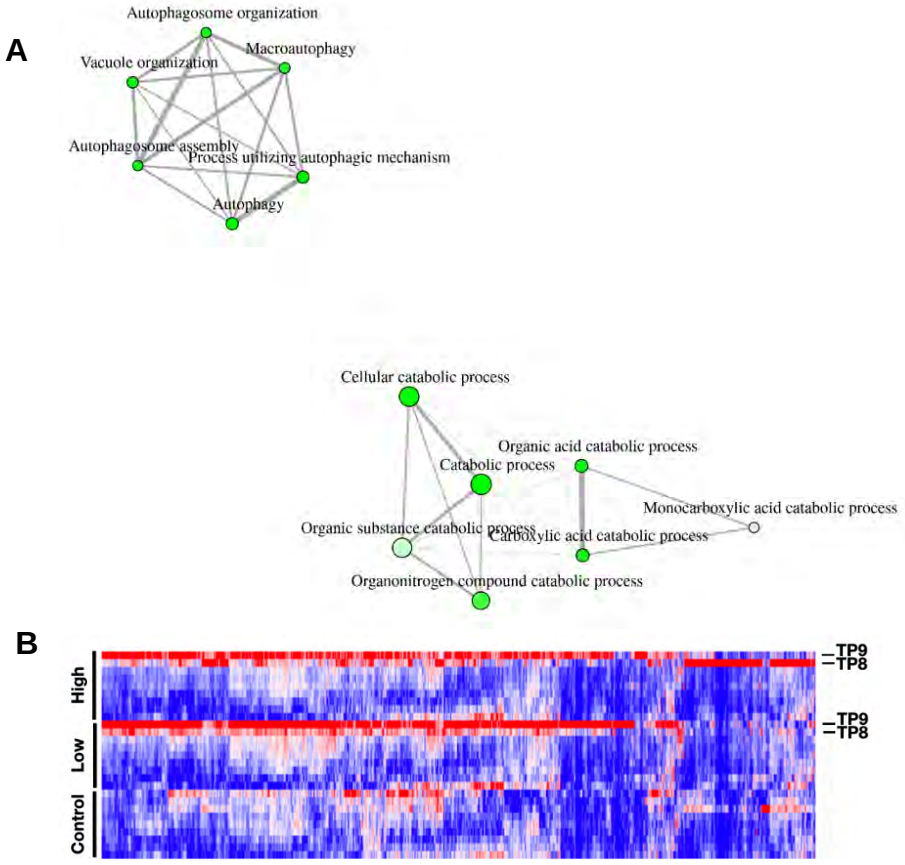


Figure 47. Representation of the genes associated with JGI-GOs comprising autophagic mechanisms and catabolism of organic substances. Distance of the lines (“edges”) is a measure of similarity, size of the nodes (bright green) is relative to significance of enrichment of the ontology term. (A) Network map for, and (B) expression heatmap of maSigPro “Cluster01” genes enriching said JGI-GOs, indicating relative increase (red) or reduction (blue) in gene expression. Time-points 8 and 9 (TP8/9) are marked on the heatmap for exposure groups “Low” and “High”.

Inhibition-induced ROS induction in *C. reinhardtii*, increased expression of ATG8 was observed previously [543]. This autophagy in response to accumulation of degraded cellular material may be delayed by multiple hours in plants [591]. Here, time-course *omics* profiling of the *C. reinhardtii* autophagic response suggested significant and substantial increase of ATG8 but also ATG4/6 and -12 at time-points TP8 and TP9. Concordantly, upregulation of the general marker of autophagic response GPXH [531,590,592] was significant from TP6-TP9 (Suppl. Fig. SI-43).

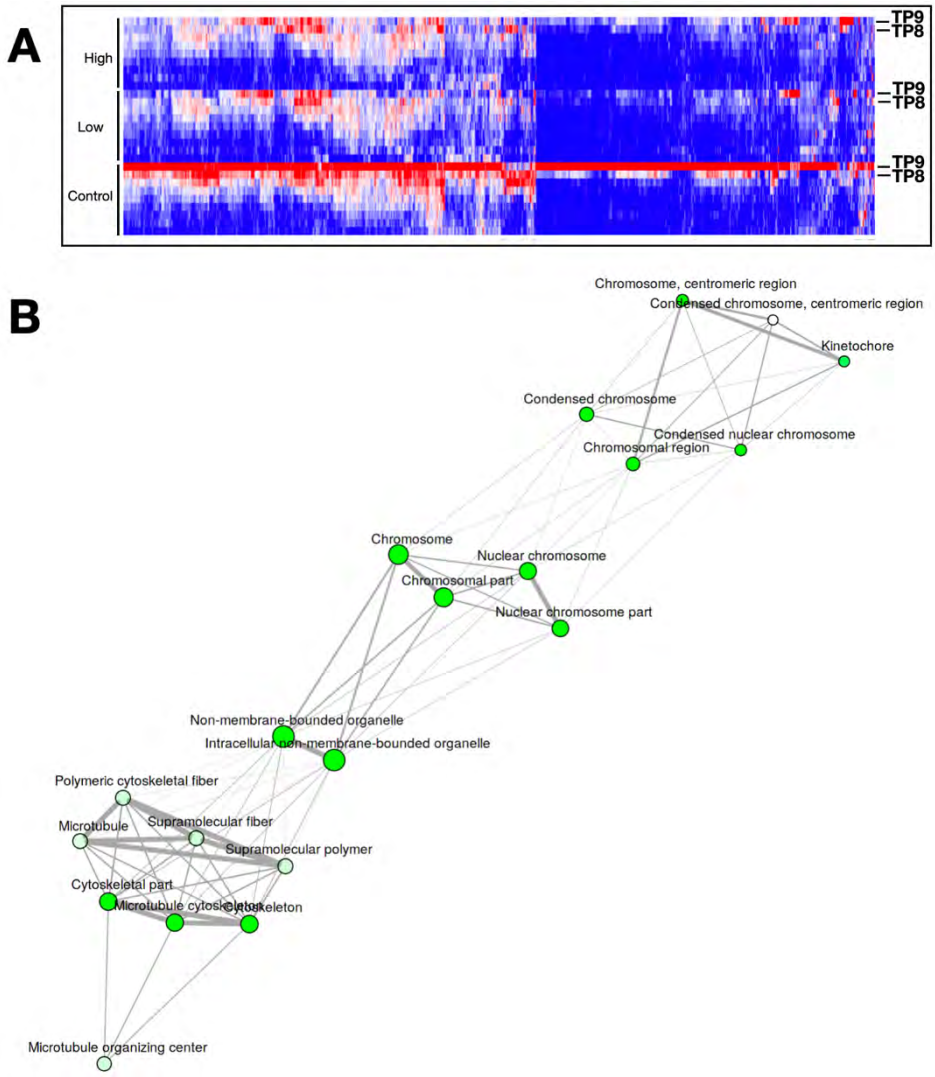


Figure 48. Heatmap (A) of gene expression (blue = relative reduction, red = relative increase) and (B) network map of JGI-GOs enriched by a gene cluster discovered by hierarchical cluster analysis, signalling activity of macromolecular mitotic processes including microtubule-/ cytoskeletal binding and chromosome organization processes, with increased expression almost exclusively only observable in control cultures. Distance of the lines ("edges") is a measure of similarity, size of the nodes (bright green) is relative to significance of enrichment of the ontology term.

More observed changes located at the tail of the cell cycle and sampling time-course were marked by JGI-GOs encompassing regulation of cell cycle progress, cell cycle checkpoints and regulation of mitotic activity. These were enriched by DEG and located in the top-30 gene sets in PGSEA at TP8 and TP9 (Suppl. Tables SI-T8 and SI-T9), comprising “Chromosome separation”, “Mitotic cell cycle”, “Microtubule organization”, “DNA replication”, “Chromosome segregation”, “Organelle fission”, “Sister chromatid segregation”, “Nuclear division”, “Protein polymerization”, “Regulation of cell cycle”, “Cytokinesis”, “Cytoskeleton organization”, “Spindle organization”, “Cell wall organization”, among others. After propagation of ROS from chloroplast into cytosol as indicated above, the cellular nucleus was likely a further target of ongoing oxidative stress propagation chains. Prior to DNA replication, cell cycle arrest was likely activated upon sensing of DNA damage to allow repair mechanisms [593,594]. Dysregulation of the JGI-GO “Cell cycle organization” was

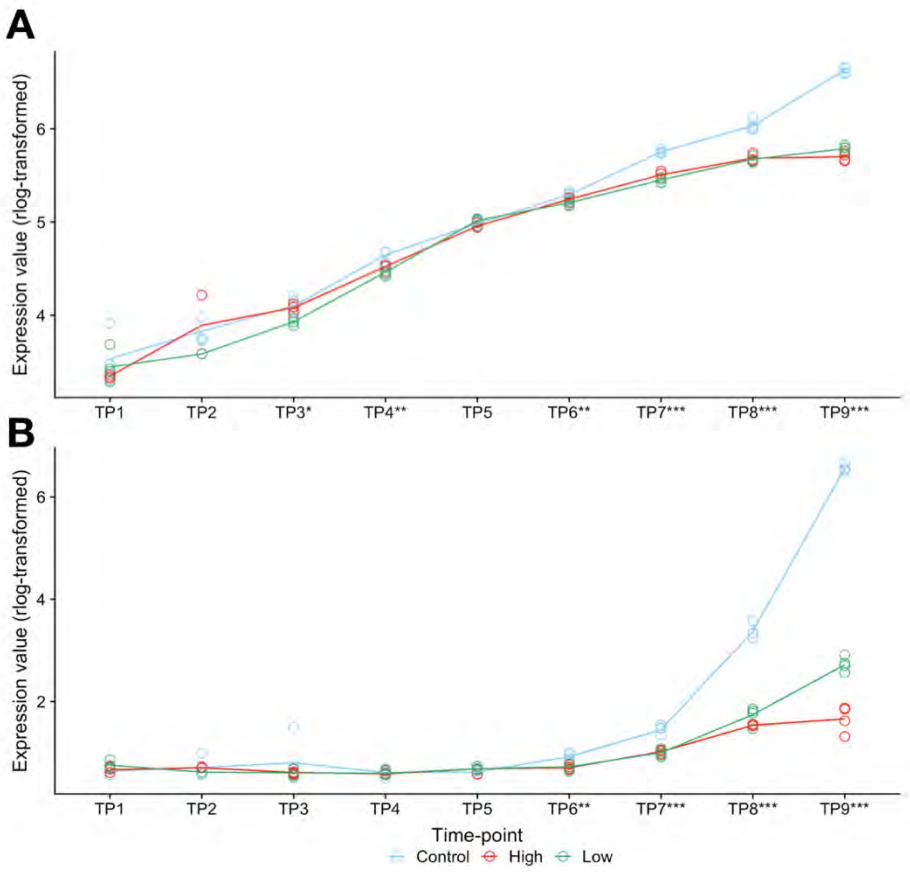


Figure 49. Time-course profiles of maSigPro (A) “Cluster02” and (B) “Cluster06”, both strongly enriched with JGI-GOs related to DNA repair mechanisms, cell cycle checkpoint activity, and mitotic and chromosomal organization (see Suppl. Fig. SI-45). Significant changes in gene expression (ANOVA) are indicated by * (FDR<0.05), ** (FDR<0.01) or *** (FDR<0.001).

reported before for *C. reinhardtii* NF exposure [424]. In the present study, expression of genes enriching discussed JGI-GOs was severely reduced in exposed cells. Actin microtubule synthesis and formation is necessary during all mitotic stages and cytokinesis [595], with cytoskeleton and microtubule assembly activated slightly before and during cell division [192] – here as expected, expression of these spiked at TP8 and TP9 almost exclusively in “Control” cultures (Fig. 48). Similarly, DNA unwinding by helicase activity and associated processes including initiation of DNA replication was observed almost exclusively in “Control” cultures (Suppl. Fig. SI-44). As previously reported [424], related topoisomerase SPO11a and septin-like protein SPE1 were downregulated significantly in exposed cultures, however only at TP8-TP9 (Suppl. Fig. SI-46).

maSigPro “Cluster02” and “Cluster06” (Fig. 49) confirmed these findings, identifying subsets of genes enriching JGI-GOs for various DNA repair processes and chromosomal organization (Suppl. Fig. SI-45), along KEGG pathways involved in DNA repair processes, including “Base-excision repair”, “Mismatch repair”, “Nucleotide excision repair”, “Homologous recombination” and “Non-homologous end-joining” (Suppl. Table SI-T15). Ultimately, significant expression of apoptotic markers (Fig. 50) could be observed at TP8 and TP9 for expose cells in a concentration-dependent relationship. Genomic and cellular damage was likely sensed as exceeding repair capacity, and programmed cell death was induced as the final effect of oxidative stress propagation as described before in plants [596]. The target-of-rampamycin (TOR)-kinase was equally upregulated at these late stages (TP8, TP9) of exposure (Suppl. Fig. SI-47). TOR in plants mediates photosynthetic function, but more importantly is directly controlling autophagic mechanisms, phytohormone signaling, control of actin-like cytoskeleton assembly, cell wall elongation during growth, and apoptosis [597,598]. This is supported by above findings along observed decrease in “Plant-type cell wall” JGI-GO at TP9 (PGSEA; Suppl. Table SI-T9; Suppl. Fig. SI-48).

Summarizing, the final downstream effect of NF proposed here involved an apparent accumulation and monotonous increase of degraded cellular components exceeding the recycling capacity during the light zone, which induced an autophagic response at late timepoints [531,543,566,590,592,599]. Excessive ROS damage to

cellular-, nuclear components but specifically genomic material then likely effected cell cycle arrest [593,600,601], followed by further accumulation of ROS, excessive and irreparable damage to the nuclear genome, ultimately succeeded by programmed cell death [542,596,599,602].

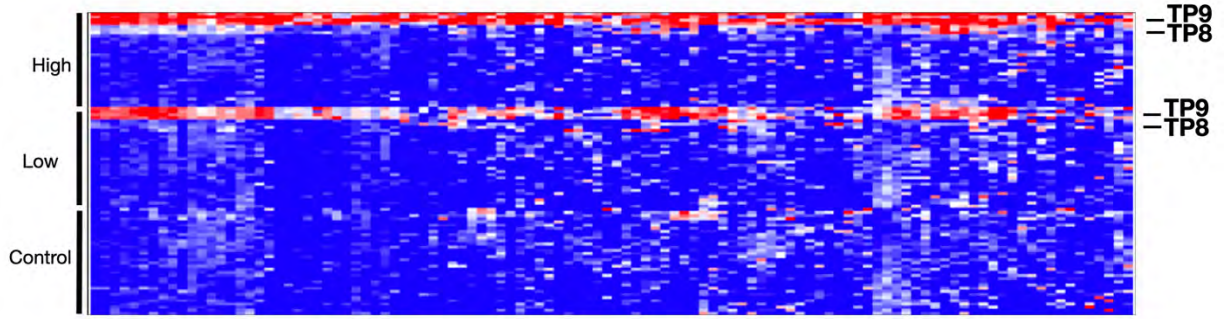


Figure 50. Heatmap of GO comprising apoptotic mechanisms, visible induction only at “Low” and “High” concentrations at the last time-points, TP8 and TP9. Time-points 8 and 9 (TP8/9) are marked, color red indicates relatively increased gene expression, blue relatively decreased.

3.6. Time-course multi-omics exposure data support existing understanding of acute NF chemical MoA and aid construction of a hypothetical AOP draft for C. reinhardtii

The main scientific objective of the present study (Scientific Objective III, see Chapter 1) was to perform an *omics*-driven hypothesis of acute chemical MoA for model toxicants – initially guided by existing knowledge on MoA to show general applicability of the approach (norflurazon, this chapter), and subsequently applied to a toxicant with a poorly described MoA in algae (chlorobenzene, next chapter). To summarize the insights gained through multi-*omics* time-profiling of the *C. reinhardtii* molecular stress response to NF, a time-resolved hypothetical schematic of NF's acute chemical MoA was constructed using only the novel generated data (Fig. 51). The schematic juxtaposes the changes of measured molecular effect categories over time, and is anchored to both the start of exposure and the narrow time-window during which of adverse outcome occurs. Previously, different (multi-)*omics* approaches were applied to gain insights into molecular toxic effects in algae, and first valuable insights into *C. reinhardtii* proteomic and transcriptomic changes and global molecular effects were achieved [246,247,424,524,525]. Further, the importance of introducing time as a variable to study perturbation processes, and discerning reversible adaptive from irreversible adverse effects, was stressed [426]. However as argued in Chapters 2 and 3, the majority of existing work still features the application of single time-point experimental designs ([246,253,256,258–260,424] or only relatively short time-course [426], using non-synchronized cultures [231,243,257,263,426] and/or sampling times indiscriminate of explicit biological anchoring to adverse outcome [251,254,255,261,262,425,427]. Overall, cause-effect relationships can be assumed to be conceptually difficult to deduce in such manner [352–354,388,389,394,395,400].

Here, the transcriptome and metabolome of *C. reinhardtii* were for the first time profiled over a wider time-course at higher temporal resolution (9 sampling time-points), with explicit application of synchronized cell cultures and anchoring of the experimental time-frame to the cell cycle as well as to the terminal time window during which adverse outcome occurs, with the aim of hypothesizing on a time-resolved acute chemical MoA. The tailored experimental design allowed hypothesis of time-resolved interrelation of molecular perturbations caused by the herbicide NF, proposing hypothetical cause-effect chains specific to subcellular locations and spanning from the initial exposure to the ultimate induction of cellular apoptosis. Due to the choice of NF as model toxicant, the analytical approach could be 'calibrated' by comparison of

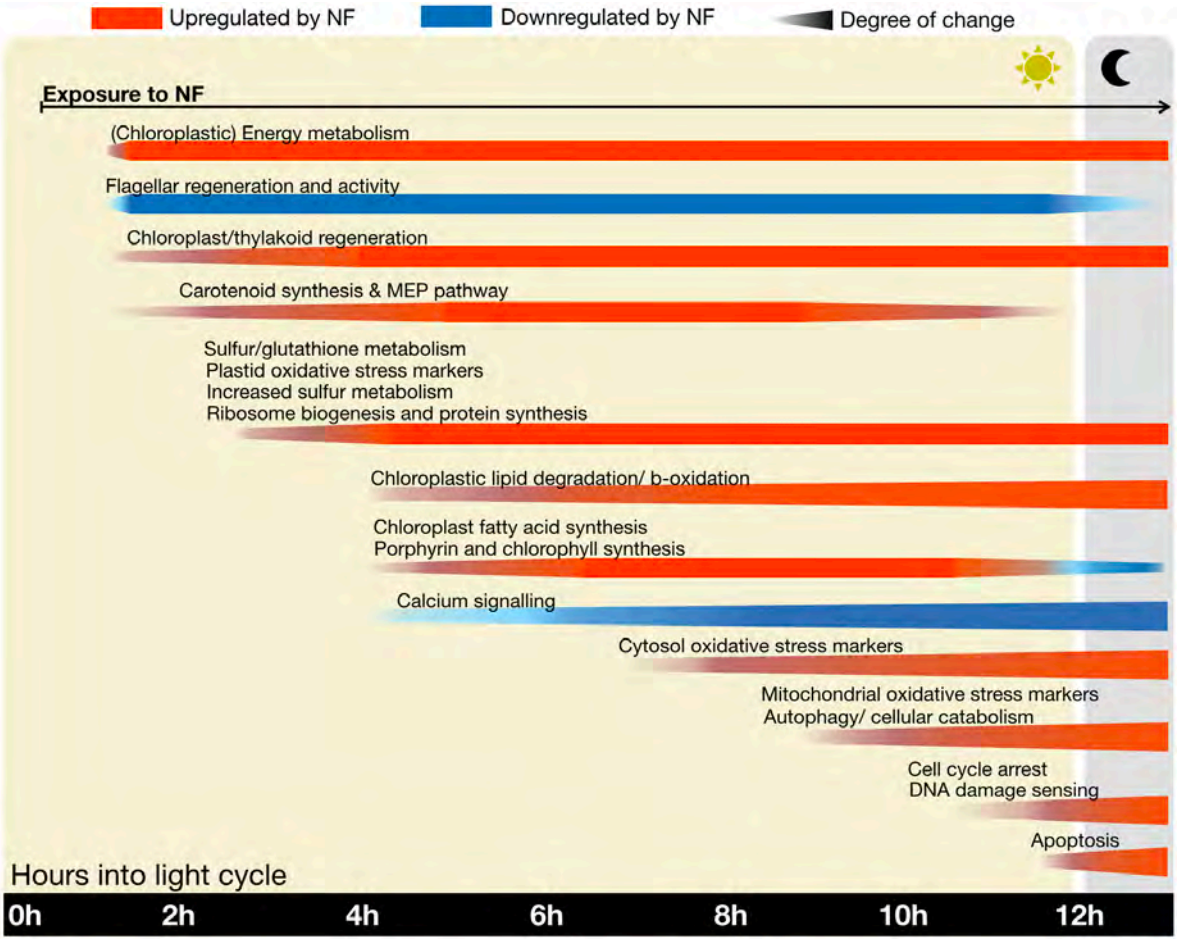


Figure 51. Time-resolved chemical MoA hypothesis of norflurazon toxicity in *C. reinhardtii.* The intensity of molecular effects (marked by increasing or decreasing width of the bars) and direction of change (marked by color of bars) is represented over the sampling time-course. The molecular effects here are anchored to both the 12h: 12h light:dark cycle (at the beginning of the 12h light period and transition into the 12h dark period) and the window of adverse outcome occurrence (inhibition of algal cell division and decrease of population growth rate), with cellular and nuclear division occurring slightly before, during and after the light:dark transition.

generated *omics* data to a known set of expected molecular results, to a) show applicability of the experimental design and *omics* to reliably re-discover known effects of chemicals on *C. reinhardtii,* and b) allow discovery of novel insights into unknown perturbations of NF, here including effects on calcium signalling, flagellar activity/regeneration and induction of programmed cell death. Specifically, the application of PGSEA [508,517] and maSigPro [510,511] allowed unsupervised, statistically powerful and biologically meaningful identification of changes on the transcriptome, and their evolution over time in relation to cell cycle. For metabolomics and lipidomics data, difficulties during initial instrumental sample acquisition and limited success of unique putative spectral peak annotations restricted meaningful analysis to datasets. However, supporting orthogonal information was gained.

To emphasize utility of the presented experimental design and the overall multi-*omics* approach towards potential future application in uncovering molecular toxicity within the scope of informing AOPs or IATA, a draft AOP for “Phytoene desaturase inhibition leading to algal growth inhibition” (Fig. 52) was constructed by listing proposed successive points of *C. reinhardtii* systemic failures to compensate for NF exposure effects [603]. Key events were hypothesized as to their qualitative necessity in a cause-effect chain to induce the adjacent downstream event as indicated by retrievable existing information and supported by novel *omics* insights. Fundamentally, the attribution of “necessary” and “sufficient” as characteristics of key events may only be assigned once the weight of evidence for key events is strong [175,604,605], however the nature of AOPs as living and often incomplete frameworks collating toxicological knowledge permits their initial drafting and suggestion of putative key events for future downstream evaluation and application towards regulatory purposes [117].

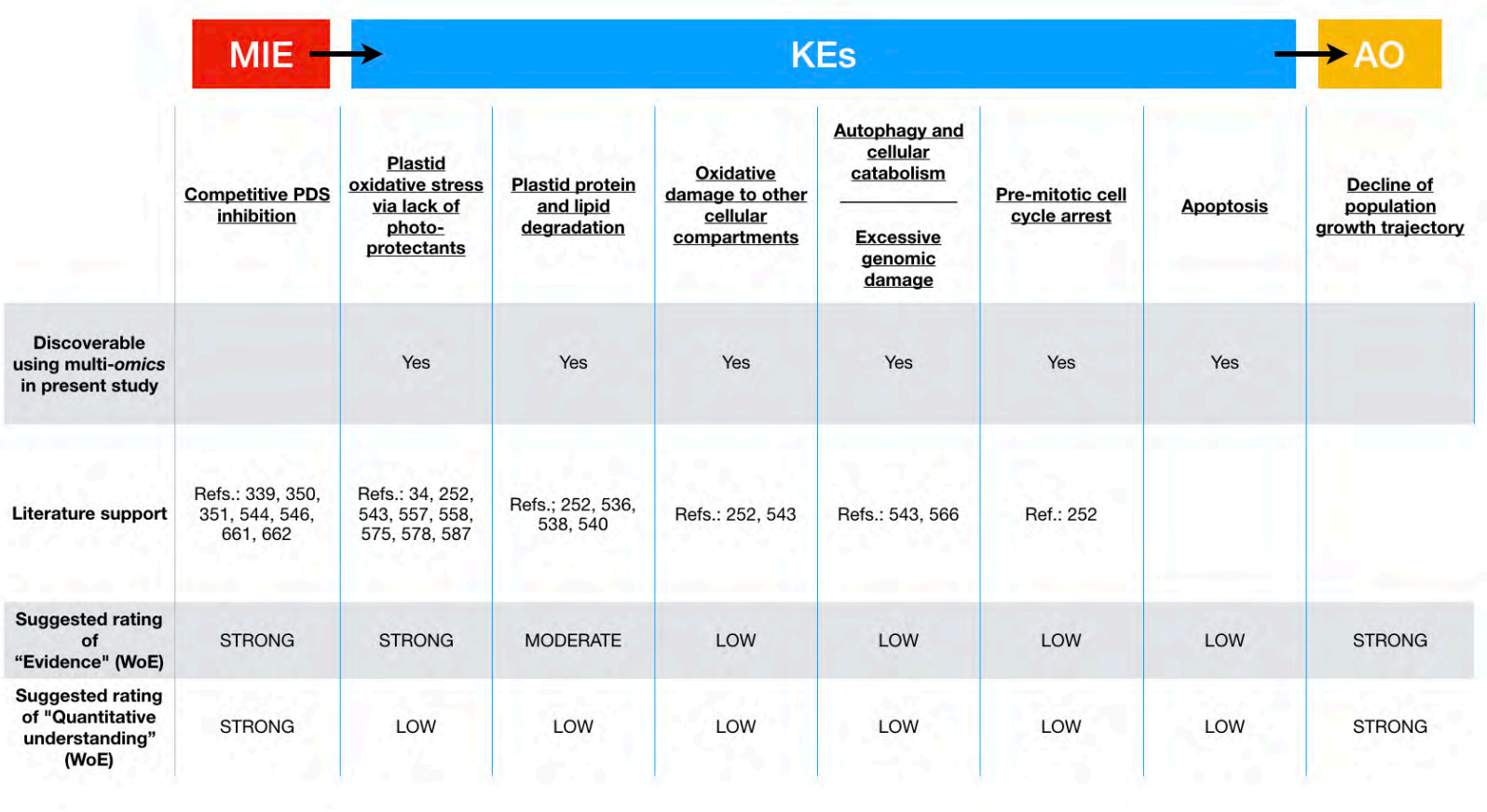


Figure 52. A potential AOP draft for "Phytoene desaturase inhibition leading to algal growth inhibition", along with an indication of whether the new phenotypically-anchored *omics* data juxtaposed to literature support and/or Weight of Evidence (WoE; a conceptual framework to rate confidence in data and specifically key events, including strength of "Evidence", and "Quantitative understanding" of key events and key event relationships [175,603,604]) have contributed to the derivation of that knowledge. PDS = Phytoene desaturase.

Ultimately, the tangible benefit of high-content technologies such as *omics* in the context of chemical MoA hypothesis is the possibility of discovering putative key events that are a) predictive of adverse outcome, b) specific to chemical MoA, c) candidates for inclusion in assay panels to screen for MoA (or even the MIE that triggers the AOPs) towards application in early tiers of chemical safety assessment [57,146]. Unsupervised analysis requires few to no prior knowledge of toxicant effects, and might permit more objective interrogation of generated datasets for putative biomarker identification. maSigPro and metaboClust software for instance were able to perform unsupervised identification of clusters of spectral peaks or genes that have expression levels or peak intensities, respectively, that behave similarly over time-course in exposed cultures, but was significantly different from non-exposed samples. As in the case for metaboClust, increase over exposure concentration could be used as an additional feature selection criterion. Such criteria can be valuable filtering steps to suggest individual markers putatively specific to chemical MoA pending targeted experimental characterization and counter-factual evaluation (for instance comprising investigations into specificity to single toxicant, specificity to class of toxicants, and specificity to overall chemical MoA) to yield clearer assessment of reproducibility and robustness of discovered biomarkers, quantitative understanding of their interrelationships, and specificity of these putative biomarkers to acute chemical MoA [109,166,167,606]. For metabolomics and lipidomics data, clusters of spectral peaks with similar time-profiles identified by metaboClust software could not be satisfactorily annotated and showed no significant metabolic pathway enrichments, however such spectral peaks lacking putative annotation could serve as valuable biomarkers if deemed predictive of adverse outcome, pending future characterization and annotation using follow-up targeted analytical methods such as LC-MS/MS.

4. Conclusion

In conclusion, the tailored experimental design (see Chapter 2) applied to a model toxicant norflurazon, and using the developed algal exposure system (see Chapter 3), led to time-resolved multi-*omics* profiling of the molecular stress response of *C. reinhardtii* to herbicide exposure. This further validated the utility of the developed exposure algal exposure system through its first application to a large-scale experimental investigation. The conducted time-course multi-*omics* study is to date the largest of its type compared the existing literature, factoring multiple concentrations and biological replication over an extensive sampling time-profile. Despite analytical and statistical limitations due to loss of sample size during sample acquisition, supervised analysis of multi-*omics* data collected in the demonstrated approach gave major time-resolved molecular insights into NF toxicity in *C. reinhardtii,* confirming and extending known effects of NFs molecular effects on algae. An acute chemical MoA for NF toxicity and a draft AOP for “Phytoene desaturase inhibition leading to algal growth inhibition” could be hypothesized, thereby achieving part 1 of the dual approach towards Scientific Objective III. In this context, the conceptual validity and value of the applied approach was discussed for possible utility of *omics* for supporting early tiers of future chemical safety assessment.

Chapter 5

Time-resolved multi-*omics* profiling of the *Chlamydomonas reinhardtii* stress response to chlorobenzene drives chemical MoA hypothesis

1. Introduction

As discussed in earlier chapters, *omics* technologies are argued to have matured to provide greater certainty about the causal relationships between chemical exposure and adverse effects to biological systems. By profiling biological stress signatures, information is provided that should be valuable for regulatory applications in the protection of environmental health. One way of emphasizing this utility is through the provision of proof-of-concept studies that showcase *omics*-driven hypotheses of acute chemical Modes of Action (MoA) thus increasing confidence in *omics-based* data for discovering mechanisms of molecular toxicity with value to chemical risk assessment [70,124,127,146].

Previously in this thesis, chapters 2 and 3 described an integrated experimental approach (experimental design, exposure system) at obtaining a time-resolved multi-omics profile of the *Chlamydomonas reinhardtii* molecular stress response to toxicants. Chapter 4 applied and validated such an approach to the model toxicant Norflurazon – a herbicide with moderate- to well-established understanding of molecular effects of toxicity. This was to 'calibrate' the applied data analysis approach to re-discover known and expected molecular effects by *omics*. Chlorobenzene (CB) is a highly lipophilic and volatile compound, and part of the chemical class refered to as base-line toxicants. Baseline toxicity is a poorly-understood effect in non-vertebrates, specifically concerning interactions at the molecular level [128,146,343,607]. An estimated 60% of all industrial chemicals are believed to belong to this chemical class, indicating the importance of understanding its potential adverse effects on environmental organisms [343].

Therefore, the research that is described in this chapter aims to apply the experimental design and exposure approach developed within this thesis, to perform an hypothesis-free investigation of the acute chemical MoA of CB (and baseline toxicity in the broader sense) in algae to underscore the discovery potential of *omics* data for toxicology and their future applications by regulatory bodies.

2. Materials and Methods

2.1. Algae culturing

Chlamydomonas reinhardtii cultures were incubated in liquid CGM under a 12h:12h light:dark cycle as described in Chapter 2.

2.2. Multi-omics time-course exposure experiment

The chlorobenzene multi-*omics* profiling exposure experiment was prepared and conducted equivalently to the norflurazon experiment as described in Chapter 4. In brief, algae were exposed to CB dissolved in CGM and seeded in 72 vials per exposure concentration plus 4 additional vials per exposure level for measuring of cell density post division, within 30min of onset of light phase. Phenotypic anchoring of molecular effects to the adverse outcome of algal growth inhibition within the boundaries of the experimental design (Chapter 2) was achieved by designating exposure concentrations of CB to two midrange concentrations ("Low" at 14mg/L for ~EC_{20}; "High" at 24mg/L for ~EC_{40}) from initially conducted concentration-response experiments (see Chapter 3).

2.3. Multi-omics sampling procedure and instrumental analysis

Sampling, washing and quenching procedures of cell pellets towards downstream Illumina RNA-Seq transcriptomics, and DIMS lipidomics and metabolomics analysis were conducted as described in Chapters 2 and 4, for 8 sample vials per concentration (n = 4 for transcriptomics) per sampling time-point, for a total of 9 time-points. Additionally at each time-point, 100µL of cell suspension was collected and stored in the dark at 4 °C for analytical measurements to confirm medium CB concentrations levels using gas-chromatography mass-spectrometry as described in Chapter 3.

2.4. Metabolomics, lipidomics and transcriptomics processing and data analysis

Acquired DIMS and Illumina HiSeq4000 raw data processing, putative spectral peak annotation, *C. reinhardtii* genome mapping of transcripts, outlier removal, normalization procedures, time-profile clustering, and statistical- and enrichment analyses were performed as described in Chapters 2 and 4. No spectral peaks of chlorobenzene were subtracted from DIMS datasets due to its high volatility and assumed loss during Speedvac solvent evaporation. Analysis reports of metaboClust and maSigPro time-profile clustering can be found in Suppl. Tables SI-T16/-17 and Suppl. Figs. SI-50/-51/-52.

3. Results and Discussion

3.1. Quality assurance of omics data acquired from time-course exposure experiment

Subsequent to multi-*omics* instrumental analysis of samples of *C. reinhardtii* exposed to CB over the time-course, quality of the gained data was assessed for the individual *omics* platforms. As for norflurazon data, low-quality samples and -variables and outliers from the 95%-confidence interval were excluded from the dataset.

3.1.1. Quality assurance – Mass spectrometry data

During DIMS acquisition of non-polar extracts from algae (lipidomics), persistent loss of spray stability in the nESI component led to highly inconsistent mass spectra and generation of missing values for most samples from the first analytical batch (Fig. 53). For the subsequent analytical batches, capillary voltage of the nESI source was increased from 1.5kV to 2kV to achieve stable spray and Triversa chip current. Variation of capillary voltage however induces significant alterations in total number and intensity of measurable spectral peaks [608], thus to enable comparability and filter out data with high percentages of missing values, samples from analytical batch 1 had to be omitted from the dataset prior to further processing steps and analysis. As a result, certain individual lipidomics sample groups displayed substantially reduced sample size. TP1 “Low” exposure group contained only a single replicate and was merged with TP1 “High” group replicates into a generic “Treatment” group to increase statistical power (Suppl. Fig. SI-49). TP5 “Low”, “Control” and TP7 “High” groups only contained a sample size of each n=3, and TP9 “Low” contained no single replicate and had to be removed from analysis. After all data processing steps and outlier removal were completed, the following numbers of samples could be retained in the dataset: Lipidomics assay = 113 of 216 samples (43% retained), metabolomics negative ion mode assay = 193 of 216 (89% retained), and 197 of 216 (91% retained) in the positive metabolomics assay. Overall, RSD distributions (see Chapter 3; [276,465]) as a measure of technical instrument variance using QC samples

suggested high-quality data in all three DIMS assays (Fig. 54), with mRSD values in approximately the expected magnitute of 11% (positive ion metabolomics), 14.7% (lipidomics) and 13.6% (negative ion metabolomics).

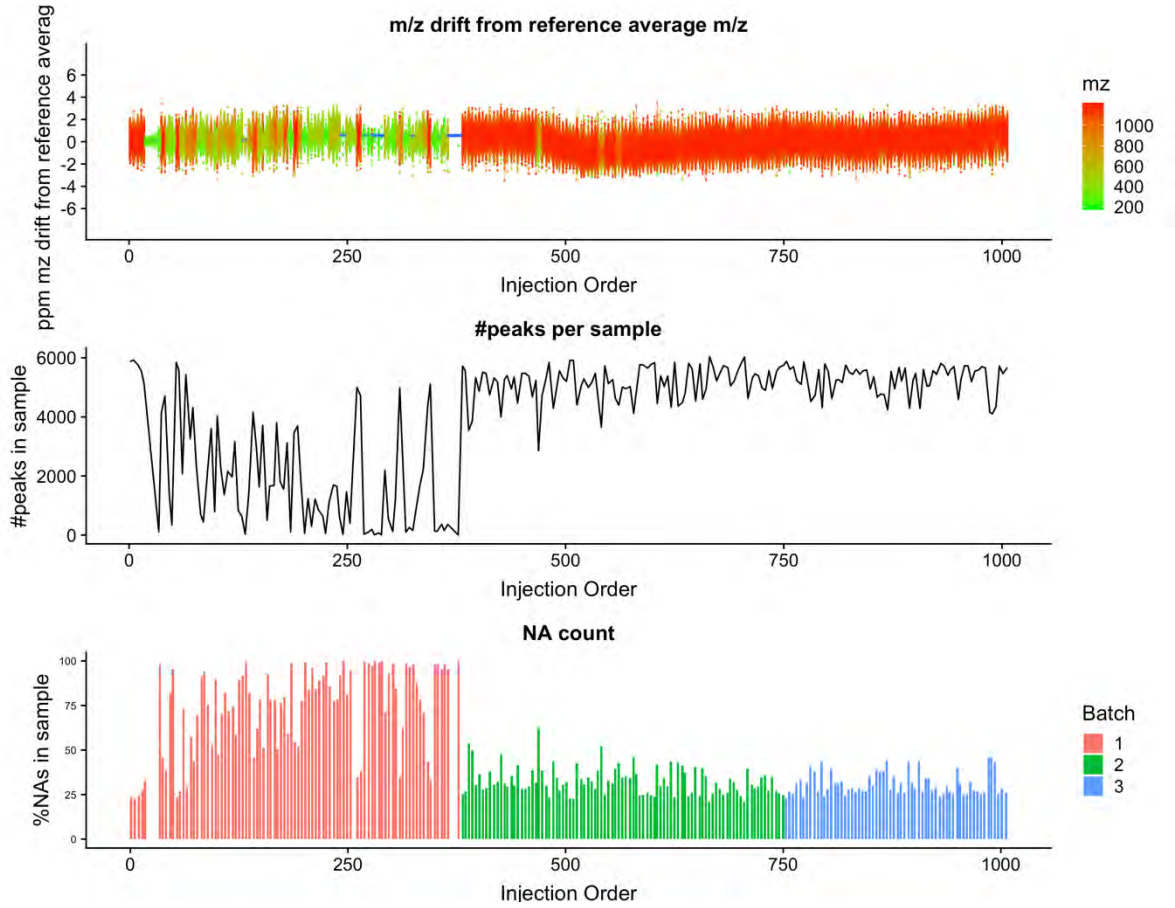


Figure 53. DIMS lipidomics sample acquisition over randomised sample sequence and effects of instable nESI spray in analytical batch 1, compared with higher data quality after increased nESI capillary voltage in batches 2 and 3. The top panel describes the m/z-distance of each individual mass spectral peak to its assigned peak cluster centroid during global dataset peak alignment at a 2ppm tolerance window. Strong loss of peak-cluster assignments is visible here in the first analytical batch (specifically higher m/z features), reinforced by a consistent reduction in the number of measurable spectral peaks (middle panel) and increased generation of missing values post peak alignment over the dataset (bottom panel).

Data were categorized into time-points, significantly different spectral peaks (Welch's t-test, FDR ≤ 0.05) were determined between exposure groups (High-vs-Control, Low-vs-Control) per time point, and putative peak annotation was attempted using *ChlamyCyc* spectral database and MI-Pack [187,498] with ppm error tolerance < 5. Significantly different spectral peaks were uniquely and putatively annotated (Suppl. Tables SI-T5, SI-T6, SI-T7) with moderate success rate: between 0-37.5% for

lipidomics datasets, 0-8.6% for the positive ion metabolomics assay, and 0-8.4% for the negative ion metabolomics assays.

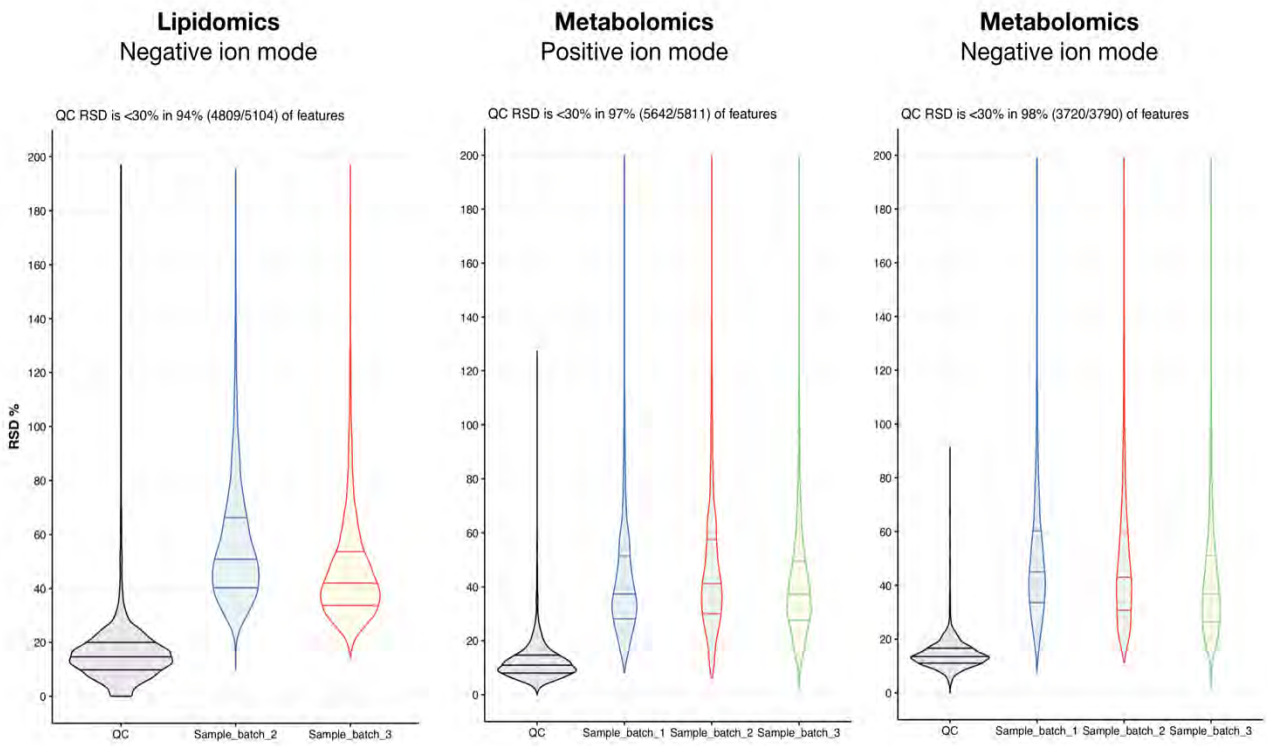


Figure 54. Violin-plot of RSD distribution and Quality Control sample (QC) RSD metrics per DIMS assay (Lipidomics, positive and negative ion mode metabolomics). QC mRSD were at or below 14.7% for all assays. RSD distributions for sample batches 1/2/3 are drastically higher as these groups contain diverse samples from all exposure groups and time-points randomised over run sequence. Each violin plot shows the value range (vertical lines), density of values (width of plot), and the 25th, 50th and 75th percentile of values (horizontal lines). Due to data loss and discarding during instrumental acquisition, batch 1 in the lipidomics dataset is missing.

3.1.2. Quality assurance – Transcriptomics data

Data acquisition and raw data processing of norflurazon and chlorobenzene samples were conducted as a single analytical batch, which is described in detail in Chapter 4. A subset of samples exhibited reduced extraction yields (Suppl. Fig. SI-10). Subsequent library preparation was ultimately unsuccessful for a total 29 samples. Thus, only 79 out of 108 samples (73%) could be successfully sequenced for the CB time-course experiment. For the total dataset, quality metrics suggested high quality of collected transcriptomics data. Phred scores above 35 (likelihood of correct base call = 99.97%) were measured for all samples (Fig. 29). The ultimate sample size of certain sample groups was decreased, with loss of “Low” and “High” exposure groups

for TP1. TP2-, TP5-, TP9 “High”- and TP4 “Low” groups displayed n=2, and TP5 “Control” group a sample size of n=1.

3.2. Confirmation of exposure concentration and adverse outcome induction

Successful induction of an adverse outcome (growth rate inhibition) and the accuracy at achieving the desired nominal medium concentrations of CB in cell suspensions were measured to increase confidence in the experimental results and achieve phenotypic anchoring. Measured medium concentrations of CB using GC-MS (Fig. 55A) were approximately 20% below the expected range of the nominal exposure concentrations (median 11.19mg/L measured for “Low” group at nominal 14mg/L; median 19.02mg/L measured for “High” group at nominal 24mg/L). The measured induction of growth rate inhibition (Fig. 55B) of both exposure concentrations was equally lower than expected (~EC_5-$EC_{12.5}$ for “Low”, ~EC_{15}-EC_{20} for “High”), in line with GC-MS results. A clear concentration-response increase of AO-induction caused by CB was however still appreciable despite the reduced exposure concentrations, enabling successful downstream anchoring of adverse molecular effects to phenotype

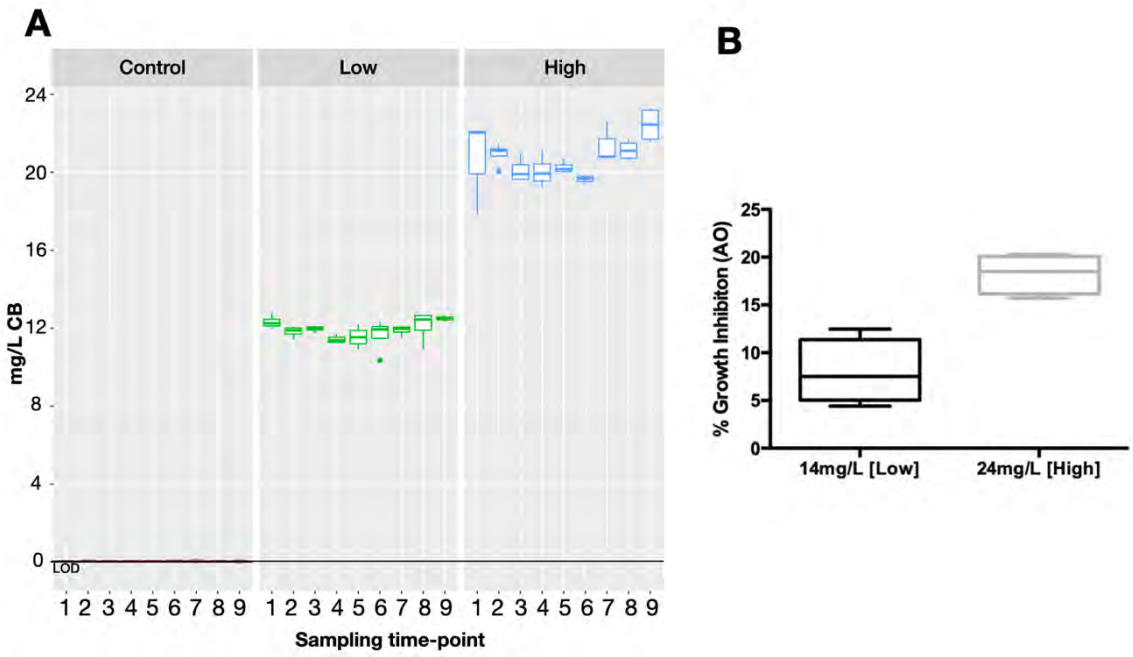


Figure 55. (A) Boxplots of exposure concentrations per group over time-course, measured by GC-MS, and (B) boxplots of growth rate inhibition measured via CASY cell counting at 24h, post induction of the adverse outcome. Marked in (A) is the limit of detection (LOD) for the applied GC-MS method.

[108,165,352–355]. The strong decrease in CB medium concentrations was likely due to substantial loss of the highly volatile CB during chemical solvation in medium and serial dilutions in exposure stock preparation, not only during experimental setup but also during CB calibrant preparations for GC-MS analysis [455,609]. To a lesser degree, biological culture drift might have led to results diverging from those of previous concentration-response assays in Chapter 3 [486,487,489,490]. Such strong loss of exposure concentrations will need to be factored into future chemical stock preparation steps during experimental setup. Although not ideal, here the presence of induced adverse outcome of growth inhibition as measured via cell counting still indicated that the experimental results are valid and thus enabled linking of molecular measurements to observed adverse apical phenotype.

3.3. Global effects of chlorobenzene on Chlamydomonas reinhardtii biology

As for the previous norflurazon experiment, scrutiny of the complete datasets generated by the various *omics* platforms using PCA (Fig. 56) revealed that the developmental trajectory over experimental time-course represented the greatest variance within the CB dataset [193,390,515]. However, PCA of the collapsed

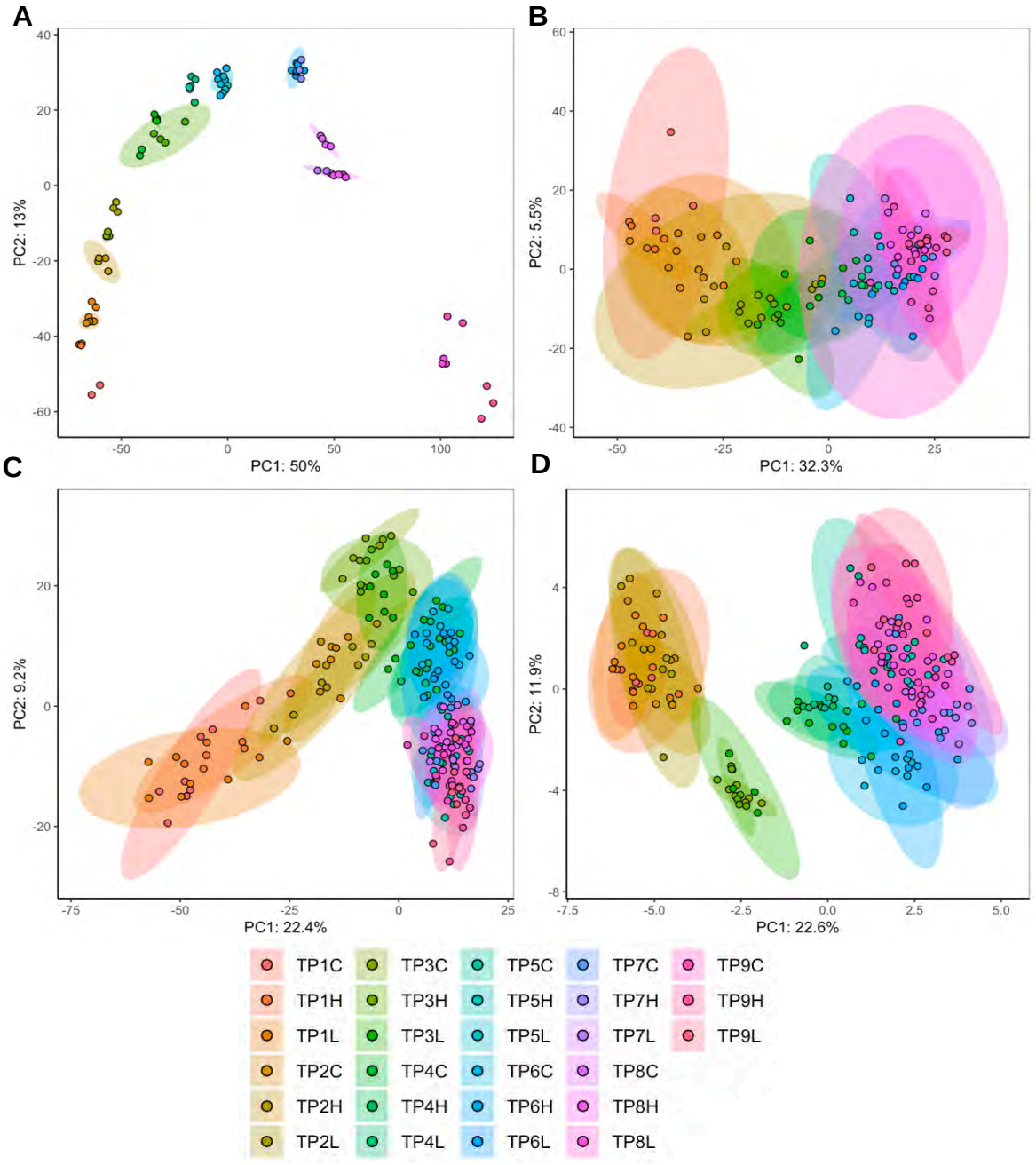


Figure 56. PCA of complete dataset (time-point "TP" 1-9, "C" = Control, "L" = Low, "H" = High), for (A) transcriptomics, (B) lipidomics, (C) metabolomics positive ion mode, (D) metabolomics negative ion mode. Colored regions indicate the 95%-confidence intervals. Scaling differences between Illumina and DIMS data stem from different data processing pipelines and are not indicative of quantity of molecular effects.

datasets (omission of time variable) revealed no immediately appreciable molecular effects on any the first 6 principal components for lipidomics or metabolomics datasets, as opposed to the NF experiment. This was likely due to the substantially lower numbers of significantly different spectral peaks between exposure groups (Fig. 57), indicating either more subtle acute chemical MoA for CB in general, lower molecular stress response due to the decreased actual CB exposure concentrations and adverse outcome induction over the algae population, or both. However, principal component 4 of the transcriptomics data indicated a subtle but consistent effect over the collapsed dataset, incorporating 3.38% of variability of the collapsed dataset (Suppl. Fig. SI-53).

The effects of CB on the transcriptome were overall strong and increasing over concentration (Fig. 57), with >100 differentially expressed genes (DEG) at TP3 to TP7 and >1000 DEG at TP2, -8 and -9 for the Low-vs-Control comparison group, and consistently above 1000 DEG at TP2 to TP9 for the High-vs-Control comparison (No comparison at TP1 possible due to high loss of samples). For mass spectral data of

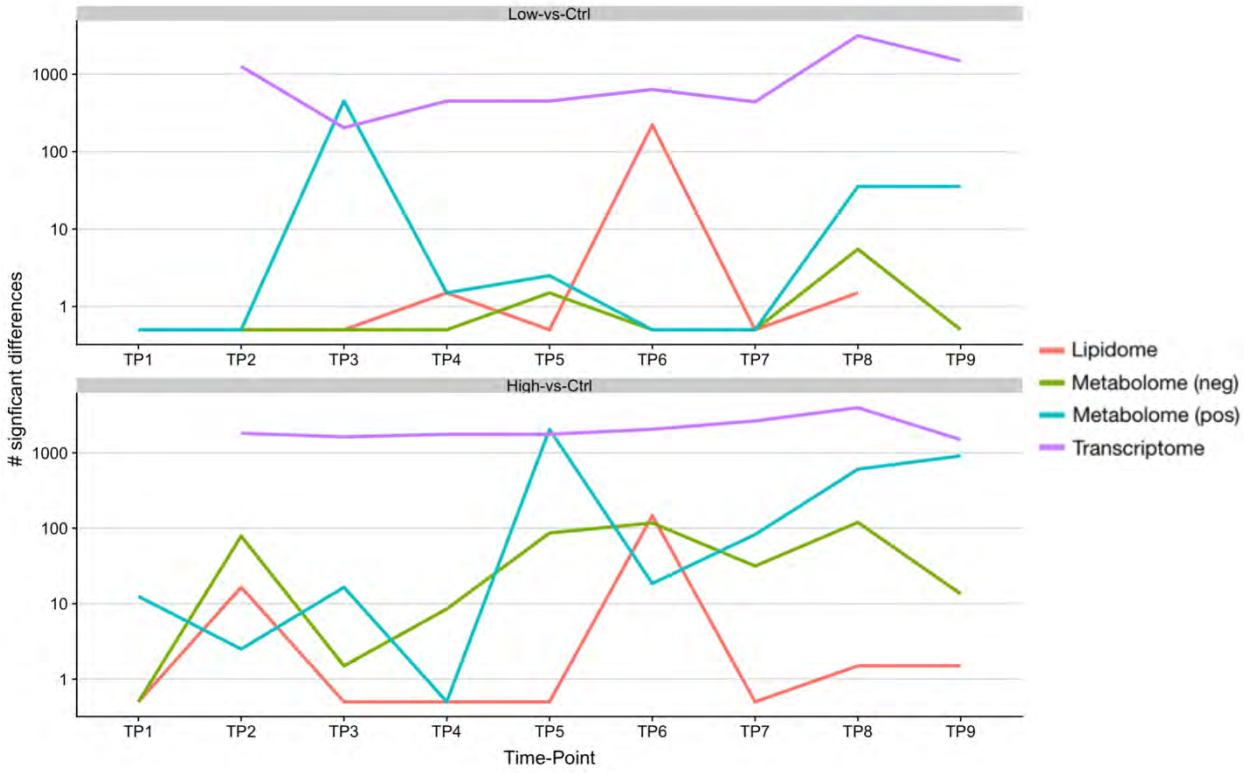


Figure 57. Significantly different variables between exposure groups (Top = Low vs Control, Bottom = High vs Control), as represented by differentially expressed genes for RNA data (FDR ≤ 0.05, log2-fold change ≥ 2) and as spectral peaks significant between groups (t-test, FDR ≤ 0.05).

the Low-vs-Control comparison, significantly different features were below 10 in number or absent for the lipidomics and metabolomics data over complete time-course, with the exception of a spike at TP6 for lipidomics data >100 features, and for the positive metabolomics data at TP3, -8 and -9 (tens to low hundreds of features). In the High-vs-Control comparison, the lipidomics data showed similarly small numbers of significant features (below 10 or none) over time-course, with spikes into the low tens and hundreds at TP3 and -6. The positive and negative metabolomics data showed increased number of significant features, in the low tens at TP1 to TP4 and hundreds to thousands at TP5 to TP9. Here, the overall low number in significantly different lipid spectral peaks was most likely caused by low statistical power in statistical tests due to omission of analytical batch 1 from analysis (Fig. 53). In PCA, separate exposure classes were obtained at TP3, -6, -8, and -9 in the lipidomics data (Suppl. Fig. SI-54), whereas in negative ion metabolomics data, exposure classes tended to aggregate over the complete time-course with few significant changes in the ANOVA of PC scores (Suppl. Fig. SI-54). In positive ion metabolomics and transcriptomics data, exposure classes separated more clearly in PCA at TP3 and

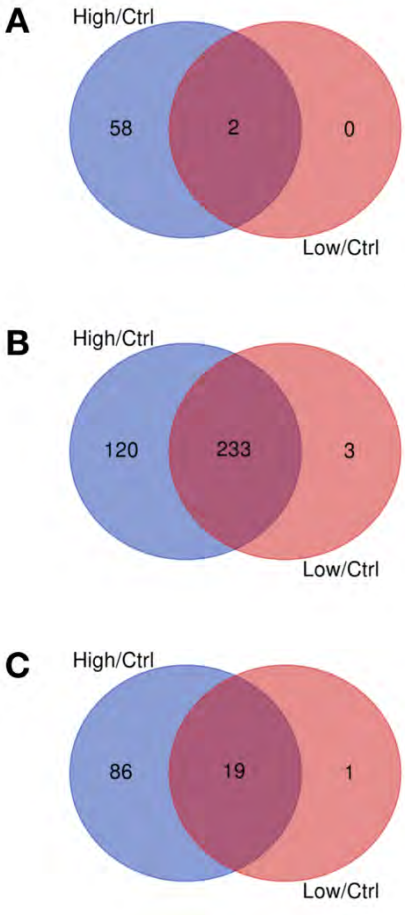


Figure 58. Venn diagrams of significantly different spectral peaks in (A) lipidomics data, (B) positive metabolomics data, and of differentially expressed genes in (C) transcriptomics data. Negative metabolomics data showed no significantly different spectral peaks of the Low vs. Control comparison over the collapsed dataset. Comparisons of “High”-concentration to “Control” (“High/Ctrl”) and of “Low”-concentration to “Control” (“Low/Ctrl”) are shown, intersections of circles show numbers of the differences that could be found within both comparisons.

TP2, respectively, with significantly different PC score distributions at almost all time-points. However, loss of TP1 transcriptomics “Low” and “High” samples obscured insight into earlier gene expression changes.

Venn diagrams of the collapsed datasets suggest large overlay of significantly different spectral peaks and DEG within all *omics* datasets for effects related to “Low”- and “High” exposure in reference to “Control” (Fig. 58), with the exception of negative ion mode metabolomics where the Low-vs-Control comparison generated no significant differences. Zero, 3 and 1 unique significant changes for Low-vs-Control comparisons could be pinpointed in lipidomics, positive ion metabolomics and transcriptomics data, respectively (no significant changes in negative ion metabolomics data), with the overwhelming majority of “Low”-induced changes also found in the High-vs-Control comparison. This observation, along with the increase of significantly different spectral peaks and DEG in the High-vs-Control comparison, suggested similarity of effects between the two exposure levels indicating concentration-response behavior of at least a subset of molecular perturbations [610]. Similar to NF, however, a more diverse biological stress response was mediated by the higher CB exposure level.

To achieve initial interpretations of the results, Joint Genome Institute gene ontology (JGI-GO) enrichments were determined for functionally annotated DEG within the collapsed dataset (Suppl. Fig. SI-55), indicating upregulation of redox processes and glucose metabolism in the High-vs-Control group comparison. Low-vs-Control comparison DEG did not significantly enrich any GO, likely due to overshadowing of the statistical significance of the more subtle Low-vs-Control DEG (low concentration effects) by large-magnitude developmental changes in the collapsed dataset, as argued earlier for norflurazon data. PGSEA yielded a more detailed picture on global effects of exposure (Fig. 59) identifying significant perturbation of multiple large clusters of JGI-GOs, including processes involving cellular motility, sugar- and energy metabolism, membrane- and vesicle docking processes, peroxisomal activity, membrane potential regulation, ion homeostasis and -transport processes. Metabolite set enrichment analysis of the collapsed lipidomics and metabolomics datasets on *Arabidopsis* metabolic pathways revealed only

marginally meaningful information, indicating upregulation of KEGG pathway "Porphyrin and chlorophyll metabolism" (FDR = 2.1 x 10^{-3}) in the High-vs-Control comparison, whereas significant spectral peaks in the Low-vs-Control comparison showed no significant enrichments. Overall, when omitting time as independent variable from the dataset, the determined significant alterations caused by CB-exposure did enrich gene sets and metabolic pathways associated with algal energy metabolism and processes involved with membrane functionality. Exposure of non-synchronized *C. reinhardtii* to butanol, a nonpolar baseline toxicant previously utilized in optimizing biofuel production in algae, similarly indicated non-specific perturbation of energy metabolism and photosynthesis, but also of intracellular trafficking and membrane transporters, amongst others [263,611]. Together, these initial analyses supplied a first empirically-based insight into molecular effects associated with CB

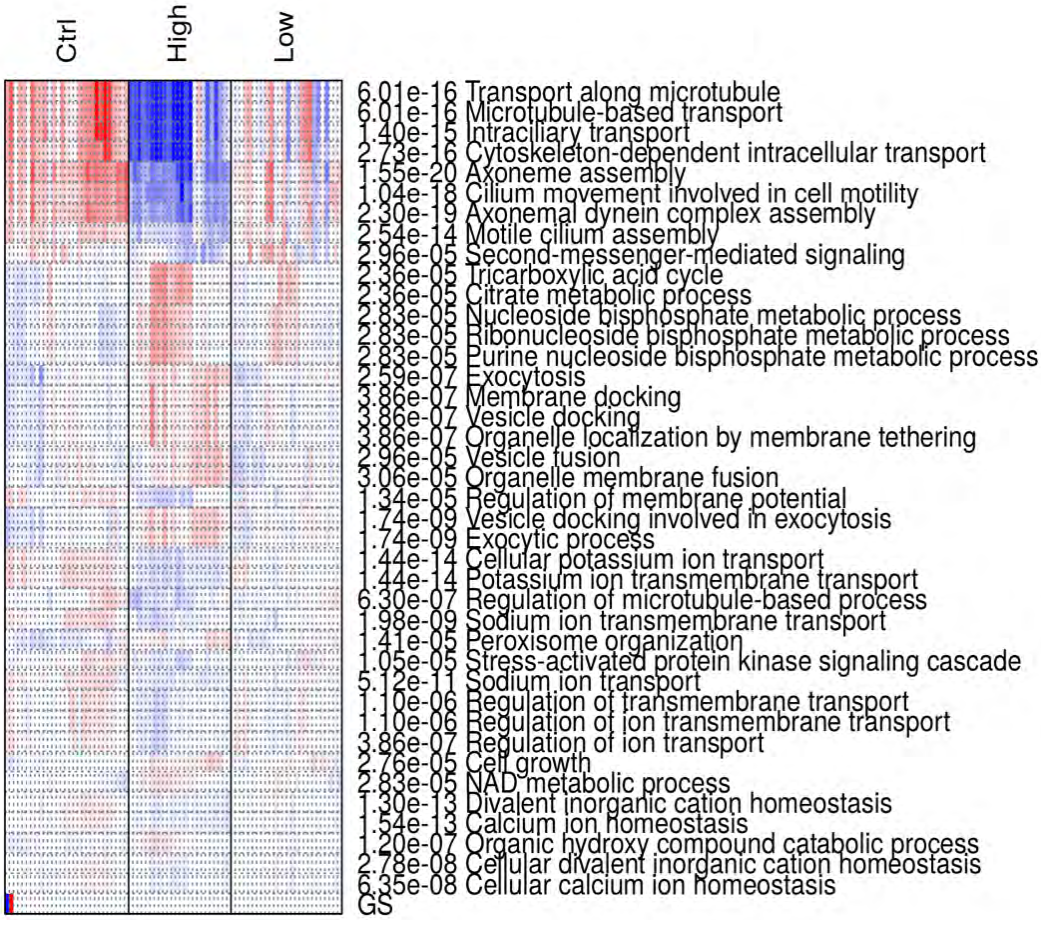


Figure 59. JGI-GO enrichments of CB-induced changes in the collapsed transcriptomics dataset, identified by parametric gene set enrichment analysis (PGSEA). Gene ontologies are presented and ranked along their FDR. PGSEA allowed first insight into exposure effects even when collapsing the time variable, and indicated monotonous changes from "Control" over "Low" and "High" exposures in most GO categories. Time-points plotted from TP1-9 per group left to right.

toxicity to *C. reinhardtii*, while indicating potential value of described molecular effects as putatively diagnostic of baseline toxicity [612,613]. For a more meaningful exploration of biological and toxicological information, exposure time in synchronized cultures was reintroduced into the dataset as independent variable [388]. Individual sampling time-points were analyzed independently regarding gene-/metabolite set enrichment and DEGs, and genes and spectral peaks were clustered along similarity in time-course profiles.

3.4. Time-course analysis of chlorobenzene toxicity on algae

Time-points and time-profiles were analyzed individually regarding significantly different gene expression and metabolite levels and gene ontology or metabolic pathway enrichments. As for the NF data, clusters of spectral peaks with similar time-profiles identified by metaboClust software could not be satisfactorily annotated and showed no significant metabolic pathway enrichments (Suppl. Table SI-T16, Suppl. Figs. SI-51/-52/-53).

3.4.1. Reduced algal motility and flagellar regeneration as generic marker of aquatic pollution

The maSigPro package time-profile clustering identified two clusters, “Cluster08” and “Cluster09”, containing genes enriching JGI-GO categories comprising flagellar activity and synthesis of flagellar structural components (significant downregulation at all time-points, Fig. 60). Similar categories were found enriched within the top-30 gene sets of PGSEA applied to the collapsed transcriptomics dataset as well as at individual time-points TP2, -4, -6, -7, -8 and -9 (Suppl. Table SI-T19). Subtle reduction of flagellar activity and regeneration was previously observed after exposure of *C. reinhardtii* or other motile algae to various toxicants, including cyanobacterial toxins, ethanol, various metals [246,247,263,520–526] or the herbicide NF, the context of which was more extensively discussed in Chapter 4. Steady-state loss and regeneration of flagella proteins is a constitutive process in healthy *C. reinhardtii* [192,527–529]. Due to the repeated observation of reduction of flagellar activity and regeneration after

exposure to various inorganic and organic toxicants with discrete chemical MoA, a hypothesized redirection of bioenergetic flux from cellular motility towards regulatory and compensatory metabolic adaptation to toxicant stress is proposed here for motile algae [614,615]. Reduced expression of gene clusters enriching GOs of cellular motility and flagellar growth/-regeneration could serve as a viable and generic

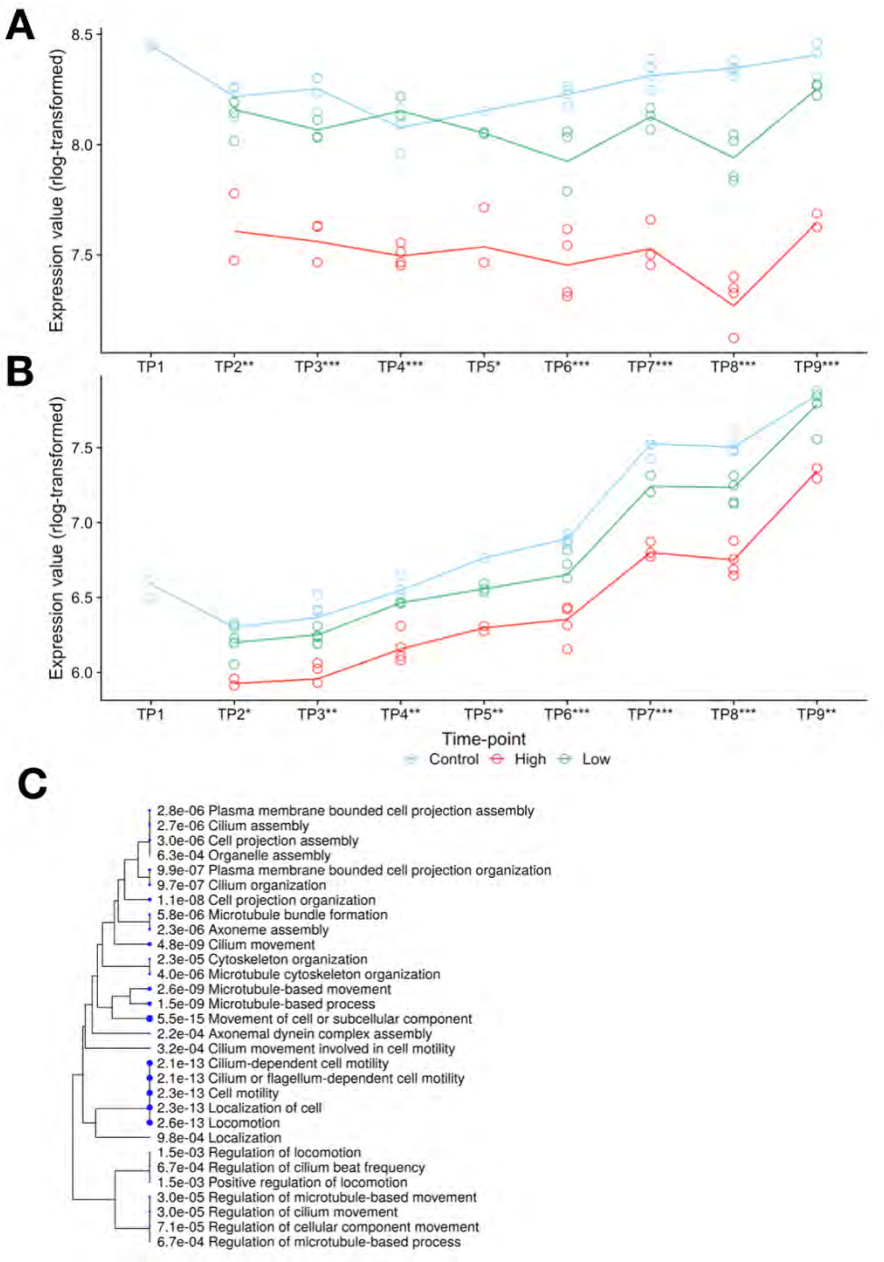


Figure 60. Time-profile plots of maSigPro gene clusters (A) “Cluster08”, (B) “Cluster09” along significant differences of expression at each time-point (ANOVA), and (C) hierarchical enrichment tree of JGI-GO enrichments of genes pooled from both clusters. FDR of JGI-GO enrichments are displayed next to JGI-GO labels. Size of the nodes indicates degree of significance, the distance of the clusters connected by the branches of the dendogram is relative to the ontological similarity of gene sets. Significant changes in gene expression (ANOVA) are indicated by * (FDR<0.05), ** (FDR<0.01) or *** (FDR<0.001).

biomarker on the molecular level for toxicity screening or biomonitoring of aquatic pollution, an approach unfeasible on the physiological level due to high variance [522].

3.4.2. CB perturbs membrane-bound homeostatic processes

Regulation of membrane ion transport processes is a lynchpin of sustaining crucial biological processes including photosynthesis, respiratory electron-transport chain, osmoregulation, or protein- and lipid trafficking [192,616–619]. Analysis of the collapsed transcriptomics dataset revealed enrichment of various JGI-GOs indicating up-regulation of “Membrane docking”, “Vesicle fusion” and “Exocytotic process” as found within the top-30 gene sets of PGSEA, along down-regulation of “Regulation of membrane potential” and JGI-GOs comprising potassium-, sodium- and calcium transmembrane transport and -homeostasis (Fig. 59). Over the exposure time-course, more subtle nuances of these effects could be identified. TP1 and TP5 did not contain replicates in either exposure group, however PGSEA on TP2 samples uncovered up-regulation of JGI-GOs “Monovalent inorganic cation homeostasis”, “Regulation of intracellular pH”, “Vesicle-docking involved in exocytosis”, “Exocytic process” or “Regulation of cellular component size” in “High", but lack of substantial up-regulation of these GOs in “Low”, suggesting a discrete and concentration-dependent molecular response to CB (Suppl. Table SI-T19). PGSEA on TP3 samples showed associated up-regulation of JGI-GOs including “Membrane docking”, “Vesicle docking” and “Retrograde endosome-to-Golgi transport”, and DEG in both “Low” and “High" groups enriched JGI-GOs for down-regulation of various ion transmembrane transport processes (Suppl. Table SI-T18). Down-regulation of “Potassium ion transmembrane transport” processes was similarly identified at TP4 by PGSEA, whereas TP6 and TP7 exhibited down-regulation of enriched JGI-GOs “Sodium ion transport”, “Potassium ion transmembrane transport” or “Calcium ion homeostasis” and “Divalent inorganic cation homeostasis”, reinforced by TP7 High-vs-Control DEG enriching down-regulation of “Ion transport” and “Metal ion transport”. Further, up-regulation of JGI-GOs “Vesicle docking”, “Membrane docking”, and “Organelle localization by membrane tethering” were indicated by PGSEA at TP7. At TP8, a similar pattern emerged, with observed down-regulation of various JGI-GOs involving sodium-,

potassium transport, and “Regulation of membrane potential” in the top-30-ranked PGSEA gene sets and enriched by DEG of “Low" group.

Despite increased variance of intra-group gene expression distributions as a result of strong losses of sample size in some exposure groups, the here observed perturbation of osmotic homeostasis and intracellular pH regulation, along various sodium-, potassium-, calcium- and associated proton antiporter activity points towards an acute chemical MoA of CB involving interactions with lipid membranes and their components regulating ion permeability consistent over the majority of exposure duration [619–621]. The set of genes enriching JGI-GOs involving membrane docking-, vesicle fusion- and exocytotic processes in the collapsed dataset and at individual time-points further enriched the KEGG pathway “SNARE interactions in vesicular transport” (FDR = 2.57 x 10^{-24}). SNARE (soluble N-ethylmaleimide-sensitive-factor attachment protein receptor) proteins are involved in lipid homeostasis and biogenesis, vesicle-target membrane fusion and the associated trafficking of lipids and proteins [622–624]. Expression of genes enriching the JGI-GOs “Polyol metabolic process” and “Protein N-linked glycolization” in PGSEA at TP2 were found significantly upregulated specifically at the “High” exposure level at multiple time-points (Suppl. Fig. SI-61) and enriched KEGG pathways “N-glycan biosynthesis” (FDR = 1.16 x 10^{-10}), “Inositol phosphate metabolism” (FDR = 1.73 x 10^{-7}) and “Phosphatidylinositol

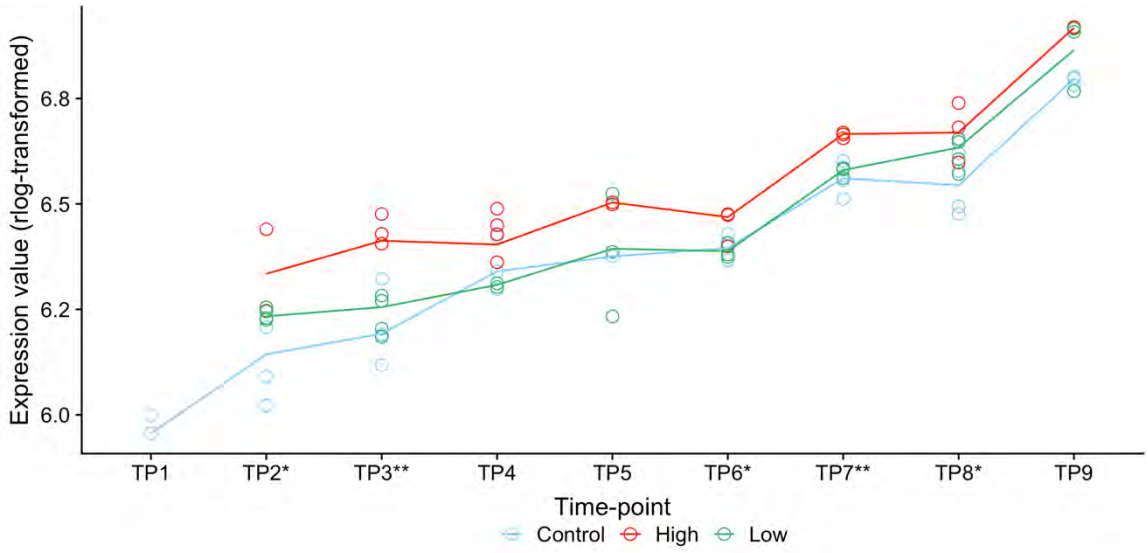


Figure 61. Time-course plot, median of genes per replicate and median of medians with connection line. Showing expression of genes within the JGI-GOs 'Polyol metabolic process' and ‘Protein N-linked glycolization’ (as identified by PGSEA at TP2), using the CB transcriptomics dataset. Significant changes in expression (ANOVA) are indicated by * (FDR<0.05), ** (FDR<0.01) or *** (FDR<0.001).

signalling system" (FDR = 1.7 x 10^{-4}). N-glycans represent major structural components of the *C. reinhardtii* cell wall, with their biogenesis, vesicular transport and -exocytosis driven by the endoplasmatic reticulum (ER)-Golgi system [625,626], whereas the inositol phosphate/ phosphatidylinositol signaling system is a key regulator of ER-Golgi-membrane vesicle trafficking, membrane internalization, lipid homeostasis and damaged membrane lipid breakdown in plants and algae, and regulates responses to disturbed ion homeostasis and osmotic potentials across membranes [627–629].

Together, a stimulation of ER-Golgi-driven transport vesicle membrane-targeting, exocytosis of newly-synthesized lipid and protein, and recycling and internalization of damaged membrane components might be inferred here from data [618,624,630,631]. The observed perturbation of ion transmembrane transport processes, osmotic potential regulation, intracellular pH regulation, and stimulation of vesicular trafficking suggested that molecular effects induced by exposure of *C. reinhardtii* to CB manifested themselves by interactions with lipid membranes and their components, comparatively similar to those induced by ionic or osmotic stress [621,630,632–634].

3.4.3. Induced alterations to energy metabolism, lipid metabolism and photosynthetic machinery

Substantial perturbation of membrane-bound homeostatic processes necessarily results in alteration of metabolic energy equilibria [635]. maSigPro time-profile clustering identified 2 gene clusters "Cluster01" and "Cluster03" enriching various bioenergetic KEGG pathways (Suppl. Figs. SI-56 and SI-57, Suppl. Table SI-T20). Here, stimulation of glycolysis, pentose-phosphate pathway, fatty acid synthesis and carbon fixation at TP2, -4, -6, -8 (and apparent down-regulation at TP9) was observed in "Cluster01" for CB-exposed algae. Genes enriching KEGG pathway "Fatty acid synthesis" (Suppl. Fig. SI-58) comprised enzymes catalyzing biogenesis of various fatty acids, triacylglycerols but also enzymes involved in chloroplast- or ER-localized membrane glycerolipid and glyercophospholipid metabolism [636], in line with hypothesized CB-induced membrane damage. Increased lipid synthesis, carbon

fixation and sugar metabolic pathways were previously observed as compensatory reactions to ionic or osmotic stress in algae and plants [629,637].

Enrichment analysis of maSigPro time-profile “Cluster03” further indicated up-regulation of citric acid cycle and propanoate metabolism (both however marginally non-significant at FDR = 0.07) in specifically the “High” exposure group at all sampling time-points except TP6; in the “Low” exposure group, up-regulation was observed at TP2, -3, -7, -8, and -9 and down-regulation at TP4 (Suppl. Fig. SI-57), signaling concentration-dependent and potentially low-dose adaptive processes [638]. “Cluster03” genes that enriched above KEGG pathways comprised almost exclusively enzymes catalyzing malonyl-CoA to acetyl-CoA-, and succinate to succinyl-CoA interconversion steps. An associated trend for up-regulation of multiple acetyl-CoA synthetases was further identified within the top-30 FDR-ranked gene sets in PGSEA at TP3, -4, -6 (contained within gene set enriching JGI-GO “Thioester metabolism”; Suppl. Table SI-T19). Up-regulation of acetyl-CoA synthetases was previously specifically observed in *C. reinhardtii* after perturbation of ion and osmotic homeostasis [621]. Based on lack of up-regulation of further enzymes catalyzing generation of energy precursors from acetyl-CoA in KEGG pathway “Citrate cycle”, this enzyme induction might reflect increased generation of substrates for above-observed lipid biogenesis [639,640].

maSigPro time-profile “Cluster01” further enriched KEGG pathways (Suppl. Fig. 56, Suppl. Table SI-T20) indicating induced stimulation of “Porphyrin- and chlorophyll metabolism”, “Terpenoid backbone synthesis”, and “Ubiquinone and other terpenoid-quinone biosynthesis” at TP2, -4, -6, -8 (and down-regulation at TP9), while DIMS data metabolic pathway overrepresentation analysis suggested here stimulation of “Porphyrin and chlorophyll metabolism” in Low-vs-Control comparison at TP2 (FDR = 0.04). Additionally, enrichments of genes contained in maSigPro time-profile “Cluster02” and “Cluster07” suggested upregulation of gene expression for various components of the photosynthetic machinery (Fig. 62, Suppl. Table SI-T21).

Increases in carbon fixation, photosynthetic activity and photosynthetic pigment synthesis are generic stress markers in microalgae and plants, but were previously specifically observed as result of ionic and osmotic stress [630,637], specifically as a result of damage to antenna proteins, photosystem (PS)-I, -II and photosynthetic electron-transport chain (ETC) subunits [621]. Here, up-regulation of gene expression of 8 out of 12 antenna proteins, the plastocyanin subunit of the ETC, most PS-I and some PS-II subunits could be observed. This increase in gene expression was significant for maSigPro “Cluster02” genes from TP2 to TP9, with strong increases for the “High” exposure group (Fig. 62A). For maSigPro “Cluster07” genes, up-regulation was significant from TP2 to TP6 for the “High” group, followed by down-regulation of both “Low” and “High” group at TP7 and TP8 (Fig. 62B).

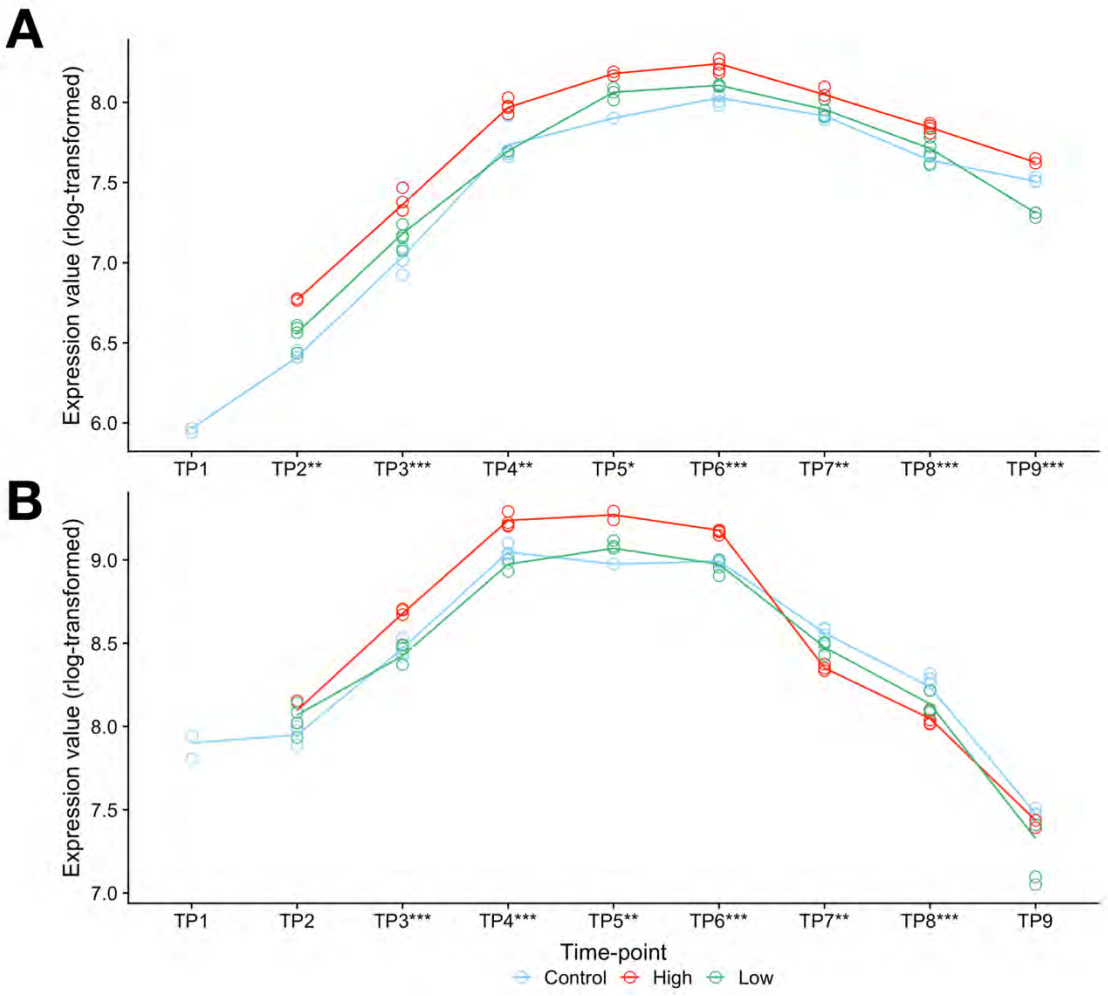


Figure 62. Time-course plot, median of genes per replicate and median of medians with connection line. Showing expression of genes within maSigPro (A) “Cluster02” and (B) “Cluster07”, comprising various elements of the photosynthetic machinery (Suppl. Table SI-T21). Significant changes in expression (ANOVA) are indicated by * (FDR<0.05), ** (FDR<0.01) or *** (FDR<0.001).

“Cluster01” genes enriching KEGG pathways “Terpenoid backbone synthesis” and “Ubiquinone and other terpenoid-quinone biosynthesis” (Suppl. Table SI-T20) particularly indicated induction of enzymes involved in Vitamin-K cycle activity and metabolism of phylloquinone and its intermediates, including specifically MenF, MenE, MenB, UbiE-MenG or MenA (Suppl. Fig. SI-59). Phylloquinone and its downstream metabolites (plastoquinone pool) have been linked to PS ETC functionality [641–645], with up-regulation further supporting CB-induced disruption of the membrane-bound photosynthetic ETC bioenergetic pathway.

Up-regulation JGI-GOs comprising “Response to hydrogen peroxide”, “Reactive oxygen species metabolic process”, “Response to reactive oxygen species”, “Glutathione metabolic process”, “Sulfur compounds transport” and “Sulfate transport” were found in the top-30 FDR-ranked gene sets in PGSEA of TP3 and TP4 and in DEG of TP9 “Low” (Suppl. Tables SI-T18 and SI-T19). As a group, these gene clusters showed increased gene expression over the complete exposure duration (with exception of TP7) for the “High” exposure group, with no significant increases in gene expression for the “Low” group (Suppl. Fig. SI-60). The genes enriching these JGI-GOs further enriched KEGG pathways “Pantothenate and CoA biosynthesis”, “Peroxisome”, “Valine, Leucine and Isoleucine synthesis”, “ABC transporters”, “Sulfur metabolism” and “Carotenoid biosynthesis” (FDR <0.05). Specifically, chloroplast sulfate transporters SULP1, -2 and SBP1, and prokaryotic (mitochondrial and chloroplastic) ABC sulfate transporters were flagged up, potentially supporting an antioxidant response to possible ROS-generation from PS-ETC and thylakoid membrane perturbation. Similar to present observations (enriched by DEG at TP9) , JGI-GO “Response to hydrogen peroxide” was previously identified as a result of ionic and osmotic stress, measurable almost immediately after exposure and in parallel with reduction of PS electron flow [621,630,637]. The KEGG pathway “Peroxisome” was enriched almost exclusively with gene expression of enzymes involved with hydrogen peroxide metabolism (PTS1-type hydrogen peroxide metabolism, specifically enzymes CAT1, SOD, NUDT12). This reactive oxygen species has before been associated specifically with photosystem radical production and is regulated by the quinone pool, cytochrome-b6f and plastocyanin [646–648]. Both perturbance of the plastoquinone pool and plastocyanin as functional units of the photosynthetic ETC

were observed here, along with earlier observed disruption of ion homeostasis adding further support to an acute chemical MoA of CB targeting the ETC or non-specific interactions with membrane-bound processes more broadly.

3.4.4. Amino acid and protein metabolism, autophagic response and perturbation of cell cycle progression

maSigPro “Cluster04” genes (Suppl. Fig. SI-61) enriched KEGG pathways “Ribosome”, Biosynthesis of amino acids”, “ Lysine biosynthesis”, “RNA transport”, “Cysteine and methionine metabolism” and “Aminoacyl-tRNA biosynthesis” (Suppl. Table SI-T22), with significant down-regulation at TP2, -3, -7 and TP9 and up-regulation at TP4 for both “Low”- and “High” exposure groups. In line with an assumed membrane-bound acute chemical MoA inducing perturbation of ionic and pH equilibria, the initially-observed reduction of ribosome biogenesis could be due to overall metabolic breakdown of cellular enzymatic machinery [649]. Top-30 FDR-ranked gene sets in PGSEA at TP2 further contained JGI-GOs “Maturation of 5.8S rRNA”, “rRNA modification”, “RNA-polymerase-II preinitiation complex assembly” or “rRNA methylation”, which combined further enriched KEGG pathways “RNA polymerase” and “Proteasome” (FDR<0.05) with up-regulation of expression at all time-points for “High” exposure group and at TP2, -4, -5, -6 and -7 for “Low” exposure

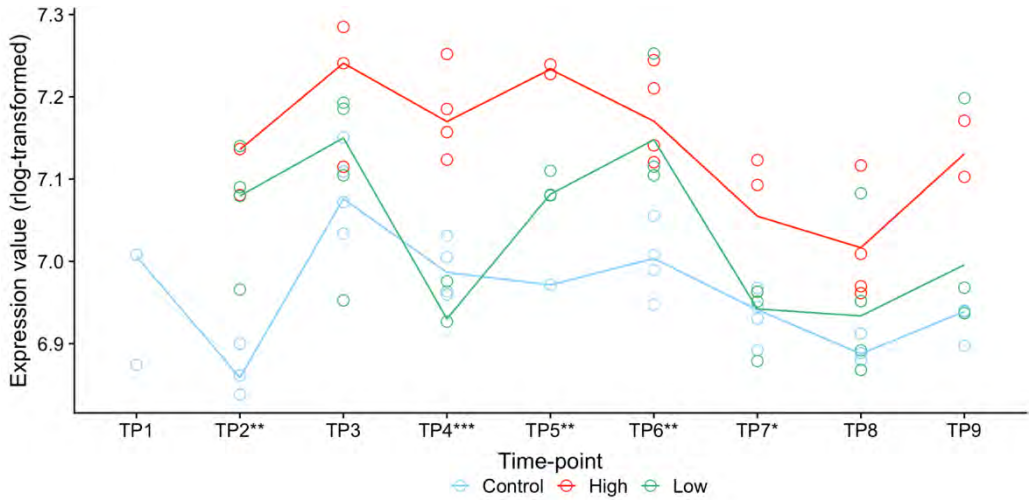


Figure 63. Time-course plot, median of genes per replicate and median of medians with connection line of genes enriching “RNA-polymerase”- and “Proteasome” KEGG pathways. Significant changes in expression (ANOVA) are indicated by * (FDR<0.05), ** (FDR<0.01) or *** (FDR<0.001).

group (Fig. 63). Consistent stimulation of RNA transcription and amino acid synthesis along proteasomal degradation could once again be construed as a generic response to CB toxicity manifesting itself as disruptive of membrane components [637,650], next to other possible explanations.

Similar to NF toxicity, CB induced an induction of autophagy. However for CB, the JGI-GOs “Autophagosome assembly”, “Macroautophagy” and “Autophagy” were found upregulated in the top-30 FDR-ranked gene sets in PGSEA at TP3 and down-regulated at TP6, while time-course plots of the genes suggest significant upregulation of autophagic mechanisms at TP8 and TP9 (Suppl. Fig. SI-62) This was here interpreted as a result of accumulated damage to membrane lipids and protein along peroxide-induced oxidative stress, as before seen for salt-induced ionic and osmotic stress in microalgae [630]. Early activation of autophagic pathways at TP3 was likely involved with breakdown of internalised vesicles containing recycled membrane components. Induction of autophagic mechanisms could arguably serve here as another non-specific biomarker for aquatic pollution, similar to inhibition of cellular motility.

Lastly, maSigPro “Cluster05” and “Cluster06” (Suppl. Figs. SI-64 and SI-64) identified differential effects of CB exposure on the algal genome. “Cluster05” genes enriched various JGI-GOs comprising cell cycle checkpoint regulation, chromosomal organization and cytoskeleton formation (Fig. 64), whereas “Cluster06” genes enriched KEGG pathways “Mismatch repair”, “Non-homologous end-joining”, “Nucleotide excision repair”, “DNA replication”, “Homologous recombination” and “Base excision repair” (Suppl. Table SI-T23). Various DNA repair mechanisms were stimulated early at TP2 and TP3 for both exposure groups, potentially indicating an early adaptive response to immediate peroxide species damage to the nuclear or organellar genomes [649]. These processes were further significantly upregulated at TP8 and TP9, with “Low” exposure group gene expression higher than “High”. At this stage of *C. reinhardtii* cell cycle, cells enter the transition from a light to dark environment and proceed through cell cycle checkpoints involving sensing of DNA damage [193,197]. Higher gene expression of DNA damage repair processes at lower exposure concentrations might have indicated here low-level genomic damage in an

adaptive and hormetic low-concentration zone (actual adverse outcome induction in “Low” group was at ~EC_5-$EC_{12.5}$, Fig. 55B), as opposed to the higher exposure concentration [638,651]. This is in line with an observed upregulation of RNA transcription for genes involved with regulation of cell cycle in “Cluster05” for the “Low” exposure group, whereas a down-regulation of such genes was observable for the “High” exposure group (Suppl. Fig. SI-63).

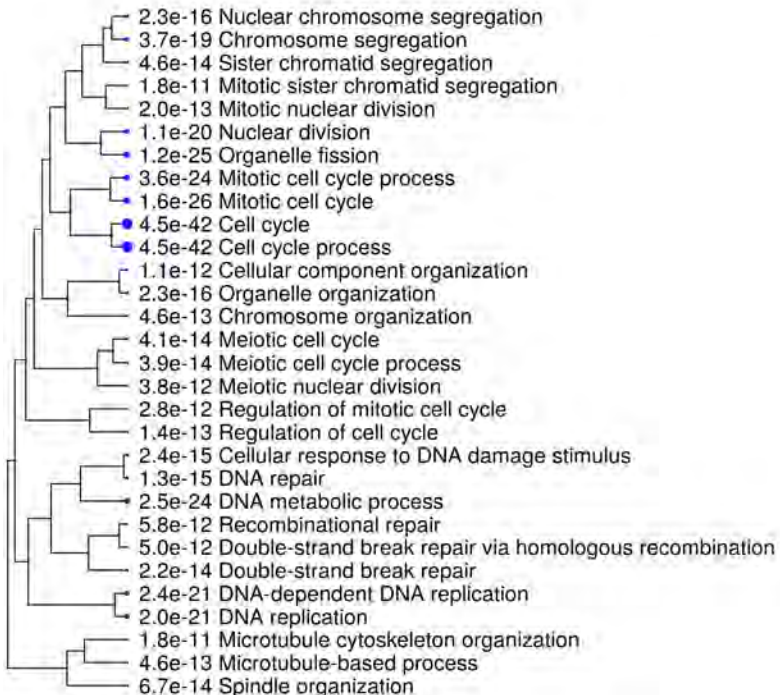


Figure 64. Hierarchical cluster plot of JGI-GOs enriched by genes of maSigPro time-profile “Cluster05”, along their FDR. Size of the nodes indicates degree of significance, the distance of the clusters connected by the branches of the dendogram is relative to the ontological similarity of gene sets.

3.5. Hypothesizing an acute chemical MoA for CB toxicity and constructing draft AOP for baseline toxicity

In this penultimate chapter, it was endeavored to conduct an *omics*-driven hypothesis of chemical MoA for a toxicant with a poorly understood molecular toxic effects in algae, in line with Scientific Objective III. Together with results of Chapter 4 which served to 'calibrate' the data analysis approaches to expected known molecular effects of NF toxicity, the overall aim was towards the purpose of giving conceptual and empirical support to the notion that a time-course multi-*omics* profiling of synchronized algal cultures may provide supporting evidence or novel insights into molecular effects of toxicity. Ultimately, such gained knowledge could be introduced into mechanistic frameworks (such as supporting draft AOP construction) in order to aid regulatory decision-making or enable early screening and prioritization approaches for testing of chemicals in the future [49,145,146,165,169–172]. For instance, panels of biomarkers predictive of adverse outcome suggested by *omics* experiments, along knowledge of the MIE, might find utility in future first-tier targeted screening assays for MoA classification or even MIE triggering of chemicals, pending downstream evaluation of biomarker specificity through follow-up experiments and counter-factual evaluation [109,134,146,166–168,606]. Additionally, *omics* data could find application in prioritization of testing by means of "chemical MoA" read-across, using *in-silico* classification methodologies to compare multivariate biological *omics* signatures of toxicant-exposed organisms.

Here, multi-*omics* time-profiling generated various insights into the stress response of *C. reinhardtii* exposed to CB. Gained knowledge on molecular effects from the previous sections was summarized in a time-resolved schematic to hypothesize on the unknown acute chemical MoA of CB (Fig. 65). The schematic juxtaposes the changes of measured molecular effect categories in dependence of time over the exposure period and is anchored to both start of exposure and the narrow time-window of adverse outcome occurrence. Little is known on the molecular basis of CB toxicity or on baseline toxicity in general - specifically to algae. In the invertebrate *Daphnia magna* exposed to a set of baseline toxicants, molecular disruption of calcium homeostasis, as similarly observed here for *C. reinhardtii*, was linked to heart rate

decrease [128]. However, wider and more resolved information on mechanism remains so far unclear [146], with membranes remaining historically speculated targets [343,652]. The baseline toxicant butanol was previously added to growth medium of non-synchronized *C. reinhardtii* cultures to optimize induction of lipids for biofuel generation, however not in context of phenotypic anchoring to inhibition of cell division or with the aim of elucidating pathways of toxicity [263,611]. Despite this disparity, the observed generic effects on energy and lipid metabolism, intracellular signaling and ion transporter activity as induced by butanol [263] could be identified as perturbed biological processes in this present CB exposure study, pointing towards similarity in molecular effects. Additionally, a captivating similarity of CB-induced molecular effects was discovered to various downstream effects observed in microalgae and plants exposed to ionic and osmotic stress [621,629,630,632–634,637]. Considering gathered data from the CB time-course exposure experiment, time-course profiles of different molecular perturbations could be anchored to adverse phenotype of algal growth inhibition. An acute chemical MoA of CB was hypothesized,

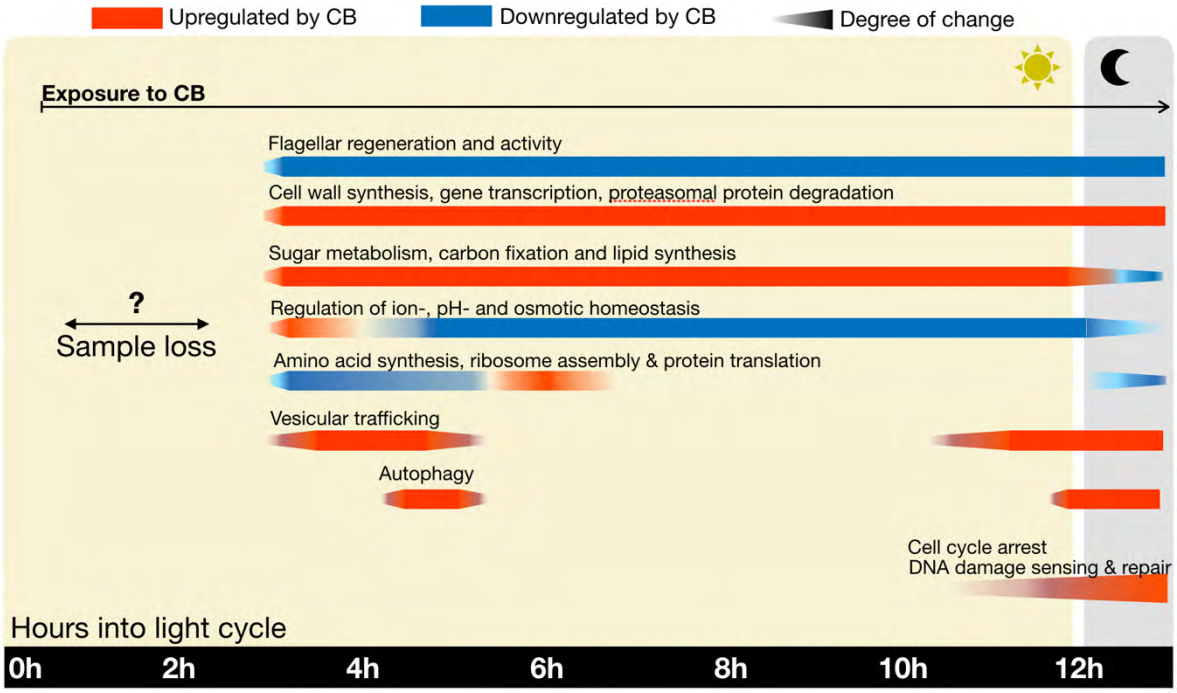


Figure 65. Time-resolved chemical MoA hypothesis of chlorobenzene toxicity in *C. reinhardtii.* The intensity of molecular effects (marked by increasing or decreasing width of the bars) and direction of change (marked by color of bars) is represented over the sampling time-course. The molecular effects here are anchored to both the 12h: 12h light:dark cycle (at the beginning of the 12h light period and transition into the 12h dark period) and the window of adverse outcome occurrence (inhibition of algal cell division and decrease of population growth rate), with cellular and nuclear division occurring slightly before, during and after the light:dark transition.

involving non-specific interactions with biological membranes and their components including various ion transporters, along a cascade of downstream perturbation of membrane-bound biological processes including photosynthetic ETC, intracellular signalling systems, osmotic potential and pH regulation, and secondary peroxide generation and potential reactive oxygen species propagation chains, thereby for the first time confirming and extending historical speculations on molecular effects of baseline toxicity specifically for microalgae [128,343,607,652]. Initial down-regulation of gene expression for amino acid- and protein synthesis processes were observed in coincidence with stimulation of vesicular trafficking of likely recycled membrane components and autophagic mechanisms, revealing activation of complex regulatory networks in adaptation to CB exposure. Results were partially obscured by substantial losses of sample size and statistical power for some experimental groups over time-course.

In addition to hypothesizing on an acute MoA for CB, a tentative draft AOP for “Baseline toxicity inducing algal growth inhibition” (Fig. 66) was hypothesized. As opposed to the hypothesized AOP for “Phytoene desaturase inhibition inducing algal growth inhibition” proposed in Chapter 4, the present AOP draft as constructed singularly using data from the present multi-*omics* exposure experiment. Due to the limitations of the latter, and relatively increased data variance and loss of sample size specifically at time-point 1 exposure groups and for DIMS spectral data in the wider sense, the perceived confidence in construction of the AOP draft and its elements was here lower than for NF. At this point of technological development of *omics* platforms and multivariate data analysis pipelines, the still prevailing inherent uncertainty of *omics* technologies and their generated data emphasizes their primary utility as tools for generating hypotheses on molecular mechanisms [653]. This further flags up the importance of follow-up experimentation to cross-verify, reproduce and quantify discovered biological perturbations and enable analysis of acute toxicant MoA from various perspectives and methodologies to gain confidence in understanding of toxicity and increase weight of evidence, ultimately enabling robust construction of AOPs [116,146,157,654]. Again - ultimately, high-content technologies such as *omics* should enable unsupervised identification of putative molecular markers diagnostic of chemical MoA towards application in chemical safety assessment, e.g. for future

downstream inclusion of any discovered biomarkers in targeted assay panels to perform first-tier screening and categorisation of chemical MoA for untested compounds [57,146].

4. Conclusion

Time-resolved multi-*omics* profiling of synchronized *C. reinhardtii* cultures exposed to the baseline toxicant chlorobenzene was conducted to gain insight into its poorly-understood mechanisms of toxicity in algae, and by extension assess utility of the tailored multi-*omics* experimental design towards *de-novo* hypothesis of acute chemical MoA. Data analysis revealed various transient and consistent molecular perturbations of the transcriptome, and to lesser degree of the metabolome and lipidome. Two gene clusters were proposed as generic markers for aquatic pollution in microalgae. Importantly, a hypothetical chemical MoA for chlorobenzene toxicity linked to non-specific interactions with biological membranes and their components was drafted despite substantial loss of sample size during analytical acquisition, for the first time delivering experimental confirmation of historical speculations on the molecular basis of baseline toxicity. Subsequently, a tentative AOP draft for “Baseline toxicity inducing algal growth inhibition” was constructed, based purely on *de-novo* generated multi-*omics* data. Lastly, the value of such experimental approach and results for application in chemical safety assessments was discussed.

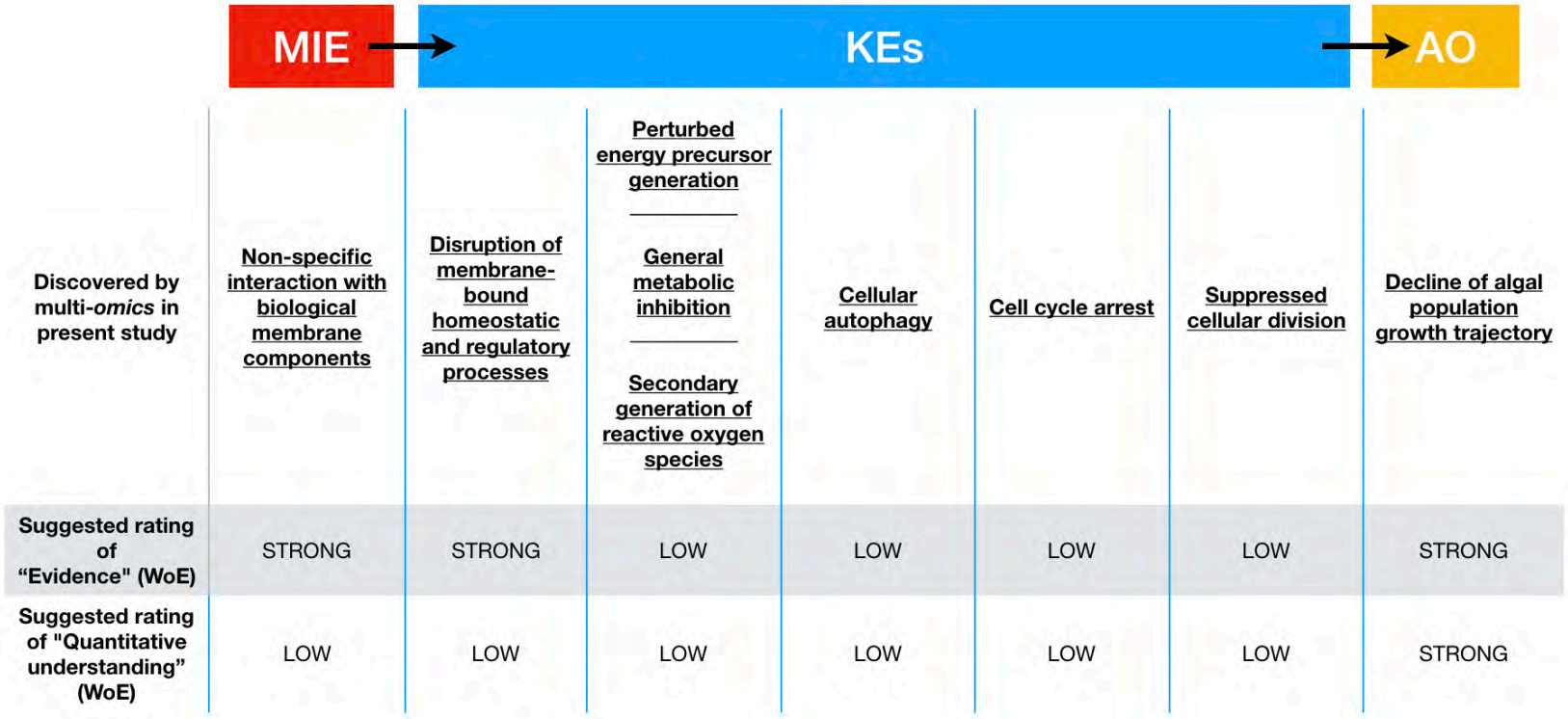


Figure 66. A potential AOP draft for “Baseline toxicity inducing algal growth inhibition”, along indication of discoverability by omics. Delineated are the AOP draft from molecular initiating event (MIE) over multiple hypothesized key events up to the adverse outcome (AO) of algal growth inhibition. Overall, perceived strength of evidence and quantitative understanding was rated low for many elements of the AOP due to high variance in the dataset and lack of existing supporting knowledge informing the construction of this AOP draft.

Chapter 6

Overall conclusions and outlook

1. Introduction

Globally, various legislations serve the purpose of guiding chemical safety assessments of synthesized or imported chemical compounds, including REACH legislation in the European Union. Hazard assessment as part of the chemical safety assessment process is to determine any intrinsic danger caused by a chemical substance to organisms. In the context of environmental hazard assessment of chemicals, this process historically focused on the determination of hazard by exposure of various sentinel organisms (e.g. microalgae, invertebrates, fish) to compounds under scrutiny, deriving toxicological understanding from observations of induced phenotypical effects.

Recently, a paradigm shift has commenced globally to modernize the process of chemical safety and hazard assessment. This effort of decreasing financial expenditure and animal sacrifice while increasing reliability and generalizability of gained toxicological knowledge is envisioned to be driven by modern conceptual models, alternative technologies, and a general core refocusing of the risk and hazard assessment procedure towards understanding the molecular basis driving an organisms adverse response to chemical exposure. An example for such alternative approaches is the various *omics* technologies, high-content analytical platforms enabling blanket profiling of various domains of biological functional units (e.g. metabolites, gene transcripts) and their response patterns to toxic insult. However, various stakeholders do not consider *omics* technologies yet sufficiently developed to inform hazard and more generally safety assessment of chemicals.

To facilitate more frequent and assured application of *omics* to environmental hazard assessment purposes, different obstacles remain to be addressed by the scientific community. Prominent among these are the establishment of tailored experimental designs and testing systems suitable for *omics*-driven hypothesis of chemical MoA and by extension discovery of molecular key events to support

construction of AOPs, and associated demonstration that *omics* applying such designs and systems can reliably hypothesize on chemical MoA in such fashion to be of utility to future hazard assessment

In this context, the present study set out to address the research question of whether an integrated and time-resolved profiling of the algal metabol-, lipid- and transcriptome during toxicant exposure can grant diagnosis of acute chemical MoA, support construction of AOP drafts, and aid in chemical hazard assessment. This chapter will briefly synthesize and evaluate findings of the present study in the light of initially posed scientific objectives and the overall research goal (see Chapter 1).

2. Evaluation of scientific objectives 1 and 2

The first scientific objective of the study was to 'outline a tailored experimental design that is effective for *omics*-driven chemical MoA diagnosis and molecular key event hypothesis in algal toxicity testing', whereas the second objective endeavored to 'develop and validate a rigorously-defined algal exposure system suitable to support the specific requirements of the outlined experimental design.'

Theoretical and practical considerations of crucial requirements to such an experimental design were delineated, and cross-disciplinary literature of existing methods in previously-conducted algal toxico-*omics* research was scrutinized to evaluate their applicability to these requirements. Various culture growth experiments over varying culturing conditions were conducted and evaluated using metabolomic-, flow cytometric- and cell density measurements. Development of a novel *C. reinhardtii* growth medium and tailored vial exposure system was achieved to suit the physical demands of the experimental design. Overall, the conventional algal toxicity test format as per official test guidelines was radically restructured to

suit a tailored and time-resolved multi-*omics* analysis of the temporal trajectory of *C. reinhardtii* biological and toxicological signatures over exposure duration with the aim of anchoring molecular signatures to cell cycle and adverse phenotype, confidence in the latter to be gained through analytical and cellular measures.

Previously, algal toxico-*omics* research with the aim of gaining insight into toxicological mechanisms focused heavily on considerations regarding optimal application of analytical and statistical methodology, with an orientation of toxicity test parameters as prescribed by conventional test guidelines. Despite serving a tremendous value to the scientific and regulatory community, conventionall test guidelines were historically developed towards deduction of hazard information using phenotypical observations, and deduction of molecular mechanisms is arguably outside their applicability domain. The prescribed legacy test format arguably contains suboptimal parameter selection (lighting, test duration, etc.) with relevance to algal cell and population biology, thus resulting in the bulk of existing algal toxico-*omics* research being dominated by low or missing deconvolution of temporal dynamics of toxicity, and lack of anchoring of test duration and sampling events to crucial biological events. Additionally, algal toxicity tests of volatile chemicals required restrictive compromise between amounts of harvestable biological material, physical scalability, and disturbance of gas equilibria in test vessels during sampling.

The originality of the outlined experimental design lies in a number of significant modifications to the conventional test format. These entail an explicit prescription of population-wide cell cycle synchronization, alignment of the test duration to a single cell cycle, and restriction of sampling events to a highly-resolved time-course pattern prior to population-harmonized window of adverse outcome induction. The experimental design extends existing test guidelines towards maximizing the utility of *omics* to discover perturbation of biological processes in *C. reinhardtii* and their specific association to cell cycle events and induction of adverse phenotype. The

abstract and thus generalizable nature of the design permits variation of many of its parameters, including employed algal species, exposure concentrations, tested toxicants and chemical MoA, *omics* platforms, or replication vs. spacing of time-points to enable flexibility to address other scientific questions. For instance, concentrations could be adjusted to simulate effects of low-concentration exposures, hormetic concentration ranges, or high concentrations mirroring chemical pulse discharge into the environment. Conceptually, the design is in a broader sense argued to be valid for applicability to other environmental sentinel species as long as synchronization of life stage can be achieved, including fish, water flea, or other invertebrates. Lastly, the design could serve application in other scientific domains, such as investigation into general biological mechanisms, algal responses to external stimuli such as radiation, starvation or eutrophication, or biotechnological applications (biofuel or hydrogen production, etc.).

The developed exposure system prominently allows miniaturization of sacrificial test vessels with previously-unachievable high levels of harvestable biomass, high scalability of applicable experimental designs in the dimensions of replication and number of sampling-points, along support of testing of volatile chemicals. Experimental evidence further suggested general validity in reproducing concentration-response curves for various toxicants, and the explicit analytical benefit of utilizing synchronized cell cultures.

The exposure system further showed an overall feasible physical implementation of the outlined experimental design, linking the two scientific objectives. It features a simple test set-up and flexibility to accommodate alternative test designs and toxicants commonly difficult to test (soluble, insoluble, volatile etc.). The conducted variability characterization using untargeted metabolomics analysis support reproducible and robust generation of data, a prime requirement for any methodologies geared for application in regulatory context. The employed batch-specific normalization strategy of multivariate signatures is argued to represent a

generalizable approach to achieve wider comparability between repeated experiments within or between scientific laboratories specifically for metabolomics data, and might potentially aid in increasing precision in classification-based read-over of chemical MoA from algal metabolomics profiles. However, empirical investigation of the validity of this notion, along the potential applicability of this batch-specific normalization strategy to other *omics* datatypes (e.g. transcriptomics) remains material for future investigations.

On the other hand, certain limitations of the outlined experimental design, the exposure system, and generated results of the variability characterization need to be noted. The current sampling procedure allows allocation of sampling events to the dark zone of the culturing light period as evidenced by the ultimate sampling time-points employed in the norflurazon and chlorobenzene time-course experiments, however initial seeding of algal test cultures prominently remains limited to the start of the light zone due to light-driven activation of cell cycle. The few but yet active metabolic pathways in *C. reinhardtii* during the experienced dark period may limit deduction of mechanistic insight for toxicants with chemical MoA specific to these pathways, and restrict generalizability of the design to other species. Due to the nature of exponential cell growth, culture set-ups on days prior to experiments strongly magnify imprecision in cell densities, a parameter in need of rigorous control in the designed exposure system (Scientific Objective 2). Further, the test design is currently restricted to investigation of acute chemical MoA, thus far ignoring transgenerational or accumulatory low-concentration (chronic) toxicity effects.

In the developed exposure system, a potential high loss of volatile test chemical during test setup was apparent, significantly reducing intended exposure concentrations from nominal levels. Preventive laboratory measures need to be taken to increase accuracy and reproducibility of future investigations applying this system. Additionally, despite the achieved high culturing cell densities and

harvestable biological material, even higher material yields might be achieved when employing growth media allowing heterotrophic growth, thereby enabling flexibility to increase technical replication, avoid substantial decrease of sample size due to material loss during metabolite-/lipid-/RNA extractions or instrumental data acquisition, or sampling for additional laboratory analyses including other *omics* platforms. Application of such media however entails the caveat of substantially increased risk of not generating axenic cultures. Further, characterization of experimental variability between experimental repeats was merely conducted using metabolomics analysis and comparability to other platforms assumed, experimental investigations into variability and repeatability of data from transcriptomics or other platforms remains an aim for future work.

Despite these limitations, the detailed deliberations of the experimental design as described in Chapter 2 are argued here to provide a flexible and useful foundation for various applications in microalgal toxicological and biological research. The developed exposure system has succeeded in attaining a physically feasible test system generating previously unachievably high biomass per experimental vessel, and enabling implementation and application of the rigorously-outlined experimental design to algal exposure studies. Thus, the first two scientific objectives were hereby successfully achieved, and general validity of phenotypic and molecular data generated by the tailored exposure system showcased and published [417].

3. Evaluation of scientific objective 3

The third objective of the research was to ‘apply the developed toxicity testing approach to selected model toxicants as an attempt to diagnose acute chemical MoA and hypothesize putative molecular key events to support construction of AOPs.’ This objective reflected the essential application of the outlined experimental design and the tailored exposure system to a set of model toxicants to probe their power in discovering toxicological mechanisms in algae. Multi-*omics* time-course experiments and analysis were here conducted on single generations of synchronized *C. reinhardtii* exposed to two model toxicants, one with well-established chemical MoA in algae (norflurazon), and one with a poorly-understood mechanism in algae (chlorobenzene). For each, time-resolved acute chemical MoA hypotheses and AOP drafts were developed using the generated *omics* data, and existing knowledge from literature background (norflurazon only). As such, the molecular stress profiles of *C. reinhardtii* to both toxicants could be recorded, and linked from exposure to induction of adverse phenotype over increasing stimulation of molecular response via two discrete concentration levels.

Single- or multiple sampling time-point experiments employing one or multiple *omics* approaches to scrutinize mechanisms of toxicity are no novelty. Experiments on various model organisms including rodents, human cell lines, fish, water flea, spring tail or algae were previously performed to elucidate molecular effects of toxicants – seminal studies include references [245,250,252,411,423,655–659]. In the present study however, experiments were performed on a previously unachievable scale of factored sampling time-point frequency, biological replication, and exposure concentration levels, particularly not in toxicological multi-*omics* research in algae. Specifically the hybrid approach of attempting to validate a multi-*omics*-driven approach of hypothesizing chemical MoA using a combination of toxicants with well-described and poorly-understood mechanisms of toxicity breaks

new ground as an evaluation strategy, indicating both reproducibility of existing knowledge and generation of novel insights into acute chemical MoA in algae. Substantial contribution to the research community was further provided by the comparison of gained insight into molecular effects of toxicants on *C. reinhardtii* between 'collapsed' datasets (omitting sampling time from data as a variable) and actual time-resolved datasets (time-course profiling and juxtaposed single time-point analysis). 'Collapsed' datasets are argued to mirror approximately those results to be gained from employing non-synchronized cultures in single sampling time-point experimental designs, which was as demonstrated a comparatively far less sophisticated and meaningful approach to gaining insight into acute chemical MoA and its temporal dynamics. Deriving hypotheses for the molecular mechanisms of toxicity for a herbicide and an industrial chemical to algae, the work conducted in Chapters 4 and 5 contributes an arguably successful evaluation of an *omics*-driven approach to hypothesize the chemical MoA of compounds, and support construction of AOP drafts. As such, these two experiments have indicated validity of the experimental approach at large.

On the other hand, reduced accuracy and precision of generated data along with non-negligible sample loss during quality assurance procedures did limit the insightfulness of findings. This was specifically prominent for the chlorobenzene exposure experiment, and was mirrored in limited accuracy and clarity of results when attempting to construct a chemical MoA hypothesis and construct an AOP draft. However, it has to be kept in mind that these hypotheses were driven purely by the generated *omics* data, whereas the acute chemical MoA schematic and AOP draft for the norflurazon experiment was at least partially supported by existing knowledge on acute chemical MoA. Further, the utility of the employed *omics* platforms in describing perturbance of biological processes was highly dichotomous. Transcriptomics data was vital in gaining biological and toxicological insights, as evidenced by its high analytical precision and almost exclusive foundation for gained

insights from enrichment analyses in the present study. DIMS-based metabolomics and lipidomics suffered from low levels of putative spectral peak annotation success and thus decreased utility in pathway enrichment analyses for the present microalgae species (similarly to other environmental model species), relatively large inter-group biological variability despite low technical variability, and instrumental sample acquisition problems, as compared to the more successful mapping of RNA transcripts to the *C. reinhardtii* genome. However, spectral peaks in the metabolomics and lipidomics datasets determined as significantly different between exposure groups may still prove a substantial asset for future follow-up experimentation and downstream application. From a perspective of untargeted analysis of the metabolome and lipidome, non-annotated significant features could be evaluated regarding their specificity to a toxicant's MoA, their concentration-response profiles characterized, and metabolite/lipid identification performed using targeted methodologies such as liquid-chromatography tandem mass-spectrometry. In such fashion, statistically important spectral features could be explored for biological relevance and chemical MoA diagnostic value.

Despite these shortcomings and particularly the increased variance of experimental results generated within the chlorobenzene exposure experiment, the third scientific objective of applying the general experimental approach towards showcasing *omics*-driven hypothesis of model toxicant chemical MoA is thus here argued to have been satisfactorily accomplished.

4. Evaluation of the overall research goal

Tying theoretical considerations and empirical insights together, the overarching research goal was ‘'to develop and trial an integrated multi-*omics*-driven algal toxicity testing approach for hypothesis of acute chemical MoA and putative

molecular key events to support construction of AOPs", which was successfully achieved upon evaluation of scientific objectives 1 to 3. Delineating chemical MoA of compounds is commonly conducted via collation, synthesis and evaluation of toxicological and supporting information stemming from various data sources, applied methodologies and experimental approaches. Here, a single large-scale experiment was showcased to yield detailed insights into mechanisms of toxicity induced by chemical compounds in microalgae. The applied multi-*omics* time-course approach could provide a highly-leveraged method for hypothesizing on the molecular effects of chemicals on environmental model species, by both increasing confidence in existing knowledge on chemical MoA but more impactfully yielding meaningful new hypotheses on compounds with little understanding of induced toxic mechanisms.

A perceived valuable contribution to the scientific community is found in the developed integrated and flexible experimental and conceptual approach, allowing them to discover molecular mechanisms using varying experimental designs and intended purposes of investigation, specifically those attempting to deconvolute effects of chemical or environmental stressors. Building on both valuable insights and perceived shortcomings of innumerable former research efforts in microalgal toxicological studies, the assembled integrated testing approach could potentially serve regulatory applications to inform environmental hazard assessment of chemical compounds, e.g. towards structuring IATA (integrated approaches to testing and assessment) or informing and supporting construction of AOPs. Multi-*omics* approaches such as those presented here are envisioned in the future to drive untargeted categorization of chemical MoA as experimental tools or to serve development of panels of targeted assays utilizing biomarkers diagnostic of chemical MoA, pending downstream follow-up experimental verification of generated molecular hypotheses.

To achieve such verification of biological insights gained through *omics* as demonstrated, a number of future experimental follow-up investigations are warranted. For each studied chemical MoA, it will be necessary to extend the application of the developed multi-*omics* discovery approach to further model toxicants to achieve insights into intersections of biomarkers and biological stress signatures specific to or shared between certain toxicants, classes of chemical compounds, or mechanisms of molecular perturbation. Such would not only demonstrate reproducible re-discovery of the generated data and the hypothesized chemical MoA but also allow confident proposal of putative biomarkers diagnostic of chemical MoA from the generated datasets. To enable future selection of potential candidate biomarkers towards application in above-mentioned panels of targeted assays, and the latter to be of utility in first-tier screening of compounds, untargeted and automated selection of features correlated between multi-*omics* datasets using advanced algorithms such as the MOCA[7] algorithm currently under development might prove valuable. Such approaches could increase throughput of analysis while reducing noise in the dataset by feature selection of markers both correlated within and between discrete datasets (e.g. from different *omics* platforms) over increasing exposure concentration. In the future, following specifically the hypothesis of single biomarkers potentially diagnostic of chemical MoA and potentially even representing molecular key events within AOPs in such approaches, targeted post-hoc tests will be ultimately required to evaluate and characterize these markers and their relationships if they are to be integrated into mechanism-based hazard assessment. For increasing confidence of such targeted test approaches within IATA, targeted test panels should contain a multitude of diagnostic markers sufficient to disambiguate different chemical MoA while accommodating for multi-layered and

[7] "Multi-omics Module Correlation Analysis"; Currently under development by Dr. Albert Zhou, School of Biosciences, University of Birmingham.

complex biological response characteristics of organisms to toxic insult, as no single biomarker will be indicative of any one single chemical MoA.

5. Outlook

Increasingly, method development of the various *omics* platforms will permit toxicological investigations with higher data-point resolution along lower financial expenditure. A lynchpin of applying *omics* technologies to toxicological investigations is an understanding of their real applicability domain. *Omics* are sophisticated tools for hypothesis generation, and if utilized as such and within the confines of tailored experimental designs such as the one presented in this study, they can prove both valuable additions or starting points for an investigation into molecular mechanisms, specifically those associated with toxicological effects. The more levels of biological functional units are explored in conjunction, the more complete the insight will be. A future trend here for instance is an application of epi-genomics investigations into low-dose chronic effects induced by chemicals. However, future applications of *omics* could well aspire to comprise not only toxicodynamic investigations into regulatory, adaptive or adverse stress profiles of organisms in response to toxic insult, but also to quantify toxicokinetic mechanisms, ecological interactions such as cell population-wide stress signaling, or serve as biomonitoring tools to assess dynamic change of environmental DNA (eDNA) in response to local, global and regional pollution.

The presented work developed and trialed an integrated, multi-*omics* driven approach to hypothesize molecular mechanisms (specifically of toxicological nature), thereby attempting to aid existing experimental designs, test guidelines and analytical methodologies to embrace the 21st-century paradigm towards mechanism-based ecotoxicology.

Appendix

A.1. Supplementary figures

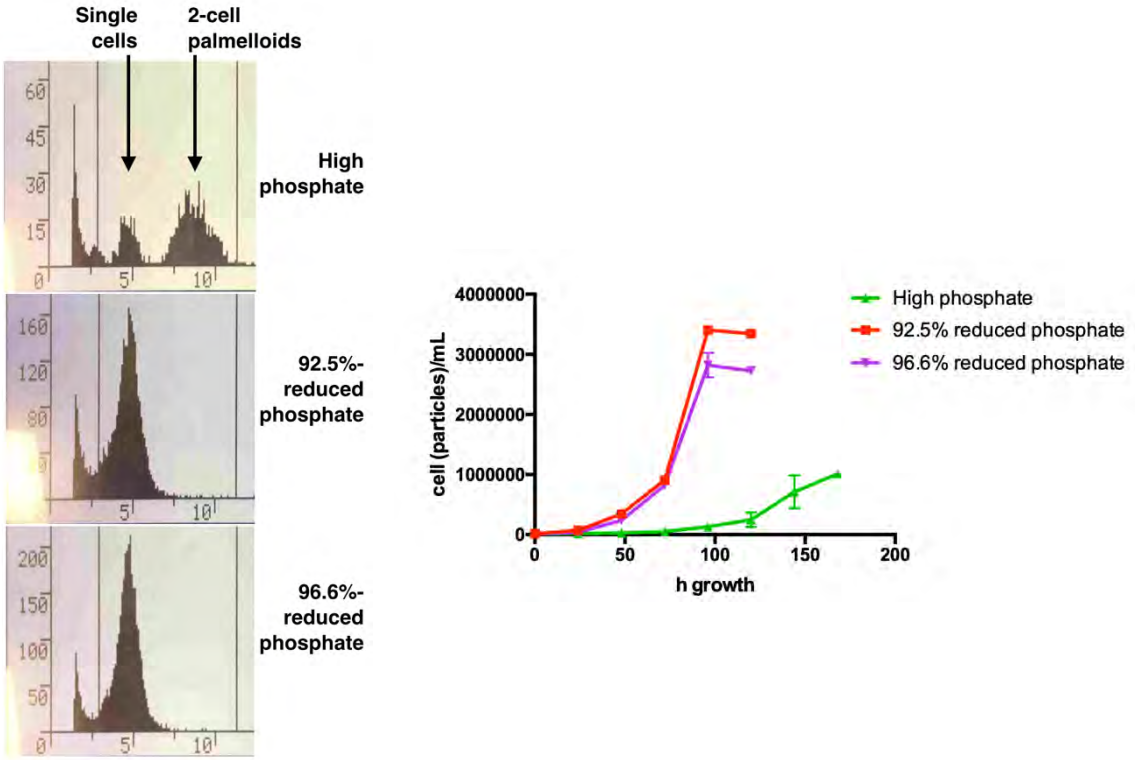


Figure SI-1. Presence of palmelloids in the three phosphate supplementation levels in *C. reinhardtii* populations after 48 h inoculation, grown under 12 h:12 h light:dark cycles in open flasks. Population size distributions [µm] in CASY cell count monitor (Left), and population growth curves (Right) for n = 4 cultures in dependence of phosphate supplementation. Palmelloid occurrence in CASY was visible as 2-cell aggregates in the selected measurement window of the capillary. The presence of larger cell aggregates was confirmed via light microscopy, and the resulting decreased growth rates can be observed in strongly-lagging population growth curve of “High”-phosphate group.

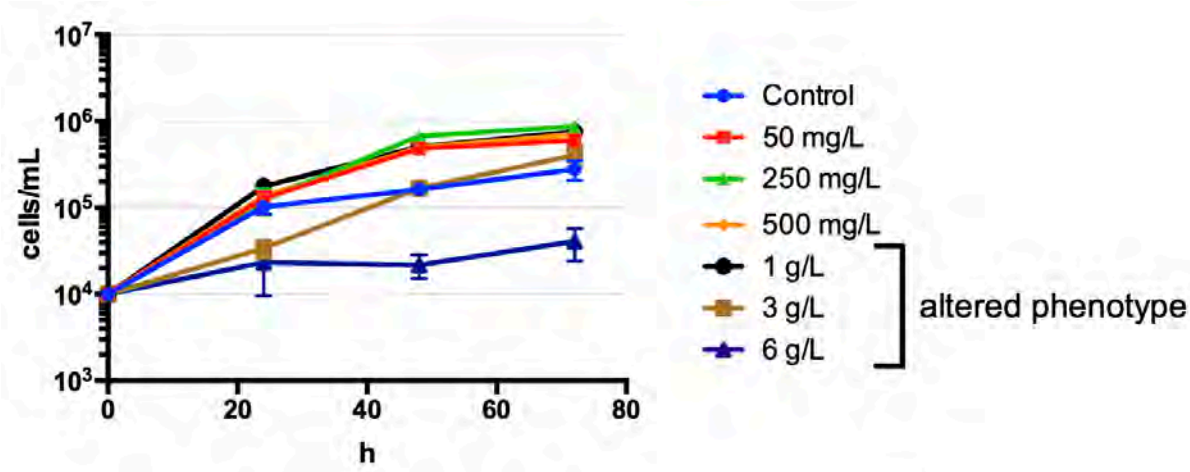


Fig SI-2. Comparison of varying NaHCO3-supplementation over 72h growth in CGM (open flasks). Growth increases with increasing carbon supplementation up to approximately 250 mg/L, and decreases with 3 g/L and 6 g/L. Altered morphology and enlarged of cells were observable in 1, 3 and 6 g/L supplementation under the microscope.

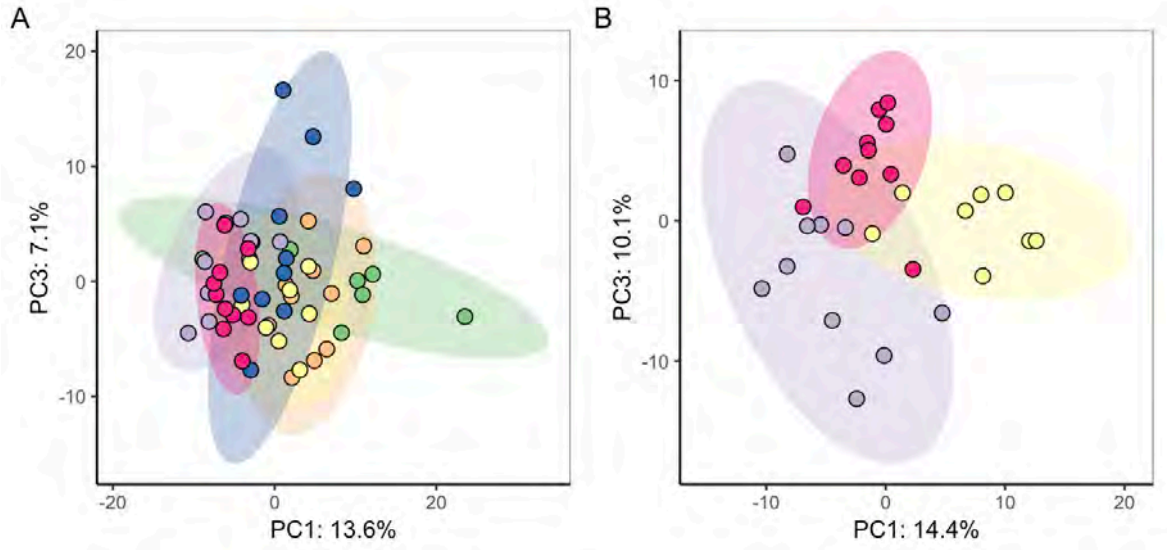


Figure SI-3. PCA scores plots (PC1 vs. PC3) visualizing the similarities and differences between three independent repeated exposure studies (biological batches), including each control and CB group (each n = 10). (A) All six control and CB groups, across all biological batches, and (B) control groups only, across the three batches. Groups were: Biological batch 1 Control (Purple), CB (Green), batch 2 Control (Yellow), CB (Orange), and batch 3 Control (Red), CB (Blue).

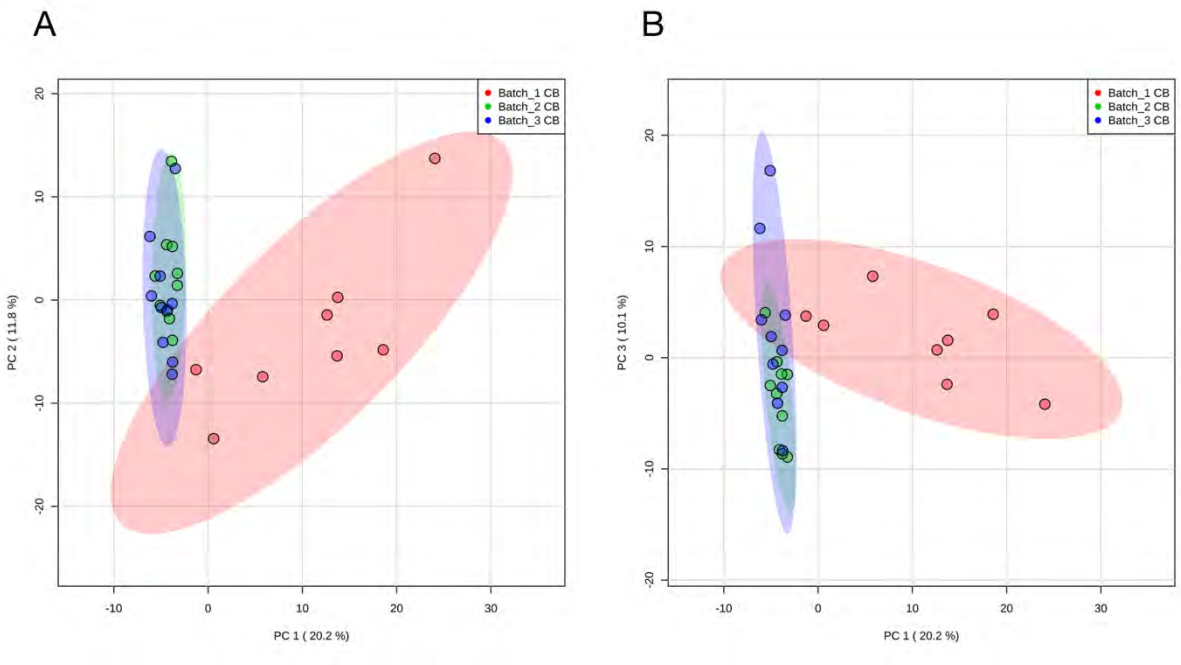


Figure SI-4. PCA scores plots (PC1 vs. PC2 (A) and PC3 (B)) visualizing the similarities and differences between three independent and identically repeated exposure studies (biological batches) for only the CB group (each n = 10. Groups were: Biological batch 1 CB (Red), batch 2 CB (Green), and batch 3 CB (Blue).

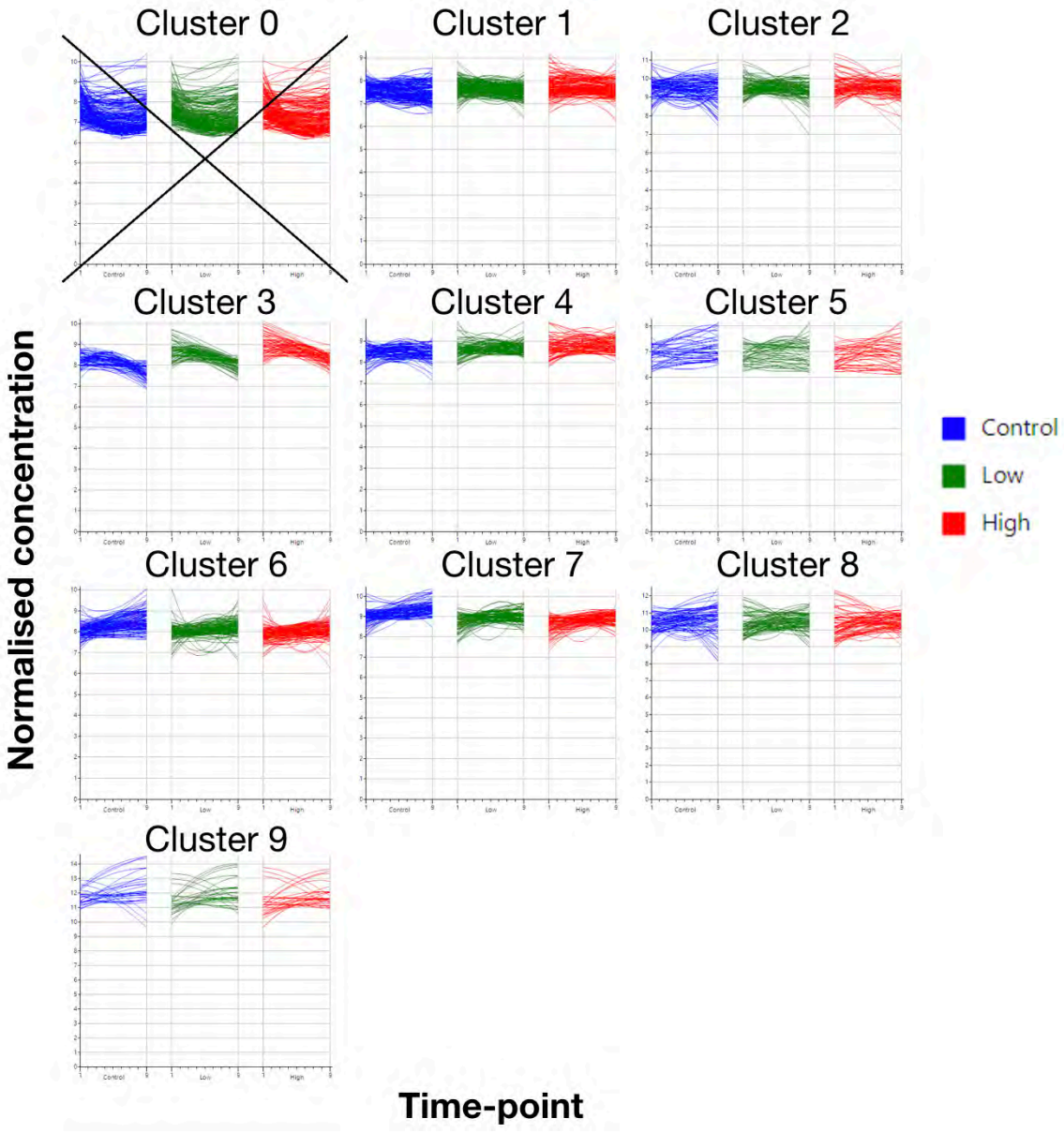


Figure SI-5. metaboClust software time-profile clusters of NF lipidomics data over time-course, with "Cluster 0" (crossed out) reflecting all insignificant spectral peaks in the dataset. K = 9 clusters of spectral peaks with similar time-profiles and displaying monotonous dose-concentration behavior were identified, however no single cluster could be meaningfully labelled with putative metabolite annotations and/or pathway enrichments.

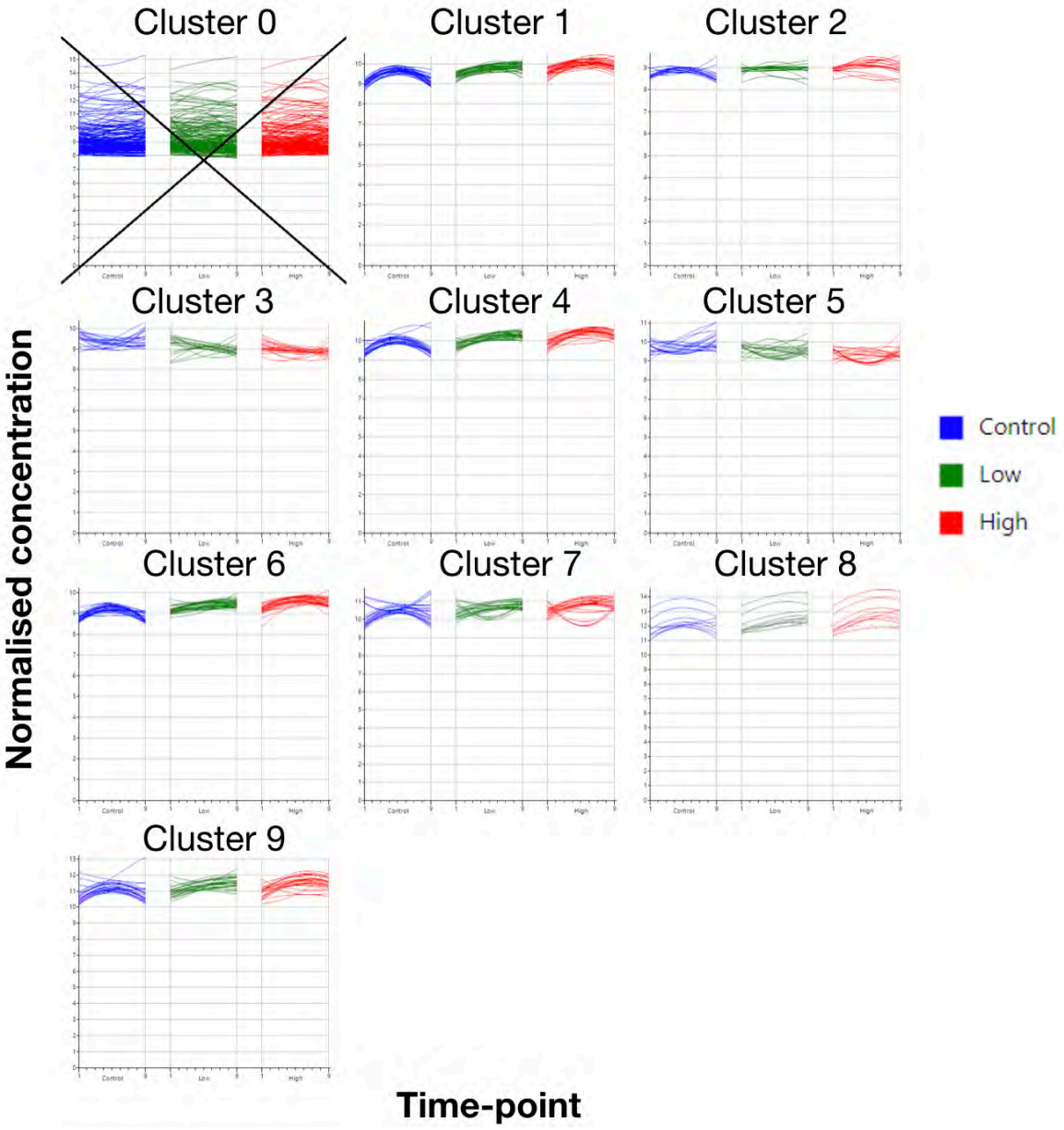


Figure SI-6. metaboClust software time-profile clusters of NF positive ion metabolomics data over time-course, with “Cluster 0” (crossed out) reflecting all insignificant spectral peaks in the dataset. K = 9 clusters of spectral peaks with similar time-profiles and displaying monotonous dose-concentration behavior were identified, however no single cluster could be meaningfully labelled with putative metabolite annotations and/or pathway enrichments.

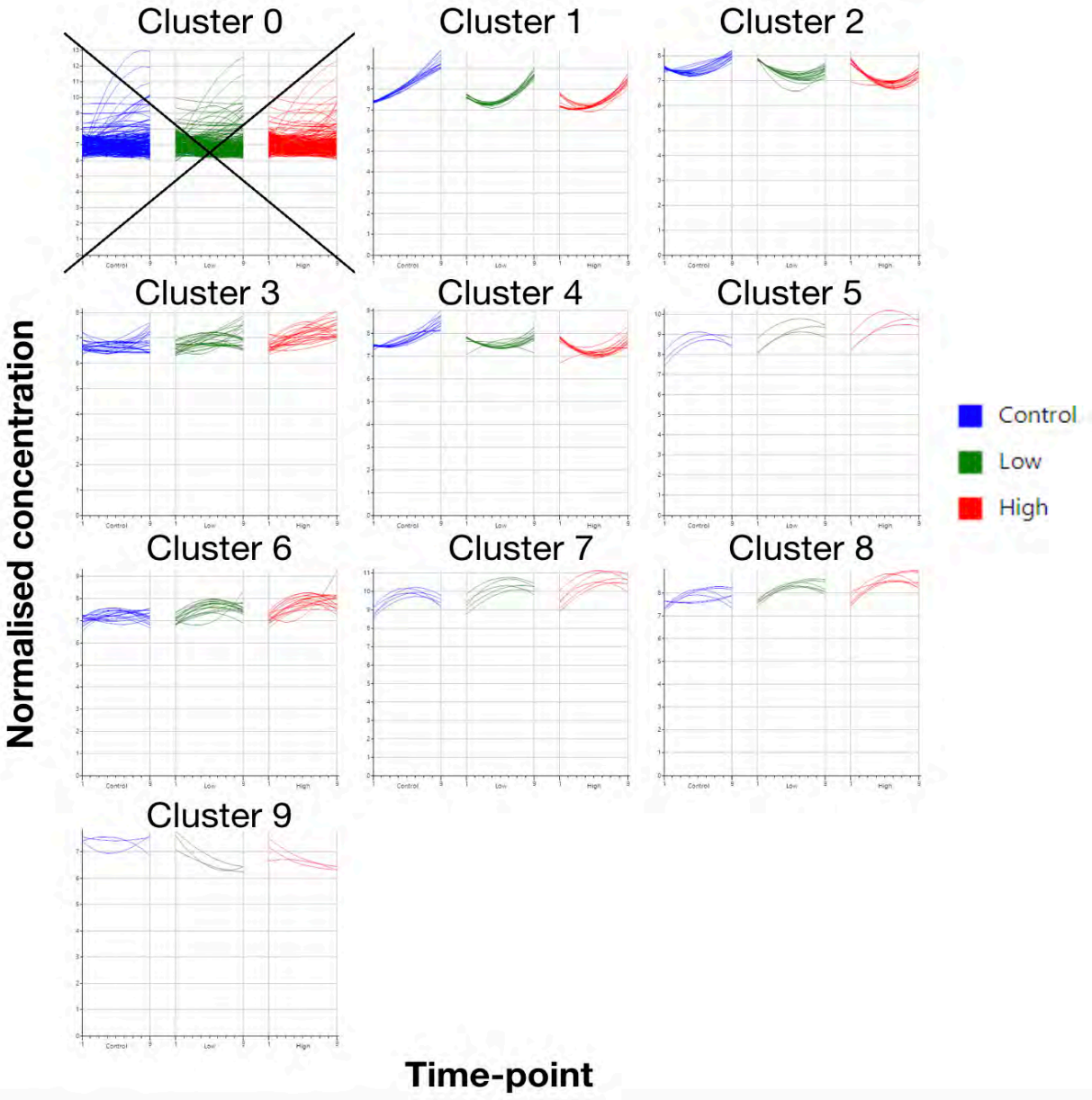


Figure SI-7. metaboClust software time-profile clusters of NF negative ion metabolomics data over time-course, with “Cluster 0” (crossed out) reflecting all insignificant spectral peaks in the dataset. K = 9 clusters of spectral peaks with similar time-profiles and displaying monotonous dose-concentration behavior were identified, however no single cluster could be meaningfully labelled with putative metabolite annotations and/or pathway enrichments.

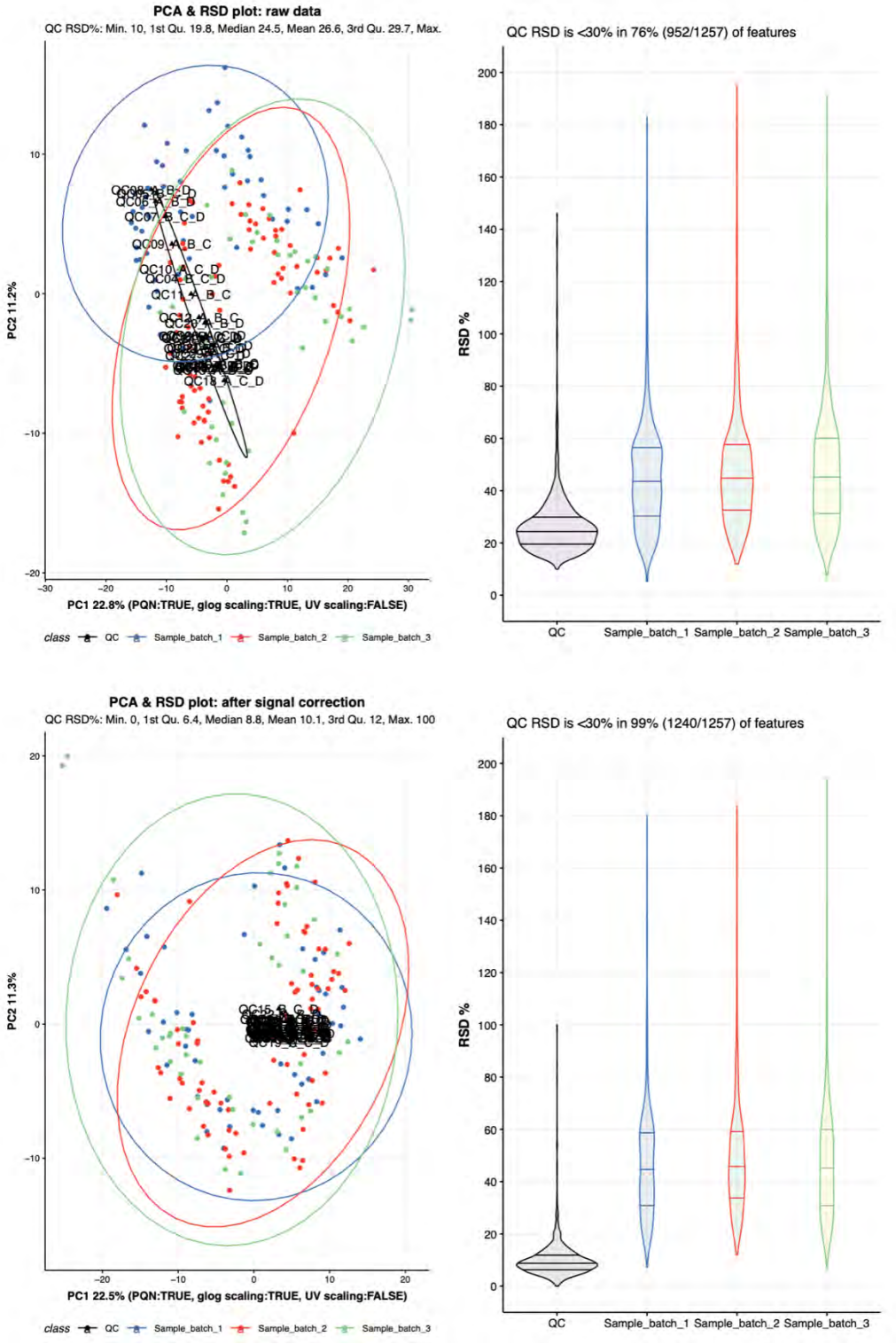


Figure SI-8. PCA and RSD violin plot of the NF dataset after global peak alignment and other processing steps, post removal of sequences sections with unacceptably large m/z calibration drift, before (Top) and after (Bottom) LOESS-signal correction. Close clustering of QC samples (black labels) with mRSD = 8.8% suggests low technical variance of QC samples after LOESS-signal correction. RSD distributions of samples batches 1-3 are higher due to their heterogeneity containing samples of all exposure groups and timepoints in a randomized sequence.

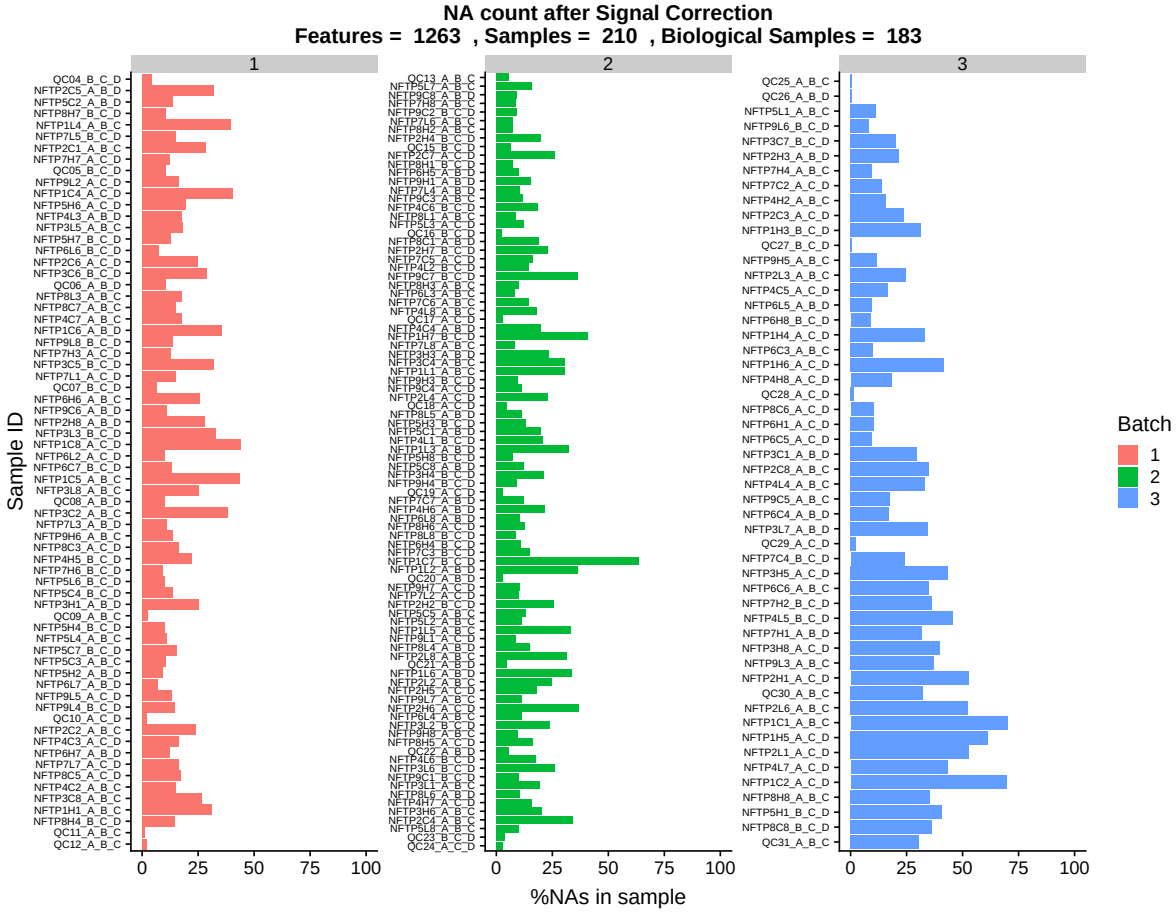


Figure SI-9. Percentage of missing values (%NAs per sample) in DIMS positive metabolomics data after global peak alignment and LOESS-signal correction of the NF dataset post removal of sequences sections with unacceptably large *m/z* calibration drift.

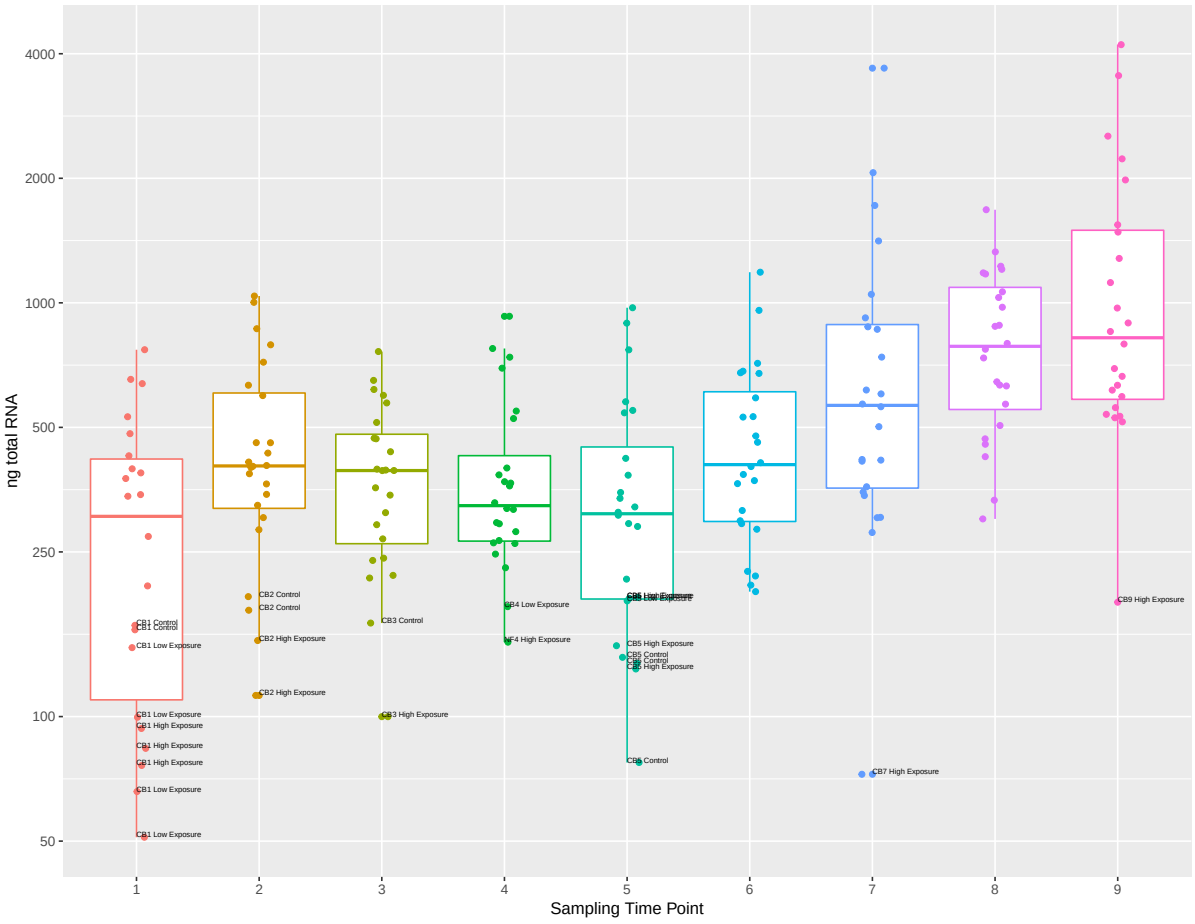


Figure SI-10. Total RNA extraction yields (ng total RNA) per sample of both CB and NF experimental samples, grouped by experimental time-point. Samples with less than 200ng total RNA yield are labelled.

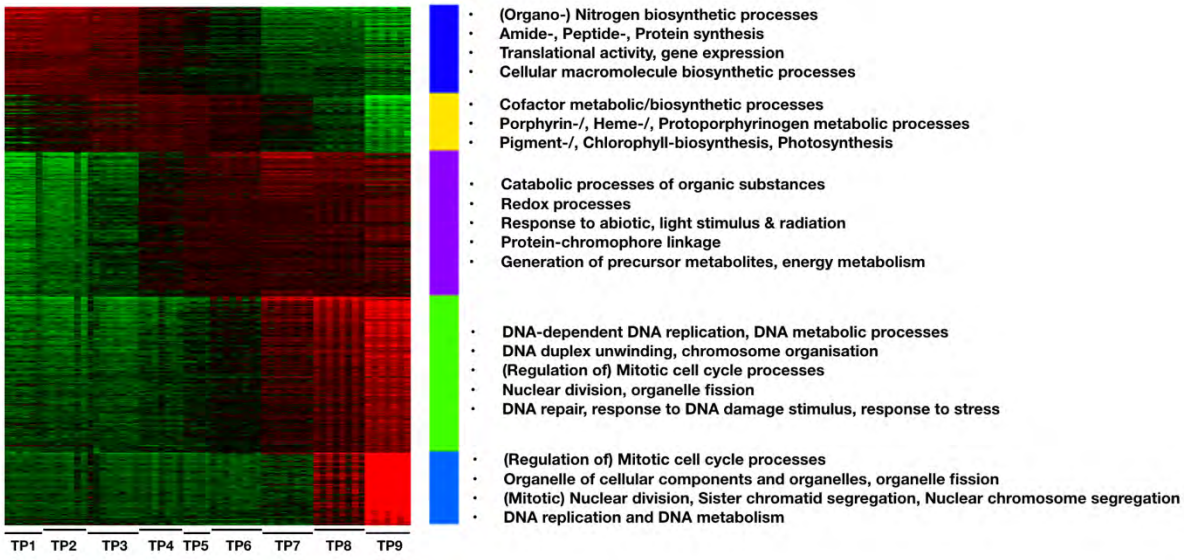
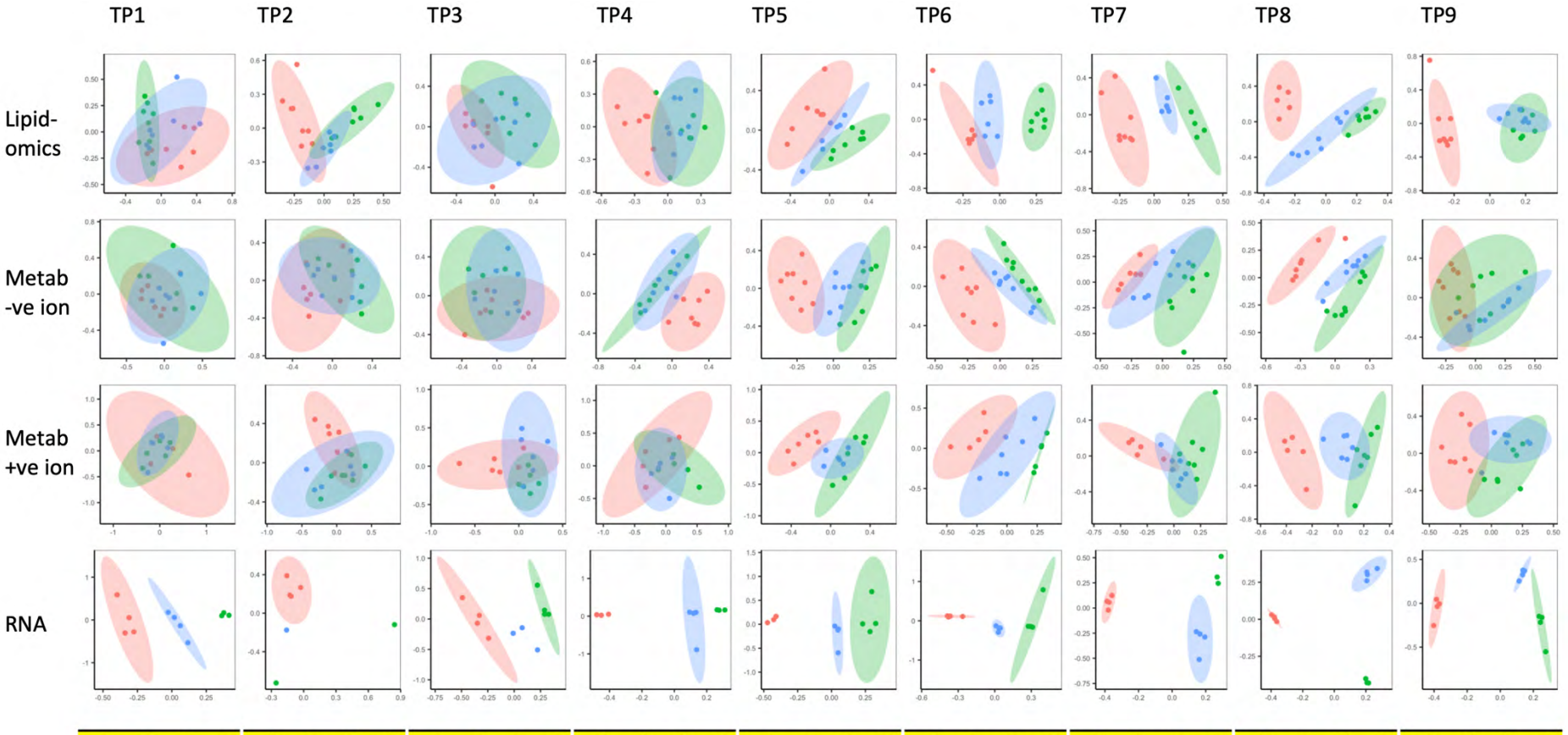


Figure SI-11. Heatmap of k-means clustering of NF and CB Control sample gene expression activity over time-course, with Joint Genome Institute Gene Ontology enrichments by genes contained within the clusters. Color red indicates relatively increased expression, color green indicates relative reduction in gene expression.



	TP1				TP2				TP3				TP4				TP5				TP6				TP7				TP8				TP9			
	PC1	PC2	p.PC1	p.PC2	PC1	PC2	p.PC1	p.PC2	PC1	PC2	p.PC1	p.PC2	PC1	PC2	p.PC1	p.PC2	PC1	PC2	p.PC1	p.PC2	PC1	PC2	p.PC1	p.PC2	PC1	PC2	p.PC1	p.PC2	PC1	PC2	p.PC1	p.PC2	PC1	PC2	p.PC1	p.PC2
Apolar	14.04%	8.21%	1.4e-02	1e-01	14.75%	11.13%	1.7e-07	8.6e-03	14.82%	11.22%	7.5e-03	2.3e-01	19.71%	11.28%	6.1e-06	6.3e-01	21.66%	13.95%	3.1e-04	2.2e-02	20.79%	13.74%	1.5e-09	6.1e-01	24.63%	15.07%	4.7e-10	2e-01	20.51%	16.96%	1e-07	7.9e-04	24.51%	14.7%	2.6e-12	6.7e-01
-ve pol	23.04%	10.86%	2.4e-01	4.1e-01	15.55%	10.39%	1.3e-02	5.7e-01	14.77%	10.23%	1.9e-01	3.7e-02	17.63%	11.15%	8.9e-04	1.8e-02	17.53%	10.74%	4.5e-10	7.6e-01	20.73%	11.49%	7.7e-07	6.9e-02	20.11%	12.63%	4.1e-06	1.9e-01	24.59%	11.37%	8.1e-05	7.9e-04	15.54%	11.52%	1.1e-03	8e-02
+ve pol	23.3%	14.7%	3.8e-01	5.6e-01	17.27%	14.3%	3.1e-01	1.4e-03	14.5%	11.92%	3.1e-03	1.6e-02	17.91%	14.15%	7.1e-02	3.2e-01	21.05%	17.63%	1.1e-05	2.8e-01	35.86%	13.64%	1.3e-05	2.4e-01	32.1%	10.28%	9.4e-07	1.6e-01	28.53%	12.21%	5.8e-09	6.4e-01	36.17%	13.04%	4.1e-06	4.3e-02
R																																			-12	5.2e-04

Figure SI-12. PCA plots and ANOVA significance table of NF dataset for lipidomics assay (Top), negative ion metabolomics assay (Mid Upper), positive ion metabolomics assay (Mid Lower) and transcriptomics data (Bottom). ANOVA was conducted on PCA scores between exposure groups, with p-values displayed below for PC1 and PC2 comparisons. Significant ($p<0.05$) values are printed in red

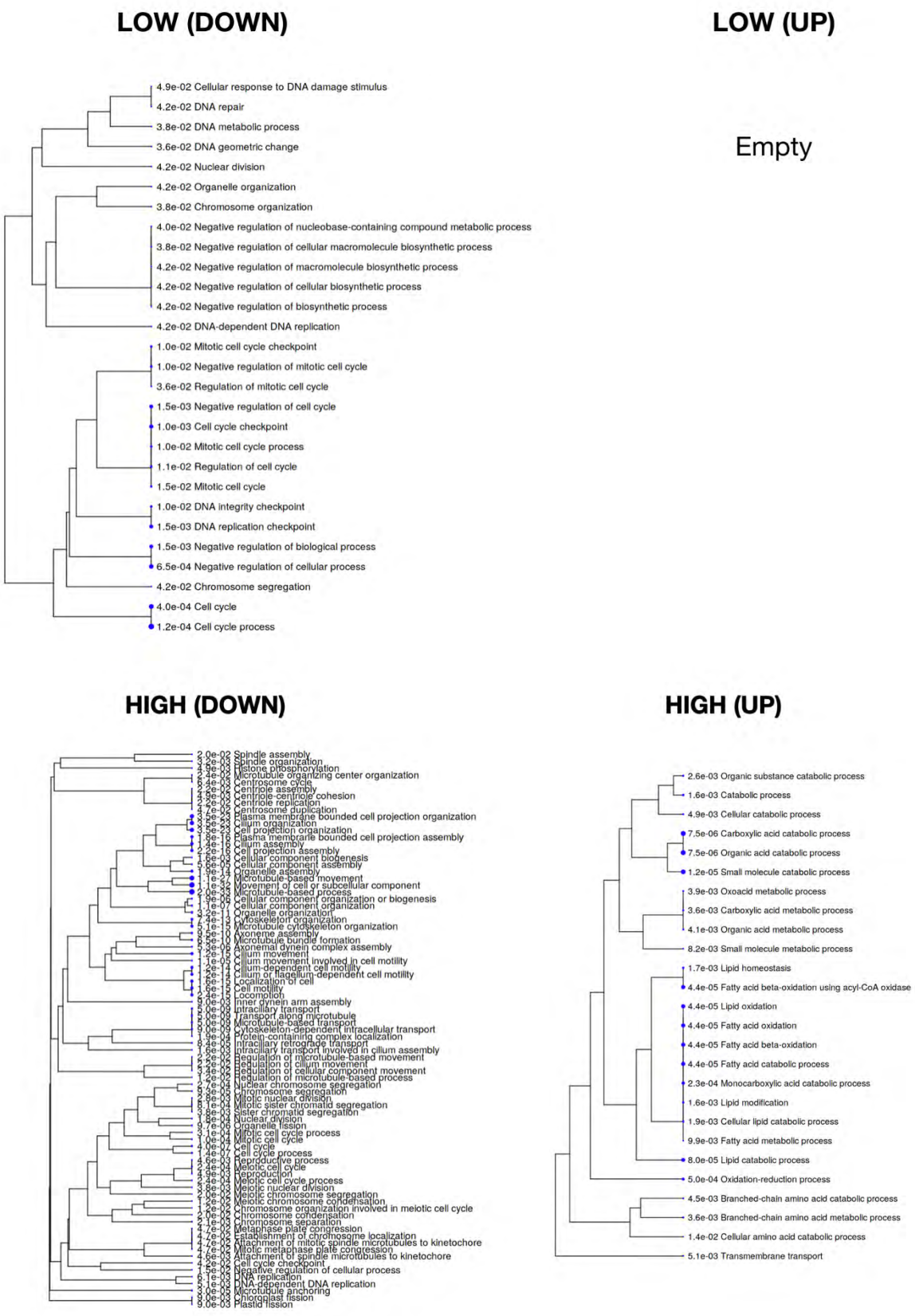


Figure SI-13. JGI-GO enrichments of DEG found in the collapsed NF dataset (omission of time as variable), split up by comparison LOW (Low-vs-Control group) and HIGH (High-vs-Control group), and by direction of changes (UP-, DOWN-regulation of gene expression). Dendogram branches suggest ontological similarity, size of nodes indicates statistical significance.

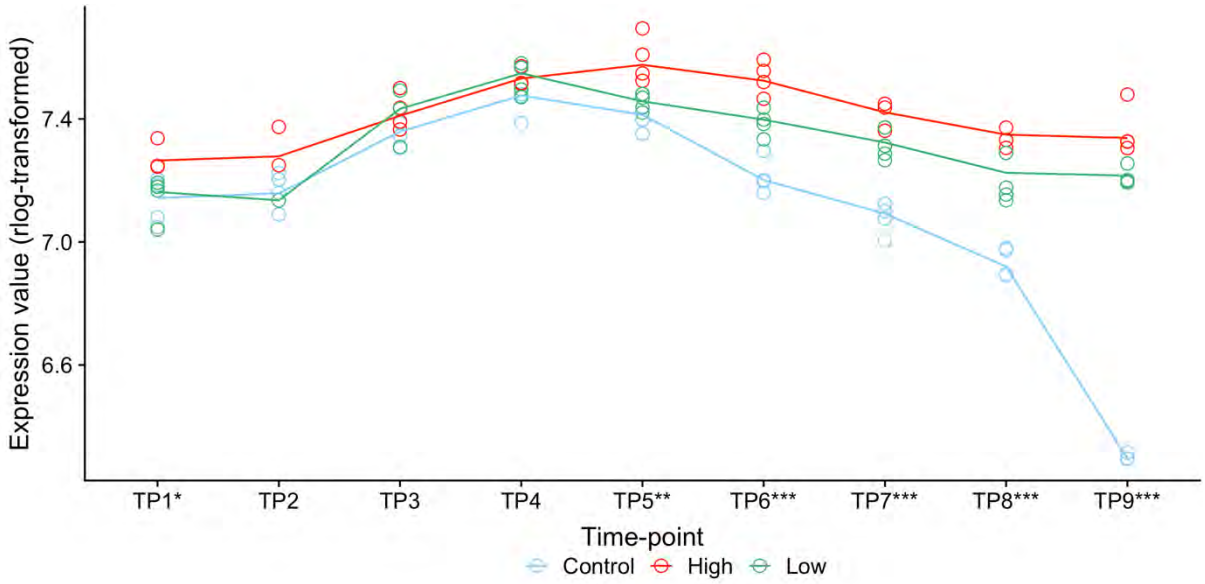


Figure SI-14. Time-course plot, median of genes per replicate and median of medians with connection line. Showing expression of the JGI gene ontology "Oxidation-reduction process" in the NF transcriptomics dataset. Significant changes in expression (ANOVA) are indicated by * (FDR<0.05), ** (FDR<0.01) or *** (FDR<0.001).

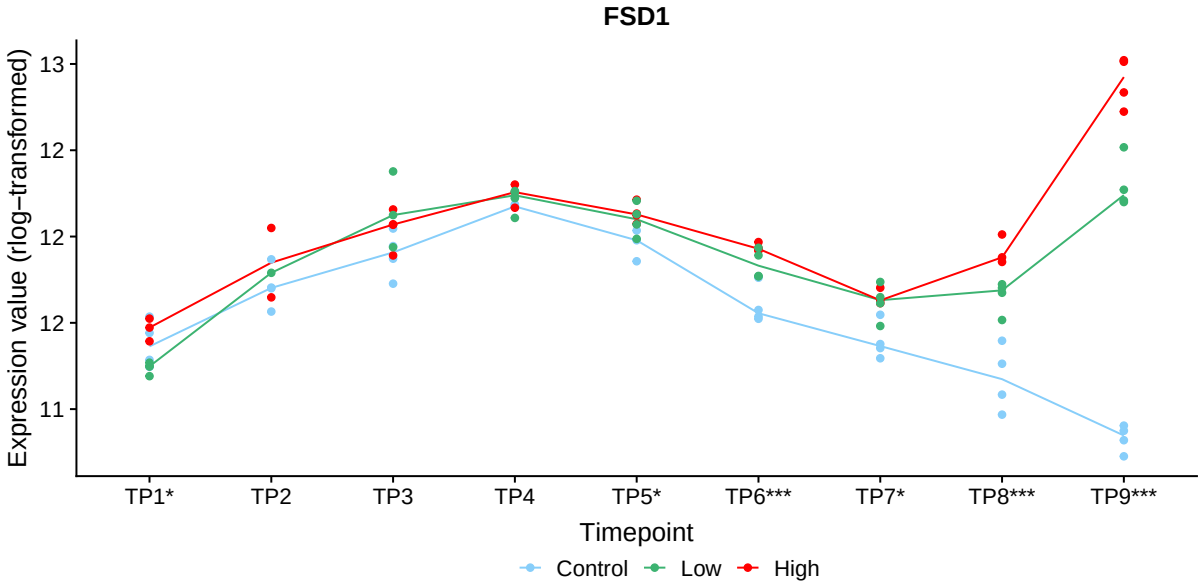


Figure SI-15. Time-course plot of replicate expression values and median connection line. Showing expression of the gene transcript for FSD1 (superoxide dismutase) in the NF transcriptomics dataset. Significant changes in expression (ANOVA) are indicated by * (FDR<0.05), ** (FDR<0.01) or *** (FDR<0.001).

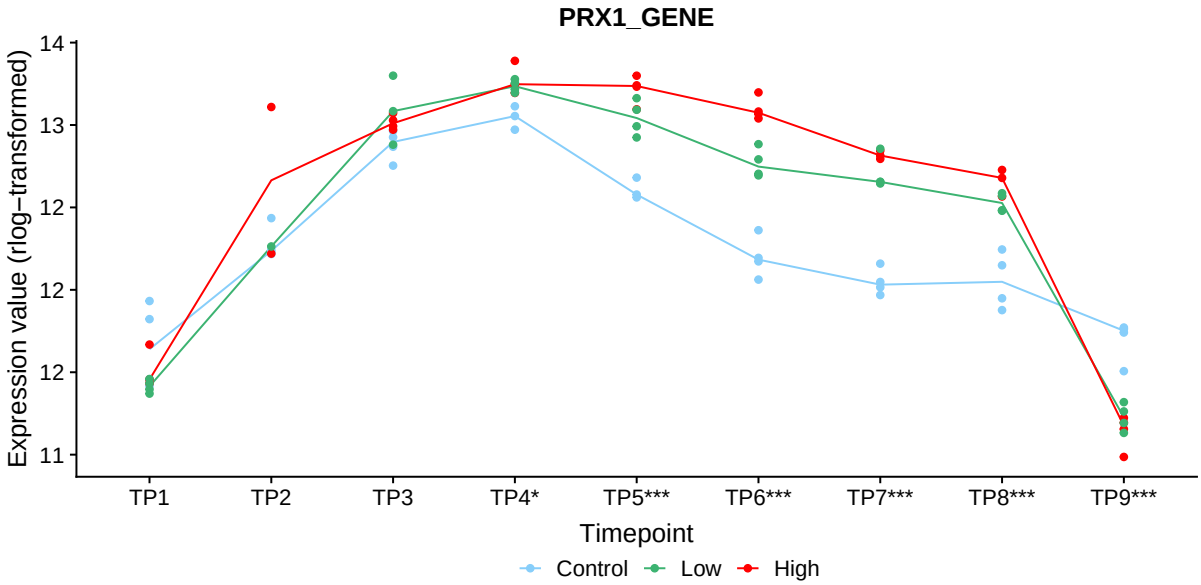


Figure SI-16. Time-course plot of replicate expression values and median connection line. Showing expression of the gene transcript for PRX1 (peroxidredoxin 1) in the NF transcriptomics dataset. Significant changes in expression (ANOVA) are indicated by * (FDR<0.05), ** (FDR<0.01) or *** (FDR<0.001).

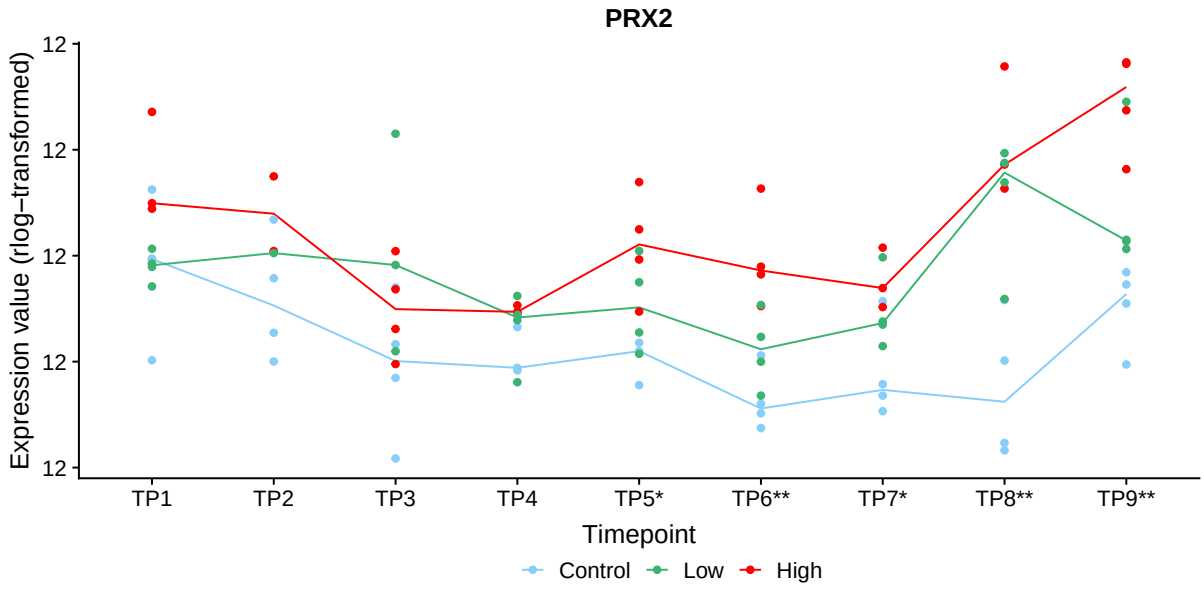


Figure SI-17. Time-course plot of replicate expression values and median connection line. Showing expression of the gene transcript for PRX2 (peroxiredoxin 2) in the NF transcriptomics dataset. Significant changes in expression (ANOVA) are indicated by * (FDR<0.05), ** (FDR<0.01) or *** (FDR<0.001).

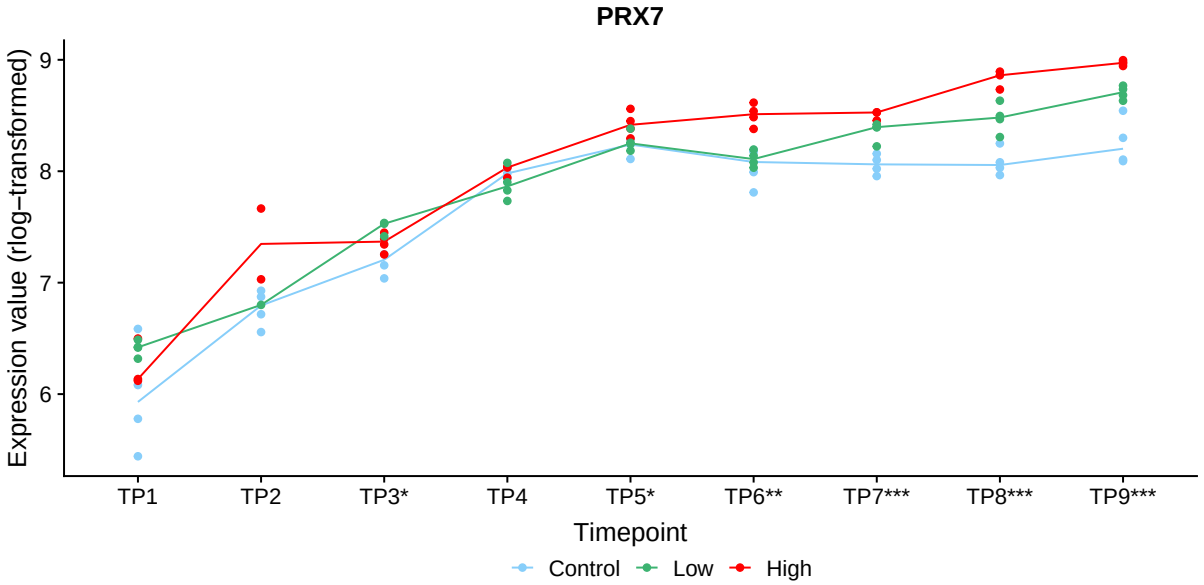


Figure SI-18. Time-course plot of replicate expression values and median connection line. Showing expression of the gene transcript for PRX7 (peroxiredoxin 7) in the NF transcriptomics dataset. Significant changes in expression (ANOVA) are indicated by * (FDR<0.05), ** (FDR<0.01) or *** (FDR<0.001).

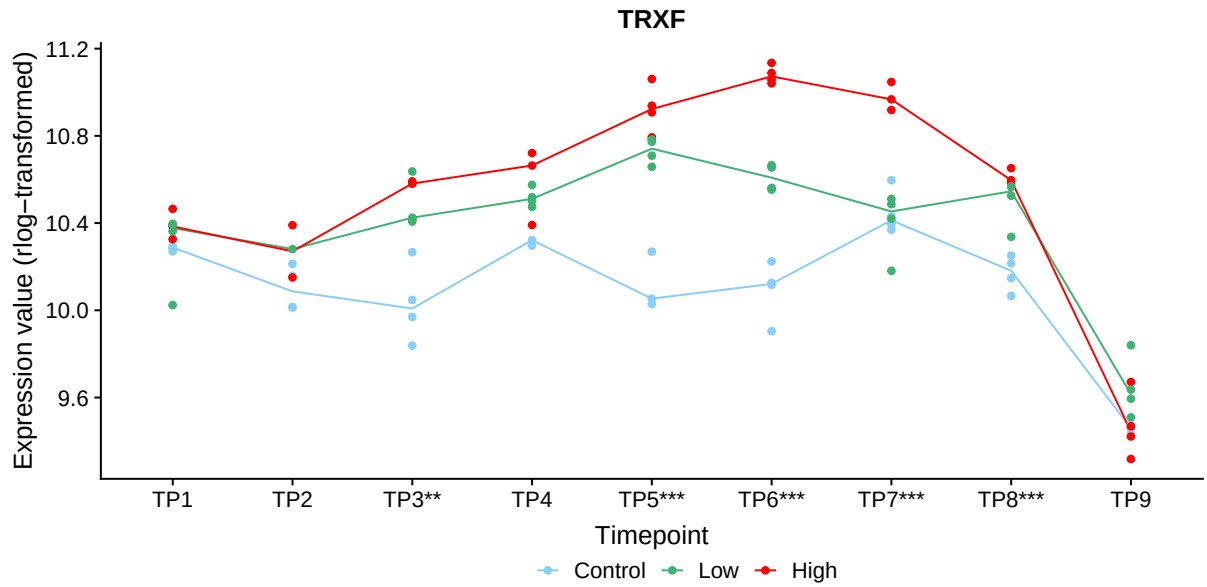


Figure SI-19. Time-course plot of replicate expression values and median connection line. Showing expression of the gene transcript for TRXF in the NF transcriptomics dataset. Significant changes in expression (ANOVA) are indicated by * (FDR<0.05), ** (FDR<0.01) or *** (FDR<0.001).

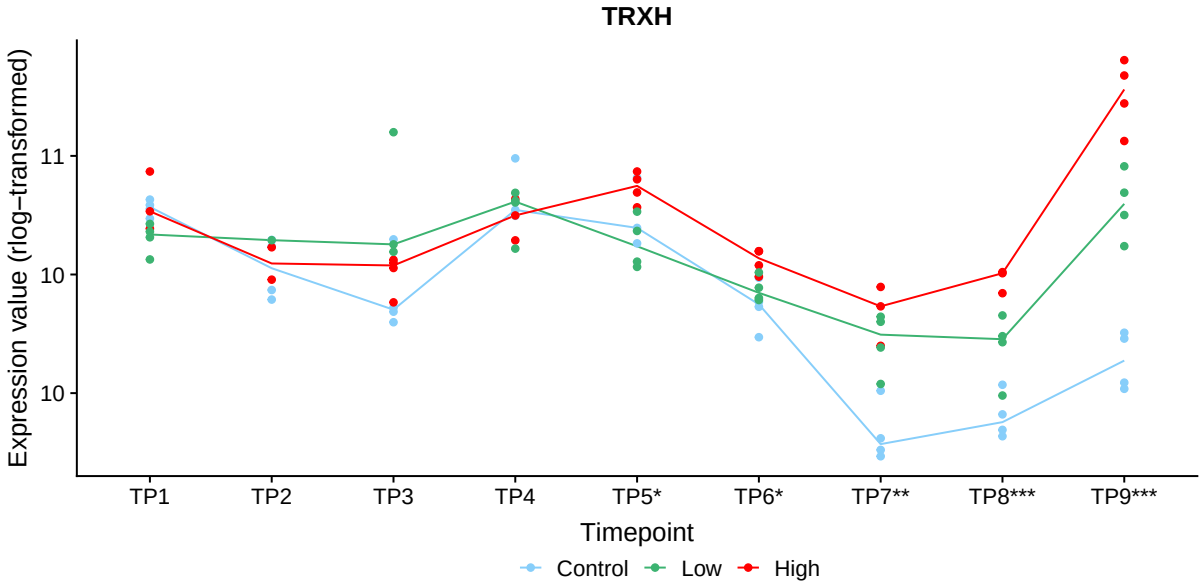


Figure SI-20. Time-course plot of replicate expression values and median connection line. Showing expression of the gene transcript for TRXH in the NF transcriptomics dataset. Significant changes in expression (ANOVA) are indicated by * (FDR<0.05), ** (FDR<0.01) or *** (FDR<0.001).

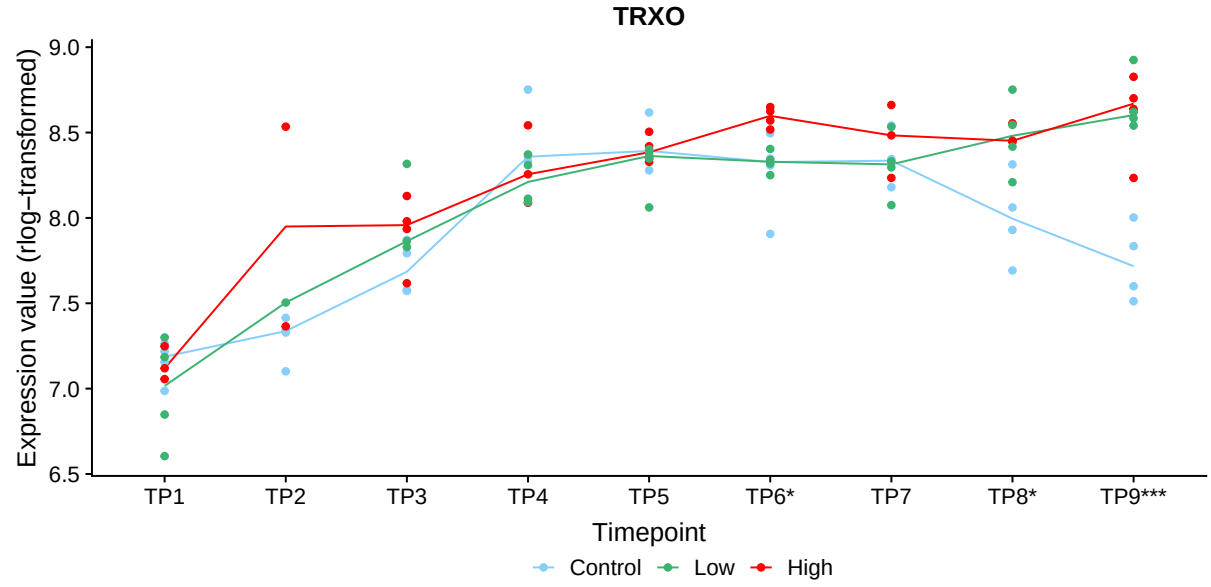


Figure SI-21. Time-course plot of replicate expression values and median connection line. Showing expression of the gene transcript for TRXO in the NF transcriptomics dataset. Significant changes in expression (ANOVA) are indicated by * (FDR<0.05), ** (FDR<0.01) or *** (FDR<0.001).

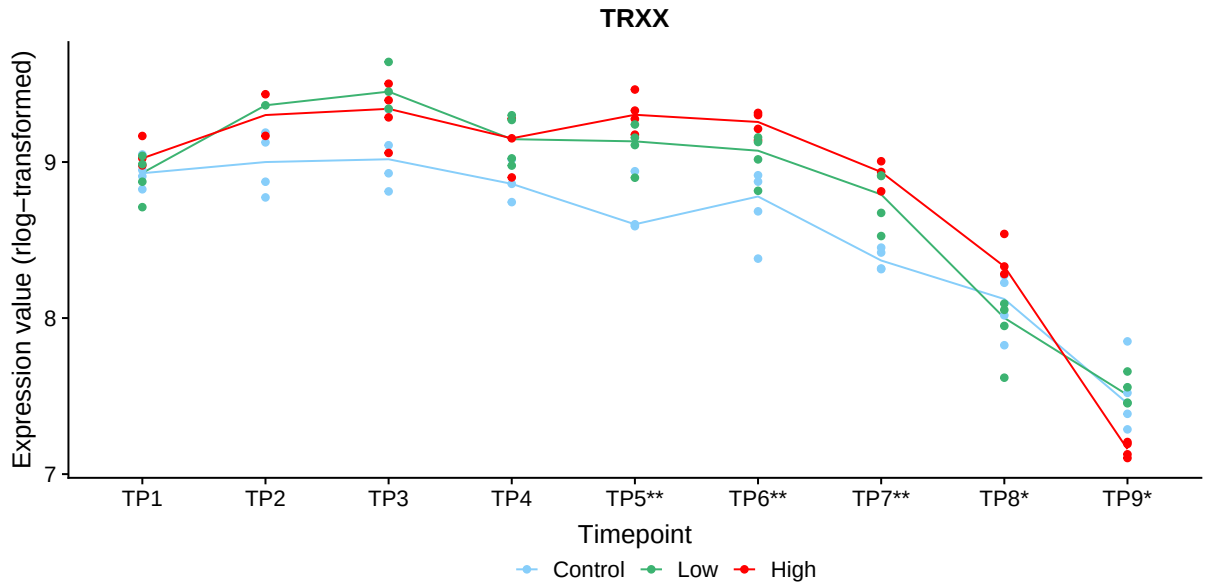


Figure SI-22. Time-course plot of replicate expression values and median connection line. Showing expression of the gene transcript for TRXX in the NF transcriptomics dataset. Significant changes in expression (ANOVA) are indicated by * (FDR<0.05), ** (FDR<0.01) or *** (FDR<0.001).

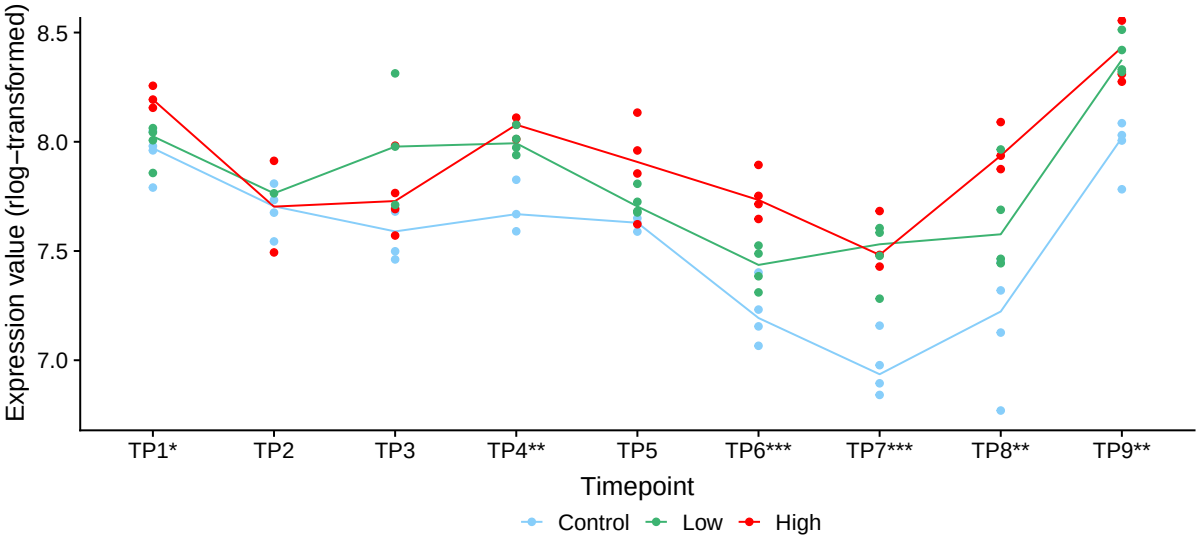


Figure SI-23. Time-course plot of replicate expression values and median connection line. Showing expression of the gene transcript for TRXY in the NF transcriptomics dataset. Significant changes in expression (ANOVA) are indicated by * (FDR<0.05), ** (FDR<0.01) or *** (FDR<0.001).

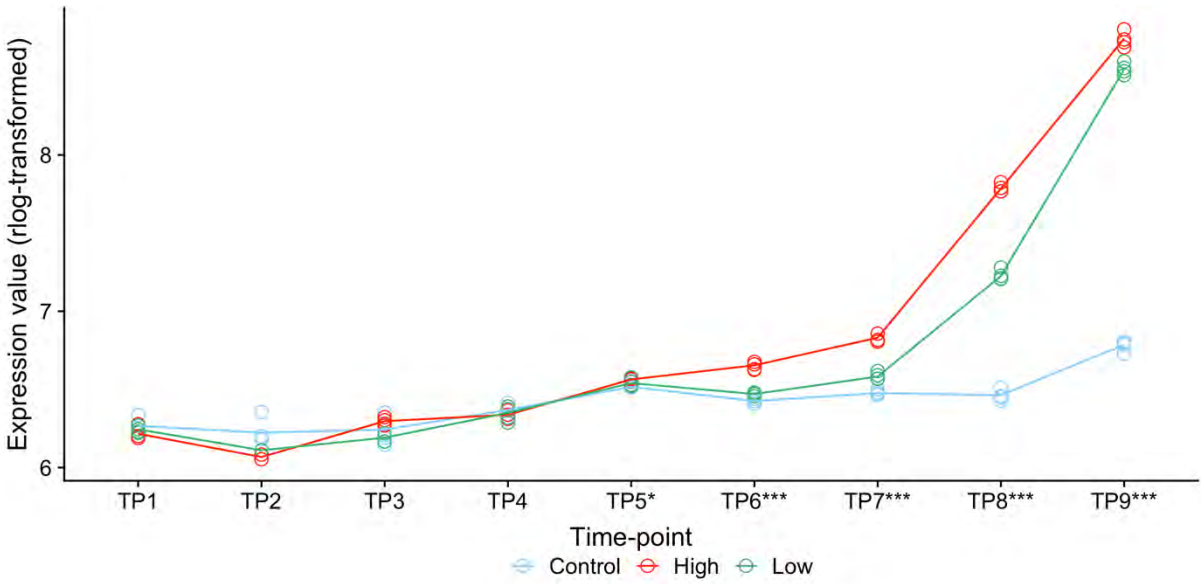


Figure SI-24. Time-course plot, median of genes per replicate and median of medians with connection line. Showing expression of genes in the maSigPro time-profile cluster "Cluster01" in the NF transcriptomics dataset. Significant changes in expression (ANOVA) are indicated by * (FDR<0.05), ** (FDR<0.01) or *** (FDR<0.001).

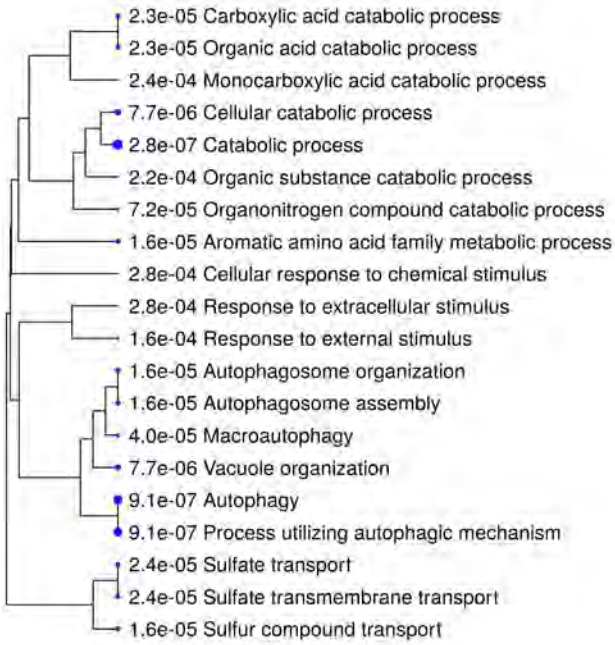


Figure SI-25. Hierarchical tree of JGI-GOs enriched by genes in maSigPro "Cluster01", along their FDR value. Dendogram branches suggest ontological similarity, size of nodes indicates statistical significance.'

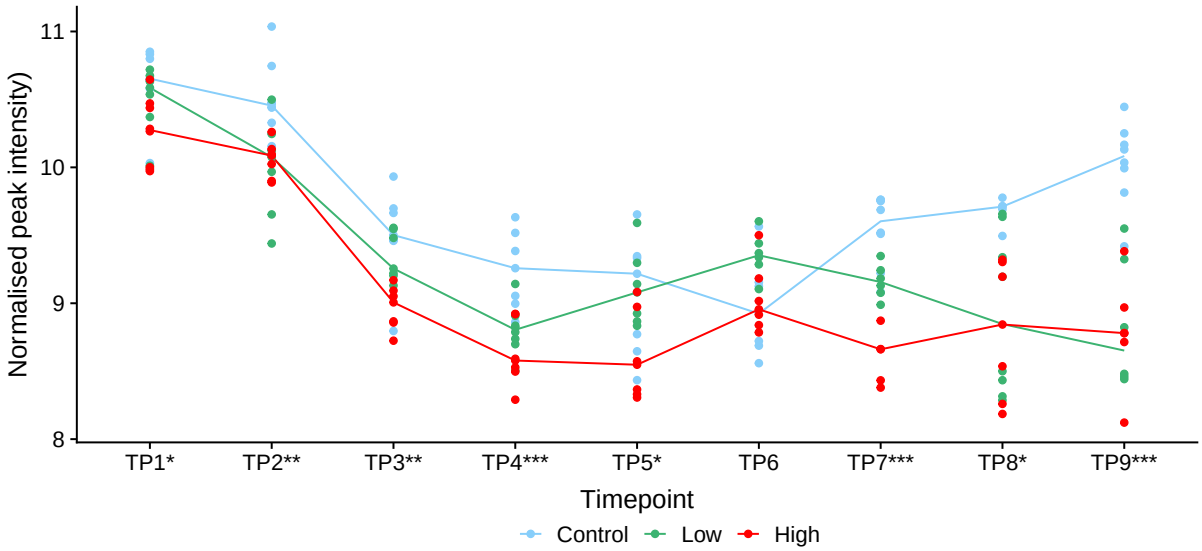


Figure SI-26. Normalized peak intensities per replicate and connection line of replicate median values for DIMS spectral peak m/z = 753.5497854449015 putatively annotated as "1-18:2-2-16:0-monogalactosyldiacylglycerol", along significance annotation (ANOVA) indicated by * (FDR<0.05), ** (FDR<0.01) or *** (FDR<0.001).

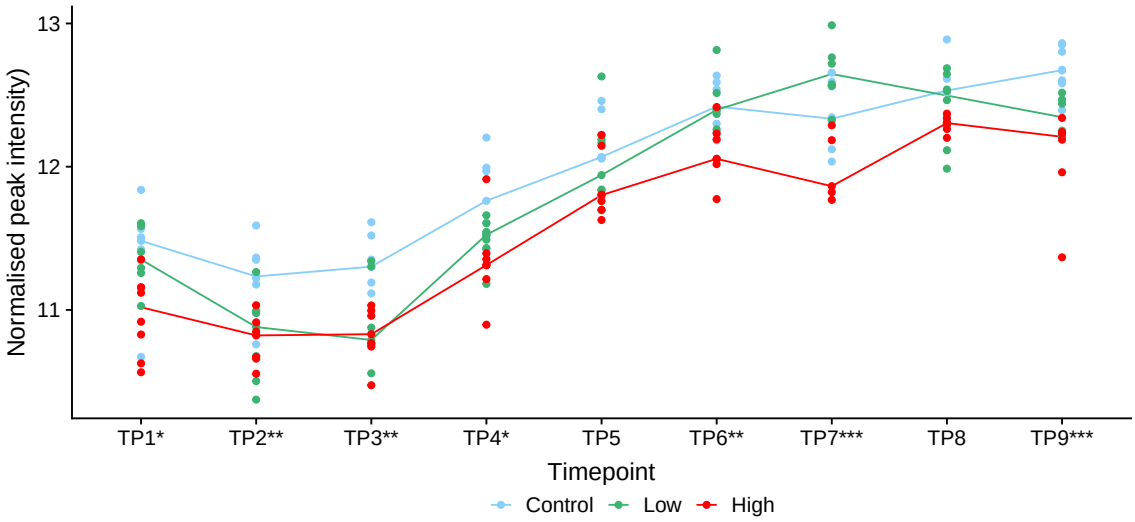


Figure SI-27. Normalized peak intensities per replicate and connection line of replicate median values for DIMS spectral peak m/z = 749.5218664989833 putatively annotated as "1-18:2-2-16:2-monogalactosyldiacylglycerol", along significance annotation (ANOVA) indicated by * (FDR<0.05), ** (FDR<0.01) or *** (FDR<0.001).

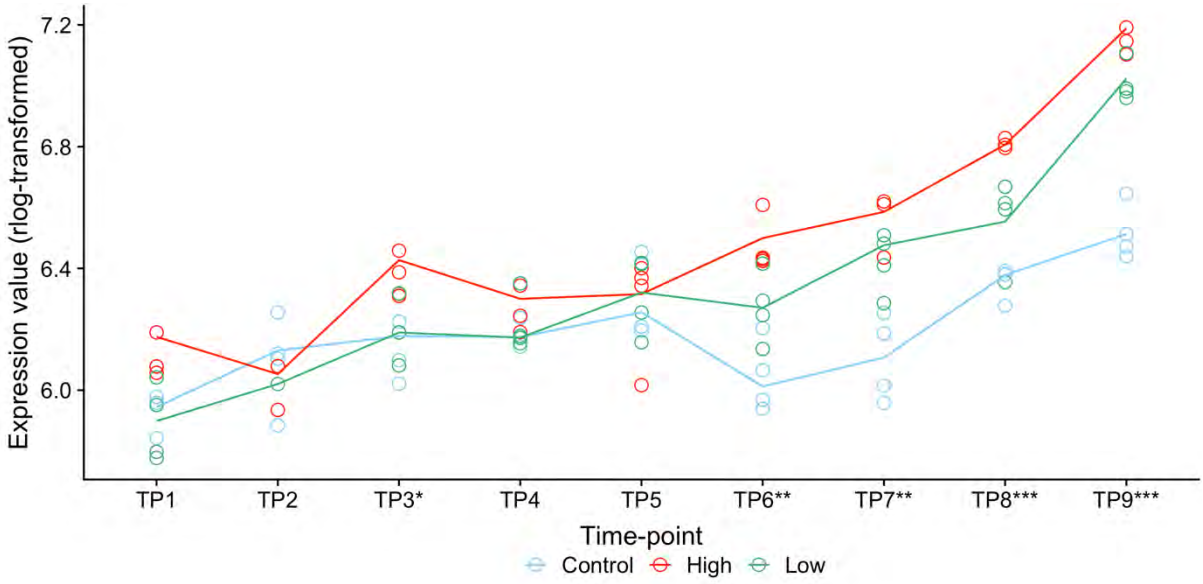


Figure SI-28. Time-course plot, median of genes per replicate and median of medians with connection line. Showing expression of non-redundant genes enriching JGI-GOs “Peroxisomal transport” and “Protein targeting to peroxisome” in the NF transcriptomics dataset. Significant changes in expression (ANOVA) are indicated by * (FDR<0.05), ** (FDR<0.01) or *** (FDR<0.001).

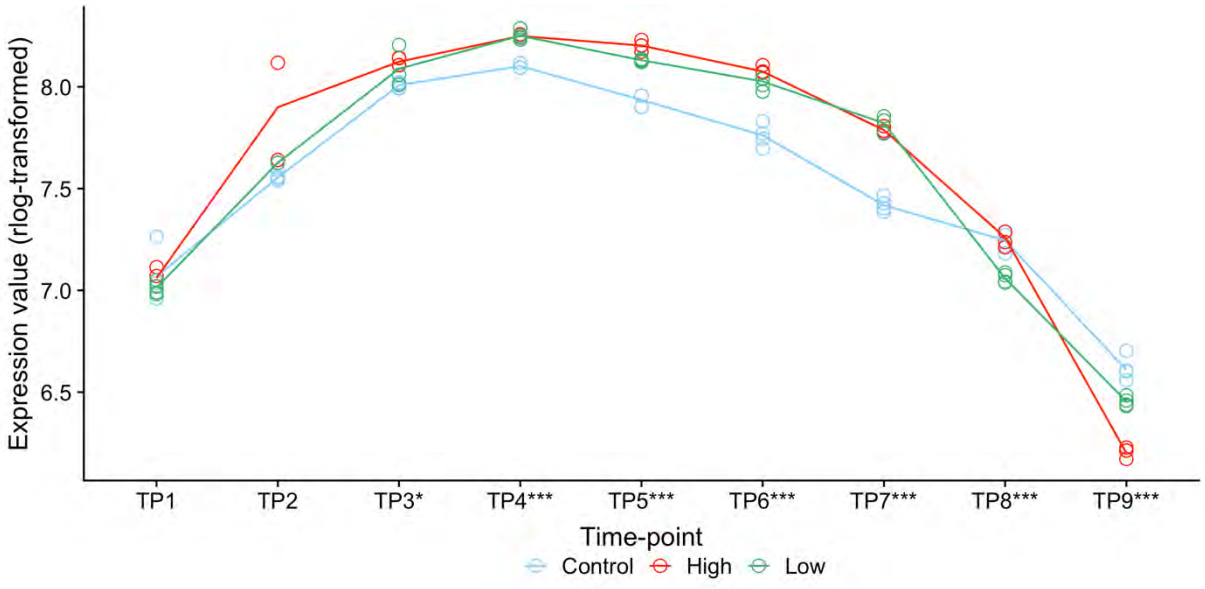


Figure SI-29. Time-course plot, median of genes per replicate and median of medians with connection line. Showing expression of genes in the maSigPro time-profile cluster “Cluster03” in the NF transcriptomics dataset. Significant changes in expression (ANOVA) are indicated by * (FDR<0.05), ** (FDR<0.01) or *** (FDR<0.001).

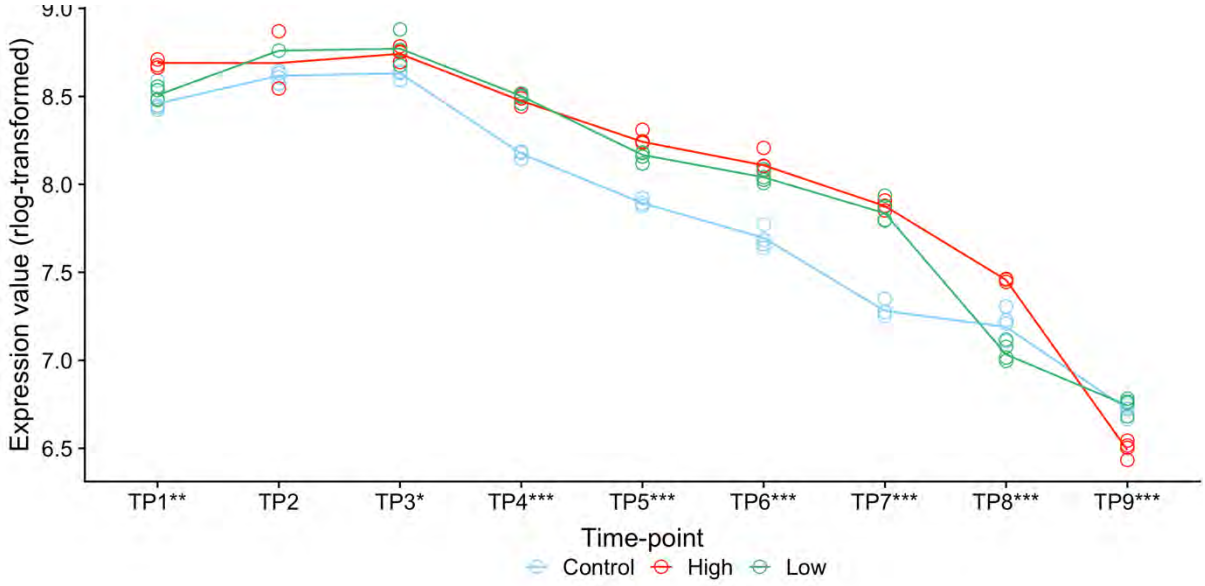


Figure SI-30. Time-course plot, median of genes per replicate and median of medians with connection line. Showing expression of genes in the maSigPro time-profile cluster "Cluster05" in the NF transcriptomics dataset. Significant changes in expression (ANOVA) are indicated by * (FDR<0.05), ** (FDR<0.01) or *** (FDR<0.001).

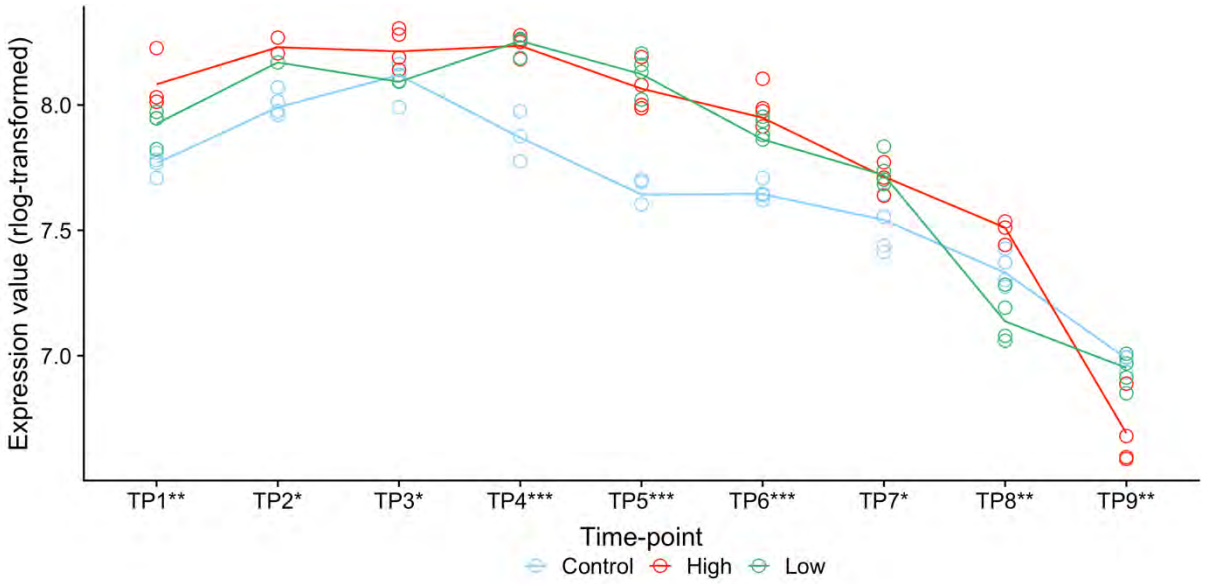


Figure SI-31. Time-course plot, median of genes per replicate and median of medians with connection line. Showing expression of genes in the KEGG carotenoid synthesis pathway (KEGG pathway code cre00906) using the NF transcriptomics dataset. Significant changes in expression (ANOVA) are indicated by * (FDR<0.05), ** (FDR<0.01) or *** (FDR<0.001).

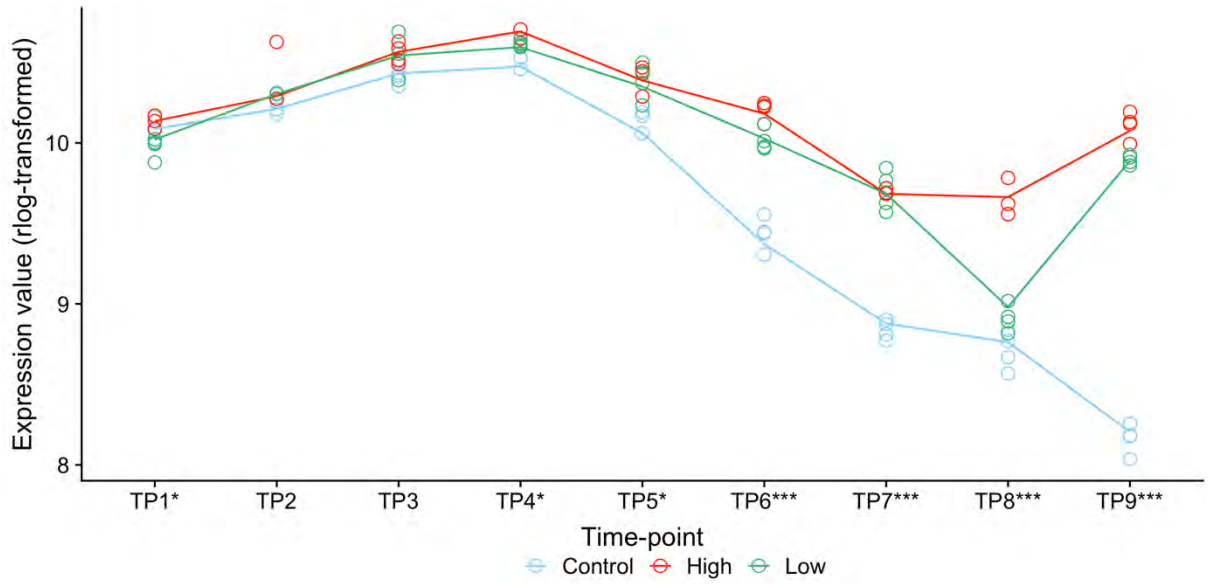


Figure SI-32. Time-course plot, median of genes per replicate and median of medians with connection line. Showing expression of genes within the KEGG Non-mevalonate pathway (KEGG module code M00096) using the NF transcriptomics dataset. Significant changes in expression (ANOVA) are indicated by * (FDR<0.05), ** (FDR<0.01) or *** (FDR<0.001).

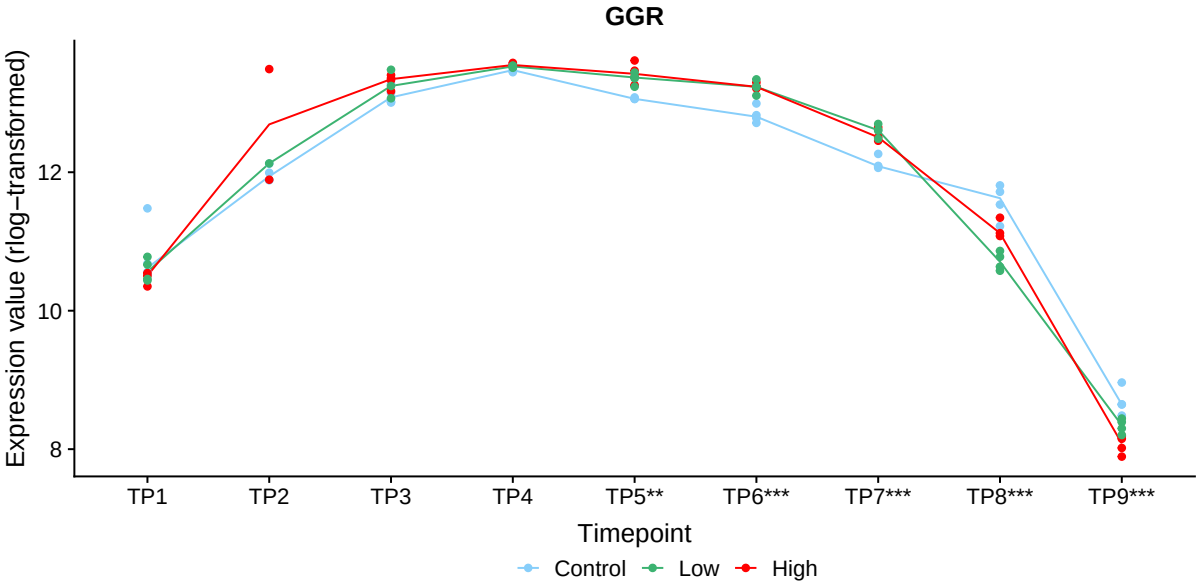


Figure SI-33. Time-course plot of replicate expression values and median connection line. Showing expression of the gene transcript for GGR (geranylgeranyl reductase) in the NF transcriptomics dataset. Significant changes in expression (ANOVA) are indicated by * (FDR<0.05), ** (FDR<0.01) or *** (FDR<0.001).

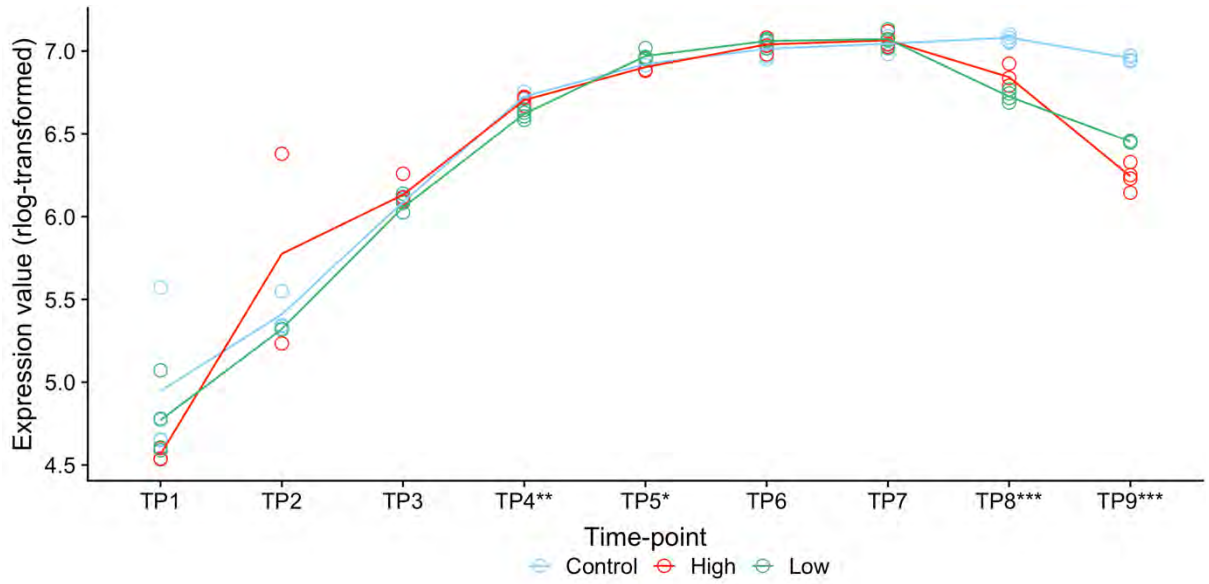


Figure SI-34. Time-course plot, median of genes per replicate and median of medians with connection line. Showing expression of genes in the maSigPro time-profile cluster "Cluster08" in the NF transcriptomics dataset. Significant changes in expression (ANOVA) are indicated by * (FDR<0.05), ** (FDR<0.01) or *** (FDR<0.001).

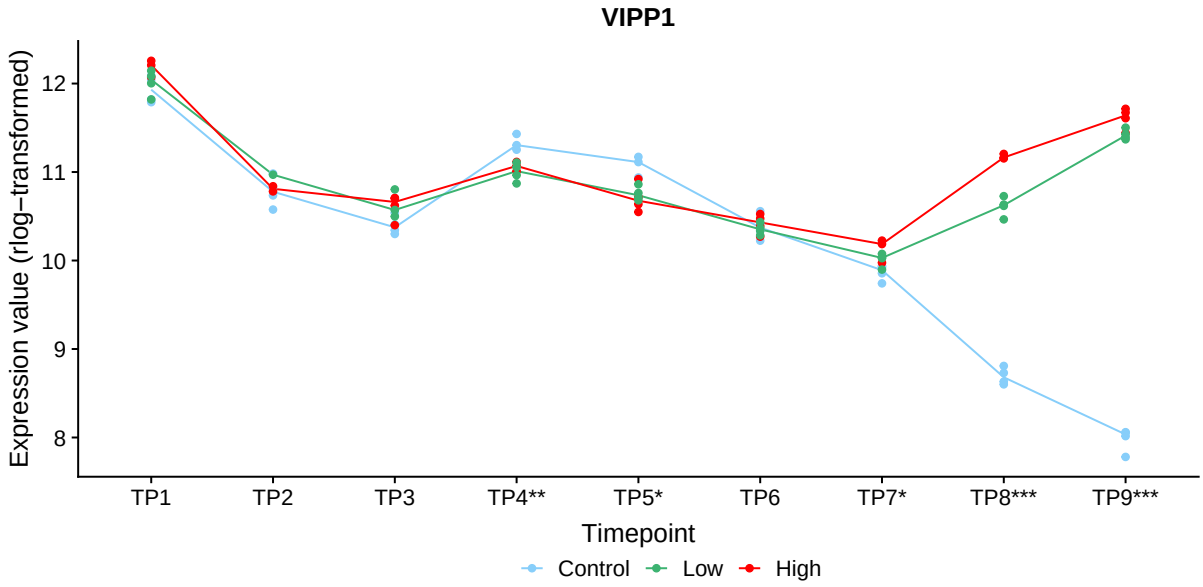


Figure SI-35. Time-course plot of replicate expression values and median connection line. Showing expression of the gene transcript for VIPP1 in the NF transcriptomics dataset. Significant changes in expression (ANOVA) are indicated by * (FDR<0.05), ** (FDR<0.01) or *** (FDR<0.001).

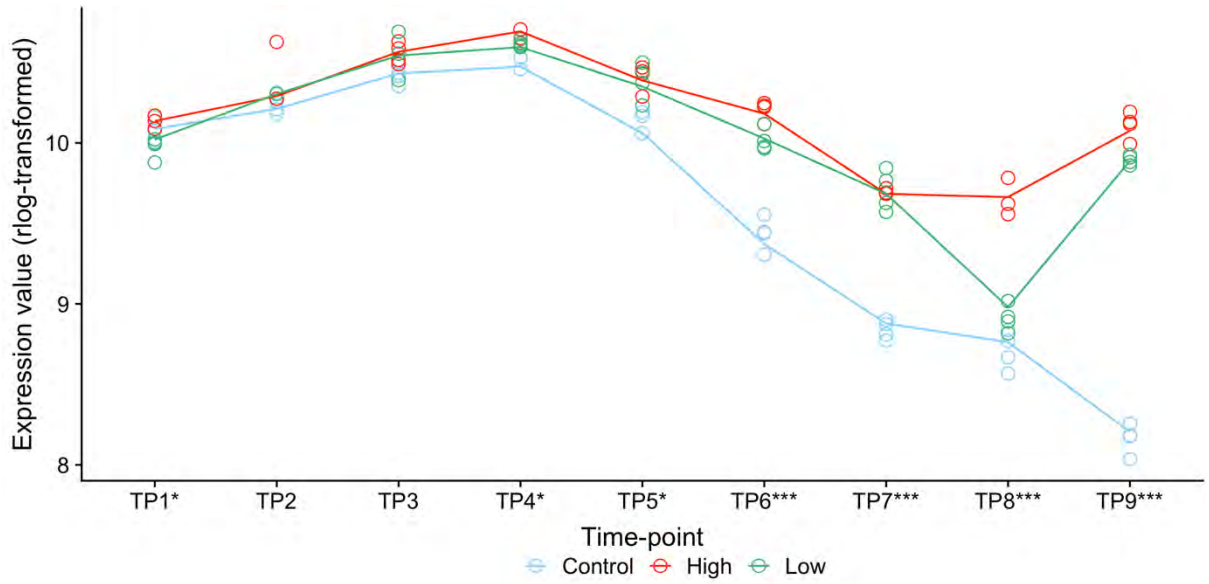


Figure SI-36. Time-course plot, median of genes per replicate and median of medians with connection line. Showing expression of genes within the JGI-GO Lysine biosynthesis (as identified by PGSEA at TP3-7), using the NF transcriptomics dataset. Significant changes in expression (ANOVA) are indicated by * (FDR<0.05), ** (FDR<0.01) or *** (FDR<0.001).

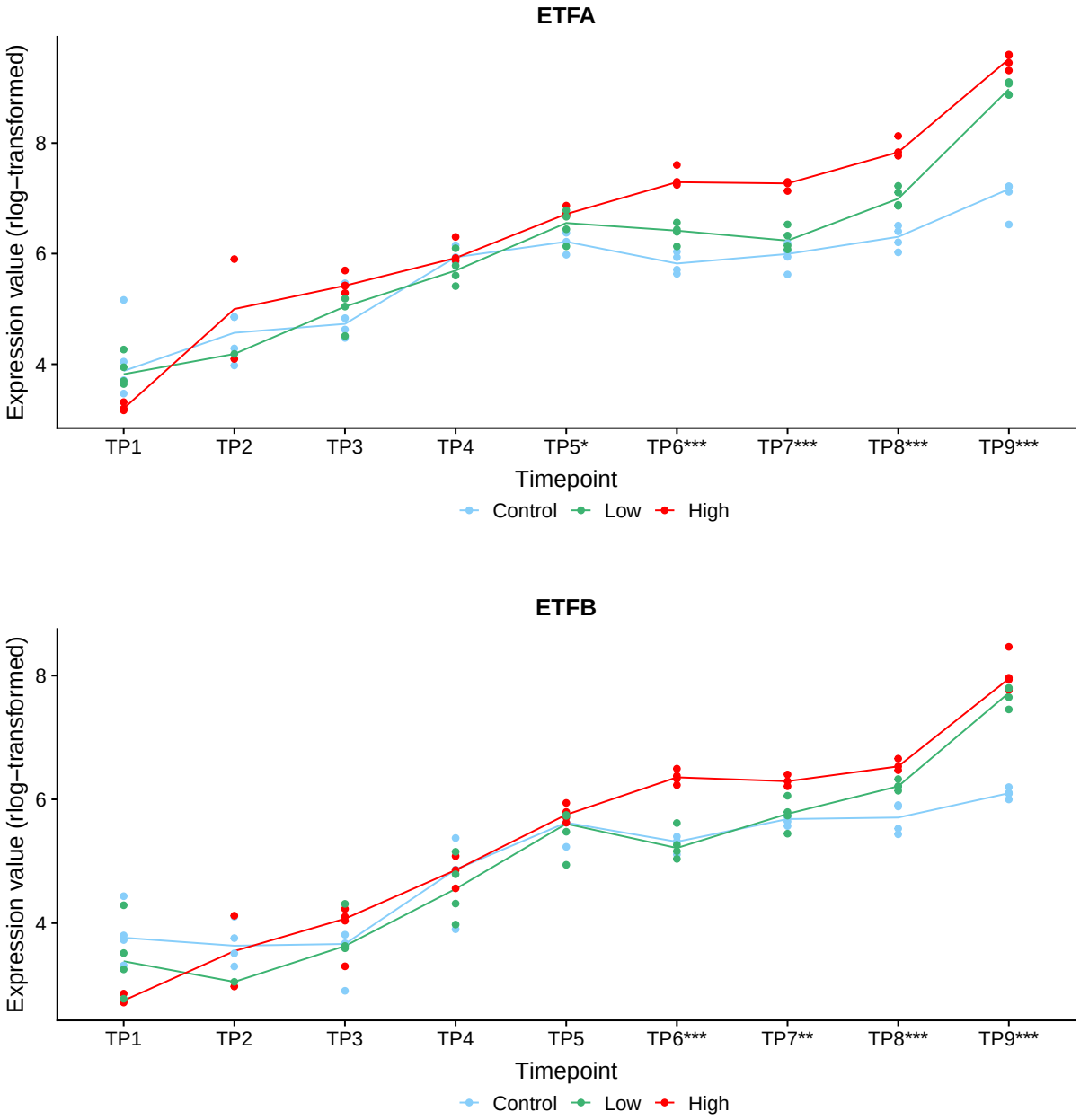


Figure SI-37. Time-course plots of replicate expression values and median connection line. Showing expression of the gene transcript for ETFa an ETFb in the NF transcriptomics dataset. Significant changes in expression (ANOVA) are indicated by * (FDR<0.05), ** (FDR<0.01) or *** (FDR<0.001).

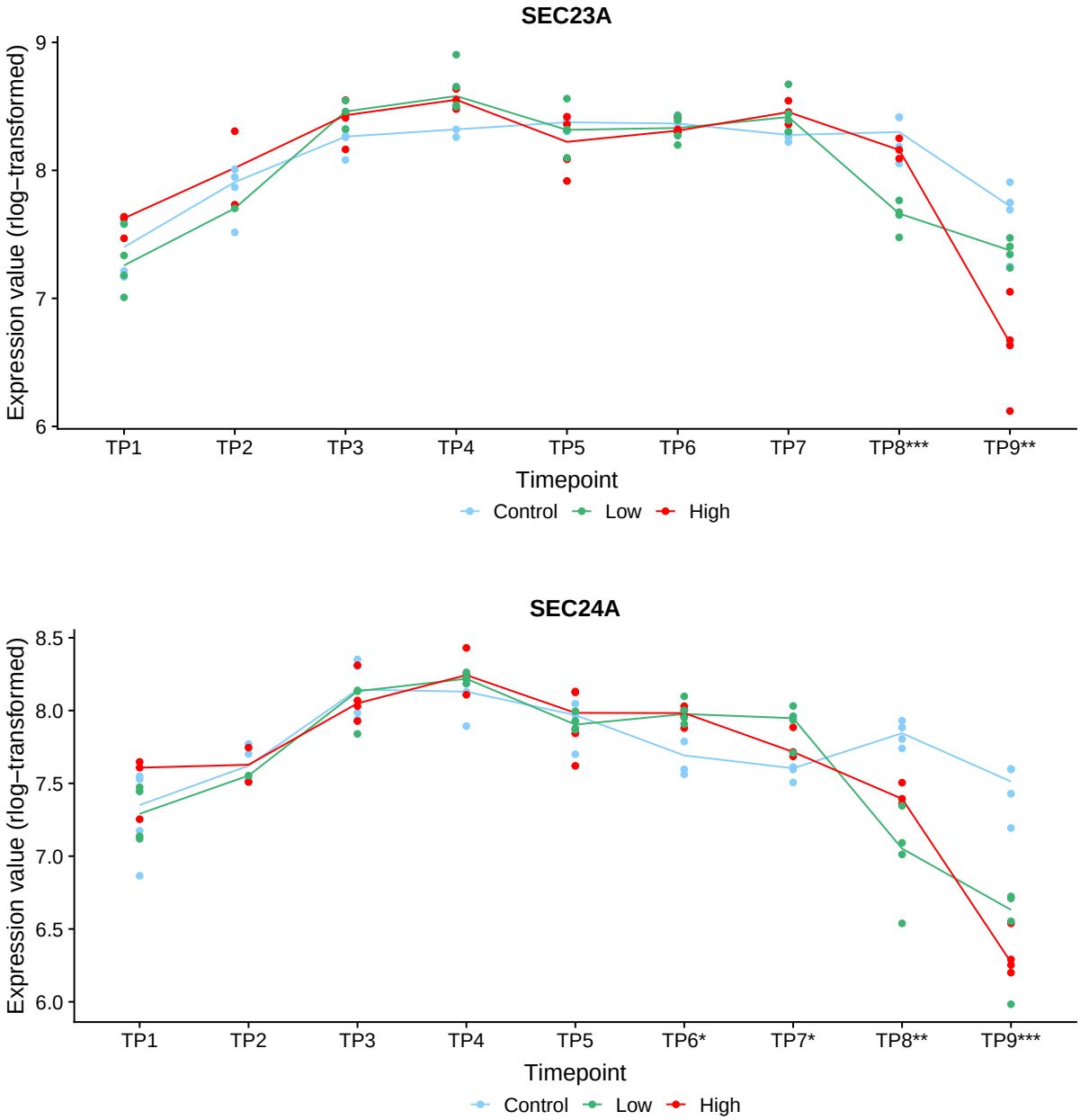


Figure SI-38. Time-course plots of replicate expression values and median connection line. Showing expression of the gene transcript for SEC23A and SEC24A in the NF transcriptomics dataset. Significant changes in expression (ANOVA) are indicated by * (FDR<0.05), ** (FDR<0.01) or *** (FDR<0.001).

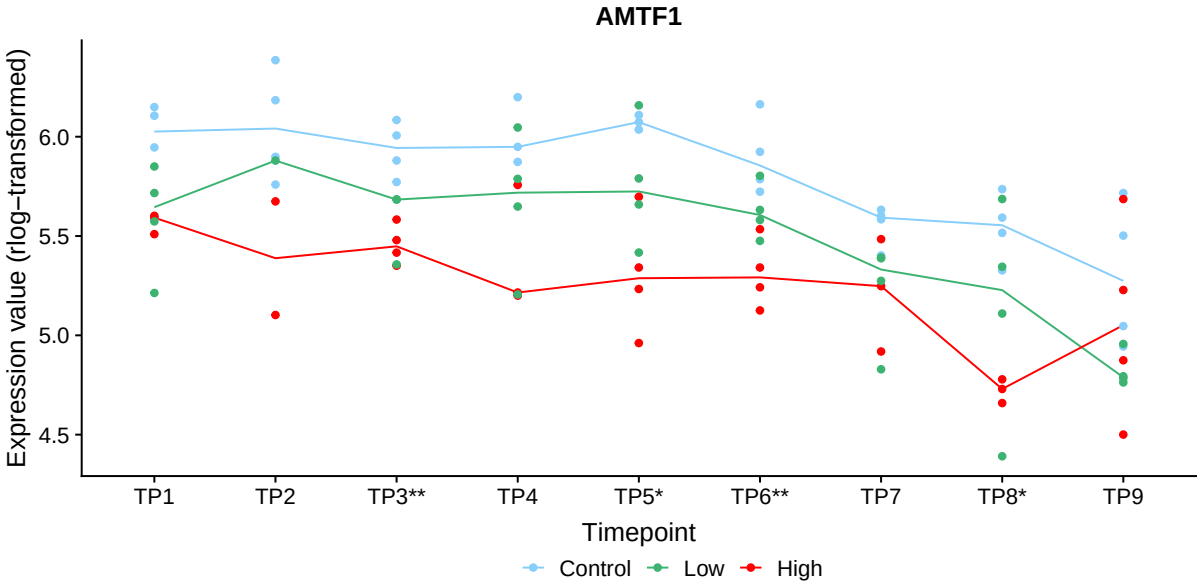


Figure SI-39. Time-course plot of replicate expression values and median connection line. Showing expression of the gene transcript for AMTF1 in the NF transcriptomics dataset. Significant changes in expression (ANOVA) are indicated by * (FDR<0.05), ** (FDR<0.01) or *** (FDR<0.001).

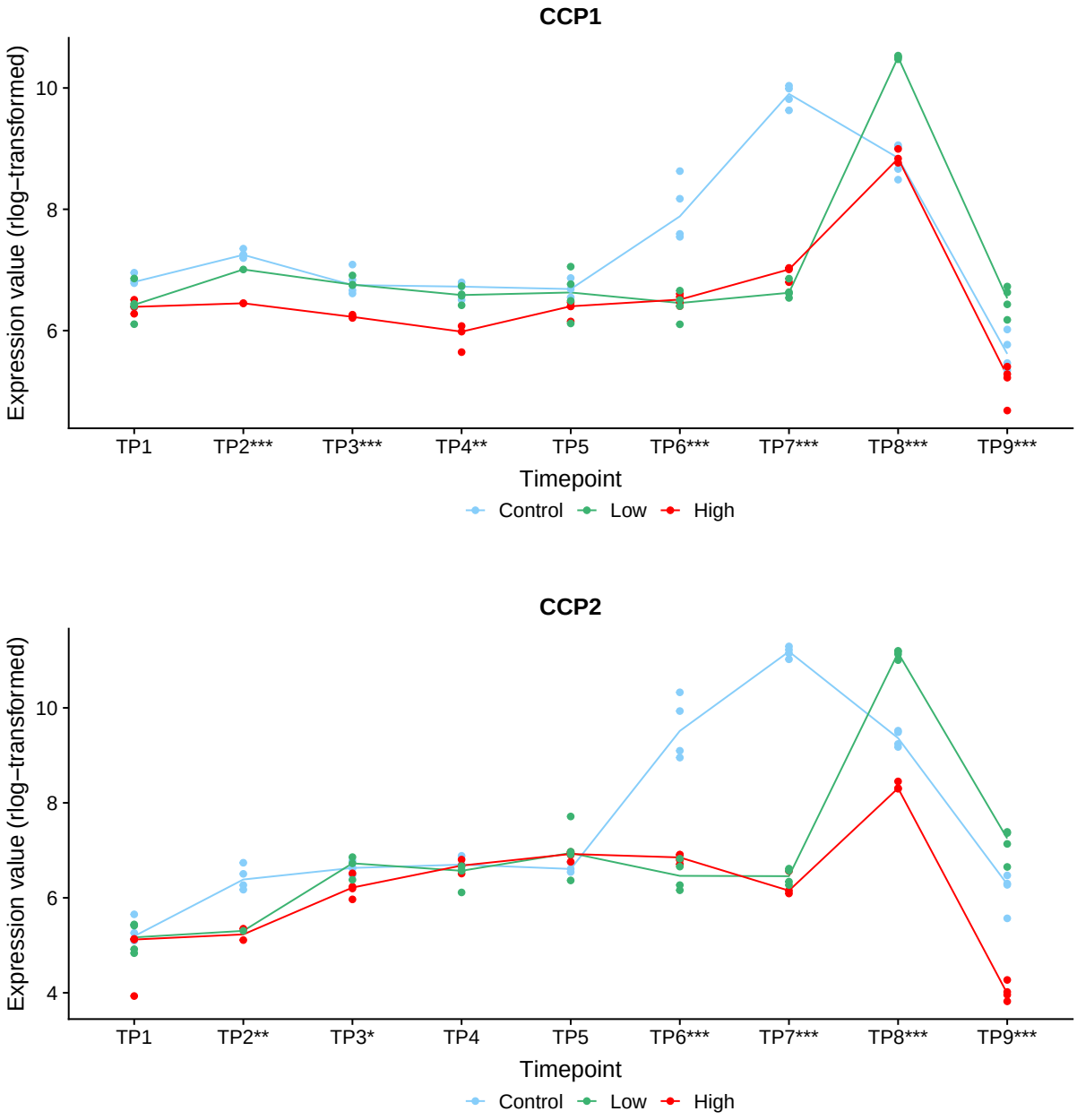


Figure SI-40. Time-course plots of replicate expression values and median connection line. Showing expression of the gene transcript for CCP1 and CCP2 in the NF transcriptomics dataset. Significant changes in expression (ANOVA) are indicated by * (FDR<0.05), ** (FDR<0.01) or *** (FDR<0.001).

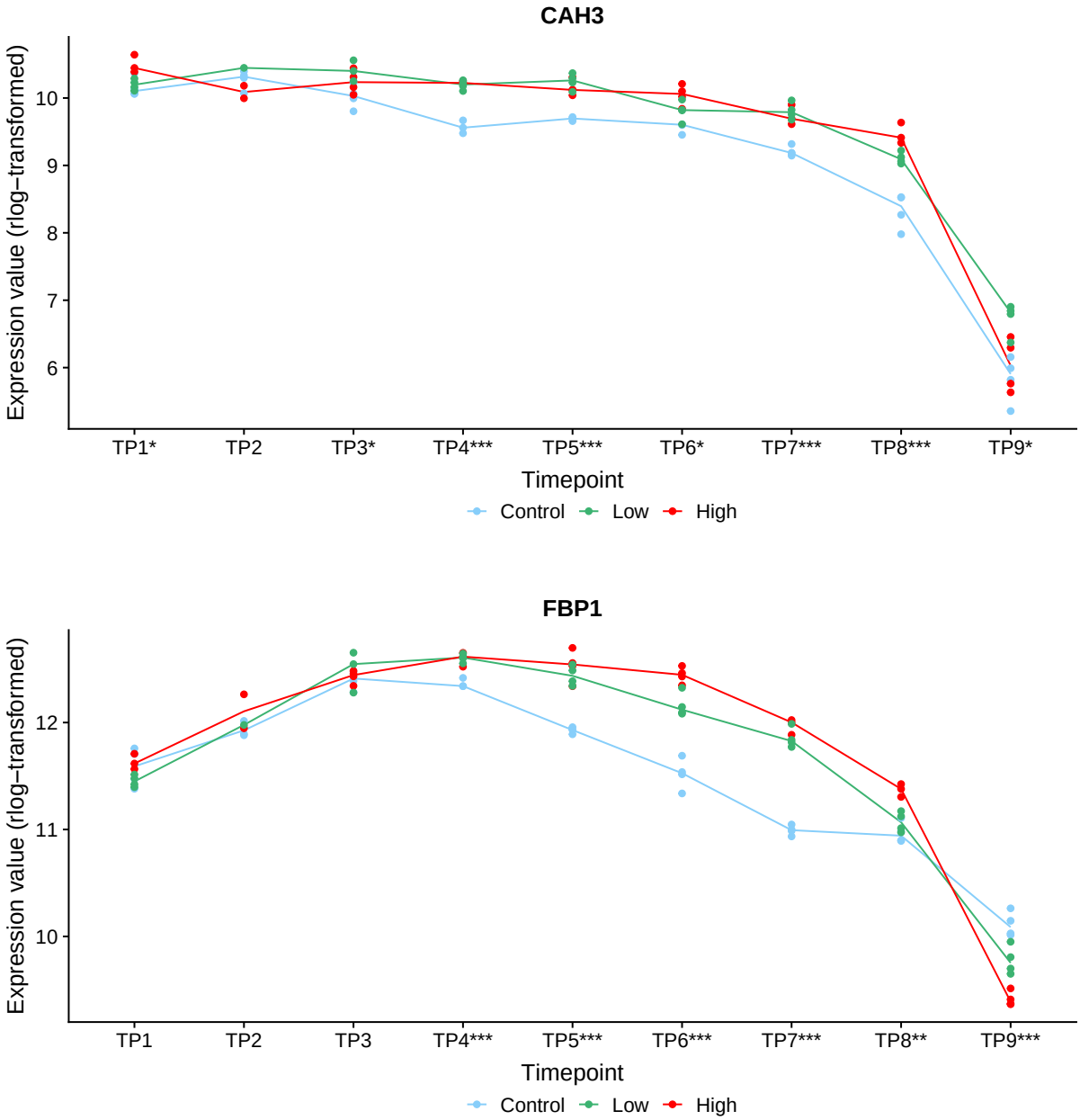


Figure SI-41. Time-course plots of replicate expression values and median connection line. Showing expression of the gene transcript for CAH1 and FBP1 in the NF transcriptomics dataset. Significant changes in expression (ANOVA) are indicated by * (FDR<0.05), ** (FDR<0.01) or *** (FDR<0.001).

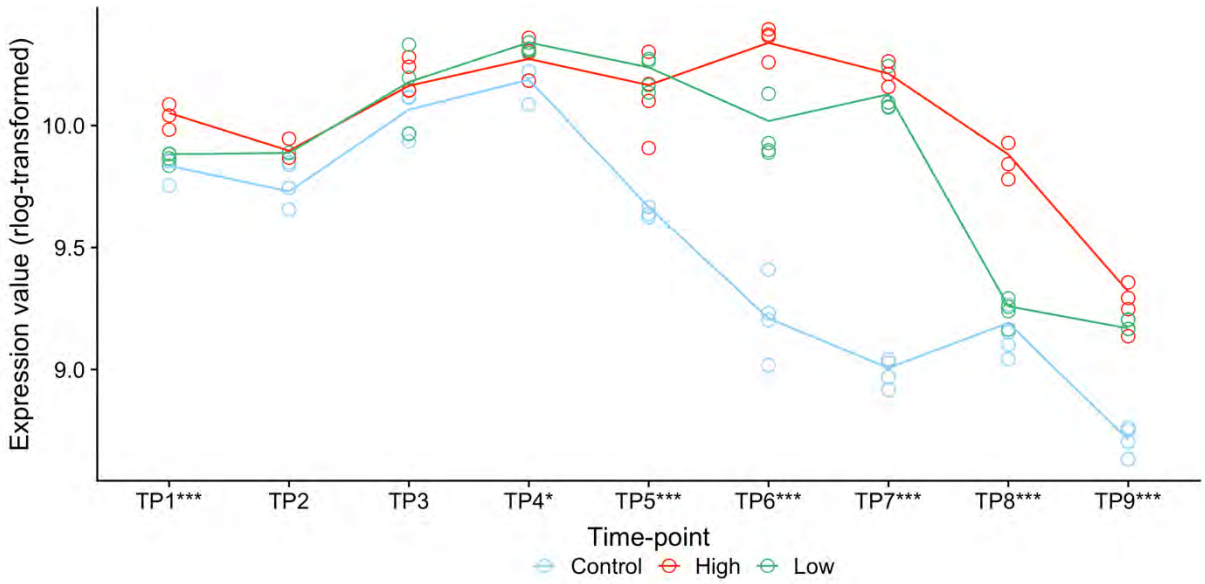


Figure SI-42. Time-course plot, median of genes per replicate and median of medians with connection line. Showing expression of genes within the JGI-GO Glyceraldehyde-3-phosphaste metabolism (as identified by PGSEA at TP6), using the NF transcriptomics dataset. Significant changes in expression (ANOVA) are indicated by * (FDR<0.05), ** (FDR<0.01) or *** (FDR<0.001).

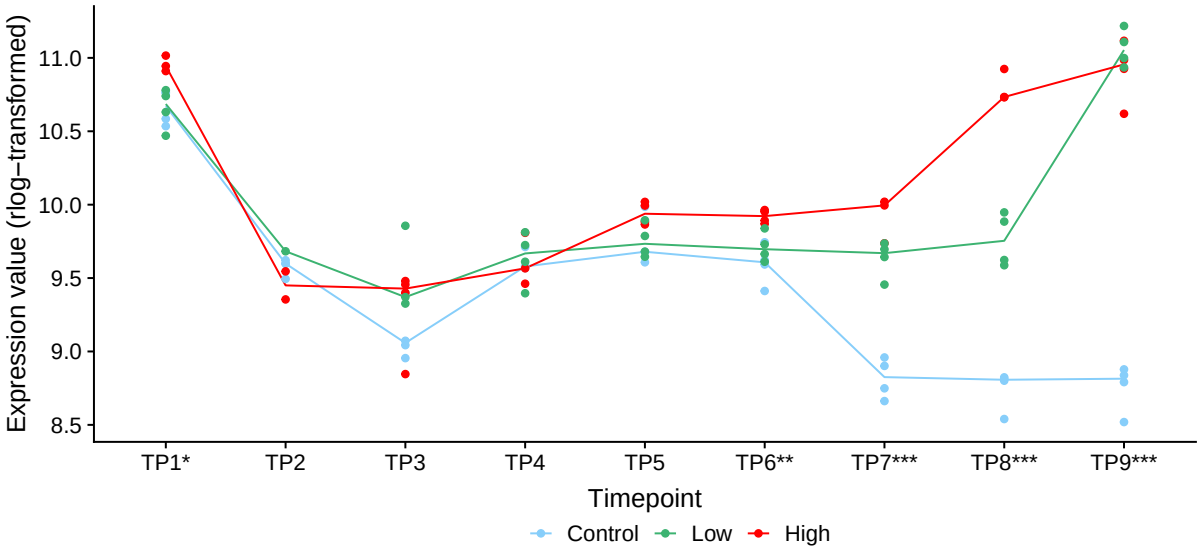


Figure SI-43. Time-course plot of replicate expression values and median connection line. Showing expression of the gene transcript for GPXH in the NF transcriptomics dataset. Significant changes in expression (ANOVA) are indicated by * (FDR<0.05), ** (FDR<0.01) or *** (FDR<0.001).

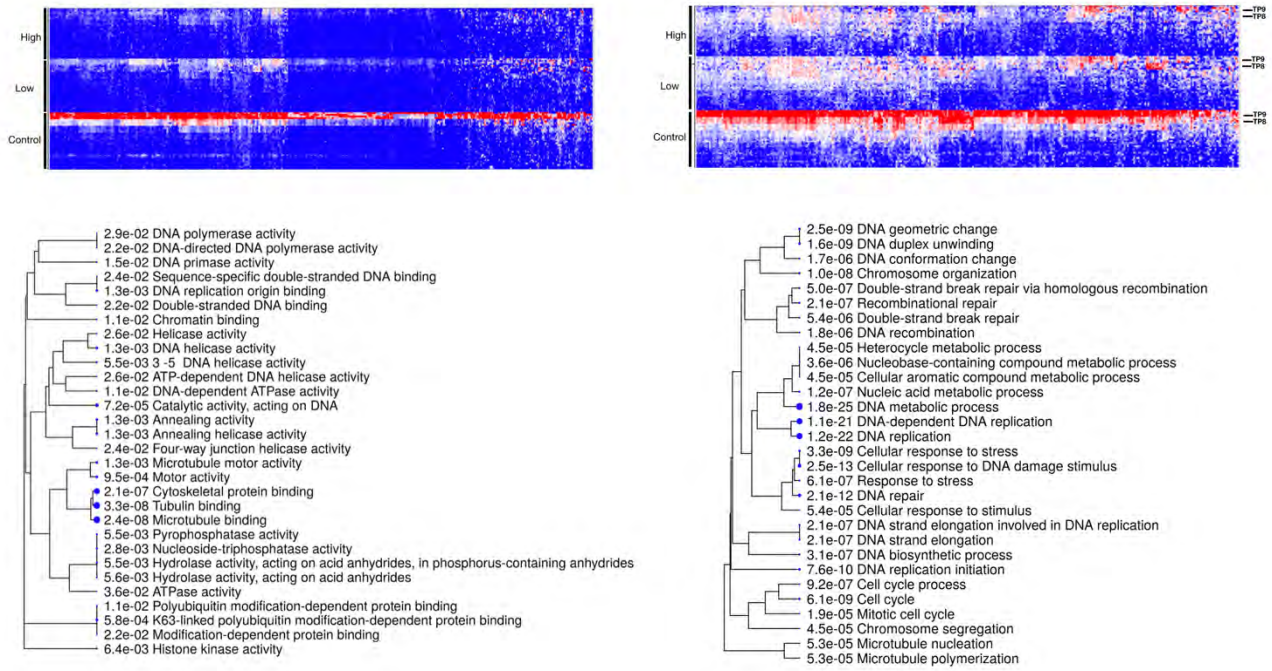


Figure SI-44. Gene expression heatmaps (red = relative increase, blue = relative decrease) and JGI-GO hierarchical enrichment trees of two gene cluster identified by hierarchical cluster analysis, of the NF experiment, indicating activity of macro- and micromolecular processes almost exclusively in non-exposed cells Dendogram branches suggest ontological similarity, size of nodes indicates statistical significance.'.

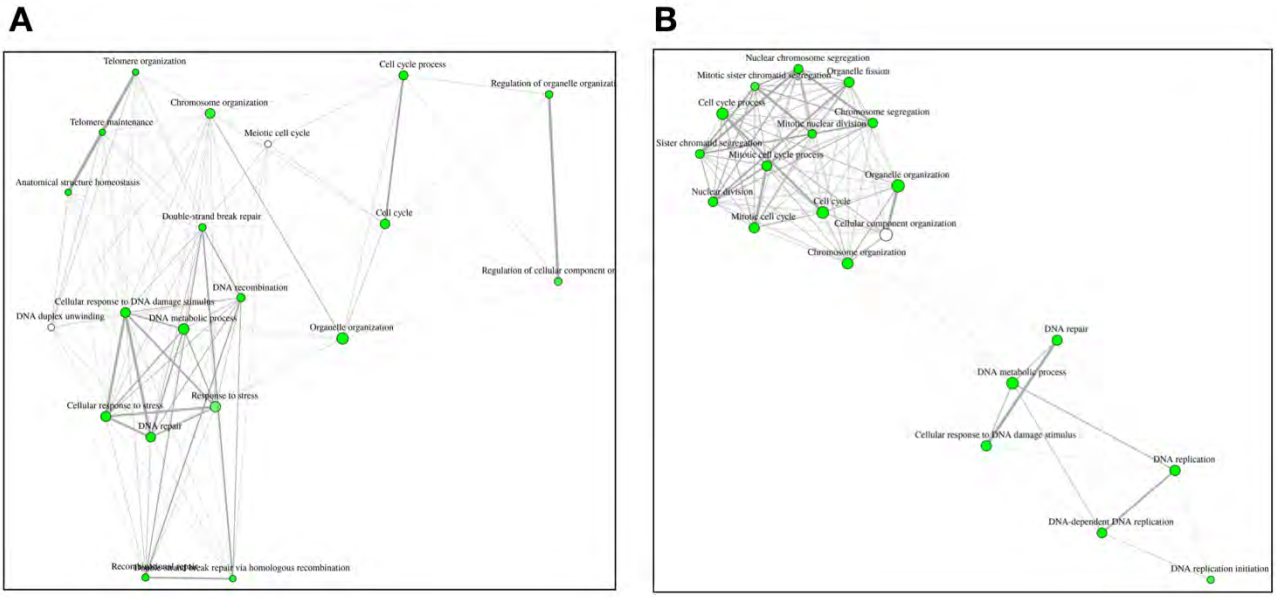


Figure SI-45. Network maps of JGI-GO enrichments of genes contained within NF experiment maSigPro (A) "Cluster02" and (B) "Cluster06". Distance of the lines ("edges") is a measure of similarity, size of the nodes (bright green) is relative to significance of enrichment of the ontology term.

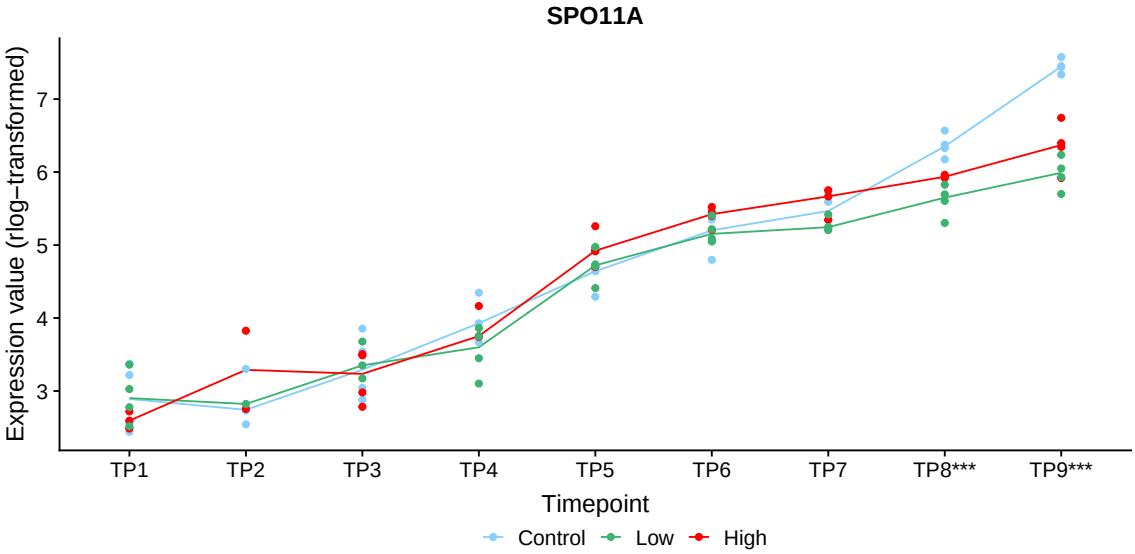


Figure SI-46. Time-course plot of replicate expression values and median connection line. Showing expression of the gene transcript for SPO11a in the NF transcriptomics dataset. Significant changes in expression (ANOVA) are indicated by * (FDR<0.05), ** (FDR<0.01) or *** (FDR<0.001).

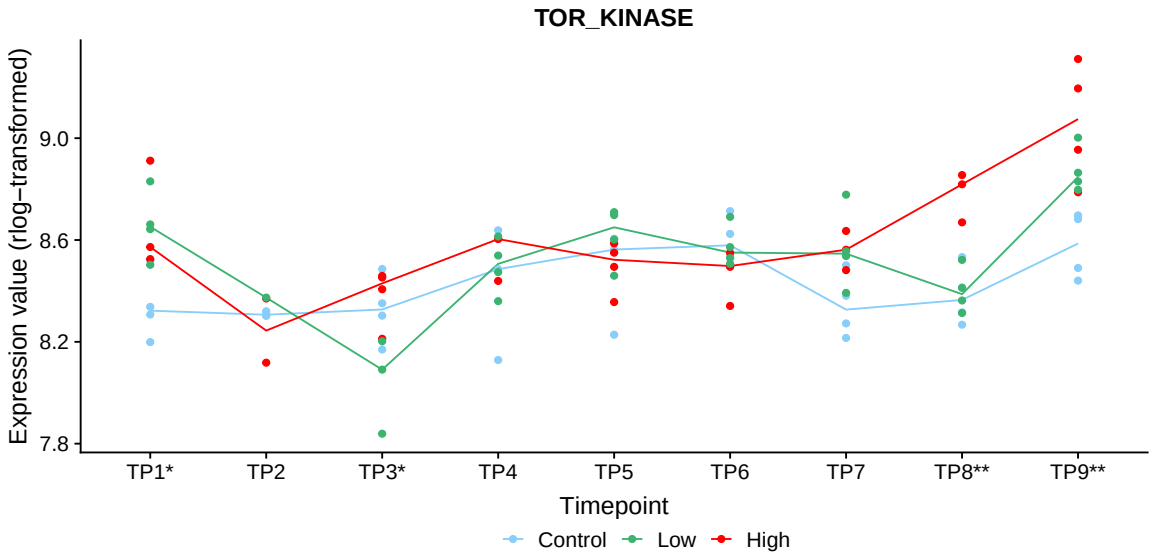


Figure SI-47. Time-course plot of replicate expression values and median connection line. Showing expression of the gene transcript for TOR-kinase in the NF transcriptomics dataset. Significant changes in expression (ANOVA) are indicated by * (FDR<0.05), ** (FDR<0.01) or *** (FDR<0.001).

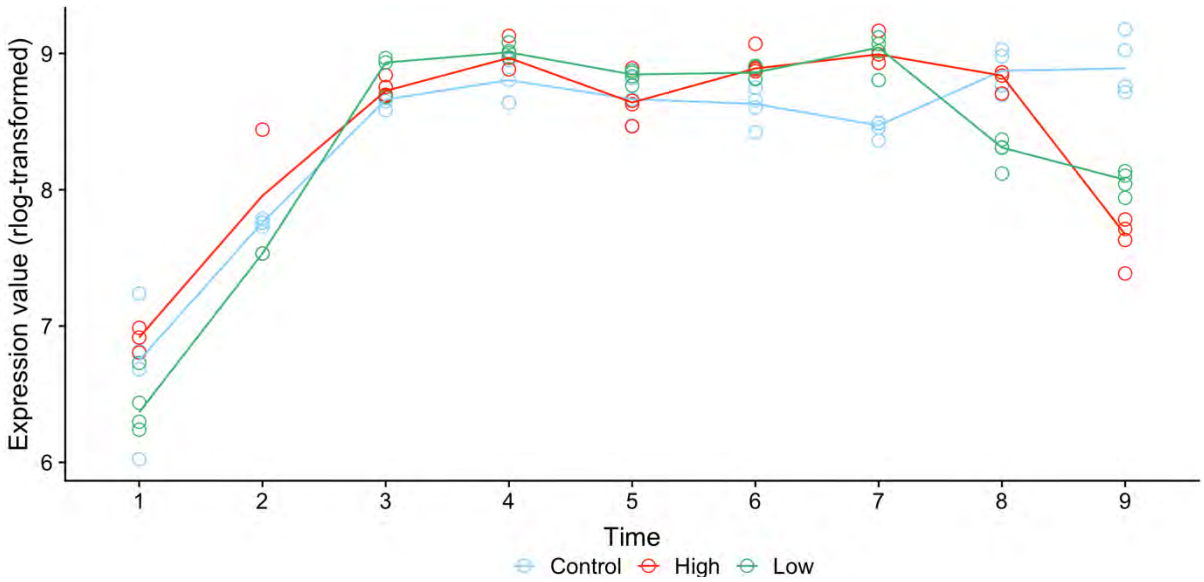


Figure SI-48. Time-course plot, median of genes per replicate and median of medians with connection line. Showing expression of genes within the JGI-GO Plant-type cell wall (as identified by PGSEA at TP9), using the NF transcriptomics dataset. Significant changes in expression (ANOVA) are indicated by * (FDR<0.05), ** (FDR<0.01) or *** (FDR<0.001).

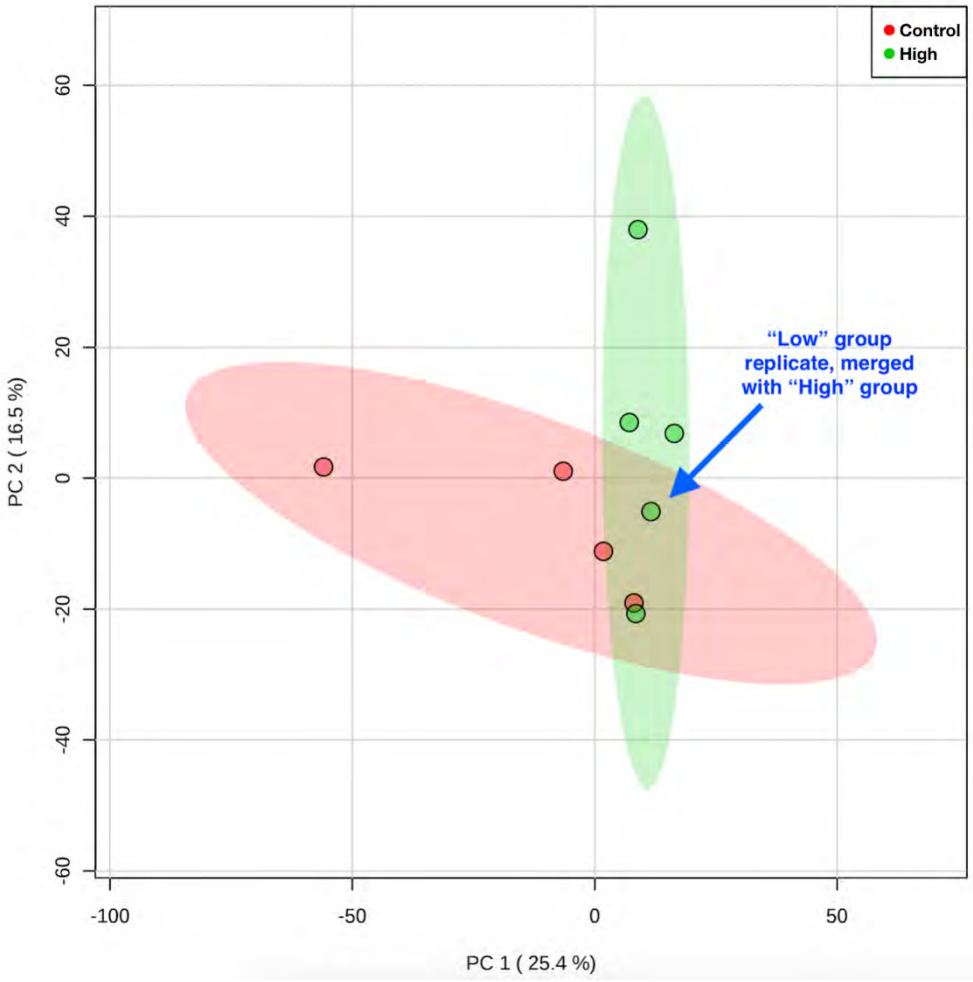


Figure SI-49. PCA scores plot of CB exposure experiment lipidomics data of experimental sampling time-point 1 (TP1). Indicated is the single replicate of "Low" exposure group that was reassigned to "High" group to increase statistical power, resulting in a generic "Treatment" group containing all "Low" and "High" replicates.

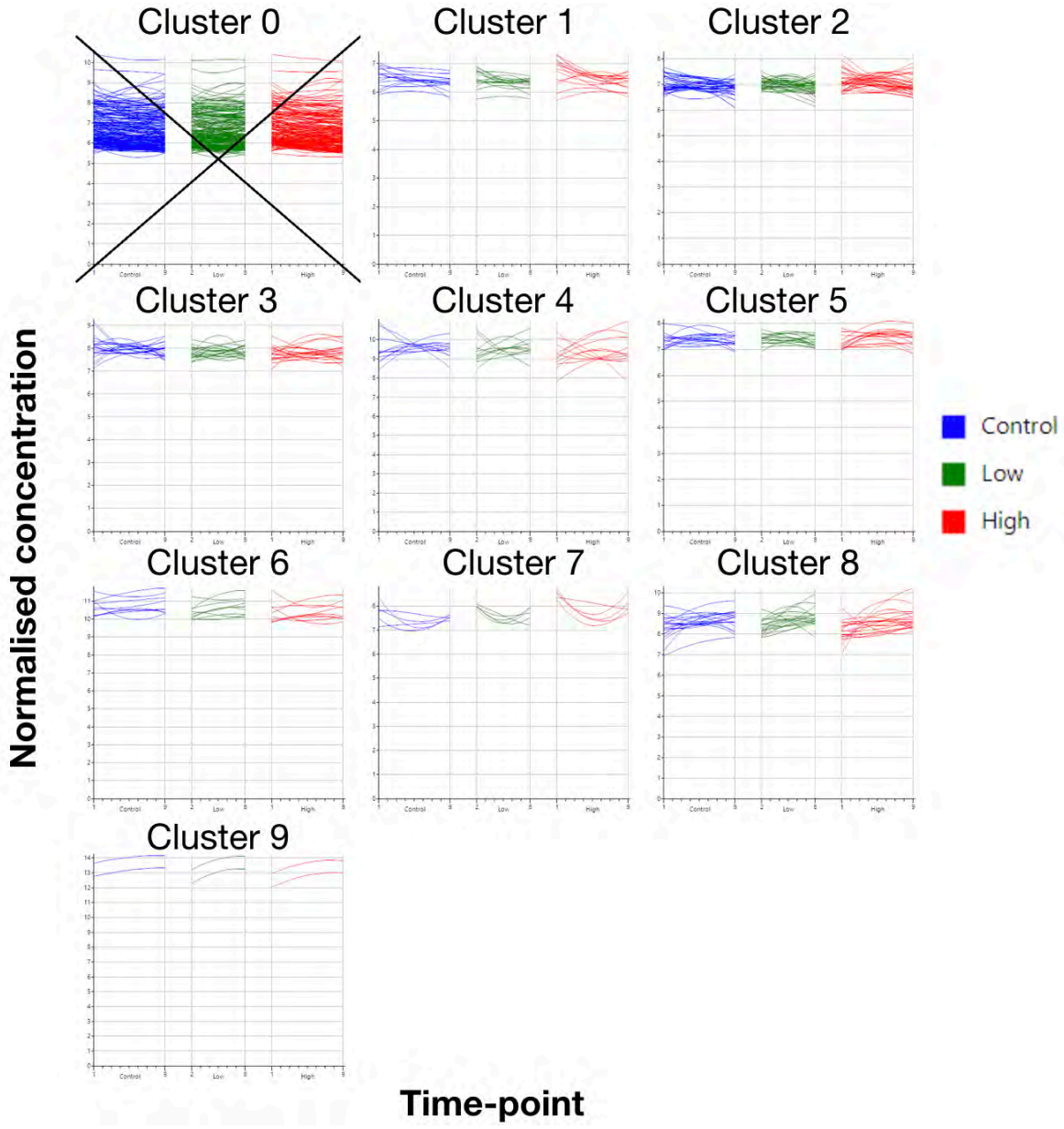


Figure SI-50. metaboClust software time-profile clusters of CB lipidomics data over time-course, with “Cluster 0” (crossed out) reflecting all insignificant spectral peaks in the dataset. K = 9 clusters of spectral peaks with similar time-profiles and displaying monotonous dose-concentration behavior were identified, however no single cluster could be meaningfully labelled with putative metabolite annotations and/or pathway enrichments.

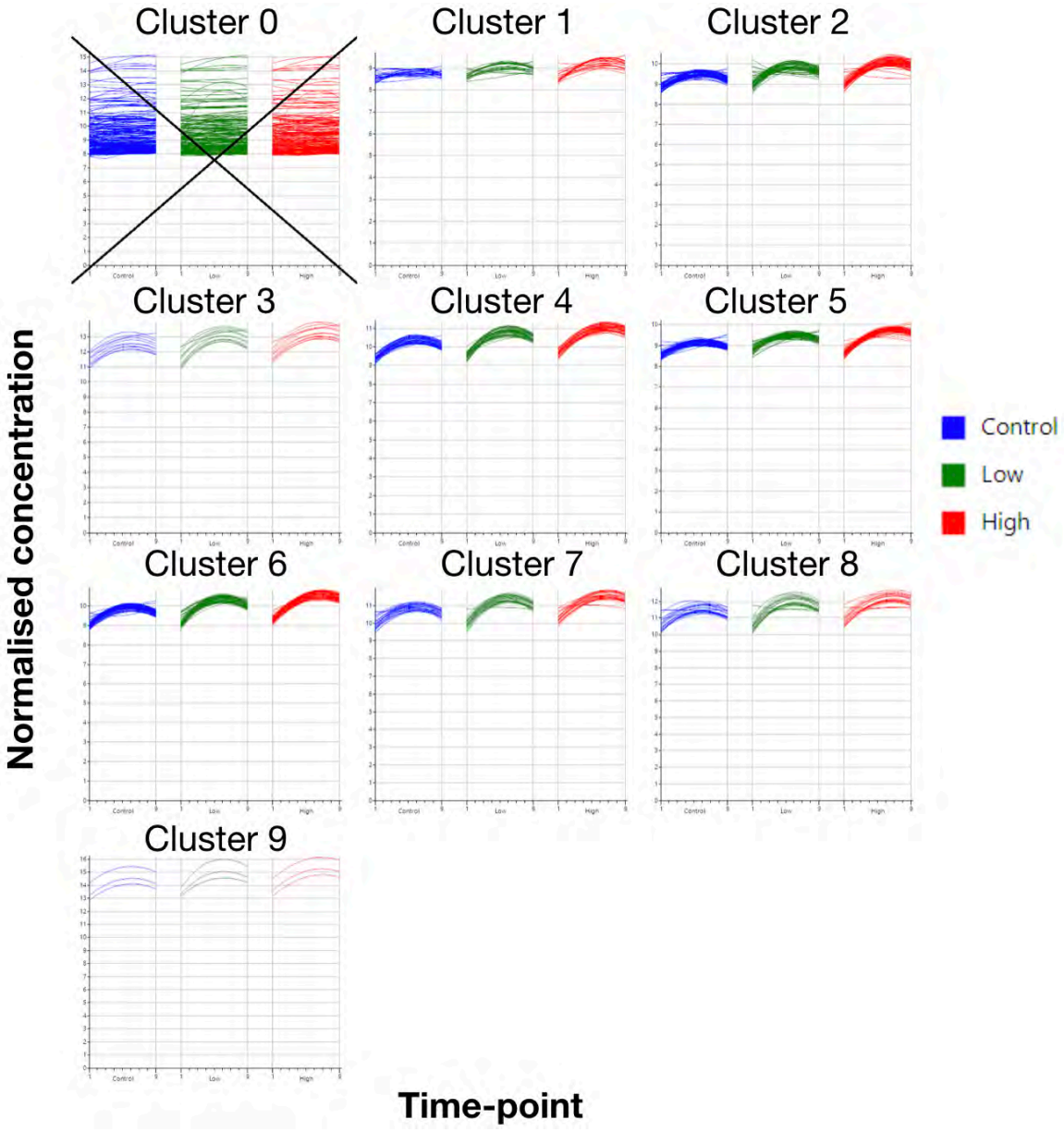


Figure SI-51. metaboClust software time-profile clusters of CB positive ion metabolomics data over time-course, with “Cluster 0” (crossed out) reflecting all insignificant spectral peaks in the dataset. K = 9 clusters of spectral peaks with similar time-profiles and displaying monotonous dose-concentration behavior were identified, however no single cluster could be meaningfully labelled with putative metabolite annotations and/or pathway enrichments.

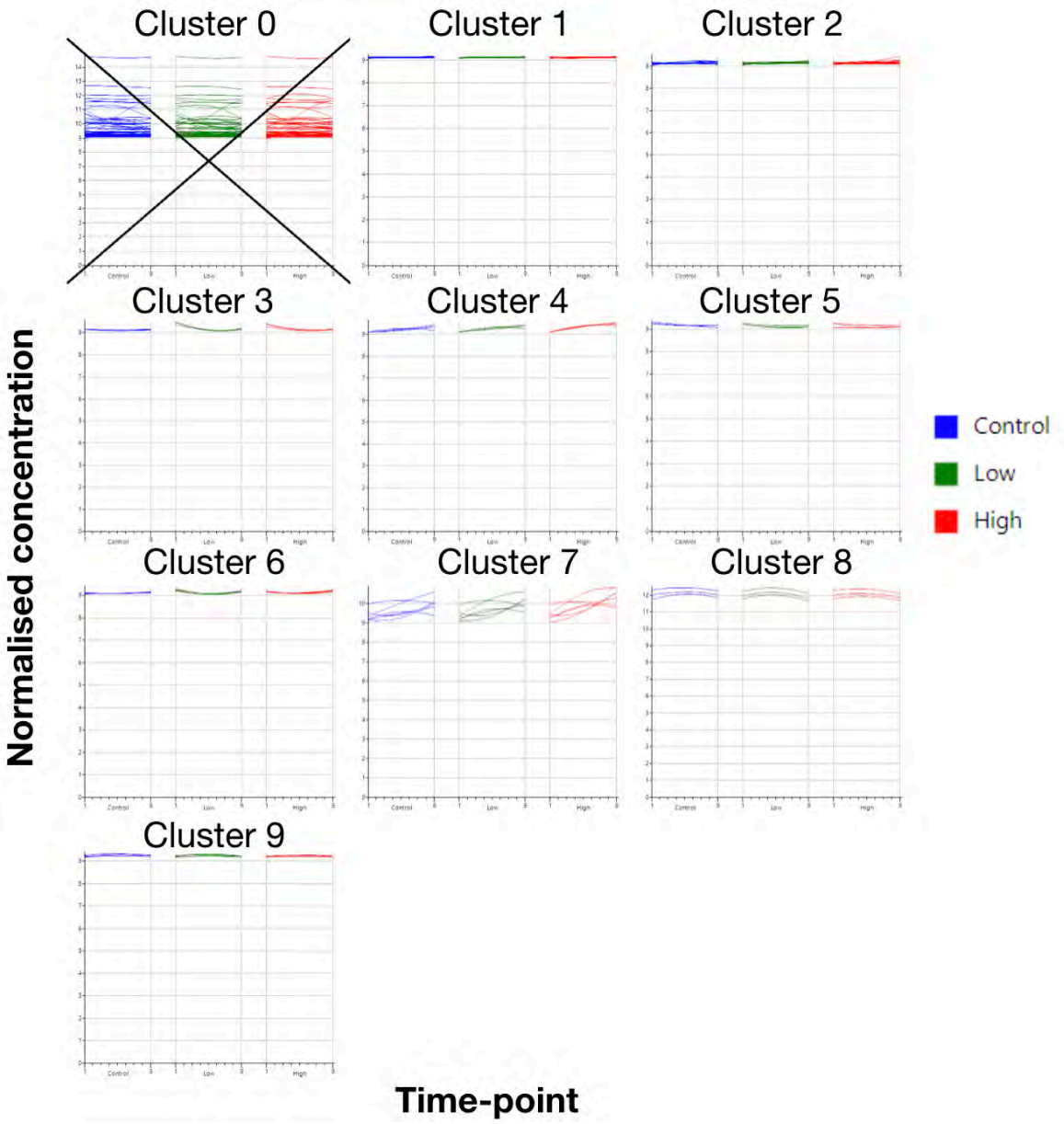


Figure SI-52. metaboClust software time-profile clusters of CB negative ion metabolomics data over time-course, with “Cluster 0” (crossed out) reflecting all insignificant spectral peaks in the dataset. K = 9 clusters of spectral peaks with similar time-profiles and displaying monotonous dose-concentration behavior were identified, however no single cluster could be meaningfully labelled with putative metabolite annotations and/or pathway enrichments.

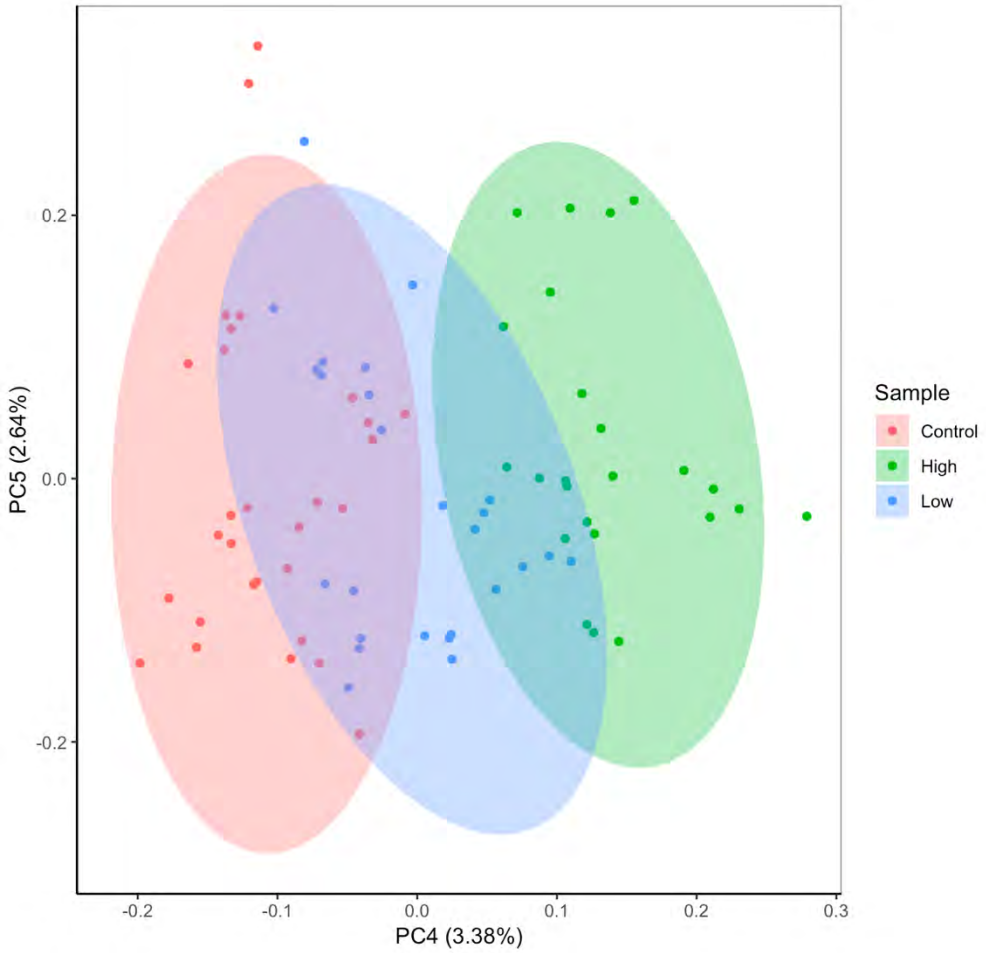


Figure SI-53. PCA scores plot (PC4 and PC5) of CB exposure experiment transcriptomics data. Consistent molecular effects of chemical exposure are appreciable on PC4 over all experimental sampling time-points.

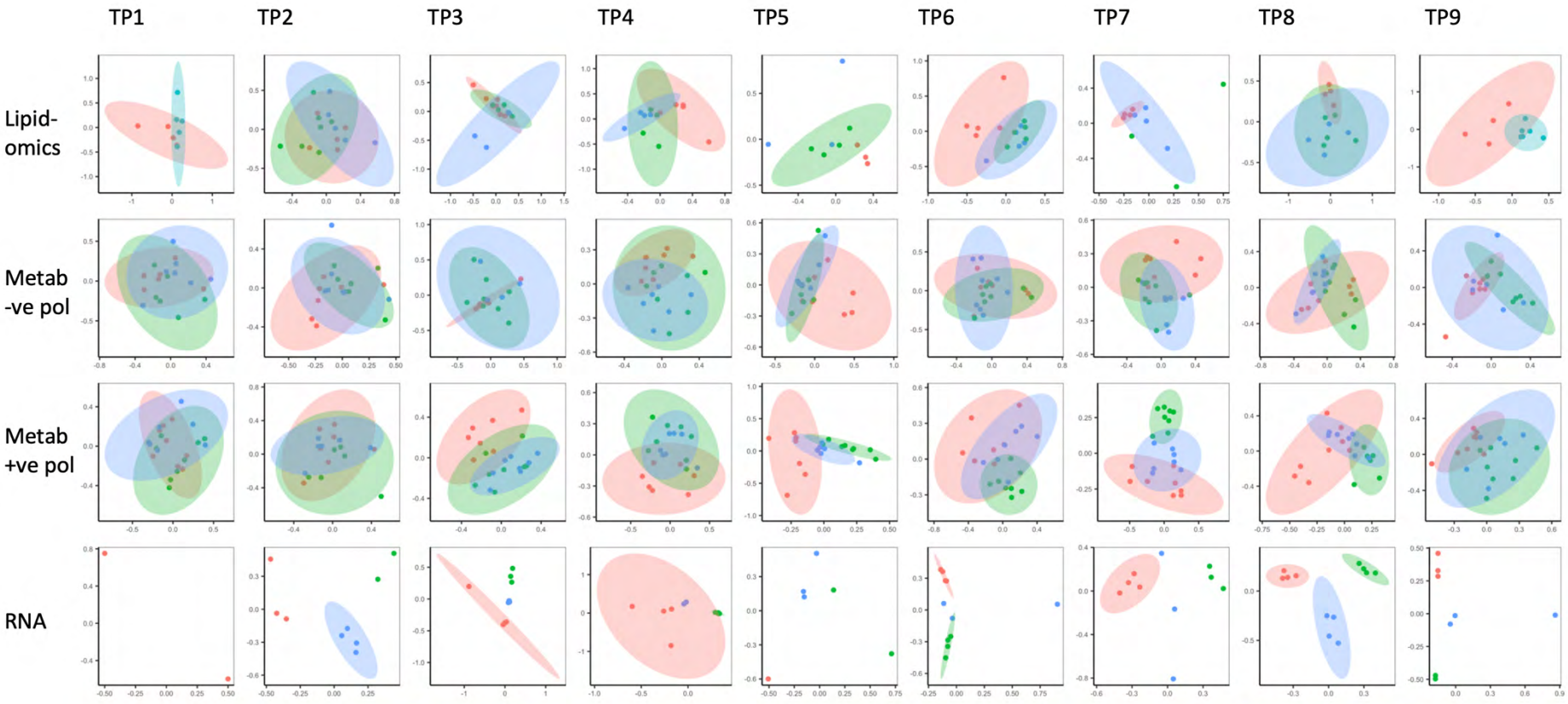


Figure SI-54. PCA plots and ANOVA significance table of the CB dataset for lipidomics assay (Top), negative ion metabolomics assay (Mid Upper), positive ion metabolomics assay (Mid Lower) and transcriptomics data (Bottom). ANOVA was conducted on PCA scores between exposure groups, with p-values displayed below for PC1 and PC2 comparisons. Significant ($p<0.05$) values are printed in red

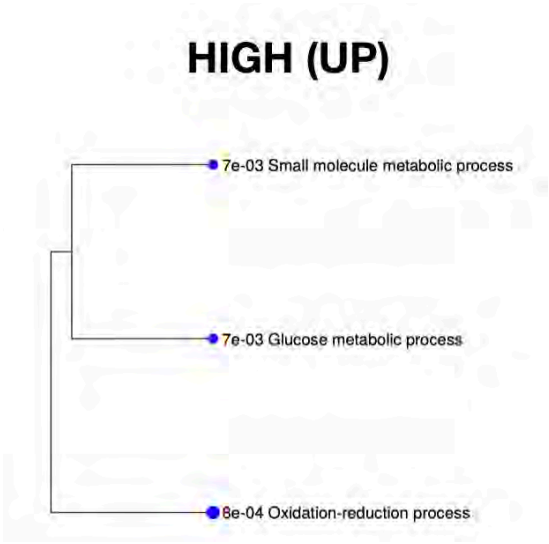


Figure SI-55. JGI-GO enrichments of DEG found in the collapsed CB dataset (omission of time as variable). DEGs for all comparisons only led to significant enrichments for the High-vs.-Control comparison, with 3 JGI-GOs upregulated. Dendogram branches suggest ontological similarity, size of nodes indicates statistical significance.'

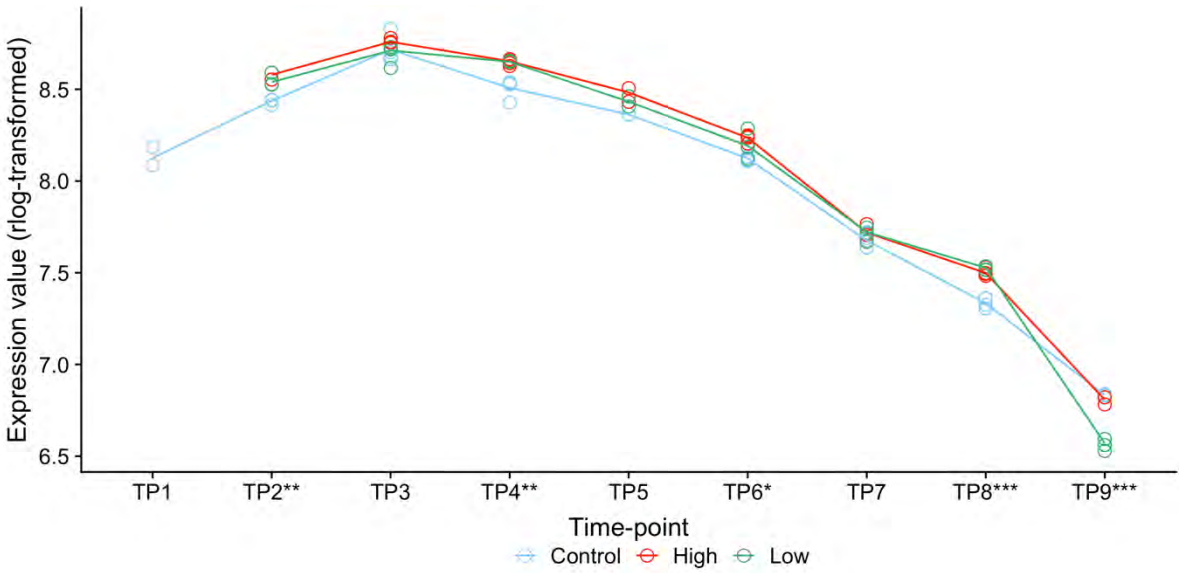


Figure SI-56. Time-course plot, median of genes per replicate and median of medians with connection line. Showing expression of genes within maSigPro "Cluster01", using the CB transcriptomics dataset. Significant changes in expression (ANOVA) are indicated by * (FDR<0.05), ** (FDR<0.01) or *** (FDR<0.001).

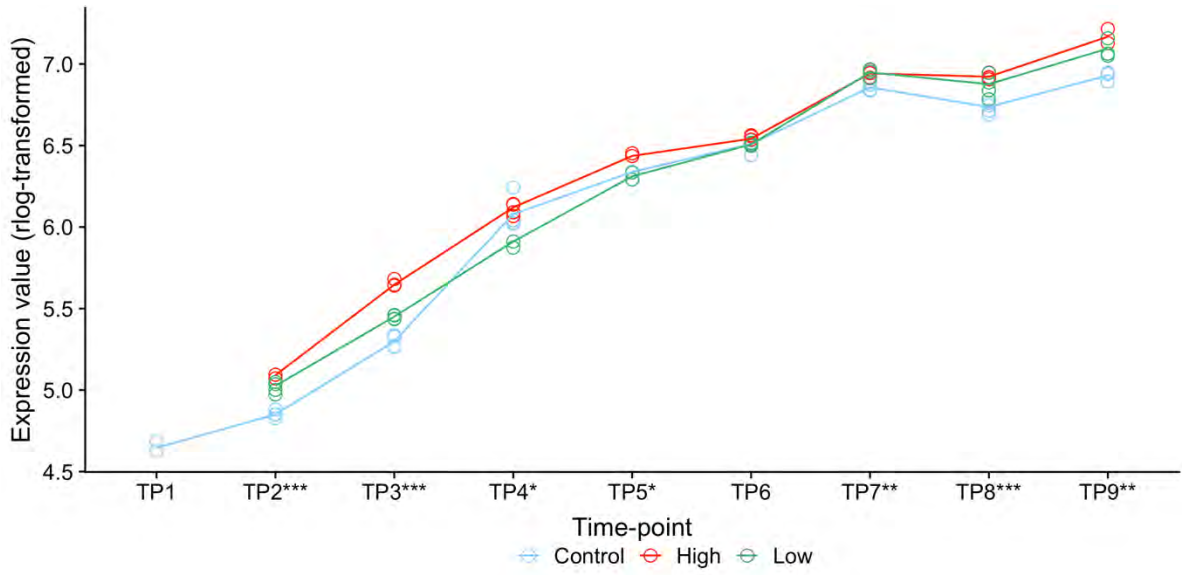


Figure SI-57. Time-course plot, median of genes per replicate and median of medians with connection line. Showing expression of genes within maSigPro “Cluster03”, using the CB transcriptomics dataset. Significant changes in expression (ANOVA) are indicated by * (FDR<0.05), ** (FDR<0.01) or *** (FDR<0.001).

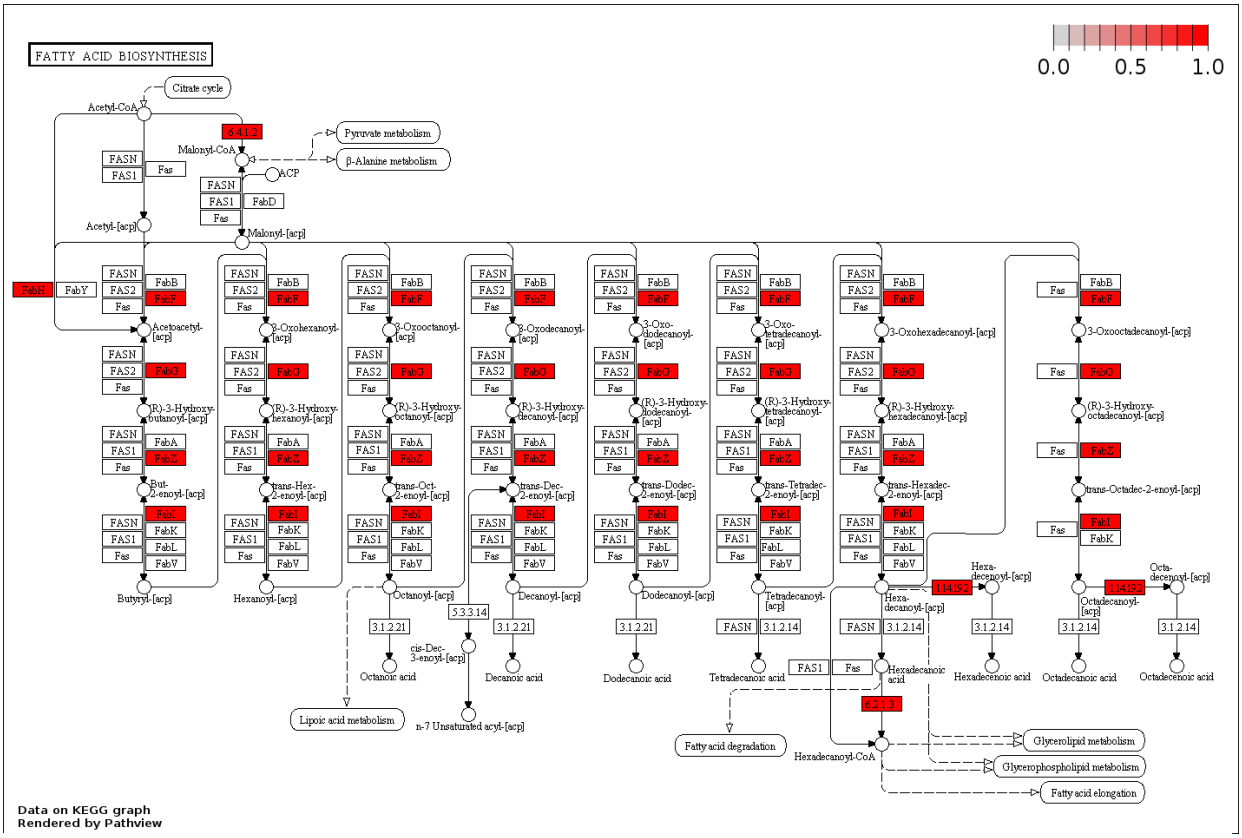


Figure SI-58. KEGG enrichment map for the KEGG pathway “Fatty acid synthesis” (KEGG code cre00061) enriched by genes from the CB experiment maSigPro “Cluster01”. Marked in red are the individual genes found both within maSigPro “Cluster01” and the KEGG pathway.

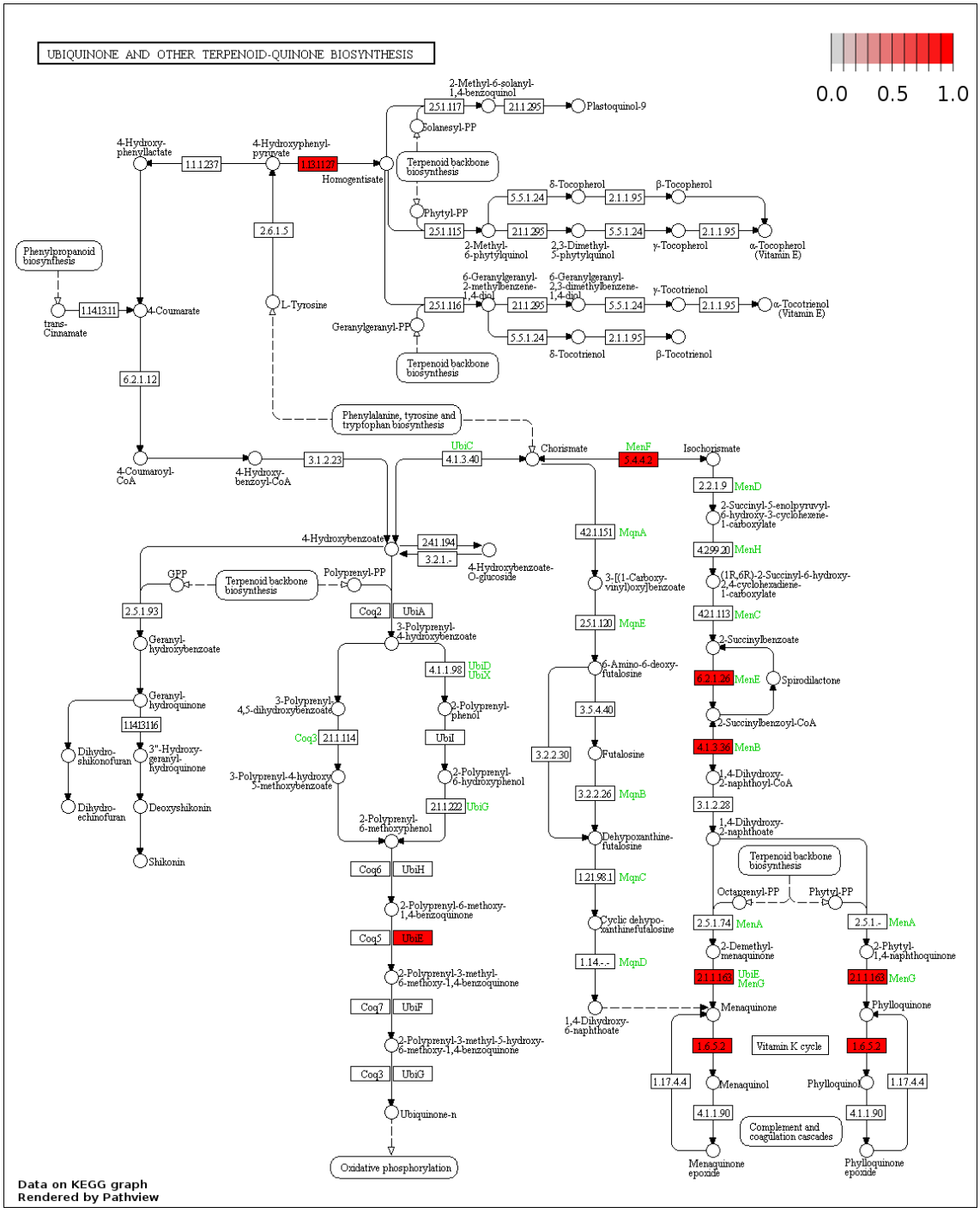


Figure SI-59. KEGG enrichment map for the KEGG pathway “Ubiquinone and other terpenoid-quinone biosynthesis” (KEGG code cre00130) enriched by genes from the CB experiment maSigPro “Cluster01”. Marked in red are the individual genes found both within maSigPro “Cluster01” and the KEGG pathway.

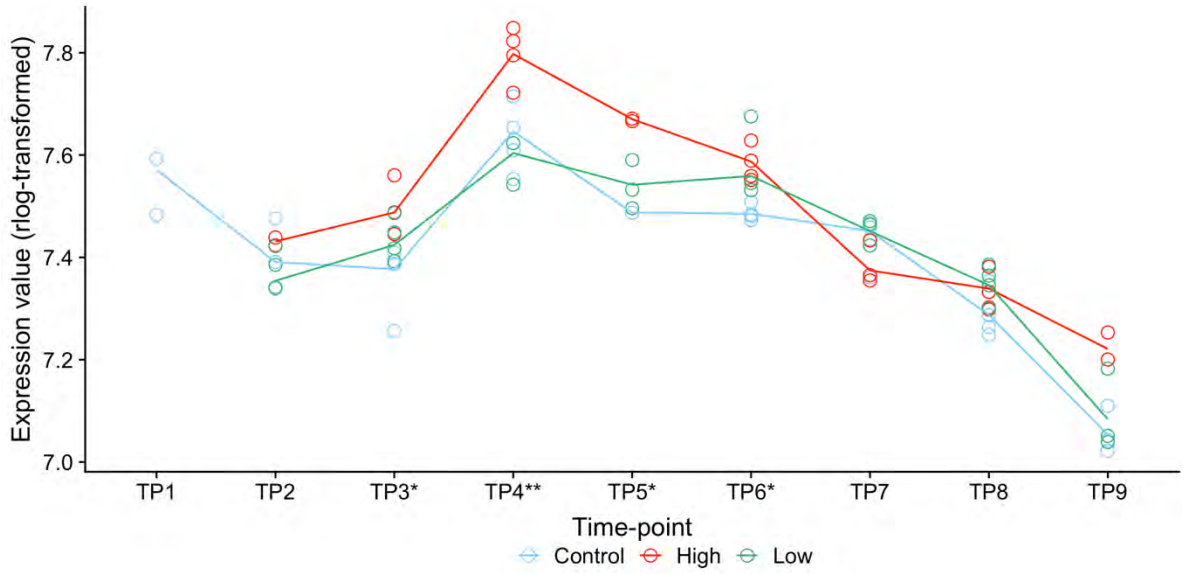


Figure SI-60. Time-course plot, median of genes per replicate and median of medians with connection line. Showing expression of genes within JGI-GOs “Response to hydrogen peroxide”, “Reactive oxygen species metabolic process”, “Response to reactive oxygen species”, “Glutathione metabolic process”, “Sulfur compounds transport” and “Sulfate transport”, using the CB transcriptomics dataset. Significant changes in expression (ANOVA) are indicated by * (FDR<0.05), ** (FDR<0.01) or *** (FDR<0.001).

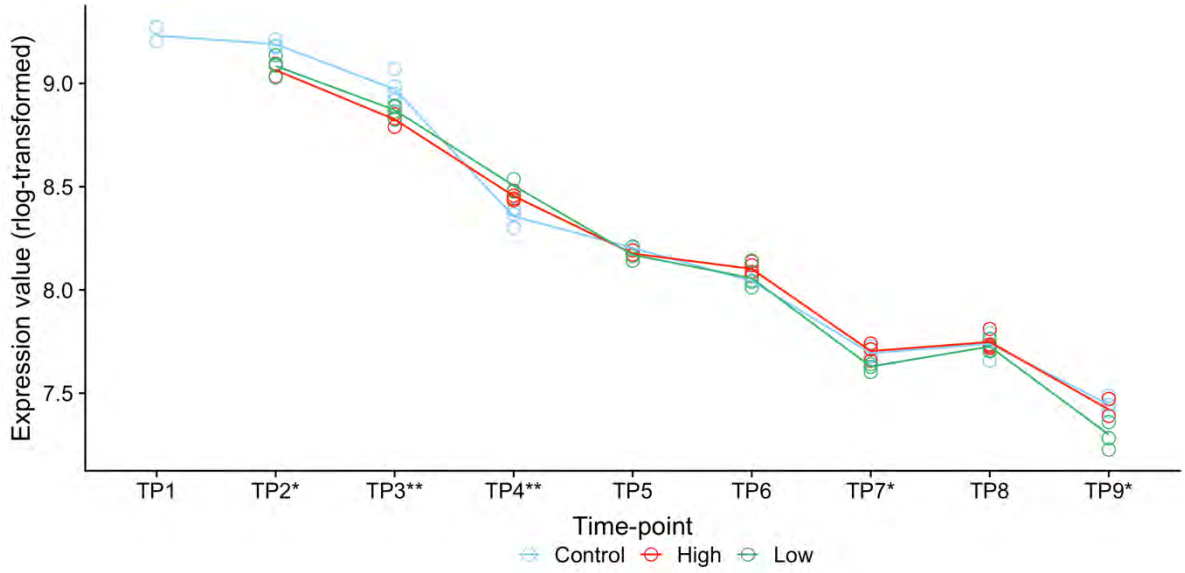


Figure SI-61. Time-course plot, median of genes per replicate and median of medians with connection line. Showing expression of genes within maSigPro “Cluster04”, using the CB transcriptomics dataset. Significant changes in expression (ANOVA) are indicated by * (FDR<0.05), ** (FDR<0.01) or *** (FDR<0.001).

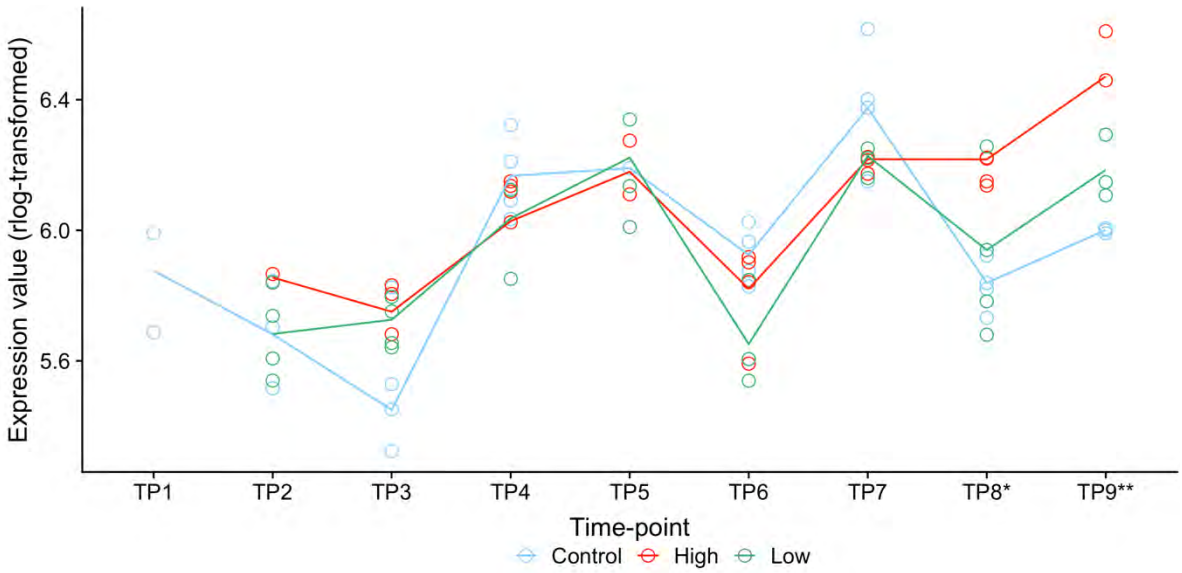


Figure SI-62. Time-course plot, median of genes per replicate and median of medians with connection line. Showing expression of genes within JGI-GOs ""Autophagosome assembly", "Macroautophagy" and "Autophagy", using the CB transcriptomics dataset. Significant changes in expression (ANOVA) are indicated by * (FDR<0.05), ** (FDR<0.01) or *** (FDR<0.001).

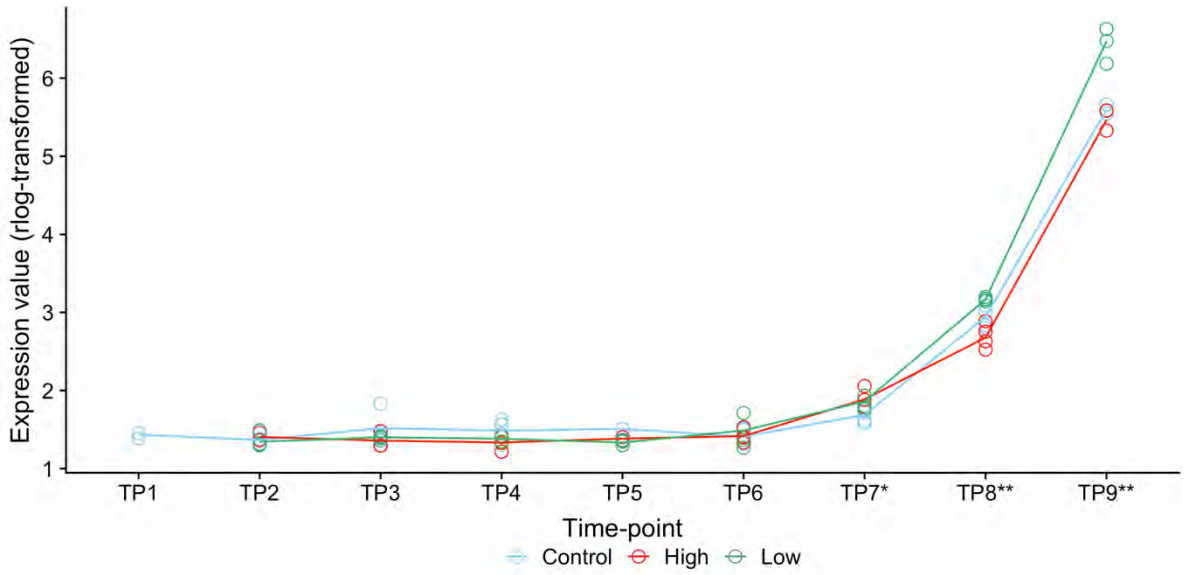


Figure SI-63. Time-course plot, median of genes per replicate and median of medians with connection line. Showing expression of genes within maSigPro "Cluster05", using the CB transcriptomics dataset. Significant changes in expression (ANOVA) are indicated by * (FDR<0.05), ** (FDR<0.01) or *** (FDR<0.001).

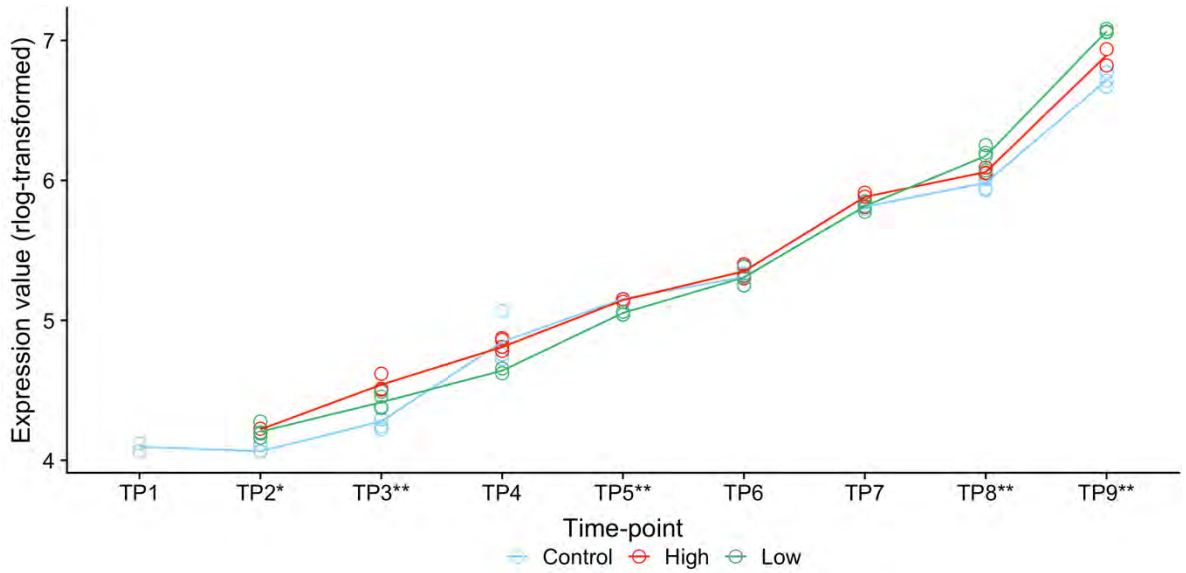


Figure SI-64. Time-course plot, median of genes per replicate and median of medians with connection line. Showing expression of genes within maSigPro "Cluster06", using the CB transcriptomics dataset. Significant changes in expression (ANOVA) are indicated by * (FDR<0.05), ** (FDR<0.01) or *** (FDR<0.001).

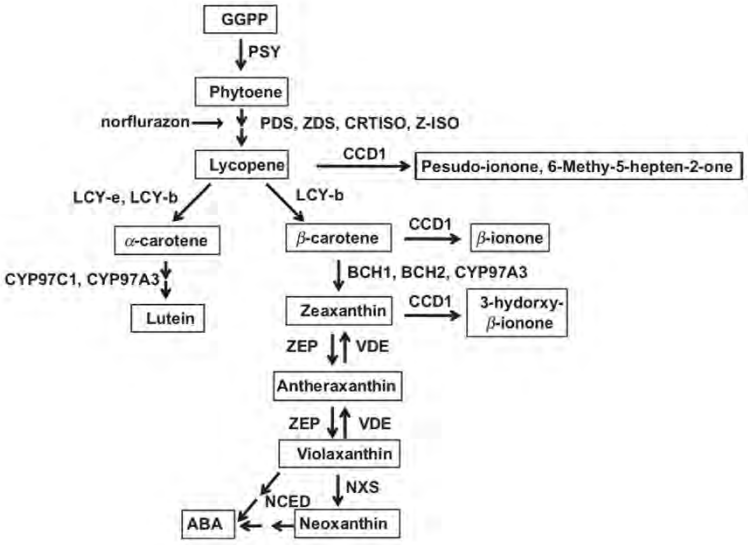


Figure SI-65. The core of the carotenoid synthesis pathway, with the molecular target site of norflurazon indicated. PSY = phytoene synthase, PDS = phytoene desaturase, ZDS = zeta-carotene desaturase, CRTISO = carotenoid isomerase, Z-ISO = 15-cis-zeta-carotene isomerase, LCY-e = lycopene e-cyclase, LCY-b = lycopene b-cyclase, BCH1/2 = beta-carotene hydroxylase 1/2, CYP97C1 = cytochrome P450 carotene e-hydroxylase, CYP97A3 = cytochrome P450 monooxygenase, ZEP = zeaxanthin epoxidase, VDE = violaxanthin de-epoxidase, NXS = neoxanthin synthase, NCED = 9-cis-epoxycarotenoid dioxygenase, CCD1 = carotenoid cleavage dioxygenase 1. Norflurazon inhibition site is indicated. Figure and caption from ref. [559].

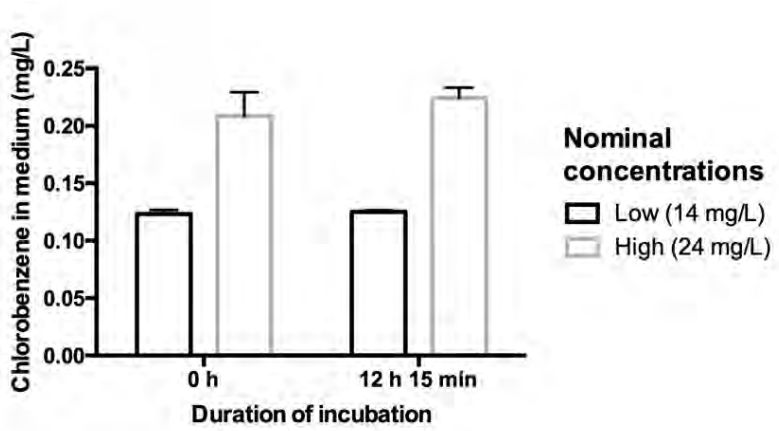


Figure SI-66. Barplots comparing chlorobenzene concentrations in test system medium, measured using GC-MS, to assess whether any loss occurs over the test duration. At 0 h and after a 12 h 15 min exposure period, two concentration groups 'Low' (nominal 14 mg/L) and 'High' (nominal 24 mg/L) test groups were measured. Bars represent mean ±sd (n = 4 per group).

A.2. Supplementary tables

Table SI-T1. Determination of mean true vial volume of T101/V4 vials. The weight of n = 10 empty vials was measured, then the vials were filled to the brim with 20°C deionized water. The weight was measured again, and the difference calculated. The average of the difference was divided by the density of water at 20 °C to yield the mean true vial volume of 11.14ml, +-0.11ml.

Weight empty [g]	**Weight filled [g]**	**Difference [g]**
8.207	19.211	11.004
8.235	19.442	11.207
8.331	19.473	11.142
8.211	19.214	11.003
8.319	19.479	11.16
8.212	19.181	10.969
8.178	19.258	11.08
8.293	19.527	11.234
8.435	19.694	11.259
	Mean	**11.118**
	Density H_2O [g/cm3] at 20 °C	**0.998203**
	True vial volume [ml]	**11.138**
	Standard deviation [ml]	**0.108**

Table SI-T2. m/z values of NF- and its main metabolite desmethyl-NF (NF-desMe)- adducts that were removed from NF metabolomics and lipidomics datasets, per ion mode. Hac = Acetate, Br = Bromine, TFA = Trifluoroacetic acid, DMSO = Dimethylsulfoxide, CH3OH = Methanol. Monoisotopic mass for NF = 303.038635 Da, for NF-desMe = 289.023 Da.

Chemical	Ion mode	Adduct	m/z
NF	Negative	M-3H	100.005602
NF	Negative	M-2H	150.512042
NF	Negative	M-H2O-H	284.020245
NF	Negative	M-H	302.031359
NF	Negative	M+Na-2H	324.013301
NF	Negative	M+Cl	338.008037
NF	Negative	M+K-2H	339.987241
NF	Negative	M+Hac-H	362.052486
NF	Negative	M+Br	381.95752
NF	Negative	M+TFA-H	416.024221
NF	Negative	2M-H	605.069994
NF	Negative	2M+Hac-H	665.091121
NF	Negative	3M-H	910.123181
NF-desMe	Negative	M-3H	95.333724
NF-desMe	Negative	M-2H	143.504224
NF-desMe	Negative	M-H2O-H	270.00461
NF-desMe	Negative	M-H	288.015724
NF-desMe	Negative	M+Na-2H	309.997666
NF-desMe	Negative	M+Cl	323.992402
NF-desMe	Negative	M+K-2H	325.971606
NF-desMe	Negative	M+Hac-H	348.036851
NF-desMe	Negative	M+Br	367.941885
NF-desMe	Negative	M+TFA-H	402.008586
NF-desMe	Negative	2M-H	577.038724
NF-desMe	Negative	2M+Hac-H	637.059851
NF-desMe	Negative	3M-H	868.076276
NF	Positive	M+3H	102.020154
NF	Positive	M+2H+Na	109.347468
NF	Positive	M+H+2Na	116.779069
NF	Positive	M+3Na	124.002096
NF	Positive	M+2H	152.526594
NF	Positive	M+H+NH4	161.039868
NF	Positive	M+H+Na	163.517565
NF	Positive	M+H+K	171.504535
NF	Positive	M+2Na	174.508536
NF	Positive	M+H	304.045911

NF	Positive	M+NH4	321.072458
NF	Positive	M+Na	326.027853
NF	Positive	M+CH3OH+H	336.072124
NF	Positive	M+K	342.001793
NF	Positive	M+2Na-H	348.009795
NF	Positive	M+2K+H	379.957675
NF	Positive	M+DMSO+H	382.059855
NF	Positive	2M+H	607.084546
NF	Positive	2M+NH4	624.111093
NF	Positive	2M+Na	629.066488
NF	Positive	2M+3H2O+2H	634.10039
NF	Positive	2M+K	645.040428
NF	Positive	M+FA+H	350.051389
NF	Positive	M+FA+K	342.001793
NF	Positive	M+FA+Na	326.027853
NF	Positive	M+FA+NH4	321.072458
NF	Positive	2M+FA+H	653.090024
NF	Positive	M/2+FA+H	198.532072
NF	Positive	M/3+FA+H	148.025632
NF-desMe	Positive	M+3H	97.348276
NF-desMe	Positive	M+2H+Na	104.67559
NF-desMe	Positive	M+H+2Na	112.10719
NF-desMe	Positive	M+3Na	119.330218
NF-desMe	Positive	M+2H	145.518776
NF-desMe	Positive	M+H+NH4	154.03205
NF-desMe	Positive	M+H+Na	156.509747
NF-desMe	Positive	M+H+K	164.496717
NF-desMe	Positive	M+2Na	167.500718
NF-desMe	Positive	M+H	290.030276
NF-desMe	Positive	M+NH4	307.056823
NF-desMe	Positive	M+Na	312.012218
NF-desMe	Positive	M+CH3OH+H	322.056489
NF-desMe	Positive	M+K	327.986158
NF-desMe	Positive	M+2Na-H	333.99416
NF-desMe	Positive	M+2K+H	365.94204
NF-desMe	Positive	M+DMSO+H	368.04422
NF-desMe	Positive	2M+H	579.053276
NF-desMe	Positive	2M+NH4	596.079823
NF-desMe	Positive	2M+Na	601.035218
NF-desMe	Positive	2M+3H2O+2H	606.06912
NF-desMe	Positive	2M+K	617.009158

NF-desMe	Positive	M+FA+H	336.035754
NF-desMe	Positive	M+FA+K	327.986158
NF-desMe	Positive	M+FA+Na	312.012218
NF-desMe	Positive	M+FA+NH4	307.056823
NF-desMe	Positive	2M+FA+H	625.058754
NF-desMe	Positive	M/2+FA+H	191.524254
NF-desMe	Positive	M/3+FA+H	143.353754

Table SI-T3. Analysis report of metaboClust time-profile clustering – NF experiment

Cluster assignments – Lipidomics, negative ion mode (see Fig. SI-5)

- Cluster 0 (Insignificant): 3882 spectral peaks
- Cluster 1: 162 spectral peaks
- Cluster 2: 61 spectral peaks
- Cluster 3: 119 spectral peaks
- Cluster 4: 41 spectral peaks
- Cluster 5: 98 spectral peaks
- Cluster 6: 103 spectral peaks
- Cluster 7: 51 spectral peaks
- Cluster 8: 48 spectral peaks
- Cluster 9: 21 spectral peaks

Cluster assignments – Metabolomics, positive ion mode (see Fig. SI-6)

- Cluster 0 (Insignificant): 103 spectral peaks
- Cluster 1: 35 spectral peaks
- Cluster 2: 17 spectral peaks
- Cluster 3: 19 spectral peaks
- Cluster 4: 27 spectral peaks
- Cluster 5: 19 spectral peaks
- Cluster 6: 32 spectral peaks
- Cluster 7: 25 spectral peaks
- Cluster 8: 9 spectral peaks
- Cluster 9: 23 spectral peaks

Cluster assignments – Metabolomics, negative ion mode (see Fig. SI-7)

- Cluster 0 (Insignificant): 992 spectral peaks
- Cluster 1: 16 spectral peaks
- Cluster 2: 18 spectral peaks
- Cluster 3: 23 spectral peaks
- Cluster 4: 14 spectral peaks
- Cluster 5: 3 spectral peaks
- Cluster 6: 16 spectral peaks
- Cluster 7: 5 spectral peaks
- Cluster 8: 6 spectral peaks
- Cluster 9: 3 spectral peaks

Table SI-T4. Analysis report of maSigPro time-profile clustering – NF experiment

- Number of total features: 17943
- Number of filtered features: 569
- Number of features after filtering: 17374
- Number of analyzed samples: 96/96
- Differentially expressed features identified (FDR <0.05): 16616
- Significant features (R-squared >0.7) according to the selection procedure:
    - All significant features: 6336
    - Significant features for each experimental group
        - Control: 6092
        - High vs Control: 5763
        - Low vs Control: 5459
    - Significant features for each regression variable[8]:
        - Start_Low: 2273
        - Start_High: 2793
        - Start_Control: 5841
        - Linear_Low: 3861
        - Linear_High: 4125
        - Linear_Control: 5175
        - Curved_Low: 4273
        - Curved_High: 4328
        - Curved_Control: 4986
- Cluster memberships in time-profile clustering
    - Cluster 1: 991
    - Cluster 2: 690
    - Cluster 3: 689
    - Cluster 4: 1296
    - Cluster 5: 542
    - Cluster 6: 583
    - Cluster 7: 470
    - Cluster 8: 392
    - Cluster 9: 683

[8] *Start*: Features with a statistically significant differential expression at the first time point. *Linear*: Features that show a statistically significant linear response of induced or repressed expression over time. *Curved*: Features that show a statistically significant change in the linear response that might be indicating a transitory or saturation behavior.

Table SI-T5. DIMS negative lipidomics assay putative spectral peak annotation success rates and median ppm error, per experimental time-point groups. Displayed are data from the NF and CB experiment.

Experiment	Timepoint	Comparison	Median ppm error	Annotation success rate
NF (Lipidomics assay)	TP1	High - Control	NA	0%
		Low - Control	Na	0%
	TP2	High - Control	2.93	4.9%
		Low - Control	1.95	3.9%
	TP3	High - Control	NA	0%
		Low - Control	NA	0%
	TP4	High - Control	3.69	6.5%
		Low - Control	1.95	3.2%
	TP5	High - Control	1.95	5%
		Low - Control	1.95	5.8%
	TP6	High - Control	2.15	5%
		Low - Control	1.95	6.1%
	TP7	High - Control	1.83	6.75%
		Low - Control	1.95	4%
	TP8	High - Control	2.22	5.1%
		Low - Control	1.95	4.8%
	TP9	High - Control	2.22	5.1%
		Low - Control	1.95	3.8%
CB (Lipidomics assay)	TP1	High - Control	NA	0%
		Low - Control	NA	0%
	TP2	High - Control	0.15	37.5%
		Low - Control	NA	0%
	TP3	High - Control	NA	0%
		Low - Control	NA	0%
	TP4	High - Control	NA	0%
		Low - Control	NA	0%
	TP5	High - Control	NA	0%
		Low - Control	NA	0%
	TP6	High - Control	NA	0%
		Low - Control	0.99	2.3%
	TP7	High - Control	NA	0%
		Low - Control	NA	0%
	TP8	High - Control	NA	0%
		Low - Control	NA	0%
	TP9	High - Control	NA	0%
		Low - Control	NA	0%

Table SI-T6. DIMS positive ion mode metabolomics assay putative spectral peak annotation success rates and median ppm error, per experimental time-point groups. Displayed are data from the NF and CB experiment.

Experiment	Timepoint	Comparison	Median ppm error	Annotation success rate
NF (Metabolomics positive ion mode assay)	TP1	High - Control	NA	0%
		Low - Control	NA	0%
	TP2	High - Control	NA	0%
		Low - Control	NA	0%
	TP3	High - Control	NA	0%
		Low - Control	NA	0%
	TP4	High - Control	NA	0%
		Low - Control	NA	0%
	TP5	High - Control	-3.46	16.4%
		Low - Control	-3.26	8%
	TP6	High - Control	-2.99	9.3%
		Low - Control	-3.26	9.3%
	TP7	High - Control	-3.12	6.1%
		Low - Control	-3.26	4.7%
	TP8	High - Control	-2.88	6.7%
		Low - Control	-3.26	6.1%
	TP9	High - Control	-3.12	5.7%
		Low - Control	-3.26	5.4%
CB (Metabolomics positive ion mode assay)	TP1	High - Control	NA	0%
		Low - Control	NA	0%
	TP2	High - Control	NA	0%
		Low - Control	NA	0%
	TP3	High - Control	NA	0%
		Low - Control	1.26	2.66%
	TP4	High - Control	NA	0%
		Low - Control	NA	0%
	TP5	High - Control	-1.03	0.9%
		Low - Control	NA	0%
	TP6	High - Control	NA	0%
		Low - Control	NA	0%
	TP7	High - Control	NA	0%
		Low - Control	NA	0%
	TP8	High - Control	0.46	2.5%
		Low - Control	1.26	5.7%
	TP9	High - Control	-0.92	0.7%
		Low - Control	1.26	8.6%

Table SI-T7. DIMS negative ion mode metabolomics assay putative spectral peak annotation success rates and median ppm error, per experimental time-point groups. Displayed are data from the NF and CB experiment.

Experiment	Timepoint	Comparison	Median ppm error	Annotation success rate
NF (Metabolomics negative ion mode assay)	TP1	High - Control	NA	0%
		Low - Control	NA	0%
	TP2	High - Control	NA	0%
		Low - Control	NA	0%
	TP3	High - Control	NA	0%
		Low - Control	-1.96	20.6%
	TP4	High - Control	-0.82	10.2%
		Low - Control	-1.96	7.8%
	TP5	High - Control	-3.11	11.2%
		Low - Control	-1.96	9.8%
	TP6	High - Control	-3.1	9.7%
		Low - Control	-1.96	6.8%
	TP7	High - Control	-2.45	14.3%
		Low - Control	NA	0%
	TP8	High - Control	-2.03	13.6%
		Low - Control	NA	0%
	TP9	High - Control	-1.42	36.1%
		Low - Control	NA	0%
CB (Metabolomics negative ion mode assay)	TP1	High - Control	NA	0%
		Low - Control	NA	0%
	TP2	High - Control	NA	0%
		Low - Control	NA	0%
	TP3	High - Control	NA	0%
		Low - Control	NA	0%
	TP4	High - Control	NA	0%
		Low - Control	NA	0%
	TP5	High - Control	NA	0%
		Low - Control	NA	0%
	TP6	High - Control	NA	0%
		Low - Control	NA	0%
	TP7	High - Control	NA	0%
		Low - Control	NA	0%
	TP8	High - Control	1.33	8.4%
		Low - Control	NA	0%
	TP9	High - Control	NA	0%
		Low - Control	NA	0%

Table SI-T8. Differentially expressed gene JGI-GO enrichments of NF data, per time-point.

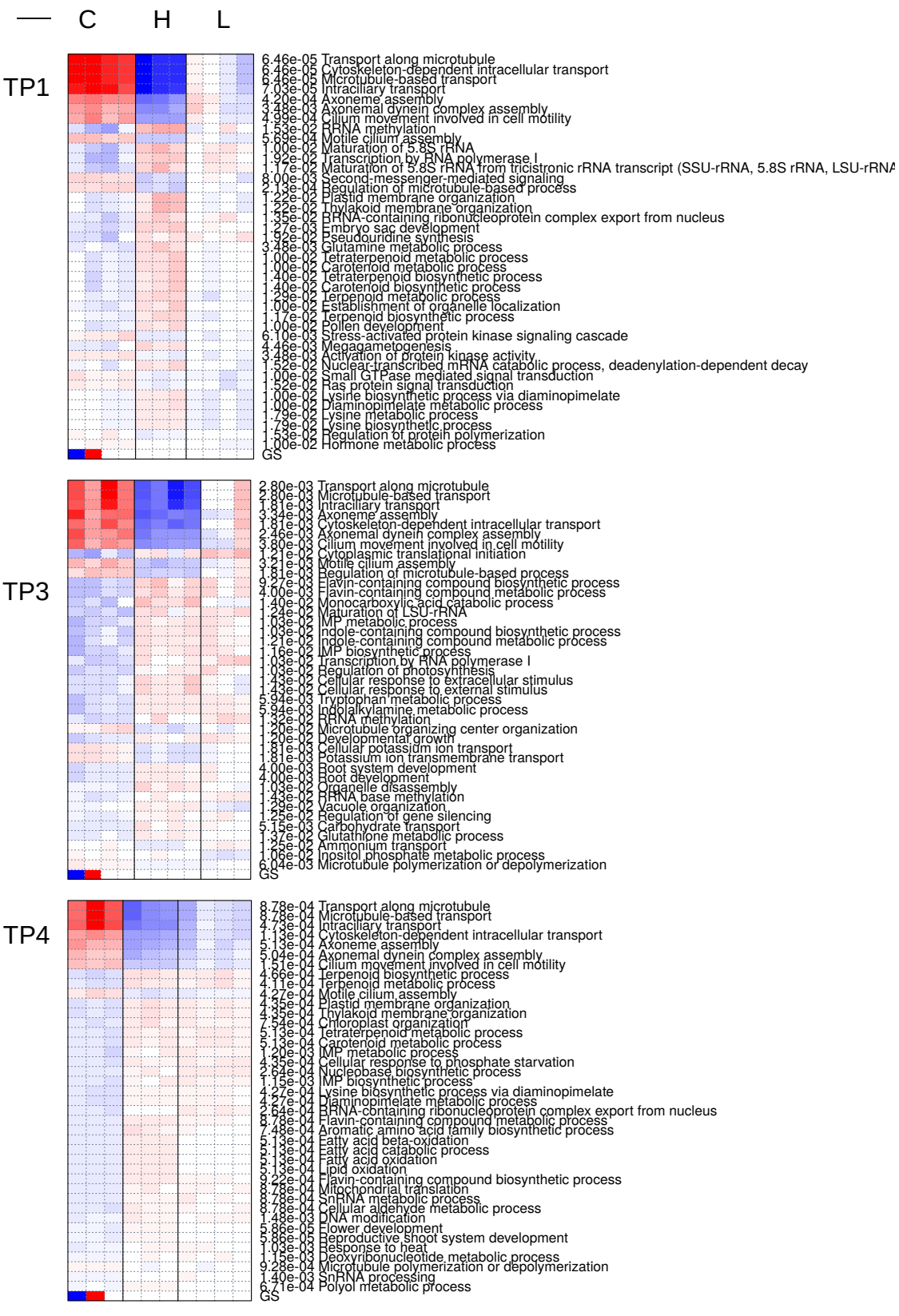
Time-point	Comparison	Direction	FDR	Number Genes	Pathways
1	Low-Vs-Control	Down	1.74E-09	14	Movement of cell or subcellular component
1	Low-Vs-Control	Down	2.89E-09	13	Microtubule-based movement
1	Low-Vs-Control	Down	9.59E-09	15	Microtubule-based process
1	Low-Vs-Control	Down	7.73E-08	10	Cilium organization
1	Low-Vs-Control	Down	1.41E-07	10	Cell projection organization
1	Low-Vs-Control	Down	1.39E-06	4	Intraciliary retrograde transport
1	Low-Vs-Control	Down	5.32E-06	5	Intraciliary transport
1	Low-Vs-Control	Down	0.00046035	6	Cilium assembly
1	Low-Vs-Control	Down	0.00046035	3	Protein localization to cilium
1	High-Vs-Control	Down	1.85E-60	83	Movement of cell or subcellular component
1	High-Vs-Control	Down	4.99E-57	67	Cell projection organization
1	High-Vs-Control	Down	2.24E-54	93	Microtubule-based process
1	High-Vs-Control	Down	5.61E-53	62	Plasma membrane bounded cell projection organization
1	High-Vs-Control	Down	1.61E-52	61	Cilium organization
1	High-Vs-Control	Down	1.03E-51	72	Microtubule-based movement
1	High-Vs-Control	Down	3.68E-45	54	Plasma membrane bounded cell projection assembly
1	High-Vs-Control	Down	1.06E-44	53	Cilium assembly
1	High-Vs-Control	Down	3.23E-34	36	Cilium movement
1	High-Vs-Control	Down	6.93E-32	35	Cell motility
1	High-Vs-Control	Down	8.72E-30	33	Cilium or flagellum-dependent cell motility
2	Treatment-Vs-C	Down	2.83E-10	16	Movement of cell or subcellular component
2	Treatment-Vs-C	Down	5.84E-08	13	Microtubule-based movement
2	Treatment-Vs-C	Down	2.13E-06	14	Microtubule-based process
2	Treatment-Vs-C	Down	1.48E-05	7	Cilium movement
2	Treatment-Vs-C	Down	0.00020821	8	Cell projection organization
2	Treatment-Vs-C	Down	0.00037445	7	Cell projection assembly
2	Treatment-Vs-C	Down	0.00114758	5	Cilium or flagellum-dependent cell motility
3	Low-Vs-Control	Down	8.69E-17	29	Movement of cell or subcellular component
3	Low-Vs-Control	Down	3.13E-14	25	Microtubule-based movement
3	Low-Vs-Control	Down	1.34E-12	29	Microtubule-based process
3	Low-Vs-Control	Down	3.78E-12	15	Cilium movement
3	Low-Vs-Control	Down	4.35E-10	18	Cell projection organization
3	Low-Vs-Control	Down	6.55E-10	17	Cilium organization
3	Low-Vs-Control	Down	9.45E-09	15	Cilium assembly
3	Low-Vs-Control	Down	9.79E-08	11	Cilium or flagellum-dependent cell motility
3	High-Vs-Control	Down	1.26E-68	87	Movement of cell or subcellular component
3	High-Vs-Control	Down	3.39E-59	95	Microtubule-based process
3	High-Vs-Control	Down	1.06E-57	75	Microtubule-based movement
3	High-Vs-Control	Down	4.02E-56	65	Cell projection organization
3	High-Vs-Control	Down	9.99E-53	60	Cilium organization
3	High-Vs-Control	Down	1.33E-44	52	Cilium assembly
3	High-Vs-Control	Down	1.06E-34	36	Cell motility
3	High-Vs-Control	Down	1.25E-33	35	Cilium movement
3	High-Vs-Control	Down	1.49E-32	34	Cilium or flagellum-dependent cell motility
4	Low-Vs-Control	Down	6.08E-57	77	Movement of cell or subcellular component
4	Low-Vs-Control	Down	2.01E-51	61	Cell projection organization
4	Low-Vs-Control	Down	5.10E-51	58	Cilium organization
4	Low-Vs-Control	Down	1.10E-47	66	Microtubule-based movement
4	Low-Vs-Control	Down	3.18E-45	80	Microtubule-based process
4	Low-Vs-Control	Down	5.63E-43	50	Cilium assembly
4	Low-Vs-Control	Down	5.74E-34	35	Cell motility
4	Low-Vs-Control	Down	9.30E-32	33	Cilium or flagellum-dependent cell motility
4	Low-Vs-Control	Down	3.29E-31	33	Cilium movement
4	Low-Vs-Control	Up	9.46E-06	9	RNA methylation
4	Low-Vs-Control	Up	9.46E-06	15	Methylation
4	Low-Vs-Control	Up	9.46E-06	12	Macromolecule methylation
4	Low-Vs-Control	Up	9.46E-06	6	Pyrimidine nucleotide metabolic process
4	Low-Vs-Control	Up	2.64E-05	11	RNA modification
4	Low-Vs-Control	Up	7.65E-05	6	TRNA methylation
4	Low-Vs-Control	Up	0.00021173	4	Pyrimidine ribonucleotide metabolic process
4	Low-Vs-Control	Up	0.00080545	12	NcRNA processing
4	Low-Vs-Control	Up	0.00080545	16	RNA processing
4	Low-Vs-Control	Up	0.00101945	7	TRNA modification
4	Low-Vs-Control	Up	0.00115252	13	NcRNA metabolic process
4	High-Vs-Control	Down	1.98E-62	87	Movement of cell or subcellular component
4	High-Vs-Control	Down	1.22E-60	71	Cell projection organization
4	High-Vs-Control	Down	6.46E-58	66	Cilium organization
4	High-Vs-Control	Down	1.26E-52	75	Microtubule-based movement
4	High-Vs-Control	Down	6.85E-50	92	Microtubule-based process
4	High-Vs-Control	Down	1.04E-48	57	Cilium assembly
4	High-Vs-Control	Down	7.36E-34	37	Cell motility
4	High-Vs-Control	Down	7.51E-33	36	Cilium movement
4	High-Vs-Control	Down	7.81E-32	35	Cilium or flagellum-dependent cell motility
4	High-Vs-Control	Up	0.00187848	16	Methylation
5	Low-Vs-Control	Down	2.74E-10	21	Movement of cell or subcellular component
5	Low-Vs-Control	Down	3.86E-09	12	Cilium or flagellum-dependent cell motility
5	Low-Vs-Control	Down	4.18E-09	12	Cell motility

5	Low-Vs-Control	Down	6.30E-07	10	Cilium movement
5	Low-Vs-Control	Down	1.38E-06	15	Microtubule-based movement
5	Low-Vs-Control	Down	7.53E-06	18	Microtubule-based process
5	Low-Vs-Control	Down	0.00023552	10	Cilium organization
5	Low-Vs-Control	Down	0.00047756	9	Cilium assembly
5	Low-Vs-Control	Up	7.60E-07	22	Peptide biosynthetic process
5	Low-Vs-Control	Up	1.03E-06	23	Amide biosynthetic process
5	Low-Vs-Control	Up	0.00037944	98	Organic substance metabolic process
5	Low-Vs-Control	Up	0.00044335	30	Organonitrogen compound biosynthetic process
5	Low-Vs-Control	Up	0.00048406	3	Fatty acid beta-oxidation using acyl-CoA oxidase
5	Low-Vs-Control	Up	0.00061544	93	Primary metabolic process
5	Low-Vs-Control	Up	0.00061544	48	Biosynthetic process
5	Low-Vs-Control	Up	0.00129453	92	Cellular metabolic process
5	Low-Vs-Control	Up	0.00129453	46	Organic substance biosynthetic process
5	Low-Vs-Control	Up	0.00138414	27	Oxidation-reduction process
5	Low-Vs-Control	Up	0.0014505	16	Lipid metabolic process
5	Low-Vs-Control	Up	0.00272091	64	Organonitrogen compound metabolic process
5	High-Vs-Control	Down	2.66E-36	51	Cell projection organization
5	High-Vs-Control	Down	2.66E-36	49	Cilium organization
5	High-Vs-Control	Down	2.66E-36	61	Movement of cell or subcellular component
5	High-Vs-Control	Down	8.28E-32	43	Cilium assembly
5	High-Vs-Control	Down	2.45E-28	64	Microtubule-based process
5	High-Vs-Control	Down	7.84E-27	49	Microtubule-based movement
5	High-Vs-Control	Down	3.60E-22	28	Cell motility
5	High-Vs-Control	Down	3.39E-20	26	Cilium or flagellum-dependent cell motility
5	High-Vs-Control	Down	2.07E-17	45	Organelle assembly
5	High-Vs-Control	Up	5.94E-15	54	Cellular amide metabolic process
5	High-Vs-Control	Up	5.94E-15	51	Amide biosynthetic process
5	High-Vs-Control	Up	5.94E-15	47	Translation
5	High-Vs-Control	Up	2.33E-14	48	Peptide metabolic process
5	High-Vs-Control	Up	4.80E-11	72	Organonitrogen compound biosynthetic process
5	High-Vs-Control	Up	1.80E-07	8	Fatty acid oxidation
5	High-Vs-Control	Up	1.80E-07	105	Biosynthetic process
5	High-Vs-Control	Up	3.23E-07	80	Cellular nitrogen compound biosynthetic process
5	High-Vs-Control	Up	3.23E-07	102	Organic substance biosynthetic process
5	High-Vs-Control	Up	5.38E-07	100	Cellular biosynthetic process
5	High-Vs-Control	Up	8.97E-07	63	Small molecule metabolic process
6	Low-Vs-Control	Down	6.22E-05	15	RRNA metabolic process
6	Low-Vs-Control	Down	0.00025652	14	Movement of cell or subcellular component
6	Low-Vs-Control	Down	0.0002771	17	Ribosome biogenesis
6	Low-Vs-Control	Down	0.00046027	19	NcRNA processing
6	Low-Vs-Control	Down	0.00069541	10	Cilium organization
6	Low-Vs-Control	Down	0.00069541	14	Organelle assembly
6	Low-Vs-Control	Down	0.00069541	12	Microtubule-based movement
6	Low-Vs-Control	Down	0.00128787	7	Cilium movement
6	Low-Vs-Control	Down	0.00128787	15	Microtubule-based process
6	Low-Vs-Control	Down	0.00533194	8	Cilium assembly
6	Low-Vs-Control	Up	3.94E-23	44	Peptide biosynthetic process
6	Low-Vs-Control	Up	5.78E-23	45	Peptide metabolic process
6	Low-Vs-Control	Up	4.19E-22	45	Amide biosynthetic process
6	Low-Vs-Control	Up	4.92E-21	46	Cellular amide metabolic process
6	Low-Vs-Control	Up	6.84E-13	52	Organonitrogen compound biosynthetic process
6	Low-Vs-Control	Up	1.03E-09	71	Organic substance biosynthetic process
6	Low-Vs-Control	Up	1.03E-09	72	Biosynthetic process
6	Low-Vs-Control	Up	1.46E-09	57	Cellular nitrogen compound biosynthetic process
6	Low-Vs-Control	Up	2.86E-09	69	Cellular biosynthetic process
6	Low-Vs-Control	Up	3.37E-09	50	Cellular macromolecule biosynthetic process
6	Low-Vs-Control	Up	5.48E-08	55	Gene expression
6	Low-Vs-Control	Up	1.49E-06	121	Cellular metabolic process
6	Low-Vs-Control	Up	1.63E-06	6	Fatty acid oxidation
6	High-Vs-Control	Down	6.04E-42	75	Movement of cell or subcellular component
6	High-Vs-Control	Down	2.28E-35	65	Microtubule-based movement
6	High-Vs-Control	Down	1.84E-34	53	Cilium organization
6	High-Vs-Control	Down	7.23E-34	55	Cell projection organization
6	High-Vs-Control	Down	3.02E-29	46	Cilium assembly
6	High-Vs-Control	Down	1.46E-28	75	Microtubule-based process
6	High-Vs-Control	Down	1.55E-26	73	Ribosome biogenesis
6	High-Vs-Control	Down	6.53E-25	33	Cell motility
6	High-Vs-Control	Down	5.14E-24	32	Cilium movement
6	High-Vs-Control	Down	1.15E-23	61	Organelle assembly
6	High-Vs-Control	Up	1.04E-15	62	Translation
6	High-Vs-Control	Up	3.55E-15	70	Cellular amide metabolic process
6	High-Vs-Control	Up	4.19E-15	65	Amide biosynthetic process
6	High-Vs-Control	Up	4.19E-15	63	Peptide metabolic process
6	High-Vs-Control	Up	1.56E-12	105	Small molecule metabolic process
6	High-Vs-Control	Up	9.38E-12	64	Oxoacid metabolic process
6	High-Vs-Control	Up	1.01E-11	63	Carboxylic acid metabolic process
6	High-Vs-Control	Up	1.65E-10	96	Organonitrogen compound biosynthetic process

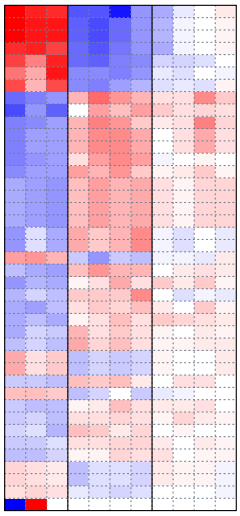
6	High-Vs-Control	Up	3.13E-10	32	Monocarboxylic acid metabolic process
6	High-Vs-Control	Up	7.17E-10	90	Oxidation-reduction process
6	High-Vs-Control	Up	3.28E-09	23	Small molecule catabolic process
6	High-Vs-Control	Up	2.93E-08	17	Organic acid catabolic process
7	Low-Vs-Control	Down	3.02E-12	47	Microtubule-based process
7	Low-Vs-Control	Down	1.06E-11	37	Movement of cell or subcellular component
7	Low-Vs-Control	Down	1.12E-09	26	Cilium organization
7	Low-Vs-Control	Down	7.54E-09	26	Cell projection organization
7	Low-Vs-Control	Down	7.54E-09	18	Cell motility
7	Low-Vs-Control	Down	8.17E-09	23	Cilium assembly
7	Low-Vs-Control	Down	8.17E-09	30	Microtubule-based movement
7	Low-Vs-Control	Down	3.94E-08	26	Microtubule cytoskeleton organization
7	Low-Vs-Control	Down	1.43E-07	16	Cilium or flagellum-dependent cell motility
7	Low-Vs-Control	Up	6.86E-27	71	Translation
7	Low-Vs-Control	Up	8.36E-26	74	Amide biosynthetic process
7	Low-Vs-Control	Up	8.36E-26	72	Peptide metabolic process
7	Low-Vs-Control	Up	6.80E-25	114	Organonitrogen compound biosynthetic process
7	Low-Vs-Control	Up	6.81E-25	77	Cellular amide metabolic process
7	Low-Vs-Control	Up	3.47E-22	74	Oxoacid metabolic process
7	Low-Vs-Control	Up	3.56E-22	112	Small molecule metabolic process
7	Low-Vs-Control	Up	1.57E-21	72	Carboxylic acid metabolic process
7	Low-Vs-Control	Up	6.82E-16	155	Biosynthetic process
7	Low-Vs-Control	Up	7.73E-16	22	Amino acid activation
7	Low-Vs-Control	Up	1.14E-14	149	Organic substance biosynthetic process
7	Low-Vs-Control	Up	1.48E-14	147	Cellular biosynthetic process
7	High-Vs-Control	Down	7.15E-38	76	Movement of cell or subcellular component
7	High-Vs-Control	Down	1.23E-35	90	Microtubule-based process
7	High-Vs-Control	Down	4.20E-30	64	Microtubule-based movement
7	High-Vs-Control	Down	1.14E-29	52	Cilium organization
7	High-Vs-Control	Down	5.37E-29	54	Cell projection organization
7	High-Vs-Control	Down	6.15E-25	45	Cilium assembly
7	High-Vs-Control	Down	1.63E-22	33	Cell motility
7	High-Vs-Control	Down	7.63E-21	31	Cilium or flagellum-dependent cell motility
7	High-Vs-Control	Down	2.19E-20	31	Cilium movement
7	High-Vs-Control	Up	3.24E-28	101	Oxoacid metabolic process
7	High-Vs-Control	Up	4.45E-28	99	Carboxylic acid metabolic process
7	High-Vs-Control	Up	2.83E-26	140	Oxidation-reduction process
7	High-Vs-Control	Up	8.80E-25	147	Small molecule metabolic process
7	High-Vs-Control	Up	1.31E-22	78	Translation
7	High-Vs-Control	Up	3.47E-21	82	Amide biosynthetic process
7	High-Vs-Control	Up	6.66E-21	79	Peptide metabolic process
7	High-Vs-Control	Up	9.90E-20	85	Cellular amide metabolic process
7	High-Vs-Control	Up	2.89E-17	126	Organonitrogen compound biosynthetic process
7	High-Vs-Control	Up	2.94E-17	34	Small molecule catabolic process
7	High-Vs-Control	Up	1.24E-14	55	Cellular amino acid metabolic process
7	High-Vs-Control	Up	1.36E-13	23	Amino acid activation
8	Low-Vs-Control	Down	1.63E-23	52	DNA replication
8	Low-Vs-Control	Down	5.50E-22	106	DNA metabolic process
8	Low-Vs-Control	Down	4.55E-21	66	Cell cycle process
8	Low-Vs-Control	Down	4.55E-21	81	Cell cycle
8	Low-Vs-Control	Down	9.20E-20	42	DNA-dependent DNA replication
8	Low-Vs-Control	Down	5.17E-16	250	Nucleic acid metabolic process
8	Low-Vs-Control	Down	3.93E-15	234	Cellular component organization or biogenesis
8	Low-Vs-Control	Down	2.98E-14	316	Cellular aromatic compound metabolic process
8	Low-Vs-Control	Down	1.22E-13	314	Heterocycle metabolic process
8	Low-Vs-Control	Down	1.40E-13	319	Organic cyclic compound metabolic process
8	Low-Vs-Control	Down	4.46E-13	293	Nucleobase-containing compound metabolic process
8	Low-Vs-Control	Down	4.46E-13	32	Chromosome segregation
8	Low-Vs-Control	Down	6.54E-13	45	Mitotic cell cycle
8	Low-Vs-Control	Down	1.33E-12	39	Mitotic cell cycle process
8	Low-Vs-Control	Down	8.17E-12	37	Organelle fission
8	Low-Vs-Control	Up	1.24E-05	31	Response to external stimulus
8	Low-Vs-Control	Up	2.06E-05	22	Response to biotic stimulus
8	Low-Vs-Control	Up	3.72E-05	21	Response to external biotic stimulus
8	Low-Vs-Control	Up	0.00041742	18	Defense response to other organism
8	Low-Vs-Control	Up	0.00061767	9	Autophagosome assembly
8	Low-Vs-Control	Up	0.00311142	20	Defense response
8	Low-Vs-Control	Up	0.00311142	91	Catabolic process
8	Low-Vs-Control	Up	0.00569079	13	Cellular amino acid catabolic process
8	Low-Vs-Control	Up	0.0074462	23	Small molecule catabolic process
8	Low-Vs-Control	Up	0.00779519	26	Multi-organism process
8	Low-Vs-Control	Up	0.00779519	11	Process utilizing autophagic mechanism
8	Low-Vs-Control	Up	0.00882362	7	Immune effector process
8	High-Vs-Control	Down	1.59E-30	93	Microtubule-based process
8	High-Vs-Control	Down	1.59E-30	98	Cell cycle
8	High-Vs-Control	Down	1.47E-28	78	Cell cycle process
8	High-Vs-Control	Down	2.04E-25	55	DNA replication
8	High-Vs-Control	Down	1.43E-22	46	DNA-dependent DNA replication

8	High-Vs-Control	Down	2.17E-21	58	Mitotic cell cycle
8	High-Vs-Control	Down	2.17E-21	64	Movement of cell or subcellular component
8	High-Vs-Control	Down	2.63E-21	109	DNA metabolic process
8	High-Vs-Control	Down	1.54E-19	49	Mitotic cell cycle process
8	High-Vs-Control	Down	7.13E-19	39	Chromosome segregation
8	High-Vs-Control	Down	1.45E-18	37	Nuclear chromosome segregation
8	High-Vs-Control	Down	5.66E-18	46	Organelle fission
8	High-Vs-Control	Down	1.25E-17	55	Microtubule-based movement
8	High-Vs-Control	Down	7.19E-17	33	Sister chromatid segregation
8	High-Vs-Control	Down	9.27E-17	39	Nuclear division
8	High-Vs-Control	Up	2.47E-22	123	Oxoacid metabolic process
8	High-Vs-Control	Up	4.85E-22	120	Carboxylic acid metabolic process
8	High-Vs-Control	Up	1.73E-16	183	Small molecule metabolic process
8	High-Vs-Control	Up	1.73E-16	77	Cellular amino acid metabolic process
8	High-Vs-Control	Up	5.88E-14	103	Cellular amide metabolic process
8	High-Vs-Control	Up	7.96E-14	95	Amide biosynthetic process
8	High-Vs-Control	Up	1.33E-13	86	Translation
8	High-Vs-Control	Up	1.37E-13	160	Oxidation-reduction process
8	High-Vs-Control	Up	3.10E-13	90	Peptide metabolic process
8	High-Vs-Control	Up	3.72E-12	163	Organonitrogen compound biosynthetic process
8	High-Vs-Control	Up	6.60E-10	25	Organic acid catabolic process
8	High-Vs-Control	Up	8.24E-10	106	Catabolic process
9	Low-Vs-Control	Down	1.80E-39	101	Cell cycle process
9	Low-Vs-Control	Down	1.80E-39	124	Cell cycle
9	Low-Vs-Control	Down	3.41E-24	135	DNA metabolic process
9	Low-Vs-Control	Down	8.78E-24	69	Mitotic cell cycle
9	Low-Vs-Control	Down	4.09E-23	58	Organelle fission
9	Low-Vs-Control	Down	1.07E-22	59	Mitotic cell cycle process
9	Low-Vs-Control	Down	3.34E-21	57	DNA replication
9	Low-Vs-Control	Down	1.31E-20	48	Nuclear division
9	Low-Vs-Control	Down	1.78E-20	45	Chromosome segregation
9	Low-Vs-Control	Down	2.53E-18	95	Cellular response to DNA damage stimulus
9	Low-Vs-Control	Down	1.47E-17	46	DNA-dependent DNA replication
9	Low-Vs-Control	Down	2.44E-17	40	Nuclear chromosome segregation
9	Low-Vs-Control	Down	3.25E-17	37	Sister chromatid segregation
9	Low-Vs-Control	Down	4.61E-17	36	Mitotic nuclear division
9	Low-Vs-Control	Down	7.88E-17	87	DNA repair
9	Low-Vs-Control	Up	4.04E-18	140	Oxoacid metabolic process
9	Low-Vs-Control	Up	1.16E-17	136	Carboxylic acid metabolic process
9	Low-Vs-Control	Up	7.66E-17	93	Cellular amino acid metabolic process
9	Low-Vs-Control	Up	2.93E-13	201	Oxidation-reduction process
9	Low-Vs-Control	Up	5.93E-13	143	Catabolic process
9	Low-Vs-Control	Up	6.81E-12	214	Small molecule metabolic process
9	Low-Vs-Control	Up	8.02E-11	29	Amino acid activation
9	Low-Vs-Control	Up	1.04E-10	125	Cellular catabolic process
9	Low-Vs-Control	Up	2.18E-10	200	Organonitrogen compound biosynthetic process
9	Low-Vs-Control	Up	3.84E-10	116	Cellular amide metabolic process
9	Low-Vs-Control	Up	4.67E-10	27	TRNA aminoacylation for protein translation
9	Low-Vs-Control	Up	1.42E-09	105	Amide biosynthetic process
9	Low-Vs-Control	Up	2.52E-09	124	Organic substance catabolic process
9	High-Vs-Control	Down	1.70E-34	129	Microtubule-based process
9	High-Vs-Control	Down	2.90E-30	131	Cell cycle
9	High-Vs-Control	Down	1.27E-27	101	Cell cycle process
9	High-Vs-Control	Down	5.57E-22	86	Movement of cell or subcellular component
9	High-Vs-Control	Down	1.42E-20	78	Microtubule-based movement
9	High-Vs-Control	Down	9.50E-20	74	Mitotic cell cycle
9	High-Vs-Control	Down	7.70E-19	67	Microtubule cytoskeleton organization
9	High-Vs-Control	Down	1.80E-17	76	Cytoskeleton organization
9	High-Vs-Control	Down	2.30E-17	147	DNA metabolic process
9	High-Vs-Control	Down	3.53E-16	59	DNA replication
9	High-Vs-Control	Down	6.93E-16	59	Mitotic cell cycle process
9	High-Vs-Control	Down	1.58E-15	286	Organelle organization
9	High-Vs-Control	Down	4.20E-14	55	Organelle fission
9	High-Vs-Control	Down	4.20E-14	105	Cellular response to DNA damage stimulus
9	High-Vs-Control	Down	4.20E-14	44	Chromosome segregation
9	High-Vs-Control	Up	1.33E-16	148	Carboxylic acid metabolic process
9	High-Vs-Control	Up	1.33E-16	151	Oxoacid metabolic process
9	High-Vs-Control	Up	1.33E-16	170	Catabolic process
9	High-Vs-Control	Up	1.75E-14	151	Cellular catabolic process
9	High-Vs-Control	Up	2.22E-14	97	Cellular amino acid metabolic process
9	High-Vs-Control	Up	1.67E-12	100	Organonitrogen compound catabolic process
9	High-Vs-Control	Up	2.64E-12	243	Small molecule metabolic process
9	High-Vs-Control	Up	4.77E-12	148	Organic substance catabolic process
9	High-Vs-Control	Up	1.75E-11	219	Oxidation-reduction process
9	High-Vs-Control	Up	7.93E-11	32	Organic acid catabolic process
9	High-Vs-Control	Up	1.53E-09	50	Cellular amino acid biosynthetic process
9	High-Vs-Control	Up	2.51E-09	109	Response to chemical
9	High-Vs-Control	Up	1.59E-08	40	Small molecule catabolic process

Table SI-T9. PGSEA JGI-GO enrichments of NF transcriptomics data, per time-point. Given are the class (C=Control, H=High and L=Low), FDR and the name of the JGI-GO. TP2 PGSEA results are missing due to too low sample size for enrichment analysis. Color red indicates relatively increased gene expression, blue indicates relative reduction in expression.

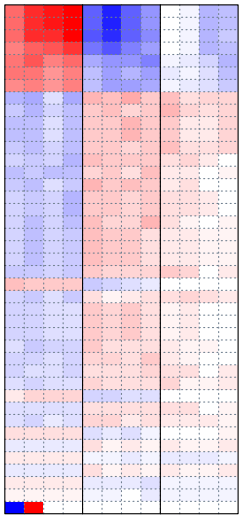


TP5



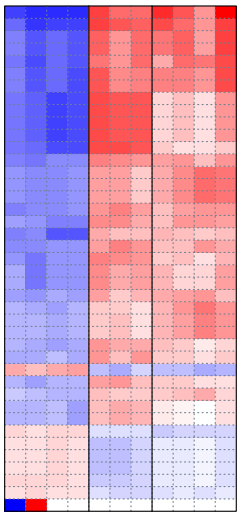
4.50e-04 Intraciliary transport
1.08e-04 Transport along microtubule
1.08e-04 Microtubule-based transport
1.55e-04 Cytoskeleton-dependent intracellular transport
2.22e-04 Axoneme assembly
1.33e-03 Axonemal dynein complex assembly
1.50e-03 Cilium movement involved in cell motility
1.07e-03 Terpenoid biosynthetic process
1.58e-03 Formation of cytoplasmic translation initiation complex
2.20e-03 Terpenoid metabolic process
1.07e-03 Tetraterpenoid biosynthetic process
1.07e-03 Carotenoid biosynthetic process
1.07e-03 Photosynthetic electron transport chain
2.12e-04 Chloroplast organization
7.38e-05 Fatty acid beta-oxidation
7.38e-05 Fatty acid catabolic process
7.38e-05 Fatty acid oxidation
7.38e-05 Lipid oxidation
1.91e-03 Riboflavin metabolic process
1.91e-03 Riboflavin biosynthetic process
1.07e-03 Motile cilium assembly
3.89e-04 Monocarboxylic acid catabolic process
1.78e-03 Methionine metabolic process
2.20e-03 Flavin-containing compound metabolic process
1.78e-03 Branched-chain amino acid metabolic process
1.07e-03 Methionine biosynthetic process
1.78e-03 Polyol catabolic process
1.33e-03 Alcohol catabolic process
1.78e-03 Cellular potassium ion transport
1.78e-03 Potassium ion transmembrane transport
1.58e-03 Organic hydroxy compound catabolic process
1.91e-03 Vesicle budding from membrane
2.20e-03 Sulfur amino acid biosynthetic process
5.12e-04 Response to hydrogen peroxide
2.05e-03 Protein localization to chloroplast
6.61e-04 Pteridine-containing compound biosynthetic process
1.33e-03 Cellular modified amino acid biosynthetic process
2.20e-03 Sulfate transport
2.20e-03 Sulfate transmembrane transport
2.12e-04 Regulation of defense response
GS

TP6



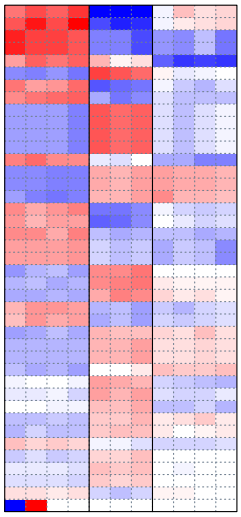
3.55e-05 Transport along microtubule
3.55e-05 Microtubule-based transport
2.52e-05 Intraciliary transport
2.52e-05 Cytoskeleton-dependent intracellular transport
1.22e-05 Axoneme assembly
1.22e-05 Axonemal dynein complex assembly
1.22e-05 Cilium movement involved in cell motility
3.55e-05 Terpenoid metabolic process
1.85e-05 Response to bacterium
2.52e-05 Tetraterpenoid metabolic process
2.52e-05 Carotenoid metabolic process
2.52e-05 Defense response to bacterium
2.52e-05 Indole-containing compound metabolic process
1.87e-05 Polyol catabolic process
4.16e-05 Acyl-CoA metabolic process
3.55e-05 Tryptophan metabolic process
3.55e-05 Indolalkylamine metabolic process
3.55e-05 Monosaccharide catabolic process
1.22e-05 Nucleoside bisphosphate metabolic process
1.22e-05 Ribonucleoside bisphosphate metabolic process
1.22e-05 Purine nucleoside bisphosphate metabolic process
3.55e-05 Glyceraldehyde-3-phosphate metabolic process
1.85e-05 SrtRNA metabolic process
1.85e-05 Aspartate family amino acid biosynthetic process
1.75e-05 Nucleoside bisphosphate biosynthetic process
1.75e-05 Ribonucleoside bisphosphate biosynthetic process
1.75e-05 Purine nucleoside bisphosphate biosynthetic process
2.52e-05 Sulfur amino acid metabolic process
2.52e-05 NADP metabolic process
3.55e-05 Glucose 6-phosphate metabolic process
3.55e-05 Glucose metabolic process
1.85e-05 Transcription by RNA polymerase I
2.52e-05 Pentose-phosphate shunt
3.55e-05 Chloroplast organization
3.55e-05 SnRNA processing
3.55e-05 Nucleoside diphosphate phosphorylation
1.22e-05 Drug transmembrane transport
3.55e-05 Nucleotide phosphorylation
1.22e-05 Ammonium transport
3.58e-05 Organic cation transport
GS

TP7



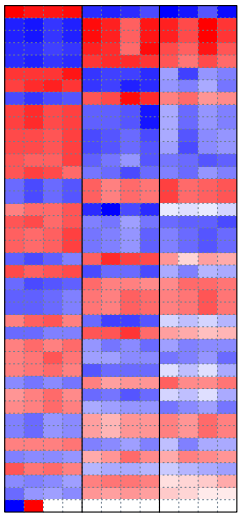
1.99e-05 Cellular aldehyde metabolic process
9.62e-06 Response to cytokinin
1.24e-05 Tetraterpenoid biosynthetic process
1.24e-05 Carotenoid biosynthetic process
1.42e-05 Mitochondrial gene expression
1.17e-05 Tetraterpenoid metabolic process
1.17e-05 Carotenoid metabolic process
9.62e-06 Fatty acid beta-oxidation
9.62e-06 Fatty acid catabolic process
9.62e-06 Fatty acid oxidation
9.62e-06 Lipid oxidation
2.85e-06 Monocarboxylic acid catabolic process
4.22e-06 NADP metabolic process
1.35e-05 Glycolytic process
1.35e-05 ATP generation from ADP
1.35e-05 ADP metabolic process
7.51e-06 Starch metabolic process
1.17e-05 Monosaccharide catabolic process
1.37e-05 Glutamate metabolic process
9.62e-06 Starch biosynthetic process
9.62e-06 Response to reactive oxygen species
1.99e-05 Response to water deprivation
1.99e-05 Response to water
1.24e-05 Phyllome development
1.35e-05 Ribonucleoside diphosphate metabolic process
1.80e-05 Purine nucleoside diphosphate metabolic process
1.80e-05 Purine ribonucleoside diphosphate metabolic process
1.24e-05 Response to antibiotic
1.83e-05 Response to auxin
1.24e-05 Positive regulation of cell cycle
1.17e-05 Response to hydrogen peroxide
1.35e-05 Floral organ development
1.17e-05 Cellular response to extracellular stimulus
1.17e-05 Cellular response to external stimulus
6.78e-07 Cofactor transport
1.17e-05 DNA alkylation
1.17e-05 DNA methylation
1.17e-05 DNA methylation or demethylation
1.17e-05 DNA modification
9.62e-06 Ammonium transport
GS

TP8



5.41e-06 Axoneme assembly
1.26e-05 Axonemal dynein complex assembly
6.71e-06 DNA strand elongation involved in DNA replication
6.71e-06 DNA strand elongation
7.25e-06 Formation of cytoplasmic translation initiation complex
3.97e-06 Monocarboxylic acid catabolic process
1.14e-05 Chromosome separation
4.06e-06 Protein polymerization
4.06e-06 Fatty acid beta-oxidation
4.06e-06 Fatty acid catabolic process
4.06e-06 Fatty acid oxidation
4.06e-06 Lipid oxidation
1.31e-05 RRNA modification
4.78e-07 Autophagosome assembly
4.78e-07 Autophagosome organization
6.76e-06 Vacuole organization
6.71e-06 Regulation of mitotic cell cycle phase transition
9.18e-06 Cell cycle checkpoint
3.97e-06 Cytokinesis
1.14e-05 Mitotic cytokinesis
1.14e-05 Cytoskeleton-dependent cytokinesis
4.06e-06 Branched-chain amino acid metabolic process
4.78e-07 Starch metabolic process
4.06e-06 Starch biosynthetic process
7.09e-06 Cell proliferation
6.71e-06 Regulation of cell proliferation
1.13e-05 Organelle disassembly
4.83e-07 Autophagy
4.83e-07 Process utilizing autophagic mechanism
9.40e-06 Exocytosis
1.12e-05 Phyllome development
9.37e-06 Response to auxin
9.09e-06 Sulfur amino acid biosynthetic process
7.53e-06 Macroautophagy
6.71e-06 Organic hydroxy compound catabolic process
6.71e-06 Plant organ morphogenesis
1.12e-05 Oligosaccharide biosynthetic process
6.59e-06 Regulation of catabolic process
3.97e-06 Regulation of cellular catabolic process
1.31e-05 DNA alkylation
GS

TP9



6.30e-08 Spindle organization
1.60e-07 Autophagosome assembly
1.60e-07 Autophagosome organization
3.23e-07 Vacuole organization
3.00e-09 Alpha-amino acid catabolic process
2.37e-07 Cell cycle checkpoint
4.21e-08 Meiotic nuclear division
9.47e-08 Branched-chain amino acid metabolic process
3.23e-07 Negative regulation of organelle organization
3.23e-07 Negative regulation of cellular component organization
1.63e-07 Mitotic cell cycle checkpoint
2.22e-07 Negative regulation of mitotic cell cycle
1.12e-07 Cytokinesis
4.21e-08 Chromosome condensation
4.21e-08 Autophagy
4.21e-08 Process utilizing autophagic mechanism
1.15e-07 Chromosome organization involved in meiotic cell cycle
4.21e-08 Cell proliferation
1.45e-07 Mitotic cytokinesis
1.45e-07 Cytoskeleton-dependent cytokinesis
3.23e-07 Neurotransmitter metabolic process
9.47e-08 Negative regulation of cell cycle process
4.21e-08 Response to heat
4.21e-08 Sulfate transport
4.21e-08 Sulfate transmembrane transport
2.22e-07 Meiotic chromosome segregation
7.56e-08 Branched-chain amino acid biosynthetic process
1.21e-07 Positive regulation of cell cycle
7.68e-08 Plant-type cell wall organization or biogenesis
1.45e-07 Meiosis I cell cycle process
5.99e-08 Macroautophagy
2.06e-07 Meiosis I
1.15e-07 Plant-type cell wall biogenesis
2.87e-07 Cellular biogenic amine metabolic process
2.87e-07 Cellular amine metabolic process
3.23e-07 Negative regulation of cell cycle phase transition
3.23e-07 Sulfur compound transport
1.45e-07 Transcription by RNA polymerase I
1.21e-07 Inorganic anion transmembrane transport
2.20e-07 Disaccharide metabolic process
GS

Table SI-T10. maSigPro time-profile JGI-GO enrichments of NF transcriptomics data, per time-point. Given are the class (C=Control, H=High and L=Low), FDR and the name of the JGI-GO. TP2 PGSEA results are missing due to too low sample size for enrichment analysis.

maSigPro Cluster	FDR	#Genes	Gene Set size	Functional Category
Cluster01	2.77E-07	65	511	Catabolic process
Cluster01	9.12E-07	12	26	Process utilizing autophagic mechanism
Cluster01	9.12E-07	12	26	Autophagy
Cluster01	7.70E-06	55	454	Cellular catabolic process
Cluster01	7.70E-06	10	21	Vacuole organization
Cluster01	1.64E-05	8	14	Autophagosome assembly
Cluster01	1.64E-05	9	18	Sulfur compound transport
Cluster01	1.64E-05	8	14	Autophagosome organization
Cluster01	1.64E-05	12	35	Aromatic amino acid family metabolic process
Cluster01	2.30E-05	14	50	Organic acid catabolic process
Cluster01	2.30E-05	14	50	Carboxylic acid catabolic process
Cluster01	2.35E-05	7	11	Sulfate transmembrane transport
Cluster01	2.35E-05	7	11	Sulfate transport
Cluster01	3.96E-05	9	21	Macroautophagy
Cluster01	7.19E-05	36	274	Organonitrogen compound catabolic process
Cluster01	0.00016204	17	85	Response to external stimulus
Cluster01	0.0002184	51	474	Organic substance catabolic process
Cluster01	0.00023981	8	20	Monocarboxylic acid catabolic process
Cluster01	0.0002812	24	159	Cellular response to chemical stimulus
Cluster01	0.0002812	10	33	Response to extracellular stimulus
Cluster01	0.00057197	9	29	Cellular response to extracellular stimulus
Cluster01	0.00057197	9	29	Cellular response to external stimulus
Cluster01	0.00075529	37	322	Response to chemical
Cluster01	0.00126887	38	343	Lipid metabolic process
Cluster01	0.00135714	72	805	Oxidation-reduction process
Cluster01	0.00148872	15	84	Small molecule catabolic process
Cluster01	0.00153437	6	14	Lipid homeostasis
Cluster01	0.00159348	30	250	Cellular amino acid metabolic process
Cluster01	0.00172899	8	27	Alpha-amino acid catabolic process
Cluster01	0.00172899	49	496	Proteolysis
Cluster02	1.62E-11	47	337	DNA metabolic process
Cluster02	5.69E-10	35	223	Cellular response to DNA damage stimulus
Cluster02	1.06E-09	33	207	DNA repair
Cluster02	2.31E-09	33	215	Cell cycle
Cluster02	7.03E-09	27	155	Cell cycle process
Cluster02	6.84E-08	14	44	Recombinational repair
Cluster02	3.19E-07	20	105	DNA recombination
Cluster02	3.64E-07	38	338	Cellular response to stress
Cluster02	1.09E-06	16	73	Regulation of organelle organization
Cluster02	1.09E-06	15	64	Double-strand break repair
Cluster02	1.14E-06	10	26	Telomere organization
Cluster02	1.14E-06	10	26	Anatomical structure homeostasis
Cluster02	1.14E-06	10	26	Telomere maintenance
Cluster02	1.59E-06	64	800	Organelle organization
Cluster02	4.27E-06	11	37	Double-strand break repair via homologous recombir
Cluster02	4.38E-06	35	334	Chromosome organization
Cluster02	6.03E-06	17	96	Regulation of cellular component organization
Cluster02	1.25E-05	44	497	Response to stress
Cluster02	2.72E-05	11	45	DNA duplex unwinding
Cluster02	2.72E-05	11	45	Meiotic cell cycle
Cluster02	2.72E-05	16	96	Regulation of cell cycle
Cluster02	2.99E-05	8	22	Protein polymerization
Cluster02	3.32E-05	17	110	Mitotic cell cycle
Cluster02	3.81E-05	11	47	DNA geometric change
Cluster02	6.51E-05	15	92	DNA replication
Cluster02	0.00015923	59	833	Cellular response to stimulus
Cluster02	0.00017532	11	55	Regulation of cell cycle process
Cluster02	0.00021409	9	37	Negative regulation of cell cycle
Cluster02	0.00028699	12	69	Nuclear division
Cluster02	0.00034105	10	49	Regulation of mitotic cell cycle

Cluster03	1.08E-56	62	107	Photosynthesis
Cluster03	7.05E-32	60	218	Generation of precursor metabolites and energy
Cluster03	1.06E-28	33	60	Photosynthesis, light reaction
Cluster03	9.79E-24	56	263	Cofactor metabolic process
Cluster03	1.35E-21	23	37	Porphyrin-containing compound biosynthetic process
Cluster03	1.61E-21	26	51	Porphyrin-containing compound metabolic process
Cluster03	2.01E-20	41	161	Cofactor biosynthetic process
Cluster03	2.38E-20	28	67	Pigment metabolic process
Cluster03	4.10E-20	26	57	Tetrapyrrole metabolic process
Cluster03	4.10E-20	23	42	Tetrapyrrole biosynthetic process
Cluster03	7.24E-19	25	57	Pigment biosynthetic process
Cluster03	1.62E-16	93	899	Small molecule metabolic process
Cluster03	2.77E-14	14	20	Chlorophyll biosynthetic process
Cluster03	7.59E-14	259	4307	Cellular metabolic process
Cluster03	9.59E-14	24	80	Response to light stimulus
Cluster03	1.15E-13	81	805	Oxidation-reduction process
Cluster03	3.11E-13	16	32	Chlorophyll metabolic process
Cluster03	3.11E-13	16	32	Photosynthesis, light harvesting
Cluster03	2.43E-12	24	92	Response to radiation
Cluster03	6.72E-12	9	9	Protoporphyrinogen IX metabolic process
Cluster04	9.59E-91	122	184	Ribosome biogenesis
Cluster04	1.80E-85	133	238	Ribonucleoprotein complex biogenesis
Cluster04	4.01E-80	132	252	NcRNA processing
Cluster04	1.29E-74	141	313	NcRNA metabolic process
Cluster04	9.28E-71	281	1231	Gene expression
Cluster04	1.48E-64	85	125	RRNA metabolic process
Cluster04	6.63E-64	369	2077	Cellular nitrogen compound metabolic process
Cluster04	1.29E-63	83	121	RRNA processing
Cluster04	3.91E-59	147	429	RNA processing
Cluster04	4.63E-50	213	961	RNA metabolic process
Cluster04	3.51E-43	302	1840	Organic cyclic compound metabolic process
Cluster04	1.35E-42	296	1796	Cellular aromatic compound metabolic process
Cluster04	1.97E-42	296	1800	Heterocycle metabolic process
Cluster04	5.91E-42	280	1661	Nucleobase-containing compound metabolic process
Cluster04	1.53E-36	226	1274	Nucleic acid metabolic process
Cluster04	3.86E-36	67	144	RNA modification
Cluster04	1.03E-34	507	4258	Primary metabolic process
Cluster04	1.22E-34	525	4473	Organic substance metabolic process
Cluster04	4.01E-34	481	3978	Nitrogen compound metabolic process
Cluster04	4.74E-33	506	4307	Cellular metabolic process
Cluster05	1.47E-64	144	864	Organonitrogen compound biosynthetic process
Cluster05	4.60E-59	91	330	Translation
Cluster05	1.33E-58	91	335	Peptide biosynthetic process
Cluster05	4.48E-58	95	378	Amide biosynthetic process
Cluster05	2.83E-57	92	357	Peptide metabolic process
Cluster05	8.01E-57	98	421	Cellular amide metabolic process
Cluster05	1.46E-46	173	1718	Biosynthetic process
Cluster05	2.17E-45	169	1677	Organic substance biosynthetic process
Cluster05	3.88E-45	167	1648	Cellular biosynthetic process
Cluster05	2.88E-35	126	1173	Cellular nitrogen compound biosynthetic process
Cluster05	2.66E-31	104	899	Small molecule metabolic process
Cluster05	7.10E-31	56	250	Cellular amino acid metabolic process
Cluster05	1.22E-30	71	427	Carboxylic acid metabolic process
Cluster05	3.31E-30	71	434	Oxoacid metabolic process
Cluster05	6.54E-30	71	439	Organic acid metabolic process
Cluster05	1.32E-28	192	2797	Organonitrogen compound metabolic process
Cluster05	1.84E-24	242	4307	Cellular metabolic process
Cluster05	1.80E-22	148	2077	Cellular nitrogen compound metabolic process
Cluster05	2.19E-22	94	972	Cellular macromolecule biosynthetic process
Cluster05	4.99E-22	107	1231	Gene expression
Cluster06	1.29E-46	69	215	Cell cycle

Cluster06	4.11E-46	60	155	Cell cycle process
Cluster06	4.67E-37	43	92	DNA replication
Cluster06	3.76E-34	70	337	DNA metabolic process
Cluster06	6.34E-31	35	72	DNA-dependent DNA replication
Cluster06	6.66E-30	37	88	Organelle fission
Cluster06	1.76E-29	40	110	Mitotic cell cycle
Cluster06	2.93E-28	36	90	Mitotic cell cycle process
Cluster06	1.75E-27	31	64	Chromosome segregation
Cluster06	7.48E-25	30	69	Nuclear division
Cluster06	4.19E-23	27	59	Nuclear chromosome segregation
Cluster06	9.70E-22	87	800	Organelle organization
Cluster06	5.45E-21	54	334	Chromosome organization
Cluster06	1.05E-20	24	52	Sister chromatid segregation
Cluster06	1.85E-17	39	207	DNA repair
Cluster06	2.65E-17	21	49	Mitotic nuclear division
Cluster06	3.58E-17	40	223	Cellular response to DNA damage stimulus
Cluster06	9.73E-17	19	40	Mitotic sister chromatid segregation
Cluster06	1.08E-16	14	18	DNA replication initiation
Cluster06	4.42E-16	90	1040	Cellular component organization
Cluster07	1.24E-66	67	137	Movement of cell or subcellular component
Cluster07	1.24E-53	67	200	Microtubule-based process
Cluster07	1.24E-53	56	122	Microtubule-based movement
Cluster07	2.07E-47	46	88	Cell projection organization
Cluster07	2.18E-43	42	80	Cilium organization
Cluster07	3.68E-43	42	81	Plasma membrane bounded cell projection organizat
Cluster07	2.15E-37	31	45	Cell motility
Cluster07	2.15E-37	31	45	Localization of cell
Cluster07	5.71E-37	31	46	Locomotion
Cluster07	1.18E-34	29	43	Cilium or flagellum-dependent cell motility
Cluster07	1.18E-34	29	43	Cilium-dependent cell motility
Cluster07	4.61E-33	33	67	Cilium assembly
Cluster07	8.06E-33	33	68	Plasma membrane bounded cell projection assembly
Cluster07	1.40E-32	33	69	Cell projection assembly
Cluster07	1.13E-30	27	44	Cilium movement
Cluster07	2.23E-20	15	18	Transport along microtubule
Cluster07	2.23E-20	15	18	Intraciliary transport
Cluster07	2.23E-20	15	18	Microtubule-based transport
Cluster07	4.51E-20	33	150	Organelle assembly
Cluster07	9.30E-20	15	19	Cytoskeleton-dependent intracellular transport
Cluster08	0.0012275	3	3	Peptidyl-asparagine modification
Cluster08	0.0012275	3	3	Protein N-linked glycosylation via asparagine
Cluster08	0.0012275	6	25	Protein-chromophore linkage
Cluster08	0.0012275	39	805	Oxidation-reduction process
Cluster08	0.0012275	6	25	Photosynthesis, light harvesting in photosystem I
Cluster08	0.0012521	8	52	Cellular polysaccharide metabolic process
Cluster08	0.00160239	8	55	Polysaccharide metabolic process
Cluster08	0.00160239	16	218	Generation of precursor metabolites and energy
Cluster08	0.00225924	6	32	Cellular polysaccharide biosynthetic process
Cluster08	0.00225924	16	235	Carbohydrate metabolic process
Cluster08	0.00225924	4	11	Plant-type cell wall organization or biogenesis
Cluster08	0.00225924	6	32	Polysaccharide biosynthetic process
Cluster08	0.00225924	8	63	Protein peptidyl-prolyl isomerization
Cluster08	0.00225924	6	32	Photosynthesis, light harvesting
Cluster08	0.00262662	6	34	Cell wall organization or biogenesis
Cluster08	0.00278767	4	12	Nucleotide-sugar metabolic process
Cluster08	0.0050017	3	6	Unsaturated fatty acid metabolic process
Cluster08	0.0050017	3	6	Unsaturated fatty acid biosynthetic process
Cluster08	0.00583455	4	15	Glycogen metabolic process
Cluster08	0.00583455	4	15	Energy reserve metabolic process

Table SI-T11. KEGG pathways significantly enriched by genes in NF experiment maSigPro "Cluster01", along their FDR value.

KEGG pathway	FDR
cre00280 Valine, leucine and isoleucine degradation	0.032741
cre00400 Phenylalanine, tyrosine and tryptophan biosynthesis	0.032741
cre00590 Arachidonic acid metabolism	0.032741
cre00920 Sulfur metabolism	0.032741
cre00350 Tyrosine metabolism	0.032741

Table SI-T12. KEGG pathways significantly enriched by genes in NF experiment maSigPro "Cluster03", along their FDR value.

KEGG pathway	FDR
cre01110 Biosynthesis of secondary metabolites	2.11E-11
cre01100 Metabolic pathways	6.33E-11
cre00195 Photosynthesis	3.71E-07
cre00860 Porphyrin and chlorophyll metabolism	1.77E-06
cre01200 Carbon metabolism	3.15E-05
cre00710 Carbon fixation in photosynthetic organisms	7.94E-05
cre00010 Glycolysis / Gluconeogenesis	0.00014246
cre00061 Fatty acid biosynthesis	0.00030961
cre01212 Fatty acid metabolism	0.00065515
cre00620 Pyruvate metabolism	0.00213146
cre00030 Pentose phosphate pathway	0.00221585
cre00196 Photosynthesis - antenna proteins	0.00314768
cre00520 Amino sugar and nucleotide sugar metabolism	0.01693031
cre00640 Propanoate metabolism	0.02608397
cre00130 Ubiquinone and other terpenoid-quinone biosynthesis	0.03302794
cre04141 Protein processing in endoplasmic reticulum	0.03446916
cre00052 Galactose metabolism	0.03446916

Table SI-T13. KEGG pathways significantly enriched by genes in NF experiment maSigPro "Cluster05", along their FDR value.

KEGG pathway	FDR
cre01230 Biosynthesis of amino acids	1.31E-07
cre03010 Ribosome	0.00117918
cre03060 Protein export	0.00117918
cre01110 Biosynthesis of secondary metabolites	0.00164596
cre00970 Aminoacyl-tRNA biosynthesis	0.00191285
cre00300 Lysine biosynthesis	0.00395942
cre00906 Carotenoid biosynthesis	0.01774766
cre00400 Phenylalanine, tyrosine and tryptophan biosynthesis	0.03491124
cre00270 Cysteine and methionine metabolism	0.13023047

Table SI-T14. KEGG pathways significantly enriched by genes in NF experiment maSigPro "Cluster03", along their FDR value.

KEG pathway	FDR
cre00520 Amino sugar and nucleotide sugar metabolism	0.00203103
cre00196 Photosynthesis - antenna proteins	0.00957121
cre01100 Metabolic pathways	0.00957121
cre00630 Glyoxylate and dicarboxylate metabolism	0.01350485
cre00514 Other types of O-glycan biosynthesis	0.01784003

Table SI-T15. KEGG pathways significantly enriched by genes in NF experiment maSigPro "Cluster02" or "Cluster06", along their FDR value.

	KEGG pathway	FDR
Cluster 02	cre03430 Mismatch repair	1.82E-07
	cre03030 DNA replication	1.72E-05
	cre03450 Non-homologous end-joining	0.00010673
	cre03440 Homologous recombination	0.00016032
	cre03420 Nucleotide excision repair	0.00019902
Cluster 06	cre03030 DNA replication	5.51E-15
	cre00240 Pyrimidine metabolism	2.94E-07
	cre03410 Base excision repair	5.30E-07
	cre03430 Mismatch repair	0.00013524
	cre03420 Nucleotide excision repair	0.00022185
	cre03440 Homologous recombination	0.00025048
	cre00230 Purine metabolism	0.00386034

Table SI-T16. Analysis report of metaboClust time-profile clustering – CB

Cluster assignments – Lipidomics, negative ion mode (see Fig. SI-50)

- Cluster 0 (Insignificant): 4672 spectral peaks
- Cluster 1: 15 spectral peaks
- Cluster 2: 35 spectral peaks
- Cluster 3: 20 spectral peaks
- Cluster 4: 11 spectral peaks
- Cluster 5: 15 spectral peaks
- Cluster 6: 9 spectral peaks
- Cluster 7: 5 spectral peaks
- Cluster 8: 18 spectral peaks
- Cluster 9: 2 spectral peaks

Cluster assignments – Metabolomics, positive ion mode (see Fig. SI-51)

- Cluster 0 (Insignificant): 5329 spectral peaks
- Cluster 1: 24 spectral peaks
- Cluster 2: 60 spectral peaks
- Cluster 3: 11 spectral peaks
- Cluster 4: 44 spectral peaks
- Cluster 5: 55 spectral peaks
- Cluster 6: 58 spectral peaks
- Cluster 7: 26 spectral peaks
- Cluster 8: 21 spectral peaks
- Cluster 9: 3 spectral peaks

Cluster assignments – Metabolomics, negative ion mode (see Fig. SI-52)

- Cluster 0 (Insignificant): 3601 spectral peaks
- Cluster 1: 49 spectral peaks
- Cluster 2: 16 spectral peaks
- Cluster 3: 5 spectral peaks
- Cluster 4: 4 spectral peaks
- Cluster 5: 3 spectral peaks
- Cluster 6: 10 spectral peaks
- Cluster 7: 6 spectral peaks
- Cluster 8: 3 spectral peaks
- Cluster 9: 4 spectral peaks

Table SI-T17. Analysis report of maSigPro time-profile clustering – CB experiment

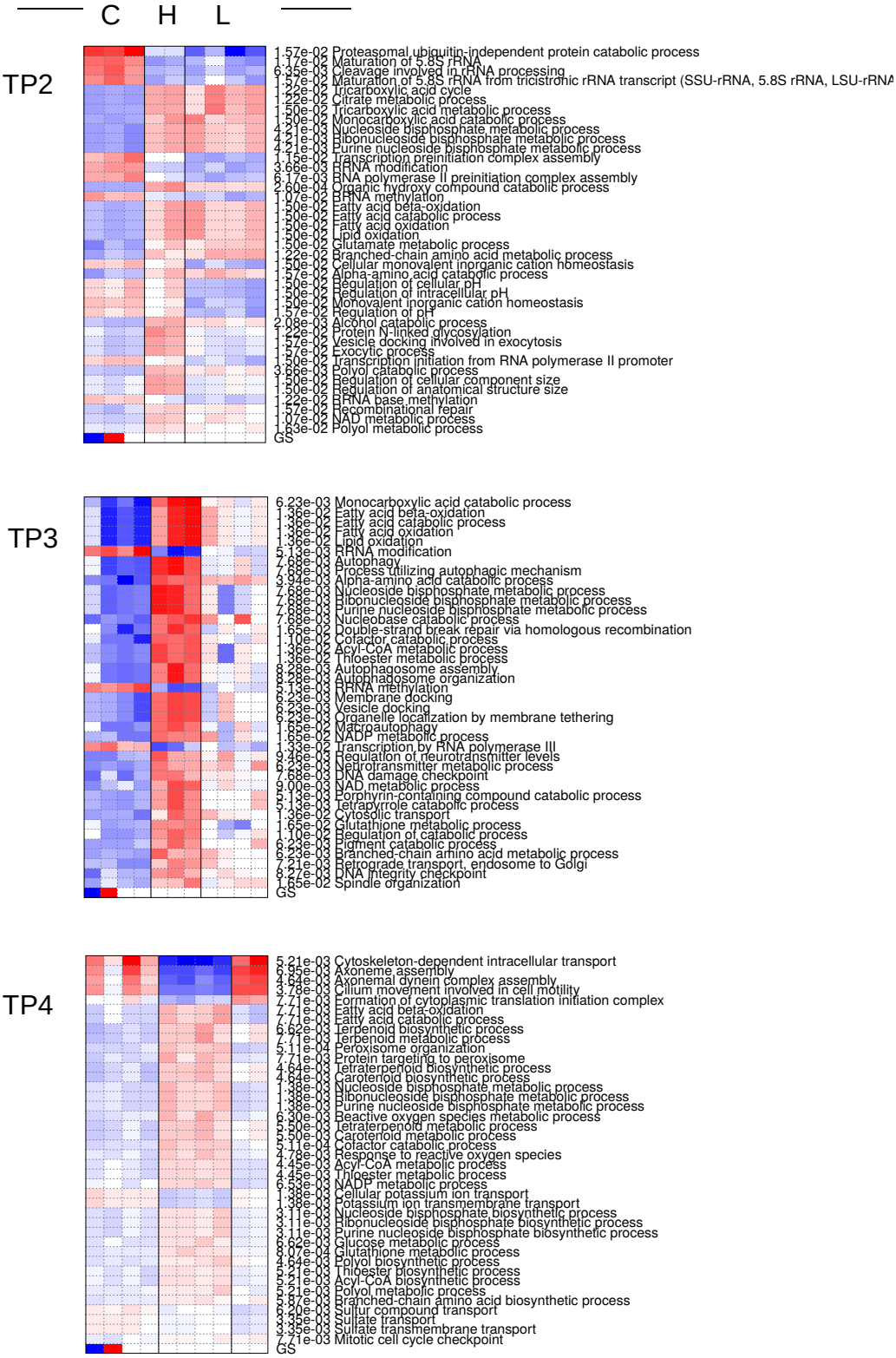
- Number of total features: 17943
- Number of filtered features: 627
- Number of features after filtering: 17316
- Number of analyzed samples: 79/79
- Differentially expressed features identified (FDR <0.05): 15520
- Significant features (R-squared >0.7) according to the selection procedure:
    - All significant features: 4091
    - Significant features for each experimental group
        - Control: 4069
        - High vs Control: 2485
        - Low vs Control: 2146
    - Significant features for each regression variable:
        - Start_Low: 1264
        - Start_High: 1585
        - Start_Control: 3764
        - Linear_Low: 1348
        - Linear_High: 1530
        - Linear_Control: 3325
        - Curved_Low: 1307
        - Curved_High: 1173
        - Curved_Control: 3213
- Cluster memberships in time-profile clustering
    - Cluster 1: 639
    - Cluster 2: 181
    - Cluster 3: 649
    - Cluster 4: 944
    - Cluster 5: 585
    - Cluster 6: 699
    - Cluster 7: 111
    - Cluster 8: 164
    - Cluster 9: 119

Table SI-T18. Differentially expressed gene JGI-GO enrichments of CB data, per time-point.

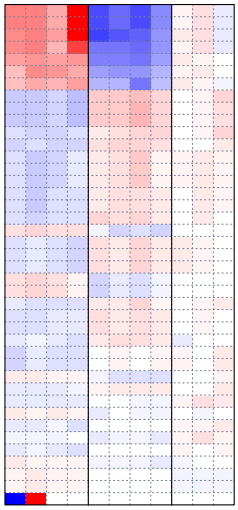
Sampling tim	Comparison	Direction	FDR	Gene set size	Pathways
2	Low-vs.-Cont	Up regulatec	1.33E-06	9	Organic acid catabolic process
2	Low-vs.-Cont	Up regulatec	3.45E-06	32	Small molecule metabolic process
2	Low-vs.-Cont	Up regulatec	5.20E-06	10	Small molecule catabolic process
2	Low-vs.-Cont	Up regulatec	7.16E-06	29	Oxidation-reduction process
2	Low-vs.-Cont	Up regulatec	7.76E-06	6	Monocarboxylic acid catabolic process
2	Low-vs.-Cont	Up regulatec	1.15E-05	5	Fatty acid oxidation
2	Low-vs.-Cont	Up regulatec	2.50E-05	19	Carboxylic acid metabolic process
2	Low-vs.-Cont	Up regulatec	0.00012861	3	Fatty acid beta-oxidation using acyl-CoA oxidase
2	Low-vs.-Cont	Up regulatec	0.00054681	12	Carbohydrate metabolic process
2	High-vs.-Con	Down regula	6.86E-11	19	Movement of cell or subcellular component
2	High-vs.-Con	Down regula	1.42E-10	12	Cell motility
2	High-vs.-Con	Down regula	9.89E-10	11	Cilium or flagellum-dependent cell motility
2	High-vs.-Con	Down regula	1.15E-08	13	Cilium organization
2	High-vs.-Con	Down regula	1.43E-08	15	Microtubule-based movement
2	High-vs.-Con	Down regula	2.59E-08	12	Cilium assembly
2	High-vs.-Con	Down regula	2.13E-07	17	Microtubule-based process
2	High-vs.-Con	Down regula	3.66E-06	8	Cilium movement
2	High-vs.-Con	Up regulatec	5.08E-09	46	Oxidation-reduction process
2	High-vs.-Con	Up regulatec	8.72E-06	42	Small molecule metabolic process
2	High-vs.-Con	Up regulatec	1.29E-05	19	Carbohydrate metabolic process
2	High-vs.-Con	Up regulatec	1.51E-05	7	Nucleoside bisphosphate metabolic process
2	High-vs.-Con	Up regulatec	2.74E-05	11	Small molecule catabolic process
2	High-vs.-Con	Up regulatec	9.98E-05	6	Monocarboxylic acid catabolic process
2	High-vs.-Con	Up regulatec	0.00010921	5	Fatty acid oxidation
2	High-vs.-Con	Up regulatec	0.00012067	8	Organic acid catabolic process
2	High-vs.-Con	Up regulatec	0.00013786	23	Carboxylic acid metabolic process
3	Low-vs.-Cont	Up regulatec	0.00034995	7	Carbohydrate metabolic process
3	Low-vs.-Cont	Up regulatec	0.00089374	3	Glucose metabolic process
3	Low-vs.-Cont	Up regulatec	0.00089374	11	Small molecule metabolic process
3	Low-vs.-Cont	Up regulatec	0.00101672	3	Process utilizing autophagic mechanism
3	Low-vs.-Cont	Up regulatec	0.00199045	7	Carboxylic acid metabolic process
3	Low-vs.-Cont	Up regulatec	0.00278376	9	Oxidation-reduction process
3	Low-vs.-Cont	Up regulatec	0.00342867	2	Hexose biosynthetic process
3	Low-vs.-Cont	Up regulatec	0.00408265	2	Autophagosome assembly
3	High-vs.-Con	Down regula	0.00038015	13	Movement of cell or subcellular component
3	High-vs.-Con	Down regula	0.00187173	14	Microtubule-based process
3	High-vs.-Con	Down regula	0.00187173	11	Microtubule-based movement
3	High-vs.-Con	Down regula	0.00348704	17	Ion transmembrane transport
3	High-vs.-Con	Down regula	0.00490327	19	Ion transport
3	High-vs.-Con	Down regula	0.0053103	6	Cilium movement
3	High-vs.-Con	Up regulatec	3.83E-05	9	Organic acid catabolic process
3	High-vs.-Con	Up regulatec	4.08E-05	27	Catabolic process
3	High-vs.-Con	Up regulatec	4.28E-05	25	Cellular catabolic process
3	High-vs.-Con	Up regulatec	4.89E-05	24	Organic acid metabolic process
3	High-vs.-Con	Up regulatec	7.18E-05	5	Fatty acid oxidation
3	High-vs.-Con	Up regulatec	7.18E-05	23	Carboxylic acid metabolic process
3	High-vs.-Con	Up regulatec	7.18E-05	36	Small molecule metabolic process
3	High-vs.-Con	Up regulatec	7.18E-05	6	Monocarboxylic acid catabolic process
3	High-vs.-Con	Up regulatec	8.26E-05	24	Organic substance catabolic process
3	High-vs.-Con	Up regulatec	9.73E-05	33	Oxidation-reduction process
4	High-vs.-Con	Down regula	0.00603556	11	Movement of cell or subcellular component
6	Low-vs.-Cont	Up regulatec	0.00410706	2	Quaternary ammonium group transport
6	Low-vs.-Cont	Up regulatec	0.00545634	12	Transmembrane transport
6	High-vs.-Con	Up regulatec	1.00E-03	NA	Small molecule metabolic process
6	High-vs.-Con	Up regulatec	3.00E-05	NA	Oxidation-reduction process
6	High-vs.-Con	Down regula	4.00E-08	NA	Microtubule bundle formation
6	High-vs.-Con	Down regula	7.00E-09	NA	Cilium movement
6	High-vs.-Con	Down regula	2.00E-11	NA	Cilium assembly
6	High-vs.-Con	Down regula	2.00E-11	NA	Cilium organization
6	High-vs.-Con	Down regula	2.00E-11	NA	Cell projection organization
6	High-vs.-Con	Down regula	8.00E-12	NA	Plasma membrane bounded cell projection
6	High-vs.-Con	Down regula	8.00E-12	NA	Cell projection assembly
6	High-vs.-Con	Down regula	3.00E-09	NA	Microtubule-based movement
6	High-vs.-Con	Down regula	3.00E-12	NA	Movement of cell or subcellular component
6	High-vs.-Con	Down regula	8.00E-10	NA	Cell motility
6	High-vs.-Con	Down regula	5.00E-10	NA	Cilium or flagellum-dependent cell motility
7	Low-vs.-Cont	Down regula	4.00E-03	NA	Cation transmembrane transport

7	Low-vs.-Cont	Down regula	7.00E-04	NA	Metal ion transport
7	Low-vs.-Cont	Down regula	3.00E-05	NA	Potassium ion transport
7	Low-vs.-Cont	Down regula	8.00E-05	NA	Inorganic ion transmembrane transport
7	Low-vs.-Cont	Down regula	6.00E-05	NA	Ion transport
7	Low-vs.-Cont	Down regula	1.00E-05	NA	Ion transmembrane transport
7	Low-vs.-Cont	Down regula	7.00E-04	NA	Transmembrane transport
7	Low-vs.-Cont	Down regula	1.00E-05	NA	Inorganic anion transmembrane transport
7	Low-vs.-Cont	Down regula	8.00E-06	NA	Sulfate transmembrane transport
7	Low-vs.-Cont	Down regula	2.00E-06	NA	Anion transmembrane transport
7	High-vs.-Con	Down regula	2.49E-08	14	Locomotion
7	High-vs.-Con	Down regula	7.41E-08	13	Cilium or flagellum-dependent cell motility
7	High-vs.-Con	Down regula	9.83E-08	22	Movement of cell or subcellular component
7	High-vs.-Con	Down regula	9.41E-06	11	Cilium movement
7	High-vs.-Con	Down regula	5.04E-05	9	Microtubule bundle formation
7	High-vs.-Con	Down regula	9.10E-05	8	Axoneme assembly
7	High-vs.-Con	Down regula	0.00016372	17	Metal ion transport
7	High-vs.-Con	Down regula	0.00016372	16	Microtubule-based movement
7	High-vs.-Con	Down regula	0.00065212	26	Ion transmembrane transport
7	High-vs.-Con	Down regula	0.00074152	12	Cilium organization
7	High-vs.-Con	Down regula	0.00078448	6	Axonemal dynein complex assembly
8	Low-vs.-Cont	Down regula	2.27E-05	24	Ion transmembrane transport
8	Low-vs.-Cont	Down regula	2.27E-05	27	Ion transport
8	Low-vs.-Cont	Down regula	3.50E-05	35	Transmembrane transport
8	Low-vs.-Cont	Down regula	0.00042346	9	Anion transmembrane transport
8	Low-vs.-Cont	Down regula	0.00078157	13	Metal ion transport
8	Low-vs.-Cont	Down regula	0.00167439	15	Inorganic ion transmembrane transport
8	Low-vs.-Cont	Down regula	0.00181643	11	Anion transport
8	Low-vs.-Cont	Down regula	0.00227277	6	Organic acid transport
8	Low-vs.-Cont	Down regula	0.00227277	48	Localization
8	Low-vs.-Cont	Down regula	0.00227277	46	Establishment of localization
8	Low-vs.-Cont	Down regula	0.00245774	14	Cation transmembrane transport
8	Low-vs.-Cont	Down regula	0.00251989	4	Amino acid transmembrane transport
8	Low-vs.-Cont	Down regula	0.00251989	45	Transport
8	Low-vs.-Cont	Down regula	0.0026172	15	Cation transport
8	High-vs.-Con	Down regula	4.68E-48	72	Movement of cell or subcellular component
8	High-vs.-Con	Down regula	5.52E-39	61	Microtubule-based movement
8	High-vs.-Con	Down regula	1.22E-35	51	Cell projection organization
8	High-vs.-Con	Down regula	9.30E-35	48	Cilium organization
8	High-vs.-Con	Down regula	7.81E-34	71	Microtubule-based process
8	High-vs.-Con	Down regula	1.00E-28	41	Cilium assembly
8	High-vs.-Con	Down regula	3.23E-28	32	Cilium movement
8	High-vs.-Con	Down regula	7.86E-28	32	Cell motility
8	High-vs.-Con	Down regula	9.31E-26	30	Cilium or flagellum-dependent cell motility
9	Low-vs.-Cont	Down regula	7.46E-23	64	Organonitrogen compound biosynthetic process
9	Low-vs.-Cont	Down regula	7.52E-16	34	Peptide biosynthetic process
9	Low-vs.-Cont	Down regula	7.52E-16	36	Amide biosynthetic process
9	Low-vs.-Cont	Down regula	7.52E-16	78	Cellular biosynthetic process
9	Low-vs.-Cont	Down regula	8.61E-16	79	Biosynthetic process
9	Low-vs.-Cont	Down regula	1.54E-15	64	Cellular nitrogen compound biosynthetic process
9	Low-vs.-Cont	Down regula	3.27E-13	13	Porphyrin-containing compound biosynthetic process
9	Low-vs.-Cont	Down regula	5.31E-13	19	Photosynthesis
9	Low-vs.-Cont	Down regula	1.27E-12	14	Porphyrin-containing compound metabolic process
9	Low-vs.-Cont	Down regula	3.36E-12	21	Cofactor biosynthetic process
9	Low-vs.-Cont	Up regulatec	0.00364488	4	Response to hydrogen peroxide
9	High-vs.-Con	Down regula	1.20E-27	40	Movement of cell or subcellular component
9	High-vs.-Con	Down regula	5.76E-24	35	Microtubule-based movement
9	High-vs.-Con	Down regula	3.09E-20	39	Microtubule-based process
9	High-vs.-Con	Down regula	2.62E-18	20	Cilium movement
9	High-vs.-Con	Down regula	9.26E-18	28	Photosynthesis
9	High-vs.-Con	Down regula	1.51E-15	24	Cell projection organization
9	High-vs.-Con	Down regula	2.04E-14	22	Cilium organization
9	High-vs.-Con	Down regula	3.34E-13	16	Cilium or flagellum-dependent cell motility
9	High-vs.-Con	Down regula	2.15E-12	19	Cilium assembly
9	High-vs.-Con	Up regulatec	0.00315224	8	Response to drug
9	High-vs.-Con	Up regulatec	0.00315224	4	Response to hydrogen peroxide
9	High-vs.-Con	Up regulatec	0.00315224	28	Oxidation-reduction process
9	High-vs.-Con	Up regulatec	0.00315224	9	Response to oxygen-containing compound
9	High-vs.-Con	Up regulatec	0.00593079	8	Response to oxidative stress

Table SI-T19. PGSEA JGI-GO enrichments of CB transcriptomics data, per time-point. Given are the class (C=Control, H=High and L=Low), FDR and the name of the JGI-GO. TP1 and TP5 PGSEA results are missing due to too low sample size for enrichment analysis. Color red indicates relatively increased gene expression, blue indicates relative reduction in expression.

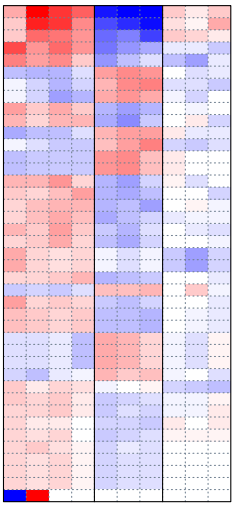


TP6



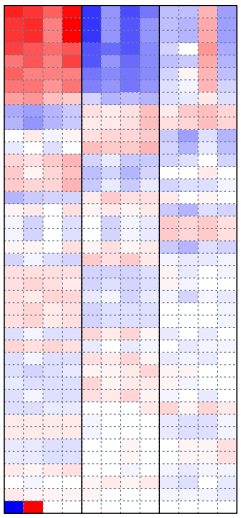
2.30e-03 Transport along microtubule
2.30e-03 Microtubule-based transport
2.33e-03 Intraciliary transport
8.26e-04 Cytoskeleton-dependent intracellular transport
1.81e-05 Axoneme assembly
2.73e-04 Axonemal dynein complex assembly
8.40e-04 Cilium movement involved in cell motility
4.34e-04 Tricarboxylic acid metabolic process
4.34e-04 Tricarboxylic acid cycle
4.34e-04 Citrate metabolic process
3.47e-03 Branched-chain amino acid biosynthetic process
1.88e-04 Branched-chain amino acid metabolic process
2.37e-03 Nucleoside bisphosphate biosynthetic process
2.37e-03 Ribonucleoside bisphosphate biosynthetic process
2.37e-03 Purine nucleoside bisphosphate biosynthetic process
7.24e-04 Thioester biosynthetic process
7.24e-04 Acyl-CoA biosynthetic process
1.49e-03 Acetyl-CoA metabolic process
9.71e-04 Sodium ion transmembrane transport
5.72e-04 Nucleoside bisphosphate metabolic process
5.72e-04 Ribonucleoside bisphosphate metabolic process
5.72e-04 Purine nucleoside bisphosphate metabolic process
1.49e-03 Cellular potassium ion transport
1.49e-03 Potassium ion transmembrane transport
8.40e-04 Alpha-amino acid catabolic process
5.22e-06 Acyl-CoA metabolic process
5.22e-06 Thioester metabolic process
3.47e-03 Embryo sac development
1.49e-03 Organic acid transmembrane transport
1.49e-03 Carboxylic acid transmembrane transport
1.49e-03 Sodium ion transport
2.92e-03 Steroid metabolic process
1.49e-03 Organic cation transport
3.81e-03 Divalent inorganic cation homeostasis
1.49e-03 Amino acid transport
3.00e-03 Cofactor transport
3.47e-03 Amino acid transmembrane transport
3.47e-03 Positive regulation of cell cycle
7.24e-04 Autophagosome assembly
7.24e-04 Autophagosome organization
GS

TP7



2.50e-03 Axoneme assembly
5.74e-03 Axonemal dynein complex assembly
2.91e-03 Cilium movement involved in cell motility
2.36e-03 Carbon fixation
8.81e-03 Response to cytokinin
2.36e-03 tRNA wobble base modification
3.27e-03 Maturation of 5.8S rRNA from tricistronic rRNA transcript (SSU-rRNA, 5.8S rRNA, LSU-rRNA
3.38e-03 rRNA methylation
2.36e-03 Response to light intensity
8.81e-03 Regulation of generation of precursor metabolites and energy
3.47e-03 tRNA wobble uridine modification
3.38e-03 Maturation of 5.8S rRNA
2.50e-03 Vesicle docking involved in exocytosis
2.50e-03 Exocytic process
7.58e-03 Starch biosynthetic process
3.60e-03 Sodium ion transport
1.69e-03 Photosynthetic electron transport chain
3.38e-03 Monosaccharide catabolic process
4.84e-03 Starch metabolic process
3.90e-03 Regulation of photosynthesis
9.10e-03 Sulfate transport
9.10e-03 Sulfate transmembrane transport
2.91e-03 Sodium ion transmembrane transport
9.38e-03 mRNA cleavage
5.74e-03 Response to high light intensity
5.30e-04 Cellular potassium ion transport
5.30e-04 Potassium ion transmembrane transport
8.12e-03 Membrane docking
8.12e-03 Vesicle docking
8.12e-03 Organelle localization by membrane tethering
5.74e-03 Mismatch repair
5.27e-03 Glutamine metabolic process
7.70e-03 Divalent inorganic cation homeostasis
8.12e-03 Calcium ion homeostasis
5.74e-03 Stress-activated protein kinase signaling cascade
4.88e-03 Activation of protein kinase activity
6.38e-03 Positive regulation of kinase activity
3.38e-03 Positive regulation of phosphorus metabolic process
3.38e-03 Positive regulation of phosphorylation
3.38e-03 Positive regulation of phosphate metabolic process
GS

TP8



1.10e-03 Intraciliary transport
1.67e-03 Transport along microtubule
1.67e-03 Microtubule-based transport
1.27e-03 Axoneme assembly
1.67e-03 Cytoskeleton-dependent intracellular transport
1.10e-03 Axonemal dynein complex assembly
1.10e-03 Cilium movement involved in cell motility
1.10e-03 Motile cilium assembly
8.00e-04 Heme metabolic process
8.00e-04 Heme biosynthetic process
1.44e-03 Cellular response to heat
1.10e-03 Response to heat
2.57e-03 Arginine biosynthetic process
1.40e-03 Carbon fixation
1.10e-03 Nucleobase biosynthetic process
8.00e-04 Cell growth
1.67e-03 Cellular response to unfolded protein
1.85e-03 DNA strand elongation involved in DNA replication
1.85e-03 DNA strand elongation
1.10e-03 Cellular response to topologically incorrect protein
1.39e-03 Regulation of RNA splicing
1.10e-03 Sodium ion transport
1.10e-03 Sodium ion transmembrane transport
1.40e-03 Neurotransmitter metabolic process
2.73e-05 Cellular potassium ion transport
2.73e-05 Potassium ion transmembrane transport
1.84e-03 Regulation of mRNA splicing, via spliceosome
1.10e-03 Regulation of membrane potential
1.67e-03 Alternative mRNA splicing, via spliceosome
1.84e-03 Carbohydrate derivative catabolic process
2.57e-03 Regulation of cellular catabolic process
1.10e-03 Regulation of alternative mRNA splicing, via spliceosome
2.07e-03 Monosaccharide biosynthetic process
1.40e-03 Sulfate transport
1.40e-03 Sulfate transmembrane transport
1.85e-03 GPI anchor metabolic process
1.85e-03 GPI anchor biosynthetic process
1.10e-03 Ammonium transport
2.28e-03 Cellular modified amino acid biosynthetic process
1.60e-03 Regulation of cellular protein localization
GS

TP9

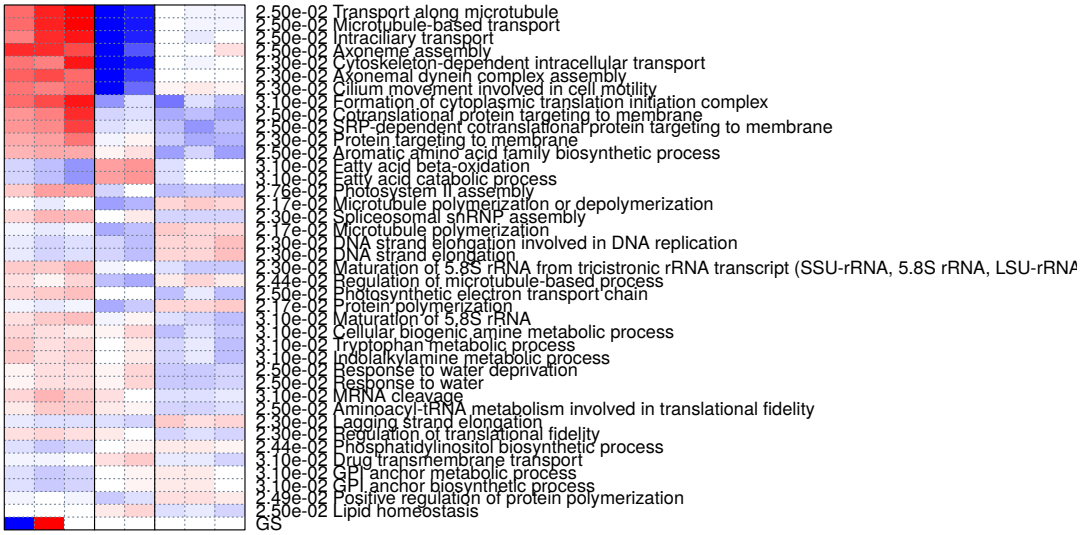


Table SI-T20. KEGG pathways significantly enriched by genes in CB experiment maSigPro "Cluster01" or "Cluster03", along their FDR value. KEGG pathways with enrichment FDR>0.05

maSigPro cluster	KEGG pathway	FDR
Cluster01	cre01110 Biosynthesis of secondary metabolites	6.08E-18
	cre01100 Metabolic pathways	4.94E-09
	cre00061 Fatty acid biosynthesis	8.12E-07
	cre00860 Porphyrin and chlorophyll metabolism	1.47E-06
	cre00710 Carbon fixation in photosynthetic organisms	1.30E-05
	cre01212 Fatty acid metabolism	2.39E-05
	cre01200 Carbon metabolism	0.00017725
	cre00010 Glycolysis / Gluconeogenesis	0.0023645
	cre00030 Pentose phosphate pathway	0.00247529
	cre01230 Biosynthesis of amino acids	0.0028242
	cre00900 Terpenoid backbone biosynthesis	0.0045001
	cre00620 Pyruvate metabolism	0.00633367
	cre00195 Photosynthesis	0.00993788
	cre00640 Propanoate metabolism	0.0245807
	cre00780 Biotin metabolism	0.02565848
	cre00130 Ubiquinone and other terpenoid-quinone biosynthesis	0.02920538
	cre00400 Phenylalanine, tyrosine and tryptophan biosynthesis	0.03648694
	cre00920 Sulfur metabolism	0.04483282
Cluster03	cre01110 Biosynthesis of secondary metabolites	0.04594604
	cre00640 Propanoate metabolism	0.07439422
	cre00020 Citrate cycle (TCA cycle)	0.07439422

Table SI-T21. KEGG pathways significantly enriched by genes in CB experiment maSigPro "Cluster02" or "Cluster07", along their FDR value.

maSigPro cluster	KEGG pathway	FDR
Cluster02	cre00196 Photosynthesis - antenna proteins	1.12E-06
Cluster07	cre00195 Photosynthesis	4.96E-12
	cre00196 Photosynthesis - antenna proteins	7.99E-08

Table SI-T22. KEGG pathways significantly enriched by genes in CB experiment maSigPro "Cluster04" along their FDR value.

KEGG pathway	FDR
cre03010 Ribosome	3.55E-38
cre01230 Biosynthesis of amino acids	7.43E-06
cre00300 Lysine biosynthesis	0.00126337
cre03013 RNA transport	0.01807192
cre00270 Cysteine and methionine metabolism	0.03054878
cre00970 Aminoacyl-tRNA biosynthesis	0.03054878

Table SI-T23. KEGG pathways significantly enriched by genes in CB experiment maSigPro "Cluster06" along their FDR value.

KEGG pathway	FDR
cre03030 DNA replication	5.54E-15
cre03430 Mismatch repair	9.00E-10
cre03450 Non-homologous end-joining	4.05E-06
cre03420 Nucleotide excision repair	1.58E-05
cre03410 Base excision repair	0.00773412
cre03440 Homologous recombination	0.00773412

References

1. Tundisi, J.G.; Tundisi, T.M. *Limnology*; CRC Press: Leiden, The Netherlands, **2012**; ISBN 978-0-203-80395-0.

2. Castro, P.; Huber, M.E. *Marine biology*; Tenth edition.; McGraw-Hill Education: New York, NY, **2016**; ISBN 978-0-07-802306-4.

3. Malaj, E.; von der Ohe, P.C.; Grote, M.; Kühne, R.; Mondy, C.P.; Usseglio-Polatera, P.; Brack, W.; Schäfer, R.B. Organic chemicals jeopardize the health of freshwater ecosystems on the continental scale. *Proc. Natl. Acad. Sci.* **2014**, *111*, 9549–9554.

4. Prüss-Üstün, A.; Wolf, J.; Corvalán, C.; Bos, R.; Neira, M. *Preventing disease through healthy environments: a global assessment of the burden of disease from environmental risks*; Second edition.; World Health Organization: Geneva, Switzerland, **2016**; ISBN 978-92-4-156519-6.

5. EU Parliament Directive 2000/60/EC of the European Parliament and of the Council of 23 October 2000 establishing a framework for Community action in the field of water policy 2000.

6. EU Parliament Regulation (EC) No 1907/2006 of the European Parliament and of the Council of 18 December 2006 concerning the Registration, Evaluation, Authorisation and Restriction of Chemicals (REACH), establishing a European Chemicals Agency, amending Directive 1999/4 2006.

7. Chartres, N.; Bero, L.A.; Norris, S.L. A review of methods used for hazard identification and risk assessment of environmental hazards. *Environ. Int.* **2019**, *123*, 231–239.

8. Villeneuve, D.L.; Coady, K.; Escher, B.I.; Mihaich, E.; Murphy, C.A.; Schlekat, T.; Garcia-Reyero, N. High-throughput screening and environmental risk assessment: State of the science and emerging applications: High-throughput screening and environmental risk assessment. *Environ. Toxicol. Chem.* **2019**, *38*, 12–26.

9. Nicolotti, O.; Benfenati, E.; Carotti, A.; Gadaleta, D.; Gissi, A.; Mangiatordi, G.F.; Novellino, E. REACH and in silico methods: an attractive opportunity for medicinal chemists. *Drug Discov. Today* **2014**, *19*, 1757–1768.

10. Ahlers, J.; Nendza, M.; Schwartz, D. Environmental hazard and risk assessment of thiochemicals. Application of integrated testing and intelligent assessment strategies (ITS) to fulfil the REACH requirements for aquatic toxicity. *Chemosphere* **2019**, *214*, 480–490.

11. Lombardo, A.; Roncaglioni, A.; Benfenati, E.; Nendza, M.; Segner, H.; Jeram, S.; Pauné, E.; Schüürmann, G. Optimizing the aquatic toxicity assessment under REACH through an integrated testing strategy (ITS). *Environ. Res.* **2014**, *135*, 156–164.

12. Organization for Economic Co-Operation and Development (OECD) *Test No. 201: Alga, Growth Inhibition Test*; OECD Publishing, **2011**.

13. International organization for Standardization (ISO) *Water quality - algal growth inhibition test. ISO/DIS 8692*; Geneva, Switzerland, **2012**.

14. OECD *Test No. 202: Daphnia sp., Acute Immobilisation Test*; **2004**.

15. OECD *Test No. 211: Daphnia magna reproduction test*; **2012**.

16. OECD *Test No. 205: Avian Dietary Toxicity Test*; **1984**.

17. OECD *Test No. 230: 21 days Fish assay*; **2009**.

18. OECD *Test No. 234: Fish Sexual Development Test*; **2011**.

19. OECD *Test No. 229: Fish Short Term Reproduction Test*; **2012**.

20. OECD *Test No. 236: Fish embryo toxicity test*; **2013**.

21. OECD *Test No. 240: Medaka Extended One Generation Reproduction Test*; **2015**.

22. Hamm, J.; Sullivan, K.; Clippinger, A.J.; Strickland, J.; Bell, S.; Bhhatarai, B.; Blaauboer, B.; Casey, W.; Dorman, D.; Forsby, A.; et al. Alternative approaches for identifying acute systemic toxicity: Moving from research to regulatory testing. *Toxicol. In Vitro* **2017**, *41*, 245–259.

23. Zaunbrecher, V.; Beryt, E.; Parodi, D.; Telesca, D.; Doherty, J.; Malloy, T.; Allard, P. Has Toxicity Testing Moved into the 21st Century? A Survey and Analysis of Perceptions in the Field of Toxicology. *Environ. Health Perspect.* **2017**, *125*, 087024.

24. Meek, M.E.B.; Palermo, C.M.; Bachman, A.N.; North, C.M.; Jeffrey Lewis, R. Mode of action human relevance (species concordance) framework: Evolution of the Bradford Hill considerations and comparative analysis of weight of evidence. *J. Appl. Toxicol. JAT* **2014**, *34*, 595–606.

25. Xie, L.; Gomes, T.; Solhaug, K.A.; Song, Y.; Tollefsen, K.E. Linking mode of action of the model respiratory and photosynthesis uncoupler 3,5-dichlorophenol to adverse outcomes in Lemna minor. *Aquat. Toxicol.* **2018**, *197*, 98–108.

26. Samadani, M.; Dewez, D. Cadmium accumulation and toxicity affect the extracytoplasmic polyphosphate level in Chlamydomonas reinhardtii. *Ecotoxicol. Environ. Saf.* **2018**, *166*, 200–206.

27. Intrchom, W.; Thakkar, M.; Hamilton, R.F.; Holian, A.; Mitra, S. Effect of Carbon Nanotube-Metal Hybrid Particle Exposure to Freshwater Algae Chlamydomonas reinhardtii. *Sci. Rep.* **2018**, *8,* e15301.

28. Nowicka, B.; Pluciński, B.; Kuczyńska, P.; Kruk, J. Physiological characterization of Chlamydomonas reinhardtii acclimated to chronic stress induced by Ag, Cd, Cr, Cu and Hg ions. *Ecotoxicol. Environ. Saf.* **2016**, *130*, 133–145.

29. Jiang, Y.; Zhu, Y.; Hu, Z.; Lei, A.; Wang, J. Towards elucidation of the toxic mechanism of copper on the model green alga Chlamydomonas reinhardtii. *Ecotoxicology* **2016**, *25*, 1417–1425.

30. Esperanza, M.; Cid, Á.; Herrero, C.; Rioboo, C. Acute effects of a prooxidant herbicide on the microalga Chlamydomonas reinhardtii: Screening cytotoxicity and genotoxicity endpoints. *Aquat. Toxicol.* **2015**, *165*, 210–221.

31. Machado, M.D.; Lopes, A.R.; Soares, E.V. Responses of the alga Pseudokirchneriella subcapitata to long-term exposure to metal stress. *J. Hazard. Mater.* **2015**, *296*, 82–92.

32. Prado, R.; García, R.; Rioboo, C.; Herrero, C.; Cid, Á. Suitability of cytotoxicity endpoints and test microalgal species to disclose the toxic effect of common aquatic pollutants. *Ecotoxicol. Environ. Saf.* **2015**, *114*, 117–125.

33. Aksmann, A.; Pokora, W.; Baścik-Remisiewicz, A.; Dettlaff-Pokora, A.; Wielgomas, B.; Dziadziuszko, M.; Tukaj, Z. Time-dependent changes in antioxidative enzyme expression and photosynthetic activity of Chlamydomonas reinhardtii cells under acute exposure to cadmium and anthracene. *Ecotoxicol. Environ. Saf.* **2014**, *110*, 31–40.

34. Nestler, H.; Groh, K.J.; Schönenberger, R.; Behra, R.; Schirmer, K.; Eggen, R.I.L.; Suter, M.J.F. Multiple-endpoint assay provides a detailed mechanistic view of responses to herbicide exposure in Chlamydomonas reinhardtii. *Aquat. Toxicol.* **2012**, *110–111*, 214–224.

35. Sanchez, D.; Houde, M.; Douville, M.; De Silva, A.O.; Spencer, C.; Verreault, J. Transcriptional and cellular responses of the green alga Chlamydomonas reinhardtii to perfluoroalkyl phosphonic acids. *Aquat. Toxicol.* **2015**, *160*, 31–38.

36. Stoiber, T.L.; Shafer, M.M.; Armstrong, D.E. Differential effects of copper and cadmium exposure on toxicity endpoints and gene expression in *Chlamydomonas reinhardtii*. *Environ. Toxicol. Chem.* **2010**, *29*, 191–200.

37. Majewska, M.; Harshkova, D.; Guściora, M.; Aksmann, A. Phytotoxic activity of diclofenac: Evaluation using a model green alga Chlamydomonas reinhardtii with atrazine as a reference substance. *Chemosphere* **2018**, *209*, 989–997.

38. de Boissel, P.G.J.; Gonzalez, P.; Buleté, A.; Daffe, G.; Clérandeau, C.; Vulliet, E.; Cachot, J. An innovative and integrative assay for toxicity testing using individual fish embryos. Application to oxazepam. *Chemosphere* **2017**, *181*, 468–477.

39. Dang, Z.; van der Ven, L.T.M.; Kienhuis, A.S. Fish embryo toxicity test, threshold approach, and moribund as approaches to implement 3R principles to the acute fish toxicity test. *Chemosphere* **2017**, *186*, 677–685.

40. Galbis-Martínez, L.; Fernández-Cruz, M.L.; Alte, L.; Valdehita, A.; Rucandio, I.; Navas, J.M. Development of a new tool for the long term in vitro ecotoxicity testing of nanomaterials using a rainbow-trout cell line (RTL-W1). *Toxicol. In Vitro* **2018**, *50*, 305–317.

41. Oliveira, G.A.R. de; Leme, D.M.; de Lapuente, J.; Brito, L.B.; Porredón, C.; Rodrigues, L. de B.; Brull, N.; Serret, J.T.; Borràs, M.; Disner, G.R.; et al. A test battery for assessing the ecotoxic effects of textile dyes. *Chem. Biol. Interact.* **2018**, *291*, 171–179.

42. Tsiridis, V.; Petala, M.; Samaras, P.; Kungolos, A.; Sakellaropoulos, G.P. Environmental hazard assessment of coal fly ashes using leaching and ecotoxicity tests. *Ecotoxicol. Environ. Saf.* **2012**, *84*, 212–220.

43. Henschel, K.-P.; Wenzel, A.; Diedrich, M.; Fliedner, A. Environmental Hazard Assessment of Pharmaceuticals. *Regul. Toxicol. Pharmacol.* **1997**, *25*, 220–225.

44. Lemly, A.D. A Protocol for Aquatic Hazard Assessment of Selenium. *Ecotoxicol. Environ. Saf.* **1995**, *32*, 280–288.

45. Thomas, P.C.; Bicherel, P.; Bauer, F.J. How in silico and QSAR approaches can increase confidence in environmental hazard and risk assessment: How QSAR Models Can Improve Environmental Risk Assessment. *Integr. Environ. Assess. Manag.* **2019**, *15*, 40–50.

46. Gramatica, P.; Papa, E.; Sangion, A. QSAR modeling of cumulative environmental end-points for the prioritization of hazardous chemicals. *Environ. Sci. Process. Impacts* **2018**, *20*, 38–47.

47. Polanski, J. Receptor dependent multidimensional QSAR for modeling drug--receptor interactions. *Curr. Med. Chem.* **2009**, *16*, 3243–57.

48. Browne, P.; Delrue, N.; Gourmelon, A. Regulatory use and acceptance of alternative methods for chemical hazard identification. *Curr. Opin. Toxicol.* **2019,** *15*, 18-25.

49. Sauer, U.G.; Deferme, L.; Gribaldo, L.; Hackermüller, J.; Tralau, T.; van Ravenzwaay, B.; Yauk, C.; Poole, A.; Tong, W.; Gant, T.W. The challenge of the application of 'omics technologies in chemicals risk assessment: Background and outlook. *Regul. Toxicol. Pharmacol.* **2017**, *91*, 14–26.

50. Sneddon, L.U.; Halsey, L.G.; Bury, N.R. Considering aspects of the 3Rs principles within experimental animal biology. *J. Exp. Biol.* **2017**, *220*, 3007–3016.

51. National Research Council (NRC) *Toxicity Testing in the 21st Century: A Vision and a Strategy*; National Academies Press: Washington, D.C., **2007**; ISBN 978-0-309-15173-3.

52. Villeneuve, D.L.; Garcia-Reyero, N. Vision & strategy: Predictive ecotoxicology in the 21st century. *Environ. Toxicol. Chem.* **2011**, *30*, 1–8.

53. Eriksson, J.; Gilek, M.; Rudén, C. (eds.) Regulating chemical risks: European and global challenges*;* Springer: Netherlands, **2010**, ISBN 978-90-481-9428-5.

54. McCarty, L.S. Are we in the dark ages of environmental toxicology? *Regul. Toxicol. Pharmacol.* **2013**, *67*, 321–324.

55. ECHA *REACH Registration Statistics Infograph, URL: https://www.echa.europa.eu/registration-statistics-infograph. Retrieved 12 March 2019*; 2019.

56. Willett, C. The Use of Adverse Outcome Pathways (AOPs) to Support Chemical Safety Decisions Within the Context of Integrated Approaches to Testing and Assessment (IATA). In *Alternatives to Animal Testing*; Kojima, H., Seidle, T., Spielmann, H., Eds.; Springer Singapore: Singapore, **2019**. ISBN 9789811324468.

57. Campos, B.; Colbourne, J.K.; Brown, J.B.; Viant, M.R.; Biales, A.D.; Gallagher, K.; Henry, T.R.; Sappington, K.G.; Marshall, S.; Whale, G. How omics technologies can enhance chemical safety regulation: perspectives from academia, government, and industry: The Perspectives column is a regular series designed to discuss and evaluate potentially competing viewpoints and research findings on current environ. *Environ. Toxicol. Chem.* **2018**, *37*, 1252–1259.

58. Brack, W.; Escher, B.I.; Müller, E.; Schmitt-Jansen, M.; Schulze, T.; Slobodnik, J.; Hollert, H. Towards a holistic and solution-oriented monitoring of chemical status of European water bodies: how to support the EU strategy for a non-toxic environment? *Environ. Sci. Eur.* **2018**, *30,* 1-11.

59. Hartung, T. Food for thought … on alternative methods for chemical safety testing. *ALTEX* **2010**, *27*, 3–14.

60. *Validation of alternative methods for toxicity testing*; Eskes, C., Whelan, M., Eds.; Advances in experimental medicine and biology; Springer: Switzerland, **2016**; ISBN 978-3-319-33826-2.

61. Belanger, S.E.; Sanderson, H.; Embry, M.R.; Coady, K.; DeZwart, D.; Farr, B.A.; Gutsell, S.; Halder, M.; Sternberg, R.; Wilson, P. It is time to develop ecological thresholds of toxicological concern to assist environmental hazard assessment: Development of ecological thresholds of toxicological concern. *Environ. Toxicol. Chem.* **2015**, *34*, 2864–2869.

62. Tice, R.R.; Austin, C.P.; Kavlock, R.J.; Bucher, J.R. Improving the Human Hazard Characterization of Chemicals: A Tox21 Update. *Environ. Health Perspect.* **2013**, *121*, 756–765.

63. *Extrapolation practice for ecotoxicological effect characterization of chemicals*; Solomon, K.R., Brock, T.C.M., De Zwart, D., Dyer, S.D., Posthuma, L., Richards, S., Sanderson, H., Sibley, P., van den Brink, P.J., Eds.; SETAC Publications; CRC Press: Boca Raton, **2008**; ISBN 978-1-4200-7390-4.

64. Ankley, G.T.; Gray, L.E. CROSS-SPECIES CONSERVATION OF ENDOCRINE PATHWAYS: A CRITICAL ANALYSIS OF TIER 1 FISH AND RAT SCREENING ASSAYS WITH 12 MODEL CHEMICALS: Conservation of vertebrate endocrine pathways. *Environ. Toxicol. Chem.* **2013**, *32*, 1084–1087.

65. Ankley, G.T.; Daston, G.P.; Degitz, S.J.; Denslow, N.D.; Hoke, R.A.; Kennedy, S.W.; Miracle, A.L.; Perkins, E.J.; Snape, J.; Tillitt, D.E.; et al. Toxicogenomics in regulatory ecotoxicology. *Environ. Sci. Technol.* **2006**, *40*, 4055–65.

66. UK REACH Competent Authority *Information Leaflet Number 18 – Minimisation of Animal Testing*; **2016**;

67. Burden, N.; Benstead, R.; Clook, M.; Doyle, I.; Edwards, P.; Maynard, S.K.; Ryder, K.; Sheahan, D.; Whale, G.; van Egmond, R.; et al. Advancing the 3Rs in regulatory ecotoxicology: A pragmatic cross-sector approach: Advancing the 3Rs in Regulatory Ecotoxicology. *Integr. Environ. Assess. Manag.* **2016**, *12*, 417–421.

68. Krimsky, S. The unsteady state and inertia of chemical regulation under the US Toxic Substances Control Act. *PLOS Biol.* **2017**, *15*, e2002404.

69. Hartung, T.; Rovida, C. Chemical regulators have overreached. *Nature* **2009**, *460*, 1080–1081.

70. Hartung, T.; Hoffmann, S.; Stephens, M. Food for thought Mechanistic validation. *Altex* **2013**, *30*, 119–130.

71. Hartung, T. Evidence-based toxicology – the toolbox of validation for the 21st century? *ALTEX* **2010**, 253–263.

72. Hodgson, E. Introduction to Toxicology. In; Hodgson, E., Ed.; John Wiley & Sons, Inc.: Hoboken, New Jersey, **2010**.

73. Becker, R.A.; Ankley, G.T.; Edwards, S.W.; Kennedy, S.W.; Linkov, I.; Meek, B.; Sachana, M.; Segner, H.; Van Der Burg, B.; Villeneuve, D.L.; et al. Increasing Scientific Confidence in Adverse Outcome Pathways: Application of Tailored Bradford-Hill Considerations for Evaluating Weight of Evidence. *Regul. Toxicol. Pharmacol. RTP* **2015**, *72*, 514–37.

74. Piersma, A.H.; Burgdorf, T.; Louekari, K.; Desprez, B.; Taalman, R.; Landsiedel, R.; Barroso, J.; Rogiers, V.; Eskes, C.; Oelgeschläger, M.; et al. Workshop on acceleration of the validation and regulatory acceptance of alternative methods and implementation of testing strategies. *Toxicol. In Vitro* **2018**, *50*, 62–74.

75. Scholz, S.; Sela, E.; Blaha, L.; Braunbeck, T.; Galay-Burgos, M.; García-Franco, M.; Guinea, J.; Klüver, N.; Schirmer, K.; Tanneberger, K.; et al. A European perspective on alternatives to animal testing for environmental hazard identification and risk assessment. *Regul. Toxicol. Pharmacol.* **2013**, *67*, 506–530.

76. Bus, J.S.; Becker, R.A. Toxicity testing in the 21st century: a view from the chemical industry. *Toxicol. Sci.* **2009**, *112*, 297–302.

77. Altenburger, R.; Brack, W.; Burgess, R.M.; Busch, W.; Escher, B.I.; Focks, A.; Mark Hewitt, L.; Jacobsen, B.N.; de Alda, M.L.; Ait-Aissa, S.; et al. Future water quality monitoring: improving the balance between exposure and toxicity assessments of real-world pollutant mixtures. *Environ. Sci. Eur.* **2019**, *31,* 1-17.

78. Harremoes, P.; Gee, D.; MacGarvin, M.; Stirling, A.; Keys, J.; Wynne, B.; Vaz, S.G. *The Precautionary Principle in the 20th Century: Late Lessons from Early Warnings.*; Taylor and Francis: Hoboken, **2013**; ISBN 978-1-134-20778-7.

79. Breitholtz, M.; Rudén, C.; Ove Hansson, S.; Bengtsson, B.-E. Ten challenges for improved ecotoxicological testing in environmental risk assessment. *Ecotoxicol. Environ. Saf.* **2006**, *63*, 324–335.

80. Chapman, P.M. Integrating toxicology and ecology: putting the “eco” into ecotoxicology. *Mar. Pollut. Bull.* **2002**, *44*, 7–15.

81. Cairns, J. Are single species toxicity tests alone adequate for estimating environmental hazard? *Environ. Monit. Assess.* **1984**, *4*, 259–273.

82. Leist, M.; Hartung, T. Inflammatory findings on species extrapolations: humans are definitely no 70-kg mice. *Arch. Toxicol.* **2013**, *87*, 563–567.

83. LaLone, C.A.; Villeneuve, D.L.; Lyons, D.; Helgen, H.W.; Robinson, S.L.; Swintek, J.A.; Saari, T.W.; Ankley, G.T. Sequence Alignment to Predict Across Species Susceptibility (SeqAPASS): A Web-Based Tool for Addressing the Challenges of Cross-Species Extrapolation of Chemical Toxicity. *Toxicol. Sci.* **2016**, *153*, 228–245.

84. LaLone, C.A.; Villeneuve, D.L.; Burgoon, L.D.; Russom, C.L.; Helgen, H.W.; Berninger, J.P.; Tietge, J.E.; Severson, M.N.; Cavallin, J.E.; Ankley, G.T. Molecular target sequence similarity as a basis for species extrapolation to assess the ecological risk of chemicals with known modes of action. *Aquat. Toxicol.* **2013**, *144–145*, 141–154.

85. Adeleye, Y.; Andersen, M.; Clewell, R.; Davies, M.; Dent, M.; Edwards, S.; Fowler, P.; Malcomber, S.; Nicol, B.; Scott, A.; et al. Implementing Toxicity Testing in the 21st Century (TT21C): Making safety decisions using toxicity pathways, and progress in a prototype risk assessment. *Toxicology* **2015**, *332*, 102–111.

86. Chapman, P.M.; Fairbrother, A.; Brown, D. A critical evaluation of safety (uncertainty) factors for ecological risk assessment. *Environ. Toxicol. Chem.* **2009**, *17*, 99–108.

87. Celander, M.C.; Goldstone, J.V.; Denslow, N.D.; Iguchi, T.; Kille, P.; Meyerhoff, R.D.; Smith, B.A.; Hutchinson, T.H.; Wheeler, J.R. Species extrapolation for the 21st century. *Environ. Toxicol. Chem.* **2011**, *30*, 52–63.

88. Benson, W.H. *Genomic approaches for cross-species extrapolation in toxicology proceedings from the Workshop on Emerging Molecular and Computational Approaches for Cross-Species Extrapolations, 18-22 July 2004, Portland, Oregon, USA*; CRC: Boca Raton, **2007**; ISBN 978-1-4200-4334-1.

89. Raunio, H. In Silico Toxicology – Non-Testing Methods. *Front. Pharmacol.* **2011**, *2,* 1-8.

90. Cronin, M.T.D. (Q)SARs to predict environmental toxicities: current status and future needs. *Env. Sci Process. Impacts* **2017**, *19*, 213–220.

91. Kienzler, A.; Barron, M.G.; Belanger, S.E.; Beasley, A.; Embry, M.R. Mode of Action (MOA) Assignment Classifications for Ecotoxicology: An Evaluation of Approaches. *Environ. Sci. Technol.* **2017**, *51*, 10203–10211.

92. United States Environmental Protection Agency (USEPA) Mode of Action (MOA) Assignment Classifications for Ecotoxicology: Evaluation of Available Methods. **2016**.

93. Tebby, C.; Mombelli, E.; Pandard, P.; Péry, A.R.R. Exploring an ecotoxicity database with the OECD (Q)SAR Toolbox and DRAGON descriptors in order to prioritise testing on algae, daphnids, and fish. *Sci. Total Environ.* **2011**, *409*, 3334–3343.

94. Bhatia, S.; Schultz, T.; Roberts, D.; Shen, J.; Kromidas, L.; Marie Api, A. Comparison of Cramer classification between Toxtree, the OECD QSAR Toolbox and expert judgment. *Regul. Toxicol. Pharmacol.* **2015**, *71*, 52–62.

95. *In silico toxicology: principles and applications*; Cronin, M.T.D., Madden, J.C., Royal Society of Chemistry (Great Britain), Eds.; Issues in toxicology; RSC Pub: Cambridge, UK, 2010; ISBN 978-1-84973-004-4.

96. Lillicrap, A.; Belanger, S.; Burden, N.; Pasquier, D.D.; Embry, M.R.; Halder, M.; Lampi, M.A.; Lee, L.; Norberg-King, T.; Rattner, B.A.; et al. Alternative approaches to vertebrate ecotoxicity tests in the 21st century: A review of developments over the last 2 decades and current status. *Environ. Toxicol. Chem.* **2016**, *35*, 2637–2646.

97. Ellison, C.M.; Piechota, P.; Madden, J.C.; Enoch, S.J.; Cronin, M.T.D. Adverse Outcome Pathway (AOP) Informed Modeling of Aquatic Toxicology: QSARs, Read-Across, and Interspecies Verification of Modes of Action. *Environ. Sci. Technol.* **2016**, *50*, 3995–4007.

98. Escher, B.I.; Hermens, J.L.M. Modes of action in ecotoxicology: Their role in body burdens, species sensitivity, QSARs, and mixture effects. *Environ. Sci. Technol.* **2002**, *36*, 4201–4217.

99. Schüürmann, G.; Segner, H.; Jung, K. Multivariate mode-of-action analysis of acute toxicity of phenols. *Aquat. Toxicol.* **1997**, *38*, 277–296.

100. ECHA *Practical guide 5. How to use and report (Q)SARs: version 3.1. Helsinki: ECHA (Practical guide).*; 2016;

101. Holsapple, M.P.; Afshari, C.A.; Lehman-McKeeman, L.D. Forum Series: the “Vision” for Toxicity Testing in the 21st Century: promises and conundrums. *Toxicol. Sci.* **2009**, *107*, 307–8.

102. Seidle, T.; Stephens, M.L. Bringing toxicology into the 21st century: A global call to action. *Toxicol. In Vitro* **2009**, *23*, 1576–1579.

103. Cohen Hubal, E.A.; Wetmore, B.A.; Wambaugh, J.F.; El-Masri, H.; Sobus, J.R.; Bahadori, T. Advancing internal exposure and physiologically-based toxicokinetic modeling for 21st-century risk assessments. *J. Expo. Sci. Environ. Epidemiol.* **2019**, *29*, 11–20.

104. Cohen Hubal, E.A. Biologically relevant exposure science for 21st century toxicity testing. *Toxicol. Sci.* **2009**, *111*, 226–32.

105. Sheldon, L.S.; Cohen Hubal, E.A. Exposure as part of a systems approach for assessing risk. *Environ. Health Perspect.* **2009**, *117*, 119–1194.

106. Krewski, D.; Acosta, D.; Andersen, M.; Anderson, H.; Bailar, J.C.; Boekelheide, K.; Brent, R.; Charnley, G.; Cheung, V.G.; Green, S.; et al. Toxicity testing in the 21st century: a vision and a strategy. *J. Toxicol. Environ. Health* **2010**, *13*, 51–138.

107. Krewski, D.; Westphal, M.; Al-Zoughool, M.; Croteau, M.C.; Andersen, M.E. New directions in toxicity testing. *Annu. Rev. Public Health* **2011**, *32*, 161–78.

108. Ankley, G.T.; Bennett, R.S.; Erickson, R.J.; Hoff, D.J.; Hornung, M.W.; Johnson, R.D.; Mount, D.R.; Nichols, J.W.; Russom, C.L.; Schmieder, P.K.; et al. Adverse outcome pathways: A conceptual framework to support ecotoxicology research and risk assessment. *Environ. Toxicol. Chem.* **2010**, *29*, 730–741.

109. Perkins, E.; Gayen, K; Shoemaker, J. E.; Antczak, P. Chemical hazard prediction and hypothesis testing using quantitative adverse outcome pathways. *ALTEX* **2019**, *36*, 91–102.

110. Lee, J.W.; Won, E.-J.; Raisuddin, S.; Lee, J.-S. Significance of adverse outcome pathways in biomarker-based environmental risk assessment in aquatic organisms. *J. Environ. Sci. China* **2015**, *35*, 115–27.

111. Perkins, E.J.; Antczak, P.; Burgoon, L.; Falciani, F.; Garcia-Reyero, N.; Gutsell, S.; Hodges, G.; Kienzler, A.; Knapen, D.; McBride, M.; et al. Adverse Outcome Pathways for Regulatory Applications: Examination of Four Case Studies With Different Degrees of Completeness and Scientific Confidence. *Toxicol. Sci.* **2015**, *148*, 14–25.

112. Ankley, G. Webinar: Evolution of the Adverse Outcome Pathway as a tool supporting chemical risk assessment in the 21st century. **2016**.

113. Carusi, A.; Davies, M.R.; De Grandis, G.; Escher, B.I.; Hodges, G.; Leung, K.M.Y.; Whelan, M.; Willett, C.; Ankley, G.T. Harvesting the promise of AOPs: An assessment and recommendations. *Sci. Total Environ.* **2018**, *628–629*, 1542–1556.

114. Edwards, S.W.; Tan, Y.M.; Villeneuve, D.L.; Meek, M.E.; McQueen, C.A. Adverse Outcome Pathways--Organizing Toxicological Information to Improve Decision Making. *J. Pharmacol. Exp. Ther.* **2015**, *356*, 170–181.

115. McKim, J.; Goldberg, A.; Kleinstreuer, N.; Busquet, F.; Andersen, M. Comments on How to Make the New Vision of Toxicity Testing in the 21st Century a Reality. *Appl. Vitro Toxicol.* **2014**, *1*, 5–10.

116. Knapen, D.; Angrish, M.M.; Fortin, M.C.; Katsiadaki, I.; Leonard, M.; Margiotta-Casaluci, L.; Munn, S.; O'Brien, J.M.; Pollesch, N.; Smith, L.C.; et al. Adverse outcome pathway networks I: Development and applications: Advancing adverse outcome pathway networks. *Environ. Toxicol. Chem.* **2018**, *37*, 1723–1733.

117. Villeneuve, D.L.; Crump, D.; Garcia-Reyero, N.; Hecker, M.; Hutchinson, T.H.; LaLone, C.A.; Landesmann, B.; Lettieri, T.; Munn, S.; Nepelska, M.; et al. Adverse Outcome Pathway (AOP) Development I: Strategies and Principles. *Toxicol. Sci.* **2014**, *142*, 312–320.

118. Athersuch, T. Metabolome Analyses in Exposome Studies: Profiling Methods for a Vast Chemical Space. *Arch. Biochem. Biophys.* **2016**, *589*, 177–186.

119. Nelms, M.D.; Simmons, J.E.; Edwards, S.W. Adverse Outcome Pathways to Support the Assessment of Chemical Mixtures. In *Chemical Mixtures and Combined Chemical and Nonchemical Stressors*; Rider, C.V., Simmons, J.E., Eds.; Springer International Publishing: Cham, 2018; pp. 177–201 ISBN 978-3-319-56232-2.

120. Vogs, C.; Altenburger, R. Time-Dependent Effects in Algae for Chemicals with Different Adverse Outcome Pathways: A Novel Approach. *Environ. Sci. Technol.* **2016**, *50*, 7770–7780.

121. Tan, Y.-M.; Leonard, J.A.; Edwards, S.; Teeguarden, J.; Paini, A.; Egeghy, P. Aggregate exposure pathways in support of risk assessment. *Curr. Opin. Toxicol.* **2018**, *9*, 8–13.

122. Teeguarden, J.G.; Tan, Y.-M.; Edwards, S.W.; Leonard, J.A.; Anderson, K.A.; Corley, R.A.; Kile, M.L.; Simonich, S.M.; Stone, D.; Tanguay, R.L.; et al. Completing the Link between Exposure Science and Toxicology for Improved Environmental Health Decision Making: The Aggregate Exposure Pathway Framework. *Environ. Sci. Technol.* **2016**, *50*, 4579–4586.

123. Worth, A.P.; Blaauboer, B.J. Integrated Approaches to Testing and Assessment. In *The History of Alternative Test Methods in Toxicology*; Elsevier, 2019; ISBN 978-0-12-813697-3.

124. Burden, N.; Sewell, F.; Andersen, M.E.; Boobis, A.; Chipman, J.K.; Cronin, M.T.D.; Hutchinson, T.H.; Kimber, I.; Whelan, M. Adverse Outcome Pathways can drive non-animal approaches for safety assessment. *J. Appl. Toxicol.* **2015**, *35*, 971–975.

125. Raseta, M.; Pitchford, J.; Cussens, J.; Doe, J. Integrated testing strategies can be optimal for chemical risk classification. *Math. Biosci.* **2017**, *290*, 1–8.

126. OECD *GUIDANCE DOCUMENT FOR THE USE OF ADVERSE OUTCOME PATHWAYS IN DEVELOPING INTEGRATED APPROACHES TO TESTING AND ASSESSMENT (IATA)*; Series on Testing & Assessment No. 260; OECD: Paris, **2016**.

127. Sakuratani, Y.; Horie, M.; Leinala, E. Integrated Approaches to Testing and Assessment: OECD Activities on the Development and Use of Adverse Outcome Pathways and Case Studies. *Basic Clin. Pharmacol. Toxicol.* **2018**, *123*, 20–28.

128. Antczak, P.; White, T.A.; Giri, A.; Michelangeli, F.; Viant, M.R.; Cronin, M.T.D.; Vulpe, C.; Falciani, F. Systems Biology Approach Reveals a Calcium-Dependent Mechanism for Basal Toxicity in Daphnia magna. *Environ. Sci. Technol.* **2015**, *49*, 11132–11140.

129. Patlewicz, G.; Fitzpatrick, J.M. Current and Future Perspectives on the Development, Evaluation, and Application of in Silico Approaches for Predicting Toxicity. *Chem. Res. Toxicol.* **2016**, acs.chemrestox.5b00388-acs.chemrestox.5b00388.

130. Klüver, N.; Vogs, C.; Altenburger, R.; Escher, B.I.; Scholz, S. Development of a general baseline toxicity QSAR model for the fish embryo acute toxicity test. *Chemosphere* **2016**, *164*, 164–173.

131. Klüver, N.; Bittermann, K.; Escher, B.I. QSAR for baseline toxicity and classification of specific modes of action of ionizable organic chemicals in the zebrafish embryo toxicity test. *Aquat. Toxicol.* **2019**, *207*, 110–119.

132. Burden, N.; Maynard, S.K.; Weltje, L.; Wheeler, J.R. The utility of QSARs in predicting acute fish toxicity of pesticide metabolites: A retrospective validation approach. *Regul. Toxicol. Pharmacol.* **2016**, *80*, 241–246.

133. dos Santos, C.E.M.; Nardocci, A.C. Prioritization of pharmaceuticals in drinking water exposure based on toxicity and environmental fate assessment by in silico tools: An integrated and transparent ranking. *Comput. Toxicol.* **2019**, *9*, 12–21.

134. Tollefsen, K.E.; Scholz, S.; Cronin, M.T.; Edwards, S.W.; de Knecht, J.; Crofton, K.; Garcia-Reyero, N.; Hartung, T.; Worth, A.; Patlewicz, G. Applying Adverse Outcome Pathways (AOPs) to support Integrated Approaches to Testing and Assessment (IATA). *Regul. Toxicol. Pharmacol.* **2014**, *70*, 629–640.

135. Aguayo-Orozco, A.; Taboureau, O.; Brunak, S. The use of systems biology in chemical risk assessment. *Curr. Opin. Toxicol.* **2019**, S2468202018300585.

136. ECHA *Evaluation under REACH - Progress Report 2015. ECHA-15-R-20-EN*; **2016**.

137. Judson, R.S.; Houck, K.A.; Kavlock, R.J.; Knudsen, T.B.; Martin, M.T.; Mortensen, H.M.; Reif, D.M.; Rotroff, D.M.; Shah, I.; Richard, A.M.; et al. In vitro screening of environmental chemicals for targeted testing prioritization: the ToxCast project. *Environ. Health Perspect.* **2010**, *118*, 485–92.

138. NIH *Library of Integrated Network-based Cellular Signatures (LINCS)*; 2019;

139. Pampaloni, F.; Stelzer, E.H. Three-Dimensional Cell Cultures in Toxicology. *Biotechnol. Genet. Eng. Rev.* **2009**, *26*, 117–138.

140. Barron, M.G.; Lilavois, C.R.; Martin, T.M. MOAtox: A comprehensive mode of action and acute aquatic toxicity database for predictive model development. *Aquat. Toxicol.* **2015**, *161*, 102–107.

141. Heijne, W.H.M.; Kienhuis, A.S.; van Ommen, B.; Stierum, R.H.; Groten, J.P. Systems toxicology: applications of toxicogenomics, transcriptomics, proteomics and metabolomics in toxicology. *Expert Rev. Proteomics* **2005**, *2*, 767–780.

142. Pérez-Alonso, M.-M.; Carrasco-Loba, V.; Medina, J.; Vicente-Carbajosa, J.; Pollmann, S. When Transcriptomics and Metabolomics Work Hand in Hand: A Case Study Characterizing Plant CDF Transcription Factors. *High-Throughput* **2018**, *7*, 7.

143. Roessner, U.; Willmitzer, L.; Fernie, a R. Metabolic profiling and biochemical phenotyping of plant systems. *Plant Cell Rep.* **2002**, *21*, 189–196.

144. Hong, J.; Yang, L.; Zhang, D.; Shi, J. Plant Metabolomics: An Indispensable System Biology Tool for Plant Science. *Int. J. Mol. Sci.* **2016**, *17*, 767–767.

145. Fent, K.; Sumpter, J.P. Progress and promises in toxicogenomics in aquatic toxicology: is technical innovation driving scientific innovation? *Aquat. Toxicol.* **2011**, *105*, 25–39.

146. Brockmeier, E.K.; Hodges, G.; Hutchinson, T.H.; Butler, E.; Hecker, M.; Tollefsen, K.E.; Garcia-Reyero, N.; Kille, P.; Becker, D.; Chipman, K.; et al. The Role of Omics in the Application of Adverse Outcome Pathways for Chemical Risk Assessment. *Toxicol. Sci.* **2017**, *158*, 252–262.

147. NRC *Application of Toxicogenomics to Cross-Species Extrapolation: A Report of a Workshop*; National Academies Press: Washington, D.C., 2006; ISBN 978-0-309-10084-7.

148. van Ravenzwaay, B.; Sperber, S.; Lemke, O.; Fabian, E.; Faulhammer, F.; Kamp, H.; Mellert, W.; Strauss, V.; Strigun, A.; Peter, E.; et al. Metabolomics as read-across tool: A case study with phenoxy herbicides. *Regul. Toxicol. Pharmacol.* **2016**, *81*, 288–304.

149. Vinken, M. Omics-based input and output in the development and use of adverse outcome pathways. *Curr. Opin. Toxicol.* **2019**, *5,* 1-15.

150. Patlewicz, G.; Simon, T.W.; Rowlands, J.C.; Budinsky, R. a; Becker, R. a Proposing a scientific confidence framework to help support the application of adverse outcome pathways for regulatory purposes. *Regul. Toxicol. Pharmacol.* **2015**, *71*, 463–477.

151. Bopp, S.K.; Barouki, R.; Brack, W.; Dalla Costa, S.; Dorne, J.-L.C.M.; Drakvik, P.E.; Faust, M.; Karjalainen, T.K.; Kephalopoulos, S.; van Klaveren, J.; et al. Current EU research activities on combined exposure to multiple chemicals. *Environ. Int.* **2018**, *120*, 544–562.

152. Bopp, S.; Berggren, E.; Kienzler, A.; Linden, S. van der; Worth, A.; Institute for Health and Consumer Protection *Scientific methodologies for the assessment of combined effects of chemicals - a survey and literature review: Use of novel and alternative methods in the assessment of effects from combined exposure to multiple chemicals.*; Publications Office: Luxembourg, 2015; ISBN 978-92-79-51925-3.

153. Zhang, X.; Xia, P.; Wang, P.; Yang, J.; Baird, D.J. Omics Advances in Ecotoxicology. *Environ. Sci. Technol.* **2018**, *52*, 3842–3851.

154. Martyniuk, C.J.; Simmons, D.B. Spotlight on environmental omics and toxicology: a long way in a short time. *Comp. Biochem. Physiol. Part D Genomics Proteomics* **2016**, *19*, 97–101.

155. Currie, R.A. Toxicogenomics: The challenges and opportunities to identify biomarkers, signatures and thresholds to support mode-of-action. *Mutat. Res. Toxicol. Environ. Mutagen.* **2012**, *746*, 97–103.

156. Bridges, J.; Sauer, U.G.; Buesen, R.; Deferme, L.; Tollefsen, K.E.; Tralau, T.; van Ravenzwaay, B.; Poole, A.; Pemberton, M. Framework for the quantitative weight-of-evidence analysis of ‘omics data for regulatory purposes. *Regul. Toxicol. Pharmacol.* **2017**, *91*, S46–S60.

157. Buesen, R.; Chorley, B.N.; da Silva Lima, B.; Daston, G.; Deferme, L.; Ebbels, T.; Gant, T.W.; Goetz, A.; Greally, J.; Gribaldo, L.; et al. Applying ’omics technologies in chemicals risk assessment: Report of an ECETOC workshop. *Regul. Toxicol. Pharmacol.* **2017**, 1–11.

158. Kauffmann, H.-M.; Kamp, H.; Fuchs, R.; Chorley, B.N.; Deferme, L.; Ebbels, T.; Hackermüller, J.; Perdichizzi, S.; Poole, A.; Sauer, U.G.; et al. Framework for the quality assurance of ’omics technologies considering GLP requirements. *Regul. Toxicol. Pharmacol.* **2017**, 1–9.

159. McBride, M.T. The Application of Omics Data to the Development of AOPs. In *A Systems Biology Approach to Advancing Adverse Outcome Pathways for Risk Assessment*; Garcia-Reyero, N., Murphy, C.A., Eds.; Springer International Publishing: Cham, 2018; ISBN 978-3-319-66082-0.

160. Corvi, R.; Ahr, H.J.; Albertini, S.; Blakey, D.H.; Clerici, L.; Coecke, S.; Douglas, G.R.; Gribaldo, L.; Groten, J.P.; Haase, B.; et al. Meeting report: Validation of toxicogenomics-based test systems: ECVAM-ICCVAM/NICEATM considerations for regulatory use. *Environ. Health Perspect.* **2006**, *114*, 420–429.

161. Kolker, E.; Özdemir, V.; Martens, L.; Hancock, W.; Anderson, G.; Anderson, N.; Aynacioglu, S.; Baranova, A.; Campagna, S.R.; Chen, R.; et al. Toward More Transparent and Reproducible Omics Studies Through a Common Metadata Checklist and Data Publications. *OMICS J. Integr. Biol.* **2014**, *18*, 10–14.

162. Taylor, N.; Gavin, A.; Viant, M. Metabolomics Discovers Early-Response Metabolic Biomarkers that Can Predict Chronic Reproductive Fitness in Individual Daphnia magna. *Metabolites* **2018**, *8*, 42.

163. Aizat, W.M.; Goh, H.-H.; Baharum, S.N. *Omics Applications for Systems Biology*; **2018**; ISBN 978-3-319-98758-3.

164. Forshed, J. Experimental Design in Clinical ‘Omics Biomarker Discovery. *J. Proteome Res.* **2017**, *16*, 3954–3960.

165. European food and Safety Authority (EFSA); Aguilera, J.; Aguilera-Gomez, M.; Barrucci, F.; Cocconcelli, P.S.; Davies, H.; Denslow, N.; Lou Dorne, J.; Grohmann, L.; Herman, L.; et al. EFSA Scientific Colloquium 24 – ’omics in risk assessment: state of the art and next steps. *EFSA Support. Publ.* **2018**, *15,* 1-30.

166. Groh, K.J.; Carvalho, R.N.; Chipman, J.K.; Denslow, N.D.; Halder, M.; Murphy, C.A.; Roelofs, D.; Rolaki, A.; Schirmer, K.; Watanabe, K.H. Development and application of the adverse outcome pathway framework for understanding and predicting chronic toxicity: I. Challenges and research needs in ecotoxicology. *Chemosphere* **2015**, *120*, 764–777.

167. Perkins, E.J.; Chipman, J.K.; Edwards, S.; Habib, T.; Falciani, F.; Taylor, R.; Van Aggelen, G.; Vulpe, C.; Antczak, P.; Loguinov, A. Reverse engineering adverse outcome pathways. *Environ. Toxicol. Chem.* **2011**, *30*, 22–38.

168. OECD *Users' Handbook supplement to the Guidance Document for developing and assessing Adverse Outcome Pathways*; Paris, **2018**.

169. Marx-Stoelting, P.; Braeuning, A.; Buhrke, T.; Lampen, A.; Niemann, L.; Oelgeschlaeger, M.; Rieke, S.; Schmidt, F.; Heise, T.; Pfeil, R.; et al. Application of omics data in regulatory toxicology: report of an international BfR expert workshop. *Arch. Toxicol.* **2015**, *89*, 2177–2184.

170. Van Aggelen, G.; Ankley, G.T.; Baldwin, W.S.; Bearden, D.W.; Benson, W.H.; Chipman, J.K.; Collette, T.W.; Craft, J.A.; Denslow, N.D.; Embry, M.R.; et al. Integrating omic technologies into aquatic ecological risk assessment and environmental monitoring: hurdles, achievements, and future outlook. *Environ. Health Perspect.* **2010**, *118*, 1–5.

171. ECHA *The Use of Alternatives to Testing on Animals for the REACH Regulation, 2nd report under Art. 117(3) of the REACH Regulation. ECHA-14-A-07-EN.*; **2014**.

172. De Wever, B.; Fuchs, H.W.; Gaca, M.; Krul, C.; Mikulowski, S.; Poth, A.; Roggen, E.L.; Vilà, M.R. Implementation challenges for designing integrated in vitro testing strategies (ITS) aiming at reducing and replacing animal experimentation. *Toxicol. In Vitro* **2012**, *26*, 526–34.

173. Garcia-Reyero, N.; Murphy, C.A. Advancing Adverse Outcome Pathways for Risk Assessment. In *A Systems Biology Approach to Advancing Adverse Outcome Pathways for Risk Assessment*; Garcia-Reyero, N., Murphy, C.A., Eds.; Springer International Publishing: Cham, **2018**; ISBN 978-3-319-66082-0.

174. Hahn, M.E. Mechanistic research in aquatic toxicology: Perspectives and future directions. *Aquat. Toxicol.* **2011**, *105*, 67–71.

175. Fay, K.A.; Villeneuve, D.L.; LaLone, C.A.; Song, Y.; Tollefsen, K.E.; Ankley, G.T. Practical approaches to adverse outcome pathway development and weight-of-evidence evaluation as illustrated by ecotoxicological case studies. *Environ. Toxicol. Chem.* **2017**, *9999*, 1–21.

176. Calzolai, L.; Ansorge, W.; Calabrese, E.; Denslow, N.; Part, P.; Lettieri, T. Transcriptomics and proteomics. Applications to ecotoxicology. *Comp. Biochem. Physiol. - Part Genomics Proteomics* **2007**, *2*, 245–249.

177. Hodges, G.; Gutsell, S.; Taylor, N.; Brockmeier, E.; Butler, E.; Rendal, C.; Colbourne, J. Invertebrate Model Species in AOP Development. In *A Systems Biology Approach to Advancing Adverse Outcome Pathways for Risk Assessment*; Garcia-Reyero, N., Murphy, C.A., Eds.; Springer International Publishing: Cham, **2018**; ISBN 978-3-319-66082-0.

178. Kim, H.; Koedrith, P.; Seo, Y. Ecotoxicogenomic Approaches for Understanding Molecular Mechanisms of Environmental Chemical Toxicity Using Aquatic Invertebrate, Daphnia Model Organism. *Int. J. Mol. Sci.* **2015**, *16*, 12261–12287.

179. Vergauwen, L.; Van Cruchten, S.; Knapen, D. The Fish Embryo as a Model for AOP Development. In *A Systems Biology Approach to Advancing Adverse Outcome Pathways for Risk Assessment*; Garcia-Reyero, N., Murphy, C.A., Eds.; Springer International Publishing: Cham, 2018; ISBN 978-3-319-66082-0.

180. Zupanic, A.; Pillai, S.; Coman Schmid, D.; Schirmer, K. Green Algae and Networks for Adverse Outcome Pathways. In *A Systems Biology Approach to Advancing Adverse Outcome Pathways for Risk Assessment*; Garcia-Reyero, N., Murphy, C.A., Eds.; Springer International Publishing: Cham, 2018; pp. 133–148 ISBN 978-3-319-66082-0.

181. Guiry, M.D. HOW MANY SPECIES OF ALGAE ARE THERE? *J. Phycol.* **2012**, *48*, 1057–1063.

182. Stevenson, J. Ecological assessments with algae: a review and synthesis. *J. Phycol.* **2014**, *50*, 437–461.

183. McCormick, P.V.; Cairns, J. Algae as indicators of environmental change. *J. Appl. Phycol.* **1994**, *6*, 509–526.

184. ECHA *Guidance on information requirements and chemical safety assessment. Chapter R.10: Characterisation of dose [concentration]-response for environment*; **2008.**

185. Pröschold, T.; Harris, E.H.; Coleman, A.W. Portrait of a Species: Chlamydomonas reinhardtii. *Genetics* **2005**, *170*, 1601–1610.

186. Merchant, S.S.; Prochnik, S.E.; Vallon, O.; Harris, E.H.; Karpowicz, S.J.; Witman, G.B.; Terry, A.; Salamov, A.; Fritz-Laylin, L.K.; Maréchal-Drouard, L.; et al. The Chlamydomonas genome reveals the evolution of key animal and plant functions. *Science* **2007**, *318*, 245–50.

187. May, P.; Christian, J.-O.; Kempa, S.; Walther, D. ChlamyCyc: an integrative systems biology database and web-portal for Chlamydomonas reinhardtii. *BMC Genomics* **2009**, *10*, 209–209.

188. Jinkerson, R.E.; Jonikas, M.C. Molecular techniques to interrogate and edit the Chlamydomonas nuclear genome. *Plant J.* **2015**, *82*, 393–412.

189. Shin, S.-E.; Lim, J.-M.; Koh, H.G.; Kim, E.K.; Kang, N.K.; Jeon, S.; Kwon, S.; Shin, W.-S.; Lee, B.; Hwangbo, K.; et al. CRISPR/Cas9-induced knockout and knock-in mutations in Chlamydomonas reinhardtii. *Sci. Rep.* **2016**, *6*, 27810–27810.

190. Romero-campero, F.J.; Ignacio, P.; Lucas-reina, E.; Valverde, F. ChlamyNET : A Chlamydomonas gene co-expression network reveals global properties of the transcriptome and the early setup of key co-expression patterns in the green lineage. *BMC Genomics* **2016**, 1–41.

191. Gumpel, N.J.; Purton, S. Playing tag with chlamydomonas. *Trends Cell Biol.* **1994**, *4*, 299–301.

192. *The Chlamydomonas Sourcebook*; Harris, E.H., Witman, G.B., Stern, D.B., Eds.; 2nd ed.; Academic Press: Oxford, UK, 2009; Vol. 3; ISBN 978-0-12-370873-1.

193. Zones, J.M.; Blaby, I.K.; Merchant, S.S.; Umen, J.G. High-Resolution Profiling of a Synchronized Diurnal Transcriptome from Chlamydomonas reinhardtii Reveals Continuous Cell and Metabolic Differentiation. *Plant Cell* **2015**, *27*, 2743–69.

194. Harris, E.H. CHLAMYDOMONAS AS A MODEL ORGANISM. *Annu. Rev. Plant Physiol. Plant Mol. Biol.* **2001**, *52*, 363–406.

195. Rochaix, J.-D. Chlamydomonas , a model system for studying the assembly and dynamics of photosynthetic complexes. *FEBS Lett.* **2002**, *529*, 34–38.

196. Oldenhof, H.; Zachleder, V.; Van Den Ende, H. Blue- and red-light regulation of the cell cycle in Chlamydomonas reinhardtii (Chlorophyta). *Eur. J. Phycol.* **2006**, *41*, 313–320.

197. Bisova, K.; Zachleder, V. Cell-cycle regulation in green algae dividing by multiple fission. *J. Exp. Bot.* **2014**, *65*, 2585–2602.

198. Cross, F.R.; Umen, J.G. The Chlamydomonas cell cycle. *Plant J.* **2015**, *82*, 370–392.

199. Lemaire, S.D.; Hours, M.; Gerard-Hirne, C.; Trouabal, A.; Roche, O.; Jacquot, J.P. Analysis of light/dark synchronization of cell-wall-less Chlamydomonas reinhardtii (Chlorophyta) cells by flow cytometry. *Eur. J. Phycol.* **1999**, *34*, 279–286.

200. Spudich, J.L.; Sager, R. Regulation of the Chlamydomonas cell cycle by light and dark. *J. Cell Biol.* **1980**, *85*, 136–145.

201. Surzycki, S. Synchronously Grown Cultures of Chlamydomonas reinhardi. *Methods Enzym.* **1971**, *23*, 67–73.

202. Zachleder, V.; Ende, H.V.D.; van den Ende, H. Cell cycle events in the green alga Chlamydomonas eugametos and their control by environmental factors. *J. Cell Sci.* **1992**, *474*, 469–474.

203. Bi, A.; Cui, J.; Ma, Y.-P.; Olshevskaya, E.; Pu, M.; Dizhoor, A.M.; Pan, Z.-H. Ectopic Expression of a Microbial-Type Rhodopsin Restores Visual Responses in Mice with Photoreceptor Degeneration. *Neuron* **2006**, *50*, 23–33.

204. Deng, X.; Fei, X.; Li, Y. The effects of nutritional restriction on neutral lipid accumulation in Chlamydomonas and Chlorella. *Afr. J. Microbiol.* **2011**, *5*, 260–270.

205. Cakmak, T.; Angun, P.; Ozkan, A.D.; Cakmak, Z.; Olmez, T.T.; Tekinay, T. Nitrogen and sulfur deprivation differentiate lipid accumulation targets of chlamydomonas reinhardtii. *Bioengineered* **2012**, *3*, 343–346.

206. Wang, Z.T.; Ullrich, N.; Joo, S.; Waffenschmidt, S.; Goodenough, U. Algal Lipid Bodies: Stress Induction, Purification, and Biochemical Characterization in Wild-Type and Starchless Chlamydomonas reinhardtii. *Eukaryot. Cell* **2009**, *8*, 1856–1868.

207. Scott, S.A.; Davey, M.P.; Dennis, J.S.; Horst, I.; Howe, C.J.; Lea-Smith, D.J.; Smith, A.G. Biodiesel from algae: challenges and prospects. *Curr. Opin. Biotechnol.* **2010**, *21*, 277–286.

208. Blaby, I.K.; Blaby-Haas, C.E.; Tourasse, N.; Hom, E.F.Y.; Lopez, D.; Aksoy, M.; Grossman, A.; Umen, J.; Dutcher, S.; Porter, M.; et al. The Chlamydomonas genome project: A decade on. *Trends Plant Sci.* **2014**, *19*, 672–680.

209. Shrager, J.; Hauser, C.; Chang, C.-W.; Harris, E.H.; Davies, J.; McDermott, J.; Tamse, R.; Zhang, Z.; Grossman, A.R. Chlamydomonas reinhardtii genome project. A guide to the generation and use of the cDNA information. *Plant Physiol.* **2003**, *131*, 401–8.

210. Weckwerth, W.; Loureiro, M.E.; Wenzel, K.; Fiehn, O. Differential metabolic networks unravel the effects of silent plant phenotypes. *Proc. Natl. Acad. Sci. U. S. A.* **2004**, *101*, 7809–7814.

211. Weckwerth, W.; Wenzel, K.; Fiehn, O. Process for the integrated extraction, identification and quantification of metabolites, proteins and RNA to reveal their co-regulation in biochemical networks. *Proteomics* **2004**, *4*, 78–83.

212. Cognat, V.; Deragon, J.M.; Vinogradova, E.; Salinas, T.; Remacle, C.; Maréchal-Drouard, L. On the evolution and expression of Chlamydomonas reinhardtii nucleus-encoded transfer RNA genes. *Genetics* **2008**, *179*, 113–123.

213. Gray, M.W. Evolution of organellar genomes. *Curr. Opin. Genet. Dev.* **1999**, *9*, 678–687.

214. Gonzalez-Ballester, D.; Pootakham, W.; Mus, F.; Yang, W.; Catalanotti, C.; Magneschi, L.; de Montaigu, A.; Higuera, J.J.; Prior, M.; Galvan, A.; et al. Reverse genetics in Chlamydomonas: a platform for isolating insertional mutants. *Plant Methods* **2011**, *7*, 24–24.

215. Grossman, A.R.; Croft, M.; Gladyshev, V.N.; Merchant, S.S.; Posewitz, M.C.; Prochnik, S.; Spalding, M.H. Novel metabolism in Chlamydomonas through the lens of genomics. *Curr. Opin. Plant Biol.* **2007**, *10*, 190–198.

216. González-Ballester, D.; de Montaigu, A.; Higuera, J.J.; Galván, A.; Fernández, E. Functional genomics of the regulation of the nitrate assimilation pathway in Chlamydomonas. *Plant Physiol.* **2005**, *137*, 522–533.

217. Dent, R.M.; Haglund, C.M.; Chin, B.L.; Kobayashi, M.C.; Niyogi, K.K. Functional genomics of eukaryotic photosynthesis using insertional mutagenesis of Chlamydomonas reinhardtii. *Plant Physiol.* **2005**, *137*, 545–56.

218. Bisova, K.; Krylov, D.M.; Umen, J.G. Genome-Wide Annotation and Expression Profiling of Cell Cycle Regulatory Genes in. *Society* **2005**, *137*, 475–491.

219. Gonzalez-Ballester, D.; Casero, D.; Cokus, S.; Pellegrini, M.; Merchant, S.S.; Grossman, a R. RNA-Seq Analysis of Sulfur-Deprived Chlamydomonas Cells Reveals Aspects of Acclimation Critical for Cell Survival. *Plant Cell* **2010**, *22*, 2058–2084.

220. Mus, F.; Dubini, A.; Seibert, M.; Posewitz, M.C.; Grossman, A.R. Anaerobic acclimation in Chlamydomonas reinhardtii: Anoxic gene expression, hydrogenase induction, and metabolic pathways. *J. Biol. Chem.* **2007**, *282*, 25475–25486.

221. Lv, H.; Qu, G.; Qi, X.; Lu, L.; Tian, C.; Ma, Y. Transcriptome analysis of Chlamydomonas reinhardtii during the process of lipid accumulation. *Genomics* **2013**, *101*, 229–237.

222. Légeret, B.; Schulz-Raffelt, M.; Nguyen, H.M.; Auroy, P.; Beisson, F.; Peltier, G.; Blanc, G.; Li-Beisson, Y. Lipidomic and transcriptomic analyses of Chlamydomonas reinhardtii under heat stress unveil a direct route for the conversion of membrane lipids into storage lipids. *Plant Cell Environ.* **2015**, *39 (4)*, 834-847.

223. Moseley, J.L.; Chang, C.W.; Grossman, A.R. Genome-based approaches to understanding phosphorus deprivation responses and PSR1 control in Chlamydomonas reinhardtii. *Eukaryot. Cell* **2006**, *5*, 26–44.

224. Yamano, T.; Fukuzawa, H. Carbon-concentrating mechanism in a green alga, Chlamydomonas reinhardtii, revealed by transcriptome analyses. *J. Basic Microbiol.* **2009**, *49*, 42–51.

225. Fang, W.; Si, Y.; Douglass, S.; Casero, D.; Merchant, S.S.; Pellegrini, M.; Ladunga, I.; Liu, P.; Spalding, M.H. Transcriptome-Wide Changes in Chlamydomonas reinhardtii Gene Expression Regulated by Carbon Dioxide and the CO2-Concentrating Mechanism Regulator CIA5/CCM1. *Plant Cell* **2012**, *24*, 1876–1893.

226. Toepel, J.; Illmer-Kephalides, M.; Jaenicke, S.; Straube, J.; May, P.; Goesmann, A.; Kruse, O. New insights into Chlamydomonas reinhardtii hydrogen production processes by combined microarray/RNA-seq transcriptomics. *Plant Biotechnol. J.* **2013**, *11*, 717–733.

227. Blaby, I.K.; Glaesener, A.G.; Mettler, T.; Fitz-Gibbon, S.T.; Gallaher, S.D.; Liu, B.; Boyle, N.R.; Kropat, J.; Stitt, M.; Johnson, S.; et al. Systems-level analysis of nitrogen starvation-induced modifications of carbon metabolism in a Chlamydomonas reinhardtii starchless mutant. *Plant Cell* **2013**, *25*, 4305–23.

228. Im, C.S.; Eberhard, S.; Huang, K.; Beck, C.F.; Grossman, A.R. Phototropin involvement in the expression of genes encoding chlorophyll and carotenoid biosynthesis enzymes and LHC apoproteins in Chlamydomonas reinhardtii. *Plant J.* **2006**, *48*, 1–16.

229. Erickson, B.; Stern, D.B.; Higgs, D.C. Microarray analysis confirms the specificity of a Chlamydomonas reinhardtii chloroplast RNA stability mutant. *Plant Physiol* **2005**, *137*, 534–544.

230. Zhang, Z.; Shrager, J.; Jain, M.; Vallon, O.; Grossman, A.R.; Chang, C. Insights into the Survival of Chlamydomonas reinhardtii during Sulfur Starvation Based on Microarray Analysis of Gene Expression Insights into the Survival of Chlamydomonas reinhardtii during Sulfur Starvation Based on Microarray Analysis of Gene Expressi. *Eukaryot. Cell* **2004**, *3*, 1331–1348.

231. Rubinelli, P.; Siripornadulsil, S.; Gao-Rubinelli, F.; Sayre, R. Cadmium- and iron-stress-inducible gene expression in the green alga Chlamydomonas reinhardtii : evidence for H43 protein function in iron assimilation. *Planta* **2002**, *215*, 1–13.

232. Lee, D.Y.; Park, J.-J.; Barupal, D.K.; Fiehn, O. System Response of Metabolic Networks in *Chlamydomonas reinhardtii* to Total Available Ammonium. *Mol. Cell. Proteomics* **2012**, *11*, 973–988.

233. Valledor, L.; Furuhashi, T.; Hanak, A.-M.; Weckwerth, W. Systemic cold stress adaptation of Chlamydomonas reinhardtii. *Mol. Cell. Proteomics MCP* **2013**, *12*, 2032–47.

234. May, P.; Wienkoop, S.; Kempa, S.; Usadel, B. rn B.; Christian, N.; Rupprecht, J.; Weiss, J.; Recuenco-Munoz, L.; Ebenhöh, O.; Weckwerth, W.; et al. Metabolomics- and proteomics-assisted genome annotation and analysis of the draft metabolic network of Chlamydomonas reinhardtii. *Genetics* **2008**, *179*, 157–166.

235. Lee, D.; Fiehn, O. High quality metabolomic data for Chlamydomonas reinhardtii. *Plant Methods* **2008**, *4*, 7–7.

236. Chang, R.L.; Ghamsari, L.; Manichaikul, A.; Hom, E.F.Y.; Balaji, S.; Fu, W.; Shen, Y.; Hao, T.; Palsson, B.O.; Salehi-Ashtiani, K.; et al. Metabolic network reconstruction of Chlamydomonas offers insight into light-driven algal metabolism. *Mol. Syst. Biol.* **2014**, *7*, 518–518.

237. Boyle, N.R.; Morgan, J.A. Flux balance analysis of primary metabolism in Chlamydomonas reinhardtii. *BMC Syst. Biol.* **2009**, *3*, 4–4.

238. Renberg, L.; Johansson, A.I.; Shutova, T.; Stenlund, H.; Aksmann, A.; Raven, J.A.; Gardeström, P.; Moritz, T.; Samuelsson, G. A metabolomic approach to study major metabolite changes during acclimation to limiting CO2 in Chlamydomonas reinhardtii. *Plant Physiol.* **2010**, *154*, 187–96.

239. Bölling, C.; Fiehn, O. Metabolite profiling of Chlamydomonas reinhardti under nutrient deprivation. *Plant Physiol.* **2005**, *139*, 1995–2005.

240. Bajhaiya, A.K.; Dean, A.P.; Driver, T.; Trivedi, D.K.; Rattray, N.J.W.; Allwood, J.W.; Goodacre, R.; Pittman, J.K. High-throughput metabolic screening of microalgae genetic variation in response to nutrient limitation. *Metabolomics* **2015,** 1-14.

241. Timmins, M.; Zhou, W.; Rupprecht, J.; Lim, L.; Thomas-Hall, S.R.; Doebbe, A.; Kruse, O.; Hankamer, B.; Marx, U.C.; Smith, S.M.; et al. The metabolome of Chlamydomonas reinhardtii following induction of anaerobic H2 production by sulfur depletion. *J. Biol. Chem.* **2009**, *284*, 35996–35996.

242. Wienkoop, S.; Weiss, J.; May, P.; Kempa, S.; Irgang, S.; Recuenco-Munoz, L.; Pietzke, M.; Schwemmer, T.; Rupprecht, J.; Egelhofer, V.; et al. Targeted proteomics for Chlamydomonas reinhardtii combined with rapid subcellular protein fractionation, metabolomics and metabolic flux analyses. *Mol. Biosyst.* **2010**, *6*, 1018–1031.

243. Gillet, S.; Decottignies, P.; Chardonnet, S.; Le Maréchal, P. Cadmium response and redoxin targets in Chlamydomonas reinhardtii: A proteomic approach. *Photosynth. Res.* **2006**, *89*, 201–211.

244. Stauber, E.J.; Hippler, M. Chlamydomonas reinhardtii proteomics. *Plant Physiol. Biochem.* **2004**, *42*, 989–1001.

245. Pillai, S.; Behra, R.; Nestler, H.; Suter, M.J.F.; Sigg, L.; Schirmer, K. Linking toxicity and adaptive responses across the transcriptome, proteome, and phenotype of Chlamydomonas reinhardtii exposed to silver. *Proc. Natl. Acad. Sci. U. S. A.* **2014**, *111*, 3490–3495.

246. Beauvais-Flück, R.; Slaveykova, V.I.; Cosio, C. Cellular toxicity pathways of inorganic and methyl mercury in the green microalga Chlamydomonas reinhardtii. *Sci. Rep.* **2017**, *7*, 1–12.

247. Beauvais-Flück, R.; Slaveykova, V.; Cosio, C. Molecular Effects of Inorganic and Methyl Mercury in Aquatic Primary Producers: Comparing Impact to A Macrophyte and A Green Microalga in Controlled Conditions. *Geosciences* **2018**, *8*, 393.

248. Jamers, A.; Van der Ven, K.; Moens, L.; Robbens, J.; Potters, G.; Guisez, Y.; Blust, R.; De Coen, W. Effect of copper exposure on gene expression profiles in Chlamydomonas reinhardtii based on microarray analysis. *Aquat. Toxicol.* **2006**, *80*, 249–260.

249. Taylor, N.S.; Kirwan, J.A.; Yan, N.D.; Viant, M.R.; Gunn, J.M.; McGeer, J.C. Metabolomics confirms that dissolved organic carbon mitigates copper toxicity. *Environ. Toxicol. Chem. SETAC* **2015,** *35 (3)*, 635-644.

250. Jamers; Blust; De, C.; Griff; Jones; Griffin; Jones An omics based assessment of cadmium toxicity in the green alga Chlamydomonas reinhardtii. *Aquat. Toxicol.* **2013**, *126*, 355–364.

251. Walliwalagedara, C.; Keulen, H.; Willard, B.; Wei, R. Differential Proteome Analysis of Chlamydomonas reinhardtii Response to Arsenic Exposure. *Am. J. Plant Sci.* **2012**, *03*, 764–772.

252. Nestler, H.; Groh, K.J.; Schönenberger, R.; Eggen, R.I.L.; Suter, M.J.F. Linking proteome responses with physiological and biochemical effects in herbicide-exposed Chlamydomonas reinhardtii. *J. Proteomics* **2012**, *75*, 5370–5385.

253. Esperanza, M.; Seoane, M.; Rioboo, C.; Herrero, C.; Cid, Á. Early alterations on photosynthesis-related parameters in Chlamydomonas reinhardtii cells exposed to atrazine: A multiple approach study. *Sci. Total Environ.* **2016**, *554–555*, 237–245.

254. Pan, C.-G.; Peng, F.-J.; Shi, W.-J.; Hu, L.-X.; Wei, X.-D.; Ying, G.-G. Triclosan-induced transcriptional and biochemical alterations in the freshwater green algae Chlamydomonas reinhardtii. *Ecotoxicol. Environ. Saf.* **2018**, *148*, 393–401.

255. González-Pleiter, M.; Rioboo, C.; Reguera, M.; Abreu, I.; Leganés, F.; Cid, Á.; Fernández-Piñas, F. Calcium mediates the cellular response of Chlamydomonas reinhardtii to the emerging aquatic pollutant Triclosan. *Aquat. Toxicol.* **2017**, *186*, 50–66.

256. Simon, D.F.; Domingos, R.F.; Hauser, C.; Hutchins, C.M.; Zerges, W.; Wilkinson, K.J. Transcriptome sequencing (RNA-seq) analysis of the effects of metal nanoparticle exposure on the transcriptome of Chlamydomonas reinhardtii. *Appl. Environ. Microbiol.* **2013**, *79*, 4774–4785.

257. Taylor, N.S.; Merrifield, R.; Williams, T.D.; Chipman, J.K.; Lead, J.R.; Viant, M.R. Molecular toxicity of cerium oxide nanoparticles to the freshwater alga Chlamydomonas reinhardtii is associated with supra-environmental exposure concentrations. *Nanotoxicology* **2015**, *5390*, 1–10.

258. Simon, D.F.; Descombes, P.; Zerges, W.; Wilkinson, K.J. GLOBAL EXPRESSION PROFILING OF CHLAMYDOMONAS REINHARDTII EXPOSED TO TRACE LEVELS OF FREE CADMIUM. *Environ. Toxicol. Chem.* **2008**, *27*, 1668–1668.

259. Du, C.; Zhang, B.; He, Y.; Hu, C.; Ng, Q.X.; Zhang, H.; Ong, C.N.; ZhifenLin Biological effect of aqueous C60 aggregates on Scenedesmus obliquus revealed by transcriptomics and non-targeted metabolomics. *J. Hazard. Mater.* **2017**, *324*, 221–229.

260. Kim, Y.K.; Yoo, W.I.; Lee, S.H.; Lee, M.Y. Proteomic analysis of cadmium-induced protein profile alterations from marine alga Nannochloropsis oculata. *Ecotoxicol. Lond. Engl.* **2005**, *14*, 589–96.

261. Patel, N.; Cardoza, V.; Christensen, E.; Rekapalli, B.; Ayalew, M.; Stewart, C.N.N. Differential gene expression of Chlamydomonas reinhardtii in response to 2,4,6-trinitrotoluene (TNT) using microarray analysis. *Plant Sci.* **2004**, *167*, 1109–1122.

262. Wang, S.-B.; Chen, F.; Sommerfeld, M.; Hu, Q. Proteomic analysis of molecular response to oxidative stress by the green alga Haematococcus pluvialis (Chlorophyceae). *Planta* **2004**, *220*, 17–29.

263. Jiang, Y.; Xiao, P.; Shao, Q.; Qin, H.; Hu, Z.; Lei, A.; Wang, J. Metabolic responses to ethanol and butanol in Chlamydomonas reinhardtii. *Biotechnol. Biofuels* **2017**, *10*, 239–239.

264. Jamers, A.; Blust, R.; De Coen, W. Omics in algae: Paving the way for a systems biological understanding of algal stress phenomena? *Aquat. Toxicol.* **2009**, *92*, 114–121.

265. Sun, Y.V.; Hu, Y.-J. Integrative Analysis of Multi-omics Data for Discovery and Functional Studies of Complex Human Diseases. In *Advances in Genetics*; Elsevier, **2016**; Vol. 93; ISBN 978-0-12-804801-6.

266. Marín-García, J. The Path to Personalized Cardiovascular Medicine. In *Post-Genomic Cardiology*; Elsevier, **2014**; ISBN 978-0-12-404599-6.

267. Wenk, M.R. The emerging field of lipidomics. *Nat. Rev. Drug Discov.* **2005**, *4*, 594–610.

268. Dettmer, K.; Aronov, P.A.; Hammock, B.D. Mass spectrometry-based metabolomics. *Mass Spectrom. Rev.* **2007**, *26*, 51–78.

269. Fiehn, O. Metabolomics--the link between genotypes and phenotypes. *Plant Mol. Biol.* **2002**, *48*, 155–71.

270. Johnson, C.H.; Ivanisevic, J.; Siuzdak, G. Metabolomics: beyond biomarkers and towards mechanisms. *Nat. Rev. Mol. Cell Biol.* **2016**.

271. Lenz, E.M.; Wilson, I.D. Analytical Strategies in Metabonomics. *J. Proteome Res.* **2007**, *6*, 443–458.

272. Putri, S.P.; Fukusaki, E. Metabolomics in a Nutshell. CRC press: Boca Raton, **2015**.

273. Christensen, E.; Sudasinghe, N.; Dandamudi, K.P.R.; Sebag, R.; Schaub, T.; Laurens, L.M.L. Rapid Analysis of Microalgal Triacylglycerols with Direct-Infusion Mass Spectrometry. *Energy Fuels* **2015**, *29*, 6443–6449.

274. Gonzalez-Dominguez, A.; Duran-Guerrero, E.; Fernandez-Recamales, A.; Lechuga-Sancho, A.M.; Sayago, A.; Schwarz, M.; Segundo, C.; Gonzalez-Dominguez, R. An Overview on the Importance of Combining Complementary Analytical Platforms in Metabolomic Research. *Curr. Top. Med. Chem.* **2018**, *17*, 3289–3295.

275. Lin, L.; Yu, Q.; Yan, X.; Hang, W.; Zheng, J.; Xing, J.; Huang, B. Direct infusion mass spectrometry or liquid chromatography mass spectrometry for human metabonomics? A serum metabonomic study of kidney cancer. *The Analyst* **2010**, *135*, 2970.

276. Southam, A.D.; Weber, R.J.M.; Engel, J.; Jones, M.R.; Viant, M.R. A complete workflow for high-resolution spectral-stitching nanoelectrospray direct-infusion mass-spectrometry-based metabolomics and lipidomics. *Nat. Protoc.* **2017**, *12*, 255–273.

277. Kirwan, J.A.; Weber, R.J.M.; Broadhurst, D.I.; Viant, M.R. Direct infusion mass spectrometry metabolomics dataset: a benchmark for data processing and quality control. *Sci. Data* **2014**, *1*, 140012–140012.

278. González-Domínguez, R.; García-Barrera, T.; Gómez-Ariza, J.L. Using direct infusion mass spectrometry for serum metabolomics in Alzheimer's disease. *Anal. Bioanal. Chem.* **2014**, *406*, 7137–7148.

279. González-Domínguez, R.; Sayago, A.; Fernández-Recamales, Á. Direct infusion mass spectrometry for metabolomic phenotyping of diseases. *Bioanalysis* **2017**, *9*, 131–148.

280. Lísa, M.; Cífková, E.; Khalikova, M.; Ovčačíková, M.; Holčapek, M. Lipidomic analysis of biological samples: Comparison of liquid chromatography, supercritical fluid chromatography and direct infusion mass spectrometry methods. *J. Chromatogr. A* **2017**, *1525*, 96–108.

281. Giavalisco, P.; Hummel, J.; Lisec, J.; Inostroza, A.C.; Catchpole, G.; Willmitzer, L. High-Resolution Direct Infusion-Based Mass Spectrometry in Combination with Whole ^{13}C Metabolome Isotope Labeling Allows Unambiguous Assignment of Chemical Sum Formulas. *Anal. Chem.* **2008**, *80*, 9417–9425.

282. Kind, T.; Meissen, J.K.; Yang, D.; Nocito, F.; Vaniya, A.; Cheng, Y.-S.; VanderGheynst, J.S.; Fiehn, O. Qualitative analysis of algal secretions with multiple mass spectrometric platforms. *J. Chromatogr. A* **2012**, *1244*, 139–147.

283. Holguin, F.O.; Schaub, T. Characterization of microalgal lipid feedstock by direct-infusion FT-ICR mass spectrometry. *Algal Res.* **2013**, *2*, 43–50.

284. Yang, D.; Song, D.; Kind, T.; Ma, Y.; Hoefkens, J.; Fiehn, O. Lipidomic analysis of chlamydomonas reinhardtii under nitrogen and sulfur deprivation. *PLoS ONE* **2015**, *10*, 1–16.

285. Yang, D.; Fan, X.; Kind, T.; Fiehn, O.; Guo, R. Analysis of Polar Lipids in *Chlamydomonas reinhardtii* Using Nanoelectrospray Direct Infusion Method and Gas Chromatography and Mass Spectrometric Detection. *Acta Chim. Sin.* **2013**, *71*, 663.

286. McLean, T.I. “Eco-omics”: A Review of the Application of Genomics, Transcriptomics, and Proteomics for the Study of the Ecology of Harmful Algae. *Microb. Ecol.* **2013**, *65*, 901–915.

287. Lowe, R.; Shirley, N.; Bleackley, M.; Dolan, S.; Shafee, T. Transcriptomics technologies. *PLOS Comput. Biol.* **2017**, *13*, e1005457.

288. Brauer, E.K.; Singh, D.K.; Popescu, S.C. Next-generation plant science: putting big data to work. *Genome Biol.* **2014**, *15*, 301–301.

289. Li, S.; Todor, A.; Luo, R. Blood transcriptomics and metabolomics for personalized medicine. *Comput. Struct. Biotechnol. J.* **2016**, *14*, 1–7.

290. Wang, Z.; Gerstein, M.; Snyder, M. RNA-Seq: a revolutionary tool for transcriptomics. *Nat. Rev. Genet.* **2009**, *10*, 57–63.

291. Li, W.V.; Li, J.J. Modeling and analysis of RNA-seq data: a review from a statistical perspective. *Quant. Biol.* **2018**, *6*, 195–209.

292. Costa-Silva, J.; Domingues, D.; Lopes, F.M. RNA-Seq differential expression analysis: An extended review and a software tool. *PLOS ONE* **2017**, *12*, e0190152.

293. Lee, H.C.; Lai, K.; Lorenc, M.T.; Imelfort, M.; Duran, C.; Edwards, D. Bioinformatics tools and databases for analysis of next-generation sequence data. *Brief. Funct. Genomics* **2012**, *11*, 12–24.

294. Miller, R.; Wu, G.; Deshpande, R.R.; Vieler, A.; Gartner, K.; Li, X.; Moellering, E.R.; Zauner, S.; Cornish, A.J.; Liu, B.; et al. Changes in Transcript Abundance in Chlamydomonas reinhardtii following Nitrogen Deprivation Predict Diversion of Metabolism. *Plant Physiol.* **2010**, *154*, 1737–1752.

295. Delseny, M.; Han, B.; Hsing, Y.I. High throughput DNA sequencing: The new sequencing revolution. *Plant Sci.* **2010**, *179*, 407–422.

296. Quail, M.; Smith, M.E.; Coupland, P.; Otto, T.D.; Harris, S.R.; Connor, T.R.; Bertoni, A.; Swerdlow, H.P.; Gu, Y. A tale of three next generation sequencing platforms: comparison of

Ion torrent, pacific biosciences and illumina MiSeq sequencers. *BMC Genomics* **2012**, *13*, 341.

297. Ari, Ş.; Arikan, M. Next-Generation Sequencing: Advantages, Disadvantages, and Future. In *Plant Omics: Trends and Applications*; Hakeem, K.R., Tombuloğlu, H., Tombuloğlu, G., Eds.; Springer International Publishing: Cham, 2016; pp. 109–135 ISBN 978-3-319-31701-4.

298. Erguner, B.; Ustek, D.; Sagiroglu, M.S. Performance comparison of Next Generation sequencing platforms. In Proceedings of the 2015 37th Annual International Conference of the IEEE Engineering in Medicine and Biology Society (EMBC); IEEE: Milan, 2015; pp. 6453–6456.

299. Liu, L.; Li, Y.; Li, S.; Hu, N.; He, Y.; Pong, R.; Lin, D.; Lu, L.; Law, M. Comparison of Next-Generation Sequencing Systems. *J. Biomed. Biotechnol.* **2012**, *2012*, 1–11.

300. Chu, Y.; Corey, D.R. RNA Sequencing: Platform Selection, Experimental Design, and Data Interpretation. *Nucleic Acid Ther.* **2012**, *22*, 271–274.

301. Gallagher, B.J. The economics of producing biodiesel from algae. *Renew. Energy* **2011**, *36*, 158–162.

302. Yu, M.; Yang, S.; Lin, X. De-novo assembly and characterization of Chlorella minutissima UTEX2341 transcriptome by paired-end sequencing and the identification of genes related to the biosynthesis of lipids for biodiesel. *Mar. Genomics* **2016**, *25*, 69–74.

303. Gligorijevic, V.; Przulj, N. Methods for biological data integration: perspectives and challenges. *J. R. Soc.* **2015**, *12*.

304. Cavill, R.; Jennen, D.; Kleinjans, J.; Briedé, J.J. Transcriptomic and metabolomic data integration. *Brief. Bioinform.* **2015**, 891-901.

305. Jin, J.; Zhang, H.; Zhang, J.; Liu, P.; Chen, X.; Li, Z.; Xu, Y.; Lu, P.; Cao, P. Integrated transcriptomics and metabolomics analysis to characterize cold stress responses in Nicotiana tabacum. *BMC Genomics* **2017**, *18*.

306. Hirai, M.Y.; Yano, M.; Goodenowe, D.B.; Kanaya, S.; Kimura, T.; Awazuhara, M.; Arita, M.; Fujiwara, T.; Saito, K. Integration of transcriptomics and metabolomics for understanding of global responses to nutritional stresses in Arabidopsis thaliana. *Proc. Natl. Acad. Sci. U. S. A.* **2004**, *101*, 10205–10210.

307. Meng, J.; Wang, B.; He, G.; Wang, Y.; Tang, X.; Wang, S.; Ma, Y.; Fu, C.; Chai, G.; Zhou, G. Metabolomics Integrated with Transcriptomics Reveals Redirection of the Phenylpropanoids Metabolic Flux in *Ginkgo biloba*. *J. Agric. Food Chem.* **2019**, *67*, 3284–3291.

308. Hoefgen, R.; Nikiforova, V.J. Metabolomics integrated with transcriptomics: assessing systems response to sulfur-deficiency stress. *Physiol. Plant.* **2007**, *132*, 190–198.

309. Shin, T.H.; Lee, D.Y.; Lee, H.-S.; Park, H.J.; Jin, M.S.; Paik, M.-J.; Manavalan, B.; Mo, J.-S.; Lee, G. Integration of metabolomics and transcriptomics in nanotoxicity studies. *BMB Rep.* **2018**, *51*, 14–20.

310. Cavill, R.; Kamburov, A.; Ellis, J.K.; Athersuch, T.J.; Blagrove, M.S.C.; Herwig, R.; Ebbels, T.M.D.; Keun, H.C. Consensus-Phenotype Integration of Transcriptomic and Metabolomic Data Implies a Role for Metabolism in the Chemosensitivity of Tumour Cells. *PLoS Comput. Biol.* **2011**, *7*, e1001113–e1001113.

311. Teng, M.; Zhu, W.; Wang, D.; Qi, S.; Wang, Y.; Yan, J.; Dong, K.; Zheng, M.; Wang, C. Metabolomics and transcriptomics reveal the toxicity of difenoconazole to the early life stages of zebrafish (Danio rerio). *Aquat. Toxicol.* **2018**, *194*, 112–120.

312. Huang, S.S.Y.; Benskin, J.P.; Veldhoen, N.; Chandramouli, B.; Butler, H.; Helbing, C.C.; Cosgrove, J.R. A multi-omic approach to elucidate low-dose effects of xenobiotics in zebrafish (Danio rerio) larvae. *Aquat. Toxicol.* **2017**, *182*, 102–112.

313. Coen, M.; Ruepp, S.U.; Lindon, J.C.; Nicholson, J.K.; Pognan, F.; Lenz, E.M.; Wilson, I.D. Integrated application of transcriptomics and metabonomics yields new insight into the toxicity due to paracetamol in the mouse. *J. Pharm. Biomed. Anal.* **2004**, *35*, 93–105.

314. Jennen, D.; Ruiz-Aracama, A.; Magkoufopoulou, C.; Peijnenburg, A.; Lommen, A.; van Delft, J.; Kleinjans, J. Integrating transcriptomics and metabonomics to unravel modes-of-action of 2,3,7,8-tetrachlorodibenzo-p-dioxin (TCDD) in HepG2 cells. *BMC Syst. Biol.* **2011**, *5*, 139.

315. Mesnage, R.; Biserni, M.; Balu, S.; Frainay, C.; Poupin, N.; Jourdan, F.; Wozniak, E.; Xenakis, T.; Mein, C.A.; Antoniou, M.N. Integrated transcriptomics and metabolomics reveal signatures of lipid metabolism dysregulation in HepaRG liver cells exposed to PCB 126. *Arch. Toxicol.* **2018**, *92*, 2533–2547.

316. Bersanelli, M.; Mosca, E.; Remondini, D.; Giampieri, E.; Sala, C.; Milanesi, L. Methods for the Integration of Multi-omics Data: Mathematical Aspects. **2016**, *17*, 1–15.

317. Huang, S.; Chaudhary, K.; Garmire, L.X. More Is Better: Recent Progress in Multi-Omics Data Integration Methods. *Front. Genet.* **2017**, *8*.

318. Santos, E.M.; Ball, J.S.; Williams, T.D.; Wu, H.; Ortega, F.; van Aerle, R.; Katsiadaki, I.; Falciani, F.; Viant, M.R.; Chipman, J.K.; et al. Identifying health impacts of exposure to copper using transcriptomics and metabolomics in a fish model. *Environ. Sci. Technol.* **2010**, *44*, 820–6.

319. Sueoka, N. Mitotic Replication of Deoxyribonucleic Acid in Chlamydomonas Reinhardi. *Proc. Natl. Acad. Sci. U. S. A.* **1960**, *46*, 83–91.

320. Kropat, J.; Hong-Hermesdorf, A.; Casero, D.; Ent, P.; Castruita, M.; Pellegrini, M.; Merchant, S.S.; Malasarn, D. A revised mineral nutrient supplement increases biomass and growth rate in Chlamydomonas reinhardtii. *Plant J* **2011**, *66*, 770–80.

321. Kiefer, P.; Portais, J.C.; Vorholt, J.A. Quantitative metabolome analysis using liquid chromatography-high-resolution mass spectrometry. *Anal. Biochem.* **2008**, *382*, 94–100.

322. Khona, D.K.; Shirolikar, S.M.; Gawde, K.K.; Hom, E.; Deodhar, M.A.; D'Souza, J.S. Characterization of salt stress-induced palmelloids in the green alga, Chlamydomonas reinhardtii. *Algal Res.* **2016**, *16*, 434–448.

323. Iwasa, K.; Murakami, S. Palmelloid formation of \emph{Chlamydomonas} II . Mechanism of palmelloid formation by organic acids. *Physiol. Plant.* **1969**, *22*, 43–50.

324. Messerli, M.A.; Amaral-Zettler, L.A.; Zettler, E.; Jung, S.-K.; Smith, P.J.S.; Sogin, M.L. Life at acidic pH imposes an increased energetic cost for a eukaryotic acidophile. *J. Exp. Biol.* **2005**, *208*, 2569–79.

325. Küsel, A.C.; Sianoudis, J.; Leibfritz, D.; Grimme, L.H.; Mayer, A. The dependence of the cytoplasmic pH in aerobic and anaerobic cells of the green algae Chlorella fusca and Chlorella vulgaris on the pH of the medium as determined by 31P in vivo NMR spectroscopy. *Arch. Microbiol.* **1990**, *153*, 254–258.

326. Arensberg, P.; Hemmingsen, V.H.; Nyholm, N. A miniscale algal toxicity test. *Chemosphere* **1995**, *30*, 2103–2115.

327. Jutson, M.G.S.; Pipe, R.K.; Thomas, C.R. The Cultivation of Marine Phytoplankton. In; Tsaloglou, M.N., Ed.; Caister Academic Press, U.K., **2016**.

328. Bligh, E.G.; Dyer, W.J. A Rapid Method Of Total Lipid Extration And Purification. *J. Biochem. Physiol.* **1959**, *37*, 911–917.

329. Dunn, W.B.; Broadhurst, D.; Begley, P.; Zelena, E.; Francis-Mcintyre, S.; Anderson, N.; Brown, M.; Knowles, J.D.; Halsall, A.; Haselden, J.N.; et al. Procedures for large-scale metabolic profiling of serum and plasma using gas chromatography and liquid chromatography coupled to mass spectrometry. *Nat. Protoc.* **2011**, *6*, 1060–1083.

330. Dieterle, F.; Ross, A.; Schlotterbeck, G.; Senn, H. Probabilistic Quotient Normalization as Robust Method to Account for Dilution of Complex Biological Mixtures. Application in 1 H NMR Metabonomics. *Anal. Chem.* **2006**, *78*, 4281–4290.

331. R Development Core Team *R: A language and environment for statistical computing*; R Foundation for Statistical Computing: Vienna, 2012;

332. Chong, J.; Soufan, O.; Li, C.; Caraus, I.; Li, S.; Bourque, G.; Wishart, D.S.; Xia, J. MetaboAnalyst 4.0: towards more transparent and integrative metabolomics analysis. *Nucleic Acids Res.* **2018**, *46*, W486–W494.

333. Marioni, J.C.; Mason, C.E.; Mane, S.M.; Stephens, M.; Gilad, Y. RNA-seq: An assessment of technical reproducibility and comparison with gene expression arrays. *Genome Res.* **2008**, *18*, 1509–1517.

334. Bolger, A.M.; Lohse, M.; Usadel, B. Trimmomatic: a flexible trimmer for Illumina sequence data. *Bioinformatics* **2014**, *30*, 2114–2120.

335. Fu, J.; Frazee, A.C.; Leek, J.T.; Collado-Torres, L.; Jaffe, A.E. *ballgown*; Bioconductor, 2017;

336. Dobin, A.; Davis, C.A.; Schlesinger, F.; Drenkow, J.; Zaleski, C.; Jha, S.; Batut, P.; Chaisson, M.; Gingeras, T.R. STAR: ultrafast universal RNA-seq aligner. *Bioinformatics* **2013**, *29*, 15–21.

337. Liao, Y.; Smyth, G.K.; Shi, W. featureCounts: an efficient general purpose program for assigning sequence reads to genomic features. *Bioinformatics* **2014**, *30*, 923–930.

338. Bartley, G.E.; Scolnik, P.A. Plant Carotenoids: Pigments for Photoprotection, Visual Attraction, and Human Health. *PLANT CELL ONLINE* **1995**, *7*, 1027–1038.

339. Sandmann, G.; Bramley, P.M.; Böger, P. The inhibitory mode of action of the pyridazinone herbicide norflurazon on a cell-free carotenogenic enzyme system. *Pestic. Biochem. Physiol.* **1980**, *14*, 185–191.

340. Sandmann, G.; Linden, H.; Böger, P. Enzyme-Kinetic Studies on the Interaction of Norflurazon with Phytoene Desaturase. *Z. Für Naturforschung C* **1989**, *44*, 787–790.

341. Bartley, G.E. Plant Carotenoids: Pigments for Photoprotection, Visual Attraction, and Human Health. *PLANT CELL ONLINE* **1995**, *7*, 1027–1038.

342. Demmig-Adams, B.; Gilmore, A.M.; Adams, W.W. Carotenoids 3: in vivo function of carotenoids in higher plants. *FASEB J.* **1996**, *10*, 403–412.

343. van Wezel, A.P.; Opperhuizen, A. Narcosis due to environmental pollutants in aquatic organisms: residue-based toxicity, mechanisms, and membrane burdens. *Crit. Rev. Toxicol.* **1995**, *25*, 255–79.

344. OECD *GUIDANCE DOCUMENT ON AQUATIC TOXICITY TESTING OF DIFFICULT SUBSTANCES AND MIXTURES; OECD SERIES ON TESTING AND ASSESSMENT Number 23 (ENV/JM/MONO(2000)6)*; Paris, 2000;

345. European Centre for, E.; Toxicology of, C. *ECETOC. Activity-Based Relationships for Aquatic Ecotoxicology Data: Use of the Activity Approach to Strengthen MoA Predictions, Technical Report No. 120*; Brussels, Belgium, 2013;

346. Dix, D.J.; Houck, K.A.; Martin, M.T.; Richard, A.M.; Setzer, R.W.; Kavlock, R.J. The ToxCast program for prioritizing toxicity testing of environmental chemicals. *Toxicol. Sci.* **2007**, *95*, 5–12.

347. Howard, P.H.; Boethling, R.S.; Jarvis, W.F.; Meylan, W.M.; Michalenko, E.M. *Handbook of Environmental Degradation Rates*; CRC Press: Chelsea, MI, 1991;

348. Verschueren, K. *Handbook of Environmental Data on Organic Chemicals*; Van Nostrand Reinholf Company: London, 1977;

349. Tomlin, C.D.S. *The Pesticide Manual, A World Compendium*; 14th ed.; British Crop Protection Council: Alton, Hampshire, **2006**.

350. Sandmann, G. Bleaching Herbicides: Action Mechanism in Carotenoid Biosynthesis, Structural Requirements and Engineering of Resistance. In *Herbicide Classes in Development*; Böger, P., Wakabayashi, K., Hirai, K., (eds.) Springer Berlin Heidelberg: Berlin, Heidelberg, **2002**; ISBN 978-3-642-63972-2.

351. Breitenbach, J.; Zhu, C.; Sandmann, G. Bleaching Herbicide Norflurazon Inhibits Phytoene Desaturase by Competition with the Cofactors. *J. Agric. Food Chem.* **2001**, *49*, 5270–5272.

352. Shostak, S. *Exposed science: genes, the environment, and the politics of population health*; University of California Press: Berkeley, **2013**; ISBN 978-0-520-27517-1.

353. ICCVAM *Validation and Regulatory Acceptance of Toxicological Test Methods. A Report of the ad hoc Interagency Coordinating Committee on the Validation of Alternative Methods*; ICCVAM, **1997**.

354. ECETOC *Workshop Report No. 25: 'Omics and Risk Assessment Science'";* Málaga, 2013;

355. Viant, M. Metabolomics of aquatic organisms: the new "omics" on the block. *Mar. Ecol. Prog. Ser.* **2007**, *332*, 301–306.

356. Keller, D.A.; Juberg, D.R.; Catlin, N.; Farland, W.H.; Hess, F.G.; Wolf, D.C.; Doerrer, N.G. Identification and Characterization of Adverse Effects in 21st Century Toxicology. *Toxicol. Sci.* **2012**, *126*, 291–297.

357. *Toxicogenomics in predictive carcinogenicity*; Waters, M.D., Thomas, R.S., Royal Society of Chemistry (Great Britain), Eds.; Issues in toxicology; Royal Society of Chemistry: Cambridge, UK, **2016**; ISBN 978-1-78262-162-1.

358. Oziolor, E.M.; Bickham, J.W.; Matson, C.W. Evolutionary toxicology in an omics world. *Evol. Appl.* **2017**, *10*, 752–761.

359. OECD *Test No. 201: Alga, Growth Inhibition Test*; OECD Guidelines for the Testing of Chemicals, Section 2: Effects on Biotic Systems; OECD Publishing, 2011;

360. ISO *Water quality - algal growth inhibition test. ISO/DIS 8692.*; Geneva, 1987;

361. Zhu, C.J.; Lee, Y.K. Determination of biomass dry weight of marine microalgae. *J. Appl. Phycol.* **1997**, *9*, 189–194.

362. Kruskopf, M.; Flynn, K.J. Chlorophyll content and fluorescence responses cannot be used to gauge reliably phytoplankton biomass, nutrient status or growth rate (vol 169, pg 525, 2006). *New Phytol* **2006**, *169*, 841–842.

363. Phelan, M.C.; Lawler, G. Cell Counting. *Curr. Protoc. Cytom.* **1997**, *00*, A.3A.1-A.3A.4.

364. OECD *Test No. 202: Daphnia sp., Acute Immobilisation Test.*; **2004**.

365. OECD *Test No. 211: Daphnia magna reproduction test.*; **2012**.

366. OECD *Test No. 206: Avian Reproduction Test*; **1984**.

367. OECD *Test No. 223: Avian Acute Oral Toxicity Test*; **2002**.

368. OECD *Test No. 214: Honeybees, Acute Contact Toxicity Test*; **1998**.

369. OECD *Test No. 237: Honeybee larval toxicity test*; **2013**.

370. OECD *Test No. 220: Enchytraeid Reproduction Test*; **2016**.

371. OECD *Test No.: 222 Earthworms reproduction test*; **2016**.

372. OECD *Test No. 232: Collembolan Reproduction Test in Soil*; **2016**.

373. OECD *Test No. 242: Potamopyrgus antipodarum Reproduction Test*; **2016**.

374. OECD *Test No. 231: Amphibian Metamorphosis Assay*; **2009**.

375. OECD *Test No. 241: Larval Amphibian Growth and Development Assay*; **2015**.

376. OECD *Test No. 234: Fish Sexual Development Test*; **2011**.

377. OECD *Test No. 236: Fish embryo toxicity test*; **2013**.

378. OECD *Test No. 229: Fish Short Term Reproduction Test*; **2012**.

379. OECD *Test No. 230: 21 days Fish assay*; **2009**.

380. OECD *Test No. 240: Medaka Extended One Generation Reproduction Test*; **2015**.

381. Bisova, K.; Zachleder, V. Cell-cycle regulation in green algae dividing by multiple fission. *J. Exp. Bot.* **2014**, *65*, 2585–2602.

382. Grabski, K.; Aksmann, A.; Mucha, P.; Tukaj, Z. Conditioned medium factor produced and released by Desmosdemus subspicatus and its effect on the cell cycle of the producer. *J. Appl. Phycol.* **2010**, *22*, 517–524.

383. Faetsch, S.; Matzke, M.; Stolte, S. *Monitoring the Cell Cycle of the Unicellular Green Algae Raphidocelis subcapitata. Analysis of cell growth and proliferation using CASY. Application Note Omni Life Sciences*; **2017**.

384. Vítová, M.; Bišová, K.; Hlavová, M.; Kawano, S.; Zachleder, V.; Čížková, M. Chlamydomonas reinhardtii: duration of its cell cycle and phases at growth rates affected by temperature. *Planta* **2011**, *234*, 599–608.

385. Bisova, K.; Krylov, D.M.; Umen, J.G. Genome-Wide Annotation and Expression Profiling of Cell Cycle Regulatory Genes in. *Society* **2005**, *137*, 475–491.

386. Zones, J.M.; Blaby, I.K.; Merchant, S.S.; Umen, J.G. High-Resolution Profiling of a Synchronized Diurnal Transcriptome from Chlamydomonas reinhardtii Reveals Continuous Cell and Metabolic Differentiation. *Plant Cell* **2015**, *27*, 2743–69.

387. Banfalvi, G. Overview of Cell Synchronization. In *Cell Cycle Synchronization*; Banfalvi, G., Ed.; Humana Press: Totowa, NJ, **2011**; Vol. 761; ISBN 978-1-61779-181-9.

388. Grigorov, M.G. Analysis of Time Course Omics Datasets. In *Bioinformatic for Omics Data*; Mayer, B., Ed.; Springer: Heidelberg, 2011; Vol. 719.

389. Spies, D.; Ciaudo, C. Dynamics in Transcriptomics: Advancements in RNA-seq Time Course and Downstream Analysis. *Comput. Struct. Biotechnol. J.* **2015**, *13*, 469–477.

390. Strenkert, D.; Schmollinger, S.; Gallaher, S.D.; Salomé, P.A.; Purvine, S.O.; Nicora, C.D.; Mettler-Altmann, T.; Soubeyrand, E.; Weber, A.P.M.; Lipton, M.S.; et al. Multiomics resolution of molecular events during a day in the life of Chlamydomonas. *Proc. Natl. Acad. Sci.* **2019**, *116*, 2374–2383.

391. Willamme, R.; Alsafra, Z.; Arumugam, R.; Eppe, G.; Remacle, F.; Levine, R.D.; Remacle, C. Metabolomic analysis of the green microalga Chlamydomonas reinhardtii cultivated under day/night conditions. *J. Biotechnol.* **2015**, *215*, 20–26.

392. Ehara, T.; Osafune, T.; Hase, E. Behavior of mitochondria in synchronized cells of Chlamydomonas reinhardtii (Chlorophyta). *J. Cell Sci.* **1995**, *108 (Pt 2*, 499–507.

393. Sorokin, C. Time course of oxygen evolution during photosynthesis in synchronized cultures of algae. *Plant Physiol* **1961**, *36*, 232–239.

394. Kluender, C.; Sans-Piché, F.; Riedl, J.; Altenburger, R.; Härtig, C.; Laue, G.; Schmitt-Jansen, M. A metabolomics approach to assessing phytotoxic effects on the green alga Scenedesmus vacuolatus. *Metabolomics* **2009**, *5*, 59–71.

395. Vogs, C.; Bandow, N.; Altenburger, R. Effect propagation in a toxicokinetic/toxicodynamic model explains delayed effects on the growth of unicellular green algae Scenedesmus vacuolatus. *Environ. Toxicol. Chem. SETAC* **2013**, *32*, 1161–72.

396. Esperanza, M.; Seoane, M.; Rioboo, C.; Herrero, C.; Cid, Á. Differential toxicity of the UV-filters BP-3 and BP-4 in Chlamydomonas reinhardtii: A flow cytometric approach. *Sci. Total Environ.* **2019**, *669*, 412–420.

397. Esperanza, M.; Seoane, M.; Rioboo, C.; Herrero, C.; Cid, Á. Chlamydomonas reinhardtii cells adjust the metabolism to maintain viability in response to atrazine stress. *Aquat. Toxicol.* **2015**, *165*, 64–72.

398. Kanesaki, Y.; Imamura, S.; Minoda, A.; Tanaka, K. External Light Conditions and Internal Cell Cycle Phases Coordinate Accumulation of Chloroplast and Mitochondrial Transcripts in the Red Alga Cyanidioschyzon merolae. *DNA Res.* **2012**, *19*, 289–303.

399. Singh, S.P.; Singh, P. Effect of temperature and light on the growth of algae species: A review. *Renew. Sustain. Energy Rev.* **2015**, *50*, 431–444.

400. Kleyman, M.; Sefer, E.; Nicola, T.; Espinoza, C.; Chhabra, D.; Hagood, J.S.; Kaminski, N.; Ambalavanan, N.; Bar-Joseph, Z. Selecting the most appropriate time points to profile in high-throughput studies. *eLife* **2017**, *6*.

401. Bruning, O.; Rodenburg, W.; van Oostrom, C.T.; Jonker, M.J.; de Jong, M.; Dekker, R.J.; Rauwerda, H.; Ensink, W.A.; de Vries, A.; Breit, T.M. A Range Finding Protocol to Support Design for Transcriptomics Experimentation: Examples of In-Vitro and In-Vivo Murine UV Exposure. *PLoS ONE* **2014**, *9*, e97089.

402. Ogut, F.; Newman, J.; Bacher, R.; Concannon, P.; Verhoeven, K.; McIntyre, L. *Experimental design for large scale omic studies*; Genetics, **2019**.

403. Rozman, K.K.; Doull, J. Dose and time as variables of toxicity. *Toxicology* **2000**, *144*, 169–178.

404. Simmons, D.B.D.; Benskin, J.P.; Cosgrove, J.R.; Duncker, B.P.; Ekman, D.R.; Martyniuk, C.J.; Sherry, J.P. Omics for aquatic ecotoxicology: Control of extraneous variability to enhance the analysis of environmental effects: Variability of omics data in aquatic ecotoxicology. *Environ. Toxicol. Chem.* **2015**, *34*, 1693–1704.

405. Tarazona, S.; Balzano-Nogueira, L.; Conesa, A. Multiomics Data Integration in Time Series Experiments. In *Comprehensive Analytical Chemistry*; Elsevier, **2018**; Vol. 82; ISBN 978-0-444-64044-4.

406. Spies, D.; Renz, P.; Beyer, T.; Ciaudo, C. Comparative analysis of differential gene expression tools for RNA sequencing time course data. *Brief. Bioinform.* **2017**, *20*.

407. Jüppner, J.; Mubeen, U.; Leisse, A.; Caldana, C.; Brust, H.; Steup, M.; Herrmann, M.; Steinhauser, D.; Giavalisco, P. Dynamics of lipids and metabolites during the cell cycle of Chlamydomonas reinhardtii. *Plant J.* **2017**, 1–13.

408. Shene, C.; Asenjo, J.A.; Chisti, Y. Metabolic modelling and simulation of the light and dark metabolism of Chlamydomonas reinhardtii. *Plant J.* **2018**.

409. Johnson, X.; Alric, J. Central Carbon Metabolism and Electron Transport in Chlamydomonas reinhardtii: Metabolic Constraints for Carbon Partitioning between Oil and Starch. *Eukaryot. Cell* **2013**, *12*, 776–793.

410. Peltier, G.; Thibault, P. O2-Uptake in the Light in Chlamydomonas: Evidence for Persistent Mitochondrial Respiration. *Plant Physiol.* **1985**, *79*, 225–230.

411. Bercu, J.P.; Jolly, R.A.; Flagella, K.M.; Baker, T.K.; Romero, P.; Stevens, J.L. Toxicogenomics and cancer risk assessment: A framework for key event analysis and dose-response assessment for nongenotoxic carcinogens. *Regul. Toxicol. Pharmacol.* **2010**, *58*, 369–381.

412. Villeneuve, D.L.; Angrish, M.M.; Fortin, M.C.; Katsiadaki, I.; Leonard, M.; Margiotta-Casaluci, L.; Munn, S.; O'Brien, J.M.; Pollesch, N.L.; Smith, L.C.; et al. Adverse outcome pathway

networks II: Network analytics: Adverse outcome pathway network analytics. *Environ. Toxicol. Chem.* **2018**, *37*, 1734–1748.

413. Wittwehr, C.; Aladjov, H.; Ankley, G.; Byrne, H.J.; de Knecht, J.; Heinzle, E.; Klambauer, G.; Landesmann, B.; Luijten, M.; MacKay, C.; et al. How Adverse Outcome Pathways Can Aid the Development and Use of Computational Prediction Models for Regulatory Toxicology. *Toxicol. Sci.* **2017**, *155*, 326–336.

414. Smetanová, S.; Riedl, J.; Zitzkat, D.; Altenburger, R.; Busch, W. High-throughput concentration-response analysis for omics datasets: Concentration-response analysis for omics datasets. *Environ. Toxicol. Chem.* **2015**, *34*, 2167–2180.

415. Saccenti, E.; Timmerman, M.E. Approaches to Sample Size Determination for Multivariate Data: Applications to PCA and PLS-DA of Omics Data. *J. Proteome Res.* **2016**, *15*, 2379–2393.

416. Yu, D.; Huber, W.; Vitek, O. Shrinkage estimation of dispersion in Negative Binomial models for RNA-seq experiments with small sample size. *Bioinformatics* **2013**, *29*, 1275–1282.

417. Schade, S.; Butler, E.; Gutsell, S.; Hodges, G.; Colbourne, J.K.; Viant, M.R. Improved Algal Toxicity Test System for Robust Omics-Driven Mode-of-Action Discovery in Chlamydomonas reinhardtii. *Metabolites* **2019**, *9*, 94.

418. ECHA *Usage of (eco)toxicological data for bridg- ing data gaps between and grouping of nanoforms of the same substance. Elements to consider. ED- 02-16-228-EN-N*; Helsinki, 2016;

419. Haas, R.; Zelezniak, A.; Iacovacci, J.; Kamrad, S.; Townsend, S.; Ralser, M. Designing and interpreting ‘multi-omic’ experiments that may change our understanding of biology. *Curr. Opin. Syst. Biol.* **2017**, *6*, 37–45.

420. Aliferis, K.A.; Jabaji, S. Metabolomics – A robust bioanalytical approach for the discovery of the modes-of-action of pesticides: A review. *Pestic. Biochem. Physiol.* **2011**, *100*, 105–117.

421. Perkins, E.J.; Chipman, J.K.; Edwards, S.; Habib, T.; Falciani, F.; Taylor, R.; Van Aggelen, G.; Vulpe, C.; Antczak, P.; Loguinov, A. Reverse engineering adverse outcome pathways. *Environ. Toxicol. Chem.* **2011**, *30*, 22–38.

422. OECD *Guidance Document On Developing And Assessing Adverse Outcome Pathways*; Paris, 2017;

423. Norris, J.L.; Farrow, M.A.; Gutierrez, D.B.; Palmer, L.D.; Muszynski, N.; Sherrod, S.D.; Pino, J.C.; Allen, J.L.; Spraggins, J.M.; Lubbock, A.L.R.; et al. Integrated, High-Throughput, Multiomics Platform Enables Data-Driven Construction of Cellular Responses and Reveals Global Drug Mechanisms of Action. *J. Proteome Res.* **2017**, *16*, 1364–1375.

424. Nestler, H.; Groh, K.J.; Schönenberger, R.; Eggen, R.I.L.; Suter, M.J.-F. Linking proteome responses with physiological and biochemical effects in herbicide-exposed Chlamydomonas reinhardtii. *J. Proteomics* **2012**, *75*, 5370–5385.

425. Jamers, A.; Van der Ven, K.; Moens, L.; Robbens, J.; Potters, G.; Guisez, Y.; Blust, R.; De Coen, W. Effect of copper exposure on gene expression profiles in Chlamydomonas reinhardtii based on microarray analysis. *Aquat. Toxicol.* **2006**, *80*, 249–260.

426. Pillai, S.; Behra, R.; Nestler, H.; Suter, M.J.-F.; Sigg, L.; Schirmer, K. Linking toxicity and adaptive responses across the transcriptome, proteome, and phenotype of Chlamydomonas reinhardtii exposed to silver. *Proc. Natl. Acad. Sci. U. S. A.* **2014**, *111*, 3490–5.

427. Jamers; Blust; De, C.; Griffin; Jones Copper toxicity in the microalga Chlamydomonas reinhardtii: an integrated approach. *BioMetals* **2013**, *26*, 731–740.

428. De Vos, R.C.H.; Moco, S.; Lommen, A.; Keurentjes, J.J.B.; Bino, R.J.; Hall, R.D. Untargeted large-scale plant metabolomics using liquid chromatography coupled to mass spectrometry. *Nat. Protoc.* **2007**, *2*, 778–791.

429. Galassi, S.; Vighi, M. Testing toxicity of volatile substances with algae. *Chemosphere* **1981**, *10*, 1123–1126.

430. Brack, W.; Rottler, H. Toxicity testing of highly volatile chemicals with green algae. *Environ. Sci. Pollut. Res.* **1994**, *1*, 223–228.

431. Hailing-Sørensen, B.; Nyhohn, N.; Baun, A. Algal toxicity tests with volatile and hazardous compounds in air-tight test flasks with CO2 enriched headspace. *Chemosphere* **1996**, *32*, 1513–1526.

432. Lin, J.H.; Kao, W.C.; Tsai, K.P.; Chen, C.Y. A novel algal toxicity testing technique for assessing the toxicity of both metallic and organic toxicants. *Water Res.* **2005**, *39*, 1869–1877.

433. Yeh, H.J.; Chen, C.Y. Toxicity assessment of pesticides to Pseudokirchneriella subcapitata under air-tight test environment. *J. Hazard. Mater.* **2006**, *131*, 6–12.

434. Hsieh, S.-H.; Tsai, K.-P.; Chen, C.-Y. The combined toxic effects of nonpolar narcotic chemicals to Pseudokirchneriella subcapitata. *Water Res.* **2006**, *40*, 1957–1964.

435. Chen, C.Y.; Yan, Y.K.; Yang, C.F. Toxicity assessment of polycyclic aromatic hydrocarbons using an air-tight algal toxicity test. *Water Sci. Technol.* **2006**, *54*, 309.

436. Tsai, K.P.; Chen, C.Y. An algal toxicity database of organic toxicants derived by a closed-system technique. *Environ. Toxicol. Chem.* **2007**, *26*, 1931–1939.

437. Mayer, P.; Nyholm, N.; Verbruggen, E.M.J.; Hermens, J.L.M.; Tolls, J. ALGAL GROWTH INHIBITION TEST IN FILLED, CLOSED BOTTLES FOR VOLATILE AND SORPTIVE MATERIALS. *Environ. Toxicol. Chem.* **2000**, *19*, 2551.

438. Herman, D.C.; Inniss, W.E.; Mayfield, C.I. Impact of volatile aromatic hydrocarbons, alone and in combination, on growth of the freshwater alga Selenastrum capricornutum. *Aquat. Toxicol.* **1990**, *18*, 87–100.

439. Fairchild, J.F.; Ruessler, D.S.; Carlson, A.R. Comparative Sensitivity of Five Species of Macrophytes and Six Species of Algae To Atrazine , Metribuzin , Alachlor , and Metolachlor. *Environ. Toxicol. Chem.* **1998**, *17*, 1830–1834.

440. Shurong, D.; Fengfen, Z.; Min, Z. Toxicity of fenvalerate to six species of fish and two species of fishfood organisms. In *Fish Physiology, Fish Toxicology, and Fisheries Management, Proceedings of an International Symposium*; Ryans, R.C., Ed.; United States Environmental Protection Agency: Guangzhou, PRC, **1988**.

441. Bischoff, H.W.; Bold, H.C. *Phycological Studies IV. Some Soil Algae from Enchanted Rock and Related Algal Species, **1963***; University of Texas Publications: University of Texas, 1963.

442. Zeb, A.; Ullah, F. Reversed Phase HPLC-DAD Profiling of Carotenoids, Chlorophylls and Phenolic Compounds in Adiantum capillus-veneris Leaves. *Front. Chem.* **2017**, *5*, 29.

443. Rowan, B.A.; Oldenburg, D.J.; Bendich, A.J. A high-throughput method for detection of DNA in chloroplasts using flow cytometry. *Plant Methods* **2007**, *3*, 5.

444. Ritz, C.; Baty, F.; Streibig, J.C.; Gerhard, D. Dose-Response Analysis Using R. *PLOS ONE* **2015**, *10*, e0146021.

445. Chong, J.; Soufan, O.; Li, C.; Caraus, I.; Li, S.; Bourque, G.; Wishart, D.S.; Xia, J. MetaboAnalyst 4.0: towards more transparent and integrative metabolomics analysis. *Nucleic Acids Res.* **2018**, *46*, W486–W494.

446. Subramanian, A.; Tamayo, P.; Mootha, V.K.; Mukherjee, S.; Ebert, B.L.; Gillette, M.A.; Paulovich, A.; Pomeroy, S.L.; Golub, T.R.; Lander, E.S.; et al. Gene set enrichment analysis: a knowledge-based approach for interpreting genome-wide expression profiles. *Proc. Natl. Acad. Sci. U. S. A.* **2005**, *102*, 15545–50.

447. Schmollinger, S.; Muhlhaus, T.; Boyle, N.R.; Blaby, I.K.; Casero, D.; Mettler, T.; Moseley, J.L.; Kropat, J.; Sommer, F.; Strenkert, D.; et al. Nitrogen-Sparing Mechanisms in Chlamydomonas Affect the Transcriptome, the Proteome, and Photosynthetic Metabolism. *Plant Cell* **2014**, *26*, 1410–1435.

448. Dos Reis Falcão, V.; Pedroso Tonon, A.; Cabral Oliveira, M.; Colepicolo, P. RNA Isolation method for polysaccharide rich algae: agar producing Gracilaria tenuistipitata (Rhodophyta). *J. Appl. Phycol.* **2008**, *20*, 9–12.

449. Kightlinger, W.; Chen, K.; Pourmir, A.; Crunkleton, D.W.; Price, G.L.; Johannes, T.W. Production and characterization of algae extract from Chlamydomonas reinhardtii. *Electron. J. Biotechnol.* **2014**, *17*, 14–18.

450. Iwasa, K.; Murakami, S. Palmelloid Formation of Chlamydomonas I. Palmelloid Induction by Organic Acids. *Physiol. Plant.* **1968**, *21*, 1224–1233.

451. Scherholz, M.L.; Curtis, W.R. Achieving pH control in microalgal cultures through fed-batch addition of stoichiometrically-balanced growth media. *BMC Biotechnol.* **2013**, *13*, 39.

452. Altenburger, R.; Krüger, J.; Eisenträger, A. Proposing a pH stabilised nutrient medium for algal growth bioassays. *Chemosphere* **2010**, *78*, 864–870.

453. Li, J.; Li, C.; Lan, C.Q.; Liao, D. Effects of sodium bicarbonate on cell growth, lipid accumulation, and morphology of Chlorella vulgaris. *Microb. Cell Factories* **2018**, *17*, 111.

454. Xing, J.; Dinney, C.P.; Shete, S.; Huang, M.; Hildebrandt, M.A.; Chen, Z.; Gu, J. Comprehensive pathway-based interrogation of genetic variations in the nucleotide excision DNA repair pathway and risk of bladder cancer. *Cancer* **2012**, *118*, 205–15.

455. Brack, W.; Rottler, H. Toxicity testing of highly volatile chemicals with green algae. *Environ. Sci. Pollut. Res.* **1994**, *1*, 223–228.

456. Faetsch, S.; Matzke, M.; Stolte, S. *Monitoring the Cell Cycle of the Unicellular Green Algae Raphidocelis subcapitata. Analysis of cell growth and proliferation using CASY. Application Note Omni Life Sciences*; 2017;

457. Grabski, K.; Aksmann, A.; Mucha, P.; Tukaj, Z. Conditioned medium factor produced and released by Desmosdemus subspicatus and its effect on the cell cycle of the producer. *J. Appl. Phycol.* **2010**, *22*, 517–524.

458. Vítová, M.; Bišová, K.; Umysová, D.; Hlavová, M.; Kawano, S.; Zachleder, V.; Cížková, M. Chlamydomonas reinhardtii: duration of its cell cycle and phases at growth rates affected by light intensity. *Planta* **2011**, *233*, 75–86.

459. Kacew, S. Confounding factors in toxicity testing. *Toxicology* **2001**, *160*, 87–96.

460. OECD *Test Guidelines for the Chemicals;* OECD: Paris, [multiple date].

461. Chisholm, S.W.; Brand, L.E. Persistence of cell division phasing in marine phytoplankton in continuous light after entrainment to light: Dark cycles. *J. Exp. Mar. Biol. Ecol.* **1981**, *51*, 107–118.

462. Singh, S.P.; Singh, P. Effect of temperature and light on the growth of algae species: A review. *Renew. Sustain. Energy Rev.* **2015**, *50*, 431–444.

463. Borgert, C.J.; Wise, K.; Becker, R. a Modernizing problem formulation for risk assessment necessitates articulation of mode of action. *Regul. Toxicol. Pharmacol.* **2015**, *72*, 538–551.

464. Kapoore, R.V.; Coyle, R.; Staton, C.A.; Brown, N.J.; Vaidyanathan, S. Influence of washing and quenching in profiling the metabolome of adherent mammalian cells: a case study with the metastatic breast cancer cell line MDA-MB-231. *The Analyst* **2017**, *142*, 2038–2049.

465. Parsons, H.M.; Ekman, D.R.; Collette, T.W.; Viant, M.R. Spectral relative standard deviation: A practical benchmark in metabolomics. *Analyst* **2009**, *134*, 478–485.

466. Ser, Z.; Liu, X.; Tang, N.N.; Locasale, J.W. Extraction parameters for metabolomics from cultured cells. *Anal. Biochem.* **2015**, *475*, 22–28.

467. Rombouts, C.; De Spiegeleer, M.; Van Meulebroek, L.; De Vos, W.H.; Vanhaecke, L. Validated comprehensive metabolomics and lipidomics analysis of colon tissue and cell lines. *Anal. Chim. Acta* **2019**, *1066*, 79–92.

468. Mitchell, M.C.; Meyer, M.T.; Griffiths, H. Dynamics of carbon-concentrating mechanism induction and protein relocalization during the dark-to-light transition in synchronized Chlamydomonas reinhardtii. *Plant Physiol.* **2014**, *166*, 1073–82.

469. Garz, A.; Sandmann, M.; Rading, M.; Ramm, S.; Menzel, R.; Steup, M. Cell-to-cell diversity in a synchronized chlamydomonas culture as revealed by single-cell analyses. *Biophys. J.* **2012**, *103*, 1078–1086.

470. Hlavová, M.; Vítová, M.; Bišová, K. Synchronization of Green Algae by Light and Dark Regimes for Cell Cycle and Cell Division Studies; **2016**.

471. Kalucka, J.; Missiaen, R.; Georgiadou, M.; Schoors, S.; Lange, C.; De Bock, K.; Dewerchin, M.; Carmeliet, P. Metabolic control of the cell cycle. *Cell Cycle* **2015**, *14*, 3379–3388.

472. Sperber, A.M.; Herman, J.K. Metabolism shapes the cell. *J. Bacteriol.* **2017**, *199*, 1–14.

473. Hailing-Sørensen, B.; Nyhohn, N.; Baun, A. Algal toxicity tests with volatile and hazardous compounds in air-tight test flasks with CO2 enriched headspace. *Chemosphere* **1996**, *32*, 1513–1526.

474. Yeh, H.J.; Chen, C.Y. Toxicity assessment of pesticides to Pseudokirchneriella subcapitata under air-tight test environment. *J. Hazard. Mater.* **2006**, *131*, 6–12.

475. Chen, C.Y.; Yan, Y.K.; Yang, C.F. Toxicity assessment of polycyclic aromatic hydrocarbons using an air-tight algal toxicity test. *Water Sci. Technol.* **2006**, *54*, 309–309.

476. Tsai, K.P.; Chen, C.Y. An algal toxicity database of organic toxicants derived by a closed-system technique. *Environ. Toxicol. Chem.* **2007**, *26*, 1931–1939.

477. Shurong, D.; Fengfen, Z.; Min, Z. Toxicity of fenvalerate to six species of fish and two species of fishfood organisms. In; Ryans, R.C., Ed.; United States Environmental Protection Agency: Guangzhou, PRC, **1988**.

478. Hsieh, S.-H.; Tsai, K.-P.; Chen, C.-Y. The combined toxic effects of nonpolar narcotic chemicals to Pseudokirchneriella subcapitata. *Water Res.* **2006**, *40*, 1957–1964.

479. Bedient, P.B.; Rifai, H.S.; Newell, C.J. *Ground water contamination: transport and remediation*; 2nd ed.; Prentice Hall PTR: Upper Saddle River, NJ, 1999; ISBN 978-0-13-013840-8.

480. USEPA CERCLIS3 Available online: https://iaspub.epa.gov/sor_internet/registry/substreg/substance/details.do?displayPopup=&id=83723.

481. USEPA ECOTOXicology knowledgebase (ECOTOX). **2019**.

482. ECHA *Registration Dossier: Potassium dichromate. EC number: 231-906-6.*; European Chemicals Agency, 2019;

483. USEPA *Ambient Water Quality Criteria for Chlorinated Benzenes. Report EPA 440/5-80-028*; 1980;

484. Martyniuk, C.J. Are we closer to the vision? A proposed framework for incorporating omics into environmental assessments. *Environ. Toxicol. Pharmacol.* **2018**, *59*, 87–93.

485. Kluender, Christina Metabolomics for toxicity analysis using the chlorophyte Scenedesmus vacuolatus. PhD Dissertation, TU Bergakademie Freiberg; Helmholtz-Zentrum für Umweltforschung GmbH - UFZ: Freiberg; Leipzig, 2009.

486. Altenburger, R.; Schmitt-Jansen, M.; Riedl, J. Bioassays with Unicellular Algae: Deviations from Exponential Growth and Its Implications for Toxicity Test Results. *J. Environ. Qual.* **2008**, *37*, 16–16.

487. Puzanskiy, R.; Tarakhovskaya, E.; Shavarda, A.; Shishova, M. Metabolomic and physiological changes of Chlamydomonas reinhardtii (Chlorophyceae, Chlorophyta) during batch culture development. *J. Appl. Phycol.* **2017**, 1–16.

488. Tawfik, D.S. Messy biology and the origins of evolutionary innovations. *Nat. Chem. Biol.* **2010**, *6*, 692–696.

489. Janssen, C.R.; Heijerick, D.G. Algal Toxicity Tests for Environmental Risk Assessments of Metals. **2003**.

490. Hörnström, E. Toxicity test with algae--a discussion on the batch method. *Ecotoxicol. Environ. Saf.* **1990**, *20*, 343–53.

491. Xia, J.; Wishart, D.S. MSEA: a web-based tool to identify biologically meaningful patterns in quantitative metabolomic data. *Nucleic Acids Res.* **2010**, *38*, W71-7.

492. Booth, S.C.; Weljie, A.M.; Turner, R.J. COMPUTATIONAL TOOLS FOR THE SECONDARY ANALYSIS OF METABOLOMICS EXPERIMENTS. *Comput. Struct. Biotechnol. J.* **2013**, *4*, e201301003.

493. Rosato, A.; Tenori, L.; Cascante, M.; De Atauri Carulla, P.R.; Martins dos Santos, V.A.P.; Saccenti, E. From correlation to causation: analysis of metabolomics data using systems biology approaches. *Metabolomics* **2018**, *14*.

494. Chagoyen, M.; Pazos, F. MBRole: enrichment analysis of metabolomic data. *Bioinformatics* **2011**, *27*, 730–731.

495. Hartung, T.; Luechtefeld, T.; Maertens, A.; Kleensang, A. Integrated testing strategies for safety assessments. *ALTEX* **2013**, *30*, 3–18.

496. Alfred, S.E.; Surendra, A.; Le, C.; Lin, K.; Mok, A.; Wallace, I.M.; Proctor, M.; Urbanus, M.L.; Giaever, G.; Nislow, C. A phenotypic screening platform to identify small molecule

modulators of Chlamydomonas reinhardtii growth, motility and photosynthesis. *Genome Biol.* **2012**, *13*, R105.

497. Strang, R.H. A Study of the Absorption, Translocation and Metabolism of Two Pyridazinone Herbicides (San6706, San9789) by Cotton, Corn and Soybean. LSU Historical Dissertations and Theses. 2361. PhD Dissertation, Louisiana State University: Louisiana, US, 1972.

498. Weber, R.J.M.; Viant, M.R. MI-Pack: Increased confidence of metabolite identification in mass spectra by integrating accurate masses and metabolic pathways. *Chemom. Intell. Lab. Syst.* **2010**, *104*, 75–82.

499. Kanehisa, M.; Goto, S. KEGG: kyoto encyclopedia of genes and genomes. *Nucleic Acids Res.* **2000**, *28*, 27–30.

500. Luo, W.; Pant, G.; Bhavnasi, Y.K.; Blanchard, S.G.; Brouwer, C. Pathview Web: user friendly pathway visualization and data integration. *Nucleic Acids Res.* **2017**, *45*, W501–W508.

501. Rusilowicz, M.J.; Dickinson, M.; Charlton, A.J.; O'Keefe, S.; Wilson, J. MetaboClust: Using interactive time-series cluster analysis to relate metabolomic data with perturbed pathways. *PLOS ONE* **2018**, *13*, e0205968.

502. Love, M.I.; Huber, W.; Anders, S. Moderated estimation of fold change and dispersion for RNA-seq data with DESeq2. *Genome Biol.* **2014**, *15*, 550.

503. Zhu, A.; Ibrahim, J.G.; Love, M.I. Heavy-tailed prior distributions for sequence count data: removing the noise and preserving large differences. *Bioinformatics* **2019**, *35*, 2084–2092.

504. Lopez, D.; Casero, D.; Cokus, S.J.; Merchant, S.S.; Pellegrini, M. Algal Functional Annotation Tool: a web-based analysis suite to functionally interpret large gene lists using integrated annotation and expression data. *BMC Bioinformatics* **2011**, *12*, 282–282.

505. Huang, D.; Sherman, B.T.; Tan, Q.; Collins, J.R.; Alvord, W.G.; Roayaei, J.; Stephens, R.; Baseler, M.W.; Lane, H.C.; Lempicki, R.A. The DAVID Gene Functional Classification Tool: a novel biological module-centric algorithm to functionally analyze large gene lists. *Genome Biol.* **2007**, *8*, R183.

506. Luo, W.; Friedman, M.S.; Shedden, K.; Hankenson, K.D.; Woolf, P.J. GAGE: generally applicable gene set enrichment for pathway analysis. *BMC Bioinformatics* **2009**, *10*, 161.

507. Luo, W.; Brouwer, C. Pathview: an R/Bioconductor package for pathway-based data integration and visualization. *Bioinformatics* **2013**, *29*, 1830–1831.

508. Ge, S.X.; Son, E.W.; Yao, R. iDEP: an integrated web application for differential expression and pathway analysis of RNA-Seq data. *BMC Bioinformatics* **2018**, *19*, 534.

509. Ghosh, S.; Datta, A.; Tan, K.; Choi, H. SLIDE – a web-based tool for interactive visualization of large-scale – omics data. *Bioinformatics* **2019**, *35*, 346–348.

510. Conesa, A; Nueda, M.J. *maSigPro: Significant Gene Expression Profile Differences in Time Course Gene Expression Data. R package version 1.54.0.*; Bioconductor, 2018;

511. Nueda, M.J.; Tarazona, S.; Conesa, A. Next maSigPro: updating maSigPro bioconductor package for RNA-seq time series. *Bioinformatics* **2014**, *30*, 2598–2602.

512. Ge, S.; Jung, D. ShinyGO: a graphical enrichment tool for animals and plants 2018.

513. Tulin, F.; Cross, F.R. Patching Holes in the *Chlamydomonas* Genome. *G3amp58 GenesGenomesGenetics* **2016**, *6*, 1899–1910.

514. Labadorf, A.; Link, A.; Rogers, M.F.; Thomas, J.; Reddy, A.S.; Ben-Hur, A. Genome-wide analysis of alternative splicing in Chlamydomonas reinhardtii. *BMC Genomics* **2010**, *11*, 114.

515. Bläsing, O.E. Sugars and Circadian Regulation Make Major Contributions to the Global Regulation of Diurnal Gene Expression in Arabidopsis. *PLANT CELL ONLINE* **2005**, *17*, 3257–3281.

516. Alexander-Dann, B.; Pruteanu, L.L.; Oerton, E.; Sharma, N.; Berindan-Neagoe, I.; Módos, D.; Bender, A. Developments in toxicogenomics: understanding and predicting compound-induced toxicity from gene expression data. *Mol. Omics* **2018**, *14*, 218–236.

517. Kim, S.-Y.; Volsky, D.J. PAGE: Parametric Analysis of Gene Set Enrichment. *BMC Bioinformatics* **2005**, *6*, 144.

518. Jung, S. Effect of chlorophyll reduction in Arabidopsis thaliana by methyl jasmonate or norflurazon on antioxidant systems. *Plant Physiol. Biochem.* **2004**, *42*, 225–231.

519. Park, J.-H.; Jung, S. Perturbations of carotenoid and tetrapyrrole biosynthetic pathways result in differential alterations in chloroplast function and plastid signaling. *Biochem. Biophys. Res. Commun.* **2017**, *482*, 672–677.

520. Kearns, K.D.; Hunter, M.D. Toxin-Producing Anabaena flos-aquae Induces Settling of Chlamydomonas reinhardtii, a Competing Motile Alga. *Microb. Ecol.* **2001**, *42*, 80–86.

521. Wong, D.; Olivesra, L. Effects of Selenite and Selenate on the Growth and Motility of Seven Species of Marine Microalgae. *Can. J. Fish. Aquat. Sci.* **1991**, *48*, 1193–1200.

522. Danilov, R.A.; Ekelund, N.G. Effects of Cu2+, Ni2+, Pb2+, Zn2+ and pentachlorophenol on photosynthesis and motility in Chlamydomonas reinhardtii in short- term exposure experiments. *BMC Ecol.* **2001**, *1*, 1.

523. Liu, G.; Chai, X.; Shao, Y.; Hu, L.; Xie, Q.; Wu, H. Toxicity of copper, lead, and cadmium on the motility of two marine microalgae Isochrysis galbana and Tetraselmis chui. *J. Environ. Sci.* **2011**, *23*, 330–335.

524. Beauvais-Flück, R.; Slaveykova, V.I.; Cosio, C. Transcriptomic and Physiological Responses of the Green Microalga *Chlamydomonas reinhardtii* during Short-Term Exposure to Subnanomolar Methylmercury Concentrations. *Environ. Sci. Technol.* **2016**, *50*, 7126–7134.

525. Beauvais-Flück, R.; Slaveykova, V.I.; Cosio, C. Comparative study of Cu uptake and early transcriptome responses in the green microalga Chlamydomonas reinhardtii and the macrophyte Elodea nuttallii. *Environ. Pollut.* **2019**, *250*, 331–337.

526. Periz, G.; Dharia, D.; Miller, S.H.; Keller, L.R. Flagellar Elongation and Gene Expression in *Chlamydomonas reinhardtii*. *Eukaryot. Cell* **2007**, *6*, 1411–1420.

527. Liu, Y.; Visetsouk, M.; Mynlieff, M.; Qin, H.; Lechtreck, K.F.; Yang, P. H+- and Na+- elicited rapid changes of the microtubule cytoskeleton in the biflagellated green alga Chlamydomonas. *eLife* **2017**, *6*, e26002.

528. Marshall, W.F.; Rosenbaum, J.L. Intraflagellar transport balances continuous turnover of outer doublet microtubules: implications for flagellar length control. *J. Cell Biol.* **2001**, *155*, 405–414.

529. Song, L.; Dentler, W.L. Flagellar Protein Dynamics in *Chlamydomonas*. *J. Biol. Chem.* **2001**, *276*, 29754–29763.

530. Kozminski, K.G.; Johnson, K.A.; Forscher, P.; Rosenbaum, J.L. A motility in the eukaryotic flagellum unrelated to flagellar beating. *Proc. Natl. Acad. Sci.* **1993**, *90*, 5519–5523.

531. Dayer, R.; Fischer, B.B.; Eggen, R.I.L.; Lemaire, S.D. The Peroxiredoxin and Glutathione Peroxidase Families in *Chlamydomonas reinhardtii*. *Genetics* **2008**, *179*, 41–57.

532. Massad, W.; Criado, S.; Bertolotti, S.; Pajares, A.; Gianotti, J.; Escalada, J.P.; Amat-Guerri, F.; García, N.A. Photodegradation of the herbicide Norflurazon sensitised by Riboflavin. A kinetic and mechanistic study. *Chemosphere* **2004**, *57*, 455–461.

533. *Flavins: Photochemistry and Photobiology*; Silva, E., Edwards, A.M., Eds.; Comprehensive Series in Photochemical & Photobiological Sciences; Royal Society of Chemistry: London, 2006; Vol. 6; ISBN 978-0-85404-331-6.

534. Rawsthorne, S. Carbon flux and fatty acid synthesis in plants. *Prog. Lipid Res.* **2002**, *41*, 182–196.

535. Suárez, G.; Santschi, C.; Slaveykova, V.I.; Martin, O.J.F. Sensing the dynamics of oxidative stress using enhanced absorption in protein-loaded random media. *Sci. Rep.* **2013**, *3*, 3447.

536. Abrous, O.; Benhassaine-Kesri, G.; Tremolieres, A.; Mazliak, P. Effect of norflurazon on lipid metabolism in soya seedlings. *Phytochemistry* **1998**, *49*, 979–985.

537. Kong, F.; Liang, Y.; Légeret, B.; Beyly-Adriano, A.; Blangy, S.; Haslam, R.P.; Napier, J.A.; Beisson, F.; Peltier, G.; Li-Beisson, Y. Chlamydomonas carries out fatty acid β-oxidation in ancestral peroxisomes using a bona fide acyl-CoA oxidase. *Plant J.* **2017**, *90*, 358–371.

538. Kong, F.; Burlacot, A.; Liang, Y.; Légeret, B.; Alseekh, S.; Brotman, Y.; Fernie, A.R.; Krieger-Liszkay, A.; Beisson, F.; Peltier, G.; et al. Interorganelle Communication: Peroxisomal MALATE DEHYDROGENASE2 Connects Lipid Catabolism to Photosynthesis through Redox Coupling in Chlamydomonas. *Plant Cell* **2018**, *30*, 1824–1847.

539. Rinaldi, M.A.; Patel, A.B.; Park, J.; Lee, K.; Strader, L.C.; Bartel, B. The Roles of β-Oxidation and Cofactor Homeostasis in Peroxisome Distribution and Function in *Arabidopsis thaliana*. *Genetics* **2016**, *204*, 1089–1115.

540. Shi, K.; Gao, Z.; Shi, T.-Q.; Song, P.; Ren, L.-J.; Huang, H.; Ji, X.-J. Reactive Oxygen Species-Mediated Cellular Stress Response and Lipid Accumulation in Oleaginous Microorganisms: The State of the Art and Future Perspectives. *Front. Microbiol.* **2017**, *8*, 793.

541. Almeida, A.C.; Gomes, T.; Langford, K.; Thomas, K.V.; Tollefsen, K.E. Oxidative stress in the algae Chlamydomonas reinhardtii exposed to biocides. *Aquat. Toxicol.* **2017**, *189*, 50–59.

542. Hess, F.D. Light-dependent herbicides: an overview. *Weed Sci.* **2000**, *48*, 160–170.

543. Pérez-Pérez, M.E.; Couso, I.; Crespo, J.L. Carotenoid deficiency triggers autophagy in the model green alga *Chlamydomonas reinhardtii*. *Autophagy* **2012**, *8*, 376–388.

544. Qin, G.; Gu, H.; Ma, L.; Peng, Y.; Deng, X.W.; Chen, Z.; Qu, L.-J. Disruption of phytoene desaturase gene results in albino and dwarf phenotypes in Arabidopsis by impairing chlorophyll, carotenoid, and gibberellin biosynthesis. *Cell Res.* **2007**, *17*, 471–482.

545. Park, J.-H.; Tran, L.H.; Jung, S. Perturbations in the Photosynthetic Pigment Status Result in Photooxidation-Induced Crosstalk between Carotenoid and Porphyrin Biosynthetic Pathways. *Front. Plant Sci.* **2017**, *8*, 1992.

546. Wilkinson, R.E. Carotenogenic inhibition by norflurazon in wheat. *Pestic. Biochem. Physiol.* **1985**, *23*, 370–377.

547. Murphy, R.C.; Axelsen, P.H. Mass spectrometric analysis of long-chain lipids. *Mass Spectrom. Rev.* **2011**, *30*, 579–599.

548. Divya, P.; Puthusseri, B.; Savanur, M.A.; Lokesh, V.; Neelwarne, B. Effects of methyl jasmonate and carotenogenic inhibitors on gene expression and carotenoid accumulation in coriander (Coriandrum sativum L.) foliage. *Food Res. Int.* **2018**, *111*, 11–19.

549. Webb, H.; Foley, W.J.; Külheim, C. The genetic basis of foliar terpene yield: Implications for breeding and profitability of Australian essential oil crops. *Plant Biotechnol.* **2015**, *31*, 363–376.

550. Jarvis, P. Intracellular Signalling: The Language of the Chloroplast. *Curr. Biol.* **2003**, *13*, R314–R316.

551. Pogson, B.J.; Woo, N.S.; Förster, B.; Small, I.D. Plastid signalling to the nucleus and beyond. *Trends Plant Sci.* **2008**, *13*, 602–609.

552. Nisar, N.; Li, L.; Lu, S.; Khin, N.C.; Pogson, B.J. Carotenoid Metabolism in Plants. *Mol. Plant* **2015**, *8*, 68–82.

553. Tischer, W.; Strotmann, H. Relationship between inhibitor binding by chloroplasts and inhibition of photosynthetic electron transport. *Biochim. Biophys. Acta BBA - Bioenerg.* **1977**, *460*, 113–125.

554. Sandmann, S.; Böger, P. Mode of Action of Herbicidal Bleaching. In *Biochemical responses induced by herbicides: based on a symposium*; Moreland, D.E., St. John, J., Hess, F.D.,

Eds.; ACS symposium series; American Chemical Society: Washington, D.C, 1982 ISBN 978-0-8412-0699-1.

555. Devlin, R.M.; Kisiel, M.J.; Karczmarczyk, S.J. Chlorophyll production and chloroplast development in norflurazon-treated plants. *Weed Res.* **1976**, *16*, 125–129.

556. Strand, Å.; Asami, T.; Alonso, J.; Ecker, J.R.; Chory, J. Chloroplast to nucleus communication triggered by accumulation of Mg-protoporphyrinIX. *Nature* **2003**, *421*, 79–83.

557. Voss, B.; Meinecke, L.; Kurz, T.; Al-Babili, S.; Beck, C.F.; Hess, W.R. Hemin and Magnesium-Protoporphyrin IX Induce Global Changes in Gene Expression in Chlamydomonas reinhardtii. *PLANT Physiol.* **2011**, *155*, 892–905.

558. Kropat, J.; Oster, U.; Rudiger, W.; Beck, C.F. Chlorophyll precursors are signals of chloroplast origin involved in light induction of nuclear heat-shock genes. *Proc. Natl. Acad. Sci.* **1997**, *94*, 14168–14172.

559. Zhou, X.; Mcquinn, R.; Fei, Z.; Wolters, A.-M.A.; Van Eck, J.; Brown, C.; Giovannoni, J.J.; Li, L. Regulatory control of high levels of carotenoid accumulation in potato tubers: Carotenoid accumulation in potato tubers. *Plant Cell Environ.* **2011**, *34*, 1020–1030.

560. Marquardt, J. Effects of carotenoid-depletion on the photosynthetic apparatus of a Galdieria sulphuraria (rhodophyta) strain that retains its photosynthetic apparatus in the dark. *J. Plant Physiol.* **1998**, *152*, 372–380.

561. Takaichi, S. Carotenoids in Algae: Distributions, Biosyntheses and Functions. *Mar. Drugs* **2011**, *9*, 1101–1118.

562. Järvi, S.; Suorsa, M.; Aro, E.-M. Photosystem II repair in plant chloroplasts — Regulation, assisting proteins and shared components with photosystem II biogenesis. *Biochim. Biophys. Acta BBA - Bioenerg.* **2015**, *1847*, 900–909.

563. Hu, X.; Kato, Y.; Sumida, A.; Tanaka, A.; Tanaka, R. The SUFBC $_2$ D complex is required for the biogenesis of all major classes of plastid Fe-S proteins. *Plant J.* **2017**, *90*, 235–248.

564. Malnoe, A.; Wang, F.; Girard-Bascou, J.; Wollman, F.-A.; de Vitry, C. Thylakoid FtsH Protease Contributes to Photosystem II and Cytochrome b6f Remodeling in Chlamydomonas reinhardtii under Stress Conditions. *Plant Cell* **2014**, *26*, 373–390.

565. Wang, F.; Qi, Y.; Malnoë, A.; Choquet, Y.; Wollman, F.-A.; de Vitry, C. The High Light Response and Redox Control of Thylakoid FtsH Protease in Chlamydomonas reinhardtii. *Mol. Plant* **2017**, *10*, 99–114.

566. Heredia-Martínez, L.G.; Andrés-Garrido, A.; Martínez-Force, E.; Pérez-Pérez, M.E.; Crespo, J.L. Chloroplast Damage Induced by the Inhibition of Fatty Acid Synthesis Triggers Autophagy in Chlamydomonas. *Plant Physiol.* **2018**, *178*, 1112–1129.

567. Ruizzo, M.A.; Bertekap, R.; Mishkind, M.L. Consequences of herbicide-induced pigment deficiencies on thylakoid membrane proteins of Chlamydomonas reinhardtii. *Plant Sci.* **1992**, *81*, 13–20.

568. Wrischer, M.; Ljubešić, N.; Salopek, B. The role of carotenoids in the structural and functional stability of thylakoids in plastids of dark-grown spruce seedlings. *J. Plant Physiol.* **1998**, *153*, 46–52.

569. Trebst, A.; Depka, B. Role of carotene in the rapid turnover and assembly of photosystem II in *Chlamydomonas reinhardtii*. *FEBS Lett.* **1997**, *400*, 359–362.

570. Santabarbara, S.; Casazza, A.P.; Ali, K.; Economou, C.K.; Wannathong, T.; Zito, F.; Redding, K.E.; Rappaport, F.; Purton, S. The Requirement for Carotenoids in the Assembly and Function of the Photosynthetic Complexes in Chlamydomonas reinhardtii. *PLANT Physiol.* **2013**, *161*, 535–546.

571. Kroll, D.; Meierhoff, K.; Bechtold, N.; Kinoshita, M.; Westphal, S.; Vothknecht, U.C.; Soll, J.; Westhoff, P. VIPP1, a nuclear gene of Arabidopsis thaliana essential for thylakoid membrane formation. *Proc. Natl. Acad. Sci.* **2001**, *98*, 4238–4242.

572. Nordhues, A.; Schöttler, M.A.; Unger, A.-K.; Geimer, S.; Schönfelder, S.; Schmollinger, S.; Rütgers, M.; Finazzi, G.; Soppa, B.; Sommer, F.; et al. Evidence for a Role of VIPP1 in the Structural Organization of the Photosynthetic Apparatus in *Chlamydomonas*. *Plant Cell* **2012**, *24*, 637–659.

573. Cavalcanti, J.H.F.; Kirma, M.; Barros, J.A.S.; Quinhones, C.G.S.; Pereira-Lima, Í.A.; Obata, T.; Nunes-Nesi, A.; Galili, G.; Fernie, A.R.; Avin-Wittenberg, T.; et al. An L,L-diaminopimelate aminotransferase mutation leads to metabolic shifts and growth inhibition in Arabidopsis. *J. Exp. Bot.* **2018**.

574. Araujo, W.L.; Ishizaki, K.; Nunes-Nesi, A.; Larson, T.R.; Tohge, T.; Krahnert, I.; Witt, S.; Obata, T.; Schauer, N.; Graham, I.A.; et al. Identification of the 2-Hydroxyglutarate and Isovaleryl-CoA Dehydrogenases as Alternative Electron Donors Linking Lysine Catabolism to the Electron Transport Chain of Arabidopsis Mitochondria. *PLANT CELL ONLINE* **2010**, *22*, 1549–1563.

575. Yurina, N.P.; Kloppstech, K. Accumulation of plastid protein precursors under norflurazon-induced carotenoid deficiency and oxidative stress in barley. *Plant Physiol. Biochem.* **2001**, *39*, 807–814.

576. Marchand, J.; Heydarizadeh, P.; Schoefs, B.; Spetea, C. Ion and metabolite transport in the chloroplast of algae: lessons from land plants. *Cell. Mol. Life Sci.* **2018**, *75*, 2153–2176.

577. Huppe, H.C.; Turpin, D.H. Integration of Carbon and Nitrogen Metabolism in Plant and Algal Cells. *Annu. Rev. Plant Physiol. Plant Mol. Biol.* **1994**, *45*, 577–607.

578. Meyer, M.; Griffiths, H. Origins and diversity of eukaryotic CO2-concentrating mechanisms: lessons for the future. *J. Exp. Bot.* **2013**, *64*, 769–786.

579. Pollock, S.V.; Prout, D.L.; Godfrey, A.C.; Lemaire, S.D.; Moroney, J.V. The Chlamydomonas reinhardtii proteins Ccp1 and Ccp2 are required for long-term growth, but are not necessary for efficient photosynthesis, in a low-CO2 environment. *Plant Mol. Biol.* **2004**, *56*, 125–132.

580. Moroney, J.V.; Ynalvez, R.A. Proposed Carbon Dioxide Concentrating Mechanism in *Chlamydomonas reinhardtii*. *Eukaryot. Cell* **2007**, *6*, 1251–1259.

581. Hwangbo, K.; Lim, J.-M.; Jeong, S.-W.; Vikramathithan, J.; Park, Y.-I.; Jeong, W.-J. Elevated Inorganic Carbon Concentrating Mechanism Confers Tolerance to High Light in an Arctic Chlorella sp. ArM0029B. *Front. Plant Sci.* **2018**, *9*, 590.

582. Wang, X.; Perez, E.; Liu, R.; Yan, L.-J.; Mallet, R.T.; Yang, S.-H. Pyruvate protects mitochondria from oxidative stress in human neuroblastoma SK-N-SH cells. *Brain Res.* **2007**, *1132*, 1–9.

583. Wang, L.; Yamano, T.; Takane, S.; Niikawa, Y.; Toyokawa, C.; Ozawa, S.; Tokutsu, R.; Takahashi, Y.; Minagawa, J.; Kanesaki, Y.; et al. Chloroplast-mediated regulation of CO_2-concentrating mechanism by Ca^{2+}-binding protein CAS in the green alga *Chlamydomonas reinhardtii*. *Proc. Natl. Acad. Sci.* **2016**, *113*, 12586–12591.

584. Hochmal, A.K.; Schulze, S.; Trompelt, K.; Hippler, M. Calcium-dependent regulation of photosynthesis. *Biochim. Biophys. Acta BBA - Bioenerg.* **2015**, *1847*, 993–1003.

585. Pyatrikas, D.V.; Rikhvanov, E.G.; Fedoseeva, I.V.; Varakina, N.N.; Rusaleva, T.M.; Tauson, E.L.; Stepanov, A.V.; Borovskii, G.B.; Voinikov, V.K. Mitochondrial retrograde regulation of HSP101 expression in Arabidopsis thaliana under heat stress and amiodarone action. *Russ. J. Plant Physiol.* **2014**, *61*, 80–89.

586. Rikhvanov, E.G.; Fedoseeva, I.V.; Pyatrikas, D.V.; Borovskii, G.B.; Voinikov, V.K. Role of mitochondria in the operation of calcium signaling system in heat-stressed plants. *Russ. J. Plant Physiol.* **2014**, *61*, 141–153.

587. Sun, A.-Z.; Guo, F.-Q. Chloroplast Retrograde Regulation of Heat Stress Responses in Plants. *Front. Plant Sci.* **2016**, *7*.

588. Cheshire, J.L.; Evans, J.H.; Keller, L.R. Ca2+ signaling in the Chlamydomonas flagellar regeneration system: cellular and molecular responses. *J. Cell Sci.* **1994**, *107*, 2491–2498.

589. Kurusu, T.; Koyano, T.; Hanamata, S.; Kubo, T.; Noguchi, Y.; Yagi, C.; Nagata, N.; Yamamoto, T.; Ohnishi, T.; Okazaki, Y.; et al. OsATG7 is required for autophagy-dependent lipid metabolism in rice postmeiotic anther development. *Autophagy* **2014**, *10*, 878–888.

590. Perez-Martin, M.; Perez-Perez, M.E.; Lemaire, S.D.; Crespo, J.L. Oxidative Stress Contributes to Autophagy Induction in Response to Endoplasmic Reticulum Stress in Chlamydomonas reinhardtii. *PLANT Physiol.* **2014**, *166*, 997–1008.

591. Upadhyaya, S.; Agrawal, S.; Gorakshakar, A.; Rao, B.J. *Modulation of TOR kinase activity in Chlamydomonas reinhardtii: Effect of N-starvation and changing carbon pool*; Plant Biology, 2018;

592. Fischer, B.B.; Wiesendanger, M.; Eggen, R.I.L. Growth condition-dependent sensitivity, photodamage and stress response of Chlamydomonas reinhardtii exposed to high light conditions. *Plant Cell Physiol.* **2006**, *47*, 1135–1145.

593. Sarkar, N.; Lemaire, S.; Wu-Scharf, D.; Issakidis-Bourguet, E.; Cerutti, H. Functional Specialization of *Chlamydomonas reinhardtii* Cytosolic Thioredoxin h1 in the Response to Alkylation-Induced DNA Damage. *Eukaryot. Cell* **2005**, *4*, 262–273.

594. Barzilai, A.; Yamamoto, K.-I. DNA damage responses to oxidative stress. *DNA Repair* **2004**, *3*, 1109–1115.

595. Doonan, J.H.; Grief, C. Microtubule cycle inChlamydomonas reinhardtii: An Immunofluorescence study. *Cell Motil. Cytoskeleton* **1987**, *7*, 381–392.

596. Petrov, V.; Hille, J.; Mueller-Roeber, B.; Gechev, T.S. ROS-mediated abiotic stress-induced programmed cell death in plants. *Front. Plant Sci.* **2015**, *6*.

597. John, F.; Roffler, S.; Wicker, T.; Ringli, C. Plant TOR signaling components. *Plant Signal. Behav.* **2011**, *6*, 1700–1705.

598. Dong, P.; Xiong, F.; Que, Y.; Wang, K.; Yu, L.; Li, Z.; Ren, M. Expression profiling and functional analysis reveals that TOR is a key player in regulating photosynthesis and phytohormone signaling pathways in Arabidopsis. *Front. Plant Sci.* **2015**, *6*.

599. Blaby, I.K.; Blaby-Haas, C.E.; Pérez-Pérez, M.E.; Schmollinger, S.; Fitz-Gibbon, S.; Lemaire, S.D.; Merchant, S.S. Genome-wide analysis on *Chlamydomonas reinhardtii* reveals the impact of hydrogen peroxide on protein stress responses and overlap with other stress transcriptomes. *Plant J.* **2015**, *84*, 974–988.

600. Schmitt, F.-J.; Renger, G.; Friedrich, T.; Kreslavski, V.D.; Zharmukhamedov, S.K.; Los, D.A.; Kuznetsov, V.V.; Allakhverdiev, S.I. Reactive oxygen species: Re-evaluation of generation, monitoring and role in stress-signaling in phototrophic organisms. *Biochim. Biophys. Acta BBA - Bioenerg.* **2014**, *1837*, 835–848.

601. Suzuki, N.; Koussevitzky, S.; Mittler, R.; Miller, G. ROS and redox signalling in the response of plants to abiotic stress: ROS and redox signalling in plants. *Plant Cell Environ.* **2012**, *35*, 259–270.

602. Vavilala, S.L.; Gawde, K.K.; Sinha, M.; D'Souza, J.S. Programmed cell death is induced by hydrogen peroxide but not by excessive ionic stress of sodium chloride in the unicellular green alga *Chlamydomonas reinhardtii*. *Eur. J. Phycol.* **2015**, *50*, 422–438.

603. Boekelheide, K.; Campion, S.N. Toxicity testing in the 21st century: using the new toxicity testing paradigm to create a taxonomy of adverse effects. *Toxicol. Sci.* **2010**, *114*, 20–4.

604. Becker, R.A.; Dellarco, V.; Seed, J.; Kronenberg, J.M.; Meek, B.; Foreman, J.; Palermo, C.; Kirman, C.; Linkov, I.; Schoeny, R.; et al. Quantitative weight of evidence to assess confidence in potential modes of action. *Regul. Toxicol. Pharmacol.* **2017**, *86*, 205–220.

605. Collier, Z.A.; Gust, K.A.; Gonzalez-Morales, B.; Gong, P.; Wilbanks, M.S.; Linkov, I.; Perkins, E.J. A weight of evidence assessment approach for adverse outcome pathways. *Regul. Toxicol. Pharmacol.* **2016**, *75*, 46–57.

606. Groh, K.J.; Carvalho, R.N.; Chipman, J.K.; Denslow, N.D.; Halder, M.; Murphy, C.A.; Roelofs, D.; Rolaki, A.; Schirmer, K.; Watanabe, K.H. Development and application of the adverse outcome pathway framework for understanding and predicting chronic toxicity: II. A focus on growth impairment in fish. *Chemosphere* **2015**, *120*, 778–792.

607. Escher, B.; Leusch, F.; Chapman, H. *Bioanalytical tools in water quality assessment*; IWA-Publ: London, 2012; ISBN 978-1-84339-368-9.

608. Tugizimana, F.; Steenkamp, P.A.; Piater, L.A.; Dubery, I.A. Mass spectrometry in untargeted liquid chromatography/mass spectrometry metabolomics: Electrospray ionisation parameters and global coverage of the metabolome. *Rapid Commun. Mass Spectrom.* **2018**, *32*, 121–132.

609. Mayer, P.; Nyholm, N.; Verbruggen, E.M.J.; Hermens, J.L.M.; Tolls, J. ALGAL GROWTH INHIBITION TEST IN FILLED, CLOSED BOTTLES FOR VOLATILE AND SORPTIVE MATERIALS. *Environ. Toxicol. Chem.* **2000**, *19*, 2551–2551.

610. Hurem, S.; Martín, L.M.; Brede, D.A.; Skjerve, E.; Nourizadeh-Lillabadi, R.; Lind, O.C.; Christensen, T.; Berg, V.; Teien, H.-C.; Salbu, B.; et al. Dose-dependent effects of gamma radiation on the early zebrafish development and gene expression. *PLOS ONE* **2017**, *12*, e0179259.

611. Escher, B.I.; Baumer, A.; Bittermann, K.; Henneberger, L.; König, M.; Kühnert, C.; Klüver, N. General baseline toxicity QSAR for nonpolar, polar and ionisable chemicals and their mixtures in the bioluminescence inhibition assay with Aliivibrio fischeri. *Env. Sci Process. Impacts* **2017**, *19*, 414–428.

612. Escher, B.I.; Eggen, R.I.L.; Schreiber, U.; Schreiber, Z.; Vye, E.; Wisner, B.; Schwarzenbach, R.P. Baseline toxicity (narcosis) of organic chemicals determined by in vitro membrane potential measurements in energy-transducing membranes. *Environ. Sci. Technol.* **2002**, *36*, 1971–1979.

613. Mackay, D.; Arnot, J.A.; Petkova, E.P.; Wallace, K.B.; Call, D.J.; Brooke, L.T.; Veith, G.D. The physicochemical basis of QSARs for baseline toxicity. *SAR QSAR Environ. Res.* **2009**, *20*, 393–414.

614. Goodchild, C.G.; Simpson, A.M.; Minghetti, M.; DuRant, S.E. Bioenergetics-adverse outcome pathway: Linking organismal and suborganismal energetic endpoints to adverse outcomes. *Environ. Toxicol. Chem.* **2018**.

615. Murphy, C.A.; Nisbet, R.M.; Antczak, P.; Garcia-Reyero, N.; Gergs, A.; Lika, K.; Mathews, T.; Muller, E.B.; Nacci, D.; Peace, A.; et al. Linking Adverse Outcome Pathways to Dynamic Energy Budgets: A Conceptual Model. In *A Systems Biology Approach to Advancing*

Adverse Outcome Pathways for Risk Assessment; Garcia-Reyero, N., Murphy, C.A., Eds.; Springer International Publishing: Cham, **2018**; ISBN 978-3-319-66082-0.

616. Schottkowski, M.; Peters, M.; Zhan, Y.; Rifai, O.; Zhang, Y.; Zerges, W. Biogenic membranes of the chloroplast in Chlamydomonas reinhardtii. *Proc. Natl. Acad. Sci.* **2012**, *109*, 19286–19291.

617. Warakanont, J.; Tsai, C.-H.; Michel, E.J.S.; Murphy, G.R.; Hsueh, P.Y.; Roston, R.L.; Sears, B.B.; Benning, C. Chloroplast lipid transfer processes in *Chlamydomonas reinhardtii* involving a TRIGALACTOSYLDIACYLGLYCEROL 2 (TGD2) orthologue. *Plant J.* **2015**, *84*, 1005–1020.

618. Huang, S.; Jiang, L.; Zhuang, X. Possible Roles of Membrane Trafficking Components for Lipid Droplet Dynamics in Higher Plants and Green Algae. *Front. Plant Sci.* **2019**, *10*, 207.

619. Xu, F.; Wu, X.; Jiang, L.-H.; Zhao, H.; Pan, J. An organelle K^+ channel is required for osmoregulation in *Chlamydomonas reinhardtii*. *J. Cell Sci.* **2016**, *129*, 3008–3014.

620. Bickerton, P.; Sello, S.; Brownlee, C.; Pittman, J.K.; Wheeler, G.L. Spatial and temporal specificity of Ca^{2+} signalling in *Chlamydomonas reinhardtii* in response to osmotic stress. *New Phytol.* **2016**, *212*, 920–933.

621. Wang, N.; Qian, Z.; Luo, M.; Fan, S.; Zhang, X.; Zhang, L. Identification of Salt Stress Responding Genes Using Transcriptome Analysis in Green Alga Chlamydomonas reinhardtii. *Int. J. Mol. Sci.* **2018**, *19*, 3359.

622. Khan, N.Z.; Lindquist, E.; Aronsson, H. New Putative Chloroplast Vesicle Transport Components and Cargo Proteins Revealed Using a Bioinformatics Approach: An Arabidopsis Model. *PLoS ONE* **2013**, *8*, e59898.

623. Ramundo, S.; Casero, D.; Mühlhaus, T.; Hemme, D.; Sommer, F.; Crèvecoeur, M.; Rahire, M.; Schroda, M.; Rusch, J.; Goodenough, U.; et al. Conditional Depletion of the *Chlamydomonas* Chloroplast ClpP Protease Activates Nuclear Genes Involved in Autophagy and Plastid Protein Quality Control. *Plant Cell* **2014**, *26*, 2201–2222.

624. Kimura, H.; Arasaki, K.; Ohsaki, Y.; Fujimoto, T.; Ohtomo, T.; Yamada, J.; Tagaya, M. Syntaxin 17 promotes lipid droplet formation by regulating the distribution of acyl-CoA synthetase 3. *J. Lipid Res.* **2018**, *59*, 805–819.

625. Mathieu-Rivet, E.; Scholz, M.; Arias, C.; Dardelle, F.; Schulze, S.; Le Mauff, F.; Teo, G.; Hochmal, A.K.; Blanco-Rivero, A.; Loutelier-Bourhis, C.; et al. Exploring the *N* -glycosylation Pathway in *Chlamydomonas reinhardtii* Unravels Novel Complex Structures. *Mol. Cell. Proteomics* **2013**, *12*, 3160–3183.

626. Aebi, M. N-linked protein glycosylation in the ER. *Biochim. Biophys. Acta BBA - Mol. Cell Res.* **2013**, *1833*, 2430–2437.

627. Leshem, Y.; Seri, L.; Levine, A. Induction of phosphatidylinositol 3-kinase-mediated endocytosis by salt stress leads to intracellular production of reactive oxygen species and

salt tolerance: *Coordination of salt stress responses by phosphoinositides*. *Plant J.* **2007**, *51*, 185–197.

628. Molendijk, J.A.; Irvine, R.F. Inositide signalling in Chlamydomonas: characterization of a phosphatidylinositol 3-kinase gene. *Plant Mol. Biol.* **1998**, *37*, 53–66.

629. Ramanan, R.; Tran, Q.-G.; Cho, D.-H.; Jung, J.-E.; Kim, B.-H.; Shin, S.-Y.; Choi, S.-H.; Liu, K.-H.; Kim, D.-S.; Lee, S.-J.; et al. The Ancient Phosphatidylinositol 3-Kinase Signaling System Is a Master Regulator of Energy and Carbon Metabolism in Algae. *Plant Physiol.* **2018**, *177*, 1050–1065.

630. Affenzeller, M.J.; Darehshouri, A.; Andosch, A.; Lutz, C.; Lutz-Meindl, U. Salt stress-induced cell death in the unicellular green alga Micrasterias denticulata. *J. Exp. Bot.* **2009**, *60*, 939–954.

631. Chia, P.Z.C.; Gleeson, P.A. Membrane tethering. *F1000Prime Rep.* **2014**, *6*.

632. Blumwald, E.; Aharon, G.S.; Apse, M.P. Sodium transport in plant cells. *Biochim. Biophys. Acta BBA - Biomembr.* **2000**, *1465*, 140–151.

633. Szabò, I.; Spetea, C. Impact of the ion transportome of chloroplasts on the optimization of photosynthesis. *J. Exp. Bot.* **2017**, *68*, 3115–3128.

634. Pittman, J.K.; Edmond, C.; Sunderland, P.A.; Bray, C.M. A Cation-regulated and Proton Gradient-dependent Cation Transporter from *Chlamydomonas reinhardtii* Has a Role in Calcium and Sodium Homeostasis. *J. Biol. Chem.* **2009**, *284*, 525–533.

635. Ray, S.; Kassan, A.; Busija, A.R.; Rangamani, P.; Patel, H.H. The plasma membrane as a capacitor for energy and metabolism. *Am. J. Physiol.-Cell Physiol.* **2016**, *310*, C181–C192.

636. Hurlock, A.K.; Roston, R.L.; Wang, K.; Benning, C. Lipid Trafficking in Plant Cells. *Traffic* **2014**, *15*, 915–932.

637. Liu, A.; Xiao, Z.; Li, M.-W.; Wong, F.-L.; Yung, W.-S.; Ku, Y.-S.; Wang, Q.; Wang, X.; Xie, M.; Yim, A.K.-Y.; et al. Transcriptomic reprogramming in soybean seedlings under salt stress: Soybean transcriptome under salt stress. *Plant Cell Environ.* **2019**, *42*, 98–114.

638. Calabrese, E.J.; Bachmann, K.A.; Bailer, A.J.; Bolger, P.M.; Borak, J.; Cai, L.; Cedergreen, N.; Cherian, M.G.; Chiueh, C.C.; Clarkson, T.W.; et al. Biological stress response terminology: Integrating the concepts of adaptive response and preconditioning stress within a hormetic dose–response framework. *Toxicol. Appl. Pharmacol.* **2007**, *222*, 122–128.

639. Yu, W.-L.; Ansari, W.; Schoepp, N.G.; Hannon, M.J.; Mayfield, S.P.; Burkart, M.D. Modifications of the metabolic pathways of lipid and triacylglycerol production in microalgae. *Microb. Cell Factories* **2011**, *10*, 91.

640. Ohlrogge, J.; Browse, J. Lipid biosynthesis. *Plant Cell* **1995**, *7*, 957–970.

641. Lefebvre-Legendre, L.; Rappaport, F.; Finazzi, G.; Ceol, M.; Grivet, C.; Hopfgartner, G.; Rochaix, J.-D. Loss of Phylloquinone in *Chlamydomonas* Affects Plastoquinone Pool Size and Photosystem II Synthesis. *J. Biol. Chem.* **2007**, *282*, 13250–13263.

642. Ozawa, S. -i.; Kosugi, M.; Kashino, Y.; Sugimura, T.; Takahashi, Y. 5'-Monohydroxyphylloquinone is the Dominant Naphthoquinone of PSI in the Green Alga Chlamydomonas reinhardtii. *Plant Cell Physiol.* **2012**, *53*, 237–243.

643. Rigby, S.E.J.; Muhiuddin, I.P.; Evans, M.C.W.; Purton, S.; Heathcote, P. Photoaccumulation of the PsaB phyllosemiquinone in Photosystem I of Chlamydomonas reinhardtii. *Biochim. Biophys. Acta BBA - Bioenerg.* **2002**, *1556*, 13–20.

644. Purton, S.; Stevens, D.R.; Muhiuddin, I.P.; Evans, M.C.W.; Carter, S.; Rigby, S.E.J.; Heathcote, P. Site-Directed Mutagenesis of PsaA Residue W693 Affects Phylloquinone Binding and Function in the Photosystem I Reaction Center of *Chlamydomonas reinhardtii* †. *Biochemistry* **2001**, *40*, 2167–2175.

645. Emonds-Alt, B.; Coosemans, N.; Gerards, T.; Remacle, C.; Cardol, P. Isolation and characterization of mutants corresponding to the MENA, MENB, MENC and MENE enzymatic steps of 5′-monohydroxyphylloquinone biosynthesis in *Chlamydomonas reinhardtii*. *Plant J.* **2017**, *89*, 141–154.

646. Borisova-Mubarakshina, M.M.; Kozuleva, M.A.; Rudenko, N.N.; Naydov, I.A.; Klenina, I.B.; Ivanov, B.N. Photosynthetic electron flow to oxygen and diffusion of hydrogen peroxide through the chloroplast envelope via aquaporins. *Biochim. Biophys. Acta BBA - Bioenerg.* **2012**, *1817*, 1314–1321.

647. Ivanov, B.N.; Borisova-Mubarakshina, M.M.; Kozuleva, M.A. Formation mechanisms of superoxide radical and hydrogen peroxide in chloroplasts, and factors determining the signalling by hydrogen peroxide. *Funct. Plant Biol.* **2018**, *45*, 102.

648. Vetoshkina, D.V.; Borisova-Mubarakshina, M.M.; Naydov, I.A.; Kozuleva, M.A.; Ivanov, B.N. Impact of High Light on Reactive Oxygen Species Production within Photosynthetic Biological Membranes. *J. Biol. Life Sci.* **2015**, *6*, 50.

649. Carillo, P.; Grazia, M.; Pontecorvo, G.; Fuggi, A.; Woodrow, P. Salinity Stress and Salt Tolerance. In *Abiotic Stress in Plants - Mechanisms and Adaptations*; Shanker, A., Ed.; **2011**; ISBN 978-953-307-394-1.

650. Malia, P.; Numrich, J.; Nishimura, T.; González Montoro, A.; Stefan, C.J.; Ungermann, C. Control of vacuole membrane homeostasis by a resident PI-3,5-kinase inhibitor. *Proc. Natl. Acad. Sci.* **2018**, *115*, 4684–4689.

651. Bernhard, W.A.; Purkayastha, S.; Milligan, J.R. Which DNA Damage is Likely to Be Relevant in Hormetic Responses? *Dose-Response* **2008**, *6*, 184-195.

652. Overton, C.E. *Studien über die Narkose*; Gustav Fischer Verlag: Jena, **1901**.

653. Pham, L.L.; Sheffield, T.Y.; Pradeep, P.; Brown, J.; Haggard, D.E.; Wambaugh, J.; Judson, R.S.; Paul Friedman, K. Estimating uncertainty in the context of new approach methodologies for potential use in chemical safety evaluation. *Curr. Opin. Toxicol.* **2019**, *15*, 40–47.

654. Sewell, F.; Gellatly, N.; Beaumont, M.; Burden, N.; Currie, R.; de Haan, L.; Hutchinson, T.H.; Jacobs, M.; Mahony, C.; Malcomber, I.; et al. The future trajectory of adverse outcome pathways: a commentary. *Arch. Toxicol.* **2018**, *92*, 1657–1661.

655. Davis, J.M.; Ekman, D.R.; Skelton, D.M.; LaLone, C.A.; Ankley, G.T.; Cavallin, J.E.; Villeneuve, D.L.; Collette, T.W. Metabolomics for informing adverse outcome pathways: Androgen receptor activation and the pharmaceutical spironolactone. *Aquat. Toxicol.* **2017**, *184*, 103–115.

656. Chen, L.; Au, D.W.T.; Hu, C.; Zhang, W.; Zhou, B.; Cai, L.; Giesy, J.P.; Qian, P.-Y. Linking genomic responses of gonads with reproductive impairment in marine medaka (Oryzias melastigma) exposed chronically to the chemopreventive and antifouling agent, 3,3′-diindolylmethane (DIM). *Aquat. Toxicol.* **2017**, *183*, 135–143.

657. Taylor, N.S.; Weber, R.J.M.; Southam, A.D.; Payne, T.G.; Hrydziuszko, O.; Arvanitis, T.N.; Viant, M.R. A new approach to toxicity testing in Daphnia magna: application of high throughput FT-ICR mass spectrometry metabolomics. *Metabolomics* **2009**, *5*, 44–58.

658. Simões, T.; Novais, S.C.; Natal-da-Luz, T.; Devreese, B.; de Boer, T.; Roelofs, D.; Sousa, J.P.; van Straalen, N.M.; Lemos, M.F.L. An integrative omics approach to unravel toxicity mechanisms of environmental chemicals: effects of a formulated herbicide. *Sci. Rep.* **2018**, *8*, 11376–11376.

659. Simões, T.; Novais, S.C.; Natal-da-Luz, T.; Devreese, B.; de Boer, T.; Roelofs, D.; Sousa, J.P.; van Straalen, N.M.; Lemos, M.F.L. Using time-lapse omics correlations to integrate toxicological pathways of a formulated fungicide in a soil invertebrate. *Environ. Pollut.* **2019**, *246*, 845–854.

660. Vernocchi, P.; Vannini, L.; Gottardi, D.; Del Chierico, F.; Serrazanetti, D.I.; Ndagijimana, M.; Guerzoni, M.E. Integration of datasets from different analytical techniques to assess the impact of nutrition on human metabolome. *Frontiers in Cellular and Infection Microbiology* **2012**, *2,* 1-10.

661. Brausemann, A.; Gemmecker, S.; Koschmieder, J.; Ghisla, S.; Beyer, P.; Einsle, O. Structure of Phytoene Desaturase Provides Insights into Herbicide Binding and Reaction Mechanisms Involved in Carotene Desaturation. *Structure* **2017**, *25*, 1222-1232.

662. Mayer, M.P.; Bartlett, D.L.; Beyer, P.; Kleinig, H. The in vitro mode of action of bleaching herbicides on the desaturation of 15-cis-phytoene and cis-ζ-carotene in isolated daffodil chromoplasts. *Pesticide Biochemistry and Physiology* **1989**, *34*, 111–117.